Characterization of Minerals, Metals, and Materials 2021

EDITED BY

Jian Li
Mingming Zhang
Bowen Li
Sergio Neves Monteiro
Shadia Ikhmayies
Yunus Eren Kalay
Jiann-Yang Hwang
Juan P. Escobedo-Diaz
John S. Carpenter
Andrew D. Brown
Rajiv Soman
Alex Moser

TMS

Springer

The Minerals, Metals & Materials Series

Jian Li · Mingming Zhang · Bowen Li ·
Sergio Neves Monteiro · Shadia Ikhmayies ·
Yunus Eren Kalay · Jiann-Yang Hwang ·
Juan P. Escobedo-Diaz · John S. Carpenter ·
Andrew D. Brown · Rajiv Soman · Alex Moser
Editors

Characterization of Minerals, Metals, and Materials 2021

TMS

Springer

Editors
Jian Li
CanmetMATERIALS
Hamilton, ON, Canada

Bowen Li
Michigan Technological University
Houghton, MI, USA

Shadia Ikhmayies
Amman, Jordan

Jiann-Yang Hwang
Michigan Technological University
Houghton, MI, USA

John S. Carpenter
Los Alamos National Laboratory
Los Alamos, NM, USA

Rajiv Soman
Eurofins EAG Materials Science, LLC
Liverpool, NY, USA

Mingming Zhang
ArcelorMittal
Schererville, IN, USA

Sergio Neves Monteiro
Military Institute of Engineering
Rio de Janeiro, Brazil

Yunus Eren Kalay
Middle East Technical University
Ankara, Turkey

Juan P. Escobedo-Diaz
University of New South Wales
Canberra, ACT, Australia

Andrew D. Brown
United States Army Research Laboratory
Abingdon, MD, USA

Alex Moser
United States Naval Research Laboratory
Washington, DC, USA

ISSN 2367-1181 ISSN 2367-1696 (electronic)
The Minerals, Metals & Materials Series
ISBN 978-3-030-65492-4 ISBN 978-3-030-65493-1 (eBook)
https://doi.org/10.1007/978-3-030-65493-1

Cover illustration: From Chapter "Variation of the Silica Module for Dosing Activated Alkali Mortars", M. T. Marvila et al., Figure 1: Microscopy of tobermorite and secondary phases [10]. https://doi.org/10.1007/978-3-030-65493-1_62.

This Springer imprint is published by the registered company Springer Nature Switzerland AG
The registered company address is: Gewerbestrasse 11, 6330 Cham, Switzerland

Preface

Characterization of properties and microstructure are important elements in determining critical processing parameters. Recent advances in characterization instruments have contributed, in a significant way, to an in-depth understanding of materials properties and structure that enabled much precise process control.

The Characterization of Minerals, Metals, and Materials Symposium is sponsored by the Materials Characterization Committee under the Minerals, Metals & Materials Society (TMS). The main focus of this symposium includes, but is not limited to, advanced characterization of extraction and processing of minerals, process-microstructure-property relation of metal alloys, ceramics, polymers, and composites. New characterization methods, techniques, and instrumentations are also emphasized.

The Characterization of Minerals, Metals, and Materials Symposia are among one of the largest in the TMS Annual Meetings that attract researchers in the field of materials, minerals, mechanical engineering, chemistry, and physics. In the TMS 2021 Virtual Annual Meeting & Exhibition, this symposium received 168 abstract submissions, of which 78 submissions were accepted for oral presentation in 8 technical sessions, and 83 were accepted as poster presentations. This proceedings volume includes 62 peer-reviewed manuscripts from original research.

This proceedings publication is a valuable reference for academia and industry that includes advanced characterization methods and instrumentations that cover a wide range of research fields. Readers will enjoy the diversity of topics in this book with novel approaches to process and characterize materials at various length scales.

The editors of this proceedings volume are very grateful to the authors for their contribution and willingness to share their research findings. The editors would also like to thank TMS for providing this valuable opportunity to publish this stand-alone volume. Appreciations also extend to the Materials Characterization Committee and Extraction and Processing Division (EPD) for sponsoring the symposium. The editors also thank the publisher, Springer, for their timely publication of this book. Last but not least, the editors would like to thank the contribution and support from the members of the Materials Characterization Committee.

Jian Li
Lead Organizer

Contents

About the Editors

Jian Li is a senior research scientist and program manager at CanmetMATERIALS in Natural Resources Canada. He obtained his B.Sc. in Mechanical Engineering from Beijing Polytechnique University, M.Sc. in Metallurgical Engineering from the Technical University of Nova Scotia, and Ph.D. in Materials and Metallurgical Engineering from Queen's University, Kingston, Ontario, Canada. He has broad experience in materials processing and characterization including alloys deformation, recrystallization, and micro-texture development. Dr. Li has extensive experience in Focused Ion Beam (FIB) microscope techniques. He is also an expert in various aspects of SEM-EDS and EPMA techniques. Dr. Li has authored three book chapters and published more than 160 papers in scientific journals and conference proceedings.

Mingming Zhang is currently a lead research engineer at ArcelorMittal Global R&D in East Chicago, Indiana. Dr. Zhang has more than 15 years of research experience in the field of mineral processing and metallurgical and materials engineering. He obtained his Ph.D. in Metallurgical Engineering from The University of Alabama and his master's degree in Mineral Processing from the General Research Institute for Non-ferrous Metals in China. Prior to joining ArcelorMittal, he worked with Nucor Steel in Tuscaloosa, Alabama where he was a metallurgical engineer leading the development of models for simulating slab solidification and

secondary cooling process. Dr. Zhang has conducted a number of research projects involving mineral beneficiation, thermodynamics and kinetics of metallurgical reactions, electrochemical processing of light metals, metal recycling, and energy-efficient and environmentally cleaner technologies. He has published more than 50 peer-reviewed research papers and he is the recipient of several U.S. patents. Dr. Zhang also serves as editor and reviewer for a number of prestigious journals including *Metallurgical and Materials Transactions A* and *B*, *JOM*, *Journal of Phase Equilibria and Diffusion*, and *Mineral Processing and Extractive Metallurgy Review*. Dr. Zhang has made more than 30 research presentations at national and international conferences including more than 10 keynote presentations. He was the recipient of the 2015 TMS Young Leaders Professional Development Award. He has served as conference/symposium organizer and technical committee chair in several international professional organizations including The Minerals, Metals & Materials Society (TMS), the Association for Iron & Steel Technology (AIST), and the Society for Mining, Metallurgy & Exploration (SME).

Bowen Li is a research professor in the Department of Materials Science and Engineering and Institute of Materials Processing at Michigan Technological University. His research interests include materials characterization and analysis, metals extraction, ceramic process, antimicrobial additives and surface treatment, porous materials, applied mineralogy, and solid waste reuse. He has published more than 120 technical papers in peer-reviewed journals and conference proceedings, authored/co-authored 3 books, and edited/co-edited 8 books. He also holds 15 patents and has delivered more than 30 invited technical talks.

Dr. Li received a Ph.D. degree in Mineralogy and Petrology from China University of Geosciences Beijing in 1998 and a Ph.D. degree in Materials Science and Engineering from Michigan Technological University in 2008. He has been an active member in The Minerals, Metals & Materials Society (TMS), Society for Mining, Metallurgy & Exploration (SME), and China Ceramic Society. At TMS, he currently serves as the past chair of the Materials Characterization Committee and as a member of the Powder Materials Committee and the

Biomaterials Committee. He has also served as an EPD Award committee member, a *JOM* subject advisor, and a key reader for *Metallurgical and Materials Transactions A*. He has been organizer/co-organizer of a number of international symposia and sessions. He also served as an editorial board member of the *Journal of Minerals and Materials Characterization and Engineering*, *Reviews on Advanced Materials Science*, and *FUTO Journal Series.*

Sergio Neves Monteiro graduated as a metallurgical engineer (1966) at the Federal University of Rio de Janeiro (UFRJ). He received his M.Sc. (1967) and Ph.D. (1972) from the University of Florida, followed by a 1975 course in energy at the Brazilian War College, and a postdoctorate (1976) at the University of Stuttgart. In 1968, he joined the Metallurgy Department of UFRJ as full professor of the postgraduation program in engineering (COPPE). He was elected as head of department (1978), coordinator of COPPE (1982), Under-Rector for Research (1983), and was invited as Under-Secretary of Science for the State of Rio de Janeiro (1985) and Under-Secretary of the College Education for the Federal Government (1989). He retired in 1993 from the UFRJ and joined the State University of North Rio de Janeiro (UENF), where he retired in 2012. He is now a professor at the Military Institute of Engineering (IME), Rio de Janeiro. Dr. Monteiro has published more than 1,500 articles in journals and conference proceedings and has been honored with several awards including the ASM Fellowship and several TMS awards. He is the top researcher (1A) of the Brazilian Council for Scientific and Technological Development (CNPq) and Top Scientist of State of Rio de Janeiro (FAPERJ). He was president of the Superior Council of the State of Rio de Janeiro Research Foundation, FAPERJ (2012), and currently is coordinator of the Engineering Area of this foundation. He has also served as president of the Brazilian Association for Metallurgy, Materials and Mining (ABM, 2017–2019), as a consultant for the main Brazilian R&D agencies, and as a member of the editorial board of five international journals as well as associate editor-in-chief of the *Journal of Materials Research and Technology*. He is the author of 30 patents and a top world researcher in "Natural Fiber Composites" and "Ballistic Armor", Scopus 2029.

Shadia J. Ikhmayies received a B.Sc. and M.Sc. from the physics department at the University of Jordan in 1983 and 1987, respectively, and a Ph.D. in producing CdS/CdTe thin film solar cells from the same university in 2002. Her research is focused on producing and characterizing semiconductor thin films and thin film CdS/CdTe solar cells. She also works in characterizing quartz in Jordan for the extraction of silicon for solar cells and characterizing different materials by computation. She has published 56 research papers in international scientific journals, 80 research papers in conference proceedings, and 3 chapters in books. She is the founder and editor of the eBook series *Advances in Material Research and Technology* published by Springer, and the editor-in-chief/editor of several books.

Dr. Ikhmayies is a member of The Minerals, Metals & Materials Society (TMS) where she was the chair of the TMS Materials Characterization Committee (2016–2017), and the leading organizer of three symposiums; Solar Cell Silicon 2017–2020, Mechanical Characteristics and Application Properties of Metals and Nonmetals for Technology: An EPD Symposium in Honor of Donato Firrao, and Green Materials Engineering: An EPD Symposium in Honor of Sergio Monteiro. Dr. Ikhmayies is also a member of the World Renewable Energy Network/Congress (WREN/WREC) 2010–present. She is a member of the international organizing committee and the international scientific committee in the European Conference on Renewable Energy Systems (ECRES2015–ECRES2020). She is a guest editor and a member of the editorial board of several journals including *JOM* and the *Journal of Electronic Materials.* Dr. Ikhmayies is a reviewer of 24 international journals and several international conference proceedings.

Yunus Eren Kalay is an associate professor in the Metallurgical and Materials Engineering Department and assistant to the president at Middle East Technical University (METU), Ankara, Turkey. Dr. Kalay received his Ph.D. degree with Research Excellence award from Iowa State University in 2009. His Ph.D. topic was related to the metallic glass formation in Al-based metallic alloy systems. Following his Ph.D., he pursued postdoctoral research at Ames National Laboratory. In 2011, Dr. Kalay joined the Department of Metallurgical and Materials Engineering (METE) of METU as an assistant professor and in 2014 he was promoted to associate professor. His research interests span microstructural evolution in metallic alloys, rapid solidification of metallic alloys, nanostructured and amorphous alloys, high-entropy alloys, electronic packaging, and advanced characterization techniques such as scanning and transmission electron microscopy, electron and X-ray spectroscopy, atom probe tomography, and synchrotron X-ray scattering. Dr. Kalay was awarded the METU Prof. Dr. Mustafa Parlar Foundation Research Incentive Award, which is a very prestigious award that recognizes young scientists in Turkey with exceptional achievements and research productivity. He is also an active member of the TMS Materials Characterization Committee and served on organizing committees of three international and one national congress including IMMC, MS&T, and TMS. Dr. Kalay has also been involved in many synergistic activities such as being founding editor of Turkey's first undergraduate research journal, *MATTER* (http://matter.mete.metu.edu.tr/), and organizing the Materials Science Camps for K–12 students.

Jiann-Yang Hwang is a professor in the Department of Materials Science and Engineering at Michigan Technological University. He is also the Chief Energy and Environment Advisor at the Wuhan Iron and Steel Group Company, a Fortune Global 500 company. He has been the editor-in-chief of the *Journal of Minerals and Materials Characterization and Engineering* since 2002. He has founded several enterprises in areas including water desalination and treatment equipment, microwave steel production, chemicals, fly ash processing, antimicrobial materials, and plating wastes treatment. Several universities have honored him as a guest professor, including the Central South University, University of Science and Technology Beijing, Chongqing University, Kunming University of Science and Technology, and Hebei United University. Dr. Hwang received his B.S. from National Cheng Kung University in 1974, M.S. in 1980 and Ph.D. in 1982, both from Purdue University. He joined Michigan Technological University in 1984 and served as its Director of the Institute of Materials Processing from 1992 to 2011 and the Chair of Mining Engineering Department in 1995. He has been a TMS member since 1985. His research interests include the characterization and processing of materials and their applications. He has been actively involved in the areas of separation technologies, pyrometallurgy, microwaves, hydrogen storage, ceramics, recycling, water treatment, environmental protection, biomaterials, and energy and fuels. He has more than 28 patents and has published more than 200 papers. He has chaired the Materials Characterization Committee and the Pyrometallurgy Committee in TMS and has organized several symposia. He is the recipient of the TMS Technology Award and of Michigan Tech's Bhakta Rath Research Award.

Juan P. Escobedo-Diaz is a senior lecturer in the School of Engineering and Information Technology (SEIT) at UNSW Canberra. He obtained his doctoral degree in Mechanical Engineering at Washington State University. Prior to taking up this academic appointment, he held research positions at the Institute for Shock Physics at Los Alamos National Laboratory. His main research interests center on the dynamic behavior of materials under extreme conditions, in particular high pressure and high strain rate. His focus has been on investigating the effects of microstructural features on the dynamic fracture behavior of metals and metallic alloys. He has published primarily in the fields of shock physics and materials science. He has been a member of The Minerals, Metals & Materials Society (TMS) since 2011. During this time, he has co-organized more than five symposia at the Annual Meetings including the symposium on Characterization of Minerals, Metals, and Materials since 2014. He was awarded a 2014 SMD Young Leaders Professional Development Award.

John S. Carpenter is a scientist within the manufacturing and metallurgy division at Los Alamos National Laboratory. Dr. Carpenter received his Ph.D. in Materials Science and Engineering from The Ohio State University in 2010 after performing his undergraduate studies at Virginia Tech.

Dr. Carpenter's research focus is on enabling advanced manufacturing concepts through experiments employing novel processing techniques, advanced characterization, and small-scale mechanical testing. Currently, he is working on projects related to the qualification of additively manufactured components, development of new materials for high field magnets using severe plastic deformation, and using high energy X-rays to study phase transformations during solidification in MIG cladding. Throughout his career he has utilized many characterization techniques including neutron scattering, X-ray synchrotron, XCT, PED, TEM, EBSD, and SEM.

He has more than 55 journal publications, one book chapter, and 35 invited technical talks to his credit.

With regard to TMS service, Dr. Carpenter currently serves as the EPD representative on the Program Committee and the SMD representative on the Content

Development and Dissemination Committee. He is a participating member of the Mechanical Behavior of Materials Committee and has served as chair of both the Characterization Committee and the Advanced Characterization, Testing, and Simulation Committee in the past. John serves as a Key Reader for *Metallurgical and Materials Transactions A* and has co-edited special sections in *JOM* related to neutron diffraction, coherent X-ray diffraction imaging methods, and modeling in additive manufacturing. He is the 2012 recipient of the TMS EPD Young Leaders Professional Development Award. He also received the 2018 Distinguished Mentor Award at Los Alamos National Laboratory.

Andrew D. Brown is a mechanical engineer at the U.S. Army Combat Capabilities Development Command (CCDC) Army Research Laboratory (ARL), Aberdeen Proving Grounds, Maryland, USA. He obtained his B.S. in Mechanical Engineering at North Carolina State University (2009) and his doctoral degree in Mechanical Engineering at Arizona State University (2015). He spent three years (2015–2018) at UNSW Canberra as a postdoctoral researcher where he oversaw the daily operations of the Impact Dynamics Laboratory, mentored undergraduate and graduate student research projects, and performed teaching duties. His research expertise is understanding microstructural effects on the mechanical performance and damage processes of materials subjected to high dynamic pressures (shock) and high strain rates. Since joining ARL in 2018 he has shifted focus to high-rate injury biomechanics research to improve injury outcome prediction and protect the U.S. Warfighter. He has been an active member of TMS since 2011; was a co-organizer for the symposium on Characterization of Minerals, Metals, and Materials in 2018; and has been the symposium's EPD Award Representative from 2017–present. Dr. Brown has published 41 peer-reviewed articles in the fields of mechanical engineering, materials science, and biomechanics.

Rajiv Soman currently serves as Director, Purity Survey Analysis, Materials Sciences Division at Eurofins EAG Laboratories, USA. He has over 30 years of professional experience in analytical chemistry and materials sciences. He earned a doctorate in Analytical Chemistry from Northeastern University, Boston. He received his B.Sc. (Chemistry—*Principal*; Physics—*Subsidiary*) with Honors, from Bombay University, India, and M.Sc. in Applied Chemistry from the Faculty of Technology & Engineering, Maharaja Sayajirao University of Baroda, India. He commenced his professional career as an Advanced Analytical Chemist in the Engineering Materials Technology Laboratories of General Electric Aircraft Engines. Prior to joining EAG Laboratories, Dr. Soman served as professor (Full) of Chemical Engineering, Chemistry, and Chemical Technology, and served as a faculty member for 20 years. He has received numerous awards for excellence in teaching and twice has been listed in *Who's Who Among America's Teachers.*

Dr. Soman's research interests are in the areas of atomic and mass spectrometry, with an emphasis on trace element determination and chemical speciation in a wide range of sample matrices. He was an invited guest scientist at the prestigious research institute, Forschungszentrum Jülich, Germany, where he conducted research in elemental mass spectrometry. He has co-authored several publications in international journals and has made numerous presentations at national and international conferences. He holds two U.S. patents.

Dr. Soman has been a member of the Society for Applied Spectroscopy (SAS) and the American Chemical Society (ACS) since 1986 and has served in numerous leadership positions in the societies. He was an invited panel member for the American Chemical Society's National Committee on Preparing for the Workforce 2020. He is also a member of ASM International, ASTM, and TMS, where he serves as a member of the Materials Characterization Committee.

Alex Moser of the U.S. Naval Research Laboratory has over 25 years of experience in materials development, shock-physics modeling, high speed videography, and armor development. He has over 40 publications, 5 patents, and patents pending, and has led research in carbon nanotube sensors.

Dr. Moser has investigated and developed blast and ballistic amour systems for the military resulting in multiple patents (10295310, 10281242, 9879946, 9696120, 9534870), patents pending, and a +$200M procurement for lightweight amour based on his design requirements. He has also contributed to projects concerning blast testing of vests, helmets, and goggles and a novel approach for quantifying the vulnerability of helmet designs.

He has augmented ballistic and blast experimental data with high strain rate simulations using CTH, a shock-physics code developed by Sandia National Laboratories. These endeavors resulted in a better understanding of the mechanisms of blast and ballistic phenomena related to amour materials and systems.

Part I
Advanced Microstructure Characterization

Insights into the Formation of Al–Cu Intermetallic Compounds During the Solid–Liquid Reaction by High-Resolution Transmission Electron Microscopy

Jie Chen, Yongqiong Ren, and Bingge Zhao

Abstract During Al/Cu solid–liquid reaction, different intermetallic compounds (IMCs) are expected, which can affect the mechanical and electrical properties of Al/Cu joints. To tackle this challenge, it is then necessary to tune the interface structure, which requires an insight into the formation mechanism of IMCs. In the current study, Al/Cu liquid–solid reaction was used to fabricate different IMCs. With the aid of a focused ion beam (FIB) and high-resolution transmission electron microscopy (HRTEM), the distribution of IMCs along the Al/Cu interface was determined. Meanwhile, the orientation relationship among different IMCs and Cu with coherent structure was identified. This study provides a fundamental understanding of the mechanism behind the Al/Cu reaction, which may guide the performance improvement of Al/Cu dissimilar weld.

Keywords Al/Cu interface · Solid–liquid reaction · Intermetallic compounds · HRTEM · Crystallographic orientation

Introduction

Materials with different physical and mechanical properties can be combined with dissimilar welding, and the advantages of each material can be fully utilized [1–3]. Al/Cu dissimilar welding has been widely used in power generation and transfer fields [4, 5]. This approach can produce a satisfying effect in lowering cost without much expense in transmission efficiency with respect to pure Cu. However, the physical, chemical, and mechanical properties of Al and Cu are significantly different [6,

J. Chen · Y. Ren
Yonggu Co. Ltd., 328 Wei Ershi Road, Yueqing City, Zhejiang Province 325600, People's Republic of China

B. Zhao (✉)
School of Materials Science and Engineering, Shanghai University, 99 Shangda Road, Shanghai 200444, People's Republic of China
e-mail: binggezhao@shu.edu.cn

J. Li et al., *Characterization of Minerals, Metals, and Materials 2021*,
The Minerals, Metals & Materials Series,
https://doi.org/10.1007/978-3-030-65493-1_1

7], which can cause defects during dissimilar welding. Among these issues, intermetallic compounds (IMCs) are essential in influencing the property of Al/Cu joints. According to the Al–Cu binary phase diagram [8], a large number of IMCs are expected in this system. Up to now, many studies have paid attention to this area. In work by Garg, Al_2Cu, and Al_4Cu_9 are the dominant IMCs during the friction stir spot welding of AA6061-T6 and Cu [9]. Nevertheless, Al_2Cu, AlCu, and Al_3Cu_4 were the main phases in Pierpaolo's research, where AA2024-T3 and Cu were joined by friction stir welding [10]. Hwang, on the other hand, utilized cold rolling to join Al and Cu, where Al_2Cu, AlCu, Al_3Cu_4, and Al_4Cu_9 were produced after annealing [11]. In a recent work by Wang, a high-temperature phase, $Cu_{15}Al$, was deemed to form during Al/Cu solid–liquid reaction [12]. These studies suggest that the formation of IMCs is rather complex. To tune the interface and optimize the property of Al/Cu joints, understanding the structural evolution during Al/Cu reaction becomes the impending issue.

In this study, Al/Cu interface structure with different IMCs was prepared by a solid–liquid reaction. To reveal the structural evolution during this process, a focused ion beam (FIB) was used to machine the interface, which was then followed by the structure characterization with high-resolution transmission electron microscopy (HRTEM) . With these efforts, the distribution of IMCs along the Al/Cu interface was determined, and the crystallographic orientation among Cu and IMCs was revealed.

Materials and Methods

Al and Cu, with the purity of 99.99%, were used in Al/Cu solid–liquid reaction. Pure Al ingot was loaded in an Al_2O_3 crucible and then melted in a muffle furnace (SXL-1200C, Shanghai Jujing) by heating it to 780 °C and holding for 5 min. A copper rod with a diameter of 6 mm was ground by sandpaper and then washed by 4 vol.% HCl solution to remove the contaminant and oxide. After that the Cu rod was treated by KF aqueous solution with a concentration of 4 wt% for 60 s to improve the wettability of Al on Cu. After drying in air, Cu was dipped into Al melt for 60 s, which was quenched by water to prepare Al/Cu solid–liquid reaction specimen.

FIB (FEI Helios Nano 600i) was then used to machine the Al/Cu interface. The interface structure was then characterized by HRTEM (JEOL-2010F) equipped with an energy dispersive spectrometer (EDS, Oxford).

Results and Discussion

As revealed in our previous study, IMCs can form in the area close to Cu during the Al/Cu solid–liquid reaction. Figure 1 displays the morphology of the Al/Cu interface. Two different IMCs are expected to form based on the image contrasts. To demonstrate this hypothesis, the interface containing different phases was machined by FIB, as schematically indicated by the yellow frame.

Figure 2 is the bright-field (BF) TEM image of the specimen. Three different areas are obviously identified. The contrast of BF image is related to the structure orientation. Accordingly, the orientation relationship between these three areas should be different.

It was reported that diffusion plays the dominant role in the Al/Cu solid–liquid reaction, suggesting the composition discrepancy in Al/Cu interface. As a result, a high-angle annular dark-field (HAADF) image whose contrast is associated with atom number was employed to reveal this phenomenon. Figure 3 displays the HAADF image of the interface as well as the EDS line scanning results. In agreement with Fig. 2, three different layers are observed in Fig. 3a, suggesting the composition

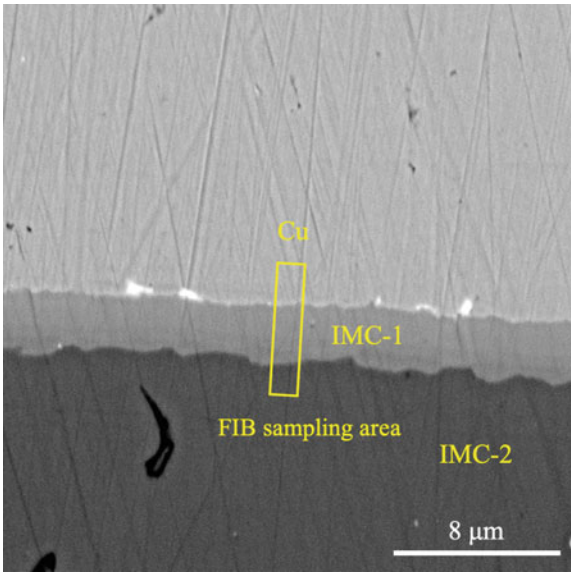

Fig. 1 Scanning electron microscopy (SEM) image of the Al/Cu interface. (Color figure online)

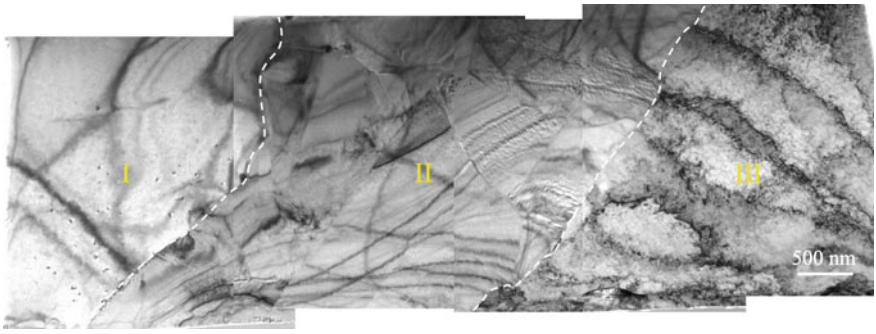

Fig. 2 Bright-field image of the Al/Cu interface. (Color figure online)

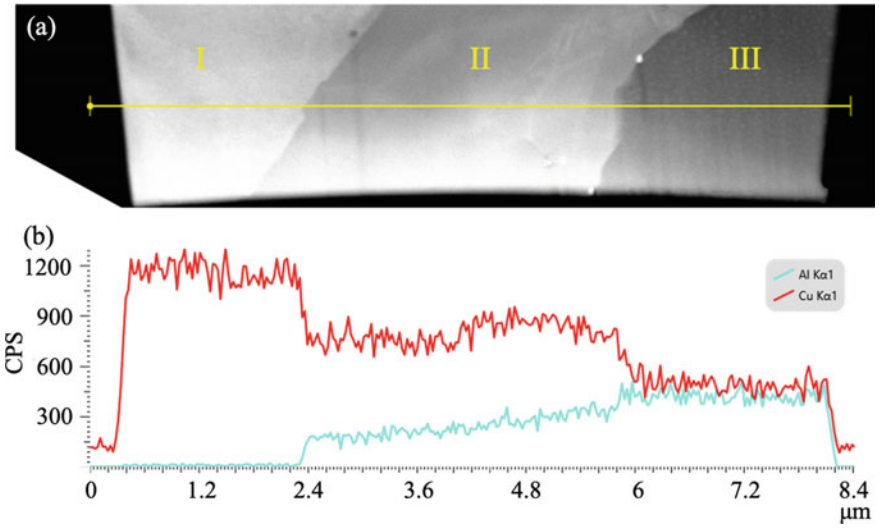

Fig. 3 HAADF image and EDS line scanning results of the specimen. (Color figure online)

difference in the specimen. As suggested by the EDS result in Fig. 3b, the area I is the Cu matrix with minor Al. During Al/Cu solid–liquid reaction, intensive diffusion of Al into Cu can occur. According to Al–Cu binary phase diagram [8], the maximum solubility of Al in Cu can reach 19.7%. That means the Cu matrix can be replaced by Cu solid solution with Al. With the distance away from Cu, the concentration of Cu decreases while it increases for Al. Meanwhile, different IMCs can form with the interdiffusion of Cu and Al.

As mentioned above, the formation of IMCs in Al/Cu system is significantly varied. Although current research uncovers the composition discrepancy in Al/Cu interface by HAADF and EDS, structure characterization is still essential to demonstrate the phase evolution. Figure 4 is the selected area electron diffraction (SAED) pattern (Fig. 4a) and HRTEM image with Fast Fourier Transformation (FFT) pattern (Fig. 4b) of area I. With the help of the SAED pattern, the area I is identified as Cu (PDF card number: 65-9743) without any IMC. Additionally, the interplanar spacing is nearly the same as that of pure Cu. Although the solid solution of Al in Cu is deemed to occur in this area, its determination is hindered by the error of SAED, which can be figured out by X-ray diffraction in our on-going work.

The structure characterization result of area II is displayed in Fig. 5. In contrast to Fig. 4a, two sets of diffraction spots with different brightness are observed: there are two weak diffraction spots between the bright ones. This phenomenon can still be detected with another incident axis (Fig. 5b). This seems like the occurrence of the superlattice, which is, however, seldom reported in the Al–Cu system. In our previous work, the kinetics of AlCu formation cannot be depicted by a single diffusion mechanism. Together with the current result, different IMCs may form in area II rather than the formation of the superlattice. By indexing the SAED patterns

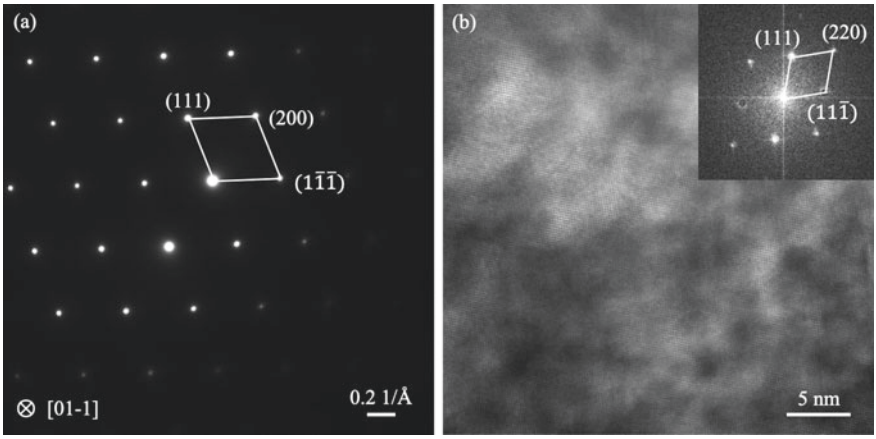

Fig. 4 Structure characterization of area I. **a** SAED pattern of area I. **b** HRTEM image with FFT pattern

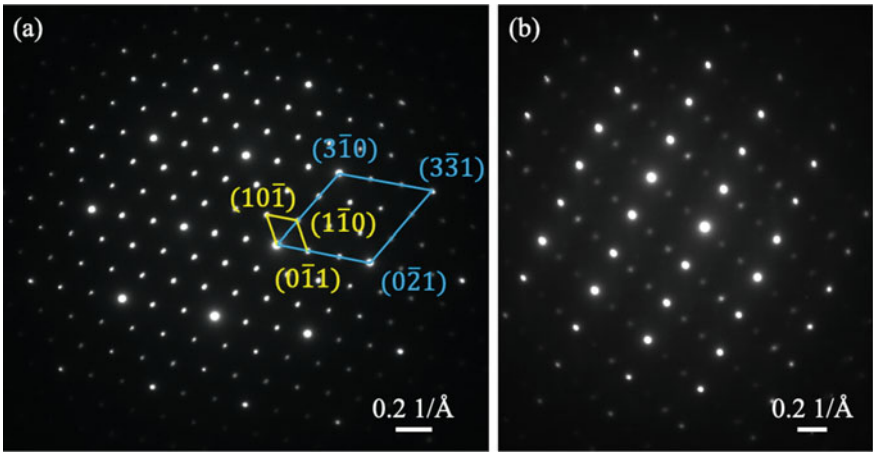

Fig. 5 SAED patterns of area II. Two sets of diffraction spots are detected. (Color figure online)

in Fig. 5a, the bright spots denote the AlCu phase with orthogonal structure (PDF card number: 39-1371) while the weak spots come from Al_4Cu_9 with primitive cubic structure (PDF card number: 65-7542). Moreover, these two IMCs are completely coherent in the microstructure. Although the Al_4Cu_9 IMC layer has been observed in Al/Cu solid reaction [13, 14], its orientation relationship with AlCu is rarely reported in solid–liquid reaction.

To further evidence this result, HRTEM image of area II is presented in Fig. 6. Based on the HRTEM image, FFT and inverse FFT patterns are obtained. By estimating the interplanar spacing, this area is identified as Al_4Cu_9.

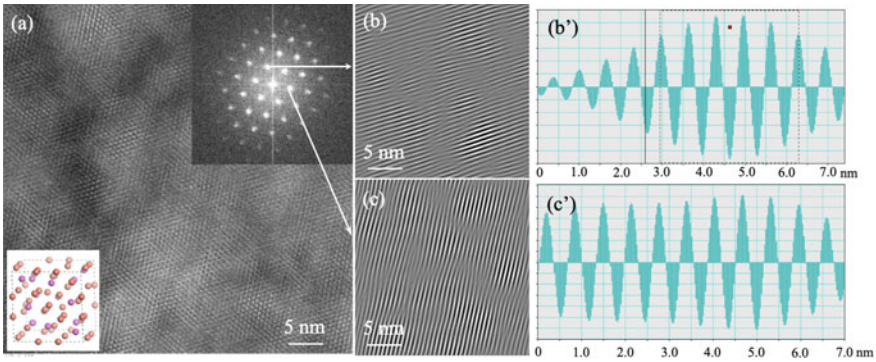

Fig. 6 Structure characterization of area II. **a** HRTEM image. The upper inset is the FFT pattern. The bottom inset is the crystal structure of Al_4Cu_9 IMC. **b** and **c** is the inverse FFT patterns with respective interplanar spacing shown in (**b**') and (**c**'). (Color figure online)

Another HRTEM image of area II is displayed in Fig. 7. In contrast to Fig. 6, AlCu is identified here. Together with Fig. 6, the coexistence of Al_4Cu_9 and AlCu IMCs in area II is further demonstrated. With the diffusion of Al and Cu, both AlCu and Al_4Cu_9 IMCs form in the area adjacent to the Cu matrix. According to Fig. 5a, their crystallographic orientation can be expressed as

$$(\bar{3}00)_{Al_4Cu_9}//(0\bar{2}1)_{AlCu},\ [111]_{Al_4Cu_9}//[1\bar{3}6]_{AlCu} \tag{1}$$

The coherence could decrease the interfacial energy during the phase transition, which facilitates the formation of Al_4Cu_9 IMC. That is why Al_4Cu_9 IMC is generally observed in solid-state reactions [11, 13].

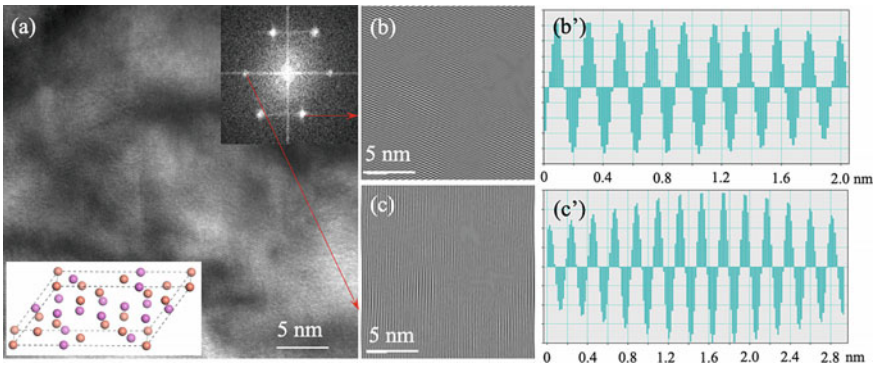

Fig. 7 Another HRTEM characterization case in area II. **a** HRTEM image. The upper inset is the FFT pattern. The bottom inset is the crystal structure of AlCu IMC. **b** and **c** is the inverse FFT patterns with respective interplanar spacing shown in (**b**') and (**c**'). (Color figure online)

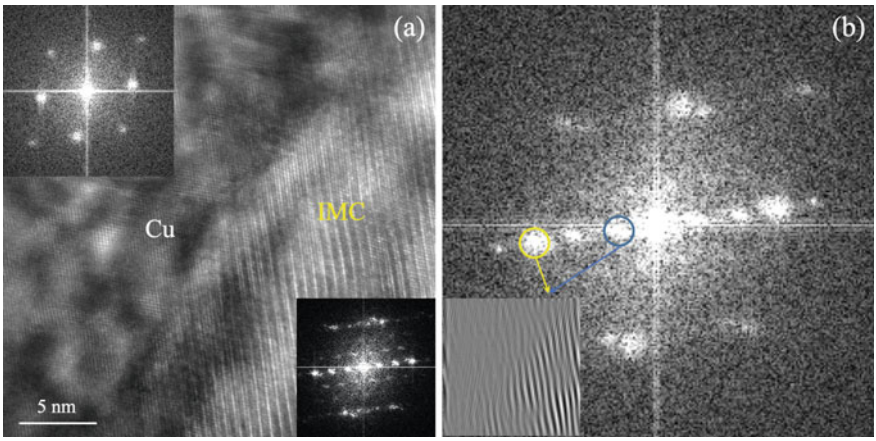

Fig. 8 The interface between Cu and IMC. **a** HRTEM image and FFT patterns of Cu and IMC. **b** FFT pattern of the interface, by which the orientation can be determined. (Color figure online)

It has to note that both AlCu and Al_4Cu_9 form from the Cu matrix, which may produce a particular orientation. The interface between areas I and II is presented in Fig. 8. The FFT pattern in the low inset suggests that both AlCu and Al_4Cu_9 are detected in this image. Moreover, FFT pattern of Cu is also contained (Fig. 8b). Accordingly, the crystallographic orientation of these three phases are illustrated as follows:

$$(\bar{1}11)_{Cu}//(\bar{3}00)_{Al_4Cu_9}//(0\bar{2}1)_{AlCu},\ [0\bar{1}1]_{Cu}//[111]_{Al_4Cu_9}//[1\bar{3}6]_{AlCu} \quad (2)$$

Moreover, they are coherent, suggesting the high potential in forming IMCs in the Al/Cu system.

The structure characterization of area III is shown in Fig. 9. Only Al_2Cu IMC with body-centered orthogonal structure (PDF card number: 65-2695) is identified by the SAED pattern. The HRETM image in Fig. 9b as well as the inverse FFT patterns in Fig. 9c and d further evidences the absence of any nano-scaled precipitates. Meanwhile, there is no obvious orientation among Al_2Cu, AlCu, and Al_4Cu_9 phases by an insight into the interface between them.

Conclusions

In this study, the formation of intermetallic compounds during Al/Cu solid–liquid reaction was revealed with the help of FIB and HRTEM. During this reaction, Al_2Cu, AlCu, and Al_4Cu_9 are the dominant IMCs. With the diffusion of Al and Cu, Al_2Cu forms in the area contacting with Al melt while AlCu and Al_4Cu_9 form in the area

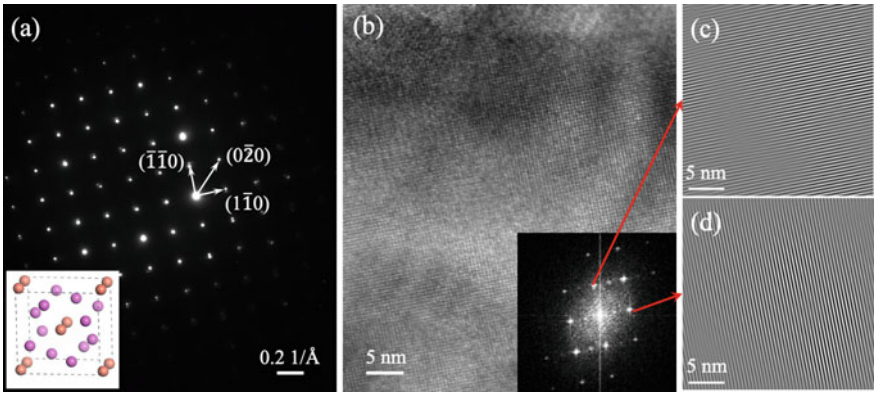

Fig. 9 Structure characterization of area III. **a** SAED pattern of this area. The bottom inset is the crystal structure of Al_2Cu IMC. **b** is the HRTEM image. **c** and **d** are the inverse FFT patterns. (Color figure online)

adjacent to the Cu matrix. AlCu, Al_4Cu_9, and Cu share coherent structure with each other, and their orientation relationship is determined as

$$(\bar{1}11)_{Cu}//(\bar{3}00)_{Al_4Cu_9}//(0\bar{2}1)_{AlCu},\ [0\bar{1}1]_{Cu}//[111]_{Al_4Cu_9}//[1\bar{3}6]_{AlCu}$$

This coherent structure can decrease the formation energy of IMCs, which is beneficial to the formation of IMCs during Al/Cu welding.

Acknowledgements This work was supported by the National Natural Science Foundation of China (Grant no. 51901125) and China Postdoctoral Science Foundation (Grant no. 2018M640376).

References

1. Ding K, Qiao S, Liu S et al (2019) Failure transition mechanism of stress rupture performance of the Inconel 625/9 Pct Cr steel dissimilar welded joint. Metall Mat Trans A 50A:4652–4664
2. Zhang Y, Fan M, Ding K et al (2020) Formation and control of the residual δ-ferrite in 9% Cr-HAZ of Alloy 617/9% Cr dissimilar welded joint. Sci Technol Weld Joining 25:398–406
3. Park G, Kim K, Uhm S, Lee C (2019) A comparison of cross-tension properties and fracture behavior between similar and dissimilar resistance spot-weldments in medium-Mn TRIP steel. Mater Sci Eng, A 752:206–216
4. Eivani AR, Mirzakoochakshirazi HR, Jafarian HR (2020) Investigation of joint interface and cracking mechanism of thick cladding of copper on aluminum by equal channel angular pressing (ECAP). J Mater Res Technol 9:3394–3405
5. Khosravifard A, Ebrahimi R (2010) Investigation of parameters affecting interface strength in Al/Cu clad bimetal rod extrusion process. Mater Des 31:493–499
6. Abbasi M, Karimi Taheri A, Salehi MT (2001) Growth rate of intermetallic compounds in Al/Cu bimetal produced by cold roll welding process. J Alloys Compd 319:233–241
7. Liu T, Wang Q, Sui Y et al (2016) An investigation into interface formation and mechanical properties of aluminum–copper bimetal by squeeze casting. Mater Des 89:1137–1146

8. Murray JL (1985) The aluminium-copper system. Int Met Rev 30:211–234
9. Garg A, Bhattacharya A (2020) Friction stir spot welding of AA6061-T6 and Cu with preheating: Strength and failure behavior at different test temperatures. Int J Adv Manuf Technol 108:1613–1629
10. Carlone P, Astarita A, Palazzo GS et al (2015) Microstructural aspects in Al–Cu dissimilar joining by FSW. Int J Adv Manuf Technol 79:1109–1116
11. Chen CY, Hwang WS (2007) Effect of annealing on the interfacial structure of aluminum-copper joints. Mater Trans 48:1938–1947
12. Liu G, Wang Q, Zhang L et al (2018) Effect of cooling rate on the microstructure and mechanical properties of Cu/Al bimetal fabricated by compound casting. Metall and Mat Trans A 49:661–672
13. Gueydan A, Domengès B, Hug E (2014) Study of the intermetallic growth in copper-clad aluminum wires after thermal aging. Intermetallics 50:34–42
14. Zhou L, Li GH, Zhang RX et al (2019) Microstructure evolution and mechanical properties of friction stir spot welded dissimilar aluminum-copper joint. J Alloys Compd 775:372–382

Part II
Advanced Characterization Methods II

Applying Stereological Characterisation to the Solidification Structure of Single Crystal Alloys to Deduce the 3D Macroscopic Solid/Liquid Interface Shape

Joel Strickland, Bogdan Nenchev, Karl Tassenberg, Samuel Perry, Gareth Sheppard, and Hongbiao Dong

Abstract Single crystals are a continuous unbroken solid crystal lattice with no grain boundaries. They find a wide range of applications, from semi-conductors, optoelectronics, to applications in aerospace engines. Primary spacing is a key phenomenon during single crystal solidification as it determines microsegregation, defect formation, and final material performance. In this work, an automatic, standardised, and comprehensive stereological single crystal characterisation methodology is applied to two sections of a CMSX-10® Ni-base superalloy bar. The Shape-Limited Primary Spacing methodology rapidly and accurately determines dendritic centres, packing pattern, and local primary spacing distribution within these bulk microstructures. Using the relationship between the radial variation of local primary spacing and isotherm curvature, the SLPS methodology has enabled the post-mortem reconstruction of the 3D macroscopic solid/liquid interface shape.

Keywords Directional solidification · Single crystal alloys · Microstructure · Dendritic growth · Primary spacing · Morphological stability · Modelling · Pattern recognition

Introduction

A wide range of imaging techniques have been developed for the study of solidification phenomena and solid-state transformations of metals. Several techniques, including SEM, CT tomography, and in situ synchrotron tomography, are widely employed to study solidification structures. High melting temperatures and sample

Joel Strickland developed the theory and wrote the manuscript. Bogdan Nenchev created the 3D macroscopic interface shapes. Karl Tassenberg optimised the software. Samuel Perry prepared and imaged the samples. All authors reviewed the manuscript and agreed to the published version.

J. Strickland (✉) · B. Nenchev · K. Tassenberg · S. Perry · G. Sheppard · H. Dong
School of Engineering, University of Leicester, Leicester LE1 7RH, UK
e-mail: jcjs2@leicester.ac.uk

J. Li et al., *Characterization of Minerals, Metals, and Materials 2021*,
The Minerals, Metals & Materials Series,
https://doi.org/10.1007/978-3-030-65493-1_2

opaqueness make the in situ observation of crystal growth evolution in metallic systems extremely challenging. Hence, post-mortem analysis of the solidified microstructure is typically required to investigate solidification processes. The standard metallographic approach involves slicing and polishing the solidified sample so that the solidification pattern can be examined using microscopy, either electron or optical.

In metallurgy, dendrites are the predominant structure that form during solidification. They are arborescent crystalline structures that grow by diffusion-limited heat and mass transfer. In most cuoppositebic metals, the preferential growth directions are <100> which results in crystallographic related features such as primary trunks, secondary, and tertiary sidearms. In directional solidification, the heat transfer is constrained through the solid, which results in arrays of dendrites aligned to the heat flow direction [1]. The variation in composition between an advancing dendrite and the surrounding inter-dendritic region gives rise to microsegregation in the solidified crystal. The solute segregation normal to the growth direction is characterised by the primary spacing, which controls the maximum length scale for segregation [2], the distribution of inhomogeneities within the microstructure [1], and mechanical properties of the material [3]. Directional solidification provides scientists a perfect opportunity to study the influence of changing process conditions on resultant microstructural formation with the least amount of feasible free solidification variables [4]. An important topic of interest for solidification scientists is predicting microstructural patterns within a directionally solidified array, as array disorder is directly related to a decrease in the mechanical behaviour of an as-cast component [5].

The morphology of the solid/liquid interface during solidification influences the final microstructural patterns within directionally solidified alloys [6]. The theory of morphological stability quantifies the stability of the interface shape that separates two phases during a phase transformation [7]. If a perturbation on the smooth surface grows the shape of the perturbation is morphologically unstable, whereas if it decays the shape is stable. One can imagine an undulating solid/liquid interface, whereby the growth of the perturbations is determined by the solute concentration ahead of the growing tips. In situ observations of the solid/liquid interface using organic analogues has been a vital tool in understanding the time-evolution of interfacial patterns [8]. Thin sample analysis (2D), has demonstrated that a small range of primary spacings are stable for any given set of experimental conditions [9], and these spacings are defined by the overgrowth and branching limits [10]. Over the last decade, more authors are becoming aware of the importance of local (3D) variations in primary spacing on defect formation within bulk microstructures [11]. As a result, significant effort has been focused on developing local characterisation techniques [12–14]. Trivedi [5] has demonstrated that spatial variation in fluid density within the melt parallel to a growing 3D array of dendritic tips can result in large variations in radial primary spacing and disorder within a bulk microstructure. This researcher highlighted thermosolutal convection and solute redistribution as the most likely perpetrator behind array disorder and linked this to variations in the shape of the solid/liquid isotherm during solidification. Consequently, small variations in the

isotherm shape will cause significant changes in solute redistribution within the melt, influencing the morphology of the solid/liquid interface [15].

In terrestrial conditions, isotherm curvature-driven lateral solute movement adds extra time and length scales to interfacial pattern evolution, which are not accounted for in the Warren and Langer model [6]. The influence of variations in lateral solute redistribution on the morphology of the solid/liquid interface and the time evolution of interfacial patterns is unknown. Unfortunately, direct observations of morphological instability in opaque 3D metallic systems are not currently possible and are limited to computer modelling of the interface [11]. Recently, Strickland et al. [15] have identified a quadratic relationship exists between the radial variation in local primary spacing, $\overline{\lambda}_{\text{Local}}$, and the macroscopic shape of the solid/liquid interface for both solutally unstable and stable alloys. In the case of solutally stable alloys, solute enriched liquid mainly flows by steepling driven convection to the most retarded part of the solid/liquid interface, which results in remelting and an increase in array disorder and $\overline{\lambda}_{\text{Local}}$. In this case, the 3D microstructures interface can be deduced post-mortem by fitting a quadratic to the reciprocal of the radial variation in $\overline{\lambda}_{\text{Local}}$. However, for solutally unstable alloys, although thermal buoyancy drives large-scale flow circulations within the melt, this is not the primary mechanism for solute flow in these systems. It has been established, that differential solutal buoyancy forces driven by curved isopleths of concentration result in solute enrichment at the most advanced part of the interface [21]. Consequently, in solutally unstable systems, solute enrichment causes an increase in $\overline{\lambda}_{\text{Local}}$ and disorder at the most advanced part of the interface rather than at the most retarded location as was previously thought.

The purpose of this work is to deduce the 3D macroscopic interface shape for a solutally unstable system using post-mortem stereological characterisation techniques. Firstly, the Shape-Limited Primary Spacing (SLPS) algorithm [15] is applied to determine the $\overline{\lambda}_{\text{Local}}$ for every dendrite within two cross-sections of a single crystal CMSX-10® Ni-base superalloy bar. The variation in $\overline{\lambda}_{\text{Local}}$ is plotted as a function of radial distance and a 3D representation of the solid/liquid interface shape is reconstructed by fitting a quadratic to the data. Lastly, the influence of changes in the bulk solidification environment and solute redistribution on the morphology of the 3D macroscopic interface shapes and their influence on defect formation are discussed.

Methodology

A single crystal CMSX-10® bar of 9.4 mm diameter and 64 mm in height (Fig. 1b) was provided by Rolls-Royce Plc; the approximate growth parameters are indicated in Table 1. The bar was solidified in a cluster mould arrangement within a Bridgman furnace (Fig. 1a) and withdrawn at a constant withdrawal velocity, V. The bar was sectioned into seven segments perpendicular to the long axes of the sample using a metallographic precision cutter. Section 1 corresponds to the part of the cast that solidified nearest to the chill plate of the Bridgman furnace and Sect. 7 furthest away (Fig. 1a). Only Sects. 1 and 7 (Fig. 1b) were used in this analysis as they

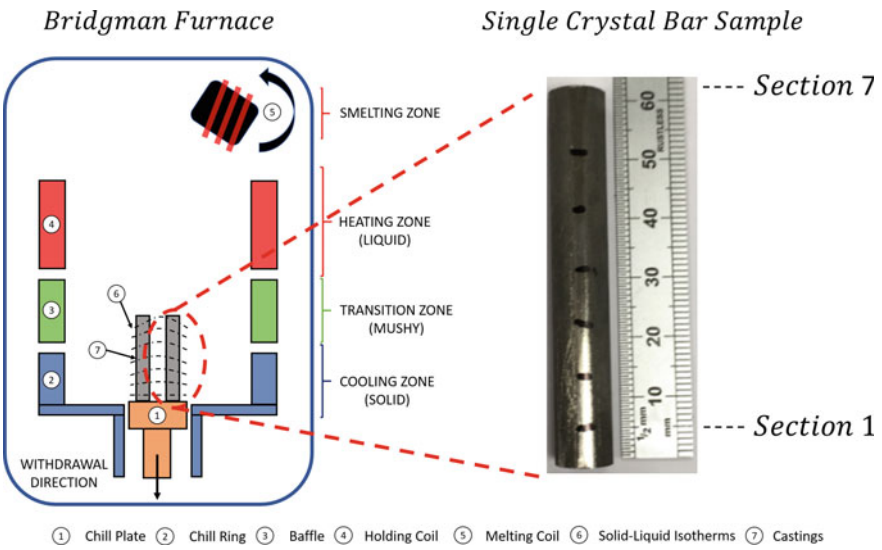

Fig. 1 **a** Schematic of Bridgman furnace. Single crystal components are manufactured via this method. Samples are withdrawn downwards through an axial thermal gradient. The solidification front is always perpendicular to the heat flow direction. Solidification occurs during the transition zone. **b** CMSX-10® sample used within this study. The sample is 9.4 mm diameter and 64 mm in height. (Color figure online)

Table 1 Growth parameters for the CMSX-10® single crystal bar used in this study. The bar was withdrawn from the Bridgman furnace at a constant velocity. The exact solidification conditions are unknown

Alloy	Morphology	G (K/cm)	V ($(\mu m/s)$)	Diameter (mm)	Height (mm)	Mould
CMSX-10®	Dendritic	10-20	5–10	9.4	64	Cluster

are taken from opposite ends of the cast, and therefore solidified under the greatest variation in bulk environmental conditions (Fig. 1a). The two sections were imaged in backscattered electron (BSE) mode to visualise the microsegregation between the dendritic core and interdendritic region. MAPS® software (ThermoFisher Scientific, Waltham, MA, USA) provided large, high resolution, stitched images of the dendritic arrays automatically, with only minor adjustments required where necessary. The BSE image was loaded into the DenMap software [16] and the exact dendritic core pixel positions were located. These coordinates were input into the SLPS algorithm [15] which determines local dendritic packing and $\overline{\lambda}_{\text{Local}}$ variation over each cross section.

Results

The variation in local dendritic packing (Fig. 2b) and $\overline{\lambda}_{\text{Local}}$ (Fig. 2c) across both single bulk single crystal microstructures were mapped using the SLPS algorithm [15]. The local dendritic packing is determined by the number of nearest neighbours around a central dendrite. For example, a dendrite with N_6 packing (hexagonal) has six nearest neighbours. The $\overline{\lambda}_{\text{Local}}$ is determined by the average primary spacing from a central dendrite to its nearest neighbours. The nearest neighbours are determined using the SLPS algorithm [15].

The packing map (N-Map) demonstrates the variation in local dendritic packing across the array, where hexagonal packing formation indicates stable growth conditions that solidified under equivalent tip compositions [15]. All other non-hexagonal packing indicates metastable regions that are forming from local variations in solute composition parallel to local arrangements of growing tips [15]. The local primary spacing map (LS-Map) in Fig. 2c demonstrates the variation in $\overline{\lambda}_{\text{Local}}$ across an array. An array whereby one unique $\overline{\lambda}_{\text{Local}}$ (average $\overline{\lambda}_{\text{Local}}$ for the bulk array) exists would obtain a uniform green LS-map. Areas of small $\overline{\lambda}_{\text{Local}}$ are indicated in the blue/dark

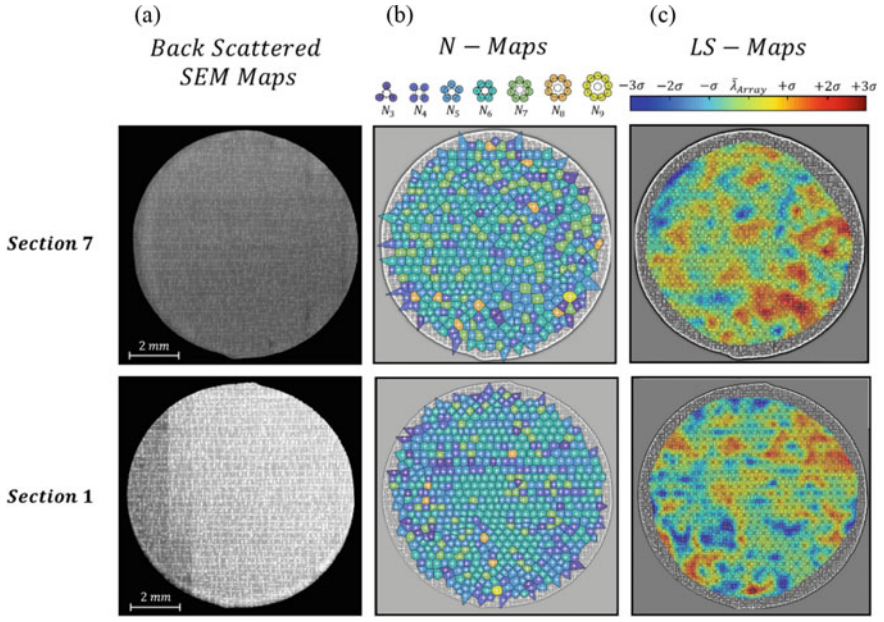

Fig. 2 **a** Backscattered SEM images comprised of 24 × 24 grid of individual SEM images taken at 300 × magnification with 20 μ s scan speed. The SLPS algorithm applied to Sect. 1 and 7 from the CMSX-10® single crystal superalloy bar from Fig. 1b. **b** Packing pattern maps (N-Maps) indicating stable and metastable packing. **c** Local primary spacing distribution maps (LS-Maps) demonstrating the variation in microsegregation across each array. The $\overline{\lambda}_{Array}$ and $\sigma_{\lambda_{Array}}$ are recorded in Table 1. The figure is adapted from [15]. (Color figure online)

Table 2 Comparison between $\overline{\lambda}_{Array}$ (calculated by SLPS [15]), $\overline{\lambda}_{N_6}$, and $\overline{\lambda}_{SCM}$ (square counting method [17]) between Sect. 1 and 7 of the CMSX-10® superalloy bar. The number of dendrites within each bulk array was determined by the DenMap software [16]. $\overline{\lambda}_{SCM}$, was calculated using the total Voronoi area of all combined patterns within an array, the number of dendrites within this combined Voronoi area, and $B = 1.075$. In both cases, $\overline{\lambda}_{N_6}$ closely matches $\overline{\lambda}_{Array}$, regardless of the array irregularity, as determined by $\sigma_{\lambda_{Array}}$. $\overline{\lambda}_{Array}$ and $\overline{\lambda}_{SCM}$ demonstrate excellent agreement

Section	No. of Dendrites	$\overline{\lambda}_{Array}$ (μm)	$\overline{\lambda}_{SCM}$ (μm)	$\overline{\lambda}_{N_6}$ (μm)	$\boldsymbol{\sigma_{\lambda_{Array}}}(\mu m)$	K_{Array}	$MLPR$
1	681	333	336	343	54	1.55	1.46
7	548	377	375	382	79	1.56	1.61

blue regions and large $\overline{\lambda}_{\text{Local}}$ the orange/red. The $\overline{\lambda}_{\text{Local}}$ and $\sigma_{\lambda_{Array}}$(standard deviation of bulk $\overline{\lambda}_{\text{Local}}$) for the single crystal microstructures in Fig. 2c are illustrated in Table 2. A full description of the SLPS algorithm and the derivation of the N-Maps (Fig. 2b) and LS-Maps (Fig. 2c) can be found in Ref. [15].

The largest variation in $\overline{\lambda}_{\text{Local}}$ versus radial distance for Sect. 1 and 7 is illustrated in Fig. 3a). The $\overline{\lambda}_{\text{Local}}$ follows a clear quadratic relationship with radial distance (Fig. 3b). The top of the sample demonstrates the greatest variation in radial $\overline{\lambda}_{\text{Local}}$ distribution across the cross section. This also corresponds with an increase in array disorder (K_{Array}), macroscopic curvature ($MLPR$), and $\sigma_{\lambda_{Array}}$ (Table 2). A perfectly hexagonal bulk array with no inherent disorder would achieve $K_{Array} = 1.52$. A perfectly flat macroscopic interface occurs when the $MLPR$ equals 1; the greater the interface curvature the larger the $MLPR$ value. For the derivations of K_{Array} and $MLPR$ the reader is referred to ref. [15].

The increase in $\overline{\lambda}_{Array}$ between Sect. 1 and 7 (Table 2) is due to a reduction in the strength of the axial thermal gradient, G, and an enrichment of solute (axial macrosegregation) at the end of the cast [15]. The increase in $\overline{\lambda}_{\text{Local}}$ observed in the bottom right part of Sect. 7 of Fig. 2c is a result of solute enrichment due at the most advanced part of the interface due to lateral fluid flow through the mush driven by isotherm curvature [15]. This flow of solute also results in an increase in array disorder (increase in K_{Array}), which is observed as an increase in non-hexagonal pattern formation in the bottom right-hand side of Sect. 7 (Fig. 2b). Regions of hexagonal packing indicate stable growth conditions and a flat macroscopic interface. Connected regions of large $\overline{\lambda}_{\text{Local}}$ correspond to solute-enriched areas where the solid/liquid interface is being remelted and is therefore lagging behind neighbouring faster growing solute-depleted areas (small $\overline{\lambda}_{\text{Local}}$). Consequently, by plotting the x-y-axes as distance, z as $1/\overline{\lambda}_{Local}$, and fitting a strong Gaussian (which corresponds to the size of the core $\approx 20 \times 20$ pixels) to the data i.e., smoothing the noise, enables a qualitative reconstruction of the undulating morphological nature of the solid/liquid interface shape (Fig. 4a); this is not be confused with the macroscopic interface curvature, which closely represents the isothermal shape. To provide a semi-quantitative representation of the average macroscopic interface concavity/convexity,

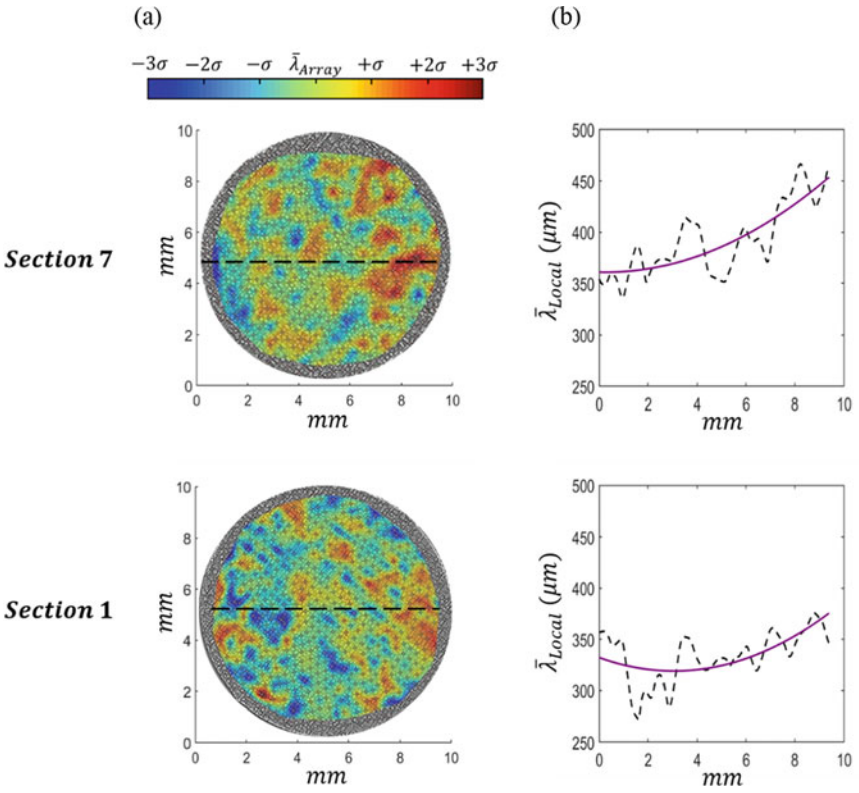

Fig. 3 **a** LS-Maps of Sect. 1 and 7 from the CMSX-10® superalloy microstructures; the $\overline{\lambda}_{Array}$ and $\sigma_{\lambda_{Array}}$ are found in Table 2. **b** The radial variation in $\overline{\lambda}_{Local}$ across the cross section is along the dashed line sketched in (**a**). The plot was taken at the point of greatest $\overline{\lambda}_{Local}$ variation. A quadratic relationship exists between radial distance and $\overline{\lambda}_{Local}$ for both samples. (Color figure online)

the x-y axes are plotted as distance, z as $\overline{\lambda}_{\text{Local}}$, and a quadratic surface fit is performed to the radial variation in the $\overline{\lambda}_{\text{Local}}$, the results are illustrated in Fig. 4(b).

Discussion

The 3D solid/liquid interface is clearly non-linear in nature (Fig. 4a), which is in keeping with the Warren and Langer non-linear stability model [6]. The bottom of the cast (Sect. 1) is more morphologically stable than the top of the cast (Sect. 7), which forms further away from the chill plate of the Bridgman furnace and under a greater curvature of the isotherm (Fig. 1a, b). The length scale of the perturbations in Sect. 1 (Fig. 4a) is on the scale of the $\overline{\lambda}_{Array}$, ($333\mu m$—Table 2, therefore, this interface is formed under mainly diffusive conditions. This interface would be well

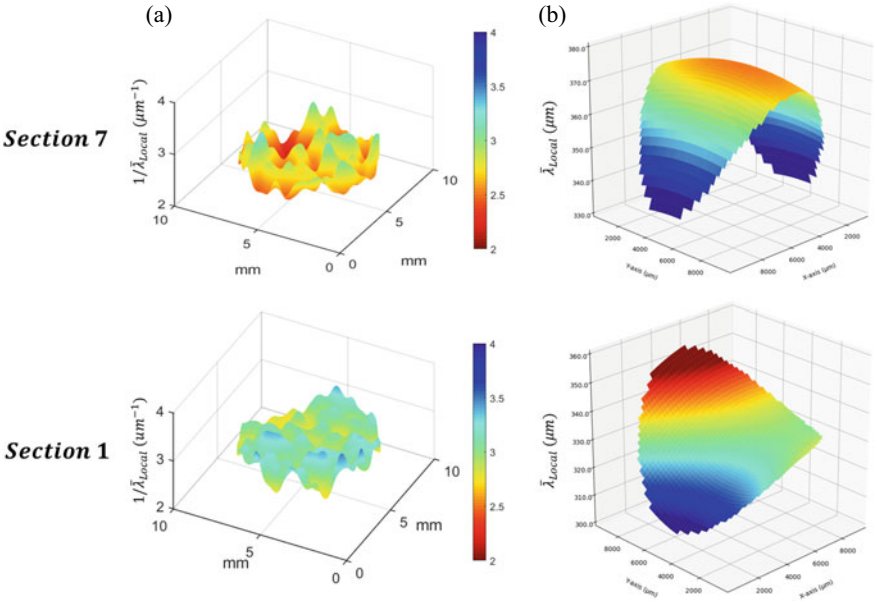

Fig. 4 **a** A post-mortem representation of the 3D macroscopic solid/liquid interface deduced from variation in local primary spacing; the colour scale corresponds to the z-axis; the perturbations are expressed in units of curvature (μm^{-1}). **b** A quadratic surface fit was performed to the variation in $\overline{\lambda}_{\text{Local}}$ and illustrates the average concavity/convexity of the interface, which closely corresponds to the shape of the isotherm during solidification. (Color figure online)

described by a Warren and Langer type non-linear stability analysis in 3D [18]. On the other hand, large perturbations are observed in Sect. 7 that are $1-2mm$ in diameter and in some cases many times larger than the $\overline{\lambda}_{Array}$, ($377\mu m$—Table 2). This cannot be accounted for by solute diffusion (D_L/V), as the length scale covers multiple connected cells/dendrites; D_L is the liquid solute diffusivity.

Under a typical V, the top of a single crystal cast (in solutally unstable systems such as CMSX-10®) becomes enriched in solute [15]. Further, in Bridgman casting of samples with uniform geometry the axial G decreases with height from the chill plate [19]. The combination of these effects changes the bulk solidification environment and the steady-state interface morphology. With sufficient time the interface responds to these environmental changes and will oscillate in a stable configuration as described by a Warren and Langer non-linear stability analysis. However, in addition to solute partitioning and buoyancy effects (dictated by the Rayleigh number), isotherm curvature has a particularly dominant effect on convection. Any isotherm curvature interacts with the solute field ahead of the tips and within the mushy zone to give rise to sideways diffusive instability [5], which is not accounted for in the Warren and Langer model [18]. Given that the existing solute gradient ahead of the moving interface is the main driving force behind the morphological instability, any lateral flow within the melt or mush that affects this solute distribution parallel to

the solidification front has a strong influence on the morphology of the resultant perturbations.

It is known, that the form of the macroscopic interface is imposed by the isotherm, which dictates the movement of solute over the bulk interface and through the mushy zone [15]. Consequently, lateral pressure gradients and fluid flow velocity are determined by the concavity/convexity of the isotherm as there is no physical driving force for lateral solute movement if the isotherm is perpendicular to the gravity vector. The severity of lateral macrosegregation (as characterised by regions of similar $\overline{\lambda}_{\text{Local}}$—Fig. 2c) is determined by the level of solute-depleted and enriched areas parallel to a growing interface. This is in turn determined by the solidification rate ($G \times V$), which dictates the time allowed for lateral fluid flow and the isotherm curvature. Consequently, to successfully predict the range of observed $\overline{\lambda}_{\text{Local}}$ within a bulk single crystal microstructure requires the inclusion of the influence of isotherm shape on lateral fluid flow.

It is clear from Fig. 4(b), that the 3D macroscopic interface shape in sample 1 is relatively flat with a region of interface advancement and retardation. Interestingly, because of mass continuity and the Gaussian nature of $\overline{\lambda}_{\text{Local}}$ [15], any interface advancement has to be balanced by an interface depression. As this effect can occur over a distance greater than that described by diffusion, it must be a bulk mass continuity phenomenon i.e., related to macroscopic convection. In essence, solute depleted liquid from the bulk melt must be being driven down into the interdendritic regions to balance the solute flowing through the mush to the most advanced part of the interface. Another interesting observation is the evolution of the interface from relatively flat in sample 1 to highly convex in sample 7. This is expected, as the axial component of G decreases under a constant V (in circular geometry samples with constant area) as the fraction of solid superalloy increases. Notice, that the increase in $\sigma_{\lambda_{Array}}$ (Table 2) in sample 7, also corresponds to an increase in interface convexity (Fig. 4(b)). Thus, the $\sigma_{\lambda_{Array}}$ quantifies the severity of the interface curvature, where decreasing the $\sigma_{\lambda_{Array}}$ is associated with a reduction in interface concavity/convexity. Another notable observation is the movement of the most advanced part of the interface from the edge of the sample (section 1) into the centre (Section 7). This modification in interface morphology must be a direct result of a change in the isotherm shape with height from the chill plate and its influence on convection through the mush and melt. For future study, research should focus on understanding how this mass continuity effect and the resulting interface undulations influence the development of low and high angle grain boundaries within the microstructure [20]. In addition, it is important to quantify how the evolving interface shape is interconnected with the elimination/creation of cells/dendrites and the mechanical properties of single crystalline materials.

Over the last twenty years, two important experimental types have come to the forefront as fundamental tools for studying metallic systems. These techniques take advantage of the penetrating nature of synchrotron and neutron radiation for investigation into material structure and property [11]; however, their application for the study of bulk metallic growth is restricted. Synchrotron X-ray methods are limited by a small voxel size and neutron source by poor spatio-temporal resolution [11].

Although, the $\overline{\lambda}_{Local}$ 3D reconstruction technique discussed in this paper is currently semi-quantitative in nature, it is the only methodology which enables ex situ observation of the bulk macroscopic solid/liquid interface on relevant length scales. It may be possible to validate this novel technique on binary systems using Phase Field computational modelling methods that are coupled with mass transport equations; however, large dendritic arrays are required to generate realistic sideways diffusive instabilities. Through application of the SLPS algorithm, it may be possible to develop a new non-linear bulk stability theory that includes the effects of isotherm curvature and the additional time and length scales added by convection. This may enable single crystal manufacturers to predict the final microstructural patterns through simulations, saving the time and labour costs associated with metallographic preparation and imaging. However, for the time being, post-mortem packing analysis is the only method to visualise the 3D macroscopic interface shape. This new technique enables the deduced 3D macroscopic interface to be compared with modelling software such as ProCAST (ESI Group, Paris, France) for validation purposes of binary and multi-component alloys (such as CMSX-10®). In addition, SLPS is the only standardised, automatic, characterisation method that enables quantification of the disorder in any single crystal array formed under any condition [15]; thus, SLPS is the only reliable method available for single crystal cast optimisation.

Conclusions

Through post-mortem microstructural analysis, Shape-Limited Primary Spacing (SLPS) enables the visualisation of the 3D macroscopic solid/liquid interface shape. For the first time, the influence of a change in processing parameters, sample geometry, and/or alloy composition on the 3D macroscopic interface shape can be visualised. From an academic viewpoint, SLPS enables quantification and understanding of the influence of the bulk solidification environment and alloy composition on the morphology of the solid/liquid interface and time-evolution of interfacial patterns. From an industrial point of view, SLPS enables the deduced shape of the solid/liquid interface to be compared with thermal models for validation purposes. By reducing the macroscopic interface curvature, either through optimisation of processing route or alloy composition, the quality of single crystal components can be improved through the reduction of array disorder and grain boundary associated defects.

Acknowledgements J.S., B.N., K.T., S.P., and G.S. acknowledge EPSRC CDT (Grant No: EP/L016206/1) in Innovative Metal Processing for providing PhD studentships for this study and Rolls-Royce Plc for providing financial support and supplying the single crystal CMSX-10® sample.

References

1. Kurz W, Rappaz M, Trivedi R (2020) Progress in modelling solidification microstructures in metals and alloys. Part II: dendrites from 2001 to 2018. Int Mater Rev 2020:1–47
2. Kurz W, Fisher D (1981) Dendrite growth at the limit of stability: tip radius and spacing. Acta Metall 29(1):11–20
3. Dong H, Wang W, Lee PD (2000) Simulation of the thermal history dependence of primary spacing during directional solidification. Superalloys 2004:925–931
4. Hunt J, Lu S-Z (1996) Numerical modeling of cellular/dendritic array growth: spacing and structure predictions. Metal Mater Trans A 27(3):611–623
5. Trivedi R, Mazumder P, Tewari SN (2002) The effect of convection on disorder in primary cellular and dendritic arrays. Metal Mater Trans A 33(12):3763–3775
6. Warren JA, Langer J (1993) Prediction of dendritic spacings in a directional-solidification experiment. Phys Rev E 47(4):2702
7. Mullins WW, Sekerka RF (1963) Morphological stability of a particle growing by diffusion or heat flow. J Appl Phys 34(2):323–329
8. Somboonsuk K, Mason J, Trivedi R (1984) Interdendritic spacing: part I. Experimental studies. Metal Mater Trans A 15(6):967–975
9. Ding G, Huang W, Lin X, Zhou Y (1997) Prediction of average spacing for constrained cellular/dendritic growth. J Cryst Growth 177(3–4):281–288
10. Weidong H, Xingguo G, Yaohe Z (1993) Primary spacing selection of constrained dendritic growth. J Cryst Growth 134(1–2):105–115
11. Strickland J, Nenchev B, Dong H (2020) On directional dendritic growth and primary spacing—a review. Crystals 10(7):627
12. Strickland J, Nenchev B, Dong H (2020) Applications of pattern recognition for dendritic microstructures. In: IOP conference series: materials science and engineering, IOP Publishing, p 012057
13. Warnken N, Reed RC (2011) On the characterization of directionally solidified dendritic microstructures. Metal Mater Trans A 42(6):1675–1683
14. Tschopp MA, Miller JD, Oppedal AL, Solanki KN (2015) Evaluating local primary dendrite arm spacing characterization techniques using synthetic directionally solidified dendritic microstructures. Metal Mater Trans A 46(10):4610–4628
15. Strickland J, Nenchev B, Perry S, Tassenberg K, Panwisawas C, Gill S, Dong H, D'Souza N, Irwin S (2020) On the nature of hexagonality within the solidification structure of single crystal alloys: mechanisms and applications. Acta Materialia
16. Nenchev B, Strickland J, Tassenberg K, Perry S, Gill S, Dong H (2020) Automatic recognition of dendritic solidification structures: DenMap. J Imaging 6(4):19
17. McCartney D, Hunt J (1981) Measurements of cell and primary dendrite arm spacings in directionally solidified aluminium alloys. Acta Metall 29(11):1851–1863
18. Warren JA, Langer J (1990) Stability of dendritic arrays. Phys Rev A 42(6):3518
19. Szeliga D, Kubiak K, Motyka M, Sieniawski J (2016) Directional solidification of Ni-based superalloy castings: thermal analysis. Vacuum 131:327–342
20. Hallensleben P, Scholz F, Thome P, Schaar H, Steinbach I, Eggeler G, Frenzel J (2019) On crystal mosaicity in single crystal Ni-based superalloys. Crystals 9(3):149
21. Kao A et al (2019) Thermal dependence of large-scale freckle defect formation. Philos Trans R Soc A 377.2143:20180206

Part III
Characterization of Composite Materials

Influence of Graphene Oxide Functionalization Strategy on the Dynamic Mechanical Response of Natural Fiber Reinforced Polymer Matrix Composites

Fabio Da Costa Garcia Filho, Michelle Souza Oliveira, Fernanda Santos da Luz, and Sergio Neves Monteiro

Abstract Since the twenty-first century began, environmental concerns related to energetic consumption and pollution have been gaining attention. In part, these could be associated with production and disregard synthetic materials. Using natural materials instead of synthetic aimed to become a trend, which has not happened. Natural lignocellulosic fibers (NLFs) were showed to be capable of replacing synthetic fibers in polymer composites. However, some limitations such as damage from heat can be considered a major constraint for wider application of NLFs/polymer composites. A novel strategy that is suggested to improve this property is the graphene oxide (GO) functionalization of NLFs. This work investigates the thermal behavior of epoxy/NLF composites, with and without GO functionalization. Two different amounts of reinforcement, low (20 vol%) and high (40 vol%), were dynamic mechanically investigated up to 160 °C. Investigated parameters revealed notable changes attributed to GO-functionalization effect on the NLF regarding viscous stiffness and damping capacity of the composite.

Keywords Natural fiber · Graphene oxide treatment · Dynamic mechanical analysis (DMA)

Introduction

In recent years, it has been an increasing effort to reduce the amount of CO_2 emission which can be associated with greenhouse effect and global warming [1, 2].

F. Da Costa Garcia Filho (✉) · M. S. Oliveira · F. S. da Luz · S. N. Monteiro
Department of Materials Science, Military Institute of Engineering—IME, Rio de Janeiro, Brazil
e-mail: fdacostagarciafilho@eng.ucsd.edu

F. Da Costa Garcia Filho
Department of Mechanical and Aerospace Engineering, University of California San Diego—UCSD, La Jolla, CA, USA

J. Li et al., *Characterization of Minerals, Metals, and Materials 2021*,
The Minerals, Metals & Materials Series,
https://doi.org/10.1007/978-3-030-65493-1_3

Energetic consumption and long-term pollution, which can be related to the production as well as the disregard of synthetic materials, motivate studies and application of eco-friendly materials. Natural lignocellulosic fibers (NLFs) are green materials as they exhibit characteristics such as renewability, recyclability, biodegradability, abundance, and low cost of production. These are considered major advantages that inspire not only researchers but also industries to invest in the use of these materials [3, 4]. It has been shown in previous years that these NLFs when employed as reinforcement for polymeric matrix composites can successfully be used in several engineering applications where synthetic fibers such as glass, carbon, or aramid fibers are the usual selection [5–9].

Many different NLFs have been extensively discussed in the literature such as jute, ramie, fique, and many others [10–14]. Yet, there are millions of other less studied fibers with great potential of being used as engineering materials, a good example is the *Attalea funifera* fiber, commonly known as piassava fiber. These are promising materials to reinforce polymeric matrices to produce stiffer and tougher composites [15–17]. The piassava fibers are extracted from palm trees that are grown in the Atlantic Rainforest in the southeast region of Brazil.

Despite the recent trend for a wider use of NLF composites for engineering applications, their use still faces some challenges and limitations. The compatibility between NLFs and polymeric materials plays a major role as it affects the mechanical and thermal properties of these composites. A way to overcome such drawback is by fiber's surface treatment, which commonly includes heat treatment and electron radiation as well as alkaline, silane, and acetylation treatments [18]. However, the improvement achieved by these physical and chemical treatments may be considered as not appreciable enough. A novel surface treatment that, recently, has been brought attention to researchers consists of the functionalization of the fiber surface with graphene oxide (GO) [19–23]. The GO treatment could significantly contribute to the thermal resistance and dynamic mechanical improvement of polymer composites. Therefore, the present work investigates the influence of the GO treatment of the dynamic mechanical response of piassava/epoxy composites.

Materials and Methods

Piassava fibers were supplied by a broom industry, Vassouras Rossi, Brazil. As-received fibers were first cleaned with running water and then dried at 60 °C in an oven for 24 h. The graphene oxide (GO) applied as piassava fiber coating was fabricated by the modified Hummers–Offeman method [22, 23]. For coating purpose, the cleaned piassava fiber was immersed in a GO solution, 0.56 mg/ml, and agitated in a shaker to guarantee optimum coating. Thereafter, the fibers already soaked with GO were placed in a stove at 80 °C for 24 h for drying.

Composites with different amount of 20 and 40 vol% of continuous and aligned piassava (untreated and GO treated) were produced using a compression molding process. Table 1 summarizes the investigated conditions in the present work. Epoxy

Table 1 Investigated conditions

Condition	Amount of fiber reinforcement (vol%)	GO treatment
Epoxy	0	No
UPF20	20	No
UPF40	40	No
TPF20	20	Yes
TPF40	40	Yes

resin was prepared by mixing bisphenol A diglycidyl ether (DGEBA) resin with triethylenetetramine (TETA) hardener with phr 13 parts of hardener ratio, both supplied by Epoxy Fiber, Brazil. Dynamic mechanical analyses (DMA) were conducted as per ASTM D7028-7 using DMA TA instruments, model Q/800 equipment in three-point flexural mode at frequency of 1 Hz, heat rate of 3 °C/min, and temperature range from 30 to 160 °C.

Results and Discussion

Figure 1 presents the results of DMA analysis of epoxy matrix reinforced with untreated piassava fiber composites and GO-treated piassava fibers, for all conditions investigated.

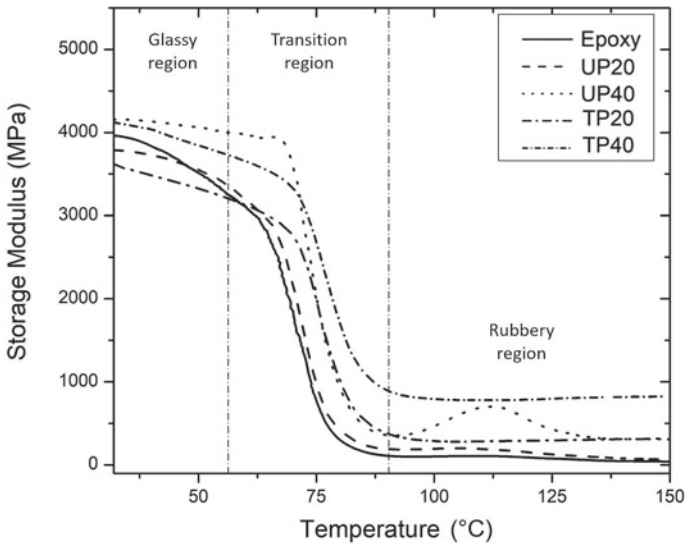

Fig. 1 Storage moduli curves of all investigated conditions

These curves are typically related to the elastic modulus associated with the material response to a viscoelastic deformation. The dynamic modulus can be directly associated with the stiffness of the material. Therefore, it measures the elastic or potential energy stored by the material [24]. It is possible to notice that the studied conditions exhibit similar behavior as three distinct regions can be identified as function of the temperature. In the first region, it takes place in relatively lower temperatures where the material tends to be a rigid solid, and this region is known as the glassy region. The second is named as transition region where the storage modulus, or dynamic modulus, displays a severe decrease. Finally, the third region is known the rubbery plateau region where a steady-state condition is observed and the material changes from stiff to soft rubber-like behavior. This may be associated with a light cross-linked material [25]. Despite the characteristic behavior displayed, some differences can also be observed, and those could be associated with both the GO treatment and/or the amount of reinforcement. The first difference between both cases lies in the measured values of dynamic modulus. The composites reinforced with GO-treated piassava tend to exhibit lower values of E' in comparison with those reinforced with untreated piassava fiber. As aforementioned, E' can be associated with the elastic energy stored by the material. It can also be noticed that when the amount of reinforcement was increased, the storage modulus was increased as well. This could be directly associated with a growth of the viscoelastic stiffness, indicating a higher energy storage by the system. Such relations might be a consequence of how the load is transferred from the epoxy matrix to the piassava fibers, either untreated or GO treated, thus indicating the quality of the adhesion between fiber and matrix, as will be further discussed.

The effectiveness of the reinforcement in polymeric matrix composites can be evaluated by the C-constant parameter, which is defined as shown in the equation below:

$$C = \frac{\left(E'_g/E'_r\right)_{composite}}{\left(E'_g/E'_r\right)_{matrix}}$$

where E'_g and E'_r are the dynamic modulus in the glassy and rubbery regions, respectively. Lower the constant (C), the higher the effectiveness of the reinforcement [26]. It is evident from Fig. 2 that TP40 showed the lowest value (i.e., 0.05051), which can be associated with excellent stress transfer between the epoxy matrix and fiber reinforcement, good dispersion of reinforcement in the epoxy matrix, and superior fiber–matrix interfacial adhesion. This provides the evidence for the effectiveness of GO treatment in enhancing the matrix/reinforcement interface.

Curves of the variation of tangent delta (tan δ) with temperature are presented in Fig. 3. The parameter tan δ can be associated with the mechanical damping factor of material. Defects contribute towards damping, especially those associated with interfaces [27].

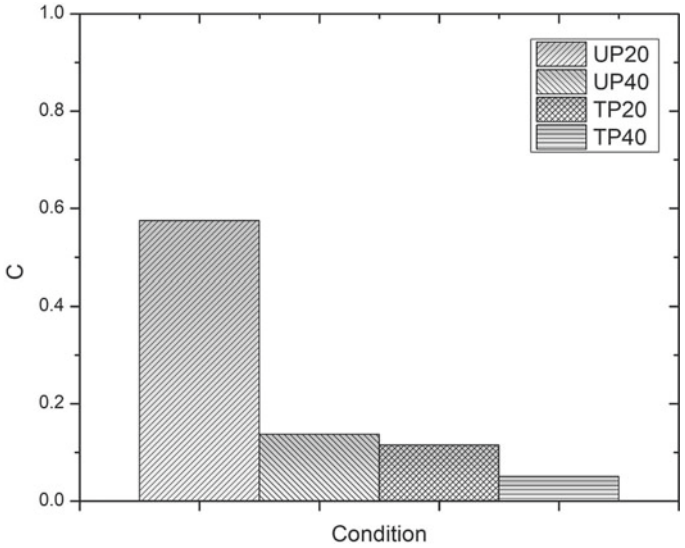

Fig. 2 Values of constant (C) for all piassava/epoxy composites

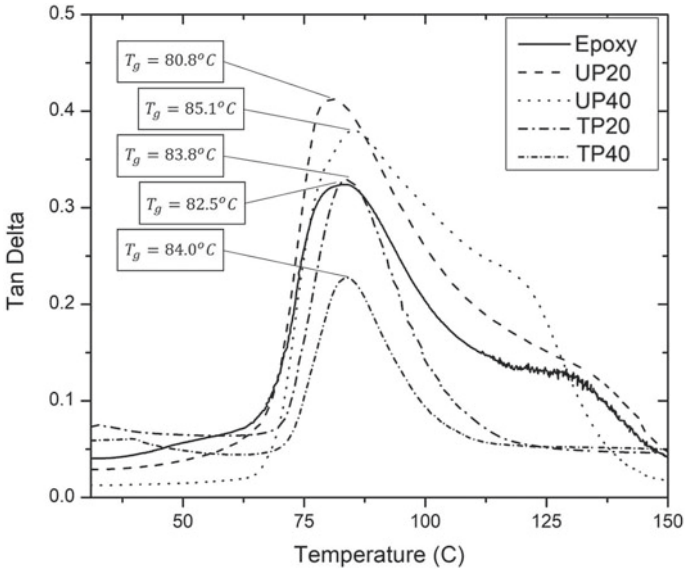

Fig. 3 Tan delta of all investigated conditions

Therefore, the condition with a lower amount of fiber reinforcement should display greater structural damping [28]. Indeed, such expected behavior was observed as the untreated condition which exhibited the highest values for tan δ. As the GO-treated conditions tend to present lower values, this suggests an improvement of the interfacial bond fiber/matrix by the GO coating. On the other hand, the glass transition temperature (Tg) could also be estimated in Fig. 3. A great variation from the measured value for the epoxy condition was not observed; however, it is suggested that higher amounts of reinforcement could shift the Tg for higher values.

Conclusions

The influence of graphene oxide (GO) treatment of the piassava fiber on the thermal behavior of epoxy/piassava composites was studied by dynamic mechanical analyses (DMA). The main results can be summarized as follows:

- The DMA results revealed remarkable changes caused by the amount of fiber reinforcement in the epoxy matrix composites as well as the GO treatment of such fibers. The main DMA parameter, dynamic modulus, showed to be sensitive to these changes.
- The C-constant parameter was used to verify the quality of the matrix/reinforcement adhesion. It was observed that the GO-treatment conditions presented the lowest values of C, thus indicating the superior interfacial adhesion.
- It was shown that the Tg was not severely impacted in any case. This suggests that the cross-linking of the epoxy during cure is relatively independent of the amount of reinforcement or its surface treatment.
- Finally, this novel result obtained by the GO treatment of the piassava fiber and therefore the enhancement of thermal properties might contribute to the applications of epoxy composites reinforced with natural fibers in conditions above room temperature.

Acknowledgements The authors thank the support of this investigation by the Brazilian agencies CNPq, FAPERJ, and CAPES. One of the authors (F.d.C.G.F) acknowledges the Coordenação de Aperfeiçoamento de Pessoal de Nível Superior-Brasil (Capes)-Finance Code 001 for the financial support.

References

1. Li M, Pu Y, Thomas VM, Yoo CG, Ozcan S, Deng Y, Nelson K, Ragauskas AJ (2020) Recent advancements of plant-based natural fiber-reinforced composites and their applications. Eng Compos Part B. https://doi.org/10.1016/j.compositesb.2020.108254
2. Sanjay MR, Madhu P, Jawaid M, Senthamaraikannan P, Senthil S, Pradeep S (2018) Characterization and properties of natural fiber polymer composites: a comprehensive review. J Clean Product 172:566–581
3. Güven O, Monteiro SN, Moura EAB, Drelich JW (2016) Re-emerging field of lignocellulosic fiber-polymer composites and ionizing radiation technology in their formulation. Polym Rev 56:706–736
4. Pickering KL, Efendy MA, Le TM (2016) A review of recent developments in natural fibre composites and their mechanical performance. Compos Appl Sci Manuf 83:98–112
5. Wambua P, Ivens J, Verpoest I (2003) Natural fibres: can they replace glass in fibre reinforced plastics? Compos Sci Technol 63(9):1259–1264
6. Monteiro SN, Drelich JW, Lopera HAC, Nascimento LFC, Luz FS, da Silva LC et al (2019) Natural fibers reinforced polymer composites applied in ballistic multilayered armor for personal protection—an overview. In: Green materials engineering. Springer, Cham, pp 33–47
7. Garcia Filho FC, Monteiro SN (2019) Piassava fiber as an epoxy matrix composite reinforcement for ballistic armor applications. JOM 71(2): 801–808
8. Demosthenes LCC, Nascimento LFC, Monteiro SN, Costa UO, Garcia Filho FC, Luz FS, Oliveira MS, Ramos FJHTV, Pereira AC, Brage FO (2020) Thermal and structural characterization of buriti fibers and their relevance in fabric reinforced composites. J Mater Res Technol 9(1):115–123
9. Reis RHM, Nunes LF, Oliveira MS, Veiga Jr VF, Garcia Filho FC, Pinheiro MA, Silva ACR, Candido VS, Monteiro SN (2020) Guaruman fiber: another possible reinforcement in composites. J Mater Res Technol 9(1):622–628
10. Garcia Filho FC, Luz FS, Nascimento LFC, Satyanarayana KG, Drelich JW, Monteiro SN (2020) Mechanical properties of Boehmeria nivea natural fabric reinforced epoxy matrix composite prepared by vacuum-assisted resin infusion molding. Polymers 12:1311. https://doi.org/10.3390/polym12061311
11. Wu C, Yang K, Gu Y, Xu J, Ritchie RO, Guan J (2019) Mechanical properties and impact performance of silk-epoxy resin composites modulated by flax fibres. Compos Appl Sci Manuf 117:357–368
12. Oliveira MS, Garcia Filho FC, Luz FS, Pereira AC, Demosthenes LCC, Nascimento LFC, Lopera HAC, Monteiro SN (2019) Statistical analysis of notch toughness of epoxy matrix composites reinforced with fique fabric. J Mater Res Technol 8(6):6051–6057
13. Chaitanya S, Singh I, Song JI (2019) Recyclability analysis of PLA/Sisal fiber biocomposites. Compos Part B Eng 173:106895
14. Depuydt DEC, Soete J, Asfaw YD, Wevers M, Ivens J, van Vuure AW (2019) Sorption behavior of bamboo fibre reinforced composites, why do they retain their properties? Compos Appl Sci Manuf 119:48–60
15. Monteiro SN (2008) Properties and structure of Attalea funifera (piassava) fibers for composite reinforcement—a critical discussion. Nat Fibers 6(2):191–203
16. Satyanarayana KG, Guimaraes JL, Wypych F (2007) Studies on lignocellulosic fibers of Brazil. Part I: source, production, morphology, properties and applications. Compos Appl Sci Manuf 38:1694–1709
17. Garcia Filho FC, Oliveira MS, Pereira AC, Nascimento LFC, Matheus JRG, Monteiro SN (2020) Ballistic behavior of epoxy matrix composites reinforced with piassava fiber against high energy ammunition. J Mater Res Technol 9(2):1734–1741
18. Hassan MM, Wagner MH (2016) Surface modification of natural fibers for reinforced polymer composites: a critical review. Rev Adhes Adhes 4(1):1–46

19. Luz FS, Garcia Filho FC, Gomez-del Rio MT, Nascimento LFC, Pinheiro WA, Monteiro SN (2020) Graphene-incorporated natural fiber polymer composites: A first overview. Polymer 12(7):1601
20. Sarker F, Karim N, Afroj S, Koncherry V, Novoselov KS, Potluri P (2018) High-performance graphene-based natural fiber composites. ACS Appl Mater Interfaces 10(40):34502–34512
21. Chen J, Huang Z, Lv W, Wang C (2018) Graphene oxide decorated sisal fiber/MAPP modified PP composites: toward high-performance biocomposites. Polym Compos 39:E113–E121
22. Costa UO, Nascimento LFC, Garcia JM, Monteiro SN, Luz FS, Pinheiro WA, Garcia Filho FC (2019) Effect of graphene oxide coating on natural fiber composite for multilayered ballistic armor. Polymers 11(8):1356
23. Garcia Filho FC, Luz FS, Oliveira MS, Pereira AC, Costa UO, Monteiro SN (2020) Thermal behavior of graphene oxide-coated piassava fiber and their epoxy composites. J Mater Res Technol 9(3):5343-5351
24. Jawaid M, Abdul Khalil HPS, Hassan A, Dungani R, Hadiyane A (2013) Effect of jute fibre loading on tensile and dynamic mechanical properties of oil palm epoxy composites. Compos Part B Eng 45:619–624
25. Saba N, Jawaid M, Alothman OY, Paridah MT (2016) A review on dynamic mechanical properties of natural fibre reinforced polymer composites. Constr Build Mater 106:149–159
26. Costa CSMF, Fonseca AC, Serra AC, Coelho JFJ (2016) Dynamic mechanical thermal analysis of polymer composites reinforced with natural fibers. Polym Rev 56:362–383. https://doi.org/10.1080/15583724.2015.1108334
27. Zhang Z, Wang P, Wu J (2012) Dynamic mechanical properties of EVA polymer modified cement paste at early age. Phys Procedia 25:305–310
28. Neuba LM, Junio RFP, Ribeiro MP, Souza AT, Lima ES, Garcia Filho FC, Figueiredo ABHS, Braga FO, Azevedo ARG, Monteiro SN (2020) Promising mechanical, thermal, and ballistic properties of novel epoxy composites reinforced with cyperus malaccensis sedge fiber. Polymers 12:1776. https://doi.org/10.3390/polym12081776

Characterization of Ultra-Hard Ceramic $AlMgB_{14}$-based Materials Obtained by Self-propagating High-Temperature Synthesis and Spark Plasma Sintering

Ilya Zhukov, Pavel Nikitin, and Alexander Vorozhtsov

Abstract In this work, $AlMgB_{14}$–TiB_2 composite materials were obtained by thermochemical-coupled self-propagating high-temperature synthesis (SHS) and subsequent spark plasma sintering. The phase composition of the raw powder mixture, the obtained SHS product, and the sintered sample was determined. The main phase in the obtained SHS product and the sintered sample is TiB_2. The structure of the sample is not uniform. Large TiB_2 agglomerates were found. The hardness of the obtained sample is 26.1 GPa.

Keywords Composite materials · $AlMgB_{14}$-TiB_2 self-propagating high-temperature synthesis · Spark plasma sintering · Hardness

Introduction

The study of polycrystalline materials based on $AlMgB_{14}$ (so-called BAM) began in 2000 in the Ames Laboratory. $AlMgB_{14}$-based materials have a high hardness (28–32 GPa) [1] and a low coefficient of friction (COF, 0.08–0.02) [2, 3] and can be used as additional wear-resistant coatings for cutting tools, as well as in the production of machine parts as a structural material [4].

It should be noted that the addition of TiB_2 to $AlMgB_{14}$ leads to a significant increase in hardness up to 46 GPa [1]. Typically, hot pressing or spark plasma sintering (SPS) methods are used to obtain dense $AlMgB_{14}$–TiB_2 composites [5–10]. A feature of these methods, in contrast to the method of high-temperature vacuum sintering [11], is that the powdered mixture is simultaneously sintered and consolidated. In this case, pre-reacted $AlMgB_{14}$ and TiB_2 are often used as raw materials.

One of the methods for preparing TiB_2 is self-propagating high-temperature synthesis (SHS) [11]. Boron and titanium powders are mixed in a (69 wt. % Ti + 31 wt. % B) stoichiometric ratio. When the reaction between the components is

I. Zhukov · P. Nikitin (✉) · A. Vorozhtsov
Tomsk State University, Tomsk 634050, Russia
e-mail: upavelru@yandex.ru

J. Li et al., *Characterization of Minerals, Metals, and Materials 2021*,
The Minerals, Metals & Materials Series,
https://doi.org/10.1007/978-3-030-65493-1_4

initiated (mainly due to the supply of heat from an external source), an exothermic reaction occurs with the release of a large amount of thermal energy (4250 kJ / kg, $T_{ad} = 3193$ K). Thus, this energy can be used to initiate a reaction in an endothermic mixture, in particular, in the initial mixture of Al: Mg: B to produce $AlMgB_{14}$.

In this work, $AlMgB_{14}$–TiB_2 powder was obtained by thermochemical-coupled self-propagating high-temperature synthesis, which was then used as the raw material for obtaining dense composite samples by spark plasma sintering. Thus, the purpose of this work is to study the phase composition, microstructure, and properties of these materials.

Methods and Materials

$Al_{12}Mg_{17}$ intermetallic powder (purity ≥ 99.2%, average particle size <d>~0 μm), amorphous black boron powder (purity ≥98.8%, <d>~1–2 μm), and titanium powder (purity ≥99.2%, <d>~140 μm) are used as the raw materials. The advantages of using $Al_{12}Mg_{17}$ intermetallic powder instead of elemental powders of aluminum and magnesium are given in [12]. $Al_{12}Mg_{17}$ and B were mixed in an atomic ratio of 2:14 and used as an acceptor mixture. Ti and B powders were mixed in a stoichiometric ratio (69 wt. % Ti + 31 wt. % B) and used as a donor mixture. Then obtained powders were mixed in a mass ratio of 60 wt. % ($Al_{12}Mg_{17}$: B) + 40 wt. % (Ti + 2B). From the obtained powder mixture, the sample was cold pressed in a 23-mm-diameter steel die. Finally, the sample was sintered in the SHS mode.

The obtained SHS product was milled by hand in a mortar. Then, the obtained SHS powder was sintered by spark plasma sintering at a temperature of 1450° C under a pressure of 70 MPa. XRD analysis was performed using a Shimadzu XRD 7000 diffractometer. The microstructure of the SHS product and sintered material was determined using Joel JSM-640 microscope. Vickers microhardness (HV) was measured using a Qness-60 microhardness tester with a load of 19.6 H and a dwell time of 30 s on polished surfaces.

Results and Discussion

Figure 1 shows the XRD patterns of the raw powder mixture, SHS product, and sintered sample. The main phase in the SHS product and the sintered sample is TiB_2. In our previous work [13], we proposed the probable mechanism for the formation of $AlMgB_{14}$ during the self-propagating high-temperature synthesis of the 70 wt. % (Al12Mg17: B)–30 wt.% (Ti + 2B) powder mixture. Briefly, in the first stage, TiB_2 is formed with the release of a large amount of thermal energy, which is spent on the endothermic reaction between aluminum, magnesium, and boron to form $AlMgB_{14}$. The $AlMgB_{14}$ content depends on the (Ti + 2B) mass content: the more (Ti + 2B) in the mixture, the higher the synthesis temperature. Temperatures above 1600 °C

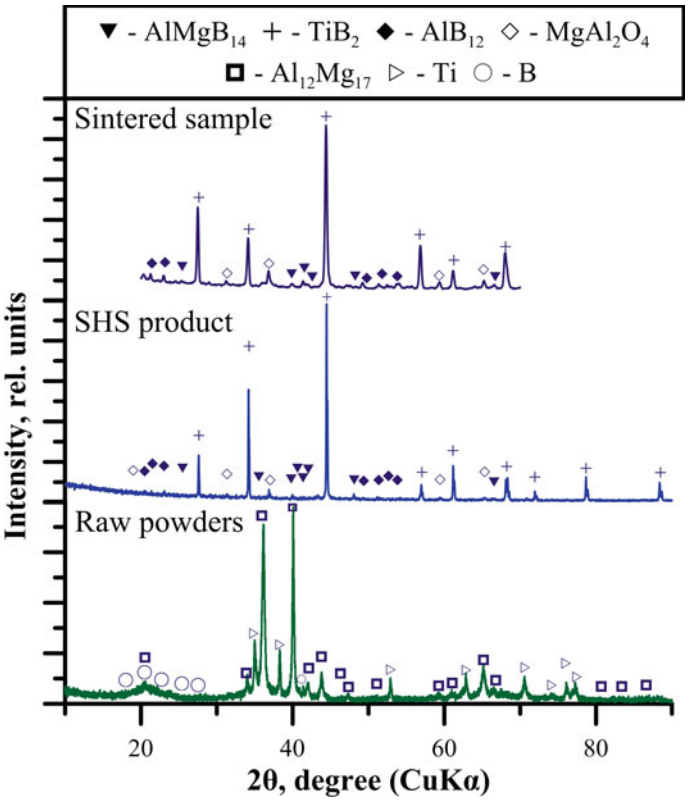

Fig. 1 XRD patterns of the raw powder mixture, SHS product, and obtained sample. (Color figure online)

lead to decomposition of $AlMgB_{14}$ into AlB_{12} and Mg, which evaporates during synthesis. A similar result is observed in this work (Fig. 1). In this case, the XRD pattern of the sintered sample does not differ from the XRD pattern of the SHS product.

The microstructure of the fracture surface of the sintered sample is shown in Fig. 2. The ceramic structure is not uniform. EDX analysis showed that Ti and B (probably TiB_2) are contained in bright regions. Al, Mg, and B are contained in dark regions, which correspond to the boron-rich compounds ($AlMgB_{14}$, AlB_{12}). The presence of agglomerates in the SHS powder leads to the formation in the ceramic structure of large areas of TiB_2 (light region). The average grain size of titanium diboride in the sintered sample is 1 μm, the density is 3.109 g/cm^3, and the microhardness is 26.1 GPa. The low hardness value may be due to the high porosity of the sample and the presence of large TiB_2 agglomerates.

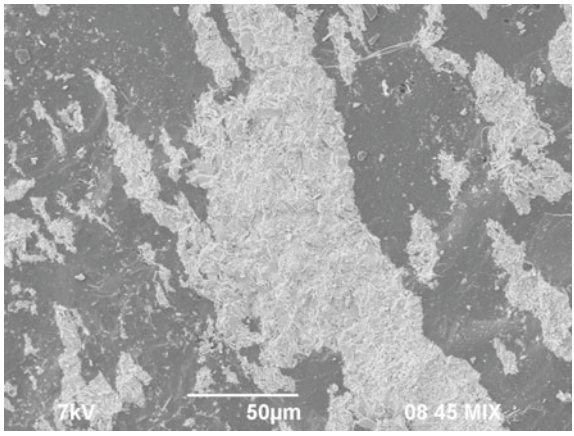

Fig. 2 SEM micrograph of the dense sintered sample

Conclusions

Studies have shown the possibility of obtaining $AlMgB_{14}$–TiB_2 composite materials by self-propagating high-temperature synthesis and subsequent spark plasma sintering. The phase composition of the raw powders, SHS product, and sintered sample was determined. The microstructure of the fracture surface of the sintered sample is shown. The microhardness of the obtained sample is 26.1 GPa. The low hardness value may be due to the high porosity of the sample and the presence of large TiB_2 agglomerates.

Acknowledgements Studies were funded by Russian Science Foundation (project no. 19-79-10042).

References

1. Cook B et al (2000) New class of ultra-hard materials based on $AlMgB_{14}$. Scripta Mater 42:597–602
2. Lu X, Yao K, Ouyang J, Tian Y (2015) Tribological characteristics and tribo-chemical mechanisms of Al–Mg–Ti–B coatings under water–glycol lubrication. Wear 326:68–73
3. Cook BA, Harringa JL, Anderegg J, Russell AM, Qu J, Blau PJ, Elmoursi AA (2010) Analysis of wear mechanisms in low-friction $AlMgB_{14}$–TiB_2 coatings. Surf Coat Technol 205(7):2296–2301
4. Ahmed A, Bahadur S, Russell AM, Cook BA (2009) Belt abrasion resistance and cutting tool studies on new ultra-hard boride materials. Tribol Int 42:706–713
5. Kevorkijan V, Škapin SD, Suvorov D (2015) Synthesis and characterisation of ultra-hard and lightweight $AlMgB_{14}$–$xTiB_2$ composites for wear-resistance and ballistic protection. Metal Mater Eng 21(1):45–56
6. Cook BA, Peters JS, Harringa JL, Russell AM (2011) Enhanced wear resistance in $AlMgB_{14}$–TiB_2 composites. Wear 271(5–6):640–646

7. Li CS, Yang F, Yan G, Xiong XM, Liu GQ, Sun YY, Feng JQ (2014) $AlMgB_{14}$–TiB_2 synthesized by a two-step heat-treatment method. J Alloy Compd 587:790–793
8. Lei Y, Meng Q, Zhuang L, Chen S, Hu L, Cheng H (2014) Friction and wear behavior of $AlMgB_{14}$–TiB_2 composite at elevated temperature. Tribol Lett 56(3):435–442
9. Lei Y, Meng QS, Zhuang L, Chen SP, Dai JJ (2015) Oxidation behavior of $AlMgB_{14}$-TiB_2 composite at elevated temperature. Appl Surf Sci 347:155–161
10. Ahmed A, Bahadur S, Cook BA, Peters J (2006) Mechanical properties and scratch test studies of new ultra-hard $AlMgB_{14}$ modified by TiB_2. Tribol Int 39:129–137
11. Matveev A, Zhukov I, Ziatdinov M, Zhukov A (2020) Planetary milling and self-propagating high-temperature synthesis of Al-TiB_2 composites. Materials 13(5):1050
12. Zhukov IA, Nikitin PY, Vorozhtsov AB, Perevislov SN, Sokolov SD, Ziatdinov MH (2020) The use of intermetallic Al_xMg_y powder to obtain $AlMgB_{14}$-based materials. Mater Today Commun 22:100848
13. NikitinPY, Zhukov IA, Matveev AE, Sokolov SD, Boldin MS, Vorozhtsov AB (2020) $AlMgB_{14}$–TiB_2 composite materials obtained by self-propagating high-temperature synthesis and spark plasma sintering. Ceramics International

Preparation of Ceramic Coating on Copper Substrate with Transitional Layer by Low-Temperature Slurry Method

Zefei Zhang, Hao Bai, Lihong Li, and Min Zhong

Abstract Ceramic coating prepared by slurry method has been applied to the metal surface for its excellent properties which can enhance the reliability and durability of industrial equipment. While, for copper as the substrate, a transition coating is needed between ceramic coating and copper substrate to solve the problem caused by the difference of their thermal expansion coefficients. In this paper, NiCoCrAlY transition coating was prepared by atmospheric plasma spraying (APS) and ceramic top coating was prepared by slurry method. The results show that the transition coating plays a key role in obtaining excellent properties. The thermal shock resistance life at 600 °C reached 110 cycles and the bonding strength was 15.04 MPa. The oxidation-resistant effect δ of the ceramic coating can reach 87.29% at 800 °C. Thus, the ceramic coating prepared can be applied to copper equipment for protection against harsh environments.

Keywords Ceramic coating · Transition coating · Copper · Thermal shock resistance

Introduction

Ceramic coating prepared by slurry method (or thermal chemical reaction method) has been applied to the metal surface, which can withstand harsh conditions to enhance the reliability and durability of industrial equipment for its excellent

Z. Zhang · H. Bai (✉)
State Key Laboratory of Advanced Metallurgy, University of Science and Technology Beijing, 30# Xueyuan Road, Beijing 100083, China
e-mail: baihao@metall.ustb.edu.cn

School of Metallurgical and Ecological Engineering, University of Science and Technology Beijing, 30# Xueyuan Road, Beijing 100083, China

L. Li · M. Zhong
Shantou Huaxing Metallurgical Equipment Co., Ltd., Shantou 515063, China

Raoping Yuexing Copper Processing Co., Ltd., Chaozhou 515726, China

J. Li et al., *Characterization of Minerals, Metals, and Materials 2021*,
The Minerals, Metals & Materials Series,
https://doi.org/10.1007/978-3-030-65493-1_5

properties [1, 2]. The advantages of ceramic materials include their high temperature stability, high melting point, good wear resistance, and excellent corrosion resistance. The preparation of ceramic coating on metal surface can be used to obtain both the strength and toughness of the metal and the high-temperature resistance, abrasion resistance, and corrosion resistance of ceramics [3], since the desired performance of the ceramic coating can be obtained by designing the raw material formula through thermodynamic calculation and dynamic condition analysis. There have been some studies on ceramic coatings by slurry method [4–6]. Xiao et al. [4] prepared ceramic coating on Q235 steel substrate using SiO_2, Cr_2O_3, Al_2O_3, and MgO as ceramic aggregates. Abbas et al. [5] prepared ceramic coating on nickel alloy substrate to prevent corrosion of nickel alloy in high-temperature applications with oxidizing environments using Y_2O_3 stabilized ZrO_2 powder and nickel powder as ceramic aggregates. Silicon-oxide series of ceramics, such as SiO_2, Al_2O_3, and ZrO_2, are valued for their hardness, high wear resistance, high corrosion resistance, and chemical stability. In this present work, SiO_2, Al_2O_3, and ZrO_2 were used as ceramic aggregates to prepare ceramic coating on copper substrate, to protect copper-made equipment from severe harsh environments for improving its performance and service life.

It is worth noting that in previous studies the substrates were mostly steel or its alloy (e.g. Q235 steel and nickel alloy). However, for the preparation of ceramic coating on copper surface by slurry method, there are two technical difficulties needing to be solved. One is that copper has a high coefficient of thermal expansion [7], which leads to high thermal stress between ceramic coating and substrate in high-temperature environment, causing the ceramic coating to crack and even fall off. This will greatly reduce the service life of the ceramic coating. The other is that copper is easily oxidized in high-temperature environment [7], which weakens the bonding between ceramic coating and substrate. The single-layer (SL) coating as mentioned in the above reports may not solve both difficulties. Therefore, we propose the scheme of double-layer (DL) coating including transition coating and ceramic top coating.

In the present work, we prepared ceramic coatings on copper substrate, by using SiO_2, Al_2O_3, and ZrO_2 as the ceramic aggregates and sodium silicate water glass as the binder. The microstructure of ceramic coatings was analyzed. And the bonding strength, oxidation resistance, and thermal shock resistance of ceramic coatings were tested.

Experimental Procedure

Coating Materials

The copper sheet which was used as substrate material was cut into specimen plates with dimensions 20 mm × 20 mm × 5 mm for the microstructure and Φ25 mm × 5 mm for the performance, using a wire cutting machine. The raw materials

as ceramic aggregates were SiO_2 (analytical reagent, China), Al_2O_3 (Analytical Reagent, China), and ZrO_2 (analytical reagent, China). Sodium silicate water glass (chemically pure, China) was used as the coating binder and its molar ratio of SiO_2/Na_2O is 3.3.

Coating Preparation

All of these copper substrates were cleaned in acetone for 30 min and in an ultrasonic bath containing an alcohol solution for 6 h to remove the grease on the surface of the substrates. The cleaned copper specimens were sandblasted with 60 mesh sand in a box-type sandblasting machine, for two purposes. One is to remove the oxide scale and the other is to increase the surface roughness and strengthen the bond between the substrate and the coating. The roughness Ra of the substrate after sandblasting was tested to be 10.82 μm. The NiCoCrAlY transition coating with a thickness of about 100 μm was plasma-sprayed on the copper surface. The spraying parameters are shown in Table 1.

The slurry preparation proceeded as follows: The different ceramic aggregates were mixed in the proportions reported in Table 2. Then, the mixed ceramic aggregates were added to water glass to obtain mixed ceramic slurry. Next, the homogeneous ceramic slurry was brushed to coat onto the specimen and before coating the surface of specimens was cleaned by alcohol. Subsequently, the coated specimen dried in shade for 5 h, and then put in drying oven at 85 °C for 5 h. Finally, the coated specimen was sintered at 600 °C for 4 h in a muffle furnace. The SL coating was fabricated according to the above procedure without the process of preparing transition coating.

Table 1 Parameters of plasma spraying

Parameter	Values	Parameter	Values
Flow rate of primary gas	45 L/min	Spray distance	100 mm
Feed stock giving rate	40 g/min	Power	500 A × 70 V
Primary gas	Ar	Secondary gas	H2
Gun moving rate	800 mm/s	Spray inclinations	90°

Table 2 Formula of ceramic slurry system

Chemical compositions	SiO_2	Al_2O_3	ZrO_2
Content/%	49.6	26.3	24.1

Microstructure Characterization

The cross section was first polished with coarse sandpaper, then with metallographic sandpaper 0#, 1#, 2#, 3#, 4#, and 5# until the surface scratches were small and uniform, and then polished with diamond polishing gypsum, until a non-diffuse, specular, reflective characteristic was obtained. The surface and cross-section microstructure of the coating was observed by scanning electron microscopy.

Bonding Strength Test

The bond strength of coating was measured by dual sample tensile method according to ASTM C633-2001 standards [8] for its application. E-7 high-temperature adhesive was selected as the interface binder in this test. The back of the specimen with coatings was coarsened by sandpaper. After that, the specimen was bonded dual tension rods by adhesive, and then clamped with fixtures, whose contact pressure was 0.05 MPa. Tensile specimens are first placed at room temperature for 3 h, then heated to 100 °C and cured for 3 h in a furnace, and finally cooled in air for tensile testing. In this experiment, a computer-controlled electronic universal testing CMT5105 machine was used at a loading speed of 0.1 mm/min. Three samples were tested, and then the average value was taken as the measured bond strength of the coating.

Oxidation Test

In order to assess the oxidation resistance of ceramic coating, isothermal oxidation tests were heat treated in ambient air at 800 °C. Each sample was placed in a corundum crucible. The DL coating was on one side of the copper substrate. Prior to the tests, the crucibles were heat treated at 800 °C for 24 h for constant weight. The samples with crucibles were cooled down to room temperature in furnace and measured using an electronic balance with a resolution of 0.1 mg. The oxidation resistance tests were conducted using the specimen mass reduction method [6, 9], where oxidation losses were determined from the difference between the mass of the specimen before and after oxidation, as shown by the following equations:

$$\text{Oxidation loss} \quad \Delta W_{\text{bare}} = (W_{\text{bare1}} - W_{\text{bare2}})/2S \tag{1}$$

$$\text{Oxidation loss} \quad \Delta W_{\text{coated}} = [(W_{\text{coated1}} - W_{\text{coated2}}) - (W_{\text{bare1}} - W_{\text{bare2}})/2]/S \tag{2}$$

$$\text{Oxidation resistant effect (\%)} \quad \delta = \frac{\Delta W_{\text{bare}} - \Delta W_{\text{coated}}}{\Delta W_{\text{bare}}} \times 100\% \tag{3}$$

where W_1 (mg) and W_2 (mg) are the weight of sample before and after heating, respectively, and S represents one side surface area of the sample.

Salt Water Test

The corrosion stability of ceramic coating was investigated through salt water test. 3.5 wt% NaCl solution was selected as the corrosion solution. Place the coating sample into the corrosion solution, and the copper substrate was also tested as a control sample. After 200 h of corrosion, the sample was taken out and rinsed with water, and then blown dry with a blower. Finally, the morphology of the sample was observed.

Thermal Shock Resistance Test

The thermal shock resistance of the coating was evaluated by water quenching method. Samples were put into a muffle furnace, heated to 600 °C, and preserved for 10 min, then taken out and quickly quenched in room temperature water, and removed after water surface was calm. After drying, the coating was observed. If there is no crack or spalling on the surface, it will be regarded as a thermal shock cycle. Repeat this process until nearly one-third of the coating peeled off [10]. The average value was calculated as a criterion for evaluating the thermal shock resistance of the coatings.

Results and Discussion

Coating Morphology Analysis

The morphology images of the SL coating sample and DL coating sample are shown in Fig. 1. The SL coating cracked and fell off after sintering, while the surface of DL coating sample remained intact. The interface between copper and ceramic coating of the SL coating sample was oxidized, and the adhesion of oxide to copper substrate is relatively small, which made the ceramic coating easy to fall off with copper oxide from the substrate. Besides, due to the high different thermal expansion coefficients of the ceramic coating and the copper substrate, the coating causes a large thermal stress, which causes the coating to be exfoliated. Therefore, without the transition layer, the ceramic coating cannot be directly prepared on the copper substrate.

The surface microstructure of the transition coating and ceramic coating of DL coating sample is shown in Fig. 2. The molten and semi-molten spraying particles

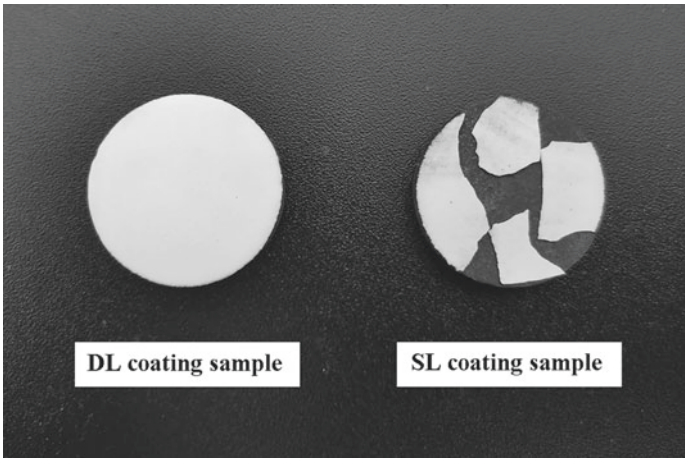

Fig. 1 Macrostructures of samples DL coating and SL coating

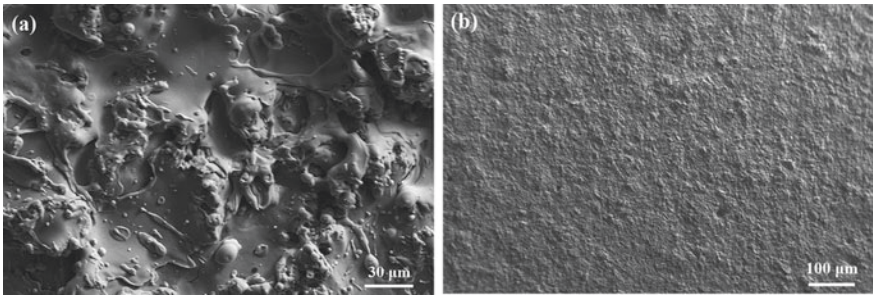

Fig. 2 Surface SEM micrographs of ceramic coatings

impact the surface of the substrate at a certain speed, so that the uneven surface is filled with deformation particles. After condensation and shrinkage, the particles and the concave and convex parts of the substrate surface are mechanically occluded together. From Fig. 2a, the surface of the NiCoCrAlY coating is uneven, which derive from the deposition of the NiCoCrAlY particles on the surface of the copper substrate after high-temperature melting and cooling in the plasma spraying process. From Fig. 2b, the surface of ceramic coating is compact and there was no evidence of defects.

The SEM image of the polished cross section of the DL coating sample is shown in Fig. 3. It can be observed that the ceramic coating was uniform and closely combined with the transition coating after sintering. This is because the sintered slurry contained sodium silicate. After the slurry solidified, the sodium silicate formed a

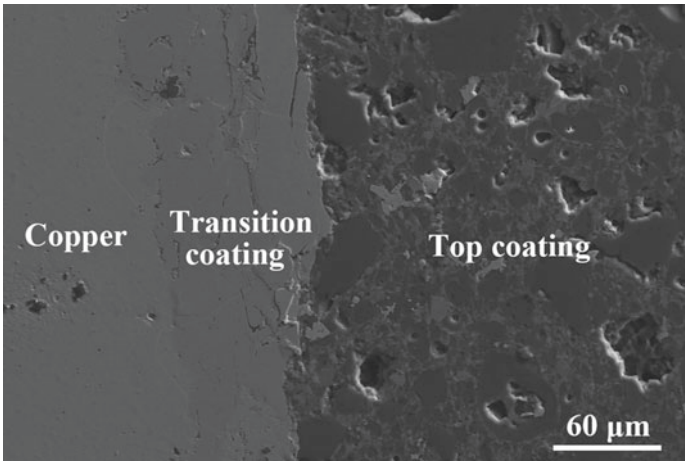

Fig. 3 Cross-sectional SEM micrograph of ceramic coatings

three-dimensional network structure, resulting in tight bonds with the ceramic aggregates and transition coating [11, 12]. Also, it could be seen that the transition coating–substrate interface and the transition coating–ceramic coating interface were rough. The roughness could enhance mechanical bonding of the interface.

Bonding Strength

Figure 4 shows the image of the broken surfaces of the DL coating samples after tensile test. The fracture position of the coating is between the ceramic coating and

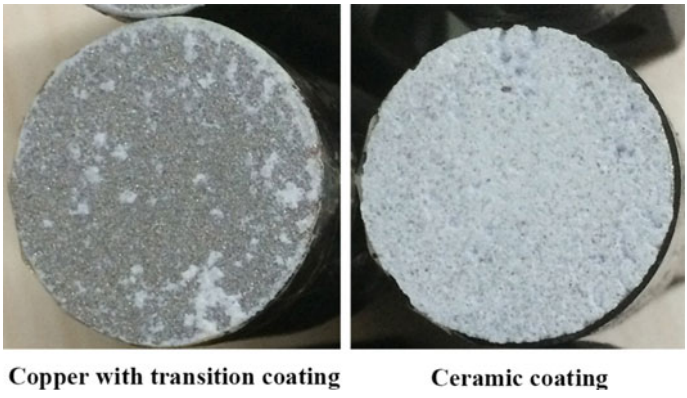

Fig. 4 Broken surfaces of the DL coating sample after tensile test. (Color figure online)

Table 3 Bonding strength of ceramic coating

Samples	1	2	3	Average value
Content/kN	6.9	7.4	7.8	7.37
Section diameter/mm	25	25	25	25
Bonding strength/Gpa	14.06	15.08	15.89	15.00

the transition coating, and there is no fracture inside the ceramic coating or transition coating, which indicated the excellent cohesion strength inside the whole coating. The results show the bonding strength between the transition coating and copper substrate is greater than between the ceramic coating and the transition coating. Table 3 shows the tensile test data of bonding strength of DL coating samples. The average bonding strength was 15.00 MPa, while the SL coating fell off after sintering and its bonding strength did not need to be tested. Because the transition coating eliminates the physical property deficiency caused by the difficult bonding between the ceramic coating and the substrate, it improves the bonding condition between the ceramic coating and substrate. From Fig. 3, roughness of the transition coating–top coating interface is a characteristic feature of plasma spraying, which could enhance mechanical bonding between the transition coating and the ceramic coating

Oxidation Test

The oxidation weight changes of bare and coated samples at 800 °C were analyzed by the specimen mass reduction method to conduct the oxidation-resistant effect of the coating. Oxide mass gains per unit area of the samples were calculated according to Eqs. (1) and (2), and isothermal oxidation kinetics curves were plotted in Fig. 5 for the blank copper substrate and the DL coating. It can be concluded from Fig. 5 after an oxidation time of 20 h, the mass gains of copper with DL coatings at 800 °C were lower than the corresponding value on the blank substrate. The oxidation-resistant effect δ of the ceramic coating can be reached at 87.29% at 800 °C. The DL coating prevented the inward diffusion of oxygen from the air to the coating–substrate interface, thereby greatly decreasing the oxidation rate of the copper. In conclusion, the ceramic coating effectively protected the copper from the harsh environment by significantly decreasing the rate of oxidation, which would correspond to increased service life of the copper or blast furnace tuyere made of copper.

Salt Water Test

Figure 6 shows the morphology of the copper substrate and DL coating before and after salt water test. When pure copper was put into sodium chloride solution,

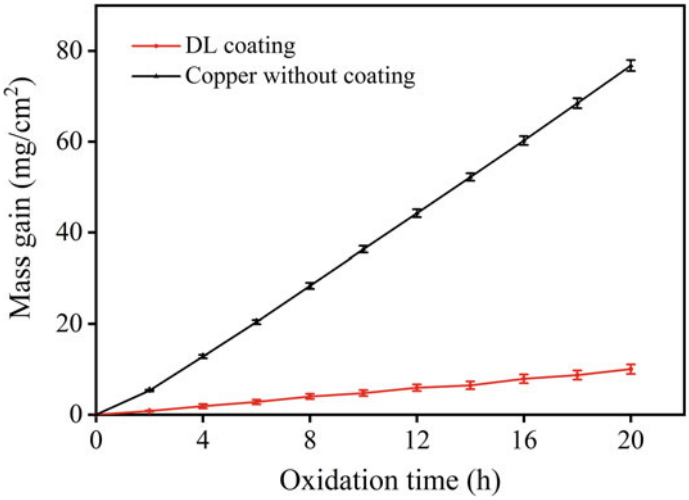

Fig. 5 Weight gains of uncoated copper and DL coating sample at 800 °C in air. (Color figure online)

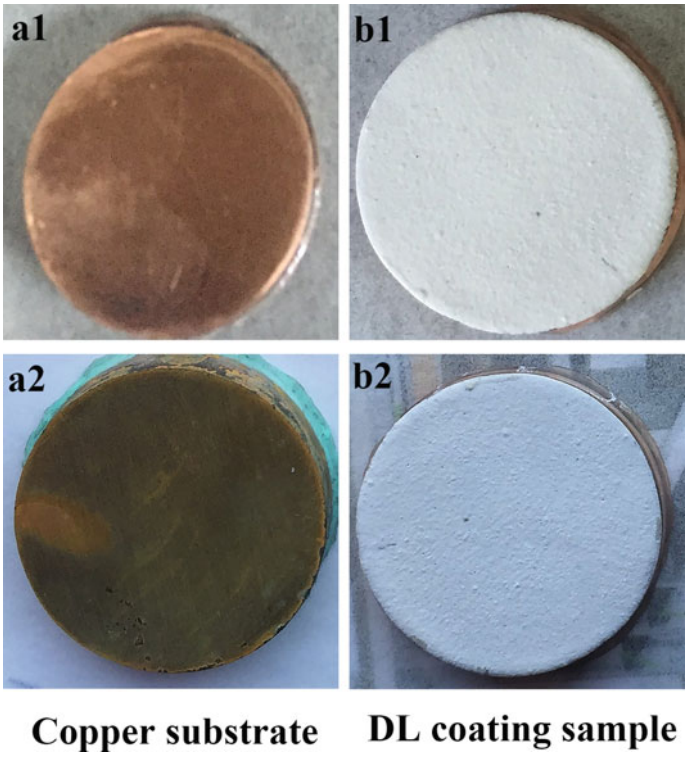

Fig. 6 Morphology of the copper substrate and DL coating before (1) and after (2) salt water test. (Color figure online)

numerous corrosion microcells were formed on the copper surface, resulting in the preferential corrosion of copper around sodium chloride. Sodium chloride can not only enhance the electrolysis, but also partially dissolve the corrosion products on the copper surface, and oxygen will be transferred to the copper, which will cause the copper to be continuously corroded. After the DL ceramic coating was prepared on copper, the ceramic coating can prevent the corrosion medium and effectively protect the copper substrate.

Thermal Shock Studies

When the ceramic coating on metal is applied in unstable high-temperature environment, the thermal stress will be produced at the interface between the ceramic coating and the substrate, due to their thermal expansion coefficient difference, and the change of thermal stress will cause the ceramic coating to crack and even fall off [13]. The thermal shock resistance of the ceramic coating can reflect the service life of the ceramic coating under the unstable high-temperature environment. The thermal shock resistance test was subjected to 600 °C for the ceramic coating samples, considering the limit temperature of tuyere surface. Thermal shock resistance test was carried out for the DL coating sample and test results are shown in Table 4**.** Figure 7 shows the optical photomicrographs of the DL coating before and after thermal shock tests at 600 °C in air. The thermal shock resistance life at 600 °C reached 110 cycles. However, the SL coating sample cracked and fell off after sintering, from Fig. 1. It can be concluded that the transition layer can significantly improve the thermal shock resistance.

Table 4 Thermal shock resistance of ceramic coating

Test temperature	600 °C
Thermal shock cycles	110 cycles

Fig. 7 Optical photomicrographs of the DL coating after thermal cycling at 600 °C in air. (Color figure online)

Conclusions

This study combined the plasma spraying method and the slurry method to prepare a double-layer (DL) coating including transition coating and ceramic top coating on the copper surface. At the same time, the single-layer (SL) coating was also prepared with the slurry spraying method for a comparative analysis. Compared with SL coating, the DL coating had good microstructure. NiCoCrAlY transition coating is helpful to the bonding strength and thermal shock resistance of the ceramic coating. The ceramic coating has high oxidation-resistant effect owing to its good structure, so that copper can be protected from high temperature.

Acknowledgements This work was supported by the Innovation Talents Fund Project of University of Science Technology Beijing and the Chaozhou Science and Technology Project of Guangdong (No. 2019ZX10).

References

1. Wang JQ, Yuan YC, Chi ZH, Zhang GX (2018) High-temperature sulfur corrosion behavior of h-BN-based ceramic coating prepared by slurry method. Mater Chem Phys 206:186–192
2. Li H, Ke Z, Li J, Xue L, Yan Y (2017) An effective low-temperature strategy for sealing plasma sprayed Al_2O_3-based coatings, J Eur Ceram Soc 38(4):1871–1877
3. Luo H, Song P, Khan A, Feng J, Zang JJ, Xiong XP, Lü JG, Lu JS (2017) Alternant phase distribution and wear mechanical properties of an Al_2O_3-40wt% TiO_2 composite coating. Ceram Int 43(9):7295–7304
4. Xiao K, Xue W, Li ZL, Wang JR, Li XM, Dong CF, Wu JS, Li XG, Wei D (2018) Effect of sintering temperature on the microstructure and performance of a ceramic coating obtained by the slurry method. Ceram Int 44(10):11180–11186
5. Abbas MR, Uday MB, Noor AM, Ahmad N, Rajoo S (2016)Microstructural evaluation of a slurry based Ni/YSZ thermal barrier coating for automotive turbocharger turbine application. Mater Design 109(November 5):47–56
6. Nguyen MD, Bang JW, Kim YH, Bin AS, Hwang KH, Pham VH, Kwon WT (2018) Slurry spray coating of carbon steel for use in oxidizing and humid environments. Ceram Int 44(7):8306–8313
7. Davis JR (2001) Copper and copper alloys. ASM Specialty Handbook
8. ASTM Standards C 633–2001, American Society of Testing and Materials, Philadelphia, PA
9. Shan X, Wei LQ, Liu P, Zhang XM, Tang WX, Qian P, He Y, Ye SF (2014) Influence of coo glass-ceramic coating on the anti-oxidation behavior and thermal shock resistance of 200 stainless steel at elevated temperature. Ceram Int 40(8):12327–12335
10. Shan X, Wei LQ, Zhang XM, Li WH, Tang WX, Liu Y, Tong J, Ye SF, Chen YF (2015) A protective ceramic coating to improve oxidation and thermal shock resistance on CrMn alloy at elevated temperatures. Ceram Int 41(3):4706–4713
11. Gao HT, Liu XH, Chen JQ, Qi JL, Wang YB, Ai ZR (2018) Preparation of glass-ceramics with low density and high strength using blast furnace slag, glass fiber and water glass. Ceram. Int. 44(6):6044–6053

12. Viktor S, Galyna K (2017) Effect of water glass on early hardening of Portland cement. Procedia Eng 172:977–981
13. Wang DS, Tian ZJ, Wang JW, Duan ZY, Shen LD, Huang YH (2010) Thermal shock behavior of laser remelting Al_2O_3-13%TiO_2 ceramic coating fabricated by plasma spraying. Appl Laser 30(4):264–269

Part IV
Characterization of Mechanical Properties

Analysis of the Elasto-Plastic Behavior of SAE 1045 Steel Submitted to Cyclic Loads

Matheus Henriques Cordeiro, Victor Barbosa Souza, Amanda Camerini Lima, and Niander Aguiar Cerqueira

Abstract This work proposes an elasto-plastic study of SAE 1045 steel through a stress versus cyclic deformation curve, which was the basis for calculating the material's hardening parameters, defining the isotropic hardening value as null and kinematic hardening value as 415.05 MPa. Therefore, due to the wide use of SAE 1045 steel in structures and elements that undergo cyclical stresses, the parameters defined in the present work are highly relevant for the analysis of structures based on this material, making it easier to meet the needs during research, diagnostics, or sizing using this steel. The mathematical model used proved to be efficient in generating results compatible with those expected based on the bibliography.

Keywords Characterization · Mechanical properties · Cyclic loads · Elasto-plasticity

Introduction

One of the uses of steel is in the construction of structural components. These elements used in engineering practice are often subjected to high stress loads and high energy impact, which can cause deterioration of the material and reduce its useful life [2].

The metallic materials have two phases, an elastic one, when a sample of a material is requested by a force and undergoes a deformation and, after the removal of the applied force, it recovers its original dimensions, and the plastic phase, where the deformation becomes permanent [3]. The linear relationship between stress and strain in an idealized material forms the basis of the mathematical theory of elasticity, however, a real structure is a very complex body, with complex stress states that defy the idealized calculation based on this theory [4]. Thus, the theory of plasticity is necessary as a complement to the theory of elasticity, concerned with making analyses of the stresses and deformations of the studied bodies, which are in the plastic or

M. H. Cordeiro · V. B. Souza · A. C. Lima · N. A. Cerqueira (✉)
SociedadeUniversitária Redentor, REDENTOR, BR 356 km 25, Itaperuna, Rio de Janeiro, Brasil
e-mail: prniander@gmail.com

J. Li et al., *Characterization of Minerals, Metals, and Materials 2021*,
The Minerals, Metals & Materials Series,
https://doi.org/10.1007/978-3-030-65493-1_6

elastic regime [5]. Plasticity plays an important role in the study of structures by describing the behavior of materials in a more realistic way than a simple linear and elastic analysis [6].

The damage induced by plastic stress is an important source of potential failure of engineering components, which is a type of permanent deformation or distortion that occurs when a material is subjected to applied stresses that exceed its yield stress, causing the material to stretch, compress, fold, or shear [1]. Therefore, for greater precision in the study of metallic materials, the two processes need to be considered, forming an elasto-plastic concept.

The elasto-plastic behavior is suitable for the study of most metals and metal alloys at room temperature, where time has no impact on the results [7]. Elasto-plasticity is the behavioral study of materials that after a loading cycle has permanent deformation, and plastic phenomena are considered instantaneous and are not affected by the loading rate [8]. There are two types of hardening as a result of these loads. The kinematic, when the material is loaded in order to overcome its flow limit in a specific direction, being subsequently loaded in the opposite direction, a reduction of its flow limit is generated, resulting in the preservation of the flow surface of the material in relation to its size, taking place in the stress space [9]. This characteristic is commonly observed, the effect being called the Bauschinger effect, being visible in materials under cyclic loading regime [8].

There is also the isotropic hardening, which consists of increasing the specific flow limit of the material, which may be linear or not, with an increase in the flow surface of the material being observed during the plastic regime, the shape and location of the material being unchanged [10]. Even though the tension is increased in each new cycle, this increase is caused by the hardening [11]. Considerando a ampla aplicação de componentes estruturais de aço e as consequências desastrosas causadas pela falha estrutural, mais trabalhos de pesquisa devem ser dedicados à análise estrutural da evolução dos danos e à sua avaliação de modo a reconhecer o mecanismo de falha do aço estrutural [12].

Materials and Methods

SAE 1045 steel is mainly used for the manufacture of axles, in general, cylinders, railway equipment, gears, and crankshafts, and is of great importance in the manufacture of products for the oil industry and for machine parts that require high mechanical resistance. This material is often used in industrial practice for components subject to cyclic loading [13]. The chemical composition of a raw material certificate is shown in Table 1.

The tensile test was carried out according to the American Society for Testing and Materials E8/8 M-13th standard [15]. Relative humidity of the environment in which the machinery is disposed of is approximately 50%; the temperature at 25 °C; definition of the applied load cell defined in the value of 10,000 Kgf; and traction application speed of 1.00 mm/min.

Table 1 Chemical composition of SAE 1045 steel

Chemical composition of the SAE 1045 (wt.%)							
C	Mn	Si	P	S	Ni	Cr	Mo
0.49	0.59	0.21	0.019	0.02	0.02	0.03	0.005

It is important to note that the speed of application of the loading has a direct impact on the yield stress, and it is essential to observe the parameters stipulated in the test standards in order to obtain reliable results [15]. The experimental results obtained in the linear tensile tests can be used to define the parameters for the load-discharge cyclic tensile test, such as the test frequency and the deformation level, in order to guarantee the progressive formation of inelastic deformation in each cycle of the cyclic test [16].

The conversion of the linear test to the cyclic test was performed using a mathematical model. The tractive-compressive traction test encounters a series of difficulties for its performance, both economic and practical, making the development of research in this field complex [17]. There is not always the possibility of execution, as the equipment that performs this test is limited and the necessary specimens have complex dimensions, not always accessible in common machining equipment, in addition to eliminating the material's buckling resistance. As the test carried out was of the monotonous type, the costs of the procedure are much lower, since it is not necessary to manufacture complex specimens or the use of more expensive equipment.

To allow the calculations to be performed, one must initially apply the hardening modeling equations in X and Y, from the coefficients a and b, making it possible to define the tension related to the traction Eq. (2) and the compression Eq. (3).

$$\begin{cases} \sigma = X + Y; Tração \\ \sigma = X - Y; Compressão \end{cases} \tag{1}$$

$$\sigma = \frac{a}{b} + \left(X_0 - \frac{a}{b}\right) e^{b\left(\varepsilon_0^p - \varepsilon^p\right)} + v_1\left(1 - e^{-v_2 p}\right) + \sigma_y, \; seX\left(\varepsilon^p = \varepsilon_0^p\right) = X_0 \tag{2}$$

$$\sigma = -\frac{a}{b} + \left(X_0 + \frac{a}{b}\right) e^{b\left(\varepsilon_0^p - \varepsilon^p\right)} - v_1\left(1 - e^{-v_2 p}\right) - \sigma_y, seX\left(\varepsilon^p = \varepsilon_0^p\right) = X_0 \tag{3}$$

The definition of the coefficients related to the isotropic hardening V1 and V2, the stabilized cycle must be obtained from an X x ε ˆ p curve, applying a limit in which the plastic deformation tends to infinity, if

$$\lim_{p \to \infty} Y = v_1 + \sigma_y = Y_{\max} \tag{4}$$

In principle, it is applied that $Y \cong Y_{\max}$, where $Y_{\max}$ x is obtained within the elastic region defined at the ends of the cycle as shown in Fig. 1.

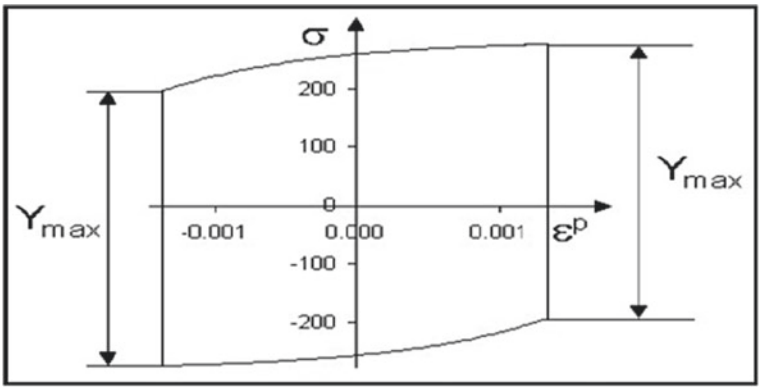

Fig. 1 Plastic deformation limit

According to Eq. (5), when it is observed that $Y_{\max}$ is less than the yield stressσ_y, it is considered that there is no isotropic hardening; therefore, the value of $Y_{\max}$ is adopted for the yield stress.

$$Y_{\max} < \sigma_y \rightarrow \dot{Y}(t) = 0 \forall t \rightarrow Y = Y_{\max} \forall t e \sigma_y = Y_{\max} \tag{5}$$

The stabilized cycle is determined from

$$\begin{cases} \sigma = X - Y; Tração \\ \sigma = X + Y; Compressão \end{cases} \tag{6}$$

The construction of the Xx ε ˆ p curve is allowed in the stabilized cycle (Figs. 2 and 3).

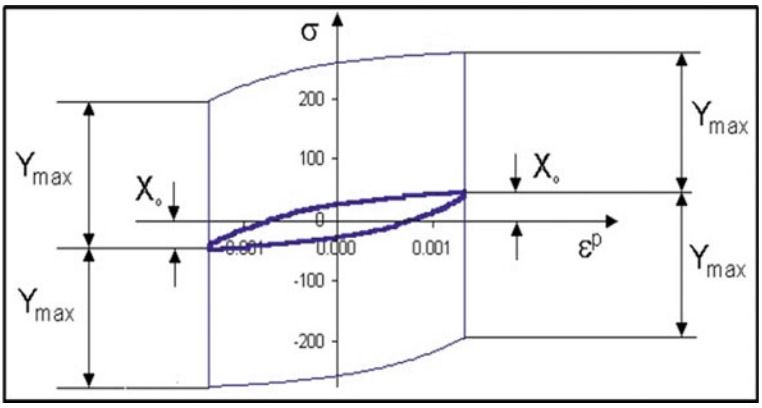

Fig. 2 Tension x plastic deformation curve. (Color figure online)

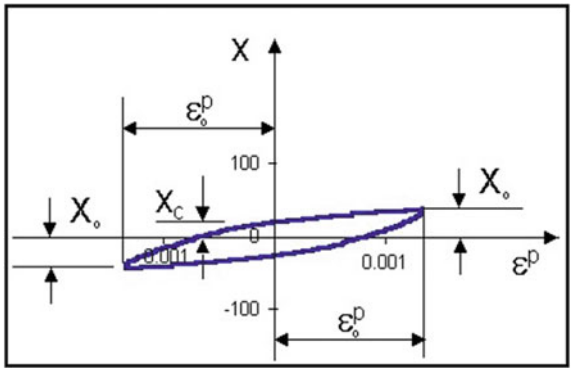

Fig. 3 Tension x isolated plastic deformation curve. (Color figure online)

The definition of the coefficients ***a*** and ***b*** can be done by analyzing the points A $= \left(\varepsilon_0^p; X_0\right)$; B $= (0; X_c)$; C $= \left(-\varepsilon_0^p; -X_0\right)$, shown in Fig. 4.

With the observation of points A, B, and C, its relationship with the kinematic hardening coefficients can be determined in Eqs. (7)–(10):

$$X_0 = \frac{a}{b} + \left(X_c - \frac{a}{b}\right)e^{-b\varepsilon_0^p} \tag{7}$$

$$X_c = \frac{a}{b} + \left(-X_0 - \frac{a}{b}\right)e^{-b\varepsilon_0^p} \tag{8}$$

$$-X_0 = \frac{a}{b} + \left(X_c - \frac{a}{b}\right)e^{b\varepsilon_0^p} \tag{9}$$

$$X_c = \frac{a}{b} + \left(X_0 - \frac{a}{b}\right)e^{-b\varepsilon_0^p} \tag{10}$$

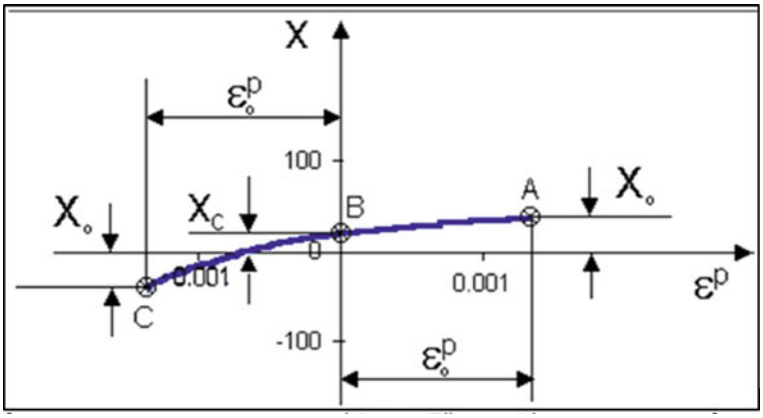

Fig. 4 Points for determining coefficients A, B, and C. (Color figure online)

Equation (11) is determined from Eqs. (7) to (10):

$$(X_0 - X_c)e^{b\varepsilon_0^p} + (X_0 + X_c)e^{-b\varepsilon_0^p} = 2X_0 \tag{11}$$

The value of ***b*** is defined using the root of Eq. (12):

$$\Phi(b) = (X_0 - X_c)e^{b\varepsilon_0^p} + (X_0 + X_c)e^{-b\varepsilon_0^p} - 2X_0 \tag{12}$$

The value of ***a*** is found in the substitution of the value of b in Eqs. (7)–(10). From Eq. (1), it is defined that Y is given by Eqs. (13) and (14):

$$Y = \sigma - \frac{a}{b}\left(1 - e^{bp}\right) - \sigma_y \tag{13}$$

$$Y = v_1\left(1 - e^{v_2\varepsilon^p}\right) \tag{14}$$

The construction of the curve Y × ε ˆ obtained from the curve σ × ε ˆ p by means of Eq. (5), and the values of V1 and V2 are defined with adjustments of Eq. (13). The representation of the elasto-viscoplastic behavior of the material is defined by the equations of Lemaitre and Chaboche, allowing the study of fluency and cyclic loads. The term viscous in uniaxial tests is shown in Eq. (15):

$$F = |\sigma - X| - Y \leq 0;\ \dot{p} = \left[\frac{F}{K}\right]^N;\ p(t=0) = 0 \tag{15}$$

Equation (15) adds the new coefficients N and K, which are associated with viscous terms.

The viscosity of the material is characterized by these new coefficients. This viscous term is presented in metal alloys subjected to temperatures above one-third of the ambient temperature. In the determination of the tensile elasticity limit, the same procedure applied to elasto-plasticity is applied to identify the elasticity limit, and this parameter must be defined by means of a tensile test with a deformation rate of $\dot{\varepsilon} \leq 10^{-5}$.

Results and Discussion

Figure 5 shows the result of the linear tensile test of the material.

The regions shown are elastic region, region of slip of discrepancies, region of uniform hardening, and the region of non-uniform hardening culminating in the failure of the material. Based on this graph, a conversion was performed on a mathematical model, generating a graphical stress x cyclic strain, simulating a tensile-compressive test. The result is shown in Fig. 6.

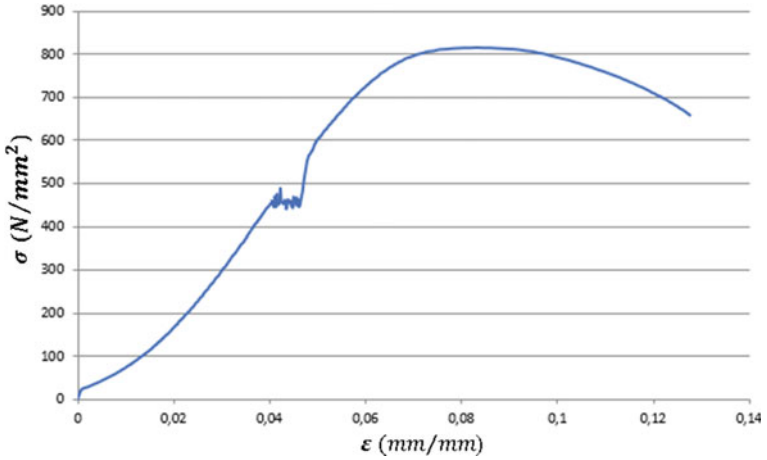

Fig. 5 Traction test result. (Color figure online)

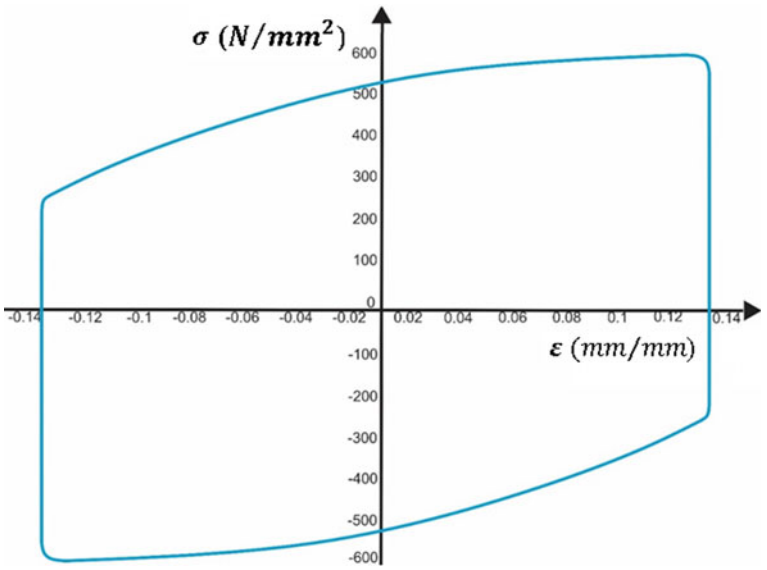

Fig. 6 Graphical stress (MPa) x deformation (mm/mm). (Color figure online)

In Fig. 6, it is necessary to highlight four different curves, the vertical elements, where the isotropic hardening of the material is observed, and the inclined curves, where the kinematic hardening is observed. From the data obtained after the conversion, it is possible to perform the calculations to define the values of the hardening of the material, thus being possible to analyze the elasto-plastic behavior of SAE 1045 steel.

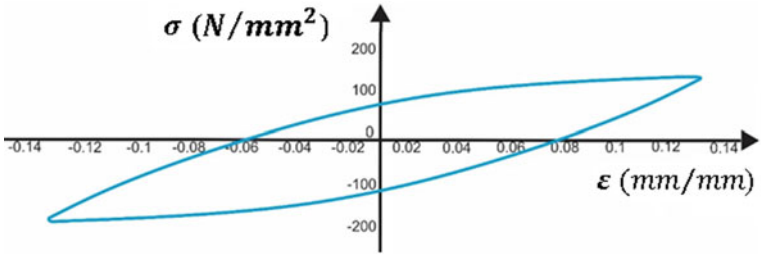

Fig. 7 Stabilized cycle (stress curve x plastic deformation). (Color figure online)

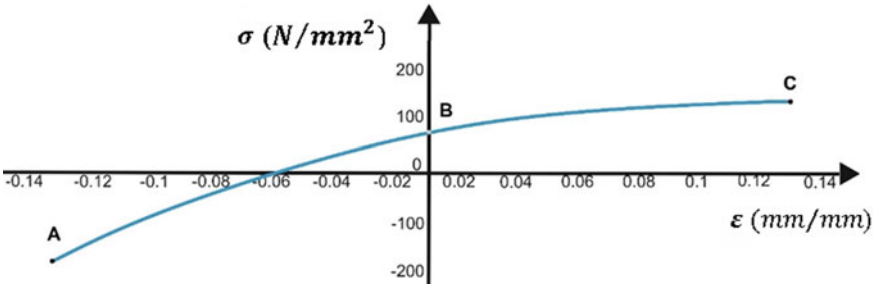

Fig. 8 Identification of points A, B and C. (Color figure online)

For analysis, it is necessary to stabilize the cycle, as shown in Figure 7.

Observing this curve of Fig. 7, it is possible to identify the necessary points for the definition of the parameters necessary for carrying out the calculations (Fig. 8).

The following coordinates are identified: A (−0.1228703; −136.4557); B (0.60.4568); and C (0.128703; 136.4557).

According to these coordinates, the values of the parameters necessary for the calculations are defined: X_0 = 136.45571 and X_c = 60.45675.

Once these variables are defined, it is possible to calculate the coefficient (b) through the roots of Eq. (12):

$$(b) = (136.45571 - 60.45675)e^{0.12870304b} + (136.45571 + 60.5675)e^{-0.12870304b} - 2(136.45571)$$
$$(b) = 7.87012$$

With the known coefficient (b), its value was replaced in Eq. (7) to obtain the value of the "a" coefficient, the result being

$$136.45571 = \frac{a}{7.87012} + \left(60.45675 - \frac{a}{7.87012}\right)e^{-(7.87012)(0.12870304)}$$
$$(a) = 415.05$$

Table 2 Results of hardening

Hardening type	Value (N/mm^2)
Isotropic	0
Kinematic	415.05

In view of these results, isotropic and kinematic hardening can be defined. Firstly, it is important to define that the isotropic hardening occurs only within the regime of elastic deformations, where the stress paths remain internal to the flow surfaces in cyclic loads [18]. Therefore, it is possible to affirm that the isotropic hardening in the tested material is null, since the stresses to which the element was subjected are above the yield stress of this steel. The isotropic constitutive model does not apply to this material, it is the use of a model that defines the hardening with stresses above the flow surface of the material, considering only the plastic deformation suffered [19]. Parameter (a) defines the kinematic hardening of the material. According to this theoretical basis, the hardening was defined as shown in Table 2.

In his work, Norman and Calmunger [20] performs tests and modeling of the cyclic behavior of bimetal steel coated with stainless steel, where it is shown that mechanical responses of bimetal steel SC under cyclic loads were significantly different from those under monotonic loads, and bimetallic steel SC exhibited Bauschinger effect visible.

Gadalińska et al. [21] studied the mechanical tests on high-performance marine steel corroded under cyclic load, where it was concluded that the influence of corrosion damage on the mechanical properties of the steel is complex and cannot be characterized by the reduction of the section alone. Cyclic loading increases the maximum tension of the steel at the expense of the final deformation capacity, which can also be noticed in the present work. According to Wang [1] when using cyclical, compressive-compressive tests in his work, where a cyclic test and a numerical analytical assessment of thin-walled cold-formed steel shear walls using tube trusses were carried out, and the results were much closer of a real situation compared to linear tensile tests.

Norman and Calmunger [20] demonstrate that the complicated cyclic constitutive behavior of cast iron, involving a non-linear elastic regime, tension and compression asymmetry, variable elastic modulus and an inflection in the tension–compression hardening curve, originates from the behavior of interaction between the constituents of the matrix and graphite, using a micromechanical model. This shows the relevance of models that are based on cyclical loads.

The distribution of stresses between the phases has a significant impact on the type of reinforcement of fully lamellar perlite. The initial flow limit is affected only by the ferrite hardness (depending on the inter-lamellar spacing), because equal stresses are located in both phases. However, during the plastic deformation, the transfer of tension from ferrite to cementite (a process independent of inter-lamellar spacing) dominates in the deformation strengthening the perlite; therefore, the effect of the ferrite's low hardness is not significant, showing that the stresses can vary in the same material depending on the crystalline formation [21].

Conclusion

The part of mechanics that studies elasto-plastic regimes is of great breadth and depth. The behavior of elasto-plastic materials needs to be formulated for the general space of stresses and deformations, which becomes very complex [22]. The area is of great importance in understanding how a material behaves in the face of different circumstances to which it can be subjected, such as analysis of metal structures in buildings [23], or analysis of cracks in gas pipelines [24], allowing for correct dimensioning and a good safety margin against project failures.

The mathematical model used was efficient in generating results compatible with those expected based on the bibliography. The relevance of this model is even more present due to its economic viability, since cyclical tests demand a high financial availability when compared to a conventional linear tensile test. The terms found in this work can be used for numerical modeling using computational software, as the necessary parameters, terms of greater complexity to be established, were defined.

These terms can be applied in failure analysis of this steel subjected to different loading conditions, for simulations of failure of metallic structures and for a better sizing both economically and in safety of mechanisms, using, for example, the finite element method. Therefore, due to the great use of SAE 1045 steel in structures and elements that undergo compressive-compressive efforts, the parameters defined in the present work are highly relevant for the analysis of structures based on this material, making it easier to meet the needs during research, diagnostics, or design using this steel.

References

1. Wang X et al (2019) Plastic damage evolution in structural steel and its non-destructive evaluation. J Mater ResTechnol
2. El Sayed T et al (2009) Computational assessment of ballistic impact on a high strength structural steel/polyurea composite plate**.** Comput Mech, Pasadena 4:525–534
3. Garcia A et al (2012) Materials testing (In Portuguese), 2nd edn. LTC, Rio de Janeiro
4. Chen, WF, Han DJ (1988) Plasticity for structural engineers. Springer, New York
5. Freitas A (2010) Modeling the evolution of orthotropic damage coupled to elastoplasticity in metals (In Portuguese).117 f. Monograph (Specialization)—Mechanical Engineering Course, Federal University of Santa Catarina, Florianópolis
6. Cecilio DL (2011) Modeling and elasto-plastic simulation in finite elements. (In Portuguese). 2011. 68 f. Dissertation (Master's)—Civil Engineering Course, Faculty of Civil Engineering, Architecture and Urbanism, State University of Campinas, Campinas**,** 2011.
7. Fernandes DHL (2015) Experimental analysis and identification of elasto-viscoplasticity properties of duplex and super duplex stainless steel (In Portuguese). 49 f. Dissertation (Master)—Mechanical Engineering Course, School of Engineering, Universidade Federal Fluminense, Niterói
8. de Souza Neto E, Peric D, Owen D (2008) Computational methods for plasticity: theory and applications. Wiley
9. Prager W (1955) The theory of plasticity: a survey of recent achievements. In: Proceedings, institution of mechanical enganes

10. Neves RS (2015) Implementation and validation of constitutive models for cyclic plasticity (In Portuguese). 106 f. Thesis (Master)—Master Course in Integrity of Engineering Materials, University of Brasília, Brasilia
11. LIRA DC (2011) Modeling and elasto-plastic simulation in finite elements (In Portuguese). Dissertation (Master in Structures)—Faculty of Civil Engineering and Architecture, State University of Campinas, Campinas
12. Yoda R et al (2010) Plastic deformation and creep damage evaluations of type 316 austenitic stainless steels by EBSD. Mater Caracterization, Osaka 10:913–922
13. Saalfeld S et al (2019) On the influence of overloads on the fatigue performance of deep rolled steel SAE 1045. Int J Fatigue, Kassel (126):221–230, maio 2019
14. Raheem Z (2019) Designation: E8/E8M—13a Standard test methods for tension testing of metallic materials 1. https://doi.org/10.1520/E0008_E0008M-13A
15. da Silva ALVC (2011) Special steels and alloys, 3rd edn. Blucher, São Paulo(In Portuguese)
16. Motta EP et al (2018) Analysis of the cyclic tensile behaviour of an elasto-viscoplastic polyvinylidene fluoride (PVDF). Poly Test, Niteroi (67), 503–512
17. Duarte RP (2015) Simplified obtaining of cyclic stress-strain curves from monotonous tests (In Portuguese). 96 f. Dissertation (Master)—Mechanical Engineering Course, School of Engineering of Federal Fluminense University, UFF, Niterói, 2015
18. Lemaitre J, Chaboche J (1994) Mechanics of solid materials. Cambridge University Press, Cambridge
19. Atkin RJ, Fox N (2015) An introduction to the theory of elasticity. Dover Publications, Dover
20. Norman V, Calmunger M (2018) On the micro- and macroscopic elastoplastic deformation behaviour of cast iron when subjected to cyclic loading.Int J Plasticity, Linköping 115:200–215, out. 2018
21. Gadalińska E et al (2019) Stress localisation in lamellar cementite and ferrite during elasto-plastic deformation of pearlitic steel studied using diffraction and modelling. Int J Plasticity, Warszawa 127: 1–67, dez. 2019
22. Zdravikovi L, Potts DM (2005) Modelling of a 3D excavation in finite element analysis. Geotechniqui
23. Teles, BO et al (2016) Assessment of overall stability in steel structures (In Portuguese). 143 f. Undergraduate degree—Civil Engineering Course, Federal University of Goiania (UFG), Goiânia
24. Torrico, IFA (2006) Fracture toughness in elastoplastic conditions with non-standard specimens for API 5L steels: numerical and experimental analysis (In Portuguese). 160 f. Thesis (Doctorate)—Mechanical Engineering Course, Faculty of Mechanical Engineering, Campinas State University (UNICAMP), Campinas

Characterization of Solidification Structure Morphology in High-Carbon Steel Billet by Fractal Dimension

Jianghai Cao, Zibing Hou, Zhiqiang Peng, Dongwei Guo, and Ping Tang

Abstract High-carbon steel is one of the typical high-end steels, and its solidification morphology has great influence on the quality of steels. In this work, fractal dimension was introduced to describe solidification structure morphology in 82B cord steel billet with 0.82 wt% carbon content. Fractal dimension was calculated using box-counting method (D_{Box}), sandbox method (D_{Sand}), and branching method (D_{Bran}). It was demonstrated that the fractal dimension is effective to characterize quantitatively the complexity of solidification structure morphology. The value of fractal dimension calculated by the above three methods is not the same as different calculation methods describe solidification structure characteristics from different angles. In addition, the relationship between fractal dimension and secondary dendrite arm spacing (SDAS) and segregation area ratio (R_{seg}) was discussed. Fractal dimension calculated by box-counting method was well correlated with SDAS and R_{seg}. This result demonstrated box-counting method can better reflect solidification characteristics of the billet than sandbox method and branching method.

Keywords Solidification structure · Fractal dimension · Morphology characteristics · High-carbon steel

Introduction

Macrosegregation in billets is non-uniformity of composition over large areas, and their size can vary from several millimeters, centimeters, or even meters [1]. Due to large sizes, macrosegregation is considered more harmful to finished steel properties, resulting in serious quality problems (such as crack or failure) of continuous casting

J. Cao · Z. Hou (✉) · Z. Peng · D. Guo · P. Tang
College of Materials Science and Engineering, Chongqing University, Chongqing 400044, China
e-mail: houzibing@cqu.edu.cn

Chongqing Key Laboratory of Vanadium-Titanium Metallurgy and New Materials, Chongqing University, Chongqing 400044, China

J. Li et al., *Characterization of Minerals, Metals, and Materials 2021*,
The Minerals, Metals & Materials Series,
https://doi.org/10.1007/978-3-030-65493-1_7

billet [2–4]. Macrosegregation in castings and ingots forms within the mush zone. In most cases, it is the result of slow interdendritic flow, driven by shrinkage, geometry, solid deformation, or gravity [5]. Solidification structure plays a very important role in governing the severity of macrosegregation. Therefore, quantitative characterization of solidification structure morphology is of great significance to effective control of macrosegregation defects in billets. To evaluate the solidification structure morphology, secondary dendrite arm spacing (SDAS), grain size, and the dendrite tip radius [6] are commonly used. However, the above parameters are mainly used to describe the local characteristics of solidification structure or calculate the growth behavior of a single dendrite. The parameters lack a quantitative description of the overall morphology of the solidification structure.

Morphology of cast structure in alloys is complex, diverse, and irregular due to the influence of solidification conditions and liquid fluid [7]. Fractal dimension is a quantitative parameter that characterizes the complexity and irregularity of fractal graphics [8]. In the field of metallic materials, fractal theory has been used to evaluate quantitatively material structures, such as dislocation patterns [9], fracture surface [10], grain boundaries [11], martensitic transformation [12], segregation morphology [13], and dendritic structure [14]. The previous studies show that fractal dimension can quantitatively characterize the complexity of overall dendrite morphology. However, there are many ways for calculating fractal dimension in fractal geometry. In general, different calculation methods describe fractal objects from different angles, and the value of fractal dimension is different. To the best of authors' knowledge, no study has discussed the similarities and differences of calculation method of fractal dimension to evaluate solidification structure.

In the present work, the fractal theory was applied to describe the overall morphology characterizations of solidification structure in 82B cord steel billet with 0.82 wt% carbon content. First, fractal dimension of solidification structure was calculated by box-counting method, sandbox method, and branching method. Then, the relationship between fractal dimension and secondary dendrite arm spacing (SDAS) and segregation area ratio (R_{seg}) was discussed.

Experiment

The 82B cord steel billet produced via continuous casting was used in this study. The specification of billet is given in Table 1. The cross-sectional area of the billet is 150 mm × 150 mm. The billet was preheated in advance and was etched with a volume

Table 1 Specification of cast billet samples considered in the present work

Casting speed, m/min	Superheat, ℃	Nominal composition of liquid steel, mass %				
		C	Si	Mn	P	S
1.9	29	0.82	0.22	0.50	0.008	0.008

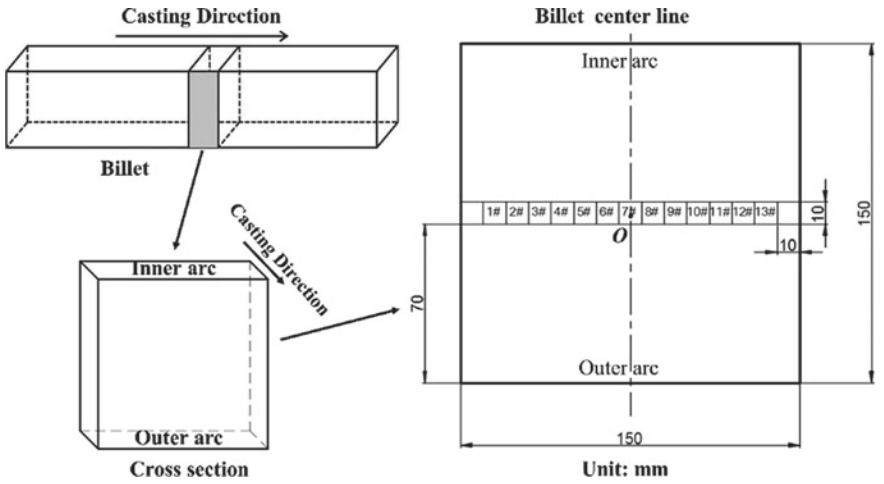

Fig. 1 Schematic of sample locations in cross section of billet [13]

ratio of 1:1 warm hydrochloric acid–water solution to reveal the cast structure. In this hot pickling experiment, the bath temperature is 60–80 °C, and the etching time is 22 min. As shown in Fig. 1, a total of 13 samples (1#–13#) were symmetrically chosen along the centerline of the billet, and each sample has a size of 10 mm × 10 mm. These macrostructures of all samples are photographed by a Sony a6000 high-definition digital camera under the same lighting conditions. According to the principle of hot pickling, the content of solute element in segregation zone is higher and the Gibbs energy is higher, the reaction with hydrochloric acid is intense, and the color becomes black when the billet is etched. After hot pickling experiment, the segregation morphology can be identified by the black zone in the macrostructure of the billet, and the white zone is solidification structure.

After obtaining macrostructure of the billet, the image was preprocessed with the image processing software without changing any morphology features. The preprocessing includes converting the original image into a grayscale image, sharpening and defogging, and adjusting the contrast. The preprocessed image of the macrostructure can clearly distinguish between the solidification structure and segregation zone, thus reducing analysis errors to a great extent.

Results and Discussion

Morphology of Solidification Structure

Macrostructure at different positions of the billet was shown in Fig. 2. The white and black regions correspond to the solidification structure and segregation, respectively.

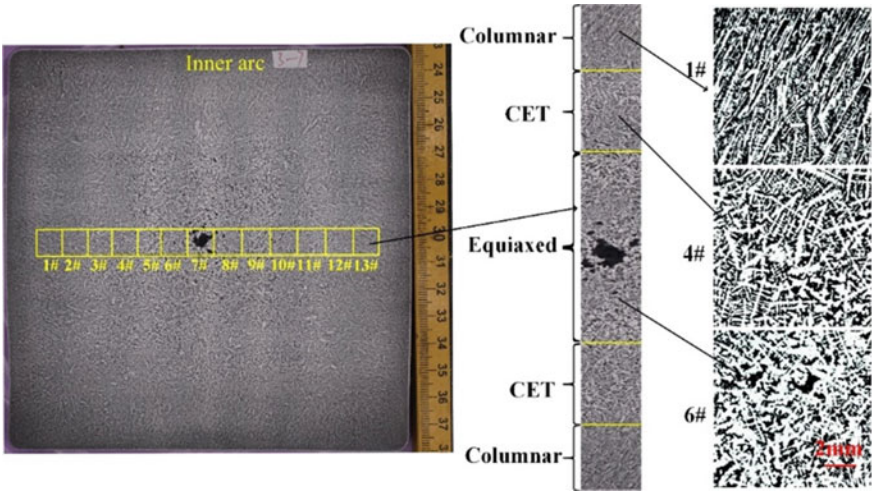

Fig. 2 Macrostructure of 82B cord steel billet produced via continuous casting [14]. (Color figure online)

The morphology of the solidification structure is different from the outer to center of the billet; it gradually changes from columnar to equiaxed grains. Samples 1#, 2#, 12#, and 13# exhibit mainly columnar grains. Samples 3#, 4#, 10#, and 11# are the columnar to equiaxed transition (CET) zone; 5#–9# exhibit equiaxed grains. Samples 1#, 4#, and 6# in Fig. 2 have the typical morphology of columnar grains, CET, and equiaxed grains, respectively.

Fractal Dimension

In fractal theory, fractal dimension is a quantitative index whose value rises with the increase of complicated shapes and forms of graphs. Effective values of fractal dimension depend on appropriate computing approaches. In general, different calculation methods describe fractal objects from different angles, and the value of fractal dimension is different. In present work, fractal dimension of solidification structure was calculated by box-counting method (D_{Box}), sandbox method (D_{Sand}), and branching method (D_{Bran}).

Box-Counting Method

Box-counting dimension [15, 16] is one of the most widely used dimension. Its popularity is largely due to its relative ease of mathematical calculation, and there are no special requirements for image morphology. Procedure of the box-counting

method is as follows: the macrostructure is covered by the square meshes with the size of r. The number of meshes, $N(r)$, in which solidification structure is included is counted. Then, the mesh size, r, is changed and the same procedure is repeated. If the following relationship (as shown in Eq. 1) is made up between the number of the meshes, $N(r)$, and the mesh size, r, the geometry of the solidification structure is fractal. In the actual calculation, a series of r and $N(r)$ are obtained. Then, the dot diagram is made with $\ln(r)$ as horizontal coordinate and $\ln(N(r))$ as vertical coordinate. The slope is obtained by linear fitting of all data points by least-square method in the diagram. Then, fractal dimension is the absolute value of slope.

$$N(r) \propto r^{D_{\text{Box}}} \tag{1}$$

where D_{Box} is the fractal dimension calculated by box-counting method; r the mesh size; and $N(r)$ the number of meshes.

Sandbox Method

The computing procedure for the sandbox method [17] was relatively simple. The calculation equations were the same as those for the box-counting method, but in the sandbox method, r was the side length of a grid that covered the macrostructure and $N(r)$ was the number of pixels of solidification structure in the grid. The procedures for box-counting method and sandbox method are presented in Fig. 3.

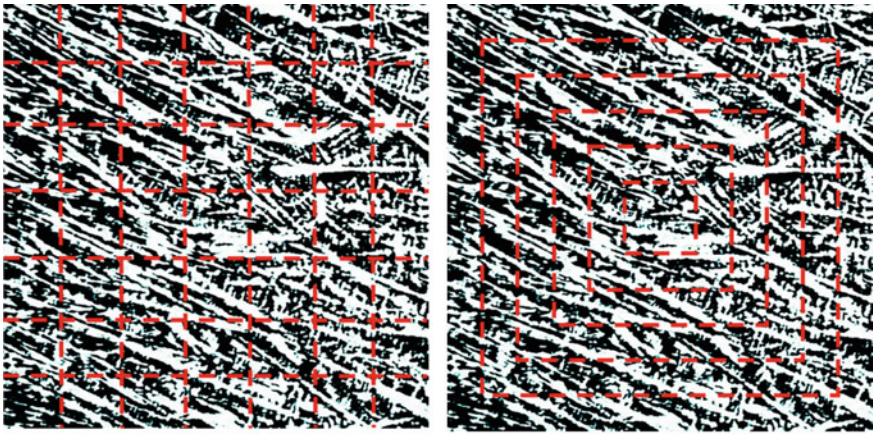

Fig. 3 Schematic of fractal dimension computational procedures: **a** box-counting method and **b** sandbox method. (Color figure online)

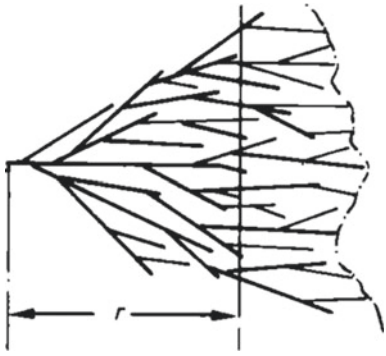

Fig. 4 Schematic of branching cluster of dendrites

Branching Method

The branching method, presented by Liu et al. [18], was applied to calculate the fractal dimension of silicon-branching clusters in Al–Si eutectic alloy. Assume that the dendrite branching initially starts at a core as shown in Fig. 4 [18]. When the dendrite branching cluster grows to $r = \mathrm{r}$, the total length of the dendrite branching cluster from 0 to r is $L(r)$. Then, r is changed and the same procedure is repeated. If the following relationship (as shown in Eq. 2) is made up between $L(r)$ and r, the geometry of the dendrite branching cluster is fractal.

$$L(r) \propto r^{D_{\mathrm{Bran}}} \tag{2}$$

where D_{Bran} is the fractal dimension calculated by branching method; r the dendrite growth length; and $L(r)$ the total length of the dendrite branching cluster from 0 to r.

D_{Box}, D_{Sand}, and D_{Bran}

Fractal dimension and corresponding fitting coefficients at different locations of billet are shown in Table 2. According to the table, the fitting coefficients are close to 1. This indicates that D_{Box}, D_{Sand}, and D_{Bran} are effective to characterize quantitatively the complexity of solidification structure morphology. In addition, the fractal dimension can characterize different types of solidification structure in a certain zone, e.g., unidirectional and equiaxed growth, without the need of a classification. This is of great significance for the effective measurement of the complex morphology of the actual billet.

Fractal dimension of solidification structure at different locations and average fractal dimension of the left–right symmetrical position are shown in Fig. 5a and b, respectively. It can be seen that fractal dimension calculated by box-counting method (D_{Box}) first increases gradually in direction from the surface to center of the billet and then fluctuates in the equiaxed grain zone. There is no obvious trend of fractal

Table 2 D_{Box}, D_{Sand}, and D_{Bran} and corresponding fitting coefficients R^2 at different locations

Sample	Box-counting method		Sandbox method		Branching method	
	D_{Box}	R^2	D_{Sand}	R^2	D_{Bran}	R^2
1#	1.7833	0.9997	2.0527	0.9984	1.8102	0.9992
2#	1.8420	0.9998	1.9642	0.9997	1.3944	0.9923
3#	1.8345	0.9998	2.0343	0.9993	1.4544	0.9844
4#	1.8331	0.9998	2.0606	0.9995	1.5757	0.9950
5#	1.8698	0.9999	2.0117	0.9997	1.2141	0.9889
6#	1.8552	0.9999	2.0728	0.9999	1.3946	0.9710
7#	1.8670	0.9999	1.8443	0.9961	1.4861	0.9931
8#	1.8465	0.9998	2.1287	0.9989	1.2887	0.9744
9#	1.8688	0.9999	1.9083	0.9995	1.3593	0.9943
10#	1.8589	0.9999	2.1912	0.9989	1.3514	0.9929
11#	1.8509	0.9999	2.0134	0.9998	1.4357	0.9903
12#	1.8139	0.9997	2.0206	0.9997	1.5312	0.9936
13#	1.7909	0.9997	1.9741	0.9998	1.7219	0.9956

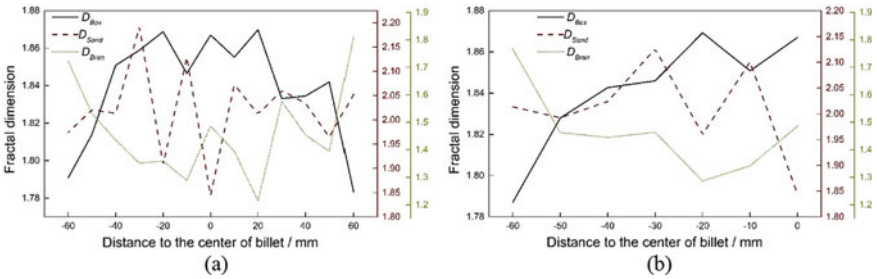

Fig. 5 D_{Box}, D_{Sand}, and D_{Bran}: **a** different locations and **b** average value of left and right sides. (Color figure online)

dimension calculated by sandbox method (D_{Sand}). Fractal dimension calculated by branching method (D_{Bran}) gradually decreases from the surface to the center of the billet.

It should be noted that fractal dimension of solidification structure calculated by different methods is different. This is mainly because the definition of fractal dimension is given on the basis of the corresponding measure, and different definitions often have different measures. Box-counting method and sandbox method are mainly based on the ratio of space occupied to describe the distribution characteristics of solidification structure in billets. Branching method mainly reflects the compactness degree of the side branches of the solidification structure.

Relation Between Fractal Dimension and SDAS

Secondary dendrite arm spacing (SDAS) reflects the solidification conditions of the billet and is closely related to the internal quality of the products. SDAS of the billet is measured with the linear intercept method, multiple typical dendrites are measured and their average values are used as SDAS.

Figure 6 shows the relationship between D_{Box}, D_{Sand}, and D_{Bran} and SDAS. Positive correlation is shown between D_{Box} and SDAS. However, there is no obvious correlation between D_{Sand}, D_{Bran}, and SDAS. It seems that the measurement of the fractal dimension of dendrites is relatively easy in comparison with the measurement of the SDAS. By obtaining a relationship between D_{Box} and SDAS, SDAS may be presumed from the D_{Box} even in a case that the measurement of SDAS is difficult.

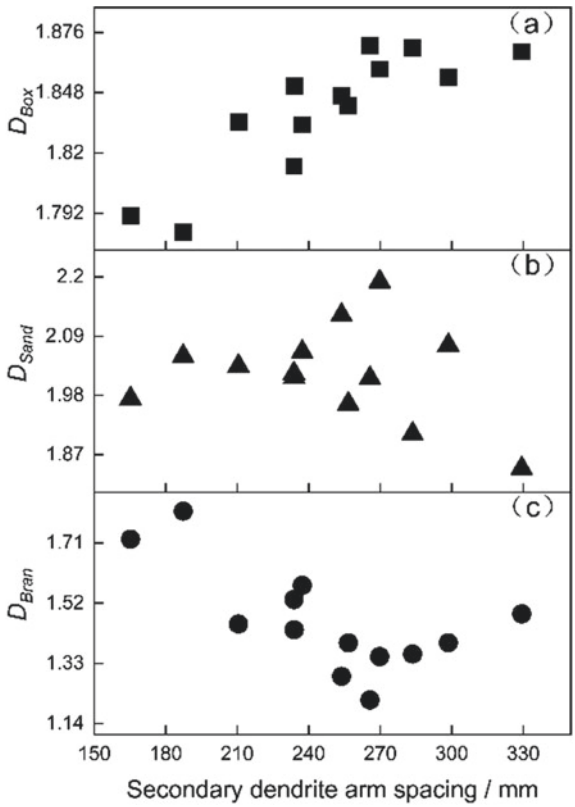

Fig. 6 Relationship between fractal dimension: **a** D_{Box}, **b** D_{Sand}, and **c** D_{Bran} and SDAS

Segregation Area Ratio and Fractal Dimension

In order to quantitatively evaluate the degree of macro/semi-macrosegregation at different locations of the billet, the segregation area ratio [19] (i.e., the ratio of the total area of all segregation points to the analytical zone area) was introduced in present study. According to the principle of hot pickling, the region with severe of C element segregation is black in macrostructure as shown in Fig. 2, so this criterion is reasonable. The calculation method of segregation area ratio is shown in Eq. (3). The greater the segregation area ratio, the more serious the segregation of billet.

$$R_{\text{seg}} = \frac{A_{\text{seg}}}{A_s} \times 100\% \tag{3}$$

where R_{seg} is segregation area ratio, %; A_{seg} the total area of all segregation points, mm^2; and A_s the area of analytical zone, mm^2.

Figure 7 shows the relationship between segregation area ratio (R_{seg}) and fractal dimension. It can be seen that R_{seg} decreases with increasing D_{Box}, and R_{seg} increases with increasing D_{Bran}. However, R_{seg} and D_{Box} have better correlation than D_{Bran}. R_{seg}

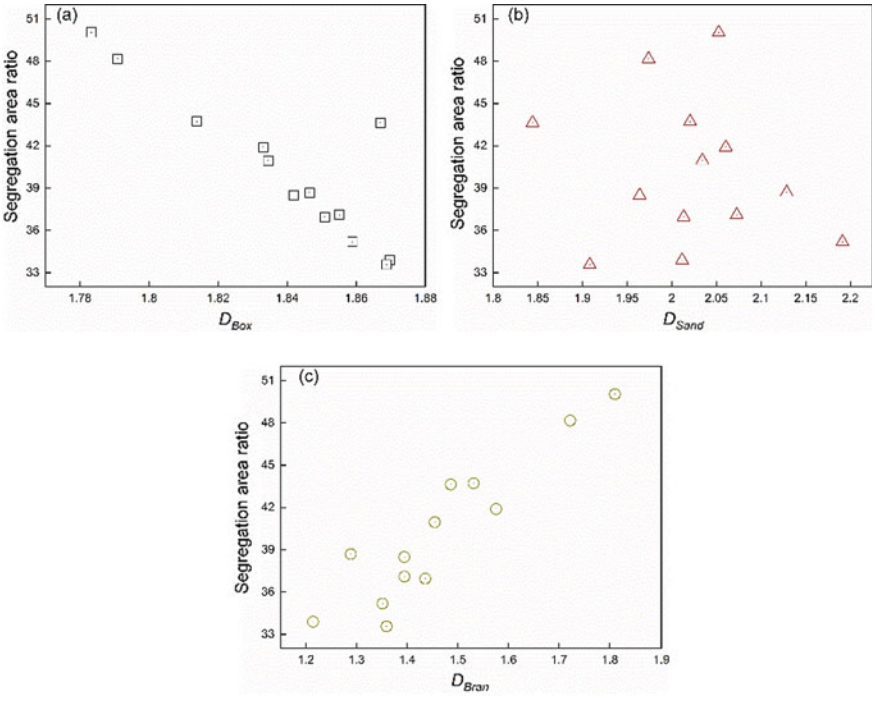

Fig. 7 Relationship between R_{seg} and fractal dimension: **a** D_{Box}, **b** D_{Sand}, and **c** D_{Bran}. (Color figure online)

has no obvious relationship with D_{Sand}. There is an outlier in Fig. 7a, this outlier is located at the center of the billet (Fig. 2; sample 7#). Sample 7# exhibits solidification shrinkage cavities according to Fig. 2. The effect of the solidification shrinkage cavities is not considered in the analysis of the present study that is treated as segregation point. Thus, the error is generated and the outlier expressed. In addition, macrosegregation is the result of interdendritic flow. The larger the fractal dimension, the more complex the dendrite morphology, which increase the flow resistance of interdendritic liquid. R_{seg} decreases with increasing D_{Box}, and this result indicates D_{Box} can better reflect the degree of macro/semi-macrosegregation in billet.

Conclusions

(1) Fractal dimension calculated by box-counting method (D_{Box}), sandbox method (D_{Sand}), and branching method (D_{Bran}) is effective to characterize quantitatively the complexity of solidification structure morphology.
(2) Positive correlation is shown between the D_{Box} and secondary dendrite arm spacing (SDAS).
(3) Negative correlation is shown between the D_{Box} and segregation area ratio (R_{seg}).
(4) D_{Box} can better reflect solidification characteristics of the billet than D_{Sand} and D_{Bran} because D_{Box} was well correlated with SDAS and R_{seg}.

Acknowledgements The authors are very grateful for support from United Funds between National Natural Science Foundation and Baowu Steel Group Corporation Limited from China (No. U1860101).

References

1. Li DZ, Chen XQ, Fu PX et al (2014) Inclusion flotation-driven channel segregation in solidifying steels. Nat Commun 5(5):5572–5578
2. Pickering EJ, Bhadeshia HKDH (2014) Macrosegregation and microstructural evolution in a pressure-vessel steel. Metall Mater Trans A 45(7):2983–2997
3. Choudhary SK, Ganguly S (2017) Morphology and segregation in continuously cast high carbon steel billets. ISIJ Int 47(12):1759–1766
4. Mayer F, Wu M, Ludwig A (2010) On the formation of centerline segregation in continuous slab casting of steel due to bulging and/or feeding. Steel Res Int 81(8):660–667
5. Flemings MC (2000) Our understanding of macrosegregation: past and present. ISIJ Int 40(9):838–841
6. Zhong XT, Rowenhorst AJ, Beladi H et al (2017) The five-parameter grain boundary curvature distribution in an austenitic and ferritic steel. Acta Mater 123:136–145
7. Li T, Chen G, Lin X et al (2006) Morphological evolution of solidification microstructure of binary alloy under stirring. Acta Metall Sin 42(6):577–583
8. Mandelbrot BB (1967) How long is the coast of britain? Statistical self-similarity and fractional dimension. Science 155(3775):636–638

9. Zaiser M, Bay K, HaHner P (1999) Fractal analysis of deformation-induced dislocation patterns. Acta Mater 47(8):2463–2476
10. Chang Q, Chen DL, Ru HQ et al (2011) Three-dimensional fractal analysis of fracture surfaces in titanium-iron particulate reinforced hydroxyapatite composites: relationship between fracture toughness and fractal dimension. J Mater Sci 46(18):6118–6123
11. Kobayashi S, Maruyama T, Tsurekawa S et al (2012) Grain boundary engineering based on fractal analysis for control of segregation-induced intergranular brittle fracture in polycrystalline nickel. Acta Mater 60:6200–6212
12. Long QY, Wen YH, Zhang XM et al (1993) Sierpinski fractal description of the martensitic transformation. Philos Mag A 68(5):885–890
13. Cao JH, Hou ZB, Guo ZA et al (2020) An application of fractal theory to complex macrostructure: quantitatively characterization of segregation morphology. ISIJ Int 60(6):1188–1195
14. Cao JH, Hou ZB, Guo DW et al (2019) Morphology characteristics of solidification structure in high-carbon steel billet based on fractal theory. J Mater Sci 54(19):12851–12862
15. Ishida H, Natsume Y, Ohsasa K (2009) Characterization of dendrite morphology for evaluating interdendritic fluidity based on phase-field simulation. ISIJ Int 49(1):37–43
16. Genau AL, Freedman AC, Ratke L (2013) Effect of solidification conditions on fractal dimension of dendrites. J Cryst Growth 363:49–54
17. Lopes R, Betrouni N (2009) Fractal and multifractal analysis: A review. Med Image Anal 13(4):634–649
18. Liu JM, Zhou YH, Shang BL (1990) On fractal of silicon-branching clusters for Al-Si eutectic growth. Materi Sci Progr 4(5):398–403
19. Wang W, Hou ZB, Chang Y et al (2018) Effect of superheat on quality of central equiaxed grain zone of continuously cast bearing steel billet based on two-dimensional segregation ratio. J Iron Steel Res Int 25(1):1–10

Part V
Advanced Characterization Methods III

A Study of the Absorption Edge of ZnO Thin Films Prepared by the Spray Pyrolysis Method

Shadia J. Ikhmayies

Abstract Zinc oxide (ZnO) thin films are produced by the spray pyrolysis method on glass substrates at 450 °C. The films are characterized using X-ray diffraction (XRD) and UV-VIS transmittance spectroscopy. XRD pattern showed that the films are polycrystalline with hexagonal (wurtzite) structure. Transmittance was measured at room temperature in the wavelength range 350–1100 nm, and used to deduce the absorbance. The fourth derivative of the absorbance is used to detect the peaks in the near-band edge region. Several peaks are found in the region of interest, from which are the free exciton peaks A, B, and C; bound exciton peaks related to defects and impurities; and very weak peaks assigned to longitudinal optical phonon replicas. These results are important for solar cells, room temperature UV laser, and other photonic and optoelectronic applications.

Keywords Zinc oxide · Absorption edge · X-ray diffraction · Optical properties · Solar cells

Introduction

ZnO is an important II–VI compound semiconductor that has direct wide bandgap energy of 3.37 eV, and large exciton binding energy of 60 meV [1] at room temperature. These properties made it attractive for several applications including solar cells, ultraviolet (UV) light emitters, detectors, room temperature (UV) lasers, high-power industry, photonics, electronics, and optoelectronics. The large exciton binding energy and strong exciton emission increase the probability of exciton-involved optical processes via interactions with excitons, electrons, and phonons [2].

In thin film form, ZnO is used as a transparent conducting oxide, and as window layer in thin film solar cells. There are several methods to prepare ZnO thin films such as thermal evaporation [3], spin coating [4], RF magnetron sputtering [5], pulsed laser deposition [6], and spray pyrolysis [7–20]. The spray pyrolysis method is used

S. J. Ikhmayies (✉)
Jabal El-Hussain, Amman 11121, Jordan
e-mail: shadia_ikhmayies@yahoo.com

J. Li et al., *Characterization of Minerals, Metals, and Materials 2021*,
The Minerals, Metals & Materials Series,
https://doi.org/10.1007/978-3-030-65493-1_8

in this work because it is a simple and cost-effective method, besides it enables the production of large area, and highly transparent thin films.

ZnO has strong absorption in the near-ultraviolet region [21], and there is a lot of experimental work in the literature conducted to explore the near-absorption edge region of ZnO single crystal and thin films using different techniques at temperatures that extend from 4.2 K to room temperature [21–23]. For example, Ohashi et al. [1] have studied room temperature emissions of doped ZnO single crystals in the near-edge UV region. Zhang et al. [2] reported the emissions of free excitons and their phonon replicas in good-quality ZnO epitaxial films from 3.5 K to room temperature. In this paper, the transmittance measurements at room temperature are used to investigate the absorption edge of as-deposited, undoped ZnO thin films prepared by the spray pyrolysis method, where the fourth derivative of the absorbance curves is used to detect the peaks in the absorption edge region. The results are discussed and compared with their counterparts obtained using photoluminescence, reflectivity, and other methods.

Materials and Methods

ZnO thin films are deposited on glass substrates of dimensions $2.5 \times 6 \times 0.1$ cm^3 using the spray pyrolysis method at a substrate temperature $T_s = 450$ °C. The precursor solution is prepared by dissolving 7.61×10^{-3} mol of $ZnCl_2$ in 300 ml of distilled water. To prevent the formation of $Zn(OH)_2$, the PH of the solution was adjusted to be 3 by adding HCl. The solution is sprayed intermittently on the hot substrates for periods that are roughly determined according to the required film thickness. Prior to deposition, the glass microslides are ultrasonically cleaned in methanol for about 30 min. Nitrogen N_2 is used as the carrier gas, and the solution spray rate is around 4 ml/min. The optimum carrier gas pressure for this rate of solution flow was around 5 kg/cm^3, and the nozzle to substrate distance is about 30 cm.

The structure of the films is explored using X-ray diffraction (XRD), where a compact X-ray diffractometer system (Philips PW1840) with Cu K_α ($\lambda = 1.5405$ Å) is used. The measurements are recorded at a diffraction angle 2θ in the range of 2–81°. Optical transmittance measurements are carried out at room temperature using a double beam Shimadzu UV 1601 (PC) spectrophotometer with respect to a piece of glass similar to the substrates in the wavelength range $\lambda = 350$–1100 nm. The values of film thickness are optically estimated as 400 nm.

Results and Discussion

The ZnO films under study are all deposited from the same precursor solution with the same deposition parameters. Figure 1 depicts the diffractogram of one of the films, where the figure shows a hexagonal (wurtzite) structure. The strongest narrow peak

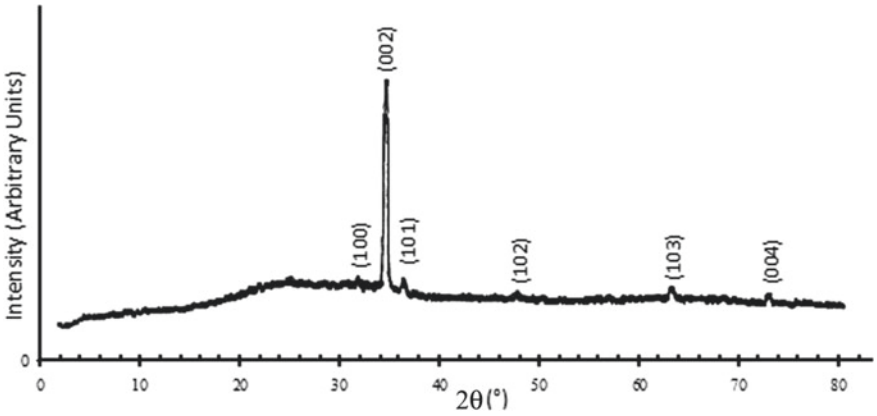

Fig. 1 X-ray diffractogram of one of the as-deposited ZnO thin films

corresponds to the reflection from the (002) plane and it confirms that the preferred growth direction is along the c-axis perpendicular to the substrate. In addition, there are five weaker diffraction peaks which correspond to reflections from (100), (101), (102), (103), and (004) planes. These weak peaks which refer to weak crystal growth in the related directions are indications of the presence of nanocrystallites in the film.

Figure 2 displays the transmittance and absorbance plotted against the wavelength of radiation, where Fig. 2a depicts the transmittance curves of two films in the range $\lambda = 350–1100$ nm, while Fig. 2b depicts the absorbance of the same films plotted in the same wavelength range. From Fig. 2a, the transmittance of the films in the visible and near-infrared region is as large as 91.9% for sample 1 and 85.2% for the sample 2. The maximum absorbance in the ultraviolet region from Fig. 2b is 5.9 for sample 1 and 4.6 for the other sample.

As a hexagonal compound, ZnO has a conduction band that is mainly constructed from s-like state, and a valence band that is constructed from a p-like state, which is split at the centre of the Brillouin zone into three bands due to the influence of crystal-field and spin–orbit interactions [5, 23], where the crystal-field splitting is about one order greater than the spin–orbit coupling [24]. These bands are labeled A, B, and C, where the energy of A is the smallest and that of C is the largest. So, there are three exciton series derived from a Zn 4 s-like conduction band, and the O 2p-like valence bands (A, B, and C). The absorption edge of ZnO comprises mainly of the peaks of the free excitons of these bands. Also, it may contain bound exciton peaks related to defects, dopants, and impurities. The peaks can be resolved usually at low temperatures using different techniques such as photoluminescence, cathodoluminescence, and reflectivity. The free exciton peaks grow with temperature, and they can merge into a broadened peak at room temperature, where broadening is related to the exciton–phonon interactions [6]. The bound exciton peaks have large oscillator strength, so they appear as strong sharp peaks, but they diminish with temperature. The energy separation of the A- and B-free exciton peaks of bulk ZnO

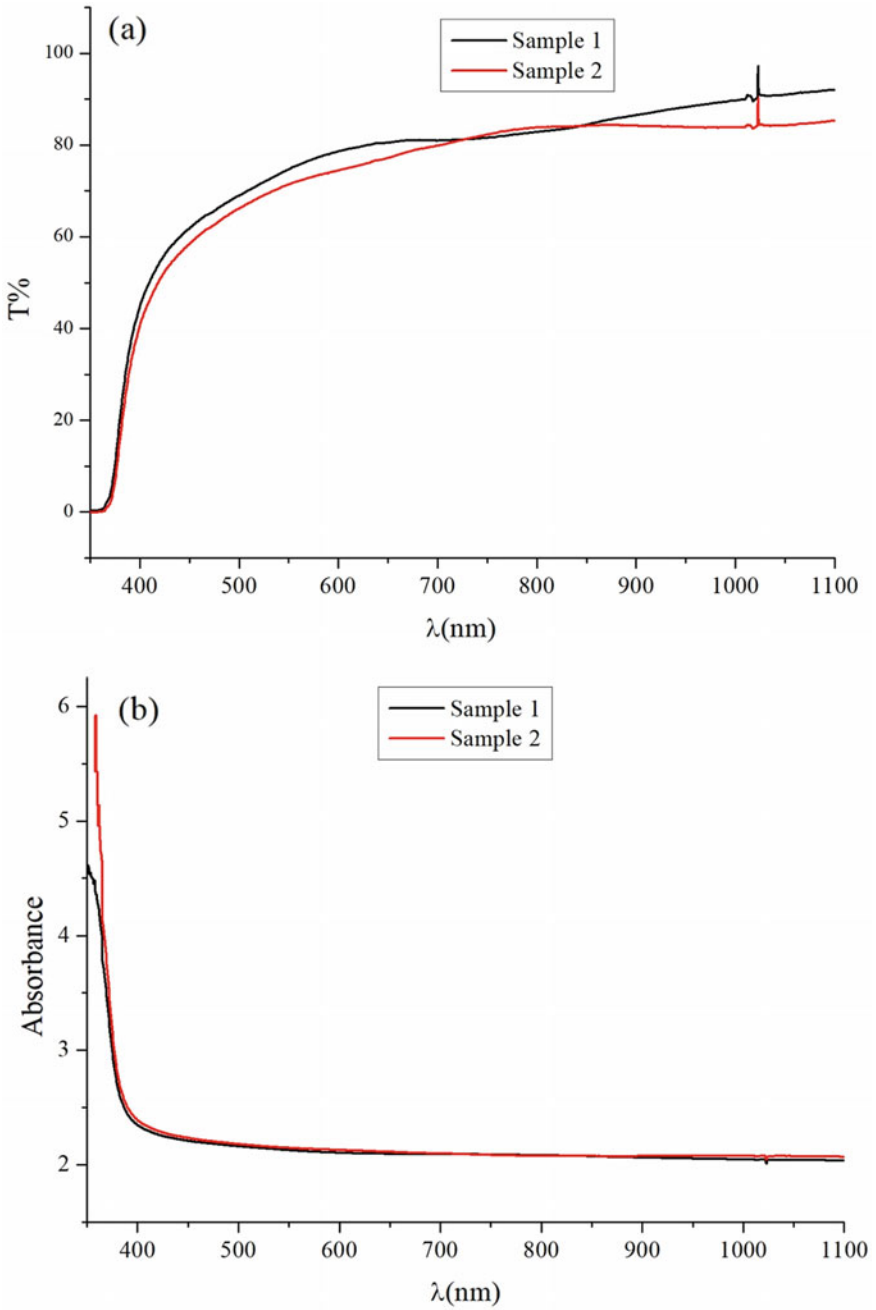

Fig. 2 The plots of transmittance (**a**) and absorbance (**b**) against wavelength of radiation for two ZnO films. (Color figure online)

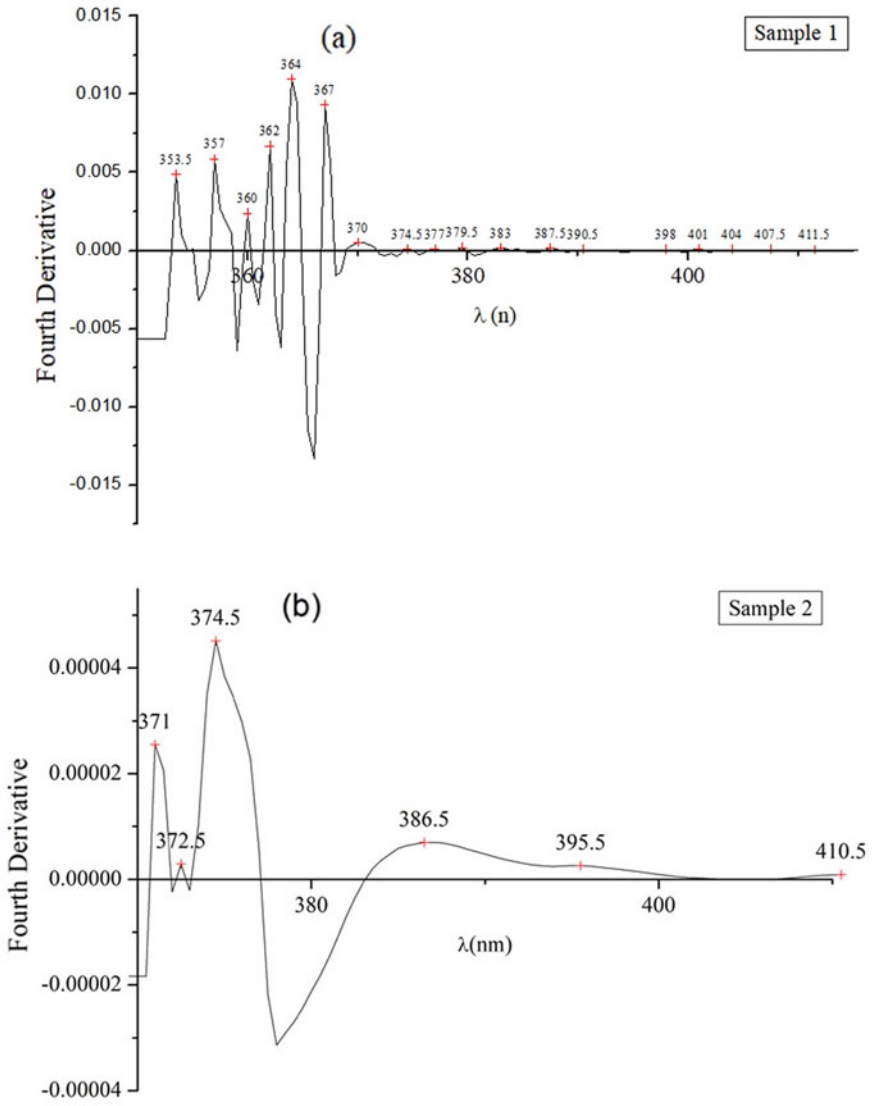

Fig. 3 The fourth derivative curves the absorbance against the wavelength of radiation for sample 1 (**a**) and sample 2 (**b**). (Color figure online)

is in the range of 9–15 meV, while the separation of B- and C-free exciton peaks for bulk ZnO is 40–45 meV [21, 23, 25, 26]. The amplitude of the peak of B-free exciton is much larger than that of A-free exciton, indicating that the former has greater oscillator strength.

To detect the peaks in the absorption edge of ZnO thin films, the fourth derivative curves of the absorbance shown in Fig. 2b are deduced and shown in Fig. 3, where

Fig. 3a represents sample 1 and Fig. 3b represents sample 2. The maxima in the fourth derivative refer to the peaks in the near-band region. So, the positions of these peaks are inserted in Tables 1 and 2 for sample 1 and sample 2, respectively. The positions of the maxima in both tables are used to find the energy at the center of each peak. The inspection of Fig. 3a and b reveals that the absorption edge contains a number of peaks, namely, the free exciton peaks of the ZnO hexagonal phase, neutral acceptor-bound exciton peaks, and neutral donor-bound exciton peaks. Following these in the low energy side there are very weak peaks that can be assigned to phonon replicas of the bound exciton peaks.

Table 1 Positions and amplitudes of peaks, and energy separation between each two successive peaks for sample 1

λ (nm)	E(eV)	Amplitude	ΔE (meV)
353.5	3.508	0.0049	
			35
357	3.473	0.00587	
			39
360	3.444	0.00238	
			19
362	3.425	0.0067	
			18
364	3.406	0.01097	
			28
367	3.379	0.00934	
			28
370	3.351	5.19158E-4	
			27
373	3.324	1.72821E-4	
			13
374.5	3.311	8.10367E-5	
			22
377	3.289	9.3168E-5	
			22
379.5	3.267	1.96924E-4	
			29
383	3.238	1.6331E-4	
			13
384.5	3.225	1.15017E-4	
			25
387.5	3.200	1.48227E-4	
			25

(continued)

Table 1 (continued)

λ (nm)	E(eV)	Amplitude	ΔE (meV)
390.5	3.175	6.11812E-5	
			12
392	3.163	5.38586E-5	
			32
396	3.131	5.152489E-5	
			15
398	3.116	6.57832E-5	
			24
401	3.092	1.09741E-4	
			23
404	3.069	6.81372E-5	
			26
407.5	3.043	5.72579E-5	
			30
411.5	3.013	4.94116E-5	

Table 2 Positions and amplitudes of peaks, and energy separation between each two successive peaks for sample 2

λ (nm)	E(eV)	Amplitude	ΔE(meV)
371	3.342	2.55072E-5	
			13
372.5	3.329	2.87677E-6	
			18
374.5	3.311	4.51552E-5	
			103
386.5	3.208	7.00603E-6	
			73
395.5	3.135	2.61586E-6	
			114
410.5	3.021	9.01201E-7	

Figure 3a shows six strong peaks followed by a set of weaker peaks in the low energy side. The first asymmetric broad peak at 353.5 nm (3.508 eV) is attributed to the first excited state of the free C-exciton, while the next asymmetric broad peak at 357 nm (3.473 eV) is assigned to the ground state of the free C-exciton, where they are separated by 35 meV. The weaker peak at 360 nm (3.444 eV) is assigned to a merged peak of the peaks attributed to the ground state of the B- and A-free excitons. The separation between this merged peak and that of the C-free exciton peak is 39 meV, which is very close to 39.7 meV given by [25]. Then the peak at 362 nm (3.425 eV) is attributed to A neutral donor-bound exciton, because its separation

from the merged peak of AB free excitons is 19 meV, where the binding energy of donor excitons is 10–20 meV [23]. Since the binding energy of the acceptor-bound exciton is larger than that of the donor-bound exciton, the largest peak at 364 nm (3.406 eV) is attributed to an A neutral acceptor-bound exciton, where its separation from the AB merged peak is 37 meV. Then the peak at 367 nm (3.379 eV) is also attributed to an A neutral acceptor-bound exciton, where it is separated from the AB merged peak by about 65 meV. The binding energies of bound excitons differ according to the donor or acceptor to which they were bound.

The weak peaks in Fig. 3a are phonon replicas of the bound excitons, and there is overlap between them. Some of them can be identified such as the peak at 370 nm (3.351 eV) which can be identified as the first-order phonon replica (1LO) of the neutral donor-bound exciton at 364 nm (3.406 eV), where the separation between it and this peak is 72 m eV. What supports this expectation is that; first, this energy separation equals the binding energy of the ZnO phonon, and second, the LO-phonon replicas are known to be roughly two orders of magnitude less intense than the neutral donor-bound exciton lines, and this is satisfied as seen in Table 1. That is, the coupling between donor-related bound exciton lines and optical phonons is weak [23, 27]. The peak at 373 nm (3.324 eV) is identified as the first-order phonon replica of the neutral acceptor-bound exciton at 367 nm (3.379 eV), where it is separated from this peak by 55 meV. The remaining peaks are all overlapped phonon replicas of different orders for the aforementioned bound excitons, and it is difficult to identify them exactly.

In Fig. 3b, the first two peaks at 371 nm (3.342 eV) and 372.5 nm (3.329) are assigned to the ground state of the B- and A-free excitons, respectively, where the separation between these two peaks is 13 meV, which is consistent with the known separation between A and B peaks of 9–15 meV. It is noticed that peak A is weaker than B, where it is known that B has greater oscillator strength [23]. The strongest peak in Fig. 3b is located at 374.5 nm (3.311 eV) and it is assigned to A neutral donor-bound exciton depending on the energy separation between it and the peak of the A-free exciton, which is 18 meV, where the binding energies of the donor-bound excitons range from 10 to 20 meV as mentioned before. This peak is broadened due to the overlap with phonon replicas of the A- and B-free excitons. The peaks at 386.5 (3.208 eV), 395.5 (3.135 eV), and 410.5 nm (3.021 eV) cannot be accurately identified because they are broadened, which means there is overlap with other peaks. These peaks are phonon replicas of different orders of the bound excitons mentioned before.

These results can be compared with those for ZnO single crystal given by different authors. The values given by Teke et al. [23] for ZnO single crystal at 10 K are 3.3772 eV for the ground state of A-free exiton, 3.3901 eV for the ground state of B-free exiton, and 3.435 eV for the ground state of C-free exciton, where these measurements were obtained from reflection spectra. But the first excited state energy of A-free exiton measured by Teke et al. [23] at 10 K is 3.421 eV. The ground state of the neutral donor-bound exciton peak measured by Teke et al. [23] at 10 K is 3.3598 eV. Thomas [21] obtained these peaks for ZnO single crystal at 77 K at 3.418 eV for the C-free exciton, 3.378 eV for B-free exciton, and 3.3708 eV for the A-free exciton. While the first excited state of the C-free exciton was found at

3.465 eV. It is confirmed that these peaks are sensitive to the conditions of the surface, and their strength increases with temperature. The values obtained in this work are higher than those of single crystal because the samples are thin films of thickness about 400 nm, which means quantum confinement will have effect due to the presence of nanocrystallites, as can be concluded from the X-ray diffractogram. Quantum confinement results in a blue shift of the exciton peaks. In addition, the measurements in this work are recorded at room temperature, which means more broadening due to phonon replicas. Another reason of broadening is the relatively large size distribution of crystallites in samples prepared by solution route-based deposition methods such as spray pyrolysis, since it results in inhomogeneous broadening of the peaks [22].

Conclusions

ZnO thin films are produced using spray pyrolysis method on glass substrates at 450 °C. The films are characterized using X-ray diffraction and UV-VIS transmittance spectroscopy. The films showed polycrystalline nature and hexagonal structure. The transmittance curves are used to deduce absorbance, and the fourth derivative of the absorbance is used to detect the peaks corresponding to absorption lines in the region near the absorption edge. The peaks are identified as free exciton C, B, and A peaks, where B and A are merged for one of the films, and separated for the other, while C-free exciton peak is observed for one of the films. Some peaks are assigned to the neutral donor-bound exciton, neutral acceptor-bound exciton, and the weaker peaks are identified as their phonon replicas. These results are important for ZnO engineering in the design of photonic, electronic, and optoelectronic devices.

References

1. Ohashi N, Sekiguchi T, Aoyama K, Ohgaki T, Terada Y, Sakaguchi I, Tsurumi T, Haneda H (2002) Band-edge emission of undoped and doped ZnO single crystals at room temperature. J Appl Phys 91(6):3658–3663
2. Zhang BP, Manh LH, Isoya G, Wakatsuki K, Usami N, Segawa Y (2002) Phonon replica of free excitons in ZnO epitaxial films. Nonlinear Optics 29(10–12):621–627
3. Fouad OA, Ismail AA, Zaki ZI, Mohamed RM (2006) Zinc oxide thin films prepared by thermal evaporation deposition and its photocatalytic activity. Appl Catal B 62:144–149
4. Amit Kumar Srivastava and Jitendra Kumar (2011) Effect of aluminum addition on the optical, morphology and electrical behavior of spin coated zinc oxide thin films. AIP Adv 1:032153
5. Adachi S (1999) Optical properties of crystalline and amorphous Semiconductors. In: Materials and fundamental principles. Kluwer Academic Publishers, Chap. 1
6. Nie JC, Yang JY, Piao Y, Li H, Sun Y, Xue QM, Xiong CM, Dou RF, Tu QY (2008) Quantum confinement effect in ZnO thin films grown by pulsed laser deposition. Appl Phys Lett 93(17):173104
7. Ikhmayies SJ (2016) Synthesis of ZnO microrods by the spray pyrolysis technique. J Electron Mater 45(8):3964–3969

8. Ikhmayies SJ, Abu El-Haija NM, Ahmad-Bitar RN (2010) Electrical and optical properties of ZnO: Al thin films prepared by the spray pyrolysis technique. Phys Scr 81:015703
9. Ikhmayies SJ, Abu El-Haija NM, Ahmad-Bitar RN (2010) Characterization of undoped spray-deposited ZnO thin films of photovoltaic applications. FDMP 6(2):165–177
10. Ikhmayies SJ, Abu El-Haija NM, Ahmad-Bitar RN (2015) A comparison between different ohmic contacts for ZnO thin films. J. Semicond. 36(3):033005
11. Ikhmayies SJ, Abu El-Haija NM, Ahmad-Bitar RN (2010) The influence of annealing in nitrogen atmosphere on the electrical, optical and structural properties of spray-deposited ZnO thin films. FDMP 6(2):219–232
12. Ikhmayies SJ, Zbib MB (2018) Synthesis of ZnO hexagonal prisms on aluminum substrates by the spray pyrolysis technique. In: Sayigh A (ed) Transition towards 100% renewable energy, innovative renewable energy. Springer International Publishing, pp 177–186
13. Ikhmayies SJ (2018) ZnO thin films of flowered-fibrous micro/nanowebs on glass substrates using the spray pyrolysis method. In: Li B, Li J, Ikhmayies S, Zhang M, Kalay YE, Carpenter JS, Hwang J-Y, Monteiro SN, Firrao D, Brown A, Bai C, Peng Z, Escobedo-Diaz JP, Goswami R, Kim J (eds) Characterization of minerals, metals, and materials, pp 209–215
14. Lahlouh BI, Ikhmayies SJ, Juwhari KH (2018) Structural, optical, and vibrational properties of ZnO microrods deposited on silicon substrate. J Electron Mater 47(8):4455–4462
15. Ikhmayies SJ, Zbib MB (2017) Spray pyrolysis synthesis of ZnO micro/nano rods on glass substrates. J Electron Mater 46(10):5629–5634
16. Ikhmayies SJ (2017) Formation of three dimensional ZnO micro flowers from self assembled ZnO micro discs. Metall Mater Trans A 48(8):3625–3629
17. Ikhmayies SJ, Zbib MB (2017) Synthesis of ZnO hexagonal micro discs on glass substrates using the spray pyrolysis technique. J Electron Mater 46(7):3982–3986
18. Juwhari KH, Ikhmayies SJ, Lahlouh BI (2017) Room temperature photoluminescence of spray-deposited ZnO thin films on glass substrates. Int. J. Hydrogen Energ. 42(28):17741–17747
19. Ikhmayies SJ (2020) Production of three-dimensional ZnO multilayered structures from self-assembled ZnO microdiscs. JOM 72:628–634. https://doi.org/10.1007/s11837-019-03953-3
20. Ikhmayies SJ (2020) Synthesis of flower-like ZnO micro/nano structures by the spray pyrolysis technique. JOM 72:621–627. https://doi.org/10.1007/s11837-019-03952-4
21. Thomas DG (1960) The exciton spectrum of zinc oxide. J Phys Chem Solids 15:86–96
22. Fonoberov VA, Alim KA, Balandin AA (2006) Photoluminescence investigation of the carrier recombination processes in ZnO quantum dots and nanocrystals. Phys. Rev. B 73:165317
23. Teke A, Özgür Ü, Doğan S, Gu X, Morkoç H, Nemeth B, Nause J (2004) Excitonic fine structure and recombination dynamics in single-crystalline ZnO. Phys. Rev. B 70:195207
24. Ding L, Yang C, He H, Wang J, Tang Z, Foreman BA, Jiang F, Ge W (2013) Verification of Γ_7 symmetry assignment for the top valence band of ZnO by magneto-optical studies of the free A exciton state. New J Phys 15:033015. https://doi.org/10.1088/1367-2630/15/3/033015
25. Reynolds DC, Look DC, Jogai B, Litton CW, Cantwell G, Harsch WC (1999) Valence-band ordering in ZnO. Phys. Rev. B 60:2340–2344
26. Boemare C, Monteiro T, Soares MJ, Guilherme JG, Alves E (2001) Photoluminescence studies in ZnO samples. Phys B 308–310:985–988
27. Thonke K, Gruber T, Teofilov N, Schönfelder R, Waag A, Sauer R (2001) Donor–acceptor pair transitions in ZnO substrate material. Phys B 308–310:945–948

Part VI
Minerals Processing and Analyses

Petrographic and SEM-EDS Analysis of Riruwai Cassiterite Ore in North Western Nigeria

Furqan Abdulfattah, Ibrahim Rafukka, Markus Bwala, Muhammad Muzzammil Abduljalal, and Kabir Isa

Abstract The petrographic and SEM-EDS analysis of Riruwai cassiterite ore located in Doguwa Local Government, Kano State, Nigeria was carried out using appropriate Scanning Electron Microscope (SEM) and optical microscope. Five representative samples of the ore were taken at intervals 50 m apart, pulverized and thoroughly mixed to give appropriate representation of the entire ore. The results obtained from SEM analysis showed that the cassiterite-bearing minerals are separated from other minerals in the ore by smooth grain boundaries that make it easily to be free from other associated minerals simply by comminution. The petrographic study using optical microscope revealed that the cassiterite-bearing minerals contains annite, microcline, cassiterite, and quartz. The petrological analysis results also reveal that the cassiterite structures are in the form of plates and river lines, which are the characteristics of cassiterite. The dark areas are mixture of cassiterite and silicate minerals. Based on the quality of the ore in comparison with cassiterite ores from other parts of Nigeria and based on the results obtained in this research work, it has been suggested that Riruwai Cassiterite ore can be a potential source of tin ore as raw material for tin production.

Keywords Cassiterite · Petrographic · SEM-EDS · Microscope

Introduction

Cassiterite popularly known as tin ore is hardly produced free from other minerals such as iron, niobium, tantalum, zinc, columbite, etc. and most of these are reduced to metal at the same time forming alloy with tin during smelting process. It is therefore necessary to beneficiate the ore.

F. Abdulfattah (✉) · M. Bwala · M. M. Abduljalal · K. Isa
Nigerian Institute of Mining and Geosciences, Jos, Plateau, Nigeria
e-mail: fa1700001.mme@buk.edu.ng

F. Abdulfattah · I. Rafukka
Mechanical Engineering Department, Bayero University Kano, Kano, Nigeria
e-mail: phurqoon93@gmail.com

J. Li et al., *Characterization of Minerals, Metals, and Materials 2021*,
The Minerals, Metals & Materials Series,
https://doi.org/10.1007/978-3-030-65493-1_9

Cassiterite (tinstone) is usually black, brown, reddish-brown, yellowish-brown, and rarely grey. It occurs as massive or fibrous or disseminated in small grains; luster usually brilliant; crystal when of pale color, rarely transparent, and always associated with impurities when occurring in pegmatite including ferrous oxide (Fe_2O_3), titanium oxide (TiO_2), manganese oxide (MnO), iron oxide (FeO), zirconium oxide (ZrO_2), and tungsten oxide (WO_2), which makes it dark brown to pitch black color. Hardness (mohs) is 6.0–7.0. Usually non-magnetic, but iron-enriched black varieties of cassiterite is electromagnetic [1]. The main commercial tin fields in the world are Malaysia, Australia, Nigeria, Bolivia, Thailand, and China [2].

There are twenty (20) known minerals of tin (Sn), the only economically important mineral of tin is cassiterie SnO_2 (78.6%Sn) and are found largely in Nigeria, other sources are Stannite or tin pyrites Cu_2FeS_4 (27.7%Sn), tealite $Pb_3Sn_3SbS_4$ (17%Sn), and cylinderite $Pb_3Sn_4Sb_2S_{14}$ (26.0%Sn). Cassiterite is the sole economic tin mineral in Nigeria: stannite has been recorded but never in economic quantities [3].

This research is aimed at mineralogical characterization of Riruwai cassiterite located in Kano, North Western Nigeria through petrographic and Scanning Electron Microscope (SEM-EDS) of the deposit.

Mineralogical Analysis Theoretical Parameters

Mineralogical analysis reveals the major and minor compounds making up the ore under investigation, grain size of each mineral in the ore, allocation of each element to each mineral present in the ore, and the degree of association of valuable mineral to the gangue mineral. Generally, the study of these properties can be achieved by chemical mineralogy, physical, and crystallography. These involved uses of petrography microscope, SEM/EDS, XRD, XRF machine, etc.

Petrography is the study of rocks using a microscope. Cross section is useful for the identification of rock minerals of the ores, their characteristics, and properties such as cleavage, twining, reflectance, and shape.

The thin section is observed with a transmitted polarized microscope [4]. The petrography microscope is a type of microscope used in the study of thin section of minerals and rocks by examining the mineral fragment; grained crystal or aggregate; and in the interpretation of texture, structure, growth pattern, and various relationships of natural or artificial substance [5].

Metallurgical Analysis Methods

Metallurgical analysis involves the qualitative as well as the quantitative analysis of various metallurgical raw materials like ores and products like metals, alloys, and slags [6]. The analytical methods employed in metallurgical analysis can be classified into classical and instrumental methods. The classical methods are slow

and for practical purposes, the instrumental methods which are faster and quite accurate are used [7].

In the instrumental methods of analysis, measurement is made upon the system as a whole. A particular physical or chemical property of the system is measured in order to get the desired analytical results. Comparison of the results of the samples of the results to be analyzed with standard samples of known composition is necessary in this method [6].

The common instrumental analytical techniques used are atomic absorption spectrophotometry, X-ray fluorescence, X-ray diffraction, scanning electron microscopy, and electron probe microanalysis.

Materials and Methods

Materials/Equipments

The following are the materials and equipment used for the experimental procedure:

1. Tin ore (cassiterite),
2. Pulverizing machine,
3. Weighing balance,
4. Petrography microscope (optical microscope),
5. Scanning electron microscope (SEM-EDS),
6. Global Positioning System (GPS),
7. Laboratory ball mill,
8. Precision thin section cutting and grinding machine, and
9. Thin section lapping machine.

Methods

Sample Collection

Representative sample of the cassiterite was collected from various points of deposit located at Riruwai Village in Doguwa Local Government Area, Kano State. GPS was used to measure the exact location points at which the samples were taken. Grab method of sampling was adopted to collect the sample. About 25 kg of the sample was collected from four (4) points at interval of 100 m apart at 5 m depth in order to have appropriate representative of the ore deposit.

Sample Preparation

Sample preparation involves crushing and grinding processes (communition process). The lump sizes of the ore sample were reduced to sizes that will be acceptable by the crusher using sledge hammer. The samples were crushed using jaw crusher. The discharge from the crusher was then ground to fine particle size using ball milling process.

Part of the sample was further prepared into thin section, for appropriate view under the optical microscope (for petrographic analysis).

Mineralogical Characteristics of Riruwai Cassiterite

Mineralogical analysis was carried out using Scanning Electron Microscope (SEM-EDS) and petrography microscope (optical microscope) . The samples were viewed under the reflected microscope for identification of mineral phases present and determination of grain size of various minerals. The results of the analysis (petrographic and SEM-EDS) are presented in result section.

Results and Discussion

Petrographic Analysis Using Optical Microscope

Images shown below are illustration derived from the optical microscope for petrographic analysis of the sample.

From the results of the petrological micrographs shown in Fig. 1a–c, four mineral phases were recognized under plane and cross-polarized light, which are identified majorly as cassiterite, annite, quartz, and ilmenite.

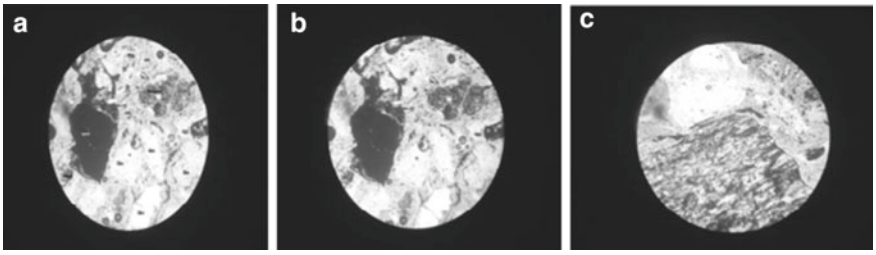

Fig. 1 **a** Optical micrograph of the sample at 50X. **b** Optical micrograph of the sample at 100X. **c** Optical micrograph of the sample at 200X

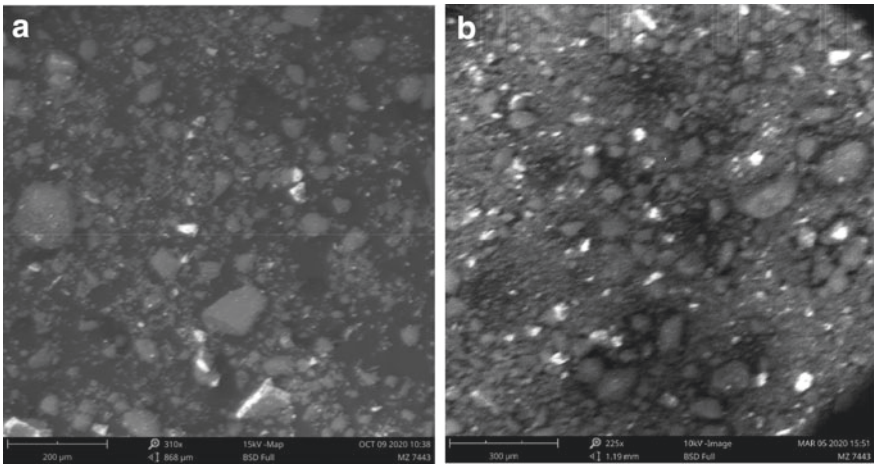

Fig. 2 **a** SEM analysis result of the sample at 310X and 200 μm. **b** SEM analysis result of the sample at 225X and 300 μm

SEM-EDS Analysis

The images below are images derived from the scanning electron microscope and EDS.

The chemical and morphological characteristics of the crushed samples in the ore were determined by means of SEM, with the chemical elements of the ore-bearing cassiterite determined by the EDS. From the result shown in Fig. 2a, b, from the SEM image, it is observed that the ore has smooth boundaries which create segregation between the cassiterite and other minerals. The EDS chemical analysis in Table 1 shows that the elements that abound in the ore-bearing cassiterite are Si, Fe, Sn, Al, K, Nb, Ag, Ti, Mn, Y, and V.

Conclusion and Recommendation

The mineralogical studies carried out with petrographic microscope and SEM-EDS showed the presence of different aggregates of minerals in the deposit. The petrographic analysis shows the presence of four of four mineral phases which are cassiterite, annite, quartz, and ilmenite. While the chemical elemental composition determined by EDS was Si, Fe, Sn, Al, K, Nb, Ag, Ti, Mn, Y, and V.

Further, mineralogical characterization can be done using XRD and XRF machine to appropriately confirm the mineral present in Riruwai deposit.

Table 1 Elemental analysis of the sample showing the atomic concentration and weight concentration of the sample using SEM-EDS

Element number	Element symbol	Element name	Atomic conc.	Weight conc.
14	Si	Silicon	51.18	34.60
26	Fe	Iron	15.64	21.03
50	Sn	Tin	6.17	17.62
13	Al	Aluminium	12.39	8.05
19	K	Potassium	3.75	3.53
41	Nb	Niobium	1.57	3.51
47	Ag	Silver	0.99	2.57
22	Ti	Titanium	2.04	2.35
25	Mn	Manganese	1.22	1.61
39	Y	Yttrium	0.58	1.24
23	V	Vanadium	0.93	1.14

References

1. Africano F, Van Rompey G, Bernard A, Le Guern F (2002) Deposition of trace elements from high temperature gases of Satsuma-Iwojima volcano. Earth Planets Space 54:275–286
2. Falcon LM (1985) Tin in South Africa J South Afr Inst Min Metall 85(10):333–345, October
3. Akanbi ES, Ugudulunwa FXO, Gyan BN (2012) Mapping Potential cassiterite deposits of Naraguta area, north central, nigeria using geophysics and geographic information. J Nat Sci Res 2:132–143
4. Beuler I (2009) Preparation petrographic thin section, vol 1 publisher Marry land 20814 U.S.A
5. Arogundade H (1999) Mineralogical of the beginners. The Godson Printers & Publishers. No. 16 OdoIdigbo street, Ado Ekiti State, pp 29–30 & 34
6. Yaro SA (1997) Development of a process route for the beneficiation of Mallam Ayuba manganese deposit to ferromanganese feed grade. Department of Metallurgical Engineering, Ahmadu Bello University, Zaria. Unpublished
7. Gilchrist JD (1989) (3rd Ed). Extraction metallurgy, Oxford: Pergamon Press Ltd

Characterization on Behavior of Al During the Oxidization Roasting Process of Polymetallic Ferruginous Manganese Ores

Yubi Wang, Li Zhang, Bingbing Liu, Bei Zhang, and Yuanbo Zhang

Abstract Polymetallic ferruginous manganese ores contain a variety of valuable metals, it is significant to realize the efficient utilization. Spinel-type composite ferrites with strong magnetism can be prepared from the polymetallic ferruginous manganese ores, while the impurities in the ores have certain impact on the properties of the ferrites. This study was mainly concentrated on the behavior of Al during the formation process of ferrites. It has been found that during the oxidation roasting process, Al element has occupied the octahedral gap (sit B) in spinel structure of ferrites, which reduced the magnetism property of ferrite. However, SiO_2 can improve the magnetism properties of Al-bearing manganese ferrites owing to that SiO_2 was able to transfer Al out of B sit of spinel via the chemical driving force generated by the formation of corresponding silicates from the SiO_2 and Al oxides. This work demonstrated that Al impurity can be regulated by adding SiO_2.

Keywords Ferrites · Element migration · Ferruginous manganese ores · Roasting · Magnetism property

Introduction

Manganese is an important metal used in many industrial fields. There are lots of impurity elements in manganese ore resources, characterized by low manganese taste, high content of impurity elements, complex ore structure, and fine intercalation

Y. Wang · B. Liu (✉)
School of Chemical Engineering, Zhengzhou University, Zhengzhou, Henan 450001, China
e-mail: liubingbing@zzu.edu.cn

L. Zhang · B. Zhang
School of Materials Science and Engineering, Zhengzhou University, Zhengzhou, Henan 450001, China

Y. Zhang
School of Minerals Processing and Bioengineering, Central South University, Changsha, Hunan 410083, China

J. Li et al., *Characterization of Minerals, Metals, and Materials 2021*,
The Minerals, Metals & Materials Series,
https://doi.org/10.1007/978-3-030-65493-1_10

particle size, such as Fe, Si, P, Al, and so on [1–3]. For the time being, the comprehensive utilization of ferromanganese ore at home and abroad is mainly concentrated in the separation of manganese and iron, and the separation methods mainly include physical beneficiation and chemical beneficiation [4]. In exploring the reasons for the difficulty in separating manganese and iron during the magnetization roasting process of ferromanganese ore, Bingbing Liu studied the reaction behavior of the MnO_2–Fe_2O_3 binary system in a weak reduction roasting atmosphere, in a weak reducing atmosphere (CO–CO_2), MnO_2 and Fe_2O_3 begin to react in a solid phase at a relatively low temperature (~900 °C) to come into being ferromanganese spinel ($MnxFe_{3-x}O_4$) with strong magnetism [5–7]. Their studies provided us with research ideas for exploring the roasting-sorting method of manganese and iron oxide minerals to directly produce spinel-type manganese ferrite functional materials.

Spinel-type ferrite functional materials are widespread consumed in the electronics industry, fine chemicals, environmental protection, and other fields, which have made great contributions to modern industrial production and development [8]. The spinel manganese ferrite structure includes tetrahedral gap (A site) and octahedral gap (B site); the A site gap is smaller, which can fill smaller metal ions; the B site gap is larger, and the size can be filled with larger metal ions [9–14]. The main phases of manganese and iron oxide minerals are MnO_2 and Fe_2O_3. Manganese and iron oxide ores still contain a certain amount of impurity elements after conventional mineral processing, which may enter the crystalline lattice of spinel manganese ferrite during high-temperature roasting, causing great influence on phase composition and magnetic properties. In order to realize the separation of impurities from target spinel manganese ferrite, the vital role is to control the directional migration of impurities and target products through roasting, which can provide mineralogical conditions for the subsequent separation of manganese ferrite products and gangue.

According to the content, type, occurrence state, and properties of impurity elements in the raw materials of manganese and iron oxidizing minerals, the impurity elements can be divided into two types: acidic SiO_2 and alkaline Al_2O_3. Al element mainly occupies the B position in spinel manganese ferrite. In this work, the characterization on the migration behavior of Al element in the process of manganese and iron oxides forming spinel manganese ferrite, and its synergistic effect or adverse effects on the magnetic properties of manganese ferrite products were investigated by X-ray diffraction (XRD) and vibrating sample magnetometer (VSM). The method of directional control of the migration of impurity elements to improve the magnetic properties of the product was developed.

Experimental

Materials

Chemically pure Fe_2O_3 and MnO_2 are used in the present work, and the molar ratio is 1: 1. In order to study the characterization on behavior of Al during the oxidization roasting process of polymetallic ferruginous manganese ores, the chemically pure Al_2O_3, and SiO_2 powders were used as the additives.

Oxidization Roasting Process

In this study, the experimental process of this experiment is shown in Fig. 1. Before roasting, the Fe_2O_3 and MnO_2 powders with Al_2O_3 additives were evenly mixed and grinded by planetary ball mill. Then the mixture was briquetted by mold into cylindrical briquette with a diameter of 10 mm and height of 20 mm at a pressure of 50 MPa, and then the cylindrical briquette was dried at 110 °C for 4 h. The dried briquettes were roasted in a horizontal resistance furnace with air atmosphere and then cooled for the phase analysis to come to being manganese aluminate. The sample is grinded by planetary ball mill. The sample with SiO_2 additives was evenly mixed and grinded by planetary ball mill. Then the mixture was briquetted by mold into cylindrical briquette with a diameter of 10 mm and height of 20 mm at a pressure of 50 MPa, and then the cylindrical briquettes were dried at 110 °C for 4 h. The dried briquettes were roasted in a horizontal resistance furnace with air atmosphere and then cooled for the phase analysis to come to being manganese ferrite and mullite ($Al_6Si_2O_{13}$).

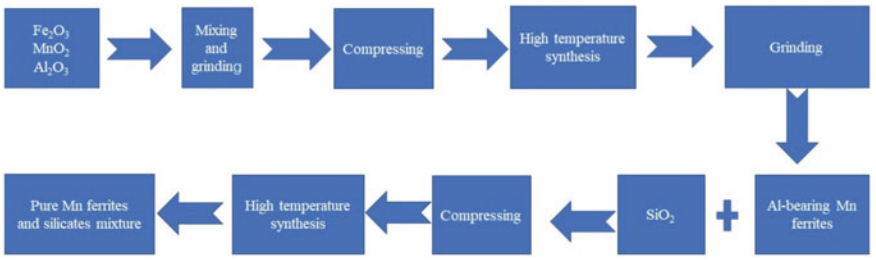

Fig. 1 The experimental process of this experiment. (Color figure online)

Characterization

FactSage7.4 thermodynamic software was used to analyze the reaction of the Al_2O_3–$Si0_2$ system. The "Equlib" module was adopted and the used databases were "FToxid" and "FactPS".

As for the migration, behavior of Al constituents in the process of manganese and ferruginous oxides forming spinel manganese ferrites was investigated by XRD. The cooled briquettes were pre-ground in an agate mortar to particle size less than 0.074 mm for the main phase identification by an X-ray diffraction using a diffractometer (X'Pert Pro MPD, Netherlands) under the conditions as follows: Cu Kα, tube current and voltage: 250 mA, 40 kV, scanning range: 10°–80° (2θ), and scanning speed: 5°/min. Note that the roasted briquettes were pre-ground in an agate mortar to a particle size passing through a 500 mesh screen (<0.025 mm) for vibrating sample magnetometer (VSM) measurements. The magnetism properties were determined by a vibrating sample magnetometer (PPMS Dynacool, Quantum Design, America) at ambient temperature.

Behaviors of Al in the MnO_2-Fe_2O_3-Al_2O_3-SiO_2 System

Effect of Al_2O_3 Content

MnO_2, Fe_2O_3, Al_2O_3, and SiO_2 are the main components of the Fe–Mn ores. MnO_2–Fe_2O_3–Al_2O_3 system is the main ternary system to research the migration behavior of Al constituents in the process of manganese and ferruginous oxides forming spinel manganese ferrites. Based on the forming spinel manganese ferrites, the molar ratio of $Mn0_2$ and Fe_2O_3 is fixed as 1:1. The dried briquettes were roasted in a horizontal resistance furnace with air atmosphere at 1300 °C for 60 min and then cooled for the phase analysis.

It can be seen from Fig. 2 that Al_2O_3 has little influence on the phase transformation of MnO_2–Fe_2O_3–Al_2O_3 system at 1300 °C, and the phases in the system are simple, mainly consisting of spinel manganese aluminate phase ($Mn_y(Al_zFe_{3-y-z})O_4$). With the increase of Al_2O_3 from 0 to 5%, Al ionics gradually enter the spinel structure's octahedral gap (B site), and the ferrite in the product changes from ($Mn_xFe_{3-x}O_4$) to manganese aluminate ($Mn_y(Al_zFe_{3-y-z})O_4$). The XRD fine scan analysis shows that the characteristic peaks of the spinel structure ferrite (311) crystal surface of the structure are gradually shifted to a large angle, indicating that the amount of Al ions entering the crystal is increasing.

Al ions entered the octahedral gap (B site) of spinel structure, and the influence of doped aluminum ions on the magnetic properties of manganese ferrite was further studied by VSM test technology, as shown in Fig. 3. The VSM test results showed that Al ion had a significant adverse effect on the magnetic properties of manganese ferrite products. When the Al_2O_3 content increased from 0 to 0.5%, the saturated

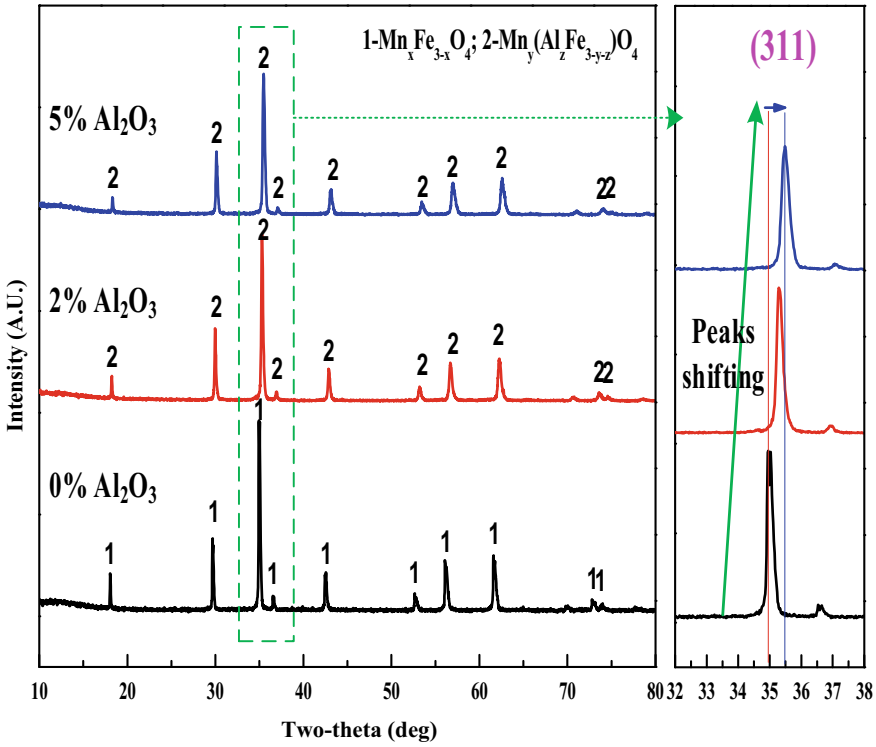

Fig. 2 Effect of Al_2O_3 content on the phase transformation of MnO_2–Fe_2O_3–Al_2O_3 system roasted at 1300 °C for 60 min. (Color figure online)

magnetization of roasted products decreased from 78.5 to 72.3 emu/g, by 7.89%. Saturation magnetization drops rapidly to 59.2 emu/g when Al_2O_3 content increases to 3%. According to the results of VSM, it can be concluded that Al element has an adverse effect on the magnetism of spinel manganese ferrite, which is not conducive to the application of spinel manganese ferrite products, and hindering the direct production of spinel manganese ferrite by oxidizing minerals. Therefore, the content of Al_2O_3 in raw materials should be controlled at a low level when preparing spinel manganese ferrite by solid reaction of manganese and ferruginous oxidizing minerals.

Effect of SiO_2

According to the binary phase diagram of Al_2O_3-SiO_2 system (Fig. 4), the reaction of silicon and alumina oxide produced mullite ($Al_6Si_2O_{13}$). The magnetic properties of $Mn(Al_{0.05}Fe_{0.95})_2O_4$ and SiO_2 samples before and after roasted were analyzed. The results are shown in Fig. 5. The saturation magnetization of samples after roasted can

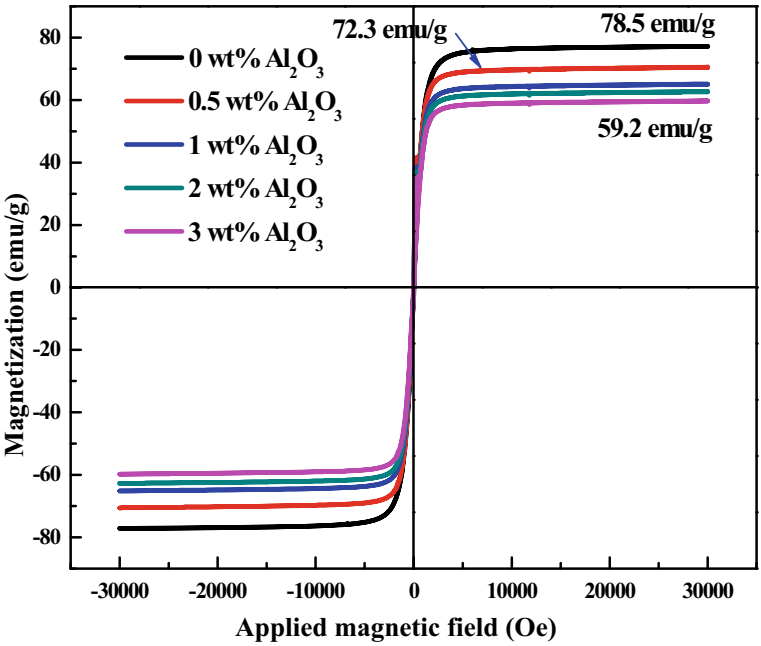

Fig. 3 Effect of Al_2O_3 content on the magnetic hysteresis loops of the MnO_2–Fe_2O_3–Al_2O_3 system roasted at 1300 °C for 2 h. (Color figure online)

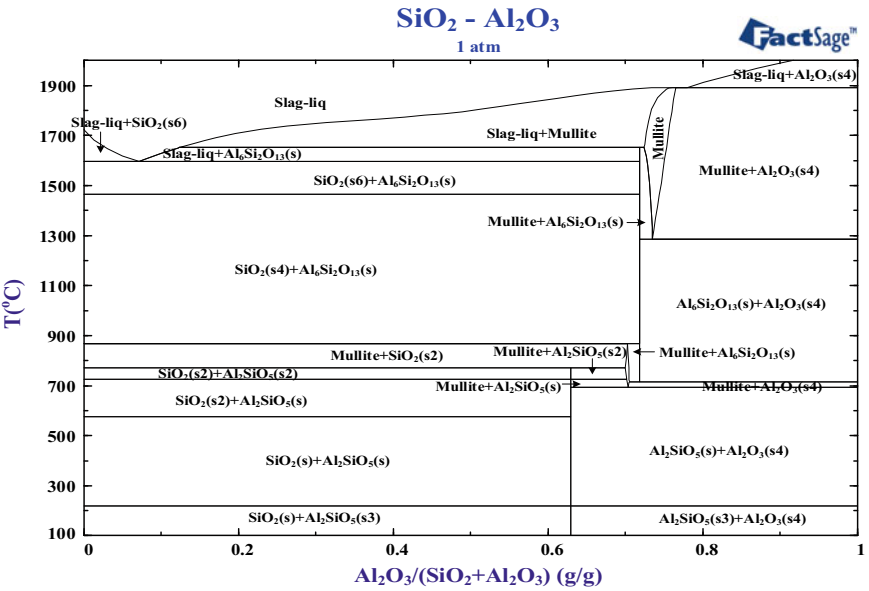

Fig. 4 Binary phase diagram of the Al_2O_3–SiO_2 system. (Color figure online)

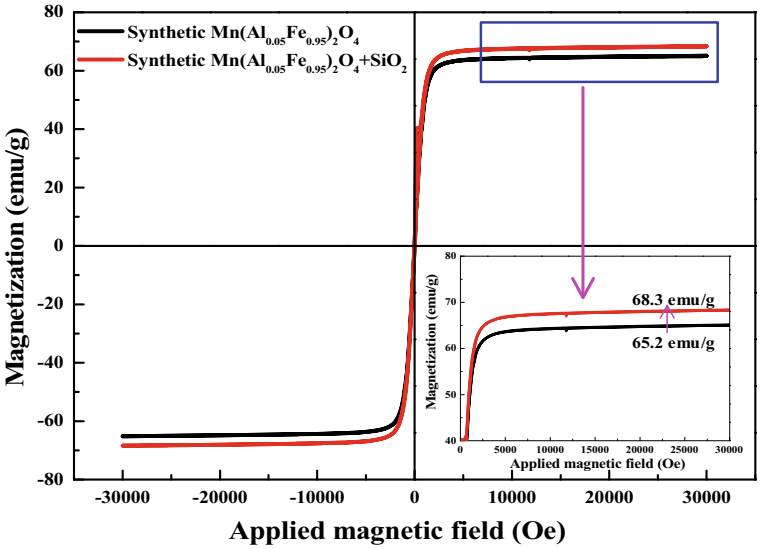

Fig. 5 Effect of SiO_2 on the VSM profiles of roasted product from the synthetic Mn $(Al_{0.05}Fe_{0.95})_2O_4$ and SiO_2. (Color figure online)

be improved from 65.2 to 68.3 emu/g, by 4.75%. Through thermodynamic analysis, the chemical driving force generated by the reaction of SiO_2 and Al_2O_3 to form mullite can move Al element out of spinel structure. The magnetic properties of spinel manganese ferrite enhanced after SiO_2 transferred Al out of B sit of spinel. The magnetic properties of spinel manganese ferrite regulated by silicon dioxide were lower than those of spinel manganese ferrite without impurity element. Therefore, it was conducive to improve the magnetic properties of the product when the raw materials used contain Al element impurities to produce the spinel manganese ferrite, which added a certain amount of silicon dioxide.

Discussion on the Mechanism

The Al element occupies the B position of spinel manganese ferrite investigated by XRD, and the reaction mechanism of MnO_2, Fe_2O_3, and Al_2O_3 is shown in Fig. 6. Because the radius difference between manganese and iron ions is smaller, manganese and iron elements occupy positions A and B in spinel structure. By comparison, the aluminum ion occupying the B position of spinel structure owe to have a bigger radius.

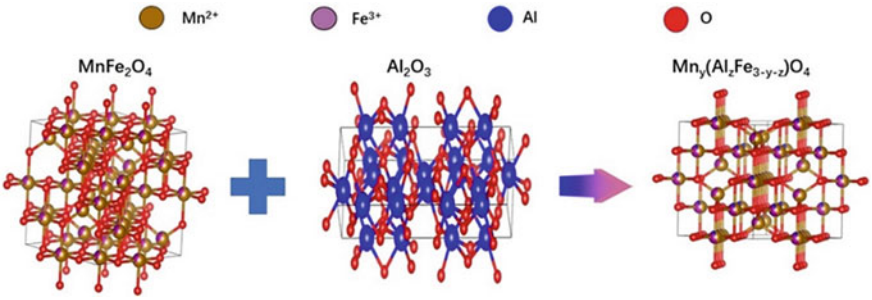

Fig. 6 Formation of $Mn_y(Al_zFe_{3-y-z})O_4$. (Color figure online)

Conclusions

In this study, it can be found that Al element entered into the spinel structure and occupied the octahedral gap (B position), which has a negative effect on the magnetism of manganese ferrite and was investigated by XRD, VSM. With the increase of Al_2O_3 content, the saturation magnetization of ferrite decreased. When Al_2O_3 content reached 3%, the saturation magnetization of ferrite decreased faster. Thermodynamic analysis showed that Al_2O_3 and SiO_2 reacted to generated mullite ($Al_6Si_2O_{13}$). SiO_2 can improve the magnetism properties of Al-bearing manganese ferrites owing to that SiO_2 was able to transfer Al out of B sit of spinel via the chemical driving force generated by the formation of mullite ($Al_6Si_2O_{13}$) from the SiO_2 and Al oxides. When producing spinel manganese ferrite with manganese and ferruginous oxides minerals, the content of Al element should be controlled lower and the corresponding amount of silicon dioxide should be added, which can reduce the adverse effect of Al element impurity on the magnetism of spinel manganese ferrite. It is instructive to provide spinel manganese ferrite from manganese and ferruginous oxide minerals.

Acknowledgements The authors wish to express their thanks to the National Natural Science Foundation of China (No. 51904273), the China Postdoctoral Science Foundation (No. 2019M660174), and the Special Support Program for High Level Talents in Henan Province (No. ZYQR201912182) for the financial support.

References

1. Fan D, Yang P (1999) Introduction to and classification of manganese deposits of China. Ore Geol Rev 15:1–13
2. Yao PH (1995) China manganese ore. Metallurgical Industry Press, Beijng, China
3. Fu Y, Xu ZG, Pei HX (2014) Preliminary study on metallogenic regularities of Manganese ore in China. J Geol 88(12):2192–2207
4. Liu BB, Zhang YB, Lu MM, Su ZJ, Li GH, Jiang T (2019) Extraction and separation of manganese and iron from ferruginous manganese ores: a review. Miner Eng 131(2019):286–303

5. Liu BB, Zhang YB, Wang (2018) New understanding on separation of Mn and Fe from ferruginous manganese ores by the magnetic reduction roasting process. Appl Surface Sci 444:133–144
6. El-Hussiny NA, El-Gawad HHA, Ahmed MM et al (2015) Reduction of low grade Egyptian manganese ore by carbon of coke breeze in the briquette form. J Multidiscip Eng Sci Technol 2(1):77–82
7. Wu Y, Shi B, Ge W et al (2014) Magnetic separation and magnetic properties of lowgrade manganese carbonate ore. JOM 67(2):361–368
8. Liu J, Lei YR, Chen X et al (2008) Recent advancement in research on spinel structural materials. Mater Rev 22(11):26–29
9. Jin HM (2013) Magnetic physics. Science Press, Beijing, China
10. Guo YC (2014) Ferromagnetics. Peking University Press, Beijing, China
11. Zhou ZG (1981) Ferrite magnetic material. Science Press, Beijing, China
12. Qu YF (2014) Functional ceramics and applications, 2nd edn. Chemical Industry Press, Beijing, China
13. Wang ZM (2013) Production technology and control technology of soft magnetic ferrite. Chemical Industry Press, Beijing, China
14. Jirák Z, Zajíček J (1978) A low temperature neutron diffraction study of manganese ferrite. Czechoslovak J Phys B 28(11):1315–1316

Preparation of Multifunctional Fused Magnesium Phosphate Fertilizer from Low-Grade Phosphate Ores

Luyi Li, Yuan Yao, Cuihong Hou, Shouyu Gu, and Haobin Wang

Abstract Low-grade phosphate ores are the main phosphorus resources in China, and it's difficult to upgrade owing to most ores belonging to collophanite with fine-grained dissemination. These inferior ores with high silicon and magnesium contents are favorable raw materials to produce fused magnesium phosphate fertilizer (FMP) for the crop growth. However, high temperature of $Ca_3(PO_4)_2$–SiO_2–MgO system for the smelting of phosphorite resulted in the energy-extensive consumption. In current study, the effect of K_2O addition on the smelting of phosphorite was investigated via thermodynamic calculations and experiment validation to reduce the smelting temperature. It has been found that 3–5% K_2O can reduce the melting temperature of the $Ca_3(PO_4)_2$–SiO_2–MgO ternary system by about 80 °C. Moreover, K_2O addition can enhance the activities of various nutrients such as potassium and magnesium in the FMP products after smelting and water quenching, and the effective conversion of the nutrients is increased by 5% compared with that without K_2O addition.

Keywords Fused magnesium phosphate fertilizer · K_2O addition · $Ca_3(PO_4)_2$–SiO_2–MgO system · Smelting temperature · Effective conversion

Introduction

Phosphate ore is a non-metallic mineral with strategic significance, and is irreplaceable and non-renewable. According to statistics from the International Fertilizer Development Center (IFDC), 82% of the phosphate rock is processed to produce phosphorus fertilizers for plants, and 4% of the phosphate rock is used as the raw material for the production of detergent additives [1, 2]. Therefore, phosphate ore resources occupy an important position in food security and the phosphorus chemical industry. With the large-scale mining of high-grade phosphate ore around the world, the reserves of rich ore have been decreasing [3], and the grade of phosphorus has

L. Li · Y. Yao · C. Hou (✉) · S. Gu · H. Wang
National Center for Research & Popularization of Calcium, Magnesium, Phosphate and Compound Fertilizer Technology, Zhengzhou University, Zhengzhou, Henan 450001, China
e-mail: hch92@zzu.edu.cn

J. Li et al., *Characterization of Minerals, Metals, and Materials 2021*,
The Minerals, Metals & Materials Series,
https://doi.org/10.1007/978-3-030-65493-1_11

continued to decline. It is foreseen that the world's phosphorus resource mining life is about 400 years, and Chinese phosphorus ore resources with a phosphorus grade of 20%–30% will be exhausted in year 2127 [4, 5].

80% of Chinese phosphate ore resources are sedimentary rocks, of which 70% are P_2O_5 15–25% middle-low-grade collophane ore containing silicon, calcium, and magnesium. Due to its small mineral grain size, densely embedded, and many harmful impurities, it makes beneficiation difficult largely, and a considerable amount of phosphorus will be lost during the beneficiation process [6]. However, middle-low-grade collophane or flotation tailings can be directly engaged in the production of fused magnesium phosphate fertilizer (FMP) . Phosphate rock and the ore containing magnesium and silicon are melted at high temperature and quenched with water to form glassy fragments with low chemical stability. FMP belongs to citric-soluble phosphate fertilizer, which can not only provide 12%–18% P_2O_5, but also 20%–35% SiO_2, 25%–40% CaO, 8%–20% MgO, and other trace elements [7–9]. In the meanwhile, the production process is simple as well as almost zero emission, and the beneficial elements in the phosphate rock and the flux are all converted into effective nutrients, which is in line with the development direction of green fertilizers. The use of these inferior minerals in the production of FMP not only avoids the high cost and phosphorus loss caused by beneficiation, as well as environmental risks caused by tailings, but also increases the utilization rate of phosphorus resources and prolongs the mining life of phosphate ore [10, 11].

However, FMP production is characterized as high temperature smelting, and electricity consumption accounts for about 80% of the total energy consumption. Due to a higher melting point of raw materials, there is an increase in the consumption of energy and the difficulty of the operation during the production process, whereas lower smelting temperature requires less time and energy. Therefore, it is of profound significance to find suitable flux to reduce the smelting temperature of the system and improve economic benefits. In this study, K_2O was selected as an additive to adjust the melting behavior of the original ore sample since it is an effective flux in other slag system. The phase transformation and characteristic fusion temperature of the $Ca(PO_4)_3$–SiO_2–MgO–K_2O system were determined based on thermodynamic analysis and XRD, and these results were verified by the smelting experiment.

Experimental Methods

Materials

Phosphate ore and dolomite used in the experiment were taken from Guizhou, China. Raw materials were dried at 120 °C for 3 h, and then ground to 100% passing 0.125 mm standard sieve. Their chemical compositions were presented in Table 1. Samples were characterized by high calcium and silica contents. XRD patterns reveal that phosphate ore mainly consists of fluorapatite, quartz, and muscovite. In order to

Table 1 Chemical compositions of the phosphate ore and dolomite/%

Composition	P_2O_5	SiO_2	CaO	MgO	Fe_2O_3	Al_2O_3	K_2O	LOI
Phosphate ore	22.33	33.79	29.65	1.67	1.74	0.5	2.45	5.67
Dolomite	–	–	29.01	17	–	1.16	–	46.59

LOI: loss on ignition

investigate the effect of different K_2O addition to the smelting of phosphorite, K_2CO_3 powder used as additive was chemically pure reagent with purity of 99.0wt%.

Smelting Process

Before oxidation smelting experiments, the raw materials consisted of phosphate ore, dolomite, with and without additives were evenly mixed and then the mixtures were put into a cylindrical heat-resistant graphite crucible with a diameter of 80 mm and height of 80 mm. The graphite crucible was loaded into the shaft furnace as illustrated in Fig. 1 and smelted isothermally in air atmosphere for 20 min. After that, melted products were quenched into cool water to attain glassy fragments. These fragments were dried and ground into pulverous samples for further characterization.

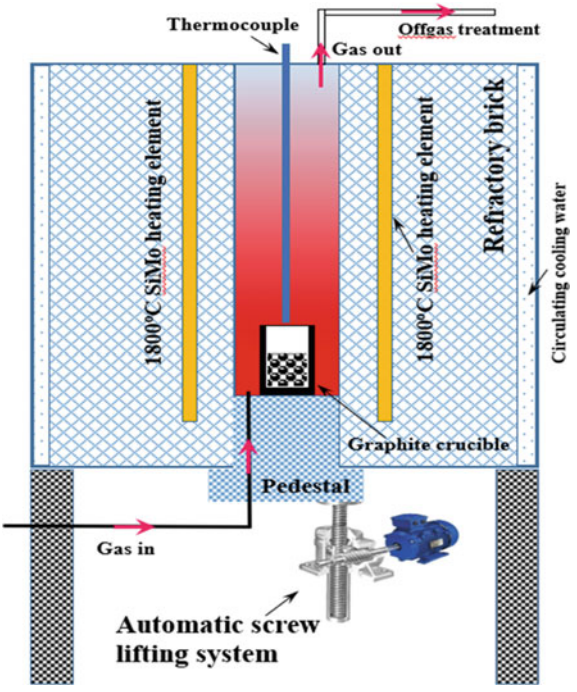

Fig. 1 The schematic diagram of shaft furnace. (Color figure online)

Characterization

FactSage7.3 software was used to analyze melting characteristics and phase diagrams of the $Ca(PO_4)_3$–SiO_2–MgO–K_2O system. The effect of K_2O content on phase diagrams and melting characteristics of the $Ca(PO_4)_3$–SiO_2–MgO system was calculated using the Phase Diagram and Equilib modules, respectively.

In terms of characteristic fusion temperatures of phosphate ore, dolomite with a certain quantity of K_2O, the mixtures were placed in a mold into pyramids with bottom side length of 8 mm and vertical height of 18 mm. The pyramids were then roasted in a microcomputer grey melting point tester with a heating rate of 5 °C/min in air atmosphere. The characteristic temperatures were identified according to (1) deformation temperature (T_D), determined by the temperature at which the tip of the pyramid becomes spherical or curved; (2) sphere temperature (T_S), determined by the temperature at which the whole pyramid deforms to be hemispheric; and (3) flow temperature (T_F), determined by the temperature at which the pyramid melts until the vertical height is less than 1.5 mm [12, 13].

Chemical Composition Analysis

To determine the effect of the addition of K_2O on the activities of a variety of nutrients in the molten pulverous sample, the effective content of nutrients was measured with reference to the 'GB/T 201412–2006 fused calcium magnesium phosphate fertilizer and fused potassium calcium magnesium phosphate fertilizer' standard, and the total element content was calculated through material balance. The effective conversion of the nutrients was calculated using Eq. (1).

$$\eta = \frac{C}{T} \times 100\% \tag{1}$$

where η is the effective conversion of the nutrients, %; C and T are the content of effective nutrient and total nutrient, respectively, %.

Results and Discussion

Effect of K_2O on Phase of $Ca_3(PO_4)_2$–SiO_2–MgO System

The main compositions of raw materials for producing FMP are P_2O_5, SiO_2, CaO, and MgO. Therefore, $Ca_3(PO_4)_2$–SiO_2–MgO system is regarded as the basic ternary system as well as the benchmark for comparative study. Phase diagrams of the

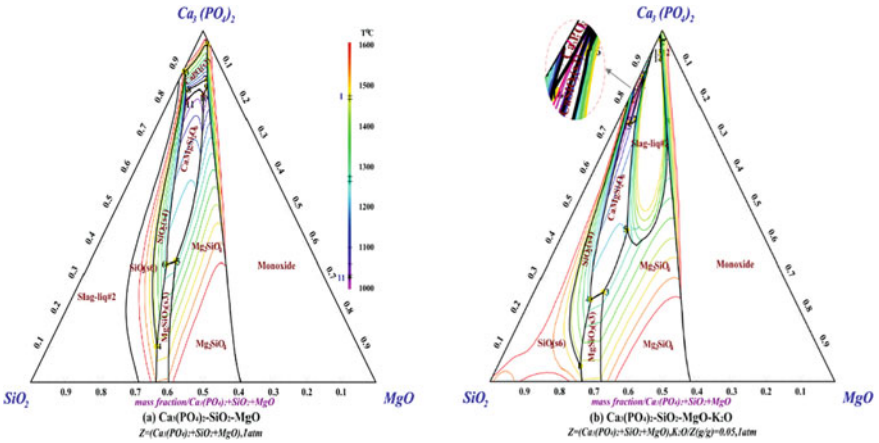

Fig. 2 $Ca_3(PO_4)_2$–SiO_2–MgO and $Ca_3(PO_4)_2$–SiO_2–MgO–K_2O phase diagrams. (Color figure online)

$Ca_3(PO_4)_2$–SiO_2–MgO system with and without a certain quantity of K_2O are calculated by software FactSage7.3 and shown in Fig. 2.

There are no significant differences between the phase of systems with and without flux. However, the lowest melting point of $Ca_3(PO_4)_2$–SiO_2–MgO–K_2O system, compared with no additive, sharply decreases from 1026 °C (point 11 in Fig. 2a) to 894 °C (point 16 in Fig. 2b), which reduces by 132 °C. It can be observed in the phase diagram that the melting point of the system will be considerably declined when the ingredients fall into the area of diopside or wollastonite, and the lowest melting point phase of the quaternary system is also transformed from diopside to wollastonite. Comparing Fig. 2a, b reveals that low-temperature wollastonite and a liquid region appear around the diopside region in the presence of 5% K_2O. The liquid phase region is altered into two larger parts. If only the phosphorus grade is supposed to be about 10% when mixing at point 3 or 4 in Fig. 2b, the production of FMP can be satisfied. This results indicates that the addition of an appropriate amount of K_2O not only reduces the smelting temperature of the system, but also the lower phosphorus grade can meet the industrial production of FMP.

Effect of K_2O Content on the Formation of Liquid Phase in the Ternary System

In order to identify the influence of K_2O on the liquid phase formation of the $Ca_3(PO_4)_2$–SiO_2–MgO system, the mass ratio of phosphate rock and dolomite (in Table 1) is fixed as 25:12. The mass percentage of the liquid phase formation of the system, consisting of P_2O_5, SiO_2, CaO, MgO, K_2O, and a few of Fe_2O_3 and Al_2O_3, is calculated using the Equilib module of Factsage 7.3 and listed in Fig. 3. K_2O content

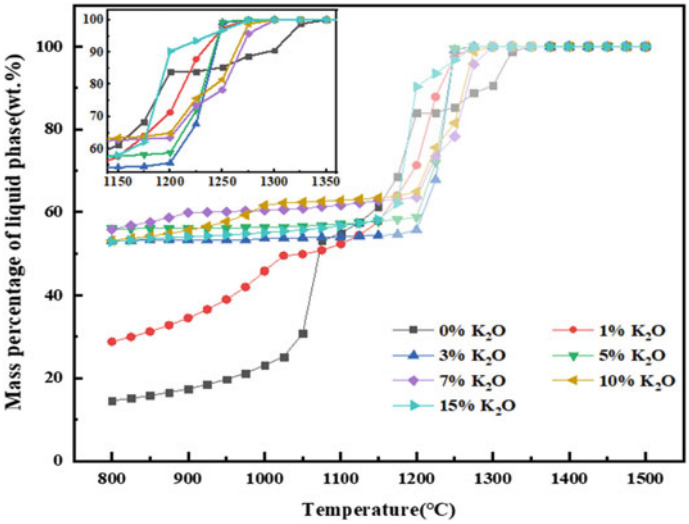

Fig. 3 Effect of K_2O content and temperature on the mass percentage of liquid phase in $Ca_3(PO_4)_2$–SiO_2–MgO system. (Color figure online)

range is 0–15% and the temperature is in the range of 800 °C–1500 °C.

The mass percentage of the liquid phase of the $Ca_3(PO_4)_2$–SiO_2–MgO system, under the constant K_2O content, has been raised markedly and then kept at a steady state with the increase of temperatures from 800 °C to 1500 °C. In the meanwhile, the liquid phase formation is much more than 50% with K_2O content within the scope of 3–15% while the mass percentage of the liquid phase is lower than 15% when K_2O is not added. It has been manifested that the liquid phase formation can speed up by adding an appropriate amount of K_2O. In particular, adding 3% or 5% of K_2O to the ternary system will almost completely form liquid phases when the temperature reaches 1250 °C, but the temperature must reach 1350 °C to melt entirely when no additive is added. The temperatures for 100% liquid phase formation of the $Ca_3(PO_4)_2$–SiO_2–MgO system decrease from 1350 °C to 1250 °C when K_2O content increases from 0% to 5%. These results indicate that the presence of K_2O can reduce the temperature of liquid phase formation and further cut down the energy consumption of FMP production.

Effect of K_2O Content on Melting Characteristics

Characteristic fusion temperatures of phosphate ore, with different K_2O content roasted in air atmosphere mixtures, are listed in Fig. 4. With K_2O content increasing from 0% to 15%, the characteristic fusion temperatures of the mixtures first decrease rapidly and then slightly increase until it tends to be stable, presenting a ‘valley’ at

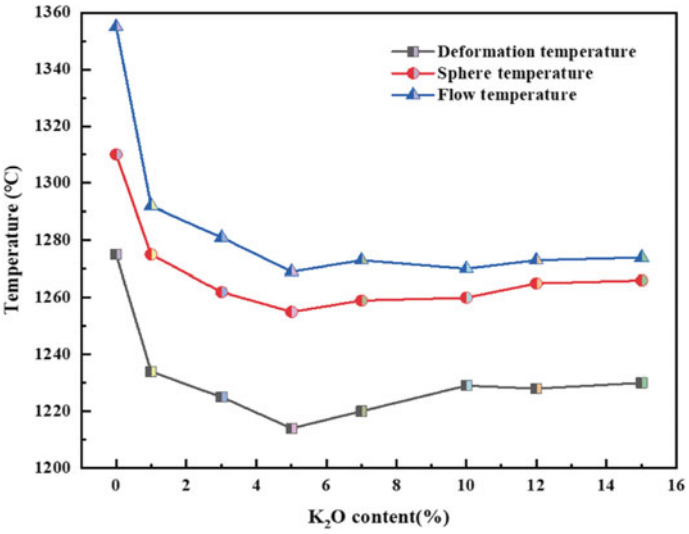

Fig. 4 Effect of K_2O content on the fusion characteristic temperatures of $Ca_3(PO_4)_2$–SiO_2–MgO system. (Color figure online)

K_2O of 5%. However, the overall trend is decreasing with the continuous increase of K_2O content. The mixtures with no additive are supplied with higher characteristic fusion temperature in air atmosphere, with the corresponding T_D, T_S, and T_F of 1275 °C, 1310 °C, and 1355 °C, respectively. Under the addition of 5% K_2O, T_D, T_S, and T_F reach the minimum values of 1214 °C, 1255 °C, and 1269 °C, respectively. Compared to the mixture with no additives, the corresponding temperatures reduce by 61 °C, 55 °C, and 86 °C, respectively. When 3–5% K_2O is added, the flow temperatures are decreased by about 80 °C. It is economically reasonable to add certain amount of K_2O to the smelting process of phosphate ore for the production of FMP since the addition of K_2O can lower the melting temperature by about 80 °C. It is also beneficial to prepare multifunctional fused magnesium phosphate fertilizer from low-grade phosphate ores at a lower oxidation temperature.

Effect of K_2O on the Activities of Various Nutrients

Potassium is one of the macronutrient elements necessary for plant growth, but potassium content in phosphate rock is generally exceedingly low. To confirm the effect of K_2O on the activities of nutrients, phosphate rock and dolomite at a mass ratio of 25:12 were mixed with different K_2O contents, and the mixture is placed in a graphite crucible to melt at 1400 °C for 20 min in the shaft furnace shown in Fig. 1. The temperature of this experiment is set at 1400 °C due to the fact that the industry requires a temperature higher than the flow temperature of 100–150 °C for

smooth slag discharge. The dried and ground pulverous samples, known as FMP, are then used for XRD detection and chemical analysis. XRD patterns and chemical compositions of FMP are listed in Fig. 5 and Table 2, respectively.

XRD patterns of pulverous samples have no obviously sharp diffraction peaks, basically showing wide-range and slowly changing diffraction peaks, which indicate that the samples made in this experiment are glassy substances with higher purity. However, it turns out that the main phases of the powder sample with 2θ between 30° and 35° are fluorapatite and zoisite without adding K_2O, implying that these substances are precipitated in the slag system, which will lead to the lowering of the effectiveness of phosphorus, silicon, and calcium in FMP product. At the same time, it has been shown in Table 2 that the activities of nutrients in the FMP product with an appropriate amount of K_2O are higher, and the effective conversion of nutrients is increased by about 5%. More significantly, the effective conversion of magnesium

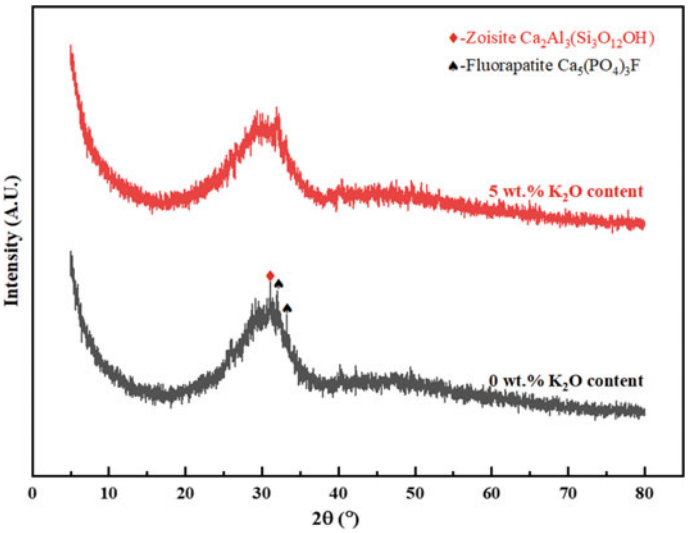

Fig. 5 XRD patterns of the mixtures smelted at 1400 °C for 20 min in air atmosphere. (Color figure online)

Table 2 The chemical compositions of FMP

K_2O content/%	Content/%	P_2O_5	SiO_2	CaO	MgO	K_2O
0	C	15.31	24.27	30.77	7.17	1.83
	T	18.01	28.33	36.59	8.30	2.07
	η	85.03	85.68	84.09	86.37	88.36
5	C	15.73	24.22	31.18	7.11	7.38
	T	17.44	26.93	34.73	7.83	7.85
	η	90.17	89.93	89.78	90.73	94.02

and potassium in the sample is higher than that of phosphorus, silicon, and calcium. It has been concluded that K_2O addition in the thermal preparation of FMP can improve the effectiveness of elements and further increase the potassium content of the sample.

Conclusions

The effect of K_2O addition on phase transformation and characteristic fusion temperature of the $Ca(PO_4)_3$–SiO_2–MgO system was investigated by thermodynamics and experimental confirmation. Thermodynamics results indicated that the lowest melting point of $Ca_3(PO_4)_2$–SiO_2–MgO–K_2O system reduced by 132 °C due to the formation of low-temperature wollastonite, and K_2O addition can decrease the temperature for liquid phase formation of the $Ca_3(PO_4)_2$–SiO_2–MgO system dramatically. The melting temperature decreased by about 80 °C with 3–5% K_2O addition.

When phosphate ore was melted with different K_2O contents at 1400 °C for 20 min in the shaft furnace, the effective conversion of nutrients in the FMP product was enhanced by 5% compared with that without K_2O addition. In particular, the effective conversion of magnesium and potassium in the sample was higher than other nutrients since the precipitation of fluorapatite and zoisite from the glass material reduced the effective content of other nutrients.

Acknowledgements The authors wish to express their thanks to the National Key Research and Development Program of China (No. 2016YFD0200401, 2018YFC1900200) and the Program for Innovative Research Team (in Science and Technology) in University of Henan Province (No. 19IRTSTHN028) for the financial support.

References

1. Van Kauwenbergh SJ (2010) World phosphate rock reserves andresources. IFDC, Savannah, pp 16–18
2. Van Kauwenbergh SJ (2014) Global phosphate rock reserves and resources, the future of phosphate fertilizer. IFDC, Savannah
3. Ganesapillai M, Simha P, Beknalkar SS, Sekhar DM (2016) Low-grade rock phosphate enriched human urine as novel fertilizer for sustaining and improving agricultural productivity of Cicer arietinum. Sustain Prod Consump, 62–66
4. Reijnders L (2014) Phosphorus resources, their depletion and conservation, a review. Resour Conserv Recycl, 32–49
5. PETEA I (2016) Phosphate depletion in china. Fertilizer International, 471:50
6. Abouzeid AZM (2008) Physical and thermal treatment of phosphate ores-An overview. Int J Miner Process 85(4):59–84
7. Zafar ZI, Anwar MM, Pritchard DW (1996) Innovations in beneficiation technology for low grade phosphate rocks. Nutr Cycl Agroecosys 46(2):135–151

8. Izbrodin IA, Ripp GS, Doroshkevich AG (2011) Aluminium phosphate and phosphate-sulphate minerals in kyanite schists of the Ichetuyskoye area, West Transbaikalia, Russia: crystal chemistry and evolution. Miner Petrol 101(1–2):81–96
9. Hou CH, Miao JY, Gu SY, Wang HB, Wang YY, Xu XC (2019) Innovation of fused calcium magnesium phosphate products to promote industry development. J Plant Nutrition Fertilizer 25(12):2162–2169
10. Cooper J, Lombardi R, Boardman DI (2011) The future distribution and production of global phosphate rock reserves. Resour Conserv Recycl, 78–86
11. Cordell D, Drangert J, White S (2009) The story of phosphorus: Global food security and food for thought. Global Environ Chang 19(2):292–305
12. Luo J, Li G, Rao M, Zhang Y, Peng Z, Zhi Q, Jiang T (2015) Evaluation of sintering behaviors of saprolitic nickeliferous laterite based on quaternary basicity. JOM 67(9):1966–1974
13. Liu BB, Li RJ, Su SP, Zhang YB (2020) Characterization on the behaviors of Ca and Si constituents during the consolidation of ferruginous manganese ores. In: TMS characterization of minerals, metals, and materials, pp 126–135

Zinc Extraction from Industrial Waste Residue by Conventional Acid Leaching

Tingfang Xie, Chengyu Sun, Guojiang Li, Yongguang Luo, Xuemei Zheng, and Aiyuan Ma

Abstract Because zinc consumption rises and the high-grade zinc ore reserves decrease year by year, the secondary zinc resources have been paid close attention. The effect of sulfuric acid solution on the zinc recovery from industrial waste residue was studied in this paper. The results showed that under the conditions of sulfuric acid concentration of 0.61 M, liquid–solid ratio of 4:1, stirring speed of 400r/min, temperature of 25 °C, and leaching time of 30 min, the system had a relatively high zinc leaching rate, which reached 86.34%.

Keywords Zinc · Leaching · Sulfuric acid · Industrial waste residue

Introduction

Industrial residue from metallurgical process is a hazardous waste material often containing valuable metal elements, such as zinc, iron, lead, cadmium, indium, and other environmentally toxic elements, while they are important secondary resources [1–4]. A large quantity of these valuable secondary resources is deposited outside plants and dumped, threatening ecological and economic sustainability [5–8].

C. Sun (✉)
Faculty of Metallurgy and Energy Engineering, Kunming University of Science and Technology, Kunming 650093, China
e-mail: chxzscyg@163.com

T. Xie
Shaanxi Key Laboratory of Electrical Materials and Infiltration Technology, School of Materials Science and Engineering, Xi'an University of Technology, Xi'an 710048, China

T. Xie · X. Zheng (✉) · A. Ma
School of Chemistry and Materials Engineering, Liupanshui Normol University, Liupanshui 553004, China
e-mail: zxm_lpssy19@163.com

C. Sun · G. Li · Y. Luo
Yunnan Chihong Zn & Ge Co., Ltd, Qujing 655011, China

J. Li et al., *Characterization of Minerals, Metals, and Materials 2021*,
The Minerals, Metals & Materials Series,
https://doi.org/10.1007/978-3-030-65493-1_12

It is well known that recycling and utilization of industrial wastes save raw materials and energy and contribute to environmental protection [9–11]. The aim of current study is to investigate the factors affecting the leaching efficiency of zinc from industrial waste residue with sulfuric acid. The effects of reaction time, sulfuric acid concentration, leaching temperature, stirring speed, and liquid–solid ratio on zinc leaching rate were studied in detail.

Materials and Methods

Materials

The zinc residue used for this study was taken from a company in Yunnan Province in China. The results of the X-ray fluorescence analysis of the residue were given in Table 1. The sample contains an average of 24.27 wt% zinc, 21.66 wt% iron, 9.14 wt% carbon, 2.94 wt% chlorine, and 4.10 wt% calcium. Si, Mg, S, and Pb are the minority elements in waste residue.

The X-ray diffraction (XRD) analysis of the waste residue was shown in Fig. 1. It has been indicated that the major mineral phases in the residue are ZnO, $Zn_2(OH)_8Cl_5H_2O$, ZnS, Zn_2SiO_4, $ZnFe_2O_4$, Fe_3O_4, Fe_2O_3, KCl, and SiO_2

Table 1 Chemical composition of waste residue sample (mass fraction, %)

Composition	Zn	Fe	C	Si	Pb	S	CaO	Mg	Cl
Content (%)	24.74	21.66	9.14	2.66	1.13	1.39	4.10	1.14	2.94

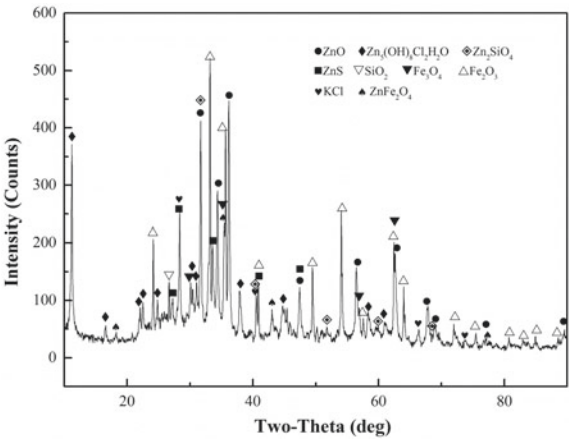

Fig. 1 X-ray diffraction (XRD) pattern of waste residue sample

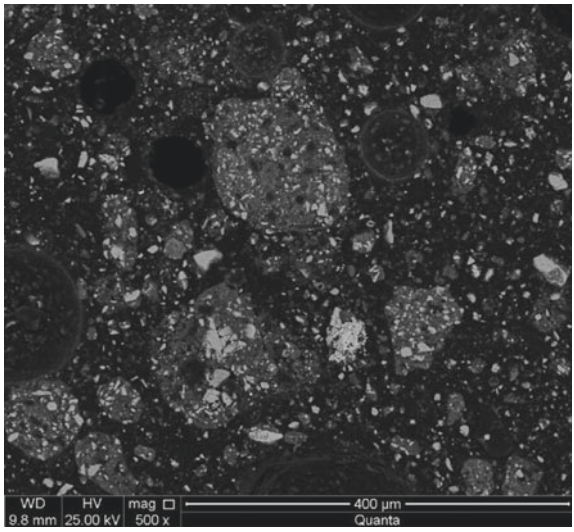

Fig. 2 Scanning electron micrograph of waste residue sample

Scanning electron microscopy (SEM) was executed to get the structure and morphology characteristics of the residue. Figure 2 shows that the particles of waste residue are evenly dispersed, most granular materials exist as inclusions.

Experimental Methods and Calculation of Metal Extraction Ratio

The dry waste residue sample (20 g) was taken and blended with sulfuric acid solution for each leaching process. All agents used in the leaching processes were analytical grade. The leaching experiments were performed in a glass reactor of 300 ml provided with a magnetic stirrer to uniformly disperse the waste residue sample with a leaching agent.

The amount of reaction time, sulfuric acid concentration, leaching temperature, stirring speed, and liquid–solid ratio on zinc leaching rate were among the investigated parameters in the leaching experiments. The detailed leaching experiments are displayed in Table 2.

The reactions of the main species that exist in the waste residue sample with sulfuric acid solution are presented in Eqs. (1–5):

$$ZnO + H_2SO_4 = ZnSO_4 + H_2O \quad (1)$$

$$FeO + H_2SO_4 = FeSO_4 + H_2O \quad (2)$$

Table 2 The leaching experiments of different leaching processes

Experiment variable	Leaching time (min)	Acid concentration (M)	Stirring speed (rpm)	L/S ratio (mL/g)	Temperature (°C)
t: 2,5,10,20,30, 40,50,60	/	0.61	400	4:1	25
C: 30,40,50,55, 60,65,70	30	/	400	4:1	25
S:100,200,300,400, 450,500,600	30	0.61	/	4:1	25
L/S: 2:1,3:1,4:1, 5:1,6:1	30	0.61	400	/	25
T: 25,35,45,55, 60,65,70	30	0.61	400	4:1	/

$$Fe_2O_3 + 3H_2SO_4 = Fe_2(SO_4)_3 + 3H_2O \tag{3}$$

$$ZnS + H_2SO_4 = ZnSO_4 + H_2S \tag{4}$$

$$ZnFe_2O_4 + 4H_2SO_4 = ZnSO_4 + Fe_2(SO_4)_3 + 4H_2O \tag{5}$$

After the leaching experiments, the zinc dissolution concentration was determined by the Ethylene Diamine Tetraacetic Acid (EDTA) titrimetric method. The zinc extraction ratio (η_{Zn}, %) was calculated as follows:

$$\mu_{Zn} = \frac{C_{Zn} \times V}{m \times w^*_{Zn}} \tag{6}$$

where η_{Zn} is the zinc extraction ratio (%); C_{Zn} is the Zn concentration of the leaching solution (g/L); V is the leaching volume (L); m is the mass of the zinc waste residue (g); and w^*_{Zn} is the Zn content of the zinc waste residue (24.74%).

Results and Discussion

Effects of Leaching Time

The leaching tests were carried out with reaction times between 2 and 60 min under constant conditions of sulfuric acid concentration of 0.61 M, reaction temperature of 25 °C, stirring speed of 400 rpm, and liquid–solid ratio of 4:1 (mL/g). The results illustrated in Fig. 3 show that the zinc extractions increased from 33.37% to 85.18% as the leaching time increased from 2 min to 30 min and the reaction was almost

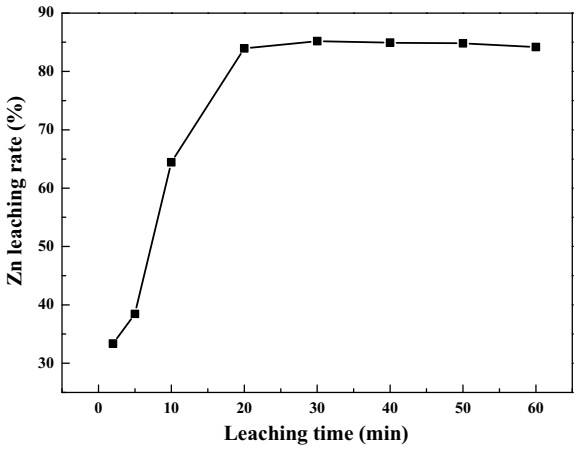

Fig. 3 Effects of different leaching times on the zinc extraction

completed in 30 min. Therefore, the leaching time should be set to 30 min in the follow-up experiment.

Effects of Sulfuric Acid Concentration

The variations of acid concentration on zinc leaching rate were investigated at a reaction temperature of 25 °C, liquid–solid ratio of 4:1 (mL/g), stirring speed of 400 rpm, and leaching time of 30 min. The result was shown in Fig. 4. It indicates that the zinc extraction rate increases from 26.49% to 84.97% with the increase in the total ammonia concentration from 0.31 M to 0.61 M. When the acid concentration

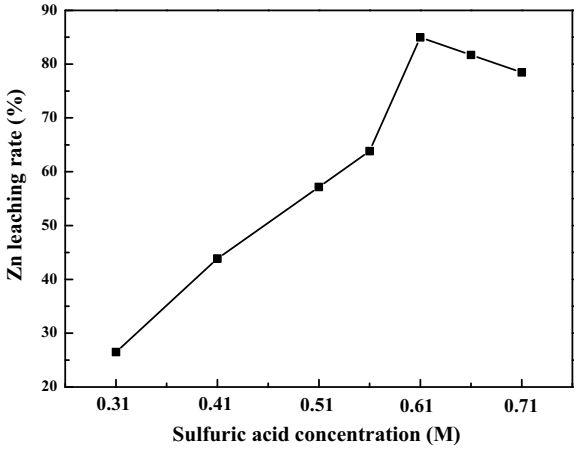

Fig. 4 Effects of different sulfuric acid concentrations on the zinc extraction

was greater than 0.61 M, the recovery of zinc first reached the maximum value and then decreased slightly. However, when production practice and economic benefits are taken into account, an acid concentration of 0.61 M is also acceptable. Hence, an appropriate sulfuric acid concentration of 0.61 M was selected to investigate the effect of the other parameters in the experiment.

Effects of Stirring Speed

The effects of stirring speeds on the dissolution of zinc were investigated at various stirring speeds (100, 200, 300, 400, 450, 500, and 600 rpm) with a sulfuric acid concentration of 0.61 M, reaction temperature of 25 °C, leaching time of 30 min, and liquid–solid ratio of 4:1 (mL/g). As Fig. 5 indicates, dissolution of zinc was affected by changes in stirring speed. The results show that the leaching rate of zinc increases quickly below 400 rpm and remains almost constant beyond this speed to 600 rpm. The zinc extraction increases from 36.46% to 85.93% with an increased stirring speed from 100 to 400 rpm. Therefore, the stirring speed was determined at 400 rpm in subsequent experiments.

Effects of Liquid–Solid Ratio

The effect of the various liquid–solid ratio on zinc extraction was evaluated in the range of 2:1 to 6:1 (mL/g), and the results are presented in Fig. 6. Other conditions included a sulfuric acid concentration of 0.61 M, a leaching temperature of 25°C, stirring speed of 400 rpm, and a leaching time of 30 min. As shown in Fig. 6, the zinc

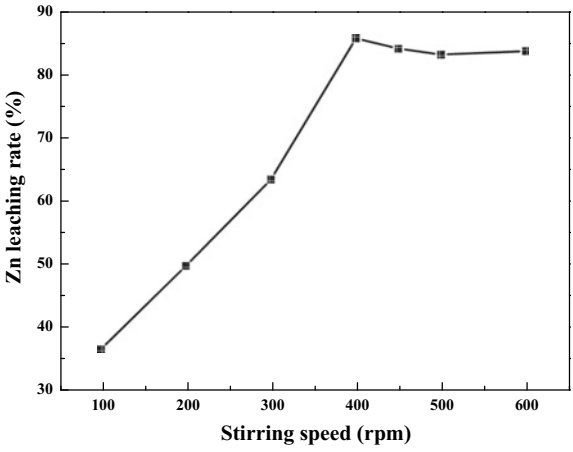

Fig. 5 Effects of different stirring speeds on the zinc extraction

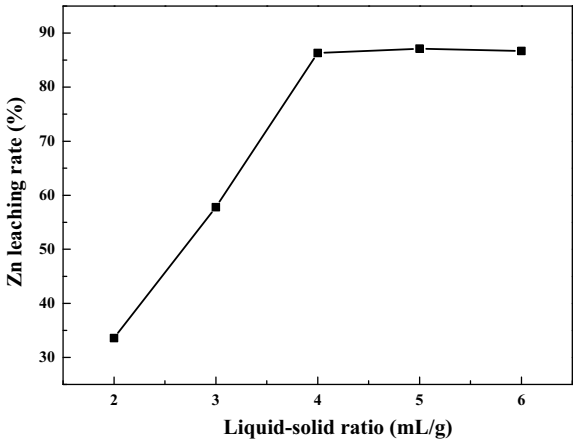

Fig. 6 Effects of different liquid–solid ratios on the zinc extraction

leaching efficiency increases significantly from 33.57% to 86.34% with an increased liquid–solid ratio from 2:1 to 4:1. With the increase of initial liquid–solid ratio from 4:1 to 7:1, the extraction of zinc did not substantially change. An excessively high liquid–solid ratio did not substantially increase the zinc leaching rate. Thus, the appropriate liquid–solid ratio was chosen as 4:1 (mL/g) for further experiments.

Effects of Leaching Temperature

The effect of temperature on zinc extraction was also performed. The waste residue sample was leached with 0.61 M sulfuric acid solution at a liquid–solid ratio of 4:1 (mL/g); stirring speed of 400 rpm; and temperatures of 25, 35, 45, 55, 60, 65, or 70 °C for 30 min. As shown in Fig. 7, the extraction of zinc slowly increased from 85.51% to 87.31% with increasing temperature from 25 °C to 70 °C. In view of these results, the optimum temperature for acid leaching was determined to be 25 °C.

On the basis of the mentioned single-factor experiments, an integrated experiment was conducted under the optimized leaching conditions. The results of the integrated acid leaching experiment are shown in Table 3

Conclusions

The study on zinc leaching from zinc industrial waste residue by conventional sulfuric acid leaching process was performed. The effects of reaction time, sulfuric acid concentration, leaching temperature, stirring speed, and liquid–solid ratio on zinc

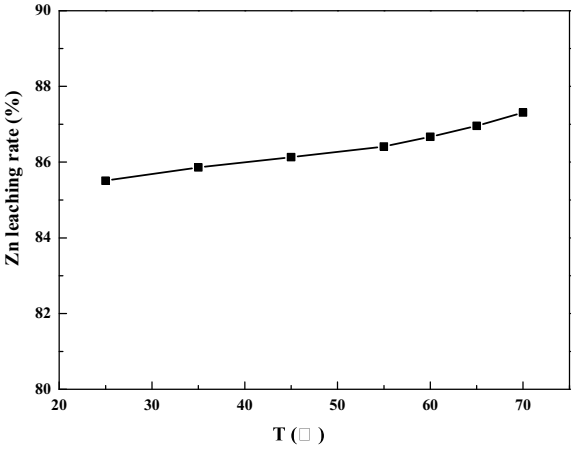

Fig. 7 Effects of different temperatures on the zinc extraction

Table 3 Results of the integrated acid leaching experiments

Optimized leaching conditions					Extraction ratio of zinc
Leaching time (min)	Acid concentration (M)	Stirring speed (rpm)	L/S ratio (mL/g)	Temperature (°C)	86.34%
30	0.61	400	4:1	25	

leaching rate were discussed. The results showed that the recovery rate of zinc extraction from waste residue reached 86.34% under the integrate condition of sulfuric acid concentration 0.61 M, reaction temperature 25 °C, liquid–solid ratio 4:1 (mL/g), stirring speed 400 rpm, and leaching time 30 min.

Acknowledgements The authors are grateful for the Nonferrous Metal Electro-deposition Technology Provincial Innovation Team of Yunnan Chihong Zn & Ge Co., Ltd (201905E160007), China Scholarship Council (CSC 202008530041), the Guizhou provincial colleges and universities science and technology top-notch talent support program project (KY [2018]066), the Guizhou province science and technology plan key project (No. [2019]1444), the Liupanshui Key Laboratory of Metallurgical Energy Saving, Environmental Protection and Recycling Economy (52020-2018-0304), and the Science and Technology Innovation Group of Liupanshui Normol University (LPSSYKJTD201801).

References

1. Holloway PC, Etsell TH (2013) Recovery of zinc, gallium and indium from La Oroya zinc ferrite using Na_2CO_3 roasting. Miner Process Extr Metall 117(3):137–146
2. Wang YL, Li X, Liu HX, Qian P, Ye SF, Chen YF (2018) Acid leaching pretreatment on two-stage roasting pyrite cinder for gold extraction and co-precipitation of arsenic with iron. Hydrometallurgy 179:192–197
3. Ma AY, Zheng XM, Li S, Wang YH, Zhu S (2018) Zinc recovery from metallurgical slag and dust by coordination leaching in NH_3–CH_3COONH_4–H_2O system. R Soc Open Sci 5:180660
4. Chen WS, Shen YH, Tsai MS, Chang FC (2011) Removal of chloride from electric arc furnace dust. J Hazard Mater 190(1–3):344–639
5. Trinkel V, Mallow O, Aschenbrenner P, Rechberger H, Fellner J (2016) Characterization of blast furnace sludge with respect to heavy metal distribution. Ind Eng Chem Res 55:5590–5597
6. Das B, Prakash S, Reddy PSR, Misra VN (2007) An overview of utilization of slag and sludge from steel industries. Resour Conserv Recycl 50:40–57
7. Ma AY, Zheng XM, Peng JH, Zhang LB, Srinivasakannan C (2017) Dechlorination of metallurgical solid waste residue derived from zinc leaching residue by microwave roasting in a rotary kiln. Braz J Chem Eng 34(1):193–202
8. Omran M, Fabritius T (2019) Utilization of blast furnace sludge for the removal of zinc from steelmaking dusts using microwave heating. Sep Purif Technol 210:867–884
9. Omran M, Fabritius T (2017) Effect of steelmaking dust characteristics on suitable recycling process determining: ferrochrome converter (CRC) and electric arc furnace (EAF) dusts. Powder Technol 308:47–60
10. Havlík T, Souza BV, Bernardes AM, Schneider IAH, Miskufova A (2006) Hydrometallurgical processing of carbon steel EAF dust. J Hazard Mater 135(1):311–318
11. Kukurugya F, Vindt T, Havlík T (2015) Behavior of zinc, iron and calcium from electric arc furnace (EAF) dust in hydrometallurgical processing in sulfuric acid solutions: Thermodynamic and kinetic aspects. Hydrometallurgy 154:20–32

Extraction of Zinc from Metallurgical Residue with a NH_3–$(NH_4)_2SO_4$–H_2O System

Chengyu Sun, Aiyuan Ma, Yongguang Luo, Guojiang Li, Tingfang Xie, and Xuemei Zheng

Abstract Metallurgical solid waste residue contains a certain amount of Zn, which is an important secondary resource for the production of Zn. In this article, a hydrometallurgical method in a NH_3–$(NH_4)_2SO_4$–H_2O system is proposed to recover Zn selectively from metallurgical solid waste residue. The results showed the highest zinc extraction of 77.55% was obtained by using a total ammonia concentration of 5 mol/L of the leaching agent, stirring speed of 400 rpm, ammonia/ammonium ratio ($[NH_3]/[NH_4]^+$) of 1:1, solid/liquid ratio of 1:4, leaching time of 30 min, and leaching temperature of 25 °C.

Keywords Metallurgical solid waste residue · Zinc · NH_3–$(NH_4)_2SO_4$–H_2O system

Introduction

Metallurgical residue of zinc is a hazardous waste material containing valuable elements, such as zinc (Zn) , iron (Fe), lead (Pb), cadmium (Cd), and other non-ferrous metals, and a small amount of rare indium (In) metals, as well as other environmentally harmful elements, which are important secondary resources for the production

C. Sun · Y. Luo (✉)
Faculty of Metallurgy and Energy Engineering, Kunming University of Science and Technology, Kunming 650093, China
e-mail: chxzscyg@163.com

A. Ma (✉) · X. Zheng
School of Chemistry and Materials Engineering, Liupanshui Normol University, Liupanshui 553004, China
e-mail: may_kmust11@163.com

T. Xie
Shaanxi Key Laboratory of Electrical Materials and Infiltration Technology, School of Materials Science and Engineering, Xi'an University of Technology, Xi'an 710048, China

C. Sun · Y. Luo · G. Li · T. Xie
Yunnan Chihong Zn & Ge Co., Ltd, Qujing 655011, China

J. Li et al., *Characterization of Minerals, Metals, and Materials 2021*,
The Minerals, Metals & Materials Series,
https://doi.org/10.1007/978-3-030-65493-1_13

of Zn [1–5]. However, the existence of chlorine (Cl) and gangue elements (Ca and Mg) in the residue makes it difficult to recover Zn by conventional acid leaching, which strongly affects its utilization in zinc-based electrical products [6, 7]. The zinc extracted from metallurgical solid waste residue has potential economic benefits in recycling, reutilization, exploitation, and application of solid waste pollutants.

Many researchers have focused on the ammonia leaching process in recent years. The selective extraction of zinc can be achieved through ammonia leaching, as the metal zinc passes into a solution, while the iron, gangue minerals, chlorides remain in the solid residue [8, 9]. Hence, this process is more environmentally friendly and cost-efficient than the conventional methods. In this article, a clean zinc production process using NH_3–$(NH_4)_2SO_4$ as a leaching agent has been developed.

Materials and Methods

Materials

The metallurgical solid waste residue material in this study was purchased from a metallurgical plant in Yunnan Province in China. Results of the XRF analysis of the waste residue sample are given in Table 1. The sample contains an average of 24.27 wt% zinc, 21.66 wt% iron, 9.14 wt% carbon, 2.94 wt% chlorine, and 4.10 wt% calcium. Both zinc and iron account for 45.93% in weight of the total sample with a zinc to iron ratio of 1.1:1.

The X-ray diffraction (XRD) analysis of the metallurgical solid waste residue samples is presented in Fig. 1. Characteristic peak intensity positions show that the main crystalline phases presented in this sample are zinc oxide and ferric oxide. Zn mainly existed in ZnO, $Zn_2(OH)_8Cl_5H_2O$, ZnS, Zn_2SiO_4, and $ZnFe_2O_4$ phase, Fe existed in the Fe_3O_4, Fe_2O_3, and $ZnFe_2O_4$ phases.

Experimental Methods

This metallurgical solid waste residue sample was fine powdered, it was screened by 200 mesh (75 μm) to remove large impurities and used without further treatment. The chemicals used in all experiments were analytical reagent grade. All solutions were prepared using deionized water. The leaching experiments were performed in a glass reactor of 300 ml provided with a magnetic stirrer to mix the metallurgical

Table 1 XRF analysis of waste residue sample (mass fraction, %)

Composition	Zn	Fe	C	Si	Pb	S	Al_2O_3	CaO	Mg	Cl
Content (%)	24.74	21.66	9.14	2.66	1.13	1.39	2.22	4.10	1.14	2.94

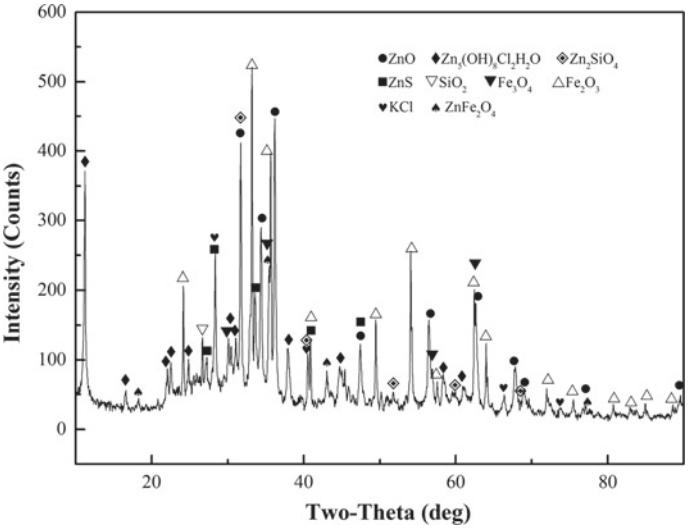

Fig. 1 X-ray diffraction analysis of metallurgical residue

solid waste residue sample with a leaching agent. The zinc leaching process was obtained by adding 20 g of a sample to the Erlenmeyer flask. A general flow sheet describing this present study is given in Fig. 2.

The amount of temperature, reaction time, stirring speed, solid/liquid ratio, total ammonia concentration, and ammonia/ammonium ratio were among the investigated parameters in the leaching experiments. The reaction of the main species that exist in the waste residue sample with ammonia solution is presented in Eqs. (1) and (2):

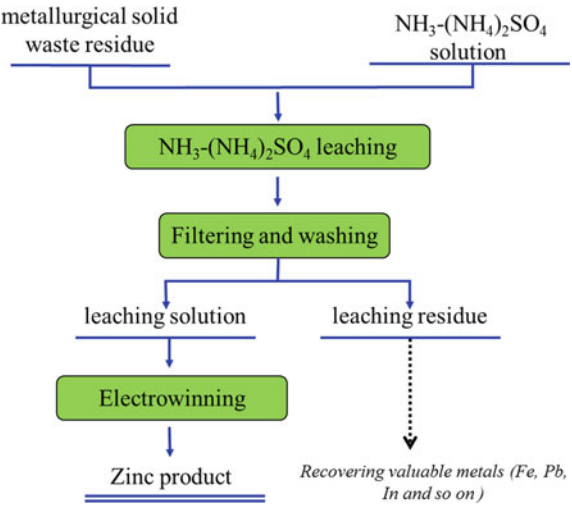

Fig. 2 Flow diagram of the leaching process. (Color figure online)

$$ZnO + iNH_4^+ = \left[Zn(NH_3)_i\right]^{2+} + H_2O + (i-2)H^+ \quad (1)$$

$$ZnO + iNH_3 + H_2O = Zn(NH_3)_i^{2+} + 2OH^- \quad (2)$$

After leaching, the concentration of zinc dissolution was determined by the Ethylene Diamine Tetraacetic Acid (EDTA) titrimetric method. The leaching rate of zinc (η_{Zn}, %) was calculated according to the following equation:

$$\eta_{Zn} = \frac{C_{Zn} \times V}{m \times w_{Zn}^*}, \quad (3)$$

where C_{Zn}, V, m, and w_{Zn}^* represent the Zn concentration of the leaching solution (g/L), the leaching volume (L), the mass of the metallurgical solid waste residue (g), and the Zn content of the metallurgical solid waste residue (%), respectively.

Results and Discussion

Effects of Leaching Time

Figure 3 shows the effect of leaching time on leaching efficiency of Zn during leaching time from 5 min to 60 min maintained at a total ammonia concentration of 5 mol/L, temperature of 25 °C, stirring speed of 400 rpm, solid/liquid ratio of 1:4, and ammonia/ammonium ratio of 1:1. The leaching efficiency of Zn increased from 72.7% to 78.62% as the leaching time increased from 5 min to 60 min and

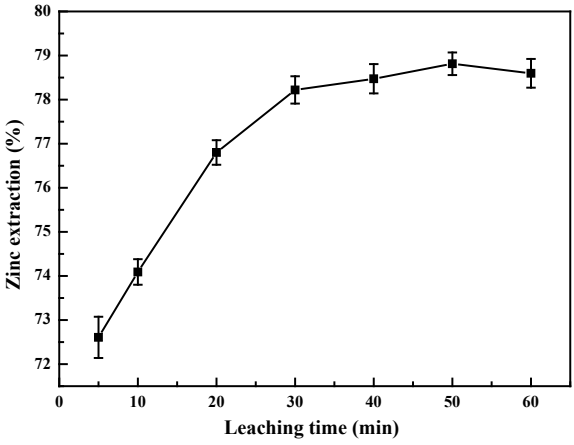

Fig. 3 Effects of different leaching times on the zinc extraction

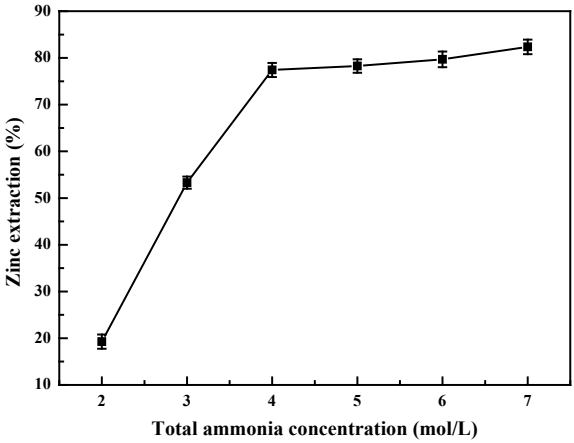

Fig. 4 Effects of different total ammonia concentrations on the zinc extraction

the reaction was almost completed in 30 min. The results demonstrated that about 30–50 min duration is sufficient to achieve maximum efficiency. While the time was more than 30 min, the zinc leaching rate changed slowly. Therefore, the leaching time should be set to 30 min.

Effects of Total Ammonia Concentration

The effects of total ammonia concentration on the extraction efficiencies of zinc are shown in Fig. 4. The total ammonia concentration was varied from 2 mol/L to 7 mol/L at a reaction time of 30 min, temperature of 25 °C, stirring speed of 400 rpm, solid/liquid ratio of 1:4, and ammonia/ammonium ratio of 1:1. It indicates that the zinc extraction rate increases from 19.39% to 77.55% with the increase in the total ammonia concentration from 1 mol/L to 4 mol/L, after which the zinc leaching rate of zinc remains approximately constant from 4 mol/L to 7 mol/L. Thus, an appropriate total ammonia concentration of 4 mol/L was selected to investigate the effect of the other parameters in the experiment.

Effects of Liquid/Solid Ratio

The leaching efficiencies of zinc in solution were evaluated using various liquid/solid ratios in the range of 2:1–7:1. The leach conditions were as follows: a stirring speed of 400 rpm, total ammonia concentration of 4 mol/L, temperature of 25 °C, leaching time of 30 min, and ammonia/ammonium ratio of 1:1. Figure 5 describes the effect

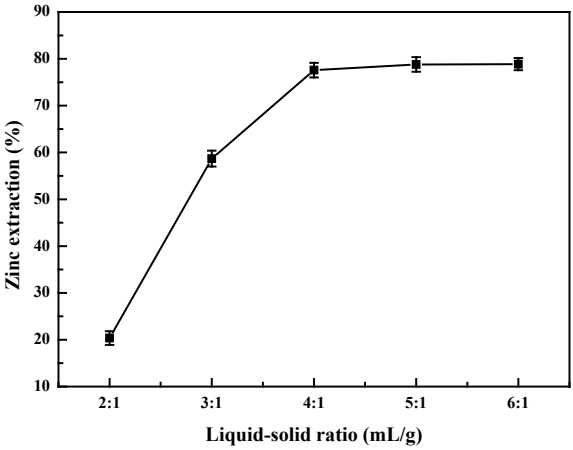

Fig. 5 Effects of different liquid–solid ratios on the zinc extraction

of the liquid/solid ratio on the dissolution of the waste residue sample. The zinc leaching efficiency increases significantly from 20.43% to 77.55% with an increased liquid/solid ratio from 2:1 to 4:1. With the increase of initial liquid–solid ratio from 4:1 to 7:1, the leaching efficiency of zinc remained basically unchanged. Therefore, an appropriate liquid/solid ratio of 4:1 is thus selected for further experiments.

Effects of Ammonia/Ammonium Ratio

Waste residue samples were leached for 30 min to investigate the influence of the ammonia/ammonium ratio ($[NH_3]/[NH_4^+]$) on the extraction of zinc. The leach conditions were as follows: stirring speed of 400 rpm, total ammonia concentration of 4 mol/L, temperature of 25 °C, and solid/liquid ratio of 1:4. In addition, the NH_3–H_2O system and $(NH_4)_2SO_4$ system were compared with the NH_3–$(NH_4)_2SO_4$–H_2O system under the same conditions. The results are shown in Fig. 6. Figure 6 shows that the effective extraction of Zn first increased and then decreased with the increase in the ammonia/ammonium ratio from 1:9 ($[NH_3]/[NH_3]_T = 0.1$) to 9:1 ($[NH_3]/[NH_3]_T = 0.9$), and the leaching rate of zinc reached the maximum value (77.55%) when the ammonia/ammonium ratio was 1:1($[NH_3]/[NH_3]_T = 0.5$). The results also suggest that the leaching rate of zinc in the NH_3–H_2O system (19.39%) and $(NH_4)_2SO_4$–H_2O system (27.7%) is relatively lower than that in the NH_3–$(NH_4)_2SO_4$–H_2O system (77.5%). In this study, zinc extraction was found to be improved with increased $(NH_4)_2SO_4$ to the NH_3–H_2O solutions. The ammonia/ammonium ratio ($[NH_3]/[NH_4^+]$) was determined at 1:1 in subsequent experiments.

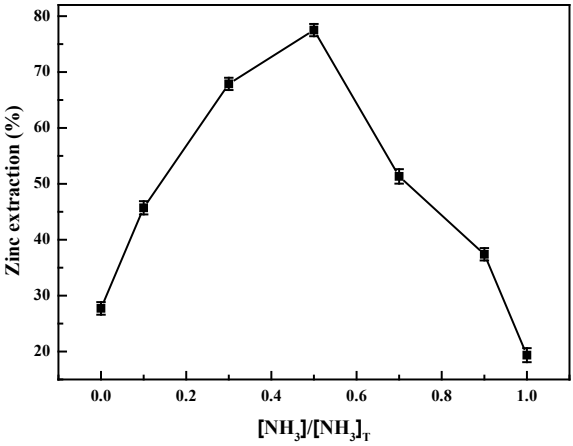

Fig. 6 Effects of different $[NH_3]/[NH_3]_T$ ratios on the zinc extraction

Effects of Stirring Speed

The effects of stirring speeds on zinc leaching rate were studied in the experiments with a total ammonia concentration of 4 mol/L, temperature of 25 °C, reaction time of 30 min, solid/liquid ratio of 1:4, and ammonia/ammonium ratio of 1:1. Figure 7 shows that the increase in agitation from 200 to 400 rpm improved the dissolution efficiency of zinc, the zinc extraction increases from 67.16% to 77.55%. With a further increase in stirring to 400 and 600 rpm, the zinc extraction remains approximately constant. Therefore, the stirring speed was determined at 400 rpm in subsequent experiments.

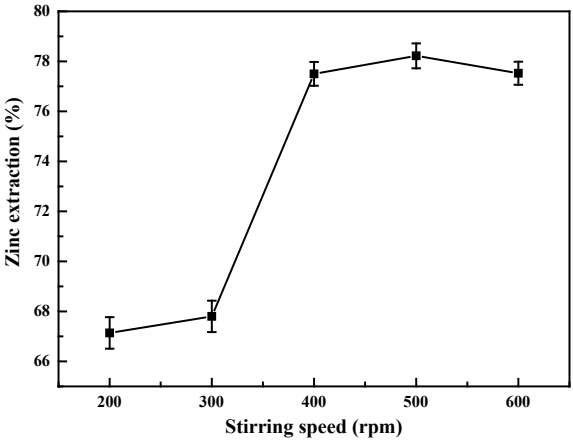

Fig. 7 Effects of different stirring speeds on the zinc extraction

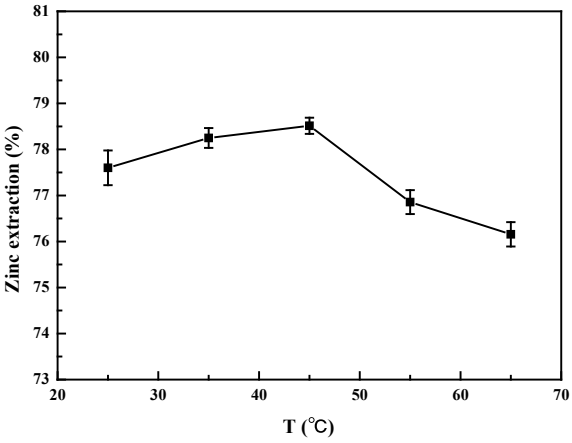

Fig. 8 Effects of different temperatures on the zinc extraction

Effects of Leaching Temperature

An investigation into the influence of temperature on zinc extraction was also performed. The leach conditions were as follows: stirring speed of 400 rpm, total ammonia concentration of 4 mol/L, leaching time of 30 min, and solid/liquid ratio of 1:4. The results are shown in Fig. 8.

The results showed that the leaching rate of zinc at 45 °C (78.53%) is significantly higher than that at 25 °C (77.55%) and 65 °C(76.16%). The main reason is that the slow diffusion of solvent molecules at low temperature directly leads to low zinc leaching rate. In addition, the solvent molecules volatilization at high temperature leads to the reduction of zinc leaching rate. Therefore, an appropriate temperature of 25 °C is considered in this paper.

Conclusions

Zinc was extracted from the metallurgical solid waste residue by NH_3–$(NH_4)_2SO_4$–H_2O system. The results indicate that a maximum zinc recovery of 77.55% was obtained by using a total ammonia concentration of 5 mol/L, stirring speed of 400 rpm, ammonia/ammonium ratio ($[NH_3]/[NH_4]^+$) of 1:1, solid/liquid ratio of 1:4, leaching time of 30 min, and leaching temperature of 25°C. The effects of leaching time, total ammonia concentration, stirring speed, ammonia/ammonium ratio, and liquid–solid ratio on zinc leaching rate were significant.

Acknowledgements The authors are grateful for Yunnan Chihong Zn & Ge Co., Ltd Nonferrous metal electro-deposition Technology Innovation Team of Yunnan Province (201905E160007), and China Scholarship Council (CSC 202008530041), the Guizhou provincial colleges and universities science and technology top-notch talent support program project (KY [2018]066), the Guizhou

province science and technology plan key project (No. [2019]1444), the Liupanshui Key Laboratory of Metallurgical Energy Saving, Environmental Protection and Recycling Economy (52020-2018-0304), the Science and Technology Innovation Group of Liupanshui Normol University (LPSSYKJTD201801).

References

1. Trinkel V, Mallow O, Aschenbrenner P, Rechberger H, Fellner J (2016) Characterization of blast furnace sludge with respect to heavy metal distribution. Ind Eng Chem Res 55:5590–5597
2. Das B, Prakash S, Reddy PSR, Misra VN (2007) An overview of utilization of slag and sludge from steel industries. Resour Conserv Recycl 50:40–57
3. Ma AY, Zheng XM, Peng JH, Zhang LB, Srinivasakannan C (2017) Dechlorination of metallurgical solid waste residue derived from zinc leaching residue by microwave roasting in a rotary kiln. Braz J Chem Eng 34(1):193–202
4. Chen WS, Shen YH, Tsai MS, Chang FC (2011) Removal of chloride from electric arc furnace dust. J Hazard Mater 190(1–3):344–639
5. Shawabkeh RA (2010) Hydrometallurgical extraction of zinc from Jordanian electric arc furnace dust. Hydrometallurgy 104(1):61–65
6. Havlík T, Souza BV, Bernardes AM, Schneider IAH, Miskufova A (2006) Hydrometallurgical processing of carbon steel EAF dust. J Hazard Mater 135(1):311–318
7. Kukurugya F, Vindt T, Havlík T (2015) Behavior of zinc, iron and calcium from electric arc furnace (EAF) dust in hydrometallurgical processing in sulfuric acid solutions: thermodynamic and kinetic aspects. Hydrometallurgy 154:20–32
8. Ma AY, Zheng XM, Li S, Wang YH, Zhu S (2018) Zinc recovery from metallurgical slag and dust by coordination leaching in NH_3–CH_3COONH_4–H_2O system. R. Soc. open sci. 5:180660
9. Shun MS, Jin GK, Dong HY, Jeong SS, Tae HK (2008) Selective leaching of zinc from spent zinc-carbon battery with ammoniacal ammonium carbonate. Mater Trans 49(9):2124–2128

Part VII
Metallurgical Process Optimization

Characterization of Brazilian Linz–Donawitz-LD Steel Sludges

Mery C. Gómez-Marroquín, Roberto R. de Avillez, Sonia Letichevsky, Dalia E. Carbonel-Ramos, Antoni L. Quintanilla-Balbuena, and Kenny A. Salazar-Yantas

Abstract Coarse sludge (sample A) and fine sludge (sample B) from a Brazilian Linz–Donawitz—LD steelworks integrated plant was characterized. Chemical analysis determined high-level content of iron (51.54–77.53%) and lower grades of zinc (0.49–1.69%). XRD analysis permitted to observe various mineralogical phases, such as metallic iron, wustite, franklinite, magnetite, portlandite, periclase, calcite, calcium oxide, silicon, moissanite-2H, and srebrodolskite. Microscopic Optical and Scanning Electron Microscopic studies shown morphologies of these residues were made up of globular and skeletal aggregates of metallic iron intergrown with crystals of iron oxides, especially wustite and a significant presence of calcite and calcium oxide in spherical nodes having particle sizes between 0.12 and 0.15 mm. Scanning Electron Microscopy–Energy-Dispersive X-ray spectroscopy studies denoted significant content of Fe, O, and Ca in both samples. In addition, a thermogravimetric analysis by DTG–DSC–TG at 1000 °C exhibited a mass loss of 97.43% for sample A and 92.57% for sample B.

M. C. Gómez-Marroquín (✉) · D. E. Carbonel-Ramos · A. L. Quintanilla-Balbuena · K. A. Salazar-Yantas
National University of Engineering, 210, Túpac Amaru Ave., Rímac, Lima LIMA 25, Peru
e-mail: mgomezm@uni.edu.pe

D. E. Carbonel-Ramos
e-mail: dcarbonelr@uni.pe

A. L. Quintanilla-Balbuena
e-mail: aquintanillab@uni.pe

K. A. Salazar-Yantas
e-mail: kenny.salazar.y@uni.pe

R. R. de Avillez · S. Letichevsky
Pontifical Catholic University of Rio de Janeiro, 225, Marquês de SãoVicente Street, Gávea, RJ 22451-900, Brazil
e-mail: avillez@puc-rio.br

S. Letichevsky
e-mail: letichevsky@puc-rio.br

J. Li et al., *Characterization of Minerals, Metals, and Materials 2021*,
The Minerals, Metals & Materials Series,
https://doi.org/10.1007/978-3-030-65493-1_14

Keywords Linz–Donawitz-LD · LD converter · BOF converter · Steel sludges · Converter process

Introduction

During the production of steel, a considerably large amount of industrial waste is generated. Various solid wastes emerging from steel plants are in the form of sludge and slag, mainly blast furnace slag, blast furnace flue dust and slag, mill scale, mill sludge, etc. [1]. Linz–Donawitz (LD) sludge is the wastes generated during the production of steel in LD converter. A huge quantity of LD sludge is generated per ton of steel produced [2]. The fine solid particles recovered after wet cleaning of the gas emerging from LD converters in the sludge form are termed as LD sludge. During this process, the furnace emits very fine iron oxide particles that are removed from the waste gases by a wet scrubbing process. This waste may contain high levels of CaO, Zn, Pb, etc., depending upon the type of limestone and chemistry of scrap used during the process of steelmaking. The sludge contains appreciable quantities of iron and lime and is therefore quite suitable for recycling in the sinter plant [3]. For example, the generation of these LD steel sludges in a Brazilian steelwork varied from 5.6 to 7.2 kg/t of crude steel for the BOF coarse sludge and from 17.0 to 22.8 kg/t of crude steel for the fine sludge. Due to its content of total iron, around 50–60% Fe, these residues could be recycled into the production process of sinter [4]. The aim of this paper was to characterize LD steel sludges using different techniques: Chemical analysis, X-ray Diffraction (XRD), Optical and Scanning Electronic Microscopy (SEM), Thermogravimetric analysis, and physical determinations in order to avoid their accumulation and suggest reuse in the steel plant itself. This reutilization would provide an added value to this material that until now is constituted as an environmental liability of considerable economic importance.

Experimental Procedures

The experiments that were part of this research involved characterization of the raw material; in this case, these were fine and coarse steel sludges sediments from an LD converter of a Brazilian integrated steelwork. For this aim, the following characterization techniques were used.

Chemical analyses were developed using an Optical Emission Spectrometer Jarrell Ash USA model Ebert 3.4 m for determining elemental composition, an Atomic Absorption Spectrometer Shimadzu (FAAS) model AA-7000 for estimating of the main oxides and a combustion analyzer Bruker, model G4 Icarus Series 2 with HF induction furnace and High-Sense detection for obtaining the contents of carbon (C) and sulfur (S).

XRD analyses were performed using a D8 Discover diffractometer, Bruker, with CuK-α radiation (λ = 1.5418 Å), Ni filter and Lynxeye detector, operating at 40 mA and 40 kV. XRD patterns were collected in the 2 θ range of 10°–90° with 0.02° increment. An energy discriminator was employed to reduce the iron fluorescence. The identification of the crystalline phases was carried out by comparison with standard patterns applying EVA program, Bruker. The crystal structures of the most probable compounds were obtained from the Inorganic Crystal Structure Database (ICSD). The experimental patterns were fitted by the Rietveld method with fundamental parameters using the TOPAS program, Bruker.

The following equipment was used in order to analyze the main morphologies of fine and coarse samples of the LD steel sludges: Polarization Microscope Carl Zeiss with image capture system, including abrasives for roughing and polishing; SEM and EDS, FEI model Quanta 650 high vacuum with 8 nA of current and 6 kV voltage, and SEM–EDAX using the quantification software TEAM.

Some physical properties were determined, such as specific gravity and average particle size. The specific gravity was calculated using the pycnometer method. The determination of the average particle size was obtained employing a series of ASTM meshes: m14, m20, m30, m50, m70, m100, m140, m200, m270, m400 and background of under m400.

Results and Discussion

Chemical Analysis

Chemical analysis determine some elements: Cu, Cd, Zn, Fe, K, Na, Ca, Pb, As, Ni, Si, Mg, Co, Hg, C, S, and some oxides: SiO_2, Al_2O_3, CaO, MgO, MnO, Na_2O, and K_2O. The chemical composition performed on both samples, A and B, of coarse and fine LD steel sludges are shown separately in Tables 1 and 2.

Table 1 Chemical compositions of oxides and elements of coarse LD steel sludges—sample A

OXIDES %							Non metals %		
SiO_2	Al_2O_3	CaO	MgO	MnO	Na_2O	K_2O	C(*)	S(*)	
0.74	0.14	3.50	1.75	0.63	0.01	0.002	0.0215	0.0219	
Metals %									
FeT	Pb	Zn	Cu	Cd	Co	Ni	Cr	As	Hg (ppm)
77.53	0.01	0.49	0.006	0.0006	0.012	0.012	0.655	0.001	0.08

(*) results of combustion analyzer

Table 2 Chemical compositions of oxides and elements of fine of LD steel sludges—sample B

Oxides %							Non metals %		
SiO_2	Al_2O_3	CaO	MgO	MnO	Na_2O	K_2O	C(*)	S(*)	
0.52	0.11	4.50	2.30	1.30	0.03	0.008	0.0347	0.0383	
METALS %									
FeT	Pb	Zn	Cu	Cd	Co	Ni	Cr	As	Hg (ppm)
51.40	0.08	1.69	0.004	0.001	0.009	0.009	0.458	0.001	0.18

(*) results of combustion analyzer

XRD Analysis

Figure 1 displays the XRD patterns of materials A—Course LD steel sludges and B-Fine LD steel sludges. The green lines, the difference between the experimental patterns (black lines) and the calculated patterns (red lines), indicate that the calculated patterns describe well the experimental data. The fitting errors estimated by the goodness-of-fit, GOF, and the weighted residual profile factor, Rwp, are listed in Table 3.

Both samples are composed by several crystalline phases. Wustite is the major individual phase observed for both samples, its content was 36.0% mass for sample A and 55.1% mass for sample B. Calcite, franklinite or zinc ferrite, silicon, and α-iron (Fe) from metallic iron were common for both samples. Portlandite, present in sample B, is probably the result of a previous free lime reaction with water after the slag cooling. The free lime observed in sample A is certainly alloyed with manganese, since its observed lattice parameter 0.4570 nm is distinct from the pure free lime parameter, 0.4810 nm. Franklinite and magnetite have the same space group: Fd-3mZ, which is an indicator that Zn and Fe atoms can be substituted in crystalline reticule from both samples. In the case of sample A, it has shown phases such as srebrodolskite and periclase. Additionally, in the case of sample B, magnetite and moissanite-2H were found.

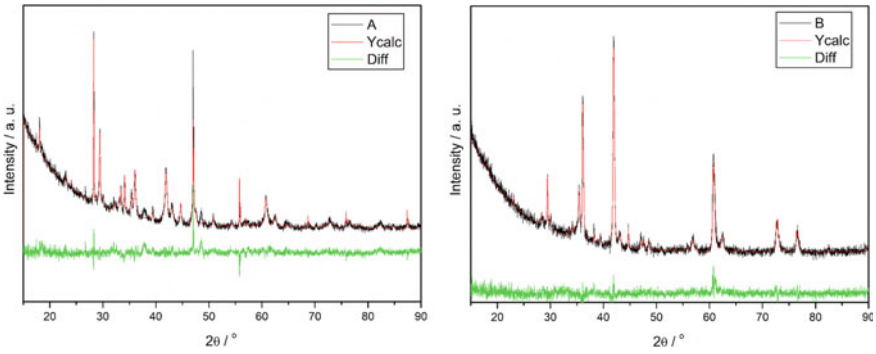

Fig. 1 XRD pattern of samples A and B including the Rietveld refinement. (Color figure online)

Table 3 Detailed information on the phases of samples A and B obtained by the Rietveld refinement

Sample	Phase name	Chemical formula	Phase %wt	Spacegroup	LVOLIB/nm	GOF	R_{wp}
A	Wustite	FeO	36.0	Fm-3 m	20	1.40	6.80
	Silicon	Si	14.3	Fd-3 mS	231		
	Srebrodolskite	$Ca_2Fe_2Al_2O_5$	12.6	Pnma	29		
	Calcite	$CaCO_3$	11.3	R-3cH	34		
	Periclase	MgO	8.0	Fm-3m	23		
	Portlandite	$Ca(OH)_2$	7.6	P-3m1	58		
	Franklinite	$ZnFe_2O_4$	5.9	Fd-3 mZ	22		
	Fe	Fe	2.5	Im-3 m	33		
	CaO	CaO	1.8	Fm-3 m	63		
B	Wustite	FeO	55.1	Fm-3m	45	1.22	4.98
	Magnetite	Fe_3O_4	14.8	Fd-3mZ	22		
	Calcite	$CaCO_3$	12.6	R-3cH	66		
	Franklinite	$ZnFe_2O_4$	5.3	Fd-3mZ	10		
	Portlandite	$Ca(OH)_2$	4.9	P-3m1	19		
	Moissanite-2H	SiC	3.9	P63 mc	64		
	Silicon	Si	2.2	Fd-3mS	43		
	Fe	Fe	1.2	Im-3m	129		

Optical and Scanning Electron Microscopic Studies

The images of optical micrographs without micron bar observed in sample A and in sample B allow to show their main mineralogical phases: hematite-Hm, magnetite-Mt, Quartz-Qz and Carbonates-Cbt, and α-iron (Fe) as can be seen in Figs. 2 and 3.

The elementary mapping, EDS, and the quantification of chemical elements identified by EDS of the selected SEM micrographs (a) and (b) of the sample of A and B are shown in Figs. 4 and 5.

In Figs. 2 and 4, the phases observed in sample A are constituted by a zone of sequential reduction of iron oxides in different shades of gray, with a porous and lamellar appearance taking the wustite as initial reduced phase. These oxides can be wustite (FeO) and franklinite ($ZnFe_2O_4$), possibly hematite (Hm) and magnetite (Mt). Hematite comes from the instantaneous decomposition of franklinite into its main oxides: hematite and zincite. It is observed that the α-iron (Fe) phase sometimes appears in circular and spherical morphologies of different diameters with a white appearance within or on the periphery of the matrix phase of iron oxides, mainly wustite. In addition, microstructures of mangano- and magnesio-wustites do not show any significant presence in wustite. Contents of MgO and MnO in chemical analysis of both samples can determinate a probably complete solubility of Mn and Mg in FeO because these elements are interchanging with iron contained into wustite,

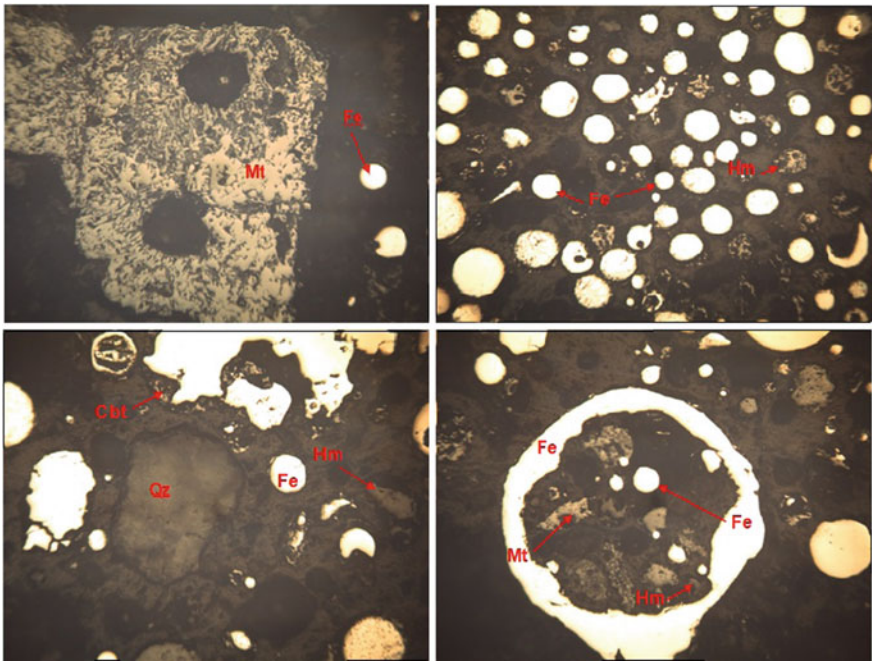

Fig. 2 Images of optical micrographs of sample A showing their main mineralogical phases. (Color figure online)

also sometimes, free lime observed in sample A is certainly alloyed with magnesium and manganese [5]. The oxidized structures of iron are almost always surrounded or accompanied by other predominant oval or spherical phases type nodes, rich in calcium carbonate—calcite or calcium oxide—CaO.

In Figs. 3 and 5, the phases observed in sample B, present whitish rounded or spherical morphologies that are not so significant compared to sample A, even some rod-like acicular grains and some dark phases of iron oxides can be observed superimposing white phases of α-iron (Fe). These optical micrographs also observe magnetite (Mt), hematite (Hm), quartz (Qz), and carbonates (Cbt). A zone of medium oxidation can also be observed in a spherical matrix with a porous appearance, probably made up of hematite (Hm), magnetite (Mt), and α-iron (Fe). Also, elongated grains like bastons were found in gray matrix of iron oxides. Some of the granules of calcite and portlandite exhibited a smooth superficial texture with regular spherical shapes of different sizes particles because Portlandite, present in sample B, is probably the result of previous free lime reaction with water after the slag cooling [6]. These results permitted to observe most of the iron-rich phase, a growing of the phase metallic iron in globular shapes like skeletal microstructures over wustite base or matrix in both samples. The carbonates including calcite occur in regular and spherical shapes sometimes enclosing metallic iron crystals in sample A but usually appear as broken

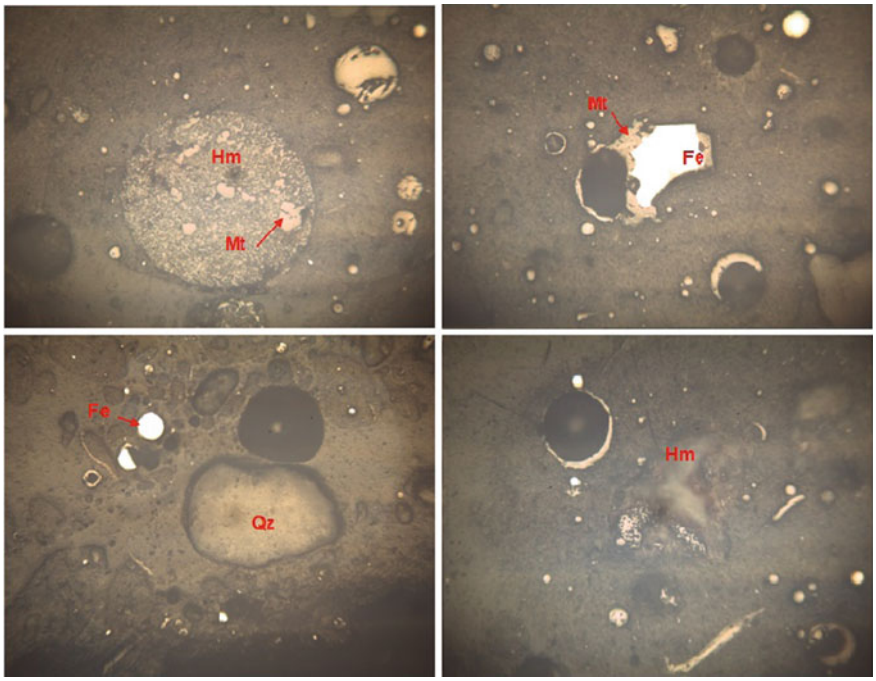

Fig. 3 Images of optical micrographs of sample B showing their main mineralogical phases. (Color figure online)

fragments in sample A. Secondary magnetite grains often coagulate and appear in spherical shape in sample B [7].

Figures 4 and 5, SEM analysis shows in (b) an elemental mapping for Fe, Zn, and O of (a). In (c) and (d) SEM–EDS studies denote significant content of Fe, O, and Ca in both samples. The absence of Zn in sample B is perceptible, however, traces of Zn are notable in their elemental mapping corresponding. Figures 4c and 5c cannot show the Fe K-line under this low acceleration voltage (6 kV). In addition, Fig. 4c shows elements that do not exist, i.e. S, Cl, and K that are label in EDS.

Finally, a morphology shown by these residues were made up of globular aggregates of metallic iron intergrown with crystals of iron oxides and zinc oxide rich in iron and zinc, probably it can come from the pelletization of the metal during the oxygen blowing in the LD converter [8, 9] .

Thermal Characterization

A thermogravimetric analysis by DTG–DSC–TG at 1000 ° C exhibited a mass loss of 97.43% for sample A and 92.57% for sample B.

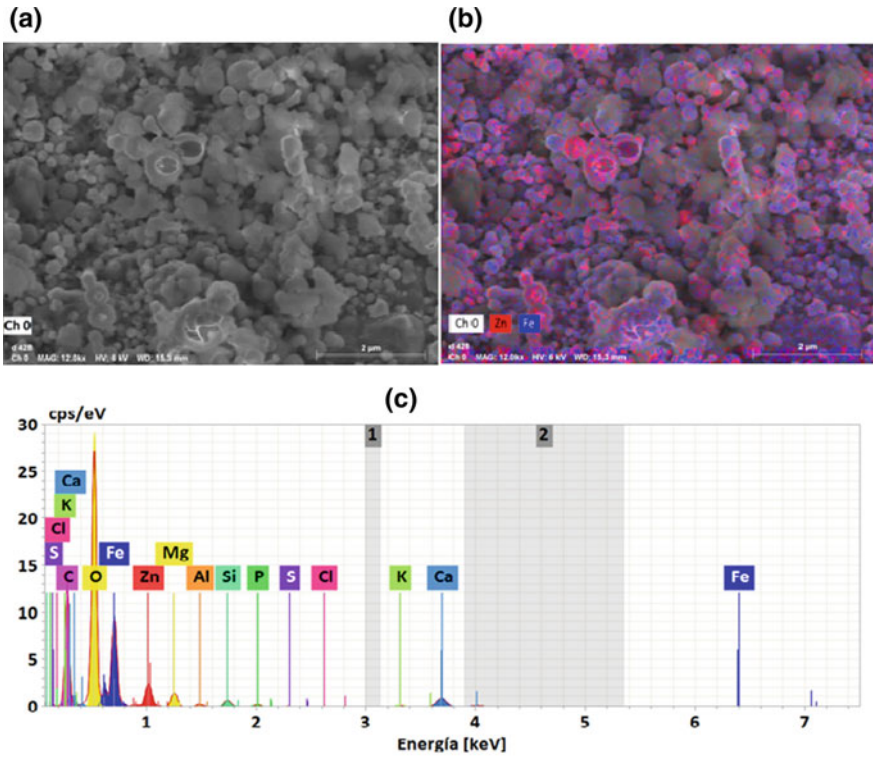

(d)

Map

Element	At. No.	Netto	Mass [%]	Mass Norm. [%]	Atom [%]	abs. error [%] (1 sigma)	rel. error [%] (1 sigma)
Carbono	6	59621	6.35	8.04	16.51	0.76	12.03
Oxígeno	8	159132	28.71	36.35	56.01	3.18	11.09
Cinc	30	19115	4.05	5.13	1.93	0.27	6.56
Hierro	26	75703	29.46	37.30	16.47	3.40	11.54
Magnesio	12	10898	1.05	1.33	1.35	0.08	7.57
Aluminio	13	1900	0.19	0.24	0.22	0.04	18.85
Silicio	14	5420	0.94	1.19	1.05	0.07	7.37
Azufre	16	298	0.05	0.06	0.05	0.00	8.32
Cloro	17	161	0.03	0.04	0.03	0.00	10.42
Potasio	19	885	0.36	0.46	0.29	0.05	13.68
Calcio	20	11156	7.56	9.58	5.89	0.45	6.00
Fósforo	15	1626	0.21	0.27	0.21	0.04	17.24
		Sum	**78.97**	**100.00**	**100.00**		

Fig. 4 Elemental mapping of SEM micrographs of the sample A (**a**), Selected SEM micrographs (**b**), O, Fe, and Zn mapping (**c**), EDS of the selected SEM micrographs in (a), and (**d**) elemental quantification of the EDS of the selected SEM micrographs in (**a**). (Color figure online)

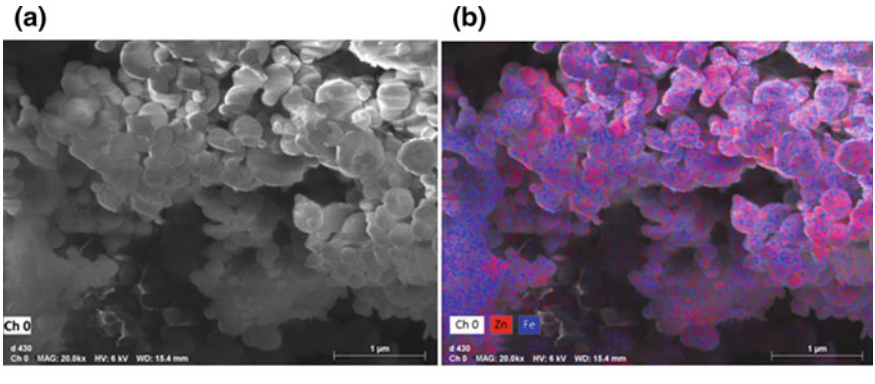

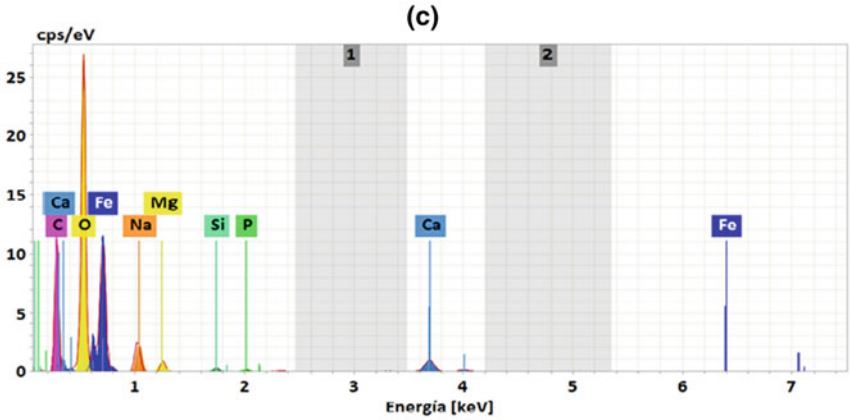

(d)

Map

Element	At. No.	Netto	Mass [%]	Mass Norm. [%]	Atom [%]	abs. error [%] (1 sigma)	rel. error [%] (1 sigma)
Carbono	6	53155	4.26	6.89	14.71	0.52	12.32
Oxígeno	8	149879	20.49	33.15	53.15	2.29	11.16
Hierro	26	92303	26.95	43.60	20.02	3.07	11.41
Sodio	11	15627	1.45	2.34	2.61	0.11	7.51
Magnesio	12	6098	0.49	0.79	0.84	0.05	10.44
Calcio	20	12934	7.66	12.39	7.93	0.46	5.97
Silicio	14	2484	0.36	0.58	0.53	0.04	12.10
Fósforo	15	1451	0.16	0.25	0.21	0.03	21.52
		Sum	**61.81**	**100.00**	**100.00**		

Fig. 5 Elemental mapping of SEM micrographs of the sample B (**a**), Selected SEM micrographs (**b**), O, Fe, and Zn mapping (**c**), EDS of the selected SEM micrographs in (a), and (**d**) elemental quantification of the EDS of the selected SEM micrographs in (**a**). (Color figure online)

Physical Determinations

The average particle size was 0.146 mm. for the coarse fraction (sample A) and 0.120 mm. for the fine fraction (sample B). The average values of specific gravity were 4.72×10^6 g/ m^3 for sample A and 3.67×10^6 g/ m^3 for the case of sample B.

Conclusions

Chemical analysis determined high levels of iron (51.54% Fe in sample A and 77.53% Fe in sample B) and low levels of zinc (0.49% Zn in sample A and 1.69% Zn in sample B). XRD analysis determined that wustite (FeO) was the major individual phase observed for both samples. Coarse of LD steel sludges (sample A) and fine of LD steel sludges (sample B) were 36.0% mass for sample A and 55.1% mass for sample B. Calcite, franklinite or zinc ferrite, silicon from quartz, and α-iron (Fe) from metallic iron were common phases for both samples. Optical Microscopic studies permitted to identify the main mineralogical phases such as wustite (FeO), hematite (Hm) from franklinite (Zf) and magnetite (Mt). The oxidized structures of iron were almost always surrounded or accompanied by other predominant oval or spherical phases type nodes, rich in calcium carbonates—calcite or calcium oxide—CaO in both samples. SEM morphologies shown by these residues were made up of globular aggregates of metallic iron intergrown with crystals of iron oxides especially wustite and zinc oxide rich in iron and zinc; this is probably the result of metal pelletization during the oxygen blowing in the LD converter. SEM–EDS studies denoted significant content of Fe, O, and Ca in both samples. A thermal characterization by DTG–DSC–TG at 1000 ° C exhibited a mass loss of 97.43% for sample A and 92.57% for sample B. The average particle size was 0.146 mm. for sample A and 0.120 mm. for sample B. The average values of specific gravity were 4.72×10^6 g/ m^3 for sample A and 3.67×10^6 g/ m^3 for sample B. Finally, these previous results of partial characterization of these residues will serve to treat or process fractions of coarse and fine of LD steel sludges until the material in particle form that are deposited in the steel mills, as well as those normally produced continuously in the ironmaking and steelmaking activities and related, such as Electric Arc Furnace (EAF), Basic Oxygen Furnace (BOF) , coke ovens, agglomeration zones, sintering, pelletizing (conventional iron ores), and other deposits of ore fines, limestone, and coal.

Acknowledgements Authors thank the Research Vice Rectorate and the College of Geological Mining and Metallurgical Engineering Research Institute of the National University of Engineering for the financial assistance granted, without which these programmed experiences could not have been carried out, and to the Brazilian Steelmaking Company for the background and the samples provided to this paper.

References

1. Drobíková K, Plachá D, Motyka O, Gabor R, Kutláková KM, Vallová S, Seidlerová J (2016) Recycling of blast furnace sludge by briquetting with starch binder: waste gas from thermal treatment utilizable as a fuel. Waste Manage 48:471–477
2. Purohit A, Swain PTR, Patnaik PK (2020) Mechanical and sliding wear characterization of LD sludge filled hybrid composites. Materials Today: Proceedings
3. Das B, Prakash S, Reddy PSR, Misra VN (2007) An overview of utilization of slag and sludge from steel industries. Resour Conserv Recy 50(1):40–57
4. Cantarino MV (2011) Estudo da remoção de zinco e de álcalis contidos em lamas de aciaria LD. Master thesis, Federal University of Minas Gerais
5. Kusinski J, Jasienska S, Monty C (1994) Microstructural and microanalytical examinations of partially reduced doped wustites. Solid State Ionics 68(3–4):185–192
6. Maggi F, Dossi S, Paravan C, Galfetti L, Rota R, Cianfanelli S, Marra G (2019) Iron oxide as solid propellant catalyst: a detailed characterization. Acta Astronaut 158:416–424
7. Jalkanen H, Holapp L (2014) Converter steelmaking. In: Seetharaman S (ed) Treatise on process metallurgy 2014. Royal Institute of Technology, Stockholm; Elsevier, pp 223–270
8. Gómez-Marroquín MC, Salazar-Yantas KA, Tinoco-Falero JA, Infante-Rojas MD (2018) Characterization of coarse and fine residues from a sludge site of an integrated steel plant in Peru. Paper presented at the Iron and Steel Technology Conference and Exposition Philadelphia, Pennsylvania, 7–10 May 2018
9. Gómez-Marroquín MC, D'Abreu JC (2017) Characterization of Peruvian Linz Donawitz-LD Steel Sludges. Paper presented at the Sustainable Industrial Processing Summit & Exhibition, Cancun, Quintana Roo, 22–26 October 2017

Study on Sinter Iron Ores and Titanium Ores Used in Pelletizing

Yan Zhang, Xiaojiang Wu, Hanglei Niu, Minge Zhao, Gele Qing, Zhixing Zhao, Yunqing Tian, Wenwang Liu, Dawei Sun, Ming Li, Luyao Zhao, Li Ma, and Tao Yang

Abstract In this paper, study on sinter iron ores and titanium ores used in pelletizing was carried out. Bond work indexes of different sinter iron ores and titanium ores were measured. Ballability would be improved, and falling strength and compression strength of green pellets would be increased after fine-grinded sinter iron ores have been added. High-titanium pellets with good metallurgical properties and high compression strength could be produced by using fine-grinded titanium ores. The application of sinter iron ores and titanium ores used in pelletizing could not only reduce the cost of ironmaking but also expand the iron ore resources for pelletizing.

Keywords Pellet · Sinter iron ores · Titanium ores · Metallurgical properties

Introduction

Pellets have the advantages of high-grade, low gangue content, and good metallurgical properties compared with sinters [1]. The energy consumption of pelletizing process is less than 50% of that of sintering process, and the emissions of flue gases, dioxins, nitrogen oxides, and dust are also significantly lower than that of sintering [2]. The development of pelletizing is an important measure for green ironmaking.

But the iron ores that can be used in pelletizing are not sufficient. Ma Li et al. studied the Mac fines used in pellets [3]. Zhang Yan et al. described the influence of different Ti-bearing materials on pellets compression strength [4]. Tian Yunqing

Y. Zhang (✉) · M. Zhao · G. Qing · Z. Zhao · Y. Tian · L. Zhao · L. Ma · T. Yang
Research Institute of Technology of Shougang Group Co., Ltd, Beijing, China
e-mail: yanzhang@shougang.com.cn

Y. Zhang · G. Qing · Z. Zhao · Y. Tian
Beijing Key Laboratory of Green Recyclable Process for Iron & Steel Production Technology, Beijing, China

X. Wu · H. Niu · W. Liu · D. Sun · M. Li
Shougang Jingtang United Iron and Steel Co., Ltd, Tangshan, Hebei, China

J. Li et al., *Characterization of Minerals, Metals, and Materials 2021*,
The Minerals, Metals & Materials Series,
https://doi.org/10.1007/978-3-030-65493-1_15

et al. carried out a series of experiments on the production of Ti-bearing pellets with titanium sands [5].

In this paper, grinding work indexes of different sinter iron ores and titanium ores were measured, and experiments of fine-grinded ores used in pelletizing and firing were conducted. Proportions of sinter iron ores and titanium ores that could be used in pellets were determined.

Materials and Experimental Methods

Chemical Compositions of the Ores

Chemical compositions of sinter iron ores and titanium ores were listed in Table 1. TiO_2 content of titanium ores A and B was 16.40% and 12.40%, respectively. Four sinter iron ores were used in the experiments including two Australian sinter ores (ASO) and two Brazilian sinter ores (BSO).

Bond Work Indexes of the Ores

Bond work index (Wi) is an index to evaluate the grindability of an ore, this index can be measured by using a Bond ball mill [6]. Bond work indexes of different ores were listed in Table 2.

As shown in Table 2, Wi of titanium ore A and B were 18.23 kwh/t and 18.89 kwh/t. ASO-B had the lowest Wi among the sinter iron ores, which was 12.88 kwh/t. Wi of the two Brazilian sinter ores was higher than the Australian sinter ores, which were 16.98kwh/t and 16.56kwh/t.

Table 1 Chemical compositions of sinter iron ores and titanium ores

Content (%)	TFe	FeO	SiO_2	Al_2O_3	CaO	MgO	TiO_2
titanium ore A	43.28	27.56	10.60	5.73	2.03	4.30	16.40
titanium ore B	48.09	27.20	7.53	5.86	1.72	3.13	12.40
ASO-A	61.50	0.69	3.60	2.31	0.15	0.29	0.34
ASO-B	62.75	0.40	3.93	2.09	0.16	0.15	0.19
BSO-A	66.00	0.20	2.0	1.91	0.19	0.19	0.21
BSO-B	60.66	1.01	6.96	1.89	0.94	0.13	0.11

Table 2 Bond work indexes of different ores

Name	Wi, kwh/t
Titanium ore A	18.23
Titanium ore B	18.89
ASO-A	14.20
ASO-B	12.88
BSO-A	16.98
BSO-B	16.56

Table 3 Chemical compositions and particle sizes of the concentrates

Content (%)	TFe	FeO	SiO_2	Al_2O_3	CaO	MgO	TiO_2	−200 mesh
High titanium concentrate	35.88	35.56	5.24	1.25	3.49	1.70	37.28	69.24
Iron concentrate A	69.52	29.35	1.86	0.37	0.40	0.64	0.026	88.58
Iron concentrate B	62.78	4.58	6.57	1.26	0.98	1.23	0.065	89.63

Pelletizing Materials

Two kinds of Iron concentrates for pellets and one kind of high titanium concentrate were also used in the pelletizing experiments. Chemical compositions and particle sizes of the concentrates used in the pelletizing experiments were listed in Table 3. Iron concentrate A was a kind of iron ore with low silica which the silica content was only 1.86%. High titanium concentrate had a high content of TiO_2, 37.28%, but it had a coarse particle size, percentage of −200 meshes was 69.24%.

Results and Discussion

Green pellets were prepared in a pelletizing disc which the diameter was 800 mm. Pellets with sizes between 10 and 12.5 mm were screened out.

Influence of Sinter Ores on Pellet Quality

The schemes of pelletizing with sinter ores were shown in Table 4, in which the sinter ores were all grinded (−200 meshes, >80%).

Table 4 Pelletizing with sinter iron ores

No.	Iron concentrate A (%)	Iron concentrate B (%)	Grinded ASO-A (%)	Grinded ASO-B (%)	Grinded BSO-A (%)	Grinded BSO-B (%)	Bentonite (%)	SiO_2 content (%)	Basicity
Base	90	10					1.5	3.25	0.15
1	90		10				1.5	2.97	0.14
2	80		20				1.5	3.16	0.12
3	70		30				1.5	3.35	0.11
4	90			10			1.5	3.00	0.14
5	80			20			1.5	3.22	0.12
6	70			30			1.5	3.45	0.11
7	90				10		1.5	2.81	0.15
8	80				20		1.5	2.84	0.14
9	70				30		1.5	2.87	0.13
10	90					10	1.5	3.30	0.16
11	80					20	1.5	3.81	0.14
12	70					30	1.5	4.32	0.14

Figure 1 showed the falling strength of green pellets with different proportions of sinter ores. As results showed, falling strength would increase while more sinter ores were added.

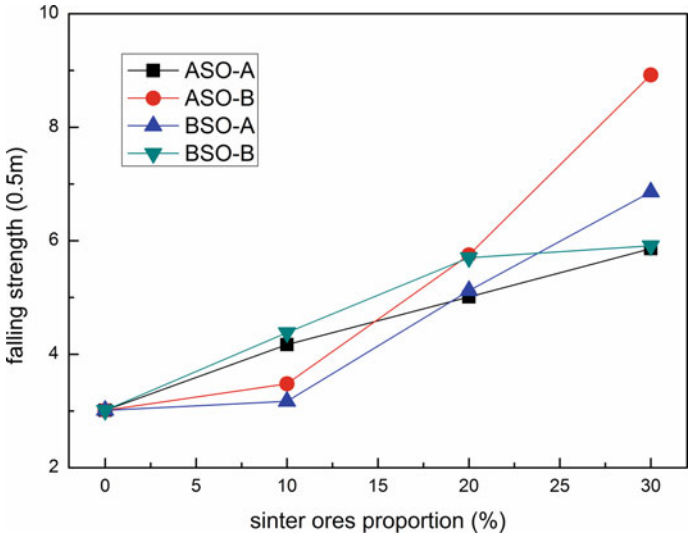

Fig. 1 Falling strength of green pellets with different proportions of sinter ores. (Color figure online)

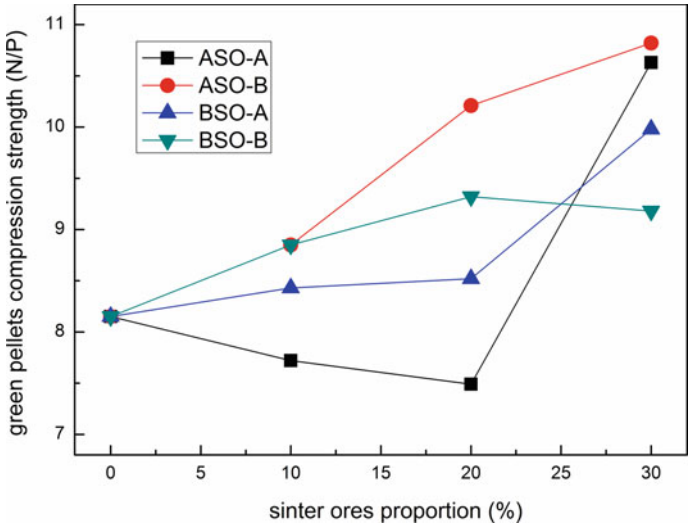

Fig. 2 Compression strength of green pellets with different proportions of sinter ores. (Color figure online)

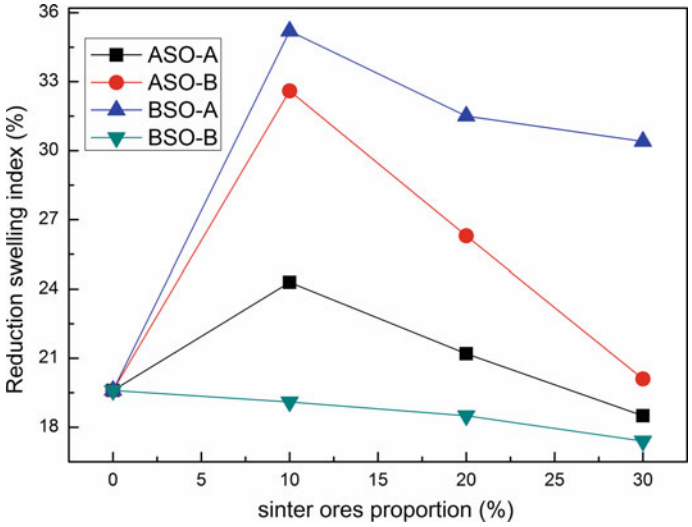

Fig. 3 Reduction swelling index of pellets with different proportions of sinter ores. (Color figure online)

Figure 2 depicted the compression strength of green pellets with different proportions of sinter ores. The green pellets compression strength would decrease and then increase, while the ASO-A was added from 20% to 30%. The other three kinds of green pellets' compression strength would increase with the increase of the sinter ores proportion.

Figure 3 illustrated the reduction swelling index (RSI) of pellets with different proportions of sinter ores. The results showed that RSI would increase when the ASO-A, ASO-B, and BSO-A were added with the proportion of 10%, and then decreased with the increase of sinter ores' proportion. Adding BSO-B would improve the pellets RSI from 19.6% to 17.4%.

Influence of Titanium Ores on Pellets

In order to confirm whether the high titanium concentrate could be added in pelletizing to produce Ti-bearing pellets with high TiO_2 content and good metallurgical properties, experiments of different proportions of high titanium concentrate added in the pellets were conducted.

Figure 4 described that compression strength would decrease as the high titanium concentrate proportion increase. And if the proportion is greater than 20%, the compression strength would be lower than 2500 N/P.

The schemes of pelletizing with titanium ores were shown in Table 5. The titanium ores were also grinded (−200 meshes, >80%).

As shown in Table 5, falling strength and compression strength of green pellets would only have a little change after the titanium ores were added.

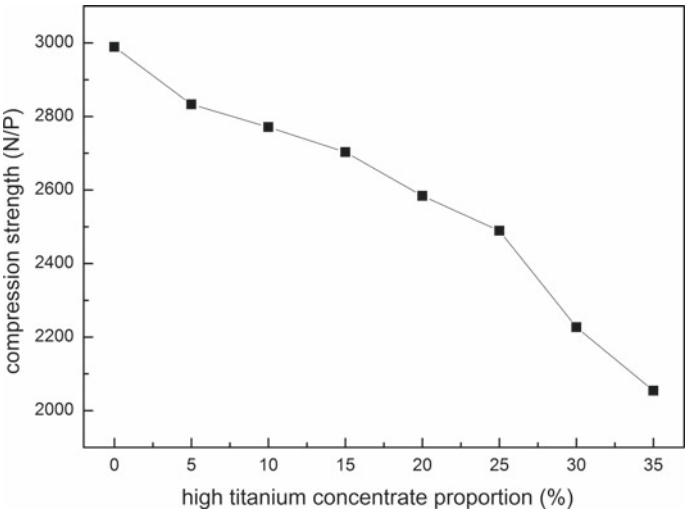

Fig. 4 Compression strength with different proportions of high titanium concentrate

If the proportion of high titanium concentrate was fixed at 20% and the proportion of grinded titanium ores was between 30% and 50%, compression strength of finished pellets would be greater than 2500 N/P and could satisfy the need of the large blast furnace.

Conclusions

Study on sinter iron ores and titanium ores used in pelletizing was carried out. Sinter iron ores and titanium ores could be used in pelletizing if they were fine-grinded. The following conclusions could be drawn from this work:

1. Bond work indexes of different sinter iron ores and titanium ores were measured, the results showed that the grinding costs of the sinter iron ores and titanium ores were not high;
2. Falling strength and compression strength of green pellets would be increased after fine-grinded sinter iron ores were added;
3. RSI of pellets would decrease while the BSO-B was added, but RSI would be increased while the ASO-A, ASO-B, and BSO-A was added;
4. Compression strength would decrease as the high titanium concentrate proportion increase, and the proportion of high titanium concentrate should not be larger than 20%;
5. Ti-bearing pellets with high titanium content could be produced by using grinded titanium ores.

Table 5 Pelletizing with titanium ores

No.	Iron concentrate A (%)	Grinded titanium ore A (%)	Grinded titanium ore B (%)	High titanium concentrate (%)	Bentonite (%)	Falling strength of green pellets (0.5 m)	Compression strength of green pellets (N/P)	Compression strength of finished pellets (N/P)
1	20	80			1.5	4.21	7.65	2315
2			100		1.5	4.38	7.89	2263
3	65			35	1.5	3.73	6.85	2054
4	45		35	20	1.5	4.56	7.37	2597
5	40		40	20	1.5	4.24	7.29	2513
6	50	30		20	1.5	4.72	7.89	2783
7	45	35		20	1.5	4.48	7.64	2654

Acknowledgements Supported by National Key R&D Program of China (2017YFB0304300 & 2017YFB0304302).

References

1. Zhu D, Huang W (2017) Technical progress in iron ore pelletization. Sintering Pelletizing 42:42–49
2. Manxing X, Zhan Y (2017) Analysis of pellet technology and production of China in 21st century. Sintering Pelletizing 42(25–30):37
3. Ma L, Qing G, Tian Y (2019) Study on grinded Mac ores in pelletizing. Sintering Pelletizing 44(39–41):49
4. Zhang Y, Qing G, Tian Y (2015) Study on influences of different Ti-bearing materials on compression strength of pellets. Sintering Pelletizing 40(28–30):44
5. Yunqing T, Qing G, Ji B (2014) Experimental research on production of Ti-bearing pellets with titanium sand. Sintering Pelletizing 39:31–35
6. Magdalinović N (1989) A procedure for rapid determination of the Bond work index. Int J Miner Process 27:125–132

Research Progress on Application of Steel Slag in Agriculture

Zha Yu-hong, Li Can-hua, and Wang Zhao-ran

Abstract The environmental pollution caused by steel slag accumulation seriously restricts the goal of green and sustainable development in China, and resource utilization is the inevitable trend of metallurgical solid waste. This paper summarizes the advantages and application status of steel slag as soil acid–base regulator, agricultural fertilizer, and soil heavy metal curing agent, and puts forward some suggestions on the utilization of steel slag in agriculture.

Keywords Steel slag · Resource utilization · Leaching toxicity

At present, the environmental pollution caused by the accumulation of steel slag in China is prominent, and the resource utilization of steel slag is urgent. Steel slag is a by-product produced by the steelmaking process. It is composed of molten iron and Si, Fe, Mn in scrap and reacts with various fluxes to form silicate substances during slagging period. According to the type of steelmaking furnace, the steel slag is divided into converter slag, electric furnace slag, and flat furnace slag. According to incomplete statistics, at present, the total stock of steel slag in china is about 1 billion tons, and its resource utilization rate is only about 30% [1]. it is mainly used in road cement, building concrete, adsorbent, and so on. Research and application in agriculture are relatively scarce [2]. It can be seen that developing the utilization of steel slag in agriculture is a means to improve the utilization rate of steel slag [3], and it is to protect the environment, prevent pollution, save resources, and ensure sustainable development of iron and steel industry. The realization of circular economy has important economic benefits and research value.

Z. Yu-hong (✉) · L. Can-hua · W. Zhao-ran
School of Metallurgical Engineering, Anhui University of Technology, Ma Anshan 243002, China
e-mail: 1059540889@qq.com

J. Li et al., *Characterization of Minerals, Metals, and Materials 2021*,
The Minerals, Metals & Materials Series,
https://doi.org/10.1007/978-3-030-65493-1_16

Utilization of Steel Slag in Agriculture

Reducing Environmental Stress

With the development of metallurgical industry, a large number of abandoned steel slag occupies a large amount of land, in which heavy metal elements are leached by rain water, surface runoff is polluted, surrounding water and groundwater are polluted, absorbed by vegetation crops, and stored in vegetation crops. It brings a potential threat to people's life and health. At the same time, the alkalinity of steel slag is long-term pollution of soil, will lead to poor soil, crop production. Therefore, it is necessary to carry out the resource utilization of steel slag, transform solid waste into agricultural resources, and alleviate the harm caused by improper solid waste disposal.

Utilization of Secondary Energy

With the in-depth research on industrial solid waste recycling technology, steel slag is widely paid attention to as an inevitable product in steelmaking process. China produces more than 100 million tons of steel slag every year [4], but 70% of steel slag is still not used rationally, and its utilization potential is huge. Using cheap steel slag as raw material for the preparation of agricultural products can reduce industrial solid waste discharge, protect the ecological environment, carry out secondary energy reuse, realize the unification of economic, environmental and social benefits, and build a resource-saving and environment-friendly society.

Characteristics of Steel Slag in Liugang China

Chemical and Mineral Composition of Steel Slag of Liugang

The main components of converter slag in Liugang are CaO, SiO_2, Fe_2O_3, and Al_2O_3, There is also a certain amount of MgO, MnO, P_2O_5, and TiO_2. A preliminary estimate of the SiO_2 in steel slag as an active component and the heavy metal content is not high. Steel slag from China's Liugang, Its chemical composition is shown in Table 1. XRD tests show that the main mineral composition is Ca_2SiO_4, $K_3(FeO_2)$,

Table 1 Main chemical constituents of steel slag of Liugang

Components	CaO	SiO_2	Fe_2O_3	Al_2O_3	MgO	P_2O_5	TiO_2	MnO
Mass fraction/%	42.59	17.05	16.33	10.78	5.83	1.81	1.76	2.55

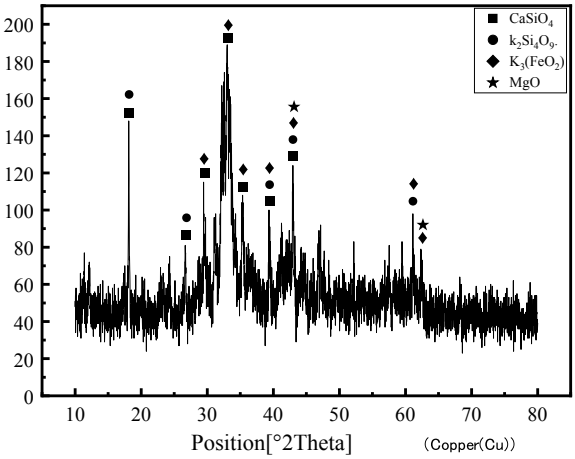

Fig. 1 XRD patterns of steel slag of Liugang

and $K_2Si_4O_9$ (as shown in Fig. 1). These minerals [5, 6], Water hydrolysis, It is difficult. Steel slag is used for relatively stable agriculture.

Leaching Toxicity of Steel Slag of Liugang

Steel slag containing a small amount of harmful heavy metal elements such as Cr^{6+}, Pb^{2+} is of the main factors hindering the application of steel slag in agriculture [7, 8]. China's Official GB8173-87—*Standard for Controlling Pollutants in Agricultural Fly Ash*, based on the total concentration of heavy metals, but the total concentration of heavy metals cannot reflect their chemical behavior and potential environmental risk [9] in soil. The methods commonly used to detect the leaching content of heavy metals in solid waste, such as *Toxicity Characteristic Leaching Procedure* developed by the EPA of the United States, the *EN 12457-3* developed by the European Union, and *Solid waste-Extraction procedure for leaching toxicity-Sulphuric acid & nitric acid metho*d HJ/T 299-2007 by China [10].

According to the HJ/T 299-2007, steel slag leaching solution was prepared GB5085.3-2007—*Identification standards for hazardous wastes-Identification for extraction toxicity* required Cd, Hg, As, Pb, Cr, Ni, Zn were tested, and the test data are shown in Table 2. Liugang steel slag leaching toxicity test is qualified.

On the basis of the above research, Liugang steel slag is a kind of fertilizer raw material which is mainly Si, Ca and contains trace Mn, P, Fe, and other elements. The content of metal elements in steel slag is high. Because it is combined in the crystal and cannot be released out [11], the leaching content of heavy metals in steel slag of Liugang conforms to the requirements of soil safety standards for agricultural land in China. Therefore, the recycling of steel slag in agriculture can be realized and used as a reference for the application of other steel slags.

Table 2 Toxicity test results of steel slag leaching solution

Projects	Results mg/L	Standard limits mg/L
Cd	nd	1
Hg	nd	0.1
As	nd	5
Pb	nd	5
Cr	0.0073	15
Ni	nd	5
Zn	nd	100

Note nd—not detected

Application of Steel Slag in Agriculture

At present, most of the studies have carried out experiments on the different properties of steel slag, according to the farmland conditions in different areas or the growth characteristics of planting products, and achieved good results. The steel slag has the characteristics of high alkalinity, nutrient elements needed for plant growth, gelling and large internal surface area, and is prepared as soil acid–base regulator, agricultural fertilizer, and soil heavy metal curing agent.

Steel Slag as Soil Acid–Base Regulator

Crop growth requires certain soil pH values [12, 13], pH is a measure of ion concentration in soil. The pH of soil will affect the absorption of mineral ions by plants, further affect the osmotic pressure of plant roots, may cause plants to lose water or even wither, and have a certain effect on the species and quantity of microorganisms in soil.

Different crops have different preferences for pH values. The soil pH value is below 7, planting Pinus koraiensis, azalea, Masson pine, and so on is more suitable; the soil pH value is above 7.5, planting willow, Platycladus orientalis, salami, and so on is more suitable; the soil pH value is 6–7.5, planting cherry blossom, lilac, cedar, and so on. Yantai Xinhua Chemical Co., Ltd [14] tested 23099 soil samples over eight years, a general rule is obtained: pH < 6 causes harm to most crops, pH 6.5–7.5 is suitable for most crops to grow, and pH < 7.5 will cause harm to crop growth (as shown in Table 3).

Basicity of steel slag is 10–13. Zhou Feng and others [15] investigate the effects of B. deformativum and steel slag on maize growth, corn was grown in acidic soils using either uninoculated B. deformativum or without steel slag (CK), inoculated with B. deformativum (Gv), added steel slag (SS) , combined with B. deformativum and steel slag (Gv SS) as soil amendments. Experiments show that the application of steel slag significantly increases the pH of soil [16], and reduced the effective states

Table 3 Effects of soil pH on crops

pH	Impact on crops
<4	Causing serious damage to crops, almost no production
4–6	Most crops are injured
6–7.5	Suitable for most crops
7.5–8	Damage to crop growth
>8	Serious damage to crop growth

of cadmium and lead (as shown in Fig. 2). The mechanism is that free calcium oxide in steel slag can hydrolyze and produce a large number of OH^-, alkaline compounds, which can hydrate with acidic compounds in farmland and improve soil pH value. Thus, the bioavailability [17] of heavy metals such as Cd, Pb, Zn can be reduced, and the mass fraction of heavy metals in the growth environment is effectively reduced.

For basylous soils, most untreated steel slag is not applicable, thus limiting the scope of application of steel slag. Hua Xiaozan and others [18, 19] made active steel slag by combining the residue produced in the steelmaking process of Taiyuan Iron and Steel Company with pH value above 12 with weathered coal at 1:2. The released H^+ binds to the OH^- in steel slag, thus reducing the basicity of steel slag. Experiments were carried out on calcareous cinnamon soil of Shanxi Province with a pH value of 8.28, set up seven treatments: treatment 1 as control, treatment 2 applies

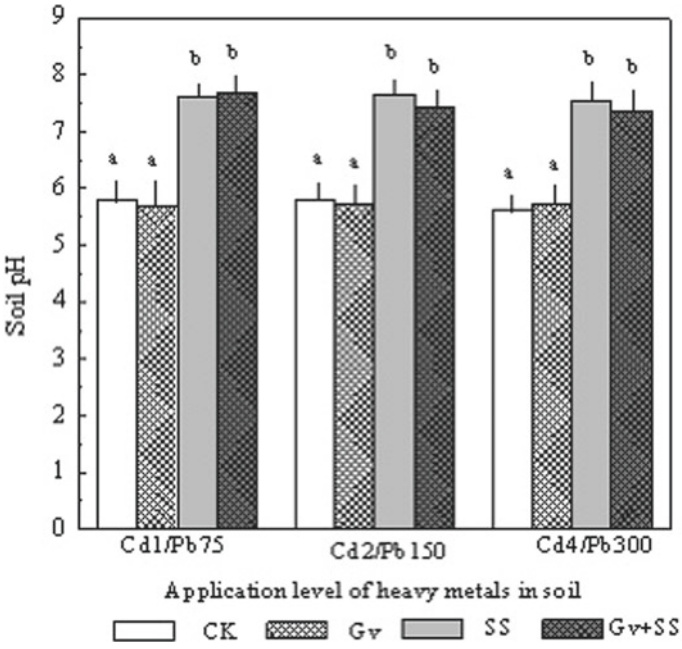

Fig. 2 The influence of Gv and SS on soil pH [15]

Table 4 Effect of application of steel slag on onion yield

Treatments	2011		2012	
	Yield/(kg/hm^2)	Increase production/%	Yield/(kg/hm^2)	Increase production/%
1(CK)	77235		70830	
2	77265	0.1	72915	2.9
3	78555	1.7	74010	4.5
4	75555	−2.2	72000	1.7
5	74550	−3.5	70200	−0.9
6	76380	−1.1	70620	−0.3
7	77910	0.9	71520	1.0

2250 kg hm^{-2} active steel slag, treatment 3 applies 4500 kg hm^{-2} reactive steel slag, treatment 4 applies 6750 kg hm^{-2} of reactive steel slag, treatment 5 applies 9000 kg hm^{-2} of reactive steel slag, treatment 6 applies 2250 kg hm^{-2} of common steel slag, treatment 7 applies 4500 kg hm^{-2} weathered coal. The results showed that the production of onion in 2011 and 2012 increased by 1.7% and 4.5% after the application of 4500 kg hm^{-2} of active steel slag (as shown in Table 4), the height of corn plant reached the highest when applied alone at 2250 kg hm^{-2}, and the application of active steel slag increased the Si content in onion and corn, and the soil and crops were not polluted when the amount of steel slag was not more than 3000 kg hm^{-2}.

From the above research, it can be seen that steel slag, as a soil acid–base regulator, is not only widely used, but also has a low cost, which has a great application prospect, but the application time and input amount of steel slag still need to be further studied.

Steel Slag as Agricultural Fertilizer

Fertilization is essential to crop yield [20], the yield of soil with different types of fertilizer increased significantly compared with that of its unfertilized control field [21]. Steel slag contains a variety of nutrients such as Si, P, Ca, Mg, which are beneficial to the growth of crops and can be used as agricultural fertilizer after proper treatment [21].

Thomas phosphatic fertilizer is a kind of slow effect agricultural fertilizer which is not absorbent, caking, and non-corrosive. It is made by cooling, crushing, magnetic separation, and grinding of steel slag into a fine powder, accounting for 13%–16% of total phosphorus fertilizer [22]. Phosphorus in Thomas phosphatic fertilizer is citric soluble and can be dissolved and released in acidic and slightly acidic environment of plant rhizosphere. Jiao [23] and others' studies have shown that excessive application of phosphorus fertilizer will lead to an increase in the bioavailability of cadmium in soil. Lower concentrations of cadmium affect the structure of crop enzymes, resulting

in slow crop growth. And excessive phosphorus will cause excessive respiration of crops, resulting in premature development of reproductive organs, resulting in low crop yield and small fruit, so it is necessary to use Thomas phosphatic fertilizer scientifically.

Silicon fertilizer can not only promote leaf photosynthesis, increase chlorophyll content but also inhibit soil bacteria and reduce crop incidence. Steel slag can be used as silicon fertilizer in agriculture [24], but different kinds of steel slag contain different amount of plant effective silicon, and its content is not less than 10% suitable for as silicon fertilizer [25]. Li Jun and others [26] applied 80-mesh sieve water quenched blast furnace slag as silicon fertilizer base in typical paddy fields of Liaoning Province. The results showed that the rice yield increased by 8.3%–20.9% after the application of steel slag silicon fertilizer(A) and the control group with conventional N–P–K fertilizer (CK) (as shown in Table 5). Wang Xiaojun and others [27] planted cabbage in Harbin by adding steel slag as silicon fertilizer to reduce the incidence of cabbage and increase plant height. However, silicon fertilizer is not volatile and does not deteriorate, the rest will remain in the soil except for the absorbed part of the crop. Therefore, silicon fertilizer application should pay attention to the amount of control [28], in the input of "prevention instead of governance" [29].

As agricultural fertilizer, steel slag can improve farmland nutrient and keep farmland fertility, but to prevent steel slag fertilizer from causing soil consolidation [30], the application amount, application mode, and application time should be studied before application.

Table 5 Effect of steel slag on rice growth rate

Test site	Treatment	Height/cm	Ripening rate/%	Yield/kg·hm^{-2}
Wu San Xiang, Dongling District, Shenyang	CK	96.0	92.8	5839.5
	A	96.0	91.2	7105.5
Shengli Township, Kangping County, Shenyang	CK	85.7	92.0	7743.0
	A	83.0	96.6	8661.0
Wu Bo Niu Xiang, Liaozhong County, Shenyang	CK	100.7	90.5	8350.0
	A	107.5	91.8	9100.5
Qiandian Town, Shuncheng District, Fushun City	CK	83.0	96.9	6883.5
	A	93.0	98.0	7450.5
Hebei Township, Shuncheng District, Fushun City	CK	83.5	89.9	6514.5
	A	87.5	92.0	7737.0
Cao Town, Qingyuan County, Fushun	CK	97.2	–	652.5
	A	98.3	–	7812.0
Tieling City	CK	98.6	66.7	8963.0
	A	99.9	70.1	9466.0

Steel Slag as Heavy Metal Curing Agent

Heavy metal pollution in soil can poison crops [31]. Hu Chao [32], Zhang Fushun [33], and Jia Xiru [34] found that the growth and development of pakchoi, beet, and cucumber were inhibited after the Cd concentration exceeded a certain concentration in the soil, and the Cr (VI) activity in the soil was strong, which caused crop distortion, carcinogenesis, or mutation [35]. And human consumption of crops with excessive heavy metals can induce various diseases [36].

Studies have shown [37, 38], the C–S–H, of Ca_2SiO_4 easy hydration into gel state in steel slag powder has certain adsorption effect on Cu, Pb, Zn, and linked to each other in a chain structure then formed Cd2SiO4, Ni2SiO4, Zn2SiO4;The OH^- released by steel slag powder and $CaCO_3$ solidify Cu, Zn, Ni, Cr, and Pb in soil, as shown in formulae (1)–(6):

$$2OH^- + Cu^{2+} = Cu(OH)_2 \tag{1}$$

$$2OH^- + Zn^{2+} = Zn(OH)_2 \tag{2}$$

$$2OH^- + Ni^{2+} = Ni(OH)_2 \tag{3}$$

$$2OH^- + Pb^{2+} = Pb(OH)_2 \tag{4}$$

$$3OH^- + Cr^{3+} = Cr(OH)_3 \tag{5}$$

$$CaCO_3 + Pb^{2+} = PbCO_3 + Ca^{2+} \tag{6}$$

On the one hand, steel slag has high basicity, large inner surface area, loose porous and so on, so it can adsorb heavy metals, thus directly reducing the DTPA effective mass fraction of heavy metals in soil [39, 40]. On the other hand, steel slag as silicon fertilizer [41] can not only promote the growth of crops but also inhibit the transport of heavy metal Cd in soil. Tong Qian and others [42] used steel slag as silicon fertilizer and calcium magnesium phosphate fertilizer. The test showed that the compound fertilizer could greatly inhibit Cd pollution in paddy soil. Liu Caifeng and others [43] proposed Si to alleviate the toxic effects of Cd by inhibiting the absorption, transport, and accumulation of crops, promoting and cooperating with Cd chelates. It should be noted that continuous application of a curing agent can reduce the curing effect of heavy metals [44], and if the soil environment changes, temporarily solidified heavy metal ions will be reactivated [45].

Steel slag as heavy metal curing agent has the characteristics of wide application range, low cost, and simple operation, but because of the different kinds of heavy metals, the effect of curing agent on reducing the effectiveness of heavy metals in plants will be different, so it needs to be adapted to local conditions.

Recommendation and Prospect

In recent years, there has been an increase in research on the effect of heavy metals in steel slag, and the heavy metal leaching amount is typically used as the evaluation standard [46, 47], but the safe level of heavy metals in the existing compound fertilizer in China is still the total amount of heavy metals used [25, 48]. It is suggested that the relevant standard in China should be revised to use heavy metal leaching amount as a measure of safety index.

Moreover, there is still a great deal of research to be focused mainly in the following areas: (1) Different types of steel slag have different effects on crops, and the tolerance of different kinds of crops to steel slag is also slightly different. Therefore, it is necessary to further explore the differences in the application of steel slag as fertilizer for different crops; (2) Although steel slag plays an active role in agriculture, little research has been done on the long-term application of steel slag, such as how much it is applied and how it is applied. Therefore, it is necessary to carry out in-depth research to ensure the safe green application of steel slag; (3) The variety and content of heavy metals in soil can be changed by human activities, natural environment, crop varieties, and geographical locations, so it is necessary to explore the application of steel slag using dynamic models in future research.

References

1. Wang SJ (2015) Promoting comprehensive utilization of steel slag to promote China's circular economy. World Metal Herald 8:B11
2. Angélica CFD, Leonardo TB, Guppy Christopher N et al (2020) Effects of lime and steel slag application on soil fertility and soybean yield under a no till-system. Soil Tillage Res 196:104422
3. Saly F, Guo LP, Ma R et al (2018) Properties of steel slag and stainless steel slag as cement replacement materials: a comparative study. J Wuhan Univ Technol (Mater Sci) 33(06):1444–1451
4. Zhang J, Yan DL, Qi YH et al (2020) Difficulty analysis on treatment and utilization of iron and steel smelting slag. Iron and Steel 55(01):1–5
5. Ma WZ, Wang H, Zhang MK (2012) Reduction of solubility, bio-availability, and bio-accessibility of heavy metals in polluted soil by mineral amendments. J Zhejiang Univ (Agricult Life Sci) 38(05):629–638
6. Zhao HJ, Yu QJ, Wei JX et al (2010) Influence on composition and morphology of mineral of steel slag and cementitious property. J Wuhan Univ Technol 32(15):22–26
7. Huang RT (2018) Study on converter steel slag mineral phase. Xi an University of Architecture and Technology
8. Lu Y, Yang LB, Lin L et al (2019) Leaching characteristics and affecting factors of total chromium and chromium in chromium-containing special steel slag. Iron Steel 54(06):103–108
9. Tian YC, Guo HW, Wang SY et al (2017) Experimental study on recycling heavy metals from steel slag sludge. Environ Eng 35:284–288
10. Chen CL, Wang G, Tian T (2019) Risk assessment based on TCLP extracted heavy metals in soil at farmlands near Molybdenum mining area. Fujian J Agricult Sci 34(04):458–464
11. Wang S, Xie L, Sheng J et al (2008) Application of steel slag to the environmental pollution treatment and its research progress. Industr Water Treatment 28(12):14–18

12. Chen YL, Zhang YN, Dai ZJ et al (2016) Effects of acidic geo-environmental on the mechanical properties of polluted soil. J Northeastern Univ Nat Sci 37(09):1343–1348
13. Zhang L, Wang J, Pang HC (2016) Decreasing soil pH value to promote spinach growth by application of urea phosphate under alkaline stress. Trans Chinese Soc Agricult Eng 32(02):148–154
14. Wang RS, Wang YH, Sui HL et al (2006) Soil amendment is the important link of formula fertilization by soil testing-improving the soil acidity and alkalinity. Phosphate Compound Fertilizer 21(06):68–70
15. Zhou F, Zhang XF, Yan TX et al (2019) The effect of combined use of Glomus versiforme and steel slag on the growth and Cd/Pb accumulation of zea mays. J South China Normal Univ (Nat Sci Edition) 5:75–83
16. Feng YS, Du YJ, Zhou SJ et al (2018) Utilization of activated steel slag to solidify/stabilize industrially heavy-metal contaminated soils. Chinese J Geotechn Eng 040(0z2):112–116
17. Zeng F, Ali S, Zhang H et al (2011) The influence of pH and organic matter content in paddy soil on heavy metal availability and their uptake by rice plants. Environ Pollut 159(1):84–91
18. Hua XZ, Chen B, Zhao RF et al (2015) Effect of steel slag application on onion production in farmland. J Shanxi Agricult Sci 43(03):293–296
19. Hua XZ, Chen B, Zhao RF et al (2015) Effect of steel slag application on corn production in farmland. J Shanxi Agricult Sci 43(01):43–46
20. Lou J, Zu Liu L, Wang T et al (2016) Effect of combined application of chemical fertilizer with organic manure on cucumber yield and soil microbial diversity. J Ecol Rural Environ 32(05):774–779
21. Liu KL, Han TF, Huang J et al (2020) Change of soil productivity in three different soils after long-term field fertilization treatments. J Integrat Agricult 19(03):848–858
22. Yang SP, Li SJ, Liu XM (2008) Reutilization and perspectives of the metallurgical waste slag. Steelmaking 24(03):59–62
23. Wang DY (2011) A new design of fe and p simultaneous recovery from steel slag. China Metall 21(8):50–54
24. Jiao Y, Grant CA, Bailey LD (2004) Effects of phosphorus and zinc fertilizer on cadmium uptake and distribution in flax and durum wheat. J Sci Food Agric 84(8):777–785
25. Ning DF (2014) Study on high efficiency utilization of steel slag silica fertilizer and risk assessment of heavy metals. Chinese Acad Agricult Sci
26. Li J, Zhang YL, Liu MD et al (2005) Effect of slag on rice in liaoning province. J Shenyang Agricult Univ 36(01):45–48
27. Wang XJ, Gao HS, Zhang L et al (2018) Application of slag calcium silicate fertilizer in chinese cabbage planting. Northern Horticult 000(22):18–22
28. Liu WQ, Fei XM, Wang CJ (2018) Factors influencing excessive application of fertilizer. J Ecol Rural Environ 34(08):726–732
29. Kang T, Mu YY, Hou LL (2019) Effect of agricultural products safety production technologies on elasticity of substitution. Trans Chinese Soc Agricult Eng 35(21):280–288
30. Zhu H, Chen C, Xu C et al (2016) Effects of soil acidification and liming on the phytoavailability of cadmium in paddy soils of central subtropical China. Environ Pollut 219(DEC):99–106
31. Chen F, Dong ZQ, Wang CC et al (2017) Heavy metal contamination of soils and crops near a zinc smelter. Environ Sci 38(10):4360–4369
32. Hu C, Fu QL (2007) Study progresses on heavy metal pollution of soil and absorption of vegetables and management. Chin Agric Sci Bull 23(06):519–523
33. Zhang FS, Liu W (2017) Heavy metal cadmium: effects on absorption of several microelements in sugar beet. Chin Agric Sci Bull 33(19):29–33
34. Jia XR, Liu FW, Fan WH et al (2019) Effect of silicon on cucumber yield and quality under cadmium stress. Chin J Soil Sci 50(01):171–176
35. Chang WY, Chen XD, Wang L et al (2008) Experimental study on reduction remediation of chromium(VI)-contaminated soil by aboriginal microbe. Environ Protect Sci 34(02):78–79, 98
36. Tan WN, Li ZA, Qiu J et al (2011) Lime and phosphate could reduce cadmium uptake by five vegetables commonly grown in South China. Pedosphere 21(02):223–229

37. Yang G, Li H, Chen H (2020) Study on remediation and mechanism of steel slag powder to heavy metal contaminated soil. J Build Mater, 1–11
38. Deng THB, Gu HH, Qiu RL (2011) Ameliorative effects of steel slag application on multi-metal contaminated soil and heavy metal uptake of rice. J Agro-Environ Sci 30(03):455–460
39. Chen BR, Xu C, Lu GM et al (2012) Effects of six kinds of curing agents on lead, cadmium, copper, zinc stabilization in the tested soil. J Agro-Environ Sci 31(07):1330–1336
40. Ran HZ, Guo ZY et al (2019) Effects of continuous application of soil amendments on cadmium availability in paddy soil and uptake by rice. China Environ Sci 39(03):1117–1123
41. Liu Y, Zhang CX (2019) The review of activation techniques of silicon in iron and steel slag silicon fertilizer preparation proces. Conservation Utilization Mineral Resour 39(01):144–149
42. Tong Q, Li J, Wang XY (2008) Effects of silicon and phosphate coordination employment on paddy soil absorbed cadmium. Acta Agriculturae Boreali-occidentalis 17(01):199–202
43. Liu CF, Shi GR, Yu RG et al (2017) Eco-physiological mechanisms of silicon-induced alleviation of cadmium toxicity in plants: a review. Acta Ecol Sin 37(23):7799–7810
44. Wu YJ, Zhou H, Yang WT et al (2016) Comparison of the persistence of a combined amendment stabilizing Pb, Cd, Cu and Zn in polluted paddy soil. Environ Sci 37(07):2791–2798
45. Qin SQ (2019) Advances in remediation of heavy metal amendments in soil. Resour Conserv Environ Protect 07:78–86
46. Zhao GH, Luo XZ, Chen G et al (2013) Progress on the testing method of heavy metals leaching toxicity of solid waste. Environ Pollut Control 35(07):80–84
47. Qu XL, Xie XS, Lu YD (2018) Study on leaching law and mechanism of heavy metals in steel slag. Environmental engineering National Annual Conference 2018. Beijing, China 36:634–639
48. Zhang XY, Zhang H, He PJ et al (2008) Beneficial reuse of stainless steel slag and its heavy metals pollution risk. Res Environ Sci 21(04):33–37

Effect of MgO on Oxidation of Vanadium Slag at High Temperature

Liang Liu, Jiang Diao, Yi-Yu Qiu, Hong-Yi Li, and Bing Xie

Abstract Based on two considerations of making full use of the residual heat of V-slag and exploring a novel green V extraction process, this paper employs MgO as the roasting additive, blows oxygen into the molten V-slag, and uses the residual heat of the V-slag for pre-roasting at high temperature. The influence of MgO on the phase structure of V-slags during oxidation has been investigated by XRD and SEM/EDS. The result shows that MgO as the roasting additive can convert V-slag at a high temperature of 1723 K. With the increase of blowing time of oxygen, the trivalent V in the spinel phase gradually disperses in the silicate matrix and then concentrates in the form of magnesium vanadate solid solution $(Mg, Mn, Ca)_2V_2O_7$. Furthermore, with the increase of MgO content, the peak intensity of the $Mg_2V_2O_7$ diffraction peak increases significantly. When the MgO content in V-slag increases from 4.01 to 12.74 wt%, the extraction efficiency increases from 18.99 to 64.07%.

Keywords V-slag · MgO · Oxidation · High temperature · Residual heat

Introduction

Vanadium is an important nonferrous metal element widely applied in metallurgical, material, and chemical industries [1, 2]. It is used as an alloy element additive in steel, as a stabilizer and strengthening agent in titanium alloys, and as a catalyst in the chemical industry. V–Ti magnetite ore is the main raw material for V extraction. About 88% of V worldwide is extracted from V–Ti magnetite ore [3, 4]. The route of extracting V from V–Ti magnetite ore is to convert the ore into V-bearing hot metal through blast furnace or other ironmaking processes and then blow oxygen into the converter to enrich V in hot metal into slag phase. The V-slag obtained with about

L. Liu · J. Diao (✉) · Y.-Y. Qiu · H.-Y. Li · B. Xie
College of Materials Science and Engineering, Chongqing University, Chongqing 400044, People's Republic of China
e-mail: diaojiang@163.com

Chongqing Key Laboratory of Vanadium-Titanium Metallurgy and Advanced Materials, Chongqing University, Chongqing 400044, People's Republic of China

J. Li et al., *Characterization of Minerals, Metals, and Materials 2021*,
The Minerals, Metals & Materials Series,
https://doi.org/10.1007/978-3-030-65493-1_17

1573 K is used as the subsequent raw material for V extraction after cooling, and V is extracted through pretreatment, roasting, leaching and, other processes [5–7].

At present, the most widely used V extraction process is the roasting–leaching method. Roasting-leaching operation requires mechanical crushing and high-temperature alkali roasting to destroy the outer package of the spinel and promote the oxidation of the low-valent V (III) in the spinel to high-valent V (V) [8]. According to different roasting additives, the industrialized V extraction methods can be divided into sodium method and calcification method [9].

Sodium roasting–water leaching method has strong adaptability to raw materials, and the obtained V_2O_5 product is of high quality. Although the V-product obtained by sodium roasting–water leaching method has high purity, it has the following problems: The low-melting sodium salt produced during the roasting process will cause the material sticking and hinder the continued oxidation of V. Harmful gases such as SO_2, SO_3, Cl_2, and HCl will be generated during the roasting process, which will corrode the equipment and pollute the environment [10, 11]. The tailings and wastewater after V extraction contain large amounts of Na^+ and cannot be recycled in the steel production process [12].

To solve the problems of waste gas pollution, agglomeration of furnace materials and the wastewater exhibits high sodium and ammonium sulfate content in the sodium roasting process, a calcium roasting–acid leaching method was proposed. During the acid leaching process, the precipitation of $CaSO_4$ could inhibit the dissolution of vanadates, thus reducing the leaching ratio of V [13]. Due to the large amount of $CaSO_4$ in the tailings of V extraction, it is difficult to use economically and can only be discarded. Moreover, the grade of V_2O_5 obtained after acid leaching is low and contains more impurity elements such as Mn^{2+}, Ca^{2+}. Difficulty in filtering residues and low V_2O_5 grade resulted in the process of not being widely used in industrial applications [14].

In this paper, to solve the pollution problem caused by the roasting agent, MgO was used to replace the existing sodium salt and calcium salt to realize the conversion of spinel to soluble magnesium vanadate. From the perspective of energy saving, the heat of V-slag discharged from the converter can provide energy support for the subsequent oxidation process. By simulating the V extraction conditions in a converter and using the residual heat of V-slag for magnesia pre-roasting, the oxidation effect of V-slag with different MgO content has been studied.

Experimental

Materials

The V-slag used in this paper was obtained from Pan-steel, China. The chemical composition of V-slag was analyzed by X-ray fluorescence spectroscopy (XRF, SHIMADZU LAB CENTER XRF-1800), as shown in No.1 in Table 1. Add different proportions of MgO to the V-slag, and the composition of V-slag obtained is shown as No.2, No.3, and No.4.

Table 1 Chemical composition of V-sla g, wt%

	FeO	V_2O_3	SiO_2	TiO_2	MnO	MgO	Al_2O_3	CaO
No.1	38.53	15.37	13.51	12.60	9.47	4.01	3.47	3.02
No.2	37.78	15.07	13.25	12.35	9.28	5.90	3.40	2.96
No.3	36.70	14.64	12.87	12.00	9.02	8.58	3.30	2.88
No.4	35.03	13.97	12.28	11.45	8.61	12.74	3.16	2.75

Experiments

Fifty grams of dried industrial V-slag were added into a corundum crucible and melted at 1723 K. After full melting, MgO was added and quickly stirred evenly to obtain V-slag with different MgO content. A double-hole alumina pipe with inner diameter of 1 mm was inserted into the molten V-slag. Then, oxygen was blown into the molten slag. The oxygen flow rate and oxygen blowing time were 3~10 L/min and 10~30 min, respectively. After oxygen blowing, the crucible was taken out from the furnace, cooled in air to room temperature, and then ground into a powder with particle size less than 74 μm.

Characterization

An X-ray diffractometer (XRD, Rigaku D/max 2500 PC) was used to characterize the phase in the powder sample. Morphology and element distribution in bulk samples were detected by a scanning electron microscope (SEM, TESCAN VEGA III) equipped with an energy-dispersive X-ray spectroscopy (EDS, INCA Energy 350). The oxidation effect of V-slag was expressed by the leaching rate of V. The elemental V concentrations in the leaching liquor were determined via an inductively coupled plasma-atomic emission spectrometer (ICP-AES, Thermo Fisher Scientific iCAP 6300 Duo) with the limit of determination of 0.001 mg/L. The thermodynamic calculations were performed using the FactSage 6.3 software.

Results and Discussion

Effect of MgO on the Phase of V-Slag

To investigate the influence of MgO addition on chemical components of the phases in the V-slag, slag samples with different MgO contents were characterized by XRD. As shown in Fig. 1a, the black line at the bottom represents the XRD pattern of industrial V-slag. The V-slag is mainly composed of spinel phase (Fe, Mg)V_2O_4,

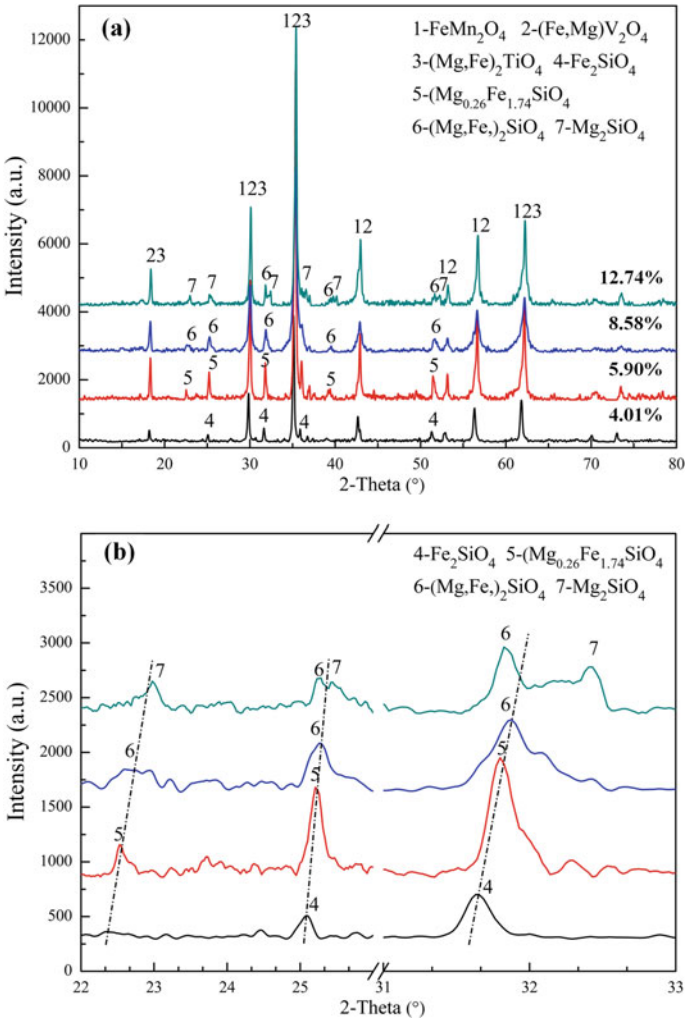

Fig. 1 XRD pattern of the samples: **a** V-slag with different MgO content; **b** partial enlarged view. (Color figure online)

$(Mg, Fe)_2TiO_4$, and olivine phase Fe_2SiO_4. V is concentrated in spinel phase and Mg distributes in each phase. The V-containing phases in all samples are concentrated in $(Mg, Fe)V_2O_4$, and the olivine phase changes. With the increase of MgO content in V-slag, part of Fe^{2+} (ion radius 0.74 Å) in Fe_2SiO_4 is replaced by Mg^{2+} (ion radius 0.66 Å) with smaller ion radius, which leads to smaller cell parameters and overall right shift of XRD peak [15]. In V-slag with MgO content as high as 12.74 wt% (No.4), Mg_2SiO_4 peaks are split from Fe_2SiO_4 peak, as shown in the partial enlargement Fig. 1b.

Effect of MgO on the Phase of Roasted V-Slag

Figure 2 shows the XRD pattern of V-slag with different MgO content after blowing oxygen for 10 min. The industrial V-slag after pre-roasting for 10 min consists of Fe_2TiO_5, Fe_2O_3, $Ca_3Mg(SiO_4)_2$, a small amount of $MgFeAlO_4$, and V-containing phases ($FeVO_4$, $(Mg, Mn)_2V_2O_7$, $Ca_7V_4O_{17}$).

After oxidation of V-slag with high MgO content for 10 min, olivine $(Mg, Fe)_2SiO_4$ oxidized to pyroxene $MgSiO_3$. The crystallinity of $MgSiO_3$ was not good, resulting in weak diffraction peaks. With the increase of MgO content in V-slag, the content of $Mg_2V_2O_7$ increased.

When the content of MgO is about 4.01wt% or 5.90 wt%(No.1 or No.2), the roasted V-slag contains a large amount of diffraction peaks of Fe_2O_3. With the increase of MgO content, the diffraction peaks of fractional Fe_2O_3 disappeared and the intensity of $MgFeAlO_4$ diffraction peak increased. Part of Fe_2O_3 and Mg^{2+} form spinel phase $MgFeAlO_4$ furtherly, which consume the content of Fe_2O_3. Under oxygen atmosphere, the binary phase diagram of MgO–Fe_2O_3 and MgO–Al_2O_3 are shown in Fig. 3a, b. Ignoring other components, MgO can form spinel with Fe_2O_3 and Al_2O_3 at 1723 K, respectively. Therefore, in the presence of MgO, Fe_2O_3, and Al_2O3, the mixed spinel phase $MgFeAlO_4$ can be generated.

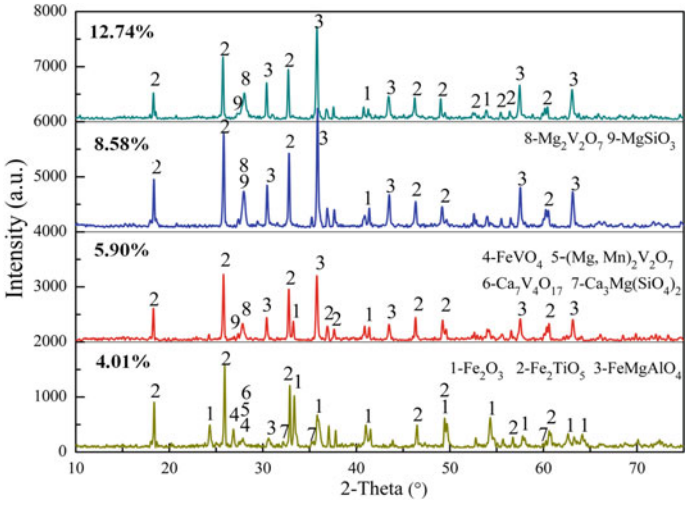

Fig. 2 XRD patterns of V-slag with different MgO content after oxygen blowing for 10 min. (Color figure online)

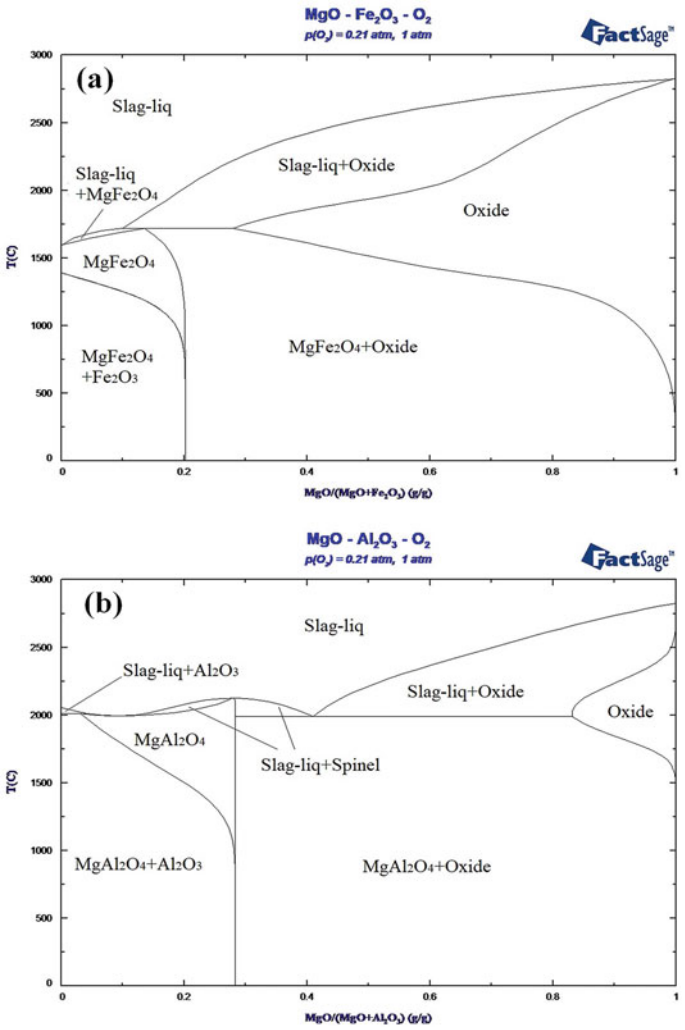

Fig. 3 The binary phase diagram: **a** MgO-Fe_2O_3; **b** MgO–Al_2O_3. (Color figure online)

Effects of Oxidation Time and MgO Content on the Leaching Rate of V

Table 2 shows the leaching rates of the roasted V-slag. The acid leaching conditions are as follows: liquid-to-solid ratio 5:1, temperature 70 °C, time 30 min, pH 0.5, stirring speed 100 rpm. The leaching rate of V of roasted V-slag increased obviously with the increase of oxidation time and MgO content. When the MgO content increased from 4.01 to 12.74 wt%, the V leaching rate increased from 18.99 to 64.09%. With

Table 2 Leaching rate of roasted V-slag, %

Raw material	Oxidation time		
	10 min	20 min	30 min
No.1	14.63	18.02	18.99
No.2	20.88	32.20	42.34
No.3	23.19	40.38	53.69
No.4	26.55	56.12	64.09

the increase of oxidation time from 10 min to 30 min, the leaching rate of V-slag with 12.74 wt% MgO, increased from 26.55 to 64.09%.

The XRD pattern of the residue of the V-slag with 8.58 wt% content oxidized for 10 min is shown in Fig. 4. The main components of the leaching residue are Fe_2TiO_5, $MgFeAlO_4$, and Fe_2O_3. The intensities of peaks corresponding to pre-roasting products Fe_2TiO_5, $MgFeAlO_4$, and Fe_2O_3 were not weakened after leaching, indicating that they did not react with H_2SO_4. The diffraction peak of magnesium pyrovanadate $Mg_2V_2O_7$ disappeared, and a weak SiO_2 diffraction peak appeared, indicating that $Mg_2V_2O_7$ is leachable. The reaction is shown in Eqs. (1–2).

$$Mg_2V_2O_7 + 3H_2SO_4 = (VO_2)_2SO_4 + 2MgSO_4 + 3H_2O \quad (1)$$

$$MgSiO_3 + H_2SO_4 = SiO_2 + MgSO_4 + H_2O \quad (2)$$

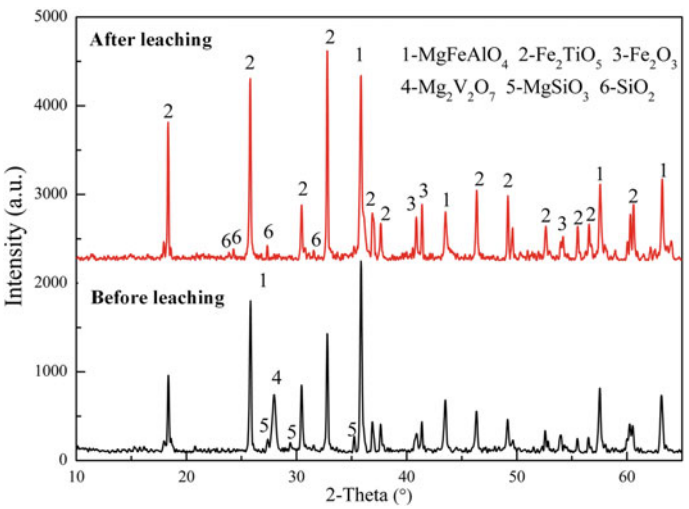

Fig. 4 XRD pattern of V-slag with 8.58% MgO before leaching and after leaching. (Color figure online)

Conclusions

The present study proposed a novel green V extraction process by magnesia pre-roasting at high temperature. The experimental results indicated that MgO as the roasting additive can convert V-slag at a high temperature of 1723 K. The added MgO entered the spinel and the olivine Fe_2SiO_4 to form (Mg, Fe)V_2O_4 and (Mg, Fe)$_2SiO_4$, respectively. The main phases of V-slag after oxidation were Fe_2TiO_5, $MgFeAlO_4$, Fe_2O_3, $Mg_2V_2O_7$. On the one hand, MgO was beneficial to the formation of magnesium pyrovanadate $Mg_2V_2O_7$. When the MgO content increased from 4.01 to 12.74 wt%, the V leaching rate increased from 18.99 to 64.09%. On the other hand, the pre-roasting time was conducive to the formation of magnesium pyrovanadate $Mg_2V_2O_7$. With the increase of oxidation time from 10 to 30 min, the leaching rate of V-slag with 12.74 wt% MgO, increased from 26.55 to 64.09%.

Acknowledgements This work was supported by the National Natural Science Foundation of China (No. 51974047) and the Natural Science Foundation of Chongqing, China (cstc2020jcyj-msxmX0043).

References

1. Moskalyk RR, Alfantazi AM (2003) Processing of vanadium: a review. Miner Eng 16(9):793–805
2. Huang DX (2000) Vanadium extraction and steelmaking. Metallurgical Industry Press, Beijing
3. Liu B, Du H, Wang SN, Zhang Y, Zheng SL, Li LJ, Chen DH (2013) A novel method to extract vanadium and chromium from vanadium slag using molten NaOH–$NaNO_3$ binary system. AIChE J 59(2):541–552
4. Lundkvist K, Brämming M, Larsson M, Samuelsson C (2013) System analysis of slag utilisation from vanadium recovery in an integrated steel plant. J Clean Prod 47:43–51
5. Kim E, Spooren J, Broos K (2016) Valorization of stainless steel slag by selective chromium recovery and subsequent carbonation of the matrix material. J Clean Prod 117:221–228
6. Ji Y, Shen S, Liu J (2017) Cleaner and effective process for extracting vanadium from vanadium slag by using an innovative three-phase roasting reaction. J Clean Prod 149:1068–1078
7. Diao J, Qiao Y, Zhang X, Ji CQ, Xie B (2015) Growth mechanisms of spinel crystals in vanadium slag under different heat treatment conditions. CrystEngComm 17(38):7300–7305
8. Zhang G, Luo D, Deng C (2018) Simultaneous extraction of vanadium and titanium from vanadium slag using ammonium sulfate roasting-leaching process. J Alloy Compd 742:504–511
9. Li XS, Xie B (2012) Extraction of vanadium from high calcium vanadium slag using direct roasting and soda leaching. Int J Miner Metall Mater. 19(7):595–601
10. Sadykhov GB (2008) Oxidation of titanium-vanadium slags with the participation of Na_2O and its effect on the behavior of vanadium. Russ Metall 2008(6):449–458
11. Mahdavian A, Shafyei A, Alamdari EK, Haghshenas DF (2006) Recovery of vanadium from esfahan steel company steel slag; optimizing of roasting and leaching parameters. Int J Iron Steel Soc 3(2):17–21
12. Wen JW, Ning PG, Cao HB, Sun Z, Zhang Y (2018) Controllable recovery of ammonium substituted polyoxovanadate acid compound (ASPOVC) from aqueous/leaching solution by primary amines. J Clean Prod 205(PT.1-1162):728–737

13. Aarabi-Karasgani M, Rashchi F, Mostoufi N, Vahidi E (2010) Leaching of vanadium from LD converter slag using sulfuric acid. Hydrometallurgy 102(1–4):14–21
14. Yang Z, Li HY, Yin XC, Yan ZM, Yan XM, Xie B (2014) Leaching kinetics of calcification roasted vanadium slag with high CaO content by sulfuric acid. Int J Miner Process 133:105–111
15. Jiang L, Bao Y, Yang Q (2017) Formation of spinel phases in oxidized BOF slag under different cooling conditions. Steel Res Int 88:e201700066. https://doi.org/10.1002/srin.201700066

Effects of Basicity, FeO, and TiO_2 on Phase Transformation and Viscosity of TiO_2-Bearing Primary Slag in Blast Furnace

Yapeng Zhang, Dongqing Wang, Shaoguo Chen, Zhengjian Liu, Wen Pan, and Zhixing Zhao

Abstract Characteristics and behaviors of primary slag are of central importance for the cohesive zone. This work focuses on phase transformation and viscosities of $CaO–SiO_2–Al_2O_3–MgO–FeO–TiO_2$ slag (TiO_2 = 4~16 wt%, CaO/SiO_2 = 1.1 ~ 1.5, FeO = 5~25 wt%). The melting process of TiO_2 bearing primary slag can be divided into three stages. With the increase of binary basicity (from 1.2 to 1.5), the viscosities of primary slag are at the same level (above 1674 K), but the T_{br} increases 40 K with it. FeO can decrease both viscosity and T_{br}. T_{br} decreases to 87 K with FeO content varying from 5 to 25 wt%. When the temperature is lower than T_{br}, TiO_2-bearing phases (titania spinel and perovskite) start to precipitate, leading to the dramatic increase of viscosity. T_{br} increases from 1578 K to 1671 K when TiO_2 content varies from 4 to 16 wt%. The effects of TiO_2 on FT and T_{br} are the same as binary basicity.

Keywords Primary slag · Wustite · Break temperature · Viscosity · Perovskite

Introduction

Burden materials of blast furnace (BF) start to soften and melt resulting from reduction and high temperature in the cohesive zone, which give rise to the formation of primary slag. Characteristics and behaviors of primary slag are of central importance for cohesive zone, because they affect gas permeability in the lower part of BF shaft, and then influence the BF operation efficiency. The composition of primary slag,

Y. Zhang (✉) · D. Wang · S. Chen · W. Pan · Z. Zhao
Shougang Group Co. Ltd. Research Institute of Technology, Beijing 100043, People's Republic of China
e-mail: andy_zhg@outlook.com

Beijing Key Laboratory of Green Recyclable Process for Iron & Steel Production Technology, Beijing 100043, People's Republic of China

Z. Liu
School of Metallurgical and Ecological Engineering, University of Science and Technology, Beijing 100083, China

J. Li et al., *Characterization of Minerals, Metals, and Materials 2021*,
The Minerals, Metals & Materials Series,
https://doi.org/10.1007/978-3-030-65493-1_18

especially FeO concentration, changes continuously as it flows and reacts with coke and reducing gases. Some scholars [1–5] tried to study and define the complex composition of primary slags with various technical methods and agreed that primary slags contain considerable FeO and are with higher basicity than typical BF slags. CaO–SiO_2–Al_2O_3–MgO–FeO slag system [2, 3, 6] had been investigated and discussed on its viscosity and structure under different composition conditions. However, it's not enough to cover and illustrate the complex primary slags, especially the TiO_2-bearing primary slag.

In some iron-making plants, a Ti-bearing sinter is charged into BF to prolong the life campaign, resulting in the formation of TiO_2-bearing primary slag. In the author's previous work [7], it was found that there were differences in phase transition between Ti-bearing sinter and ordinary sinter during reduction with the existence of titanium, which lead to the formation mechanism of TiO_2-bearing primary slag different from that of ordinary primary slag. Thus, this work focused on phase transformation and viscosities of CaO–SiO_2–Al_2O_3–MgO–FeO–TiO_2 slag system in the temperature range of 1473–1723 K to have a better understanding of TiO_2-bearing primary slag. Studies on liquid phase proportion and fluidity of slag [4], liquid phase formation during iron ores sintering [8], and Melting behavior of Ti-bearing electric furnace slag [9] were reported using FactSage to investigate the phase transition [10] in iron-making and steelmaking process. Therefore, FactSage 7.1 was applied to simulate the transition of solid and liquid phases during the formation of primary slag. Viscosities of CaO–SiO_2–Al_2O_3–MgO–FeO–TiO_2 slag system at different temperatures were measured with an accurate rotating viscometer.

Materials and Methods

Thermodynamic Calculation of Phase Transition of TiO_2-Bearing Primary Slag

TiO_2-bearing primary slag is a typical slag system composed of multiple components (including CaO, SiO_2, Al_2O_3, MgO, FeO, TiO_2) and phases. The formation of TiO_2-bearing primary slag in BF is also companied with complicated interaction and recombination of various phases and components. It is necessary to clarify the phase transition of TiO_2-bearing primary slag with temperature increasing by thermodynamic calculations. In this work, FactSageTM software, which contains two famous software packages [11, 12] (Fact-Win & ChemSage) in the field of thermodynamics, was adopted to simulate the phase transitions. The "Equilib" module was applied with the databases "FToxid" and "FactPS", as "Equilib" module has the function of completing phase equilibrium calculations under the conditions of multiple coupling reactions. According to the reports of other scholars and the author's previous work,

Table 1 Chemical compositions of primary slag samples (wt%)

Sample number	CaO	SiO_2	MgO	Al_2O_3	TiO_2	FeO	R
R1	29.86	27.14	8	12	8	15	**1.10**
R2*	31.09	25.91	8	12	8	15	**1.20**
R3	32.22	24.78	8	12	8	15	**1.30**
R4	33.25	23.75	8	12	8	15	**1.40**
R5	34.20	22.80	8	12	8	15	**1.50**
F1	36.55	30.45	8	12	8	**5**	1.20
F2	33.82	28.18	8	12	8	**10**	1.20
F3*	31.09	25.91	8	12	8	**15**	1.20
F4	28.36	23.64	8	12	8	**20**	1.20
F5	25.64	21.36	8	12	8	**25**	1.20
T1	33.27	27.73	8	12	**4**	15	1.20
T2	32.18	26.82	8	12	**6**	15	1.20
T3*	31.09	25.91	8	12	**8**	15	1.20
T4	30.00	25.00	8	12	**10**	15	1.20
T5	28.91	24.09	8	12	**12**	15	1.20
T6	27.82	23.18	8	12	**14**	15	1.20
T7	26.73	22.27	8	12	**16**	15	1.20

* Samples R2, F3, and T3 are the benchmark and have the same chemical composition.

the compositions of TiO_2-bearing primary slag were determined as shown in Table 1. Viscosity tests were conducted by picking up some of the compositions.

Sample Preparation and Viscosity Test

Samples of TiO_2-bearing primary slags were prepared with analytic reagents ($CaCO_3$, SiO_2, MgO, $Al(OH)_3$, TiO_2, and $FeC_2O_4{\cdot}2H_2O$). The components, i.e. CaO, Al_2O_3, and FeO, of the primary slag were obtained by decomposition of $CaCO_3$, $Al(OH)_3$, and $FeC_2O_4{\cdot}2H_2O$, the reaction equations are as follows:

$$CaCO_3 \rightarrow CaO + CO_2$$

$$2Al(OH)_3 \rightarrow Al_2O_3 + 3H_2O$$

$$FeC_2O_4{\cdot}2H_2O \rightarrow FeO + CO + CO_2 + 2H_2O$$

Figure 1 presents the preparation procedures of TiO_2-bearing primary slag samples. Analytic reagents ($CaCO_3$, SiO_2, MgO, $Al(OH)_3$, and TiO_2, excluding $FeC_2O_4{\bullet}2H_2O$) were weighted and mixed adequately as designed in Table 1. The mixtures were ground in a corundum mortar for 15 min. The well-mixed powders were then charged into the titanium dioxide crucibles, and put in a muffle furnace, heated to 1150 °C, and kept for 60 h. After that, analytic reagent $FeC_2O_4{\bullet}2H_2O$ was

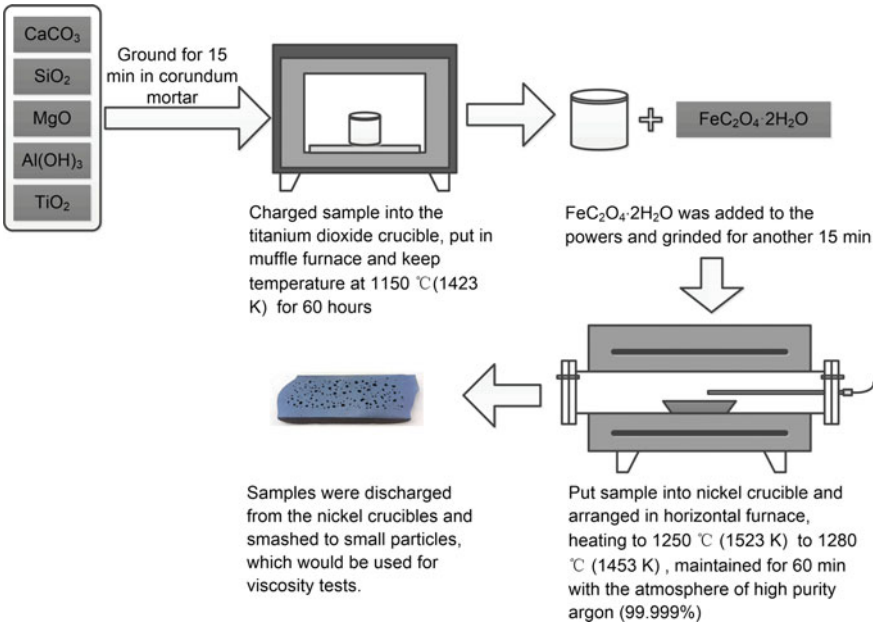

Fig. 1 Preparation procedures of TiO_2-bearing primary slag samples. (Color figure online)

added to the powers and ground for another 15 min. Then, the mixed samples were put into the nickel crucibles and arranged in a horizontal furnace, heated to 1250–1280 °C (according to the solidus temperature of samples, which was calculated by FactSage 7.1), and maintained for 60 min under the atmosphere of high purity argon (99.999%). After the furnace being cooled to room temperature under argon atmosphere, the samples were discharged from the nickel crucibles and smashed into small particles, which would be used for viscosity tests.

The viscosity tests of TiO_2-bearing primary slag were performed with typical rotating cylinder method. The viscosity measuring equipment used in this work is Rheotronic II-type viscometer (produced by Theta Industries Inc.) and its main parameters are shown in Table 2. Two types of molybdenum crucibles (Testing

Table 2 Equipment parameters of Rheotronic II-type viscometer

Items	Parameters
Type of measuring head	Brookfield DV III
Range of measurement	0.05 ~ 500 Pa·s
Range of Temperature	RT ~ 2000°C
Rotor speed	0.1 ~ 500 rpm
Type of thermocouple	S-Type
Size of chamber	Φ60 × 500 mm
Heating element	$MoSi_2$ bar

Table 3 Size parameters of crucibles and spindle (mm)

Spindle		Crucible	Testing crucible	Protecting crucible
Diameter	12	Inner-diameter	29	31.5
Height	17	Outer-diameter	31	35
Shape	Fusiform	Height	60	65

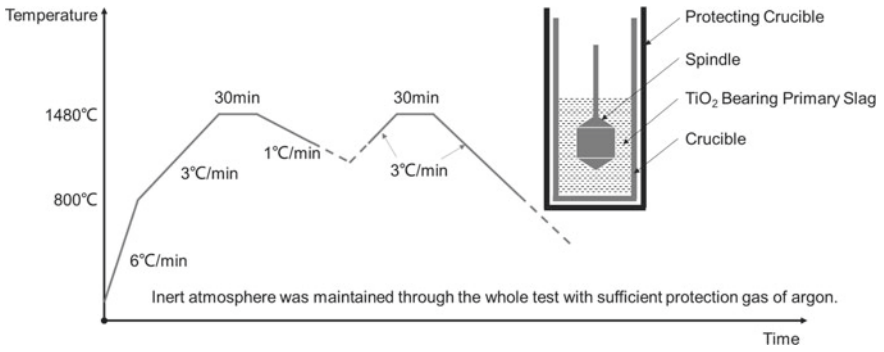

Fig. 2 Schematic diagram of viscosity tests and the temperature schedule of measurements

crucible and protecting crucible) and the molybdenum spindles were applied for viscosity tests. The size parameters were summarized in Table 3. Each time 35–45 g of prepared samples (the height of molten slag was kept at the same level in crucible) was charged into the testing crucible for viscosity test. Schematic diagram of viscosity tests and the temperature schedule were illustrated in Fig. 2.

Results and Discussion

Effects of Binary Basicity (R)

Figure 3 illustrates the phase transitions of different primary slags with binary basicity from 1.1 to 1.5. The fusion temperature (FT) of TiO_2-bearing primary rises with the increase of binary basicity.

The initial melting temperature (IMT) also rises, indicating the existence of more compounds with a high melting point in primary slag. The IMT of primary slag with $R = 1.1$ is lower than 1473 K, as some liquid phases have appeared at 1473 K. The temperature interval between IMT and FT has a small difference (124–128 K) when binary basicity varies from 1.2 to 1.5.

Interestingly, the melting process of TiO_2-bearing primary slag can be divided into three different temperature stages with distinctive features according to the phase

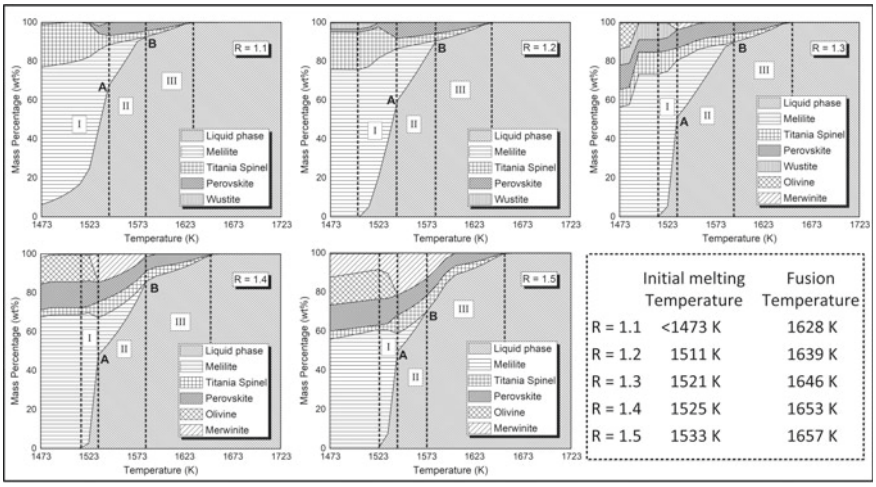

Fig. 3 Effects of binary basicity (R) on phase transformation of TiO_2-bearing primary slags

transformation and the liquid phase proportion during melting. The main features of each stage are as follows.

Stage I: From IMT to Point A, the liquid proportion increases dramatically, while melilite decreases quickly. Some FeO-containing phases, such as wustite and olivine, also decrease or disappear at the end of this stage. Meanwhile, merwinite, which has relatively high FT (1823 K), reaches its maximum proportion in the melting process, and the maximum proportion of merwinite increases with binary basicity improving from 1.1 to 1.5. The two TiO_2-bearing phases, i.e. titania spinel and perovskite, are very special in this stage. When binary basicity varies from 1.1 to 1.3, the proportion of titania spinel decreases and perovskite increases. Adversely, when binary basicity varies from 1.4 to 1.5, the titania spinel increases and the perovskite decreases. The main phase transformations in stage I are summarized:

$$\text{melilite} + \text{wustite} + \text{titania spinel} \rightarrow \text{liquid} + \text{perovskite} + \text{merwinite}\ (R = 1.1 \sim 1.3)$$

$$\text{melilite} + \text{olivine} + \text{perovskite} \rightarrow \text{liquid} + \text{titania spinel} + \text{merwinite}\ (R = 1.4 \sim 1.5)$$

Stage II: From Point A to B, the proportion of liquid increases continuously. At the end of this stage, melilite disappears gradually with temperature going higher. The proportion of TiO_2-bearing phases (titania spinel and perovskite) decreases slightly because of the existence of melilite. And merwinite also dissolves totally or partly into liquid in this stage depending on various binary basicities. Consequently, phase transformation is relatively simple:

$$\text{melilite} + \text{titania spinel} + \text{perovskite} + \text{merwinite}\ (R = 1.3 \sim 1.5) \rightarrow \text{liquid}$$

Stage III: From point B to FT, solid phases are mainly titania spinel, perovskite and some residual merwinites (at high binary basicity). The two TiO_2-bearing phases are the last to be dissolved into liquid. Thus, the phase transformation can be summarized as follows:

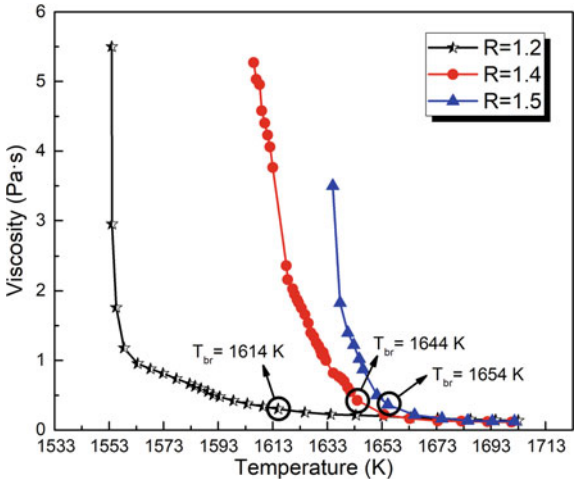

Fig. 4 Effects of binary basicity (R) on viscosity of TiO_2-bearing primary slags. (Color figure online)

titania spinel + perovskite + merwinite (R = 1.4 ~ 1.5) → liquid

Figure 4 presents the effects of binary basicity (R) on viscosity of TiO_2-bearing primary slags. The T_{br} is a point at which the viscosity increases suddenly and the slag becomes non-Newtonian in behavior because of the crystallization and solidification [13–15] when viscosity measurements are carried out during a cooling cycle. The T_{br} is usually lower than the initial crystallization temperature and higher than the ful crystallization temperature. That means T_{br} is between IMT and FT. When the temperature is higher than T_{br} and lower than FT, solid and liquid phases co-exist in the system, and the solid phases do not precipitate [16]. With the increase of binary basicity, the T_{br} on viscosity curve (circled points) increases about 50 K. Therefore, A higher binary basicity corresponds to higher T_{br}, IMT, and FT for TiO_2-bearing primary slag. Furthermore, the viscosity values of primary slag are at the same level when temperature is above 1663 K.

Effects of FeO Content

Effects of FeO on phase transformation of TiO_2-bearing primary slags are illustrated in Fig. 5. The FT decreases first and then increases with FeO content varying from 5 to 25 wt%. It means that when TiO_2 is contained in the primary slag, the FT would not always decrease with the FeO increasing. The IMT increases with FeO content increasing in the range of 5–15 wt%.

Meanwhile, IMT has no significant variation trend with FeO content increasing when FeO is between 15 and 25 wt%. Comparing the phase transformation diagrams in Fig. 5, perovskite decreases and titania spinel increases during melting process with FeO varying from 5 to 25 wt%. Interestingly, in stage III of melting process, either perovskite or titania spinel alone left would increase the FT of primary slag.

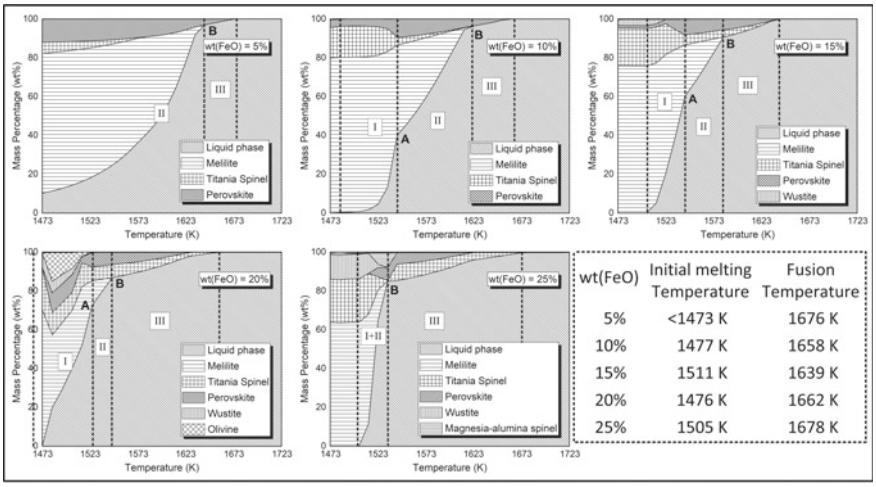

Fig. 5 Effects of FeO on phase transformation of TiO_2-bearing primary slags

However, when both of the two TiO_2-bearing phases were left, FT would decrease, as shown in Fig. 5.

Furthermore, the phase transformations of primary slags during melting are of great difference with FeO content increasing from 5 to 25 wt%, especially in stage I. Main phase transformations at different temperature stages are summarized as follows.

Stage I: From IMT to Point A.

melilite + titania spinel + wustite → liquid + perovskite (FeO = 5~15 wt%)

melilite + olivine + wustite + titania spinel → liquid + perovskite + magnesia-alumina spinel (FeO = 20 ~ 25 wt.%)

The TiO_2-bearing phase olivine is an intermedium phase when FeO is 20 wt%.

Stage II: From Point A to B.

melilite + titania spinel + perovskite → liquid

Stage III: From point B to FT

TiO_2-bearing phase + liquid → liquid

TiO_2-bearing phase represents titania spinel and (or) perovskite in different diagrams.

With the increase of FeO content, the temperature range of stage II gets narrower, while stage III gets wider. When FeO is 25 wt%, temperature stages I and II are even merged as one. Generally, TiO_2-bearing primary slags with higher FeO content melt more quickly and sharply in stages I and II.

Figure 6 shows the effects of FeO on viscosity of TiO_2-bearing primary slags. FeO has a strong influence on the viscosity. Higher FeO content corresponds to lower viscosity and T_{br}. The T_{br} decreases by 87 K with FeO varying from 5 to 25 wt%. FeO is a basic oxide and acts as a network modifier [1, 3, 9] in slag, which can decrease the viscosity of slag significantly.

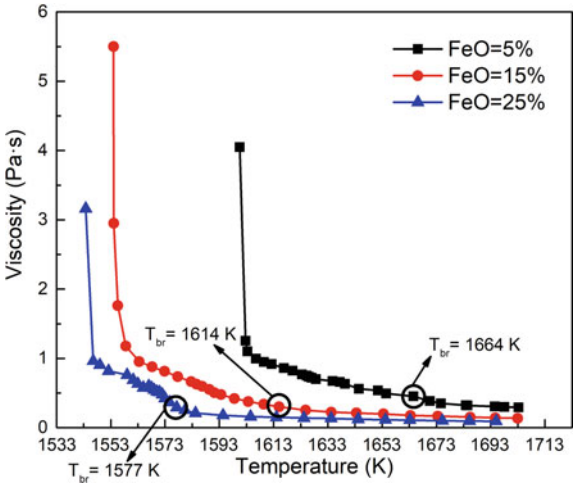

Fig. 6 Effects of FeO on viscosity of TiO_2-bearing primary slags. (Color figure online)

Effects of TiO_2 Content

Figure 7 presents the effects of TiO_2 content on phase transformation of different primary slags. The IMT decreases when more TiO_2 exists in primary slag. It even becomes lower than 1473 K with 12–16 wt% TiO_2 as considerable liquid phase has appeared at 1473 K. Interestingly, the FT increases from 1627 K to 1682 K with TiO_2 varying from 4 to 16 wt%. That means the increase of TiO_2 content in primary slag will extend the temperature interval of solid–liquid coexistence zone.

As shown in Fig. 7, the titania spinel expands while the melilite and wustite shrink with TiO_2 ranging from 4 to 16 wt% before primary slag starting to melt. Similarly, the melting process of TiO_2-bearing primary slag can be also divided into three different temperature stages. The main features of each stage are as follows.

Stage I: From IMT to Point A, liquid phase increases, while melilite and wustite decrease quickly. Wustite disappears at the end of this stage. Meanwhile, perovskite reaches its maximum proportion in melting process. Magnesia–alumina spinel starts to form when TiO_2 content increases. So the main phase transformations in stage I are summarized:

melilite + wustite + titania spinel → liquid + perovskite (TiO_2 = 4~8 wt%)

melilite + titania spinel → liquid + perovskite (TiO_2 = 10 ~ 16 wt%)

Stage II: From Point A to B, the increase of liquid proportion slows down slightly. Perovskite starts to dissolve at this stage and the melilite disappears at the end of this stage. Consequently, phase transformation is relatively simple:

melilite + titania spinel + perovskite → liquid

Stage III: From point B to FT, solid phases are only TiO_2-bearing phases, i.e. titania spinel and perovskite. The phase transformation is the dissolution of the two TiO_2-bearing phases into liquid. So the phase transformation can be summarized as follows:

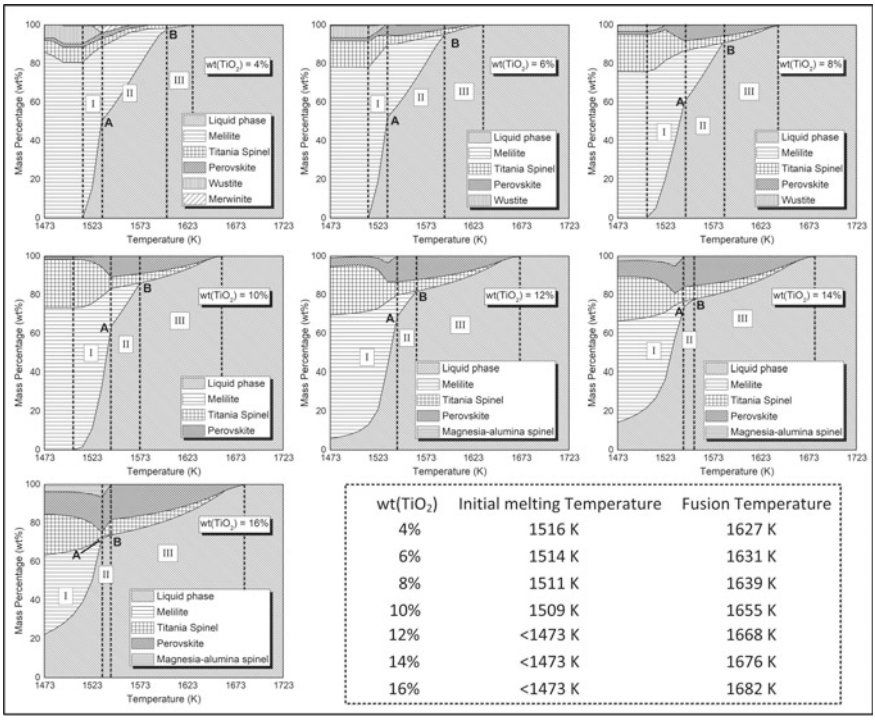

wt(TiO_2)	Initial melting Temperature	Fusion Temperature
4%	1516 K	1627 K
6%	1514 K	1631 K
8%	1511 K	1639 K
10%	1509 K	1655 K
12%	<1473 K	1668 K
14%	<1473 K	1676 K
16%	<1473 K	1682 K

Fig. 7 Effects of TiO_2 on phase transformation of TiO_2-bearing primary slags

titania spinel + perovskite → liquid

Figure 8 shows the effects of TiO_2 content on viscosity of TiO_2-bearing primary slags. The trends of the viscosity curves with relatively low TiO_2 content (4 ~ 8 wt%) are of typical "short slag". However, the viscosity curve of relatively high TiO_2 content (16 wt%) is of typical "long slag". The T_{br} increases from1578 K to 1671 K when TiO_2 content varies from 4 to 16 wt%.

As for the influence of TiO_2 on viscosity, it's more complicated than basicity and FeO because TiO_2 is an amphoteric oxide [17]. Many scholars [1, 16, 18] conducted viscosity measurements and structure analysis of slags to study and identify the role of TiO_2 in slag and found that TiO_2 behaved as a basic oxide and acted as a network modifier. That means the viscosity will decrease with the increase of TiO_2 content in slag. However, this conclusion may be correct only when the temperature is close to or higher than 1773 K. In this work, the viscosities were measured lower than 1723 K. In the temperature range of 1723 K–T_{br}, the viscosity increases with TiO_2 increasing in slag. This may indicate that TiO_2 acts as a weak acidic oxide [19] and plays the role of network former. Jiao and Zhang et al. [16, 20] explained that TiO_2 can capture oxygen ions and the existence of $Ti_2O_6^{4-}$ chain units gives rise to a higher degree of polymerization for silicate network. When the temperature is lower than T_{br}, TiO_2-bearing phases (titania spinel and perovskite) start to precipitate,

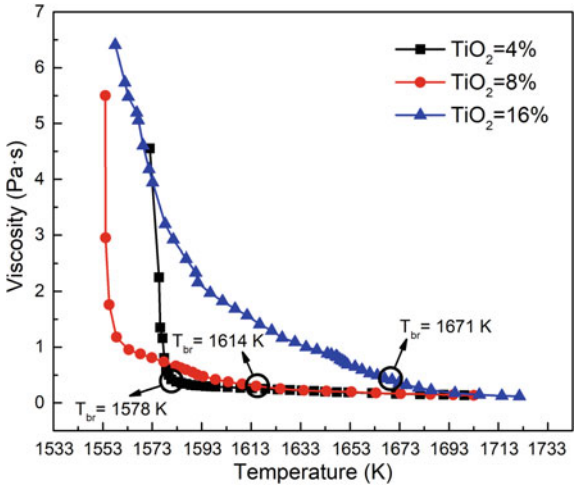

Fig. 8 Effects of TiO_2 on viscosity of TiO_2-bearing primary slags. (Color figure online)

leading to the dramatic increase of viscosity. Zhang et al. [18] also confirmed that TiO_2 would act as a network former when temperature was low in the CaO–MgO–Al_2O_3–SiO_2–TiO_2 slag system. But he found that TiO_2 mainly existed in the form of [TiO_4] which was different from the result of Jiao's work. Therefore, further study is necessary to clarify the structure of TiO_2 in Ti-bearing primary slag.

Comparison of IMT, FT, and T_{br}

Binary basicity, FeO, and TiO_2 have different influences on the melting process and viscosity of primary slag. Figure 9 gives the comparison of T_{br} with IMT and FT of TiO_2-bearing primary slag.

T_{br}, IMT, and FT all increase along with binary basicity increasing from 1.1 to 1.5, as shown in Fig. 9a. Furthermore, the temperature interval between T_{br} and FT becomes narrower. That means higher binary basicity will promote the precipitation of TiO_2-bearing phases. Besides, the cohesive zone in a blast furnace tends to be lower as IMT goes high with binary basicity.

FeO has an obvious effect on T_{br}, as shown in Fig. 9b. T_{br} decreases sharply with FeO content varying from 5 to 25 wt%. Meanwhile, FT tends to decrease first and then increase. It seems that FT will decrease when titania spinel and perovskite dissolve into liquid together at stage III.

The effect of TiO_2 on FT and T_{br} is the same as the binary basicity. However, IMT goes lower with TiO_2 increasing from 4 to 16 wt%, as shown in Fig. 9c. It will lead to the expansion of temperature interval of the cohesive zone in a blast furnace, and then affects the smooth operation of blast furnace.

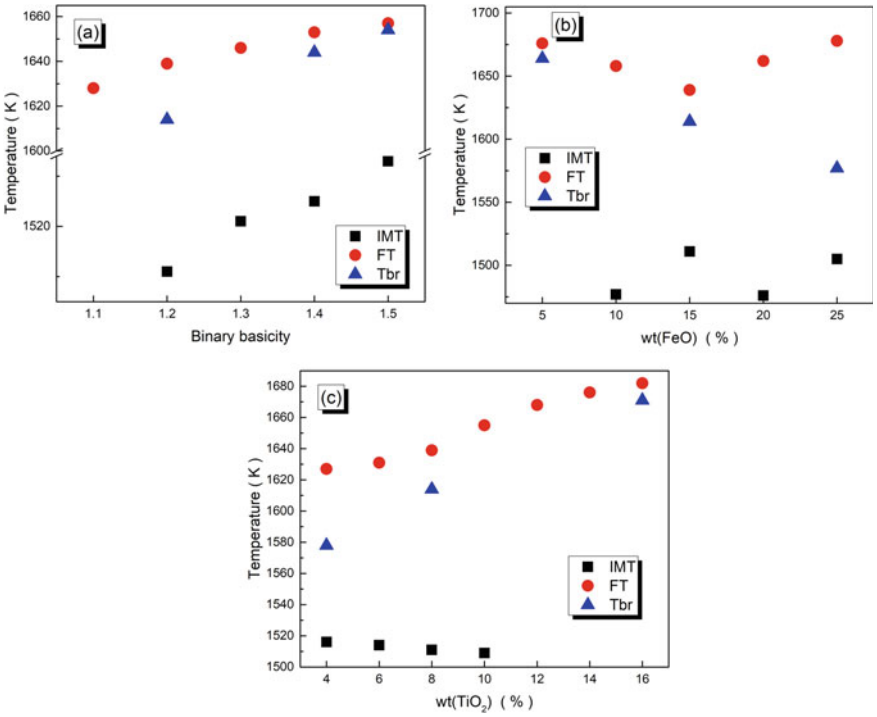

Fig. 9 Comparison of T_{br} with IMT and FT of TiO_2-bearing primary slag. (Color figure online)

Conclusions

(1) The melting process of TiO_2-bearing primary slag can be divided into three stages. The first stage mainly includes not only the melting process of melilite, titania spinel, wustite, and olivine but also the formation of perovskite and some other intermediate compounds. The second stage is the melting of melilite and TiO_2-bearing phases. The third stage is the dissolution of TiO_2-bearing phases.

(2) With the increase of binary basicity (from 1.2 to 1.5), the viscosities of primary slag are at the same level at high temperature (above 1674 K), but the T_{br} increases 40 K with it. FeO can decrease both viscosity and T_{br} because FeO acts as a network modifier in primary slag. T_{br} decreases 87 K with FeO content varying from 5 to 25 wt%. TiO_2 acts as a weak acidic oxide and plays the role of network former in cohesive zone at relatively low temperatures, and then increases the viscosity of primary slag. When the temperature is lower than T_{br}, TiO_2-bearing phases (titania spinel and perovskite) start to precipitate, leading to the dramatic increase of viscosity. T_{br} increases from 1578 K to 1671 K when TiO_2 content varies from 4 to 16 wt%.

(3) Binary basicity, FeO, and TiO_2 have different influences on the trends of T_{br}, IMT, and FT. Binary basicity has the same effect on the three temperatures. T_{br}

decreases sharply with FeO varying from 5 to 25 wt%. Meanwhile, FT tends to decrease first and then increase. The effect of TiO_2 on FT and T_{br} is the same as binary basicity. IMT goes lower with TiO_2 increasing from 4 to 16 wt%, leading to the expansion of temperature interval of the cohesive zone in a blast furnace.

Acknowledgements The authors are grateful for the financial support of the National Key R&D Program of China (2017YFB0304300&2017YFB0304302) and would like to thank Dr. Liming Lu, Dr. Hongliang Han, and Mr. Alexander Edenton from CSIRO Minerals for their generous guidance and help on the experiments of this work.

References

1. Jiao K, Zhang J, Wang Z, Chen C, Liu Y (2017) Steel Res Int 88:1600296. https://doi.org/10.1002/srin.201600296
2. Kim JR, Lee YS, Min DJ, Jung SM, Yi SH (2004) ISIJ Int 44:1291–1297
3. Lee YS, Min DJ, Jung SM, Yi SH (2004) ISIJ Int 44:1283–1290
4. Wu S, Huang W, Kou M, Liu X, Du K, Zhang K (2015) Steel Res Int 86:550–556
5. Liu X, Wu S, Huang W, Zhang K, Du K (2014) ISIJ Int 54:2089–2096
6. Sohn I, Min DJ (2012) Steel Res Int 83:611–630
7. Zhang J, Zhang Y, Li K, Wang Y, Liu Z, Wang G (2016) Metall Mater Trans B 47:3046–3055
8. van de Walle A (2018) Calphad 60:1–6
9. Wang S, Guo Y, Jiang T, Chen F, Zheng F, Yang L (2018) JOM. https://doi.org/10.1007/s11837-018-2983-0
10. Ai X, Bai H, Zhao L, Cang D, Tang Q (2013) Int J Miner Metall Mater 20:379–385
11. Bale CW, Bélisle E, Chartrand P, Decterov SA, Eriksson G, Gheribi AE, Hack K, Jung IH, Kang YB, Melançon J, Pelton AD, Petersen S, Robelin C, Sangster J, Spencer P, Van Ende MA (2016) Calphad 54:35–53
12. Lv X, Bai C, Deng Q, Huang X, Qiu G (2011) ISIJ Int 51:722–727
13. Kim BJ, Sohn J (2013) Non-Cryst Solids 379(2013):235–243
14. Sridhar S, Mills KC, Afrange ODC, Lörz HP, Carli R (2000) Ironmaking Steelmaking 27:238–242
15. Xu R, Zhang J, Fan X, Zheng W, Zhao Y (2017) ISIJ Int 57:1887–1894
16. Jiao K, Zhang J, Wang Z, Liu Y, Xu RZ (2018) High Temp Mater Proc 37:1–8
17. Zhen Y, Zhang G, Chou K (2014) ISIJ Int 54:985–989
18. Zhang S, Zhang X, Peng H, Wen L, Qiu G, Hu M, Bai C (2014) ISIJ Int 54:734–742
19. Zheng K, Zhang Z, Liu L, Wang X (2014) Metall Mater Trans B 45:1389–1397
20. Zhang L, Jahanshahi S (1998) Metall Mater Trans B 29:177–186

Manufacture of Porous Frit Vents Using Space Holder Methodology for Radioisotopic Space Power Systems

Gareth Sheppard, Karl Tassenberg, Ramy Mesalam, Bogdan Nenchev, Joel Strickland, and Hugo Williams

Abstract Porous pure copper frits were produced by sintering via both pressureless and space holder methods. Frits function both as a gas pressure release path and radioisotopic fine filter for radioisotopic thermoelectric generators (RTG's) and radioisotopic heater units (RHU's). Highly precise and reproducible flow rates are a fundamental requirement in frit vent design, hence accurate characterisation of their morphological structure is crucial. A novel bulk sample characterisation algorithm "GAKTpore" is applied to scanning electron microscope (SEM) maps to study and quantify the effects of processing parameters on sample heterogeneity, pore dispersion, and pore morphology. The purpose of the investigation is to refine the process–property relationships and achieve manufacturable repeatable homogeneous morphological structures. In this study, copper was used as a surrogate for platinum alloys. All frits were tested via a purpose-built/in-house helium precision-flow rig in order to establish a link between permeability and surface morphology. Frits manufactured via the space holder route displayed great potential for the future development of the manufacture of frit vents for European RTG and RHU development programs.

G. Sheppard (✉) · K. Tassenberg · B. Nenchev · J. Strickland · H. Williams
School of Engineering, University of Leicester, Leicester LE1 7RH, UK
e-mail: gts4@leicester.ac.uk

K. Tassenberg
e-mail: kt199@leicester.ac.uk

B. Nenchev
e-mail: bn55@leicester.ac.uk

J. Strickland
e-mail: jcjs2@leicester.ac.uk

H. Williams
e-mail: hugo.williams@leicester.ac.uk

R. Mesalam
School of Physics and Astronomy, University of Leicester, Leicester LE1 7RH, UK
e-mail: rm558@leicester.ac.uk

J. Li et al., *Characterization of Minerals, Metals, and Materials 2021*,
The Minerals, Metals & Materials Series,
https://doi.org/10.1007/978-3-030-65493-1_19

Keywords Pore analysis · Homogeneity · Metal foams · Space holders · Sintering · Permeability

Introduction

Radioisotopic thermoelectric generators (RTG's) and radioisotopic heater units (RHU's) share a similar inner containment architecture, where a ceramic radioisotopic heat source is contained within a compatible welded metallic structure, usually referred to as the cladding. The design of the containment architecture is completed to meet many safety criteria, the most important being the retention of the radioisotopic fuel within the vessel for all failure scenarios [1]. Failure via clad pressurisation from the generation of gases is a mechanism of failure [2]. Gaseous pressurisation is formed from two mechanisms; continuous helium build-up (alpha decay) from the radioisotopic source and oxygen released from the ceramic fuel at elevated temperatures. To avoid this scenario, the cladding has a small vent hole, to allow the venting of any generated gases. The hole is covered by a frit vent, a thin disk manufactured from a porous metal foam material serving a dual purpose: (1) allowing controlled gas release and (2) preventing contamination of escaping radioisotopic fuel fines [3].

The porous material covering the vent is usually produced by sintering a pure metallic powder via the pressure-less sintering route. Pure element precious metals powders such as platinum and iridium are typically used to ensure high-temperature material compatibility with the cladding. Porous frit dimensions vary but are usually a few millimetres in diameter and less than a millimetre thick [4]. Therefore, frits are challenging to manufacture and produce to the critical safety tolerances required. To the knowledge of the authors, commercially available frits made of platinum are not obtainable in Europe. Thus, the University of Leicester is currently developing alternative methods of producing porous platinum disks for the European RTG and RHU systems [5].

To bypass some of the challenges encountered of pressure-less powder sintering route, such as reproducibility and flow rate deviation [6], a new method was explored for creating controlled open porosity. The sacrificial space holder method employs the use of a sacrificial material mixed into the material matrix, which is later extracted, leaving porosity in the space it previously occupied. The quantity and particulate size of the sacrificial space holder material determine the approximate final material porosity, morphology and pore size distribution. Allowing effective tailoring of the space holder volume fraction to meet the desired material permeability.

In open porous metal foams, morphological analysis is usually carried out via simple pressure drop readings, or gas absorption methods. However, both fail to give a full morphological characterisation and provide a measure of closed porosity [7]. Pore morphological characterisation is usually carried out by manually measuring features in SEM micrographs, such as using the line tool in ImageJ (NIH, Maryland, USA). It has been recognised that these simple porosity and pore diameter measurements are insufficient to thoroughly determine the wide variety of

morphological features in metal foams, resulting in limiting their potential performance. To remedy this issue, a feature extraction algorithm titled "GAKTpore" was created at the University of Leicester to characterise bulk porous metal foams. For a full derivation and explanation of the characterisation methods used, the reader is referred to the journal paper [8]. The advantages of automatic feature extraction and bulk characterisation for the discovery of novel relationships has been increasingly highlighted in computer vision literature [9].

This paper outlines the initial design concept and characterisation of frits manufactured via the space holder route. The porous frits were manufactured using copper as an initial surrogate to platinum. The frits were characterised via both a flow permeability test and the new validated feature extraction algorithm developed at the University of Leicester "GAKTpore". The work focuses on the applicability of the novel characterisation method for the optimisation of the manufacturing process of porous frit vents for space applications. For comparison, the samples manufactured via the space holder route were assessed against the performance of frits manufactured via the traditional pressure-less sintering route, which was sintered under the same sintering cycle.

Experimental Procedure

Copper metal foams were manufactured to compare the pressure-less and space holder metal foam manufacturing techniques. Table 1 outlines the processing sequence of both metal foams. For the foams manufactured via the pressure-less sintering route, the starting materials were a 325-mesh (44 μm) dendritic copper powder from Alfa Aesar (Haverhill, Massachusetts, USA). For the space holder route, a 5 μm 99.8% spherical copper powder and 10 μm spherical PMMA powder from Goodfellow (Huntingdon, UK).

Figure 1 is the sintering cycle used to manufacture the copper frits. Tightly controlled heating rates are utilised so that frits can be produced with refined microstructures repeatably. The sintering cycle was undertaken using a 1600 °C horizontal inert gas furnace from Elite Furnaces (UK) to try to mitigate against the

Table 1 Processing sequence

	Via pressure-less sintering route	Via space holder route
1.	The powder is weighed and placed in a specially designed and manufactured crucible	The powders are weighed to give a 50% volume fraction
2.	The loaded crucibles are placed on a vibrating plate and vibrated for 20 min	Powders are mixed with 5 wt% PVA as a binder in a pestle and mortar for 5 min
3.	The loaded crucibles are placed in an inert gas furnace	Powders are cold-pressed in a 10 mm die at 300 MPa
4.	The furnace is flushed with argon and the samples are sintered at 760 °C for 60 min	

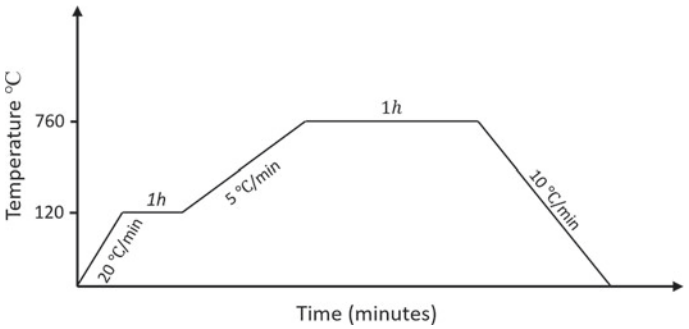

Fig. 1 Thermal heating cycle under which the porous copper frit vents were sintered

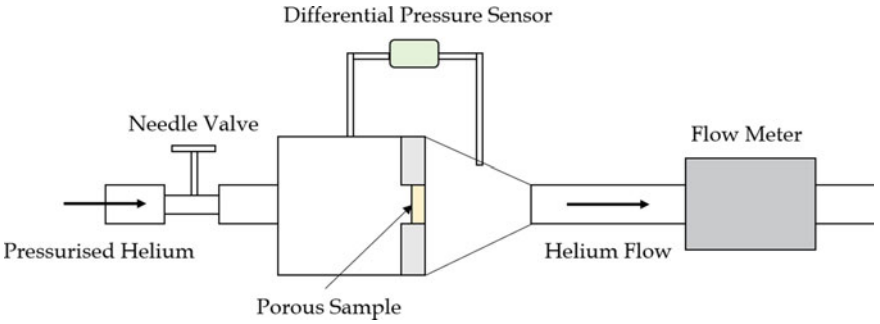

Fig. 2 Diagram of the experimental setup used for measuring helium permeability. (Color figure online)

volatile components released during the PMMA burnout, which are known to cause bulk defects such as cracks and swelling [10].

Surface Morphology Characterisation

To characterise the surface morphology, the foam samples were imaged using a Quanta 650 FEG SEM, where bulk SEM maps were produced of the full sample using FEI MAPS 2.1 software. From the bulk sample maps: local area fraction (pore dispersion/inhomogeneity), shape factor (circularity, waviness and aspect ratio), pore size and area, and largest sphere fitting through a given pore (LSTP) was calculated using the validated open-source algorithm "GAKTpore" [8].

Permeability Tests

The permeability tests were undertaken using helium, the experimental set up is displayed below in Fig. 2. The rig consists of a high-pressure helium source, needle valve, sample chamber, bespoke sample holder, differential pressure sensor, and a flow rate meter. The rig was calibrated with a solid copper disk before the experiments to check for helium leakage.

The bespoke sample holders for testing the porous copper samples were designed to replicate the helium flow route that is currently used in the European clad RTG/RHU architecture. In Fig. 3, the design uses a machined recess in which the porous material is secured. A thin disk with a 3 mm hole in the middle is then press-fitted over the top to keep the porous material tightly secured and allow helium flow in. A 1 mm hole below the porous material is used to simulate the vent hole in the cladding, where the helium is released. This provided configuration similar to that used in the lightweight radioisotopic heater unit (LWRHU) [3].

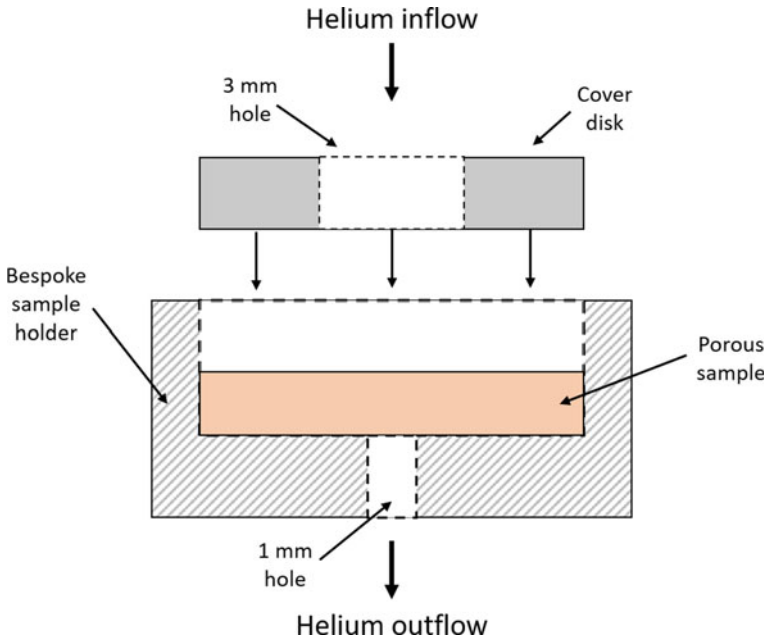

Fig. 3 Cross-sectional diagram of bespoke sample holder used to replicate cladding frit vent helium flow. A machined recess in the cylinder is utilised with a pressed cover disk fit. (Color figure online)

Results and Discussion

Surface Morphology Characterisation

Inhomogeneity bulk sample maps are plotted in Fig. 4. GAKTpore utilises a novel dedicated neighbourhood algorithm that relates every point/pixel in an image to its nearest shape/pore contour. By evaluating these relationships based on distance, an area of free space around every pore, named territory area, is identified. This territory area is influenced by the morphology of the pore, pore area, neighbouring pore areas, and their proximity. The maps visually illustrate the level of local area fraction ratio

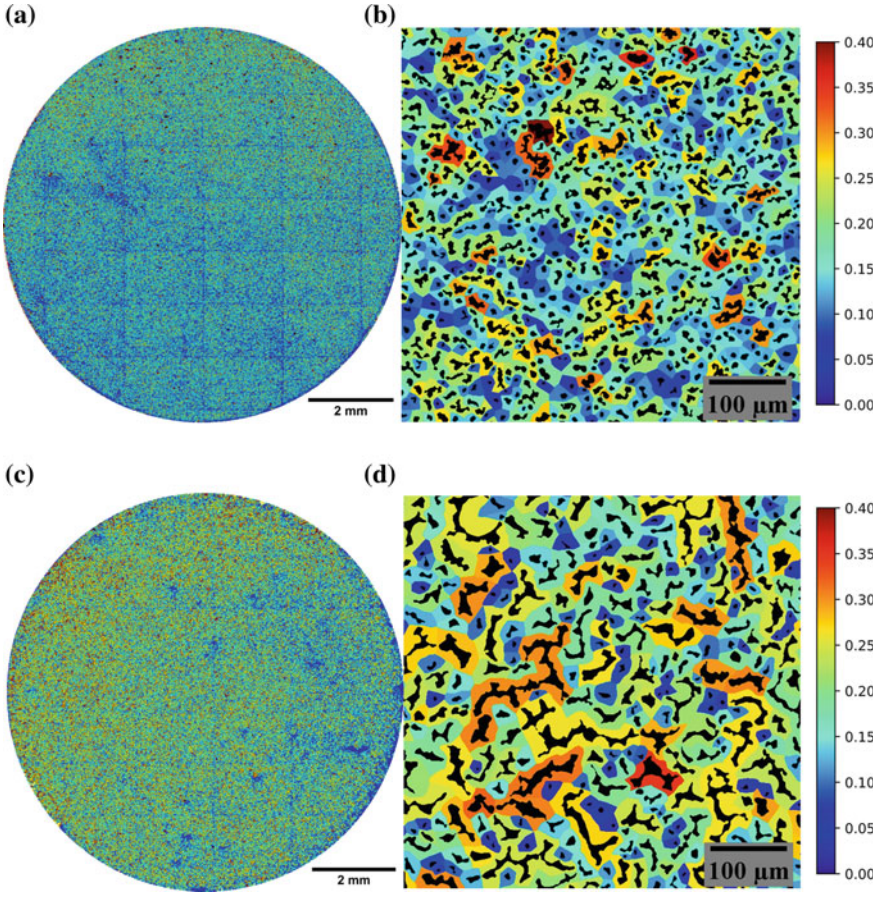

Fig. 4 Inhomogeneity maps plotting the area fraction of pore area to territory area with pores overlaid. Lower ratios (dark blue) correspond to a larger territory area to pore area, through a combination of smaller pores and greater pore spacing. **a** Sample HM3, **b** Sample HM3 micrograph, **c** Sample PFS2, **d** Sample PFS2 micrograph. (Color figure online)

(homogeneity) by plotting the local pore area over its corresponding territory area. The level of homogeneity is visualised through a colour map of contrasting colours, displaying the frequency and distribution of different local area fractions. Figure 4a–d shows the samples manufactured via the space holder route and pressure-less sintering technique, respectively. For the space holder, a 10 μm spherical PMMA powder was used. This is clearly displayed as the pores are smaller in Fig. 4b and more circular than Fig. 4d. The pores created in Fig. 4d are from natural loose particulate packing, which appear to give it a more distinct thin elongated shape.

Figure 5 allows the visualisation of the differences in samples manufactured using the exact same parameters. Figure 5a, c are the samples made with the 10 μm PMMA space holder and Fig. 5b, d are made using the pressure-less sintering route. Figure 5a displays the local area fraction distributions within the samples, where the sample HM1 is shifted slightly to the right and higher, which suggests a higher quantity of larger pores than HM2 and HM3. Whereas, in Fig. 5c, the pore size distribution data shows that HM1 has the lowest sigma, displaying the desirable narrow pore distribution required. When then compared with the permeability data in Fig. 6, it can be seen that the area fraction data is also vitally important for predicting permeability trends between samples, proving insights that the pore size distribution data is not enough to fully quantify how the pore morphology and permeability relate.

Figure 5b, d on the other hand display a much less ordered structure, where, Fig. 5b shows a much greater difference in area fraction distribution range, showing

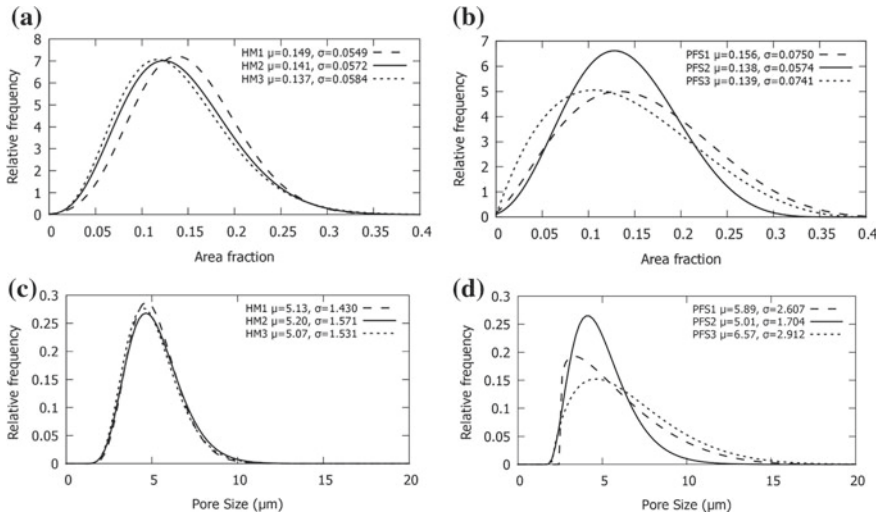

Fig. 5 Beta fits of histograms comparing data collected from the feature extraction algorithm, "GAKTpore". **a** Area fraction distributions of samples manufactured via the space holder route, **b** Area fraction distributions of samples manufactured via the pressure-less sintering route, **c** Largest sphere through a pore size distributions of samples manufactured via the space holder route, **d** Largest sphere through a pore size distributions manufactured via the pressure-less sintering route

Table 2 The mean shape factor statistics extracted from the bulk sample map micrographs

Sample	Mean Circ	σ	Mean Wav	σ	Mean AR	σ
HM1	0.63	0.24	0.36	0.15	0.64	0.17
HM2	0.73	0.23	0.27	0.17	0.64	0.17
HM3	0.73	0.23	0.26	0.17	0.64	0.17
PFS1	0.57	0.25	0.39	0.18	0.58	0.16
PFS2	0.51	0.26	0.42	0.18	0.54	0.16
PFS3	0.61	0.26	0.37	0.20	0.57	0.17

larger deviations in samples manufactured using the same method. The pore size range in Fig. 5d is shown to have a large variance in distributions, indicating a more unreliable production method when compared to the space holder method.

The shape factors in Table 2 provide an insight into the morphology of the pores and can be used to quantify the variation in the sample morphology for a specific manufacturing technique and the effect of certain process parameters, i.e. being able to quantify the effect of compaction pressure on pore morphology. This is also useful for modelling purposes as the pores can no longer be assumed to be circular. The waviness shows that the structures are convoluted, not simply elongated circles that could be inferred from just the aspect ratio and circularity. The samples manufactured through the space holder technique have pores that are more circular and less wavy than the pores produced from the pressure-less sintering route.

Permeability Characterisation

Fitted linear plots of the helium permeability data are shown in Fig. 6. The three samples that were manufactured via the space holder route are shown to have a lower permeability compared to the single sample tested via the pressure-less sintering route. Sample HM1 is shown to have the largest permeability of its sample batch and HM3, the lowest. This also matches perfectly with the data in Fig. 5a, where having the slightly larger distributions of larger pores (HM1) shows an increase in permeability, and small distributions (HM3) show lower. This is due to the reduced chance of pores connecting and creating open channels through the sample.

From the proof of concept study, the space holder technique has been shown to be a potential method to manufacture frit vents for European RHU and RTG power systems. With the aid of "GAKTpore" it is hoped that refinement of processing parameters can be carried out in order to reduce the variance within samples manufactured via the same method and conditions. The space holder method shows greater potential when compared to the pressure-less sintering route due to the greater reproducibility displayed, lowering the level of manufacture parameter refinement required, although this can only be inferred from the SEM bulk maps data as not all of the samples could be flow tested.

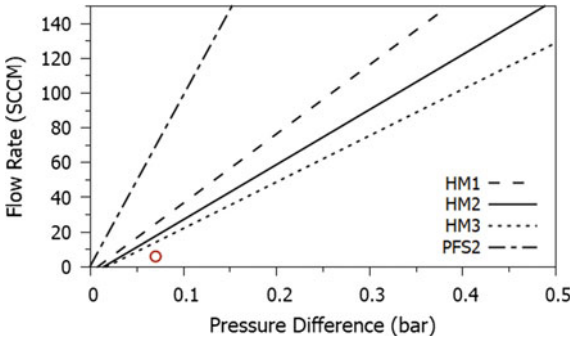

Fig. 6 Permeability testing of the porous samples produced. Hand-mixed samples 1–3 and 1 pressure-less sintered sample. The red circle shown is the average helium permeability of the multi-mission RTG (MMRTG) frit vent as a single point of reference [3]. (Color figure online)

In this study, "GAKTpore" is implemented as an alternative method for μ CT tomography quantification of porous structures, since the attenuation effects of copper significantly limit the resolution of μ CT tomography. By utilising upscaling techniques, high resolution (30 px per pore) can be attained on bulk SEM samples (10 mm diameter), allowing a much more comprehensive extraction of pore morphology information, compared to X-ray tomography techniques.

In futures studies, the volume fraction of the PMMA space holder will be varied to create a frit vent using the space holder method that aims to have the same permeability as the MMRTG frit vent system. Further refinement of processing parameters using "GAKTpore" will also be completed to try to refine flow rate reproducibility.

Conclusions

In this study, the space holder route for the manufacture of controlled morphology of porous media was explored for future European RHU and RTG vent systems. When compared against the traditional pressure-less sintering technique, the space holder route was shown to have a much lower variance between extracted surface morphological features. Pore size and local area fraction distributions confirm the reliability of manufacturing using the space holder route, producing significantly more consistent results compared to the pressure-less sintering technique. Permeability data of the space holder samples was shown to have a clear relationship linking flow rate and local area fraction distributions. It is hoped that further refinement of local area fraction distributions will produce a higher reproducibility of samples, lowering deviations in morphological and flow properties, an important criterion for the manufacture of frit vents. Future studies will be undertaken to match the permeability of the MMRGT frit vent system and refine process–property relationship to

allow this technique to be used to manufacture any required permeability with high reproducibility.

Acknowledgements G.S, K.T., B.N., and J.S. gratefully acknowledge the financial support from the Centre for Doctoral Training in Innovative Metal Processing (IMPaCT) funded by the UK Engineering and Physical Sciences Research Council (EPRSC) (Grant No: EP/L016206/1) and the Mechanics of Material Advanced Microscopy Centre at the University of Leicester.

Declaration of Competing Interests The authors declare that they have no known competing financial interests or personal relationships that could have appeared to influence the work reported in this paper.

References

1. Barco A et al (2020) Radioisotope power systems in space missions: overview of the safety aspects and recommendations for the European safety case. J Space Safety Eng. https://doi.org/10.1016/j.jsse.2020.03.001
2. Ulrich GB (1995) Examination of frit vent from sixty-watt heat source simulant fueled clad vent set. Oak Ridge Y-12 Plant, TN (United States), p Medium: ED; Size, 9 p
3. Tate RE (1982) The light weight radioisotope heater unit (LWRHU): a technical description of the reference design
4. Ulrich GB (1994) The metallurgical integrity of the frit vent assembly diffusion bond, D.o. energy. Oak Ridge
5. Ambrosi RM et al (2019) European radioisotope thermoelectric generators (RTGs) and radioisotope heater units (RHUs) for space science and exploration. Space Sci Rev 215(8):55. https://doi.org/10.1007/s11214-019-0623-9
6. Mesalam R et al (2020) A facile polymeric templating route towards fabricating RTG and RHU vent hole filters. In *NETS 2020*. Knoxville Convention Center, Knoxville, Tennessee
7. Ishizaki K, Komarneni S, Nanko M (1998) Porous materials; process technology and applications. Springer, London
8. Sheppard G et al (2020) GAKTpore: stereological characterisation methods for porous metal foams in biomedical applications
9. Nenchev B et al (2020) automatic recognition of dendritic solidification structures: DenMap. J Imaging 6(4):19. https://doi.org/10.3390/jimaging6040019
10. Lin Y-J, Hwang K-S (2010) Swelling of copper powders during sintering of heat pipes in hydrogen-containing atmospheres. Mater Trans 51(12):2251–2258. https://doi.org/10.2320/matertrans.M2010151

Utilization of Ferronickel Slag for Producing Concrete

Huimin Tang, Zhiwei Peng, Foquan Gu, Lei Yang, Wenxing Shang, Jingfeng Yu, Guangyan Zhu, Weiguang Tian, Mingjun Rao, Guanghui Li, and Tao Jiang

Abstract Ferronickel slag, featured by high contents of SiO_2 and MgO, is a kind of solid waste produced in the ferronickel alloy process. Proper utilization of ferronickel slag can not only effectively reduce the environmental risk but also realize the high value-added utilization. Based on analysis of the composition and phase characteristics of various kinds of ferronickel slag obtained by different processing methods, the applications of the slag in producing concrete were discussed for providing insight into efficient use of the waste.

Keywords Ferronickel slag · Utilization · Cement · Concrete · Strength

Introduction

Ferronickel slag is a byproduct discharged in the production of ferronickel alloy. Its chemical and phase compositions and physical properties depend on raw materials and processing methods [1]. It was estimated that approximately 6–16 tons of slag are produced in the production of 1 ton of ferronickel [2]. The annual output of ferronickel slag in China was approximately 40 million tons [3], accounting for more than 20% of the global ferronickel slag output. However, its utilization is only about 8–10% [4, 5]. Piled ferronickel slag causes large land occupation and environmental pollution.

Although the physicochemical features of ferronickel slag may vary greatly, its main chemical components are SiO_2 (30.0–54.5 wt%), Fe_2O_3 (6.4–43.8 wt%), MgO

H. Tang · Z. Peng (✉) · F. Gu · L. Yang · W. Shang · J. Yu · G. Zhu · M. Rao · G. Li · T. Jiang
School of Minerals Processing and Bioengineering, Central South University, Changsha, Hunan 410083, China
e-mail: zwpeng@csu.edu.cn

National Engineering Laboratory for High Efficiency Recovery of Refractory Nonferrous Metals, Changsha, Hunan 410083, China

W. Tian
Guangdong Guangqing Metal Technology Co. Ltd., Yangjiang, Guangdong 529500, China

J. Li et al., *Characterization of Minerals, Metals, and Materials 2021*,
The Minerals, Metals & Materials Series,
https://doi.org/10.1007/978-3-030-65493-1_20

(2.7–32.7 wt%), CaO (1.5–12.0 wt%), and Al_2O_3 (2.5–8.3 wt%). Its main crystalline minerals include enstatite, forsterite, and diopside [6]. There are mainly two types of slag, depending on the heating furnace during the production process, namely, blast furnace ferronickel slag (BFFS) and electric furnace ferronickel slag (EFFS). According to the cooling method, slag can also be classified as water-cooled ferronickel slag (W-FS) and air-cooled ferronickel slag (A-FS). Compared with W-FS, A-FS has higher density and water absorption as well as less amorphous mineral phase [7].

In the past decade, using ferronickel slag for producing concrete has been attracting tremendous attention. In this study, the representative efforts in this field were reviewed, with the aim to offer a guide for sustainable recycling and value-added utilization of the waste.

Applications of Ferronickel Slag in the Production of Concrete

In recent years, ferronickel slag has been used for the production of concrete due to its similar chemical composition, low water absorption, high density, high strength,

Table 1 Chemical compositions of different ferronickel slags (wt%)

No.	SiO_2	MgO	Fe_2O_3	Al_2O_3	CaO	Cr_2O_3	Reference
1	24.89	9.61	2.66	17.46	32.15	–	Chen et al. [2]
2	49.38	21.81	7.62	7.25	11.62	0.91	Sun et al. [3]
	31.02	10.91	0.6	24.43	27.58	0.91	
3	46.1	27.12	12.25	4.46	7.75	1.5	Huang et al. [4]
	50.48	32.61	10.37	3.08	1.01	1.37	
	44.9	23.29	14.36	4.94	8.24	2.47	
	29.95	8.93	1.55	26.31	25.19	2.3	
	33.15	12.54	2.15	21.94	22.5	2.08	
4	40.5	40.5	6.9	3.6	6.6	0.7	Kim et al. [5]
	40.7	43.4	7.9	2.7	3.6	0.8	
	40.8	40.4	9.0	2.7	4.2	1.0	
5	29.95	8.93	1.55	26.31	25.19	2.3	Wang et al. [6]
6	53.29	31.6	11.9	2.67	0.42	1.08	Saha et al. [9–12]
7	51.93	30.87	12.98	2.92	0.5	–	Nuruzzaman et al. [13]
8	41.18	7.79	40.02	5.98	4.12	2.75	Lemonis et al. [14]
9	51.67	31.56	12.58	2.29	0.31	–	Bouasria et al. [15]
10	47.61	15.94	13.24	6.56	11.49	0.70	Cao et al. [16]
11	45.90	24.14	10.30	6.39	10.25	-	You et al. [17]

Table 2 Physical properties of different ferronickel slags

No.	Apparent particle density (t/m^3)	Fineness modulus	Water absorption (%)	Density (g/cm^3)	Specific surface (m^2/kg)	Reference
1	–	–	–	2.95	430	Chen et al. [2]
2	–	3.22	0.94	2.99	–	Sun et al. [3]
	–	2.64	3.16	2.42	–	
3	–	–	–	2.97	436	Huang et al. [4]
	–	–	–	2.94	447	
	–	–	–	2.89	461	
	–	–	–	2.87	391	
	–	–	–	2.91	439	
4	2.85	4.07	0.42	–	–	Saha et al. [9–12]
5	2.92	3.42	0.42	2.86	425.6	Nuruzzaman et al. [13]
6	–	–	–	3.18	398.5	Lemonis et al. [14]
7	–	–	–	2.99	355	You et al. [17]

and strong pozzolanic activity [4, 8]. Tables 1 and 2 show the chemical compositions and physical properties of different ferronickel slags used for the purpose.

Ferronickel slag can be used as fine aggregate instead of natural sand for preparing concrete. Its use affects the durability of concrete [9–12], which is determined by measuring the volume of permeable voids (VPV), compressive strength, and chloride permeability of concrete. Compared to the use of 100% natural sand, the 28-day compressive strength and VPV of concrete prepared with the addition of 50 wt% ferronickel slag were increased by 21.5% and 4%, respectively, indicating the improved performance of concrete because of the addition of slag [9–12]. The specific results are shown in Table 3. Another study [13] showed that appropriate addition of ferronickel slag (~40%) not only increased the 28-day compressive strength and splitting tensile strength but also reduced water absorption and VPV, resulting from improved particle packing and interlocking by the angular ferronickel slag particles with rough surface texture [13]. However, excessive ferronickel slag addition would deteriorate the strength and increase water absorption due to increase of void content of concrete [13]. The detailed results are shown in Table 3.

The effect of using BFFS and EFFS to replace sand for producing concrete on the product properties was also investigated [3]. The 28-day compressive strength, splitting tensile strength, and flexural strength increased with increasing addition of BFFS, whereas the slump loss of concrete in 1 hour decreased with the increase of BFFS, as shown in Fig. 1. Compared to the concrete prepared with the addition of BFFS, the mechanical strength of concrete decreased with increasing EFFS addition. In spite of the decrease of mechanical strength, the minimum 28-day compressive

Table 3 Properties of concrete produced with different additions of ferronickel slag

No.	Addition of slag (wt%)	Compressive Strength (MPa)	Splitting tensile strength (MPa)	Flexural strength (MPa)	Slump (mm)	Charge passed (C)	Water absorption (%)	VPV (%)	Slag	Reference
1	0	–	–	–	–	2506	–	–	–	Chen et al. [2]
	30	–	–	–	–	1571	–	–		
	50	–	–	–	–	962	–	–		
	70	–	–	–	–	1094	–	–		
2	0	64.9	7.1	6.9	72	2641	3.5	–	BFFS	Sun et al. [3]
	25	68.5	7.5	7.2	15	2266	3.5	–		
	50	70.3	7.9	8.2	16	1545	3.3	–		
	75	71.5	8.2	8.2	10	1195	3	–		
	0	65.5	8.3	6.9	72	2506	3.5	–	EFFS	
	25	62.2	8.1	6.5	73	2553	3.6	–		
	50	60.1	7.7	6.5	53	2454	3.6	–		
	75	54.7	7.4	6.3	26	2610	3.7	–		
	100	55.5	7.1	6.1	12	2861	3.8	–		
3	0	40	–	–	–	–	–	17	W-FS	Saha et al. [9–12]
	25	43.3	–	–	–	–	–	20		
	50	48.6	–	–	–	–	–	21		
	75	45.4	–	–	–	–	–	23		
	100	41.6	–	–	–	–	–	24		

(continued)

Table 3 (continued)

No.	Addition of slag (wt%)	Compressive Strength (MPa)	Splitting tensile strength (MPa)	Flexural strength (MPa)	Slump (mm)	Charge passed (C)	Water absorption (%)	VPV (%)	Slag	Reference
4	0	50.5	4.4	–	–	–	3.9	9.4	–	Nuruzzaman et al. [13]
	20	52.2	5	–	–	–	3.7	8.5		
	40	65.8	4.6	–	–	–	2.6	6.3		
	60	61.4	4.3	–	–	–	2.8	6.9		
5	0	54.2	–	–	–	–	–	17	W-FS	Lemonis et al. [14]
	5	53	–	–	–	–	–	20		
	10	50.5	–	–	–	–	–	21		
	15	48.7	–	–	–	–	–	23		
	20	47.1	–	–	–	–	–	24		
6	50	61.2	8.8	–	–	–	2.0	–	–	You et al. [17]

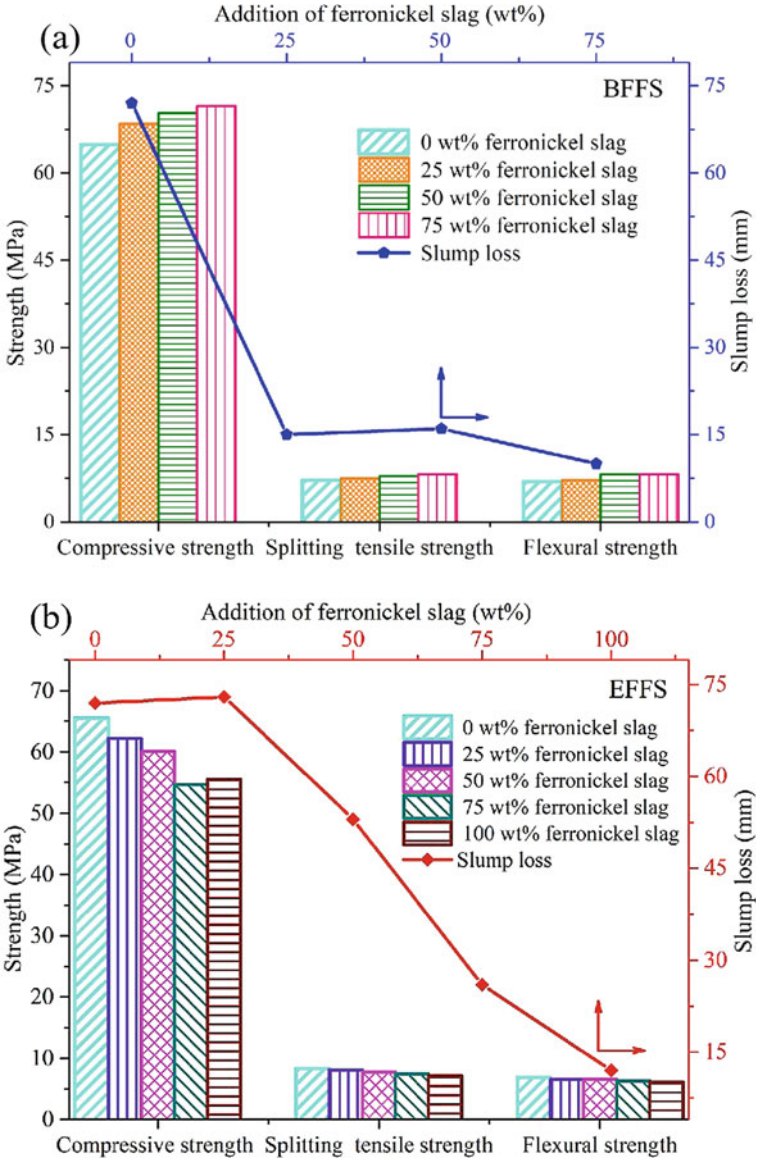

Fig. 1 Effect of addition of (a) BFFS and (b) EFFS on the strength and slump loss of concrete (Sun et al. [3]). (Color figure online)

strength with a water/binder ratio of 0.45 (E100) still reached 55 MPa, conforming to the standard of C50 concrete. In addition, adding BFFS could decrease the penetrability and water absorption of concrete, as shown in Table 3. The charge passed of concrete prepared with the additions of 50% slag and 75% slag varied in the range 1000–2000 C (low permeability) at 28 days, indicating good resistance to chloride ion penetration with high BFFS addition. The addition of EFFS obviously increased the charge passed with moderate chloride penetrability level when the addition of ferronickel slag was 100 wt% (>2000 C), as shown in Fig. 2. It demonstrated the weak influence of using EFFS as fine aggregate on the resistance of concrete to chloride ion penetration.

Ferronickel slag has also been used to replace partial Portland cement in concrete. Its effect on the properties and chloride penetration of concrete can be systematically investigated by measuring chloride permeability, corrosion current, natural diffusion, pore structure, and phase composition of product [2, 4, 5, 14]. Chen et al. [2] found that appropriate replacement amount of ferronickel slag (up to 30%) could improve the corrosion resistance by improving the pore structure of concrete. In addition, the chloride binding capacity and strength of cement pastes were also enhanced by forming hydrotalcite-like phases and higher amorphous hydrate calcium silicate (C–S–H) with gelling property due to the high contents of calcium, magnesium, and aluminum in ferronickel slag, which also delayed the occurrence of chloride corrosion [2, 4, 5, 14]. Besides, the pore structure was improved by decreasing the charge passed to a very low permeability level ($\leq$1000 C), as shown in Table 3. Compared to EFFS, BFFS had higher pozzolanic activity in association with its higher contents of CaO and Al_2O_3 as well as lower content of MgO [4].

Conclusions

Ferronickel slag is widely used for production of concrete. Appropriate addition of ferronickel slag can improve strength of concrete and delay the occurrence of chloride ion corrosion by improving the pore structure of concrete, forming hydrotalcite-like phase and increasing the C–S–H with amorphous cementitious property. By comparing the properties of concretes produced using different ferronickel slags, this review is expected to serve as a useful guide for promoting utilization of the slag for building.

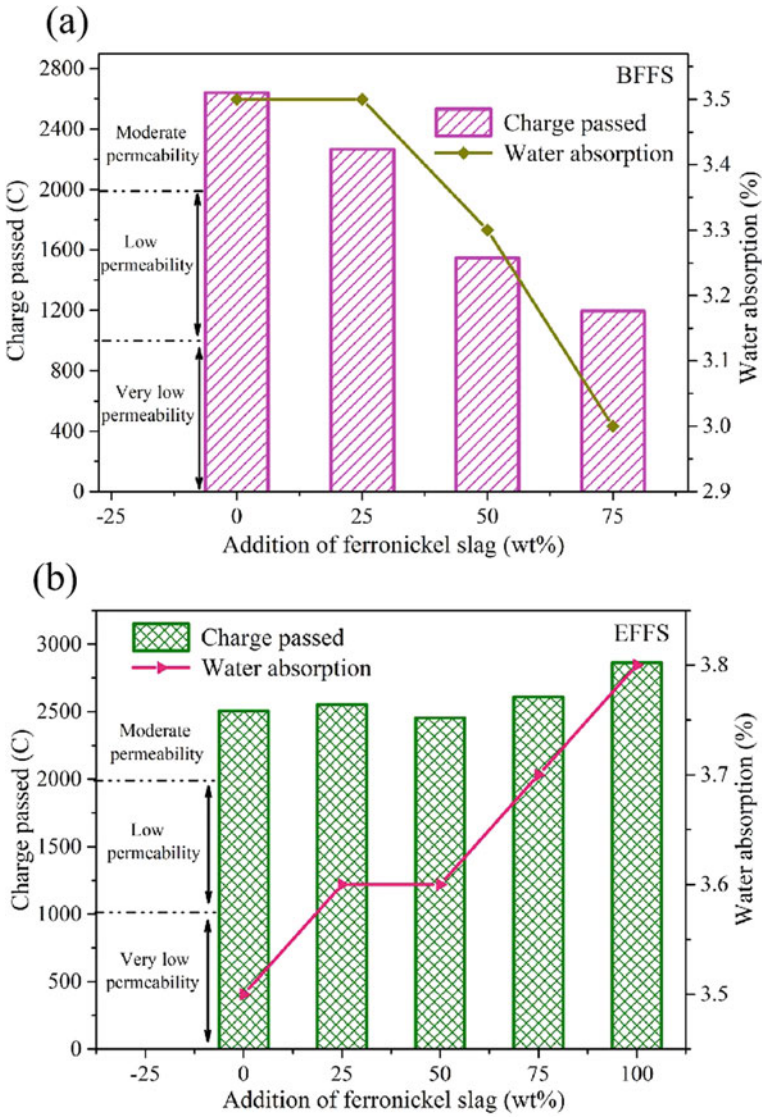

Fig. 2 Effect of addition of (a) BFFS and (b) EFFS on the charge passed and water absorption of concrete (Sun et al. [3]). (Color figure online)

Acknowledgements This work was partially supported by the Science and Technology Planning Project of Hunan Province, China, under Grant 2019RS2008, the Project of State Key Laboratory Cultivation Base for Nonmetal Composites and Functional Materials under Grant 17kffk11, and the National Key Research and Development Program of China, under Grant 2017YFB0304301.

References

1. Maragkos I, Giannopoulou IP, Panias D (2009) Synthesis of ferronickel slag-based geopolymers. Miner. Eng. 22(2):196–203
2. Chen Y, Ji T, Yang Z, Zhan W, Zhang Y (2020) Sustainable use of ferronickel slag in cementitious composites and the effect on chloride penetration resistance. Constr. Build. Mater. 240:117969
3. Sun J, Feng J, Chen Z (2019) Effect of ferronickel slag as fine aggregate on properties of concrete. Constr. Build. Mater. 206:201–209
4. Huang Y, Wang Q, Shi M (2017) Characteristics and reactivity of ferronickel slag powder. Constr. Build. Mater. 156:773–789
5. Kim H, Lee C, Ann K (2019) Feasibility of ferronickel slag powder for cementitious binder in concrete mix. Constr. Build. Mater. 207:693–705
6. Wang D, Wang Q, Zhuang S, Yang J (2018) Evaluation of alkali-activated blast furnace ferronickel slag as a cementitious material: reaction mechanism, engineering properties and leaching behaviors. Constr. Build. Mater. 188:860–873
7. Choi YC, Choi S (2015) Alkali-silica reactivity of cementitious materials using ferronickel slag fine aggregates produced in different cooling conditions. Cons. Build. Mater. 99:279–287
8. Saha AK, Khan MNN, Sarker PK (2018) Value added utilization of by-product electric furnace ferronickel slag as construction materials: A review. Resour. Conserv. Recy. 134:10–24
9. Saha AK, Sarker PK, Golovanevskiy V (2019) Thermal properties and residual strength after high temperature exposure of cement mortar using ferronickel slag aggregate. Constr. Build. Mater. 199:601–612
10. Saha AK, Sarker PK (2017) Durability characteristics of concrete using ferronickel slag fine aggregate and fly ash. Mag. Concrete Res. 70(17):875–874
11. Saha AK, Sarker PK (2020) Effect of sulphate exposure on mortar consisting of ferronickel slag aggregate and supplementary cementitious materials. J. Build. Eng. 28:101012
12. Saha AK, Majhi S, Sarker PK, Mukherjee A, Siddika A, Aslani F, Zhuge Y (2021) Non-destructive prediction of strength of concrete made by lightweight recycled aggregates and nickel slag. J. Build. Eng. 33:101614
13. Nuruzzaman MD, Casimiro JOC, Sarker PK (2020) Fresh and hardened properties of high strength self-compacting concrete using by-product ferronickel slag fine aggregate. J. Build. Eng. 32:101686
14. Lemonis N, Tsakiridis PE, Katsiotis NS, Antiohos S, Papageorgiou D, Katsiotis MS, Beazi-Katsioti M (2015) Hydration study of ternary blended cements containing ferronickel slag and natural pozzolan. Constr. Build. Mater. 81:130–139
15. Bouasria M, Khadraoui F, Benzaama MH, Touati K, Chateigner D, Gascoin S, Pralong V, Orberger B, Babouri L, Mendili YE (2021) Partial substitution of cement by the association of Ferronickel slags and Crepidula fornicata shells. J. Build. Eng. 33:101587
16. Cao R, Li B, You N, Zhang Y, Zhang Z (2018) Properties of alkali-activated ground granulated blast furnace slag blended with ferronickel slag. Constr. Build. Mater. 192:123–132
17. You N, Li B, Cao R, Shi J, Chen C, Zhang Y (2019) The influence of steel slag and ferronickel slag on the properties of alkali-activated slag mortar. Constr. Build. Mater. 227:116614

Adsorption of Methylene Blue by $CuFe_2O_4$ Prepared from Precipitation Flotation Sludge

Huanhuan Miao, Wenjuan Wang, Yanfang Huang, Guihong Han, and Shengpeng Su

Abstract The adsorption materials can be prepared from the heavy metal ions flotation sludge in the metal-containing wastewater. When the flotation sludge was pyrolyzed in the air at 800 °C for 4.0 h as a self-template, cubic copper ferrite ($CuFe_2O_4$) particle was prepared and tested as an adsorption material for the adsorption performance of the material. Structural analysis of the $CuFe_2O_4$ particle was performed using scanning electron microscope (SEM), Brunauere–Emmette–Teller (BET), X-ray diffraction (XRD), and thermogravimetric analysis (TGA) techniques. According to the measurement results, the specific surface area of copper ferrite was 10.58 m^2/g. The adsorption process of this material for the organic dye methylene blue (MB) conformed to the Freundlich isotherm adsorption model and Dubinin–Radushkevitch (D–R) isotherm adsorption models, and it was a multilayer physical adsorption process, which was proven to be an adsorbent with good adsorption performance. The sludge including heavy metal ions was effectively enriched by precipitation flotation, and the recovered sludge is pyrolyzed to form an adsorbent material, thereby achieving the effective utilization of heavy metal resources.

Keywords Precipitation flotation · Adsorption materials · Methylene blue

Introduction

The amount of organic dye wastewater discharged from the industrial production and application of dyes in China is 2.0–2.3 billion tons every year, which is characterized by high chroma, strong toxicity, and high chemical oxygen demand [1]. Methylene blue (MB) is usually discharged by several industries such as the textile industry, paper industry, and printing industry [2]. If it is not treated effectively, it will cause a decrease of light transmittance of the water body and great harm to the environment and living organisms [3].

H. Miao · W. Wang · Y. Huang · G. Han (✉) · S. Su
School of Chemical Engineering and Energy, Zhengzhou University, Zhengzhou 450001, People's Republic of China
e-mail: hanguihong@zzu.edu.cn

J. Li et al., *Characterization of Minerals, Metals, and Materials 2021*,
The Minerals, Metals & Materials Series,
https://doi.org/10.1007/978-3-030-65493-1_21

At present, there are innumerable methods to treat dye wastewater, such as nanofiltration [4], ozone oxidation [5], photodegradation [6], and adsorption [7], etc. Among them, the adsorption method is a simple, economical, and efficient method for the removal of various wastewater pollutants, especially for dyes that are difficult to be degraded by biochemical processes, adsorption is proved to be a considerable method in light of its effectiveness [8]. According to the survey, the adsorbents made from wastes such as cotton flower agro-waste [9] and cellulose fiber from newspaper waste [10] have been successfully explored, which were used to remove anionic and cationic dyes from the solution. Converting waste into useful products that can be utilized in industrial processes is a significant concept in waste recycling research [8].

Heavy metal sludge is an addendum produced after the treatment of heavy metal wastewater. The purpose of this research is to use precipitation flotation to treat heavy metal wastewater, and the heavy metal sludge obtained is pretreated to adsorb days in dye wastewater, so as to achieve the purpose of "using waste to treat waste "and realize the sustainable development of heavy metal resources.

In this study, the copper ferrite ($CuFe_2O_4$) particle made from sludge containing heavy metal ions had been conducted to remove MB dye from simulated dye solution. Through XRD, TGA, SEM, and other techniques to characterize the physicochemical properties of the material, the kinetics, isotherms, and influencing factor of the material's adsorption and removal of MB dye from water were studied, which proved that the adsorbent has practical applications in water treatment. In general, the current research showed that the research has broad application prospects in terms of waste recycle and wastewater treatment value.

Experiments

Synthesis and Processing of $CuFe_2O_4$

First of all, the HA precipitant is added to heavy metal wastewater simulated with Cu^{2+} solution to carry out the chelation reaction for 30 min. then the flocculant $FeCl_3$ is added and the solution is stirred stably for 10 min, to ensure that the molar ratio of copper and iron is 1:2. When the stable flocculation is formed, the cationic surfactant CTAB is added, and after 3 min of reaction, transfer the solution to the microbubble flotation column to collect waste residue and purified water. Finally, after the enriched precipitation flotation sludge is washed and dried, in the air atmosphere, the heavy metal sludge is heated to 800 °C at a heating rate of 5 °C/min, which are pyrolyzed at this temperature for 4.0 h to obtain the adsorbent.

Physical Characteristics

Thermo gravimetric analysis was performed under airflow from 30 to 1000 °C with a rate of 10 °C min^{-1} (TGA, DTG-60H, Shimadzu, Japan). The XRD measurements were carried out using D8 ADVANCE diffractometer (Cu K α, λ = 0.15406 nm), and 2θ was in the range of 10°–80° at a scanning rate of 0.3 s^{-1}. The particle morphology was characterized at 5.0 kV by a field emission scanning electron microscope(SEM, ZEISS MERLIN Compact). The Brunauere–Emmette–Teller (BET) specific surface area was determined using nitrogen adsorption/desorption with an automatic specific surface area measuring equipment (ASAP 2460, Mike Company, American). The functional groups of the materials were identified using Fourier transform infrared (FTIR) from Thermo Scientific/Nicolet IS50, USA. The absorbance of MB was determined by using an ultraviolet–visible spectrophotometer of Beijing General Instrument (TU-1901).

Adsorption Experiment

Five milligrams of the adsorbent were added in 30 mL of methylene blue solution with a certain concentration of 30 mg/L. The pH value of the dye solution is adjusted between 3 and 11 using diluted HCl or NaOH solution. The adsorbent was then added to the dye solution and stirred at 150 rpm and 25 °C. In each experiment, the ultraviolet–visible (UV–Vis) absorbance of the solution was estimated to determine the residue of MB at 664 nm.

The amount of adsorbed dye using the biocomposite beads was determined to the following equations:

$$q = (C_0 - C_e) * V/m, \tag{1}$$

where q is the amount of adsorbed dye on the adsorbent (mg · g^{-1}). C_0 and C_e denote the initial and equilibrium concentration of dye in solution (mg · L^{-1}), respectively. V (L) represents the volume of solution and m (g) is the mass of adsorbent in use.

Results and Discussion

Characterization of Adsorbent

The thermal behavior of the heavy mental sludge was shown in Fig. 1. The weight loss before 300 °C is generally attributed to the loss of physically adsorbed water, zeolitic water, and crystal water in precursors, respectively. The weight loss between 300 and

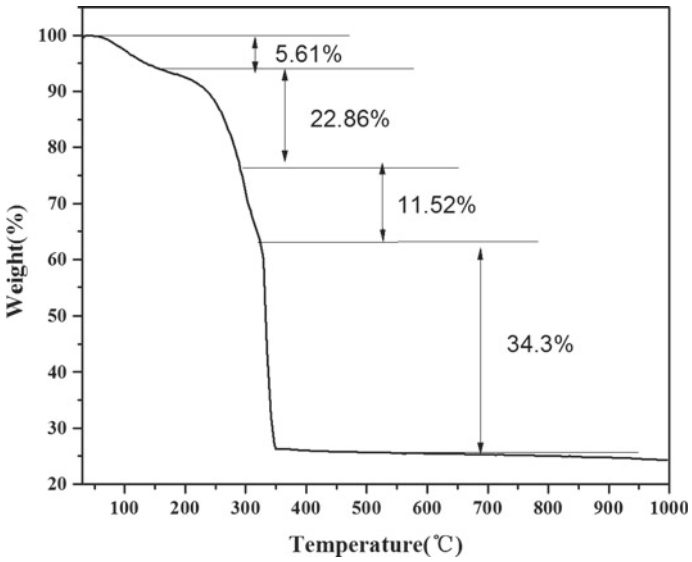

Fig. 1 TG curves of heavy mental sludge. (Color figure online)

600 °C is assigned to the decomposition of residual surfactants and organisms, along with the release of CO_x, NO_x, and H_2O gases. In this study, the calcination of the sludge was kept at 800 °C for 4.0 h, which ensures the oxidation process is entire.

The XRD diffractograms of the adsorbent were shown in Fig. 2a. Most peaks of the sample at 2 thetas of 18.51, 30.17, 35.64, 43.03, 57.05, and 62.77° matched the cubic spinel copper ferrite (which was marked as $CuFe_2O_4$) (PDF No.25-0283).

N_2-adsorption/desorption isotherms were measured using the BET method to determine the specific surface area and pore distribution of the adsorbent. As seen in Fig. 2b, the hysteresis loop appeared at the middle-higher pressure region,which means that there are mesoporous in the adsorbent sample. The BET specific surface area of adsorbent is 10.58 m^2/g, the calculated average pore diameter is 49.6 nm of desorption branch, and the total pore volume of 0.064 cm^3/g.

SEM micrographs of active materials are shown in Fig. 2c. The adsorbent displays irregular polyhedron.

Adsorption of MB

In order to determine the kinetics of MB adsorption by copper ferrite, we investigated the pseudo-first-order and pseudo-second-order kinetic equations. Pseudo-first-order and pseudo-second-order kinetics are expressed as Eqs. (2) and (3):

$$q_t = q_e\left[1 - \exp(-k_1 t)\right] \tag{2}$$

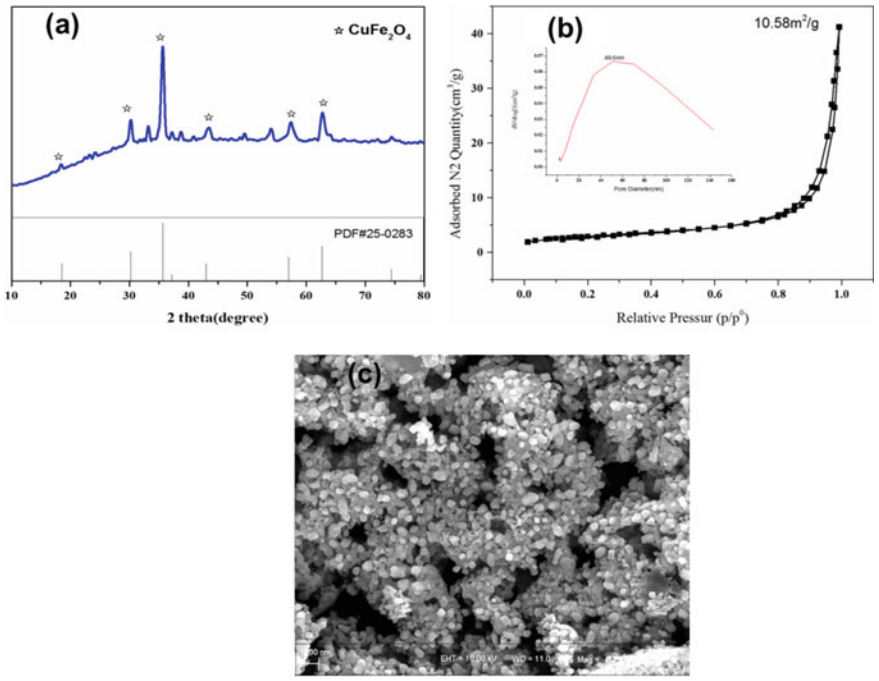

Fig. 2 Structure and morphology characterization: **a** XRD diffractograms of adsorbent material. **b** N_2-adsorption/desorption isotherms, and **c** SEM micrographs of the adsorption material. (Color figure online)

$$\frac{t}{q_t} = \frac{1}{k_2 q_e^2} + \frac{1}{q_e} t \tag{3}$$

where q_e and q_t are the adsorption uptakes at equilibrium and at any time t (mg/g), respectively. The adsorption kinetics data can be fitted well by the pseudo-first-order ($R^2 = 0.987$) (Fig. 3a) than the pseudo-second-order rate (0.824) (Fig. 3b) kinetic model. Moreover, the calculated value of the equilibrium adsorption capacity (q_e, cal = 101.929 mg/g) from pseudo-first-order kinetics shows excellent agreement with the experimental value (q_e, exp = 103 mg/g), in comparison, the calculated value of the equilibrium adsorption capacity (q_e, cal = 250 mg/g) from pseudo-second-order kinetics is far apart.

The adsorption of MB on the copper ferrite increased with increasing solution pH (Fig. 4). Zeta potential measurements show that the surface charge of the copper ferrite is negative and that its absolute value gradually increased with the increasing solution pH from 3 to 12. MB is a cationic dye, and its adsorption is favored by the more highly negatively charged adsorbent under alkaline conditions [11].

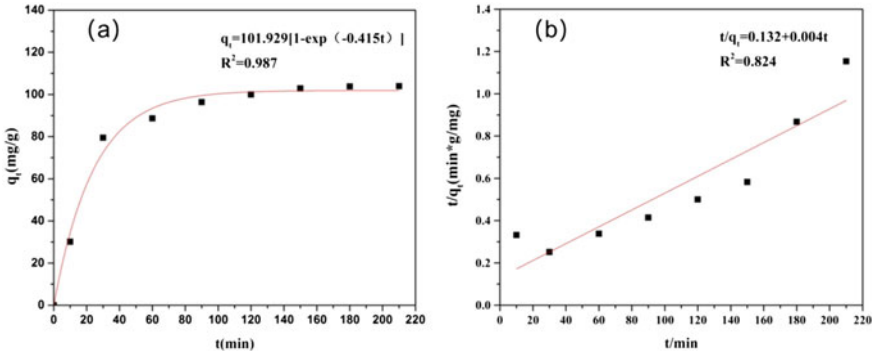

Fig. 3 Kinetics curves for the MB adsorption by $CuFe_2O_4$, fitting of **a** Pseudo-first order and **b** Pseudo-second order model. (Color figure online)

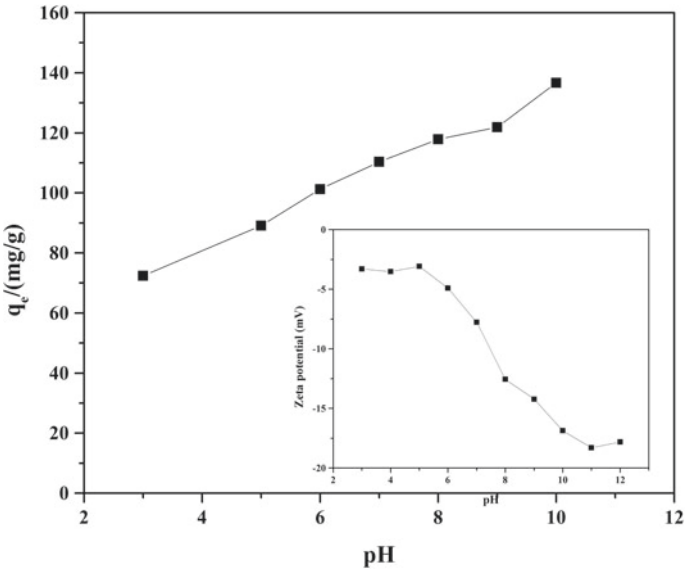

Fig. 4 Effect of solution pH on the MB adsorption by $CuFe_2O_4$ and Zeta potential as a function of pH. Adsorption conditions: T = 298 K

Langmuir, Freundlich, and Dubinin–Radushkevitch (D–R) isotherm models are part of mostly adsorption studies because of their great role to investigate the adsorption mechanism of adsorbate on the surface of the adsorbent. These equations can be described as follows:

Langmuir

$$\frac{C_e}{q_e} = \frac{1}{b * q_m} + \frac{C_e}{q_m} \tag{4}$$

Freundlich

$$Inq_e = InK_F + \frac{InC_e}{n} \tag{5}$$

D–R

$$Inq_e = Inq_{DR} - K\varepsilon^2 \tag{6}$$

$$\varepsilon = RTIn\left(1 + \frac{1}{C_e}\right) \tag{7}$$

$$E = \frac{1}{\sqrt{-2K}} \tag{8}$$

where b refers to Langmuir adsorption constant. K_F refers to Freundlich isotherm constant, and K is D–R isotherm constant which gives mean free energy (E) per molecule of adsorbate when it is transferred from the bulk solution to the surface of the solid and given by Eq. (4). ε is a temperature-dependent parameter.

As is shown in Figs. 5 and 6, the linear trends were observed upon plotting the studied models and the parameters belonging to these isotherm models for the equilibrium adsorption of MB onto $CuFe_2O_4$ surface, calculated from the slope and intercept, were also presented in Table 1.

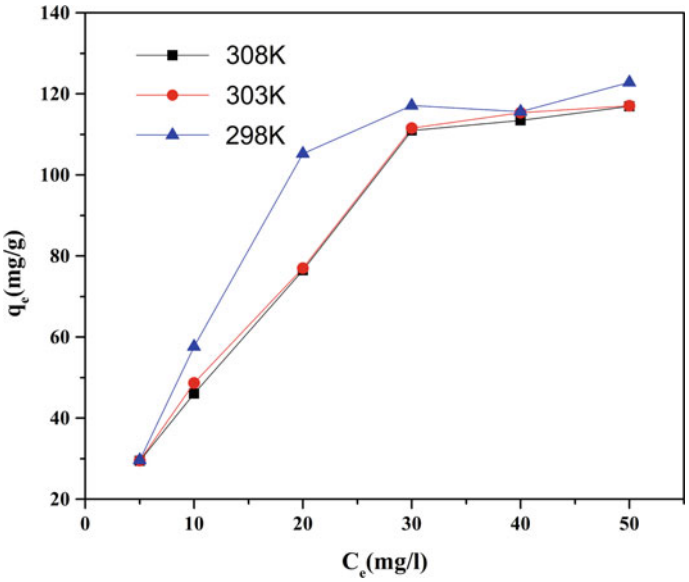

Fig. 5 Effect of solution temperature on the MB adsorption by $CuFe_2O_4$. Adsorption conditions: pH = 7. (Color figure online)

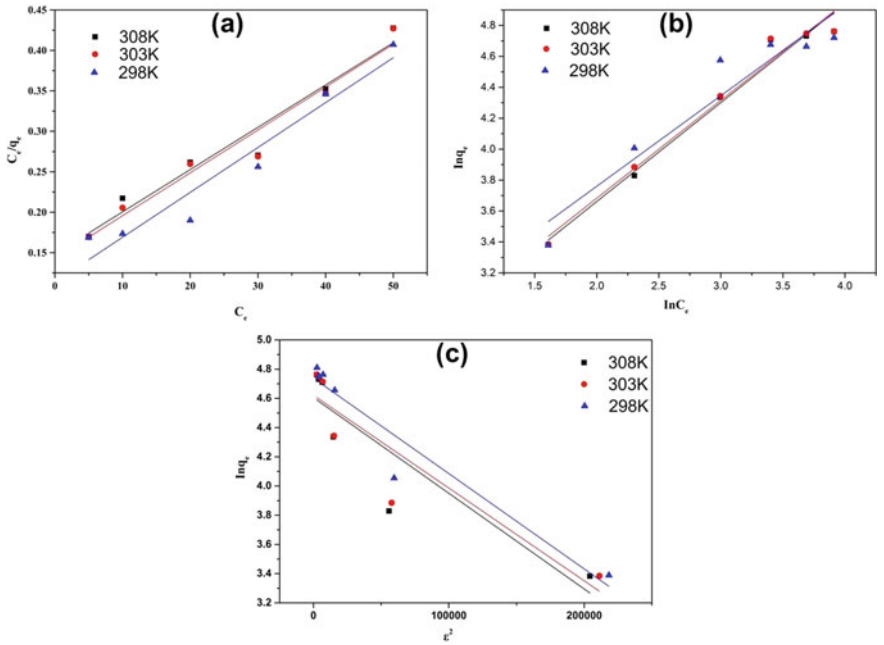

Fig. 6 Adsorption isotherms of $CuFe_2O_4$ adsorb MB: **a** Langmuir isotherms of $CuFe_2O_4$ adsorb MB; **b** Freundlich isotherms of $CuFe_2O_4$ adsorb MB; **c** D–R isotherms of $CuFe_2O_4$ adsorb MB. (Color figure online)

Table 1 The parameters of Langmuir, Freundlich, and D–R isotherms for the adsorption of MB onto $CuFe_2O_4$

Model	Parameter	T/K		
		298	303	308
Langmuir	q_m	180.1802	188.6792	191.2046
	b	0.048847	0.037138	0.035293
	R^2	0.92701	0.95135	0.94434
Freundlich	K_F	12.85972	11.21789	10.82816
	$1/n$	0.61978	0.63278	0.6397
	R^2	0.8937	0.96748	0.96844
D–R	q_{DR}	114.1907	101.5814	100.04
	K	-6.53×10^{-6}	-6.35×10^{-6}	-6.55×10^{-6}
	E	0.276769	0.280602	0.27624
	R^2	0.91778	0.80686	0.78094

It can be observed from the mathematical calculation of the experimental results that Langmuir, Freundlich, and D–R isotherms adequately described the adsorption

data in a close manner. The fitting results of the D–R model showed that the free energy of adsorption E values at 298, 303, and 308 K are 0.27624, 0.28602, and 0.276769 kJ/mol in order, all of which are <8 kJ/mol, which belong to the category of physical adsorption, indicating that the foam product adsorbs MB It is mainly adsorbed by an electrostatic effect. The Freundlich model had a good fitting correlation, which indicates that the adsorbent may adsorb MB on multiple molecular layers, and the obtained parameter $1/n$ values were between 0 and 1, which also indicates that the adsorption process is easy to proceed.

Conclusions

In this study, the cubic spinel copper ferrite with surface area (10.58 m^2/g) was prepared by heat treatment precipitation flotation heavy metal wastewater sludge, and it was successfully used as an adsorbent for simulated dye wastewater treatment. The adsorption process follows Freundlich isotherm and pseudo-first-order kinetics. The adsorption of MB on copper ferrite is mainly through electrostatic adsorption, and it is multi-molecular layer adsorption.

Acknowledgements The authors acknowledge the financial support from the National Science Fund of China (Nos. 51674225 and 51774252), the Innovative Talents Foundation in Universities in Henan Province (No. 18HASTITO11), the Educational Commission of Henan Province of China (Nos. 17A450001, 18A450001), and the China Postdoctoral Science Foundation (No. 2017M622375).

References

1. Senthil KP, Varjani SJ, Suganya S (2018) Treatment of dye wastewater using an ultrasonic aided nanoparticle stacked activated carbon: Kinetic and isotherm modelling. Bioresour Technol 250:716–722
2. Calimli MH, Nas MS, Burhan H, Mustafov SD (2020) Preparation, characterization and adsorption kinetics of methylene blue dye in reduced-graphene oxide supported nanoadsorbents. J Mol Liq 309
3. Yu J, Han Y, Jong H, Jong HI (2020) Two-step hydrothermal synthetic method of niobium-tungsten complex oxide and its adsorption of methylene blue. Inorg Chim Acta 507
4. Zahrim AY, Hilal N (2013) Treatment of highly concentrated dye solution by coagulation/flocculation–sand filtration and nanofiltration. Water Res Ind 3:23–34
5. Souza SM, Bonilla KA, Souza AA (2010) Removal of COD and color from hydrolyzed textile azo dye by combined ozonation and biological treatment. J Hazard Mater 179(1):35–42
6. Mengting Z, Kurniawan TA, Fei S (2019) Applicability of $BaTiO_3$/graphene oxide (GO) composite for enhanced photodegradation of methylene blue (MB) in synthetic wastewater under UV-vis irradiation. Environ Pollut 255:113182
7. Ozer D, Dursun G, Ozer A (2007) Methylene blue adsorption from aqueous solution by dehydrated peanut hull. J Hazard Mater 144(1):171–179

8. Uddin MK, Nasar A (2020) Walnut shell powder as a low-cost adsorbent for methylene blue dye: isotherm, kinetics, thermodynamic, desorption and response surface methodology examinations. Sci Rep 10(1):7983
9. Charola S, Yadav R, Das P, Maiti S (2018) Fixed-bed adsorption of Reactive Orange 84 dye onto activated carbon prepared from empty cotton flower agro-waste. Sustain Environ Res 28:298–308
10. Srasri K, Thongroj M, Chaijiraaree P (2018) Recovery potential of cellulose fiber from newspaper waste: an approach on magnetic cellulose aerogel for dye adsorption material. Int J Biol Macromol 119:662–668
11. Yu Y, Qiao N, Wang D (2019) Fluffy honeycomb-like activated carbon from popcorn with high surface area and well-developed porosity for ultra-high efficiency adsorption of organic dyes. Bioresour Technol 285

Part VIII
Poster Session

Analysis of Potential Applications of Kamafugite Rocks in Fertilizer

Rodrigo Lima da Motta Junior, Edson Márcio Mattiello, Patrícia Cardoso Matias, Fabiane Carvalho Ballotin, Gustavo Emílio Soares de Lima, Leonardo Gonçalves Pedroti, Jéferson Silveira Martins, and Luiz Brandão

Abstract Kamafugite is a group of ultrapotassic igneous minerals, alkaline ultrabasic rocks, composed of leucitite, olivine, leucite, kalsilite, and melilite. In Brazil, Kamafugite can be found at Minas Gerais and Goiás state. Based on its composition and the lack of national fertilizer production, it would be an alternative source of potassium, phosphorus, and other important nutrients in agriculture. This research analyzed the morphology feature, the physical and chemistry properties of the material, and its potential as an alternative fertilizer. Samples of the Kamafugite in natura, supplied by Terra Brazil Minerals, were enriched by the addition of MAP, Elementary S, and Ulexite, being the resulting powder granulated. The materials were analyzed by SEM, EDS, TGA, XRD, Raman spectroscopy, and IPC-AES. The results showed that Kamafugite rock is a potential source of nutrients for plants, once it is composed of K, P, Ca, Mg, Fe, besides Ti. However, is extremely important to analyze the material solubility in water and perform agronomic tests to assure its efficiency.

Keywords Kamafugite · Fertilizer · Potential

Introduction

Brazil is among the biggest food producers and exporters in the world [1], the national production reached 101.2 billion dollars [2] and is responsible for almost 40% of Brazilian PIB [3]. At the same time of agribusiness growth, the crop demand for fertilizer increases annually. However, the Brazilian agriculture has a high extern

R. L. da Motta Junior (✉) · E. M. Mattiello · P. C. Matias · F. C. Ballotin
Departamento de Solos, Universidade Federal de Viçosa, Viçosa, Brasil
e-mail: rodrigo.motta@ufv.br

G. E. S. de Lima · L. G. Pedroti
Departamento de Engenharia Civil, Universidade Federal de Viçosa, Viçosa, Brasil

J. S. Martins · L. Brandão
Terra Brasil Minerals, Belo Horizonte, Brasil

J. Li et al., *Characterization of Minerals, Metals, and Materials 2021*,
The Minerals, Metals & Materials Series,
https://doi.org/10.1007/978-3-030-65493-1_22

dependence on fertilizers for attending the domestic demand, being 81% of fertilizers consumption in the country imported [4, 5].

Considering the fertilizer growing demand and the low Brazilian production, alternative fertilizers sources are national product options [6]. An alternative is rock application "in natura" in the agricultural field [7]. The big problem of these materials is the low nutrient solubility in water, as happens in Brazilian potassic and ultrapotassic rocks [8]. However, some volcanic rocks like Kiberilites and Kamafugites are potential sources of potassium, calcium, and magnesium [9].

In Brazil, the biggest part of Kamafugites deposits are located at Minas Gerais and Goiás states [11]. Kamafugites are alkaline ultrabasic rocks, rich in CaO, FeO, TiO_2, and K_2O. Usually, associated with feldspar, leucites, phlogotipes, calcites, and olivines [10]. Due to high potassium contents and other elements of agricultural interest, this material arouses interest in areas where the nutrients have importance [11].

Previous works evaluated the potential of using the agrominerals as fertilizer, reminerlizers or alternative P, K, Ca, and Mg source for soil [12], mainly in Brazilian regions, where the soil are considered nutrient-poor and acids.

However, the use of additional raw materials to natural rock is an interesting strategy to add value to the final product by incorporating nutrients of great importance in fertilization. Thus, materials such as Monoammonium Phosphate (MAP), elementary S, and Ulexite, are interesting options for the production of multi-nutrient fertilizers. The use of material with a greater solubility, such as MAP, is important to supply the initial demand of the plant for P. Ulexite and elemental S will supply B and S, respectively, to the plants during their development.

Thus, in this work, Kamafugite in nature (KMF) and enriched Kamafugite (KMF^{enr}), supplied by Terra Brazil Minerals, were characterized by physical, chemical, and morphological analysis. The previous analysis showed these materials could be a potential source of nutrients for plant demand, being necessary plant tests to assure it.

Materials and Methods

Sample Collection and Preparation

The Kamafugite sample was collected in Presidente Olegário mine, at Minas Gerais state. It was grounded with a rock mill and sifted to 0.200 mm sieve. After it, it was grounded again, using ball mill, and sifted to 200 mesh sieve.

Chemistry Characterization

Kamafugite "*in natura*" was digested by EPA 3051-A method [13]. The concentration of P, K, Ca, Mg, Zn, Ni, Cu, Mn, Al, Fe, As, Co, Cr, Cd, Pb, Ti, and Si in the extract was measured using inductively coupled plasma coupled with atomic emission spectroscopy (ICP-AES Perkin Elmer 8300 DV, US).

Production of Kamafugite-Based Fertilizer

To optimize the nutritional potential of kamafugite as a more balanced fertilizer, the sample was enriched with MAP (25% w w^{-1}), elemental S (5% w w^{-1}), and ulexite (10% w w^{-1}) to produce powder or granules of enriched Kamafugite-based fertilizer.

Scanning Electron Microscopy (SEM) and Energy-Dispersive Spectrometry (EDS)

SEM and EDS were carried out at SEM Laboratory of Physics Department, at UFV. A JEOL's JSM-6010LA microscope integrated with an EDS probe operating at 20 kV was used to obtain secondary electron images of the samples, with magnification levels from 200x to 2500x. EDS operating at 12 kV was used to investigate the elementary chemical composition of Kamafugite.

X-Ray Diffraction (XRD)

XRD tests were carried, out at XRD Laboratory of Physics Department, at UFV, using a D8 Discover diffractometer with CuKα radiation (α = 1.5418 Å), working voltage of 40 kV, and electric current of 40 mA. Samples were scanned from 5º to 90º (2θ), with a 0.05º step size and 1 s per step.

Raman Spectroscopy

Raman spectra were obtained with a Renishaw inVia spectrometer with a laser of 785 nm as excitation source, available in the Raman Spectroscopy Laboratory of

Table 1 Concentration of main elements in Kamafugite (KMF) determined by ICP-AES, after acid digestion

P	K	Ca	Mg	Al	Fe	Mn
%						
1.02	2.59	2.78	4.22	3.94	9.75	0.17

Physics Department, at UFV. A randomly chosen sample point was brought into focus with 5x objective lens.

Thermogravimetric Analysis (TGA)

TGA was carried out in Packaging Laboratory of the Food Engineering Department, at UFV. A DTG-60H thermogravimetric analyzer from Shimadzu was used in the temperature range from ambient to 1000 °C, heating rate of 10 °C min^{-1}. The initial mass used in the test was about 5 mg. Atmospheric air was used to purge gas at 50 $mLmin^{-1}$.

Results and Discussion

In order to verify KMF composition, a microwave-assisted digestion with HCl/HNO_3 [14] was performed. Table 1 summarizes the content of the elements found in the sample. In fact, studies have shown that Kamafugite rocks are composed of chemical elements essential to plant growth and have potential to be used as fertilizer.

Thermogravimetric analysis was also performed to determine the material thermal stability. KMF presented 10% of weight loss in the region 0–200 °C, likely related to moisture release and dehydration of minerals, such as gibbsite [15]. At higher temperature, e.g. 400 °C, a weight loss of 3% was verified due to kaolinite dihydroxylation [16]. In fact, kaolinite dihydroxylation usually results from the interaction of two hydroxyl groups to form a water molecule leaving oxygen bounded in the lattice [17], and generally occurs at temperatures higher than 400 °C [18].

The Kamafugite morphology was also verified by SEM/EDS. The images (Fig. 2a–c) showed that it is composed of heterogeneous bulky particles of 10–30 μm, with a rounded shape. This feature can further indicate better nutrients solubility. Furthermore, an EDS-mapping also verified the presence of a great quantity of O, Mg, Si, K, Fe, and Ti (Fig. 2d–i), as showed on total digestion analysis.

As discussed in the previous analysis, Kamafugite is a rock composed of a wide variety of nutrients. Thus, Fig. 3 shows XRD of both samples: in nature (KMF) and enriched (KMF^{enr}). On KMF was verified peaks relative to Fe_3O_4 (JCPDS Card No. 1-1111), Fe_2O_3 (JCPDS Card No. 3-800), $(MgFe)SiO_4$ (JCPDS Card No. 3-195),

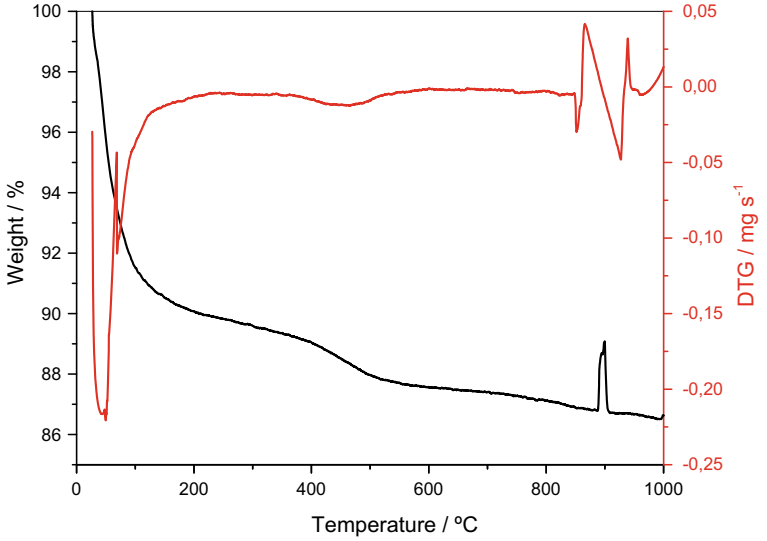

Fig. 1 TG/ DTG curves of Kamafugite, heating rate 10 °C min^{-1}, air atmosphere. (Color figure online)

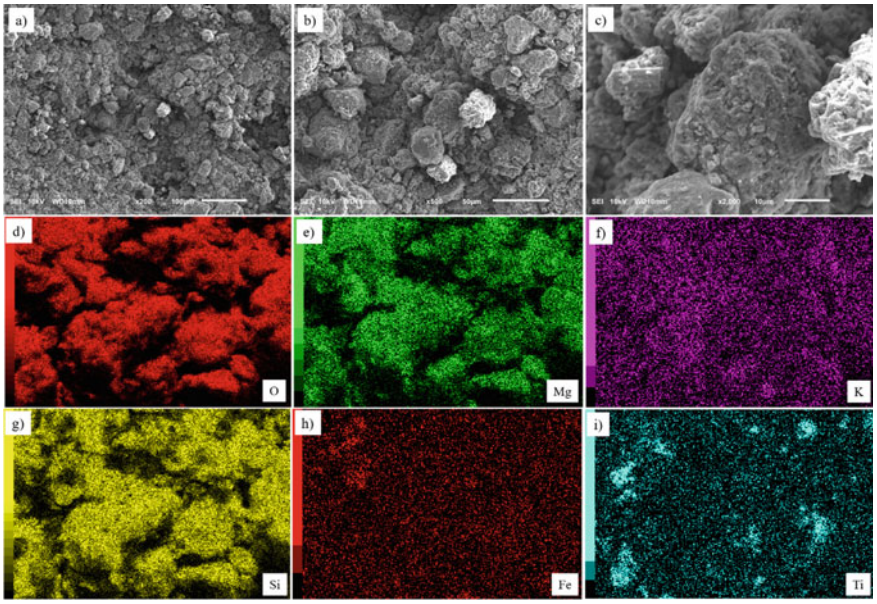

Fig. 2 Scanning electron microscopy (SEM) of KMF **a** 100 μm, **b** 50 μm, **c**10 μm; EDS mapping **d** O; **e** Mg; **f** K; **g** Si; **h** Fe; and **i** Ti. (Color figure online)

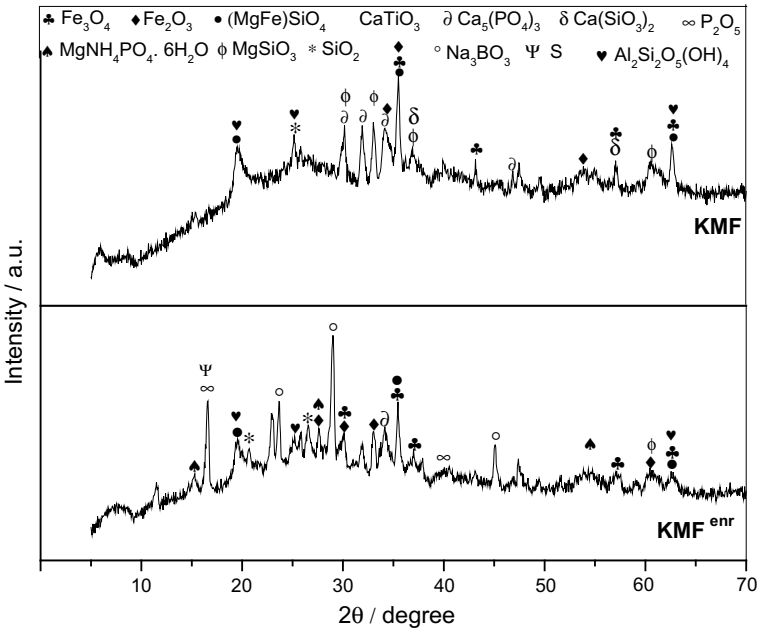

Fig. 3 XRD of Kamafugite in nature (KMF) and enriched (KMF^{enr})

$AlSi_2O_5(OH)_4$ (JCPDS Card No. 1-527), $CaTiO_3$ (JCPDS Card No. 1-1055), SiO_2 (JCPDS Card No. 3-444), $MgSiO_3$ (JCPDS Card No. 3-1173), $Ca_3(PO_4)_2$ (JCPDS Card No. 3-681), $CaSiO_3$ (JCPDS Card No. 34-612), and $Al_2Si_2O_5(OH)_4$ (JCPDS Card No. 1-527).

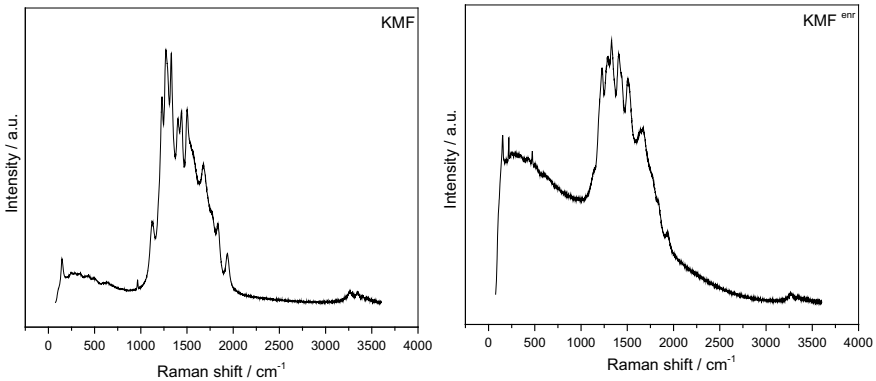

Fig. 4 Raman spectra of Kamafugite in nature (KMF) and enriched Kamafugite (KMF^{enr}), laser 785 nm, P = 5 mW, 5 accumulations.

On KMF^{enr}, was clear the presence of other minerals, confirming that the enrichment process was effective. In fact, the peak at 16.58° was observed due to elemental sulfur (JCPDS Card No. 13-144) and P_2O_5 (JCPDS Card No. 1-213) on the sample. Furthermore, at 23.75 and 28.78° was verified the presence of Na_3BO_3 (JCPDS Card No. 32-1047), which comes from ulexite. In addition, the peaks at 15.31, 27.67, and 54.36° are strictly related to mineral struvite, $MgNH_4PO_4.6H_2O$ (JCPDS Card No. 15-762), characteristic of MAP fertilizer.

A Raman analysis of each sample was performed and similar Raman spectra were obtained for both samples with a small difference on KMF^{enr}, which could be related to fluorescence during the measurement.

In general, for both samples, a broad Raman band from 1000 to 2000 cm^{-1} was verified, likely due to bands superposition related to the variety of minerals present on KMF. Hematite (Fe_2O_3) present bands at 225, 245,291, 411,500 611, and 1320 cm^{-1} [19]. Another mineral that might be responsible for the bandwidth is struvite, which has a band at 942 cm^{-1}, related to PO_4 species (P–O symmetric stretching band) and at 1477 cm^{-1} due to bending vibrations of NH_4 [20]. Furthermore, the phase P_2O_5 also presents a band at 1390 cm^{-1}, related to P = O stretching mode [21].

In addition, studies have reported that Kamafugite is frequently found associated with carbonates [22] samples. Usually, carbonates present strong Raman modes due to stretching vibrations of CO_3^{2-} at 1050 cm^{-1} and weak Raman peaks at 1400 cm^{-1}, related to asymmetric stretching [23].

Although the materials characterization showed potential and promising results of Kamafugite use in agriculture, water solubility as well as experiments with plants are important to assure Kamafugite use as fertilizer.

Conclusions

In this work, potential applications of Terra Brasil Minerals' Kamafugite rocks enriched with fertilizers were investigated. KMF and KMFenr physical, chemical, and morphological properties were analyzed with different analytical techniques.

The materials characterization showed through digestion and ICP-AES, TG, SEM/EDS, XRD, and Raman spectroscopy that Kamafugite rock is a potential source of nutrients for the plants. In fact, the material presented a wide variety of nutrients in the rock in nature, e.g. K, Ca, Mg, Fe, Al; besides B, S, and P on KMF^{enr}. Also, the quantity of phases presented in XRD confirms the potential of this material to be used as a fertilizer. However, is extremely important to analyze the material solubility in water and perform agronomic tests to assure its efficiency.

References

1. Contini E, Pena Júnior MA, Santana CAM, Martha Júnior GM (2012). Exports Engine of Braziian agribisiness. Agric Polic Rev 21(2):88–102
2. Brazilian Agribusiness Foreign Trade Statistics-AGROSTAT, Brazil (2018)
3. Silva MG, Cesario AV, Cavalcanti IR (2013) Relevance of agribusiness to the current Brazilian economy. Presented at X teaching initiation meeting, Federal University of Paraíba
4. National Fertilizer Spreading Agency-ANDA, Brazil (2019)
5. Cella D, Lima Rossi MC (2010) Analysis of the fertilizer Market in Brazil. Technol Interface Mag 7(1):41–50
6. Römheld V, Kirkby EA (2010) Research on potassium in agriculture: needs and prospects. Plant Soil 335(1–2):155–180
7. Resende ÁV, de Souza Martins É, Oliveira CG, de Sena MC, Machado CTT, Kinpara DI, Oliveira Filho EC (2006). Supply of potassium and research on the use of "in natura" rocks in Brazilian agriculture. Space Geogr Mag 9(1)
8. Ramos CG, Querol X, Oliveira ML, Pires K, Kautzmann RM, Oliveira LF (2015) A preliminary evaluation of volcanic rock powder for application in agriculture as soil a remineralizer. Sci Total Environ 512:371–380
9. Nascimento M, Monte MBDM, Loureiro FEL (2008) Agriminerals-potassium. CETEM/MCTI
10. Araujo A, Carlson RW, Gaspar JC, Bizzi LA (2001) Petrology of kamafugites and kimberlites from the Alto Paranaiba alkaline province, Minas Gerais, Brazil. Contrib Mineral Petrol 142(2):163–177
11. Sgarb PBDA, Gaspar JC, Valenca JG (2017) Brazilian kamafugites. Braz Mag Geosci 30(3):417–420
12. Loureiro FEL, Sampaio JA, Castilhos ZC, Bezerra MS, Luz ABD (2010) Rocks, minerals and technological routes for the production of alternative fertilizers. CETEM/MCT
13. Link DD, Walter PJ, Kingston HM (1998) Development and validation of the new EPA microwave-assisted leach method 3051A. Environ Sci Technol 32(22):3628–3632
14. United States Environmental Protection Agency-USEPA (1998) Method 3051A-Microwave assisted acid digestion of sediments, sludges, soils, and oils
15. Sahnoune F, Saheb N, Khamel B, Takkouk Z (2012) Thermal analysis of dehydroxylation of Algerian kaolinite. J Therm Anal Calorim 107:1067–1072
16. Kristóf J, Frost RL, Kloprogge JT, Horváth E, Makó É (2002) Detection of four different OH-groups in ground kaolinite with controlled-rate thermal analysis. J Therm Anal Calorim 69:77–83
17. Killingley JS, Day SJ (1990) Dehydroxylation kinetics of kaolinite and montmorillonite from Queensland Tertiary oil shale deposits. Fuel 69:1145–1149
18. Ptáček P, Kubátová D, Havlica J, Brandštetr J, Šoukal F, Opravil T (2010) Isothermal kinetic analysis of the thermal decomposition of kaolinite: the thermogravimetric study. Thermochim Acta 501:24–29
19. Hanesch M (2009) Raman spectroscopy of iron oxides and (oxy)hydroxides at low laser power and possible applications in environmental magnetic studies. Geophys J Int 177:941–948
20. Frost RL, Weier ML, Martens WN, Henry DA, Mills SJ (2005) Raman spectroscopy of newberyite, hannayite and struvite. Spectrochim Acta Part A Mol Biomol Spectrosc 62:181–188
21. Galeener FL, Mikkelsen JC (1979) The Raman spectra and structure of pure vitreous P2O5. Solid State Commun 30:505–510
22. Brod JA, Gibson SA, Thompson RN, Junqueira-Brod TC, Seer HJ, de Moraes LC, Boaventura GR (2017) The kamafugite-carbonatite association in the Alto Paranaíba Igneous Province (APIP) southeastern Brazil. Braz Mag Geosci 30(3):408–412
23. Buzgar N, Apopei AI (nd) The raman study of certain carbonates

Application of Desulphurization Residue in Cementitious Mortars

A. S. A. Cruz, M. T. Marvila, A. R. G. Azevedo, L. R. Cruz, J. A. L. Júnior, C. M. F. Vieira, J. Alexandre, and S. N. Monteiro

Abstract Steel residues in general have a high cementing power, which makes them potential substitutes for Portland cement. One of these residues is that of desulfurization, which currently has no technological application. In this sense, the objective of this work was to evaluate the application of this residue in mortars 1:1:6:1.5 (cement:lime:sand:water), as a substitute for cement in percentages of 0, 10, 20, and

A. S. A. Cruz · M. T. Marvila (✉) · A. R. G. Azevedo · L. R. Cruz · J. A. L. Júnior · C. M. F. Vieira
LAMAV—Advanced Materials Engineering Laboratory, UENF—State University of the Northern Rio de Janeiro, Av. Alberto Lamego, 2000, Campos dos Goytacazes, Rio de Janeiro 28013-602, Brazil
e-mail: markssuel@hotmail.com

A. S. A. Cruz
e-mail: ariana.sazeredo@gmail.com

A. R. G. Azevedo
e-mail: afons.garcez91@gmail.com

L. R. Cruz
e-mail: lucasreis1550@gmail.com

J. A. L. Júnior
e-mail: tosteslinhares@gmail.com

C. M. F. Vieira
e-mail: vieira@uenf.br

A. S. A. Cruz · L. R. Cruz · J. Alexandre
LECIV—Civil Engineering Laboratory, UENF—State University of the Northern Rio de Janeiro, Av. Alberto Lamego, 2000, Campos dos Goytacazes, Rio de Janeiro 28013-602, Brazil
e-mail: jonas.uenf@gmail.com

A. R. G. Azevedo
TER—Department of Agricultural Engineering and Environment, UFF—Federal Fluminense University, Rua Passo da Pátria, 341, Niterói, Rio de Janeiro 24210-240, Brazil

S. N. Monteiro
Department of Materials Science, IME—Military Institute of Engineering, Square General Tibúrcio, 80, Rio de Janeiro 22290-270, Brazil
e-mail: snevesmonteiro@gmail.com

J. Li et al., *Characterization of Minerals, Metals, and Materials 2021*,
The Minerals, Metals & Materials Series,
https://doi.org/10.1007/978-3-030-65493-1_23

30%. The tests carried out were consistency, mass density, compressive strength, water absorption, and porosity, in addition to incorporated air content. The results demonstrate that the application of the residue as a cementitious material is possible, due to the good mechanical parameters obtained.

Keywords Residue · Desulphurization · Mortar

Introduction

Steel is defined as a metal alloy composed of iron ore, coal (mineral or vegetable), and lime [1]. The steel production cycle has undergone profound changes from birth to the present day, developing over time. In fact, as of the 1980s, a steel industry underwent an intense restructuring, marked not by an exponential increase in production, but technological innovations in processes and products, greater shareholder interaction, and fewer employees [2].

The steel production chain can be divided into four major stages, namely: Cargo Production, Pig Iron Production, Steel Production, and finally, the Mechanical Conformation of the steel produced.

During the first phase of the production cycle, the materials that will go to the blast furnace for the production of pig iron are prepared: coke and sinter. Coke plays a fuel role in the blast furnace. For its production, several types of mineral coal are mixed and heated, at temperatures of around 1000 °C, so that the volatile moisture in the coal is eliminated [3]. The sinter, in turn, represents the main metallic source used in blast furnaces and consists of the agglomeration of iron ore fines with other raw materials [4]. To reduce iron ore to pig iron, a mixture of coke and sinter is taken to the blast furnace, which constitutes the second stage of production.

In the next phase, liquid pig iron is taken, together with iron scrap, to an oxygen converter [5], for the production of steel. Finally, the last stage of the process consists of mechanical shaping, in which the steel is subjected to suitable shapes for commercialization.

Throughout this production cycle, all stages are responsible for the generation of waste harmful to the environment, at different scales. Due to the current concern with the management of industrial waste, and with the objective of mitigating the environmental damage resulting from its inadequate disposal, it is common to reuse steel residues in other industrial activities. As an example, the Blast Furnace Slag, a residue generated during the process of obtaining pig iron, whose main destination is the cement industry, since, like clinker, has the characteristic of hydraulicity, that is, the ability to harden when in contact with water, making it a material option to be added to Portland cement production [6]. Blast furnace slag can also be added in mortars and concrete, as a partial replacement for Portland cement, being able to increase the compressive strength of the final material.

As with slag, the steel production cycle is also responsible for the waste generated by steel desulfurization, a process that aims to decrease the sulfur content present

in pig iron, or in liquid steel itself, with the purpose of conserving the quality of the final product, given that the presence of sulfur in hardened steel, often in the form of sulfides [7], not only affects the ductility, toughness, and fatigue resistance of the steel but can also play an important role in processes of corrosion of steel [8].

As a consequence of this, considering that, contrary to what occurs with blast furnace slag, the residue from steel desulfurization does not yet have an adequate destination, this work aims to evaluate the behavior of this residue when used in mortars of settlement, in partial replacement of Portland cement and gather conclusions about the technical feasibility of its use. To achieve this objective, mortar specimens were made with the introduction of 0, 10, 20, and 30% steel desulfurization residue, in relation to Portland cement, and, for experimental results, the specimens were subjected to Consistency Index, Mass Density and Incorporated Air tests, Water Absorption, and Porosity and Compression Resistance.

Materials and Methods

For the tests, specimens were made in the 1:1:6:1.5 line (cement:lime:sand:water), with the insertion of the steel desulfurization residue in the percentages of 0% (reference), 10, 20, and 30%, in relation to Portland cement mass.

The residue used in the research was obtained from the steelmaker ArcelorMittal, in Campos dos Goytacazes, and, for its use as mineral addition in mortar, passed through the # 200 sieve to achieve the necessary granulometry for the research.

All mortars were prepared in accordance with NBR 13276 [8], as well as the consistency index test. The test was carried out by filling the metal cone trunk with the mortar in a fresh state, for later activation of the table for consistency index, in this case with electric activation, to perform the 30 strokes determined by the standard. The results determined by the arithmetic mean of the three diameters measured after the test was carried out were expressed as a graph for better comparison between the tested mortars.

The Mass Density and Incorporated Air Content test, governed by NBR 13278 [9], consists of using fresh mortar to fill a previously calibrated cylindrical container. In order for the test to be as accurate as possible, it is sought to ensure that the container has approximately all its volume filled with mortar and that there is no material adhered to it from the outside.

Through this process it is possible to determine the mass of the mortar used in the test, and, having this information, using mathematical formulas, to reach the numbers that express the mass density and the air content incorporated into the mortar.

Mortars were also subjected to a water absorption test by immersion, in which results were also obtained about the porosity of the mortar. To carry out the test, the specimens were weighed and dried in an oven, and their masses were again measured at intervals of 24, 48, and 72 h. Then they were submerged in water at room temperature and the masses were measured again at the intervals already mentioned.

The test is governed by NBR 9778 [10], which provides equations through which, using the information obtained in the test, it is possible to arrive at the expected results.

Finally, all specimens were cured for 28 days in order to carry out the compressive strength test.

Results and Discussion

The results obtained in the Consistency Index test showed in Fig. 1, that the steel desulfurization residue, applied as mineral addition in mortars, implies a decrease in its consistency, and a consequent increase in fluidity [11].

The behavior observed in the Mass Density and Incorporated Air Content test, showed in Figs. 2 and 3, in turn, proved to be within the expected for mortars that use mineral additions. The increase in density presented, as well as the decrease in the content of air incorporated into the mortar, can be explained by the filler effect, which

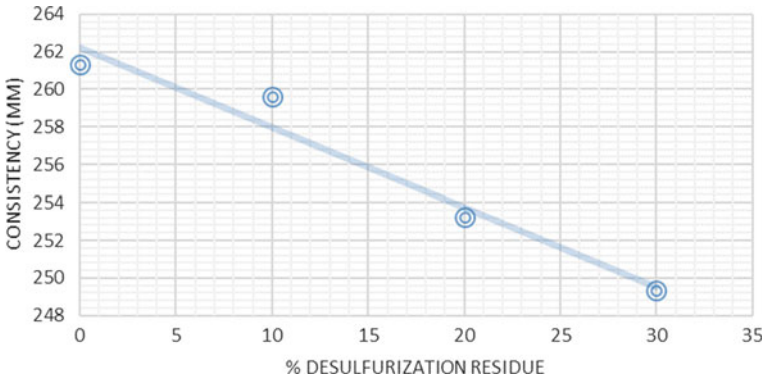

Fig. 1 Consistency × Desulfurization Residue. (Color figure online)

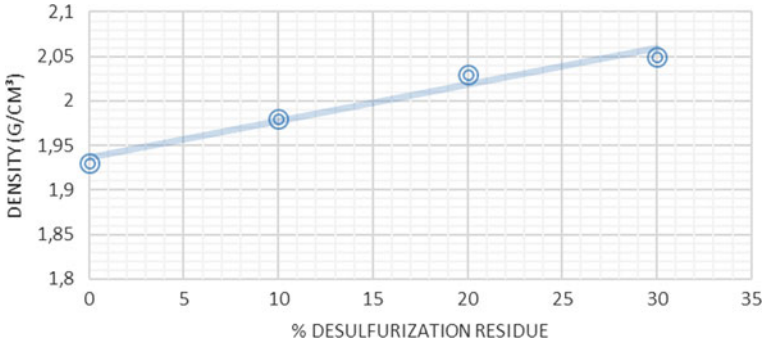

Fig. 2 Density × Desulfurization Residue. (Color figure online)

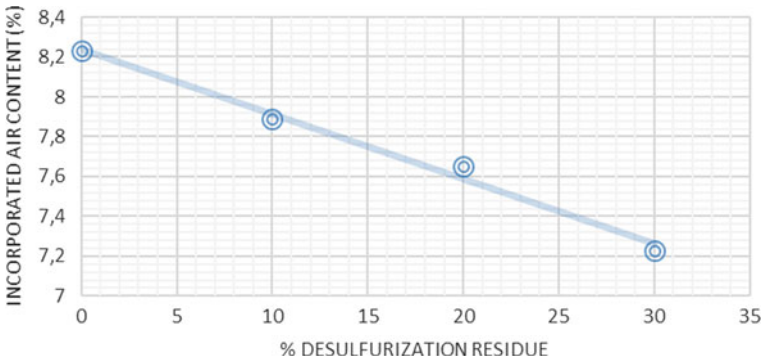

Fig. 3 Incorporated air content × Desulfurization Residue. (Color figure online)

occurs with the incorporation of a material, whose granulometry is finer than that of cement. The voids left by the cement particles will be occupied by smaller particles that, in the present research, belong to the steel desulfurization residue. The reduction of voids directly implies denser and less porous cementitious mixes [12, 13].

Also due to the increase in compaction, resulting from the insertion of very fine material in the mortar, the porosity (Fig. 4) test also showed expected results and in accordance with the theory. Note that the addition of the residue tends to decrease the porosity of the mortar [14].

The results obtained in the Water Absorption by Immersion test (Fig. 5), in turn, showed an interesting behavior. It was clear that the residue had no significant interference in this physical property [14]. There was a small drop in water absorption that remained until the percentage of 20% of residue in the mortar. Since then, water absorption has grown again.

The results of the Compression Resistance test (Fig. 6) showed an increase in resistance proportional to the increase in the residue content in the mortar, without showing any drop. This conclusion was expected and is shown to be in accordance not only with theory but also with the increase in density observed in the Mass Density and Porosity tests [15, 16].

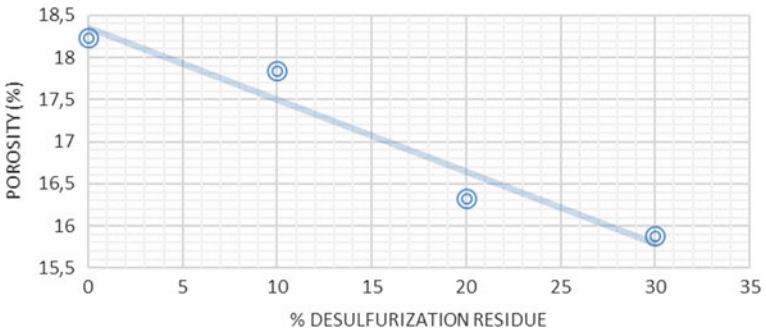

Fig. 4 Porosity × Desulfurization Residue. (Color figure online)

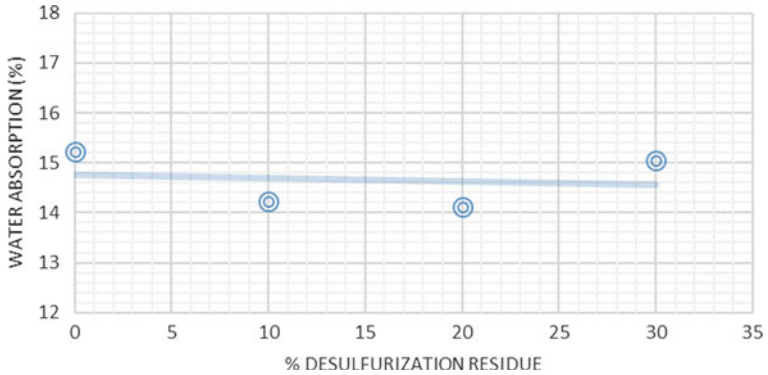

Fig. 5 Water absorption × Desulfurization Residue. (Color figure online)

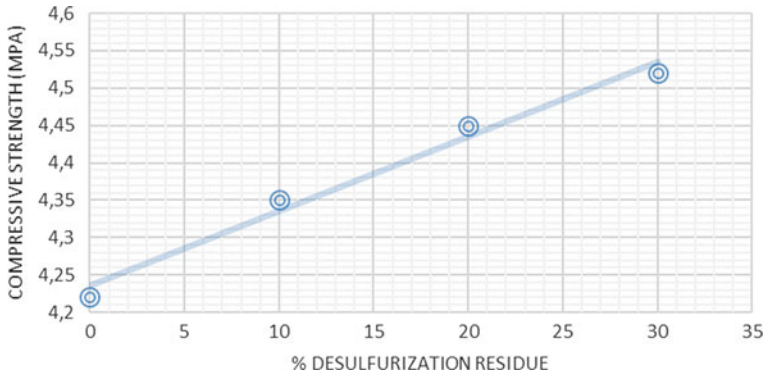

Fig. 6 Compressive strength × Desulfurization Residue. (Color figure online)

Conclusion

The insertion of steel desulfurization residue in mortar for settlement was responsible for an increase in mass density proportional to the increase in the presence of the residue. As a consequence, this behavior indicates a decrease in the mortar porosity, also confirmed by the tests. Due to these results, the growth of the mortar's compressive strength was expected and can also be confirmed.

The tests also demonstrated an increase in consistency and a decrease in the content of air incorporated into the mortar. The water absorption test showed a slight drop in absorption, up to the content of 20% replacement of the residue in relation to Portland cement.

In view of the results obtained, it can be seen that the steel desulfurization residue is a viable option to be used as mineral addition in settlement mortars. It is necessary to consider, however, the behavior observed in the Water Absorption by Immersion

test, and, as a result, the 20% substitution content of the residue in relation to Portland cement should be considered as ideal.

Acknowledgements The authors thank the Brazilian agencies CNPq, CAPES, and FAPERJ for the support provided to this investigation.

References

1. Silva VC, Pereira AF (2013) Study of Life Cycle Assessment (LCA) Aspects for reuse of solid industrial steelmaking waste. In: International interdisciplinary congress on social and humanities, Belo Horizonte, MG, Brazil, pp 8–11
2. Coast MM (2002) Principles of industrial ecology applied to environmental sustainability and steel production systems [Thesis]. Federal University of Rio de Janeiro, Rio de Janeiro
3. Telles VB, Espinosa DCR, Tenório JAS (2013) Iron Ore sinter production using electric steelmaking dust as raw material. Tecnol Metal Mater Miner 10(1):72–77
4. Silva WKC (2018) Characterization of steel slag and evaluation of its use in the production of coating mortar. Federal University of Ceará, Fortaleza
5. Lobato NCC, Villegas EA, Mansur MB (2013) Evaluation of technological alternatives for the management of solid steel waste: slag and blast mud. In: XXV national meeting on mineral treatment and extractive metallurgy & VIII meeting of the Southern Hemisphere, 20–24 October 2013, Goiânia, GO, Brazil
6. Costa LT, Margins BB, Barral CEP, Tavares RP, Heck NC (2015) Integrated analysis of desulfurization processes for optimizing routes in steel production. In: 46th steelmaking seminar—ABM week, Rio de Janeiro, RJ, Brazil
7. Santos RPM, Castro JA, Silva ALVC, Martins AAR (2015) Initial steps in the development of a sulfur forecast model in the desulphurization of pig iron in a Torpedo Car at Companhia Siderúrgica Nacional. In: 46th steelmaking seminar—ABM week, Rio de Janeiro, RJ, Brazil
8. Brazilian Association of Technical Standards. NBR 13276 (2016) Mortar for laying and covering walls and ceilings—Determination of the consistency index, Rio de Janeiro
9. Brazilian Association of Technical Standards. NBR 13278 (2005) Mortar for settlement and coating of walls and ceilings—Determination of Mass Density and Incorporated Air Content, Rio de Janeiro
10. Brazilian Association of Technical Standards. NBR 9778 (1987) Mortar and hardened concrete: determination of water absorption by immersion—Index of voids and specific mass, Rio de Janeiro
11. Zanelato EB, Alexandre J, de Azevedo ARG, Marvila MT (2019) Evaluation of roughcast on the adhesion mechanisms of mortars on ceramic substrates. Mater Struct Constr 52. https://doi.org/10.1617/s11527-019-1353-x
12. Amaral LF, Girondi Delaqua GC, Nicolite M, Marvila MT, de Azevedo ARG, Alexandre J, Fontes Vieira CM, Monteiro SN (2020) Eco-friendly mortars with addition of ornamental stone waste—a mathematical model approach for granulometric optimization. J Clean Prod 248:119283. https://doi.org/10.1016/j.jclepro.2019.119283
13. Marvila MT, Azevedo ARG, Cecchin D, Costa JM, Xavier GC, de Fátima do Carmo D, Monteiro SN (2020) Durability of coating mortars containing açaí fibers, Case Stud Constr Mater 13 e00406. https://doi.org/10.1016/j.cscm.2020.e00406
14. Marvila MT, Azevedo ARG, Monteiro SN (2020) Verification of the application potential of the mathematical models of lyse, abrams and molinari in mortars based on cement and lime. J Mater Res Technol 97327–7334. https://doi.org/10.1016/j.jmrt.2020.04.077

15. Marvila MT, Alexandre J, de Azevedo ARG, Zanelato EB (2019) Evaluation of the use of marble waste in hydrated lime cement mortar based. J Mater Cycles Waste Manag 21:1250–1261. https://doi.org/10.1007/s10163-019-00878-6
16. Marvila MT, Alexandre J, Azevedo ARG, Zanelato EB, Xavier GC, Monteiro SN (2019) Study on the replacement of the hydrated lime by kaolinitic clay in mortars. Adv Appl Ceram 118:373–380. https://doi.org/10.1080/17436753.2019.1595266

Cause Analysis on Buildup Formation of Carbon Sleeve in Continuous Annealing Furnace for Low-Temperature Grain-Oriented Silicon Steel Production

Mingsheng He

Abstract Based on the investigation and study of the topography and composition of the buildups, combined with production process of low-temperature grain-oriented silicon steel, the mechanism and major causes of forming buildups of carbon sleeve were discussed from the factors such as the quality of carbon sleeve, antioxidants, furnace atmosphere, dew point, running speed of carbon sleeve, and so forth. Meanwhile, some countermeasures to reduce the formation of the buildups were proposed.

Keywords Carbon sleeve · Causes for buildup formation · Low-temperature grain-oriented silicon steel · Continuous annealing

Introduction

Grain-oriented silicon steels are iron-silicon alloys that were developed to provide the low core loss and high permeability required for efficient and economical electrical transformers. Due to the low heating temperature and low production cost, the low-temperature grain-oriented silicon steel has been paid more and more attention. After low-temperature heating, hot rolling, and cold rolling, the steel strip must be treated by continuous decarbonization annealing. Carbon sleeve is the most important kind of hearth rolls in the annealing furnace to support and convey silicon steel strips. Under the condition of the high temperature and H_2–N_2–H_2O weak oxidation or H_2–N_2–H_2O–NH_3 weak basic and weak oxidation atmosphere in the annealing furnace for low-temperature grain-oriented silicon steel production, buildups adhered (AD-buildup) to the surface of the carbon sleeve can form after using for a period of time. Once AD-buildups come into being on the surface of carbon sleeve, they will easily indent, bruise, and scratch the surface of steel strip, which can affect the quality of steel strip surface and production efficiency.

M. He (✉)
R&D Center of Wuhan Iron & Steel Co., Ltd, Wuhan 430080, China
e-mail: hms03@tsinghua.org.cn

J. Li et al., *Characterization of Minerals, Metals, and Materials 2021*,
The Minerals, Metals & Materials Series,
https://doi.org/10.1007/978-3-030-65493-1_24

In the past, there were few buildups in the production line of grain-oriented silicon steel, but recently, AD-buildups formation occurred frequently. Impregnating phosphates is an economical, practical, and effective method to improve the oxidation resistance of graphite materials [1]. Phosphates are widely used as antioxidants for low- and medium-temperature carbon sleeve at home and abroad. Phosphate antioxidants can promote or accelerate the formation of buildups for low- and medium-temperature carbon sleeve during the continuous annealing of non-oriented silicon steel [2]. However, the real reason for buildups formation of oriented silicon steel is still unknown. The quality and life time of carbon sleeve have been troubling the production of continuous annealing line.

Materials and Methods

In order to determine the microstructure and compositions of AD-buildups, the buildups taken from the surface of the carbon sleeve were sectioned along radial or axial direction of the carbon sleeve, inlaid, ground, and polished. And then the as-prepared samples were observed and analyzed by a scanning electron microscope (SEM, Quanta 400, FEI Co., Netherland) equipped with energy-dispersive X-ray spectroscopy (EDS).

Results and Discussion

Topography and Composition of AD-Buildups

Figure 1 shows the AD-buildups forming on the surface of carbon sleeve during the decarburizing, annealing, and nitriding for low-temperature grain-oriented silicon

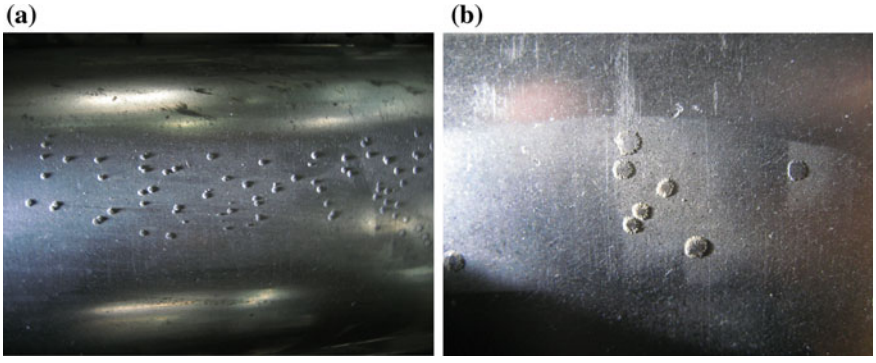

Fig. 1 Photos of AD-buildups on the surface of carbon sleeve. (Color figure online)

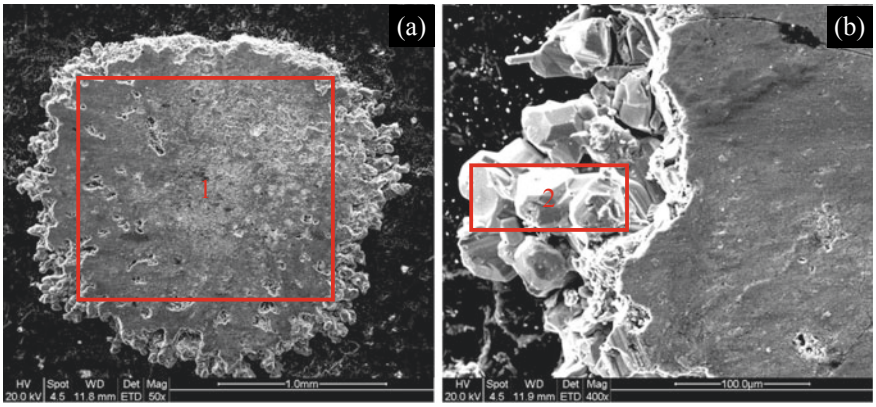

Fig. 2 SEM micrographs of AD-buildup: **a** general view, **b** partially enlarged. (Color figure online)

steel production. All the AD-buildups are irregular in shape. From the aspect of morphology, the AD-buildups are completely different from that on the surface of carbon sleeve in continuous annealing furnace for non-oriented silicon steel production.

Figure 2a, b is SEM micrographs with different magnification. As can be seen from Fig. 2a, the shape of the AD-buildup on the surface is irregular, and the outer surface has been smoothed by the steel strip. Figure 3a, b is EDS spectrums of the selected zones of the AD-buildup in Fig. 2a, b. It can be seen from Fig. 3 that the main components of the buildups are Fe, P, O, C, and a small amount of Mn and Si. The content of Si is higher and there is no Ca in the edge zone of the buildup (Fig. 2b).

Figure 4 shows SEM micrographs of the AD-buildups together with a small piece of carbon sleeve sectioned along the axial direction of the carbon sleeve. As can be seen from Fig. 4, it looks like the buildup has a lot of roots in the pores of the carbon sleeve. Therefore, once the buildup was formed, it was difficult to remove it by grinding roller. The real reason for AD-buildup formation on the surface of carbon sleeve is that there are many pores in the surface of carbon sleeve, that is to say, there are pores or holes where the AD-buildup can root and grow up.

Causes for Buildup Formation of Carbon Sleeve

According to the above results of analysis on the microstructure, topography, and composition of the AD-buildups, it can be seen that buildups on the surface of the carbon sleeve experienced the “rooting-growing up” process and the main components are Fe, P, O. The two necessary conditions for AD-buildup formation were (1) there exist big pores in the surface of carbon sleeve; (2) rich material sources such as iron scale, iron rust, greasy dirt, dust, etc. [1]. Although the surface of carbon sleeve is

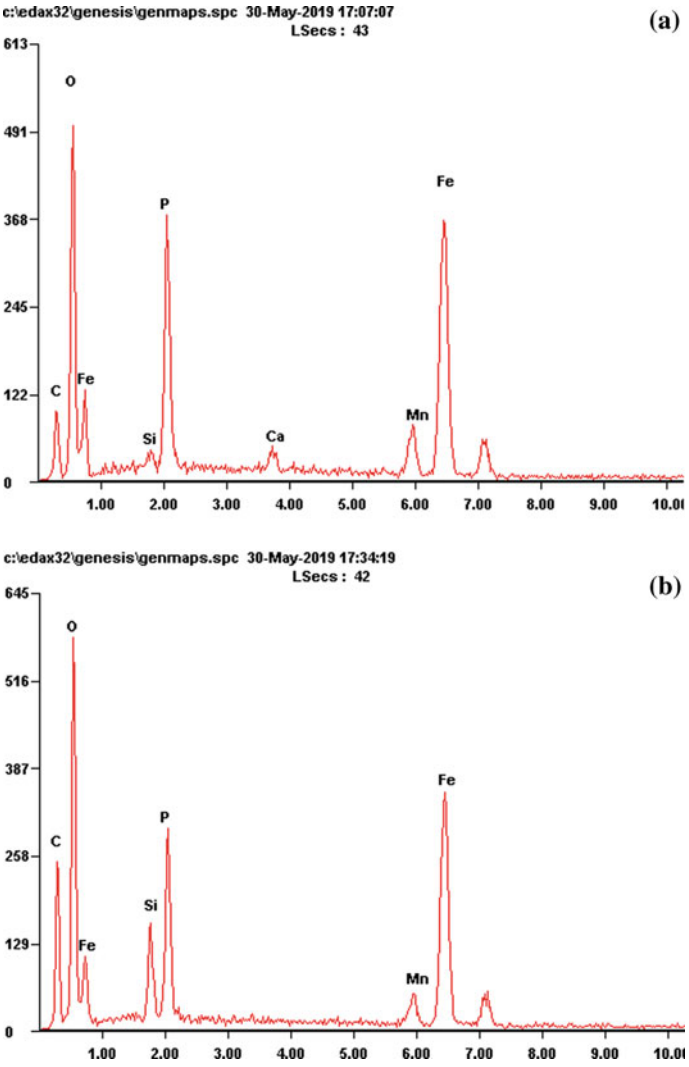

Fig. 3 EDS spectrums of the AD-buildups: Region 1 (**a**), 2 (**b**). (Color figure online)

smooth after soaking of various chemical substances and processing, graphite begin to react with water vapor over 700°C. Graphite itself is a porous material, and due to the high dew point in continuous annealing furnace for low-temperature grain-oriented silicon steel production, more and larger pores may be formed after using for a period of time.

From the above results of the composition analysis, there was a large amount of phosphide or phosphate. However, there cannot be a large amount of P in silicon steel nor can there be a large amount of P in the refractory materials in the annealing furnace. In addition to the anti-oxidation treatment of carbon sleeve, it was more

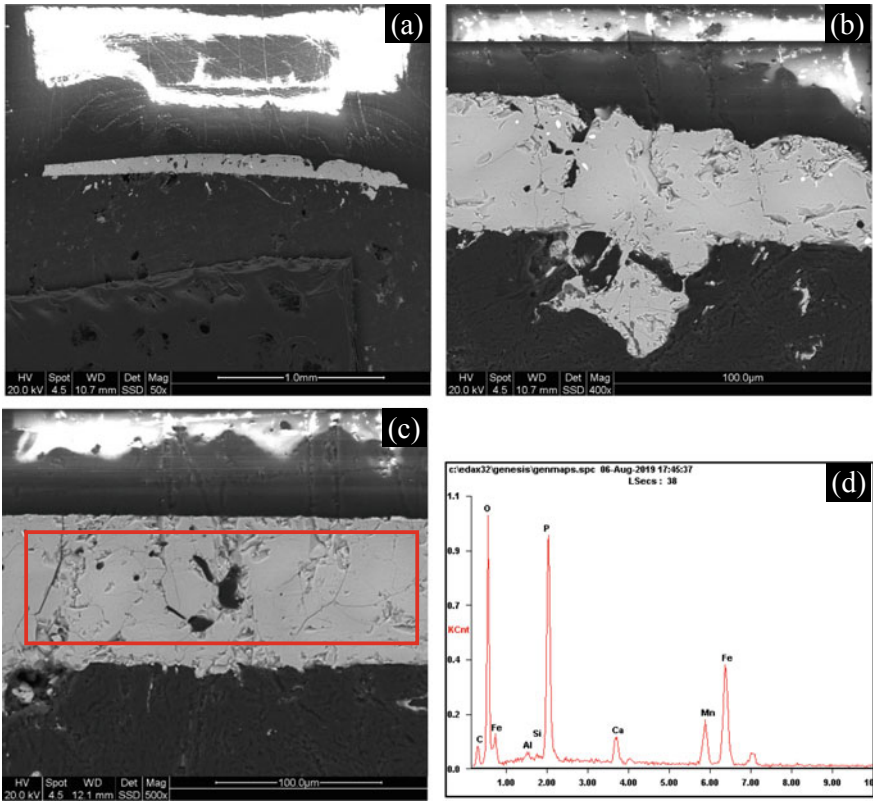

Fig. 4 SEM micrographs of AD-buildups sectioned along the axial direction of carbon sleeve: **a** general view, **b** and **c** partially enlarged, **d** EDS spectrum of the selected zone. (Color figure online)

impossible for other processes or media to bring a large amount of P into the AD-buildups. Therefore, the phosphide or phosphate in the buildups mainly came from antioxidants in carbon sleeve, and phosphate itself was an inorganic high-temperature binder, which promoted (or accelerated) the formation of buildup. Meanwhile, many other factors can influence on buildups formation, such as furnace atmosphere, residues of alkali wash, speed synchronization of steel strip and carbon sleeve, dusts inside furnace, etc.

Measures to Control and Reduce Buildups Formation

The smaller pores in the surface of carbon sleeve are, and the less material sources for forming buildups such as phosphate, iron scale, iron rust, iron oxidation, greasy dirt on the surface of silicon steel strip are, the less the possibility of buildup formation

is. In order to control and reduce buildup formation, extend the service life of carbon sleeve, the following methods and measures are proposed:

(1) Improve the surface quality of carbon sleeve, enhance its oxidation resistance, and buildup formation resistance.
(2) Develop carbon sleeve with low phosphate or no phosphate antioxidant.
(3) As long as the product meets the performance requirements, the dew point in the furnace can be reduced as much as possible.

Conclusions

Phosphate is one kind of inorganic high-temperature binder, which promoted the formation of AD-buildup on the surface of carbon sleeve. This was one of the main reasons for the buildup formation of carbon sleeve in continuous annealing furnace for low-temperature grain-oriented silicon steel production. In terms of resistance to buildup formation and water, phosphate was not a good antioxidant for carbon sleeve. If new antioxidants with low phosphate or no phosphate will be developed in the future, it is feasible and effective to take some process control in technology or preventive measures to significantly decrease buildups formation and extend the service life of carbon sleeve.

References

1. He MS, Wang XK, Zhou WZ et al (2019) Effect of microstructure on resistance to buildups formation of carbon sleeves in continuous annealing furnace for silicon steel production. Characterization Miner Metals Mater 2019:351–359
2. He MS, Peng SJ, Xue GF et al (2015) Cause analysis on buildup formation of carbon sleeve in continuous annealing furnace for non-oriented silicon steel produced by CSP process. Characterization Miner Metals Mater 2015:587–593

Characterization of Arsenopyrite Depression During Collectorless Flotation

Arturo Navarro Pérez, Martín Reyes Pérez, Elia Palacios Beas, Iván A. Reyes Domínguez, Mizraim U. Flores Guerrero, Aislinn Michelle Teja Ruiz, Miguel Pérez Labra, Julio Cesar Juárez Tapia, and Francisco Raúl Barrientos Hernández

Abstract Arsenopyrite is a mineral present in most of the world's mineral deposits, and it pollutes both the environment and base metal concentrates. In this research work, the characterization of arsenopyrite depression was studied during collectorless flotation, in the presence of $Al_2(SO_4)_3$ and Na_2SiO_3 mixtures, in a slightly acidic environment. The arsenopyrite used in this work consists of a single mineralogical phase. The use of 0.1, 0.2, and 0.4 g/ton of the mixture, depresses the presence of this phase in the concentrate by 28% w/w. The percentage of cumulative collectorless flotation and without depressant reagents was 77% w/w, while in the presence of depressants $Al_2(SO_4)_3$ and Na_2SiO_3 it was 49% w/w. The pulp potential *Eh* (mV) referred to the standard hydrogen electrode, to achieve arsenopyrite depression is around $Eh + 50$ mV.

Keywords Arsenopyrite · Depression · Flotation · Collectorless · Arseniatos

A. N. Pérez (✉) · M. Reyes Pérez (✉) · A. M. T. Ruiz · M. Pérez Labra · J. C. J. Tapia · F. R. Barrientos Hernández
Autonomous University of the State of Hidalgo, Academic Area of Earth Sciences and Materials, Road Pachuca-Tulancingo Kilometer 4.5, 42180 Mineral de La Reforma, Hidalgo, México
e-mail: arturetiom@hotmail.com

M. Reyes Pérez
e-mail: mreyes@uaeh.edu.mx

E. P. Beas
National Polytechnic Institute Unit ESIQUIE, C.P. 07738 Mexico City, D.F, México

I. A. Reyes Domínguez
Institute of Metallurgy, Autonomous University of San Luis Potosí, 78210 San Luis Potosí, SLP, México

M. U. Flores Guerrero
Industrial Electromechanics Area, Technological University of Tulancingo, 43642 Hidalgo, México

J. Li et al., *Characterization of Minerals, Metals, and Materials 2021*,
The Minerals, Metals & Materials Series,
https://doi.org/10.1007/978-3-030-65493-1_25

Introduction

Arsenic is a toxic metal, linked to numerous types of cancer (skin, bladder, lung, among others) [1]. In many countries, including Mexico, the problem of groundwater contamination is relevant, it has to do with health public, due to the fact that the water obtained from the groundwater is practically used in daily life [2, 3]. Arsenopyrite (FeAsS) is a toxic arsenic sulfide, the presence of this mineral in the mineral concentrates of the base metals (Cu, Pb, Zn) has both economic and environmental repercussions.

The flotation separation of arsenopyrite from copper ores typically uses a mixture of sodium cyanide, lime, sodium hydrosulfide, sodium sulfite, and magnesium-ammonium [4–7]. However, there are some factors that limit the industrial applications of most of these depressants, and that is that they are not friendly to the environment, due to technical and profitability reasons.

Regarding the CN^- ion as a depressant of arsenopyrite [5], it is increasingly restricted due to its high toxicity, and its application will be prohibited [8]. Lime can also be used as a depressant, but generally requires large dosages [6]. The addition of large amounts of lime also reduces the rate of flotation and recovery of base metal sulphides, also increasing plant operating costs [9].

On the subject of arsenopyrite depression, several separation technologies have been proposed to produce high quality concentrates with low arsenic content. These include; modification of pulp pH [10], control of pulp potential [10, 11], as well as the development of new selective collectors or depressants [12, 13]. The technology to control the redox potential in the flotation has turned out to be the most successful factor [14]. Until now, the removal of the arsenic sulfide ore remains an area of opportunity as a research topic in the mineral processing industry. Thus, the flotation behavior of this type of arsenic and iron sulfurous mineral, arsenopyrite, has not been clearly studied and is currently the subject of arduous research.

In this research work, the effect of aluminum sulfate-sodium silicate mixtures on the depression of arsenopyrite during flotation without collector (without xanthate) will be studied. To characterize the activation-depression process of arsenopyrite, in all flotation tests, the behavior of physicochemical variables such as pH, oxide reduction potential (ORP) mV, which refers to the potential of the standard hydrogen electrode (SHE) and the electrical conductivity (K) $\mu S \cdot cm^{-1}$. Thermodynamics will be used with the help of the Pourbaix, *Eh–pH* diagrams, to establish the thermodynamic stability conditions of the different species contained in the flotation mineral pulp.

Experimental Methodology

To carry out the characterization of the depression or activation of arsenopyrite during flotation using mixtures of aluminum sulfate and sodium silicate, a pure arsenopyrite mineral from the mining region of Zimapan, Hidalgo, Mexico was used. The ore was first fragmented to a size of approximately 2 mm, later it was ground to <74 μm in a ball mill with a milling time of 20 min. The arsenopyrite mineral was previously characterized and reported [15].

Deionized water and analytical grade chemical reagents were used for all the experiments performed. To bring about the flotation tests, a 1 L laboratory Denver cell was used, the cell made of stainless steel, the impeller and diffuser made of polypropylene, the stirring speed of the impeller was 1200 revolutions per minute RPM, measured with a tachometer. The air injected into the cell to form the bubbles is sucked into the cell by the effect of the impeller movement.

During the pulp conditioning stage and at the end of the flotation, both the pH and the potential oxide reduction ORP (mV) were monitored in each addition of reagents (mV), these variables were measured with a potentiometer, Thermo Scientific Orion 3 Star brand equipped with a pH electrode, Ross ultra triode provided with a temperature sensor. The conditioning of the pulp was carried out inside the flotation cell.

Initially with only deionized water, the pH, ORP, and K were measured, later the frother agent 0.06 g·Ton^{-1} of methyl isobutyl carbinol MIBC was added, a conditioning time was given and the arsenopyrite mineral was added 4 grams, three minutes later the depressant reagents were added, first the aluminum sulfate $Al_2(SO_4)_3$, and at the end the sodium silicate Na_2SiO_3, it should be specified that both reagents are soluble in water, using different concentrations; 0.05, 0.1, 0.2, 0.4, and 0.6 g·Ton^{-1} of each one, this procedure was repeated for all the flotation experiments carried out.

After conditioning the pulp, the flotation test was started, collecting the concentrate spills in times of 0.5, 1, 2, 4, 6, 8, and 10 min in previously weighed plastic containers. At each arsenopyrite flotation time without a collector, the foam was helped to shed with an inert material accessory. The concentrates of each time were dried at room temperature and weighed, by weight difference, the mass of arsenopyrite floated in each float time was obtained, calculating the percentage of flotation achieved in each of the analyzed times.

Results

The results of the evaluation of the depressant effect of the mixture of aluminum sulfate and sodium silicate on the flotation of arsenopyrite at slightly acidic pH is shown in Fig. 1 which presents the% cumulative recovery of arsenopyrite as a function of time (minutes) for flotation tests without a collector, in the absence and presence of a mixture of aluminum sulfate $Al_2(SO_4)_3$ and sodium silicate Na_2SiO_3,

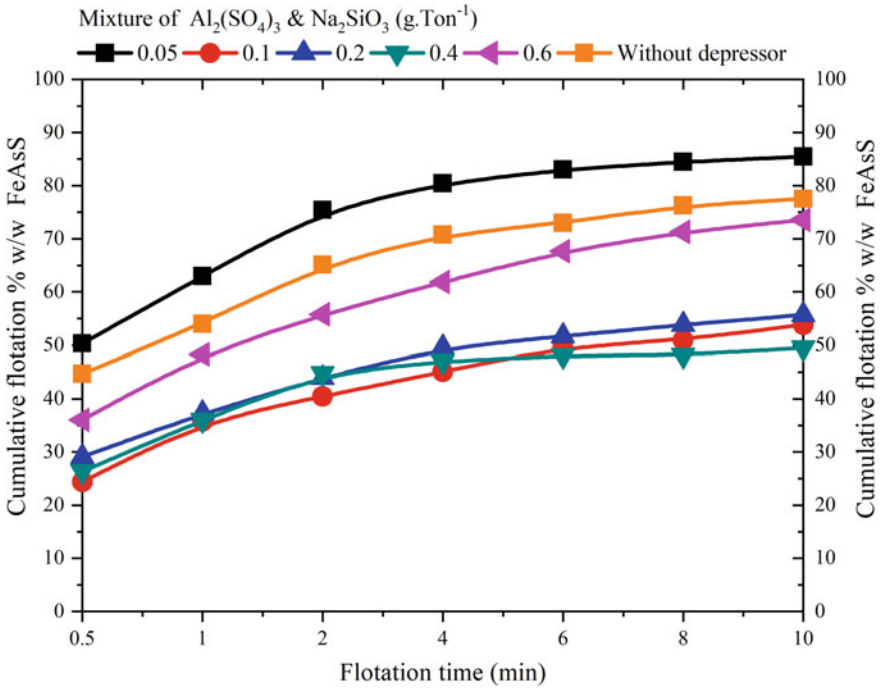

Fig. 1 % of cumulative recovery FeAsS versus flotation time. Using as depressant mixtures of $Al_2(SO_4)_3/Na_2SiO_3$. (Color figure online)

0.05, 0.1, 0.2, 0.4, and 0.6 g·Ton^{-1}, using 0.06 as frother agent g·Ton^{-1} of methyl isobutyl carbonyl MIBC.

Collectorless flotation was carried out at pH between 5.5 and 6.0. The choice of the concentration of the depressant reagents to be investigated was based on the fact of the typical concentrations of reagents used in other flotation tests, in this experimental part it began with 0.05 g·Ton^{-1}, and the value was doubled. of concentration until finding a turning point where the effect would be opposite to that of depression. The results of Fig. 1 show that the use of a concentration of 0.05 g·Ton^{-1}creates an activating effect of the arsenopyrite surface, under these conditions, the highest recoveries are achieved, in an accumulated float time of 10 min, with about 85% w/w float. This proportion of reagent activates the arsenopyrite surface, causing mineral surface rich in hydrophobic species, improving its flotation.

The best arsenopyrite depression conditions are achieved when the $Al_2(SO_4)_3/Na_2SiO_3$ mixture is 0.1, 0.2, and 0.4 g·Ton^{-1}, depressing the arsenopyrite by 28% w/w on average compared to the test of flotation without depressant reagent, tests carried out at a pH between 5.5 and 6. In addition, from Fig. 1 it is observed that the use of concentrations of depressant reagents of $Al_2(SO_4)_3/Na_2SiO_3$ of 0.1–0.4 g·Ton^{-1} in just four minutes, about 53% w/w arsenopyrite floats on average.

However, the expected depressant effect of the $Al_2(SO_4)_3/Na_2SiO_3$ mixture for the concentration of 0.6 g·Ton^{-1} is reversed and the arsenopyrite surface is activated reaching cumulative recoveries in ten minutes of flotation of 73% w/w. This clearly indicates that an excess of the proposed mixture inhibits the desired effect, so that the ideal concentration to achieve the greatest depression of arsenopyrite is between 0.1 and 0.4 g·Ton^{-1} of $Al_2(SO_4)_3/Na_2SiO_3$. Previously, it has been established that arsenopyrite depression occurs due to the formation of a layer of oxidation products on the surface of the mineral particles, both ferric hydroxide $Fe(OH)_3$ and arsenate-type species have been detected [16]. These oxidation products on the mineral surface are detrimental to flotation due to the high demand of the collecting reagent to achieve a satisfactory recovery of the metal sulfide [17].

During the study of the influence of the mixture of $Al_2(SO_4)_3$ and Na_2SiO_3 in the activation or depression of arsenopyrite, the conditions of the pulp chemistry pH, potential, and K were monitored, during the conditioning stage, at the beginning and at the end of the test. Figure 2 shows the behavior of the pH, it can be seen that the tendency of the pH is to decrease, the addition of aluminum sulfate gives an even more acid character to the pulp with pH values of around 3.7. In addition, the change in pH is observed during each of the pupal conditioning stages, the addition of sodium Na_2SiO_3 silicate increases the pH of the pulp.

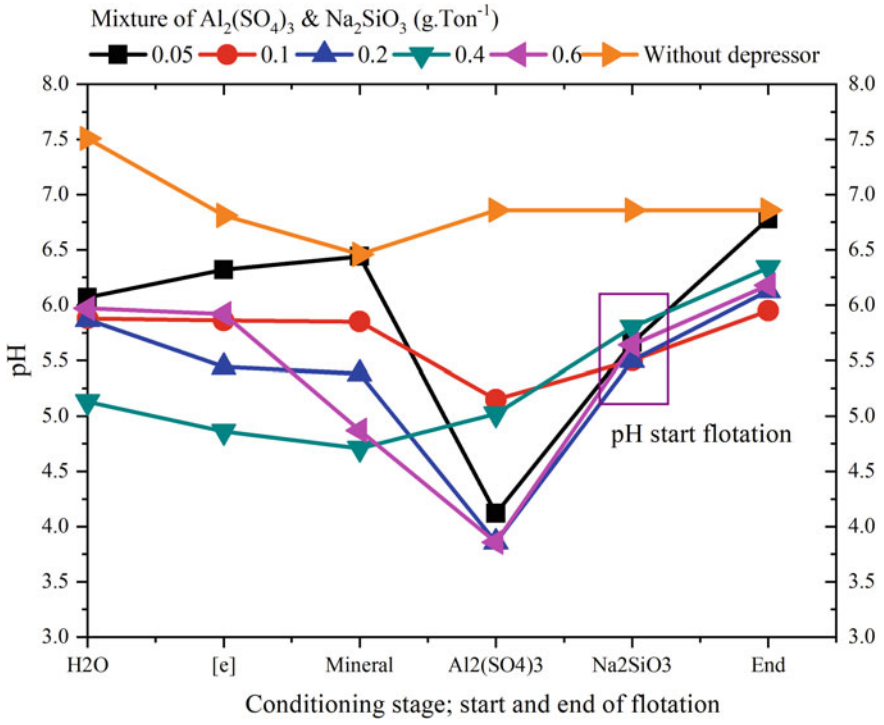

Fig. 2 Behavior of pH during the conditioning stage. Mixture of $Al_2(SO_4)_3/Na_2SiO_3$. (Color figure online)

A conditioning time of 3 min was given for each reagent addition. In this way, the starting pH of the flotation without arsenopyrite collector in the presence of different amounts of the $Al_2(SO_4)_3/Na_2SiO_3$ mixture is between 5.5 and 5.8. At the end of the flotation test, the concentration of hydrogen ions in the pulp decreases, that is, the pH tends to increase to values greater than 6.0. In the literature, it is mentioned that arsenopyrite exhibits good recovery by flotation in acidic environments and the recovery of arsenopyrite by flotation decreases rapidly at alkaline pH values [18], for this reason it was decided to test the reagent mixture in suitable flotation conditions of arsenopyrite.

It is expected that, in very alkaline environments, at a high pH value, the arsenopyrite surface is more easily oxidized, this oxidation process consists of Fe, As, and sulfur losing electrons from their last energy levels and by effect from the aqueous medium in which they are immersed, oxides, hydroxides, sulfates, oxy sulfates, oxyhydroxides among others are formed, and these oxidation products formed prevent the chemisorption of the flotation collectors on the mineral particles in this particular case of investigation the molecules of frother.

The variation of the pH previously presented will consequently cause changes in the oxidation reduction potential (ORP) mV referred to the standard hydrogen electrode (SHE) mV. The potential is a measure of the tendency of the solution to either gain or lose electrons when it is subject to change by the introduction of a new species. With a more positive potential, chemical species have a greater affinity to acquire electrons and therefore to be reduced.

The detection of changes in the redox potential of the pulp indicates changes in the surface composition of the arsenopyrite mineral particles and this surface modification can then be explained by the variation of the oxide reduction potential. Due to the difficulty of accurately measuring absolute potentials, potentials are defined in reference to the standard hydrogen electrode (SHE) mV [19].

Figure 3 shows the potential measurements, plotted with reference to the standard hydrogen electrode. Positive potentials are observed, that is, the species present tend to lose electrons, both when arsenopyrite is depressed and when there is a good response to flotation, the potentials are strongly oxidizing. The values of the potential oxide reduction referred to the standard hydrogen electrode are represented in Fig. 4 which shows in the diagram Eh–pH of the As–Fe–S–H_2O system, under saturated conditions of 1 M the species formed is iron arsenate product of the oxidation of arsenopyrite.

In the literature it has been established that many sulfides do not present natural flotation; however, collectorless flotation can be achieved based on a specific potential range [20]. For this experimental work, collectorless flotation and using 0.06 g·Ton^{-1} as frother agent methyl isobutyl carbinol MIBC, it is carried out at oxidative potentials of around +250 mV measured with reference to the standard hydrogen electrode. Even under moderately oxidizing conditions of pulp potential around +50 mV, around 50% cumulative flotation of arsenopyrite is achieved in the presence of depressants. In collectorless sulfide flotation studies using sodium sulfide as a reagent, the

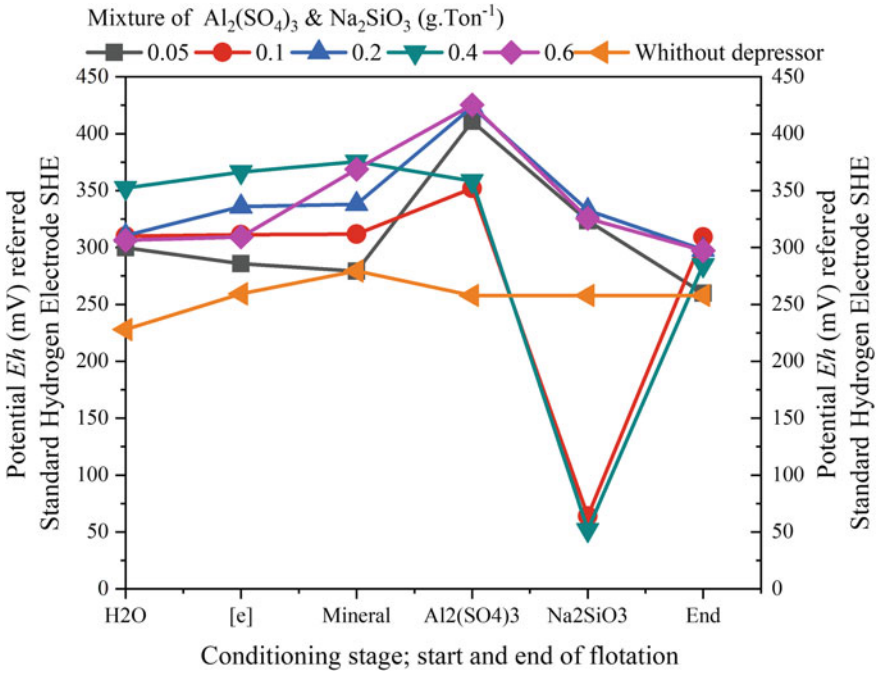

Fig. 3 Potential oxide reduction referred to the Standard Hydrogen Electrode (mV) versus the conditioning stage. Using the mixture as a depressant $Al_2(SO4)_3/Na_2SiO_3$. (Color figure online)

pulp potential decreases, and the species flotation is not carried out and is only achieved when the pulp potential reaches a positive value [20].

However, in some investigations it has been found that freshly ground arsenopyrite surfaces do not float in the absence of a collector, despite the presence of potential oxidants [20]. Figure 4 implies that the *Eh–pH* zone of the flotation without arsenopyrite collector is within the area that forms meta arsenate iron $Fe_3(AsO4)_2$, in addition, it shows that arsenopyrite is stable in aqueous environments where it is a negative reducing potential and decomposes in environments with oxidizing potentials.

On the other hand, the addition of both aluminum sulfate and sodium silicate change the electrical environment of the pulp, due to the addition of conductive ions. Figure 5 shows the changes in the electrical conductivity of the pulp during the conditioning stage, it is to be expected, the increase in electrical conductivity K (μs/cm) at a higher concentration of $Al_2\ (SO_4)_3$, as observed in the Fig. 5.

The addition of sodium silicate contributes to the increase in conductivity. In this way, the depression of arsenopyrite is accompanied by a decrease in the electrical conductivity of the pulp solution at the end of the flotation, it should be mentioned that this decrease is attributed to the reaction of ions with the surface of the arsenopyrite,

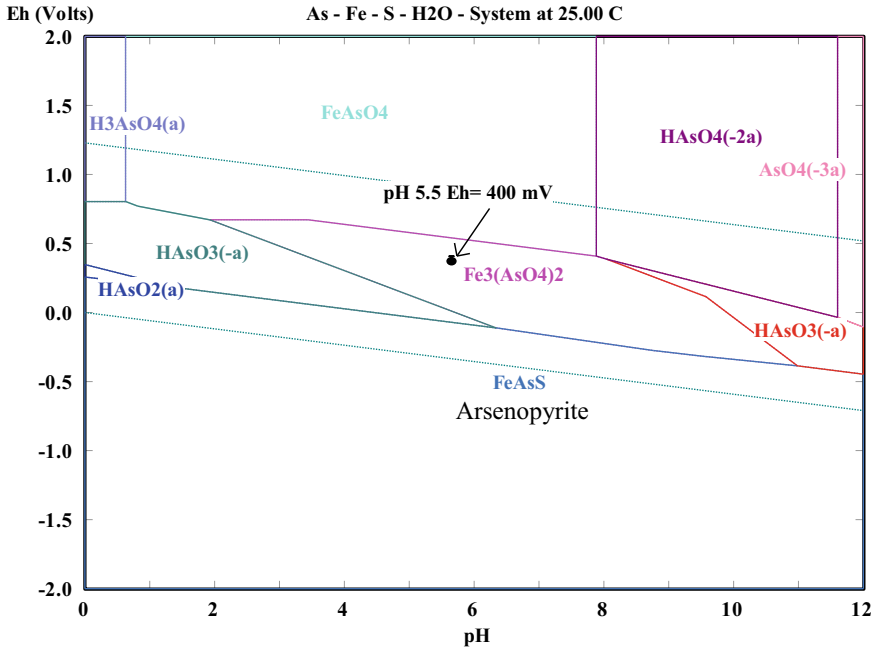

Fig. 4 Diagram of Pourbaix Eh–pH system As–Fe–S–H_2O at 25 °C and 1 M. (Color figure online)

taking conduct precipitation reactions of these ions of aluminum sulfate and sodium silicate.

Conclusions

The mixture of 0.1–0.4 g·Ton^{-1} of $Al_2(SO_4)_3$/Na_2SiO_3 depresses the flotation of arsenopyrite by 28% w/w with respect to the flotation without a collector in the absence of depressant reagents. The cumulative percentage of flotation in the absence and presence of depressants was 77% w/w and 49% w/w, respectively. An excess of the mixture 0.6 g·Ton^{-1} has an opposite effect to the depression of arsenopyrite. The pulp potential of around +50 mV provides the conditions for the depression of arsenopyrite to occur through the formation of hydrophilic species such as that detected in the *Eh–pH* $Fe_3(AsO4)_2$ diagram.

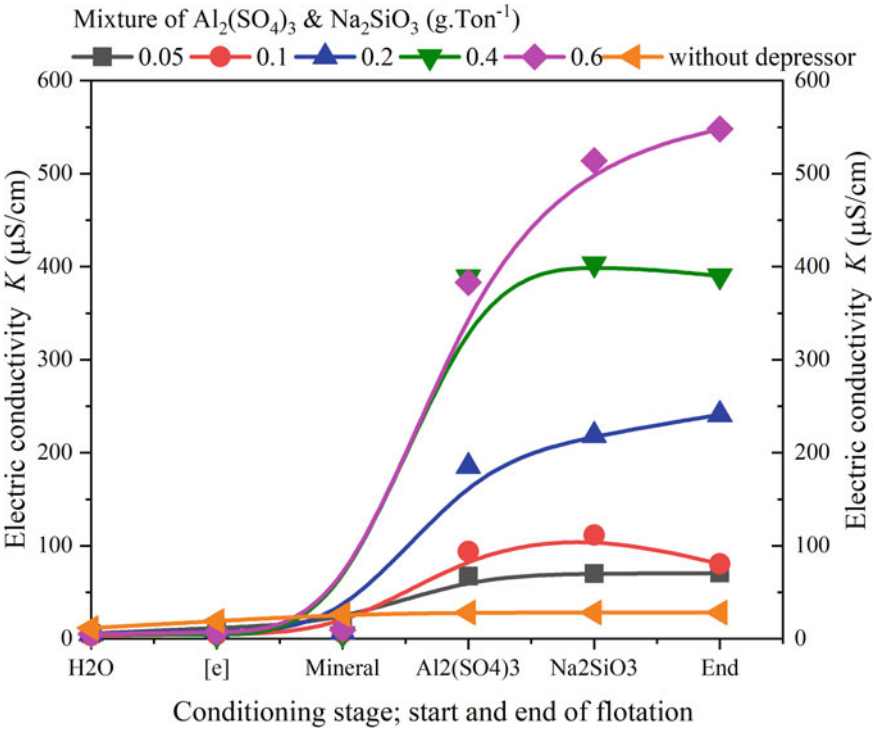

Fig. 5 Electric conductivity K ($\mu S \cdot cm^{-1}$) versus the conditioning stage. (Color figure online)

Acknowledgements To the Autonomous University of the State of Hidalgo, to the PRODEP Teacher Professional Development Program, and to the National Polytechnic Institute ESIQUIE.

References

1. Goncalves KLC, Andrade VLL, Peres AEC (2007) Minerals engineering, vol 16, pp 1213–1216
2. Wei Y, Sandenbergh RF (2007) Minerals engineering, vol 20, pp 264–272
3. Rao SR, Moon KS, Leja J, Fuerstenau MC (eds) (1976) Flotation: A.M. Gaudin memorial volume, vol 1. AIME, New York, pp 509–527
4. Smith LK, Bruckard WJ (2007) The separation of arsenic from copper in a north parkes copper–gold ore using controlled-potential flotation. Int J Miner Process 84:15–24
5. You KS, Kim HS, Ahn JW, Lee S (2013) Arsenic rejection from lead concentrate using aluminosulfate. Int J Miner Process 125:118–121
6. Matveeva TN, Gromova NK, Lantsova LB (2018) Effect of tannin on compound collector adsorption and stibnite and arsenopyrite flotation from complex ore. J Min Sci 53:1108–1115
7. Tapley B, Yan D (2003) The selective flotation of arsenopyrite from pyrite. Miner Eng 16:1217–1220
8. Lopez Valdivieso A, Orozco L (1994) The flotation column to control arsenic, zinc and insoluble in lead concentrates. In: Geomimet XXI Epoca, vol 187, pp 33–45

9. Mu Y, Peng Y, Lauten RA (2016) The depression of pyrite in selective flotation by different reagent systems—a literature review. Miner Eng 96–97:143–156
10. López Valdivieso A, Sánchez López AA, Ojeda Escamilla C, Fuerstenau MC (2006) Flotation and depression control of arsenopyrite through pH and pulp redox potential using xanthate as the collector. Int J Miner Process 81:27–34
11. Bruckard WJ, Kyriakidis I, Woodcock JT (2007) The flotation of metallic arsenic as a function of pH and pulp potential—a single mineral study. Int J Miner Process 84:25–32
12. Sirkeci AA (2010) The flotation separation of pyrite from arsenopyrite using hexyl thioethylamine as collector. Int J Miner Process 60:263–276
13. Chen J, Chen Y, Wei Z, Liu F (2010) Bulk flotation of auriferous pyrite and arsenopyrite by using tertiary dodecyl mercaptan as collector in weak alkaline pulp. Miner Eng 23:1070–1072
14. Chimonyo W, Corin KC, Wiese JG, O'Connor CT (2017) Redox potential control during flotation of a sulphide mineral ore. Miner Eng 110:57–64
15. Martín Reyes P, Ricardo A, García E, Elia Palacios B, Miguel Pérez L (2017) Arsenopirita un mineral potencialmente tóxico: caracterización. Tópicos de investigación en ciencias de la tierra y materiales, vol 4 Ed. AACTyM Universidad Autónoma del Estado de Hidalgo
16. Lin Shangyong, Liu Runqing, Yongjie Bu, Wang Chen, Wang Li, Sun Wei, Yuehua Hu (2018) Oxidative depression of arsenopyrite by using calcium hypochlorite and sodium humate. Minerals 8:463
17. Monte MBM, Dutra AJB, Albuquerque JCRF, Tondo LA, Lins FF (2002) The influence of the oxidation state of pyrite and arsenopyrite on the flotation of an auriferous sulphide ore. Miner Eng 15(12):1113–1120
18. Li Yu, Liu Quanjun, Li Shimei, Deng Jiushuai, Luo Bin, Lai Hao (2019) Depression mechanism involving Fe3 + during arsenopyrite flotation. Sep Purif Technol 222:109–116
19. Stumm W, Morgan JJ (1981) Aquatic chemistry, 2nd edn. John Wiley & Sons, New York
20. Yuehua H, Wei S, Dianzuo W (2009) Electrochemistry of flotation of sulphide minerals. Tsinghua University Press, Beijing

Chemical, Physical, and Morphological Characterization of Eco-Clinker Produced from Industrial Wastes

A. L. Oliveira, L. Pedroti, G. Brigolini, J. M. F. de Carvalho, J. C. L. Ribeiro, C. M. M. de Souza, M. Altoé, A. C. P. Martins, W. Fernandes, B. C. Mendes, C. M. Torres, G. E. S. de Lima, and M. M. S. Lopes

Abstract To mitigate the low environmental performance of civil construction, researchers began to study the incorporation of waste from other industries in construction materials. The aim of this research was to produce and characterize an eco-clinker from the reuse of grits residues (produced at cellulose manufacturing process), granite residues (produced during the processing of ornamental rocks). To produce the eco-clinker, three mixtures were formulated considering the parameters of lime saturation factor (LSF), calculation of the Bogue potential, silica ratio (SR), and alumina ratio (AR). The pellets were burnt at a temperature of 1450 ºC for 20 min and then, the mixtures were characterized. The eco-clinker produced presents large amounts of C2S-β. The mechanical properties in the early ages were out of date. At older ages the mechanical strength of the eco-clinkers can be compared with the mechanical strength of conventional cements.

Keywords Grits waste · Granite waste · Eco-clinker

Introduction

The concern about climate changes, global warming and the pollution increase has made it essential to create green policies for sustainable development. In contrast, in the civil construction, the technological process of cement production releases a large amounts of CO_2 to the atmosphere, being responsible for 5–7% of the total of CO_2 launched in the world [1–3].

A. L. Oliveira (✉) · L. Pedroti · J. M. F. de Carvalho · J. C. L. Ribeiro · C. M. M. de Souza · A. C. P. Martins · W. Fernandes · B. C. Mendes · C. M. Torres · G. E. S. de Lima · M. M. S. Lopes
DEC – Civil Engineering Department, UFV – Federal University of Viçosa, Peter Henry Rolfs Avenue, Viçosa, Minas Gerais 36570-900, Brazil
e-mail: andre.l.junior@ufv.br

G. Brigolini · M. Altoé
DEC – Civil Engineering Department, UFV – Federal University of Ouro Preto, Morro Do Cruzeiro Campus, Ouro Preto, Minas Gerais 35400-000, Brazil

J. Li et al., *Characterization of Minerals, Metals, and Materials 2021*,
The Minerals, Metals & Materials Series,
https://doi.org/10.1007/978-3-030-65493-1_26

Several studies claim that the most efficient way to the construction industry to become a sustainable activity is to incorporate waste from other industries into construction materials. Incorporating waste into construction materials is a highly effective strategy to minimize environmental impacts such as reducing the use of natural resources, saving energy in production, and recovering water resources [4]. The large generation and inadequate disposal of industrial waste, whose production is growing and whose impacts are diverse and potentially dangerous for the human community [5].

In recent years, Brazil has stood out in the group of major world producers and exporters in the ornamental rocks. Among the Brazilian states, Espírito Santo stands out as the main mining and processing pole for ornamental rocks, with emphasis on granite [6]. This implies a great concern with the waste generated in this industrial sector, since the quantity is extremely significant and there is still no detailed study of all the impacts that this waste can cause when released directly into the environment [7].

Additionally, the pulp and paper mills industry is one of the most promising business areas in the country, with an increase in production year after year. According to the Indústria Brasileira das Árvores (Brazilian Tree Industry, in English) [8], Brazil is one of the largest pulp producers in the world, producing about 20,000 tons per year. This is due to the Brazilian tropical climate, in addition to the use of biotechnology and advances in forest technology, which favor Brazilian productivity. The grits waste is produced in large quantity from the production of cellulose by the *kraft* process, industrial solid waste, Class II A that does not present adequate deposition [9].

These two residues (grits and granite residue) are rich in calcium carbonate ($CaCO_3$) and silica (SiO_2) respectively, and can replace limestone and clay commonly used in the production of clinker. The raw materials commonly used in the production of the main component of Portland cement (clinker) are high purity limestone (CaCO3) and clay (SiO_2, Al_2O_3 and Fe_2O_3). Corrective materials are also commonly used to adjust the contents of SiO_2, Al_2O_3 and Fe_2O_3 [10, 11].

This research aims to produce an ecological clinker from grits residues generated in the production of cellulose and granite residue generated in the processing of ornamental rocks. The Bogue method (1929) was used to obtain the composition of the clinker phases produced. Ritvield refinement was used to perform the validation of the results, which is a robust technique for the quantitative analysis of mineral phases, through X-ray diffraction. With the use of the above mentioned waste it is possible to take advantage of much of the material that is currently disposed of in inappropriate places, giving them a new use in civil construction.

Materials and Methods

Characterization of Raw Materials

Is this research the grits and granite residue were used to produce an eco-clinker. The collection of grits was made in CENIBRA—Celulose Nipo-Brasileira located in the city of Belo Oriente, Minas Gerais, Brazil (19.314181, −42.397282) and the granite residue was supplied by Decolores Mármores e Granitos do Brasil, located in the city of Cachoeiro de Itapemirim, Espírito Santo, Brazil (−20.867655, −41.019633).

The preparation of raw materials was divided into the following steps: air drying in the courtyard of the Construction Materials Laboratory of the Federal University of Viçosa and later in the kiln to ensure complete removal of moisture; grinding in the Abrasion Los Angeles mill; those that were underwent to the next step, also passed in the ball mill, to facilitate the sifting process; sifting: the materials which were submitted to the ball mill were subsequently screened through on a 0.074 mm mesh sieve (200 mesh).

The chemical analysis of raw materials was made by X-ray Fluorescence (XRF) in the X-ray Laboratory of Civil Engineer of the Federal University of Ouro Preto using Epsilon 3× equipment, Panalytical. The mineralogical analysis was made by X-ray Diffraction (XRD) using the D8-Discover diffractometer with Co-Kα (λ = 1,789 Å) radiation.

Preparation of Eco-Clinker: Formulation and Production

For this research, five mixtures using grits and granite residues were produced. The formulations were produced taking into account the amount of C_3S, C_2S, C_3A and C_4AF required, seeking to maximize the amounts of C_3S (variations between 35 and 60%) and smaller amounts of C_2S (variations between 20 and 30%). The formulations of the clinker compositions were performed using the parameters of lime saturation factor (Eq. 1), calculation of the Bogue potential (Eqs. 2, 3, 4 and 5), silica ratio (Eq. 6) and alumina ratio (Eq. 7).

$$\mathrm{LSF} = \frac{\mathrm{CaO}}{2,8\mathrm{SiO_2} + 1,2\mathrm{Al_2O_3} + 0,65\mathrm{Fe_2O_3}} \tag{1}$$

$$\mathrm{C_3S} = 4,07\mathrm{CaO} - 7,60\mathrm{SiO_2} - 6,72\mathrm{Al_2O_3} - 1,43\mathrm{Fe_2O_3} - 2,85\mathrm{SO_3} \tag{2}$$

$$\mathrm{C_2S} = 2,867\mathrm{SiO_2} - 0,754\mathrm{C_3S} \tag{3}$$

$$\mathrm{C_3A} = 2,650\mathrm{Al_2O_3} - 1,692\mathrm{Fe_2O_3} \tag{4}$$

Fig. 1 Molded pellets with diameter of 1–2 cm. (Color figure online)

$$C_4AF = 3,043Fe_2O_3 \tag{5}$$

$$SR = \frac{SiO_2}{Al_2O_3 + Fe_2O_3} \tag{6}$$

$$AR = \frac{Al_2O_3}{Fe_2O_3} \tag{7}$$

Based on the methodology proposed by Costa et al. [12], was added water in the raw mixtures, and hand-molded pellets with diameter of 1–2 cm (Fig. 1). The pellets were then kept in a kiln at 100 ± 5°C for at least 24 h, then be inserted into the furnace. The mixtures were burnt at a temperature of 1,450 ºC for 20 min. After burning, the pellets were cooled with compressed air until they reached room temperature. In order to obtain the eco-clinker, the cooled material was comminuted in a ball mill for a period of 30 min and passed through the 200 mesh opening sieve for subsequent performance of characterization tests of the material produced.

Characterization of the Produced Eco-Clinker

Table 1 shows if the physical tests performed based on current Brazilian standards. The eco-clinker produced was characterized in terms of its chemical, mineralogical and physical composition.

X-ray fluorescence (XRF) and X-ray diffraction (XRD) tests were performed on the five mixtures produced (M1, M2, M3, M4 and M5). The XRF and XRD tests were performed using the same configurations described in 2.1. For the quantification of the

Table 1 Physical tests performed on the produced eco-clinker

Tests	Reference	Description
Fineness	[14]	By the air permeability method (Blaine method)
Specific mass	[15]	Test performed using the Le Chatelier bottle
Residue on sieve #200	[16]	Test using sieve set #200
Setting time	[17]	Setting time using Vicat apparatus
Expansibility	[18]	Test using the Le Chatelier needles
Compressive strength	[19]	Compressive strength performed in specimens in reduced model (Ø 35 × 35 mm) applying correction factor of 0.87 according to ASTM C 42-04.

phases and amorphicity, 20% by weight of zincite (ZnO) was added to the samples and the Rietveld method was used in same software, using the ICSD (Inorganic Crystal Structure Database) database [13]. The samples were prepared using the backload method to avoid preferential orientation of the crystalline material.

Results and Discussion

Chemical and Mineralogical Analysis of Raw Materials

The results of the chemical analysis of the raw materials are shown in Table 2 and the main mineralogical phases observed in the XRD diffractograms are shown in Fig. 2.

Through the results of the X-ray fluorescence test (XRF) presented in Table 2 it was possible to observe that the grits have a large amount of calcium oxide (CaO) and minor amounts of SiO_2, Al_2O_3, Fe_2O_3 and SO_3. The granite residue has a large amount of silicon dioxide (SiO_2). The grits residue presents 53.8% of CaO in the form of calcite ($CaCO_3$), a result corroborated by XRD analysis (Fig. 2) and also by data reported in the literature [20–22]. Granite residue presents large amounts of SiO_2 (72.1%), replacing clay in cement, in addition to minority amounts of Al_2O_3 (14.1%), K_2O (4.3%) and Na_2O (4.6%). According to the mineralogical characterization obtained through XRD analysis (Fig. 2), it was found that the granite residue presents more intense peaks of quartz (SiO_2) and albita ($NaAlSi_3O_8$) and low-intense peaks of muscovite ($KAl_2Si_3AlO_{10}(OH,F)_2$).

Table 2 Chemical composition of raw materials

Materials	Compounds (%)					
	CaO	SiO_2	Al_2O_3	Fe_2O_3	SO_3	LOI
Grits	53.8	1.0	0.5	0.2	0.6	42.8
Granite	1.9	72.1	14.1	0.5	0.0	1.5

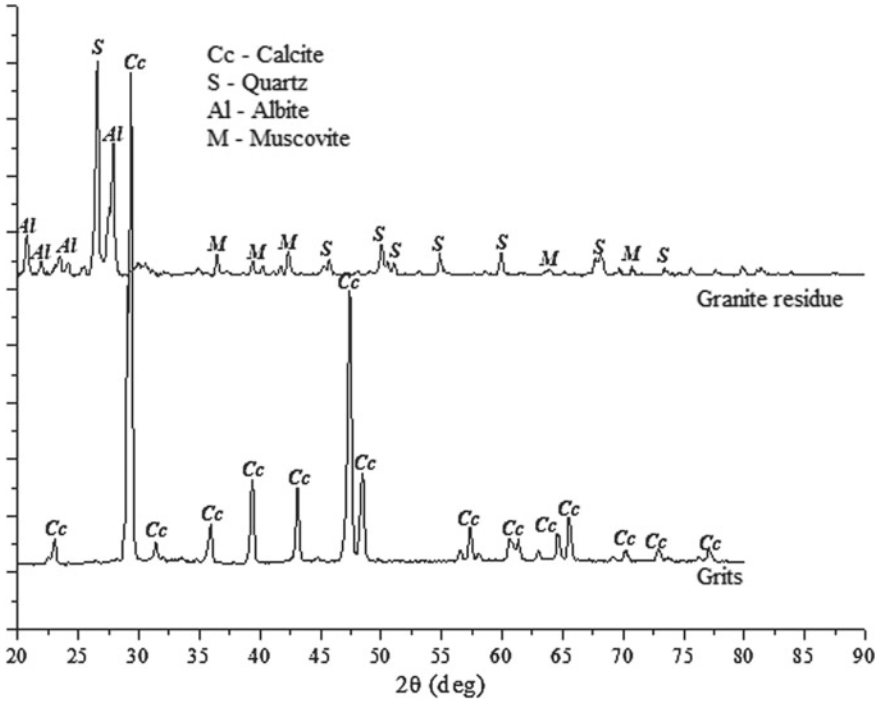

Fig. 2 Result of XRD analysis of granite residue and grits residue

Mixtures Formulation

The list of mixtures to be made (M1, M2, M3, M4 and M5) using the chemical characterization of raw materials (Table 2), Bogue's Equations, silica ratio (SR) and alumina ratio (AR) modules, and lime saturation factor (LSF) are shown in Table 3.

For the production of the five mixtures the proportion of grits residue ranged between 81% and 77%. The residue was used in large quantity because it is the source

Table 3 Mixtures to be made in the preparation of the eco-clinker

Mixtures	Residue (%)		Bogue Equation estimation				LSF	AR	SR
	Grits	Granite	C_3S	C_2S	C_3A	C_4AF			
1	81.0	19.0	77.71	4.68	6.60	2.54	100.4	3.63	5.72
2	80.0	20.0	68.77	13.25	6.92	2.59	96.3	3.71	5.67
3	79.0	21.0	59.84	21.82	7.24	2.64	92.5	3.79	5.63
4	78.0	22.0	50.90	30.40	7.55	2.69	88.9	3.87	5.58
5	77.0	23.0	41.97	38.97	7.87	2.74	85.4	3.94	5.54
Recommended							92–98	1–4	2–3

of CaO in the mixture, the main oxide present in conventional Portland clinker. The proportion of granite residue varied between 19 and 23%. Its chemical composition obtained by FRX demonstrated large amounts of SiO_2 and Al_2O_3, important oxides in the formation of C_2S, C_3S, C3A and C_4AF.

The proportion of phases estimated by Bogue are also presented in Table 3. The amount of C_3S ranged from 41.97 to 77.71% while the proportion of C_2S ranged from 38.97 to 4.68%. In addition, it was possible to estimate LSF, AR and MR. The recommended LSF values are between 92 and 98%. According to the mixtures produced, the results of this parameter are between 85.4 and 100.4%. The alumina ratio (AR) parameters are all within the recommended range while the results presented for the silica ratio (SR) showed results above the recommended ones.

Eco-Clinker Characterization

Chemical Characterization

The chemical composition (oxides) effective found through FRX analysis in the five mixtures produced is presented in Table 4.

By observing the results presented in Table 4, it is possible to notice little discrepancy between the percentages of the oxides analyzed. The mixture containing 81% grits and 19% granite residue showed a higher amount of calcium oxide (CaO) since the source of this oxide comes from the grits residue. However, the other mixtures also presented satisfactory amounts of CaO, which ranged from 57.68 to 62.23%. As for quartz (SiO_2), the percentages varied between 24.98 and 28.62%. According to Petrucci [23], Neville [24] and Taylor [25] the ideal amount of quartz for the production of a conventional clinker ranges from 20 to 25%. Minority amounts of Al_2O_3 and Fe_2O_3 were also observed. Al_2O_3 ranged from 6.67 to 7.39% and Fe_2O_3 ranged from 1.73 to 4.34%. The amount of Fe_2O_3 was not satisfactory due to the low amount of this oxide in the raw materials, as shown in Table 2.

To study the composition of phases of the five mixtures formulated, the Rietveld method was applied to quantify the present phases. The quantifications performed

Table 4 Chemical characterization of the five mixtures produced

Materials	Compounds (%)				
	CaO	SiO_2	AL_2O_3	Fe_2O_3	SO_3
81% Grits + 19% Granite	62.23	24.98	6.67	2.41	0.17
80% Grits + 20% Granite	60.74	25.04	7.39	4.34	0.15
79% Grits + 21% Granite	59.12	27.79	6.74	2.23	0.16
79% Grits + 22% Granite	57.68	28.62	6.98	1.84	0.24
77% Grits + 23% Granite	57.71	28.11	7.12	1.73	0.24

Table 5 Estimation of the phases performed by bogue equations and quantification of mineralogical phases by XRD and Rietveld method

Mixture	C_2S		C_3S		C_3A		C_4AF	
	Estimated (%)	Effective (%)	Estimated (%)	Effective (%)	Estimated (%)	Effective (%)	Estimated (%)	Effective (%)
M1	4.68	24.34	77.71	28.45	6.60	4.45	2.54	2.59
M2	13.25	26.6	68.77	19.45	6.69	5.87	2.59	4.47
M3	21.82	29.1	59.84	11.91	7.24	4.12	2.64	3.78
M4	30.40	30.15	50.90	7.91	7.55	1.07	2.69	8.64
M5	38.97	40.7	41.97	4.37	7.87	3.31	2.74	3.10

by XRD and Rietveld's method and the estimates made by Bogue equations of the four phases are presented in Table 5.

Among the results presented in Table 5, the quantifications of the phases showed great variation in all mixtures when compared to the results estimated by Bogue. It was possible to observe a large amount of C2S formed (ranging from 24.34 to 40.7%), a discrepant result of the values estimated by Bogue (between 4.68 and 38.97%). The large discrepancy also occurs in the formation of C3S, since the amount estimated by Bogue is not formed. As a consequence, the mechanical resistance in the first of the eco-clinkers produced is lame, considering that C2S presents low reactivity due to its high thermodynamic stability and dense structure that hinders hydration [26, 27].

Mineralogical Characterization

The mineralogical analysis performed in the five mixtures produced (M1, M2, M3, M4 and M5) is presented in Table 6 that informs the results obtained in the diphratograms. A total of 20% ZnO was used as an internal standard. A total of 20% ZnO was used as an internal standard. In the diffractograms are observed phase peaks normally found in clinker (i.e. larnite, brownmillerite, hatrurite).

In the table presented it is possible to notice that all the mixtures produced contain amounts of C_2S-β (crystalline structure similar to the structure of the larnite mineral),

Table 6 Minerals found in each of the mixtures by X-ray diffraction (XRD) analyses

Mixture	Mineral found
M1	Larnite, hatrurite, goethite, brownmillerite
M2	Larnite, hatrurite, gothite, gehlenite, mayneite, brownmillerite
M3	Larnite, hatrurite, brownmillerite
M4	Larnite, hatrurite, goethite, brownmillerite, magnetite
M5	Larnite, hatrurite, mayenite, magnetite, brownmillerite

Table 7 Physical and mechanical properties of the five mixtures produced and normative results for conventional clinkers according to Brazilian standards

Tests	Values recommended by Brazilian standards	M1	M2	M3	M4	M5
Fineness (cm^2/g)	≥3000	3870	3641	3204	3057	2974
Residue in the #200 (%)	≤6,0	2.87	3.12	1.03	2.26	2.98
Specific Mass (g/cm^3)	–	3.15	3.17	3.02	3.1	3.12
Initial setting time (h:min)	≥1:00	1:20	1:18	1:45	2:00	2:15
Final setting time (h:min)	≤12:00	2:45	3:30	3:15	3:30	3:45
Expansibility (mm)	≤5,0	0.0	0.0	0.0	0.0	0.0
Compressive strength at 28 days (MPa)	(≥25,0; ≥32,0; ≥45,0)	7.5	8.3	6.2	3.1	4.8

results different from the results calculated by the mathematical model proposed by Bogue. The main peaks of C_2S-β observed in the mixtures are between angles 31.8º–32.7º (2θ) and at angles 41.2º and 47.6º (2θ). Proportions can also be observed in the C_3S-T phase (crystalline structure similar to the structure of the hatrurite mineral). The main peak of C_3S for the mixtures analyzed by XRD is at the angle 29.64° (2θ). The cooling rate, oven temperature, and presence of mineralizing crystals (such as Mg2+ and K+) are crucial for the stabilization of this phase [25, 28]. Minority phases such as C_4AF and C_3A are also observed in diffractograms. All diffractograms showed main peaks of the C_4AF phase (brownmillerite).

Physical and Mechanical Characterization

Results obtained for the physical and mechanical characterization of the five mixtures produced are presented in Table 7. For comparative purposes, Table 7 also presents normative values for commercial clinkers according to Brazilian standards.

The results presented in Table 7 show that the fineness of the eco-clinkers produced ranged from 2974 cm^2/g to 3870 cm^2/g, demonstrating that the grinding of the eco-clinker was performed efficiently. The specific mass of the eco-clinker ranged from 3.02 g/cm^3 to 3.17 g/cm^3. This variation occurred due to the different specific masses (ρ) of the minerals found in the mixtures. In M1, 28.45% of larnite was quantified, which presents $\rho = 3.28$ g/cm^3 and minority amounts of brownmillerite and hatrurite, which present $\rho = 3.76$ g/cm^3 and 3.02 g/cm^3, respectively.

The initial and final settings time of the eco-clinker was also studied. The final handle time recommended by Table 7 refers to the longer catch time reported by Brazilian standards. When analyzing Table 7, it is observed that the initial setting time of the eco-clinker varied between 1 h 18 min and 2 h 15 min (M2 and M5, respectively) and the final pick time varied between 2 h 45 min and 3 h 45 min (M1 and M5, respectively). The M1 mixture showed shorter start and end time of handle.

Because there are higher amounts of alite, the hydration reaction occurs more quickly when compared to the other mixtures [30, 31].

Mechanical strength was also studied through the compressive strength assay at the ages of 28 days. The resistance acquired at established age showed a lower result when compared to results commonly obtained for Portland cement. This is due to the large amount of β-C2S and a small amount of C3S-T, considering that the hydration of β-C2S is slower due to the chemical arrangement complex, making it impossible to penetrate water and, consequently, resulting in a late hydration [32, 33].

Conclusions

In this research, the possibility of formulating and producing an eco-clinker was studied exclusively through recycled raw material. The grits residue from the kraft process in the production of cellulose and the granite residue from the cutting and processing of ornamental rocks were used. Specific conclusions were obtained at the end of this study:

- The grits residue is rich in CaO (53.8%) in the form of CaCO3, being responsible for the replacement of limestone in the production of conventional clinker. Granite waste is responsible for silica.
- The estimates of the phases for the three mixtures performed using the Bogue method showed considerable deviations when compared with effective results by X-ray diffraction.
- The quantification of oxides obtained by X-ray fluorescence for the three mixtures produced showed satisfactory results. All three mixtures presented amounts of oxides within the specifications established by several authors.
- The mineralogy of the mixtures is basically composed of larnite, hatrurita, goethite, brownmillerite, and mayenite.
- The high fineness and phase composition of the mixtures contributes to the fast initial setting time. Mixtures with higher amounts of alita (C3S) and alumina (C3A) showed faster catch time and mixtures with lower proportions of these phases showed slower pick-up.

Acknowledgements This work was carried out with the support of the Coordination for the Improvement of Higher Education Personnel - Brazil (CAPES) - Financing Code 001.

References

1. Ali MB, Hossain MS (2011) A review on emission analysis in cement industries. Renew Sustain Energy Rev 15:2252–2261
2. Iacobescu RI, Angelopoulos GN, Jones PT, Blanpain B, Pontikes Y (2016) Ladle metallurgy stainless steel slag as a raw material in Ordinary Portland Cement production: a possibility for industrial symbiosis. J Clean Prod 112(1):872–881
3. Kajaste R, Hurme M (2016) Cement industry greenhouse gas emissions e management options and abatement cost. J Clean Prod 112:4041–4052
4. Kubba S (2017) Handbook of Green Building Design and Construction. United Kingdom: © Butterworth-Heinemann
5. Simão L, Jiusti J, Lóh NJ, Hotza D, Raupp-Pereira F, Labrincha JA, Montedo RK (2017) Waste-containing clinkers: Valorization of alternative mineral sources from pulp and paper mills. Process Saf Environ Prot 109:106–116
6. Abirochas–Associação Brasileira da Indústria de Rochas Ornamentais (2017) Balanço das Exportações e Importações Brasileiras de Rochas Ornamentais em 2017. Disponível em: http://abirochas.com.br/wp-content/uploads/2018/03/Informe-01-2018-Balanco-2017.pdf. Acesso em 06 de september de 2020
7. Sardou Filho R, Matos GMM, Mendes VA, Iza ERHF (2013) Atlas de rochas ornamentais do estado do Espírito Santo. Brasília
8. IBÁ–Indústria Brasileira de Árvores. Dados Estatísticos (2017) Disponível em: https://www.iba.org/dados-estatisticos. Acesso em 29 de novembro de 2018
9. Souza TI, Cardoso AV (2014) Utilização De Resíduos Sólidos Da Indústria De Celulose Kraft Na Fabricação De Cimento: Caracterização Físico-Química, 18º CBECiMat-Brazilian Congress of Engineering and Materials Science, 24–28 November 2014, Porto de Galinhas, PE, Brazil
10. Battagin AF (2011) Cimento Portland. In: IBRACON Concreto Ciência e Tecnologia, Cap. 6. 1st ed., vol 1. Arte Interativa, São Paulo, p 185–232
11. Ishak SA, Hashim H (2015) Low carbon measures for cement plant. J Clean Prod 103:260–274
12. Costa EB, Nobre TRS, Guerreiro AQ, Mancio M, Kirchheim AP (2013) Clínquer Portland com reduzido impacto ambiental. Ambiente Construído, Porto Alegre, v. 13, n. 2, p 75–86, abr./jun. 2013
13. Leibniz Association (2019) Inorganic crystal structure database. Disponivel em: https://www.fiz-karlsruhe.de/en/produkte-und-dienstleistungen/inorganic-crystal-structure-database-icsd
14. NBR NM 76: Cimento Portland - Determinação da finura pelo método de permeabilidade ao ar (Método de Blaine). Rio de Janeiro: ABNT, 1998
15. ASSOCIAÇÃO BRASILEIRA DE NORMAS TÉCNICAS (2017) NBR 16605: Cimento Portland e outros materiais em pó — Determinação da massa específica. Rio de Janeiro: ABNT
16. ASSOCIAÇÃO BRASILEIRA DE NORMAS TÉCNICAS (1991) NBR MB 3432: Cimento Portland - Determinação da finura por meio da peneira 75 μm (nº 200). Rio de Janeiro: ABNT
17. ASSOCIAÇÃO BRASILEIRA DE NORMAS TÉCNICAS (2003) NBR NM 65: Portland Cement – Determination of setting time, Rio de Janeiro, Brazil, p 4
18. ASSOCIAÇÃO BRASILEIRA DE NORMAS TÉCNICAS (2016) NBR 11582: Cimento Portland - Determinação da expansibilidade Le Chatelier. Rio de Janeiro: ABNT
19. ASSOCIAÇÃO BRASILEIRA DE NORMAS TÉCNICAS (1996) NBR 7215: Cimento Portland - Determinação da resistência à compressão. Rio de Janeiro: ABNT
20. Oliveira Júnior AL, Pedroti LG, Oliveira JA, Fernandes WEH, Fineza AG, Monteiro SN, Nalon GH (2019) The influence of partial replacement of natural sand aggregates by grits residues on the mechanical properties of an ecological mortar. J Build Eng 26:100912
21. Torres ST, Carvalho JMF, Alvarenga RCSS, Pedroti LG, Brigolini GJ, Peixoto RAF (2017) Utilização de finos de dregs na produção de concretos. In: IBRACON Anais do 59º Congresso Brasileiro do Concreto-Bento Gonçalves-31 de outubro a 03 de novembro de 2017. Bentio Gonçalves: IBRACON, pp 1–13

22. Mymrin V, Alekseev KP, Fortini OM, Aibuldinov YK, Pedroso CL, Nagalli A, Winter E, Catai RE, Costa EBC (2017) Environmentally clean materials from hazardous red mud, ground cooled ferrous slag and lime production waste. J Clean Prod 161:376–381
23. Petrucci E (1987) Concreto de cimento Portland. Editora Globo, Rio de Janeiro
24. Neville AM (2016) Propriedades do concreto. 5ª Edição. Editora Bookman Company, Rio de Janeiro
25. Taylor HFW (1997) Cement chemistry. Academic Press, London
26. Sinyoung S, Kunchariyakun K, Asavapisit S, Mackenzie KJD (2017) Synthesis of belite cement from nano-silica extracted from two rice husk ashes. J Environ Manage 190:53–60
27. Vashistha P (2019) Sustainable utilization of paper mill solid wastes via synthesis of nano silica for production of belite based clinker. J Clean Prod 224:557–565
28. Koumpouri D, Angelopoulos GN (2016) Effect of boron waste and boric acid addition on the production of low energy belite cement. Cement Concr Compos 68:1–8
29. Carvalho JMF, Campos PAM, Defáveri K, Brigolini GJ, Pedroti LG, Peixoto RAF (2019) Low environmental impact cement produced entirely from industrial and mining waste. J Mater Civil Eng 31(2)
30. Bergold ST, Goetz-Neunhoeffer F, Neubauer J (2016) Influence of the reactivity of the amorphous part of mechanically activated alite on its hydration kinetics. Cem Concr Res 88:73–81
31. Scrivener K, Snelling R, Lothenback B (2016) A practical guide to microstructural analysis of cementitious materials. CRC Press, United States, p 530
32. Bullerjahn F, Zajac M, Skocek J, Ben Haha M (2019) The role of boron during the early hydration of belite ye'elimite ferrite cements. Constr Build Mater 215:252–263
33. Su T, Kong X, Tian H, Wang D (2019) Effects of comb-like PCE and linear copolymers on workability and early hydration of a calcium sulfoaluminate belite cement. Cement Concr Res 123(May):105801

Life Cycle Assessment Applied to Red Ceramic Bricks Production Versus Red Ceramic Bricks Incorporated with Stone Wastes: A Comparative Study

J. O. Dias, G. C. Xavier, A. R. G. Azevedo, J. Alexandre, H. A. Colorado, and C. M. F. Vieira

Abstract Ceramic bricks play an important role in the Brazilian economy and have red clay as the basic raw material for this industry. The aim of this study was to discuss the main environmental impacts related to the manufacturing of red clay bricks, comparing the conventional production versus the production of red clay brick incorporated with ornamental stone processing waste (OSPW). The environmental performance of the production of red clay bricks in Brazil was evaluated with a Life Cycle Assessment study based on the international standards ISO 14040 and ISO 14044. The main impacts of brick production are associated with atmospheric emissions at the stage of extraction and transformation. In both systems studied, the analysis showed relevance regarding the impacts related to human health. This is due to the respiratory effects caused by the clay extraction and burning process, since this step is largely responsible for CO_2 and particulates emissions. The mass reduction

J. O. Dias · A. R. G. Azevedo (✉) · C. M. F. Vieira
LAMAV – Advanced Materials Laboratory, UENF - State University of the Northern Rio de Janeiro, Av. Alberto Lamego, 2000, Campos dos Goytacazes, Rio de Janeiro 28013-602, Brazil
e-mail: afonso.garcez91@gmail.com

J. O. Dias
e-mail: josinaldo.engproducao@gmail.com

C. M. F. Vieira
e-mail: vieira@uenf.br

G. C. Xavier · J. Alexandre
LECIV – Civil Engineering Laboratory, UENF - State University of the Northern Rio de Janeiro, Av. Alberto Lamego, 2000, Campos dos Goytacazes, Rio de Janeiro 28013-602, Brazil
e-mail: gxavier@uenf.br

J. Alexandre
e-mail: jonasuenf@gmail.com

A. R. G. Azevedo
TER – Department of Agricultural Engineering and Environment, UFF - Federal Fluminense University, Rua Passo da Pátria, 341, Niterói, Rio de Janeiro 24210240, Brazil

H. A. Colorado
CCComposites Laboratory, University of Antioquia UdeA, Medellín, Colombia
e-mail: henry.colorado@udea.edu.co

J. Li et al., *Characterization of Minerals, Metals, and Materials 2021*,
The Minerals, Metals & Materials Series,
https://doi.org/10.1007/978-3-030-65493-1_27

of the red clay raw material represents a possibility to reduce environmental impacts and improve the sustainability of ceramic bricks, since the bricks incorporated with 5% of OSPW increases the useful life 2.91-fold when compared to the traditional product. The improvement in the estimated useful life of ceramic bricks can reduce the disposal of these materials in landfills, leading to reduction in the environmental impacts.

Keywords Life cycle assessment · Red ceramic · Waste

Introduction

The main requirements for sustainable development are to guarantee the protection of the environment and natural resources and providing the capacity to meet current and future demands. Hence, there is a need for functional development that, together with urban, agricultural, industrial, technological, and logistical development, establishes the bases that guarantee sustainable development. This need is due to the excessive extraction of natural resources, mainly mineral resources for civil construction, which caused the sector to adapt its processes, such as sustainable building materials [1].

Ceramic bricks are materials used widely in the civil construction, applied to sealing masonry, and both acoustic and thermal insulation. Ceramic brick production uses red clay as the base raw material. In view of the environmental impacts associated with construction activities and its segments, it is essential to obtain and evaluate reliable data on the environmental performance of various building materials, including ceramic bricks [2].

In Brazil, the state of Rio de Janeiro has the fourth largest segment of red ceramic, and the city of Campos dos Goytacazes has a considerable participation in this segment, in addition to being the second-largest producer of blocks for sealing purposes in the country, in 2017 it stood out as the largest ceramic manufacturing pole in the state with more than 120 unionized companies generating about R$ 168 million per year, and an estimated production of 90 million pieces per month [3].

In view of productive activities, the ceramic industry consumes a large amount of non-renewable resources and energy, in addition to generating gaseous emissions and waste discharges as by-product, which makes an assessment of the associated environmental impacts relevant [4, 5]. Several studies evaluated the use of industrial waste in the development of alternative construction materials, such as cementitious and ceramic matrices. However, these studies initially sought an analysis of the technological conditions of application of these materials, thus leaving questions such as environmental factors unanswered, which has demanded new research in this segment [6].

Efforts have been directed towards the development of new environmentally friendly materials and products, including ceramic bricks with the incorporation of waste. In addition, the incorporation of waste in the production of ceramic bricks

contributes to the avoided impact of the industrial waste disposal in landfills, also collaborating to solve the scarcity of natural resources [7].

The incorporation of industrial residues from ornamental stones processing waste (OSPW) in ceramic parts provided an increase in the estimated useful life of these materials [8]. In Brazil, the ornamental stone industry is mainly focused on the production of granite, slates, and siliceous rocks. The estimated amount of OSPW is 240000 tons per year [9]. The state of Espírito Santo is the main producer and largest processor of ornamental stones in Brazil, accounting for more than half of Brazilian exports. On the other hand, Espírito Santo suffers from the generation of a large amount of waste from the processing of ornamental stones, such as cutting and polishing [10].

Due to the development of alternative materials, some environmental management tools, such as Life Cycle Assessment (LCA), are important in the analysis alternatives with ecological potential. In this sense, measuring impacts over the life cycle of a product enables a comprehensive diagnosis of the environmental viability of the alternatives [11]. LCA applies to products, processes, or services, from the extraction of raw materials, through the stages of transportation, production, distribution, use, and disposal. Through the quantification and characterization of the elements flow of input and output of matter, energy, among others, it becomes possible to understand an action of a product system in the environment [12].

The main objective of this work is to study the development of environmentally friendly construction materials from the incorporation of industrial waste from ornamental stone in red clay to produce ceramic bricks.

Materials and Methods

The environmental performance of clay brick production in Brazil was assessed with a LCA study based on the international standards ISO 14040 and ISO 14044 [13, 14]. The goal of the present study is to evaluate the environmental impacts associated with the manufacture of clay bricks, comparing the conventional process and the incorporation of OSPW in the composition of clay bricks.

Scope of the Study: Functional Unit and System Boundaries

The functional unit was defined as the production of 1 kg of clay brick, according to the characteristics of the clay sample, from the city of Campos dos Goytacazes-RJ, as well as the ornamental stone processing waste incorporated in the study, from the city of Cachoeiro de Itapemirim—ES.

Two scenarios were created: the first scenario (S1) represents traditional production of clay brick (0 W), the second scenario (S2) represents the production of clay brick incorporated with 5%, in mass, of OSPW (5 W). The boundaries for both

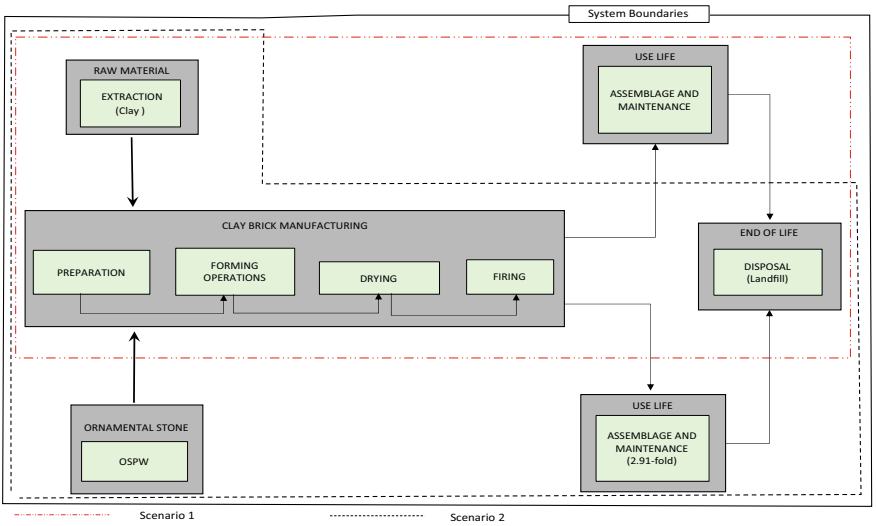

Fig. 1 System boundaries considering the S1 and S2. (Color figure online)

systems were defined from the extraction and processing of raw materials to the end-of-life stage. The system boundaries are shown in Fig. 1.

Life Cycle Inventory and Data Collection

This LCI study reports inventory and impact assessment data (Table 1) associated with the manufacturing of clay bricks from the cradle to the gate, and the end-of-life impact is generated after the useful life. This analysis assumes that the useful life of the ceramic brick incorporated with OSPW (5 W) increases 2.91-fold when compared to traditional bricks [8]. After their useful life has expired, bricks are removed and sent to a landfill.

Data input into the model is based on the Brazilian context for both alternatives. Chemical composition data in the production of red ceramic bricks (0 W) and the production of red ceramic bricks with stone waste (5 W) were collected on a laboratory scale (Table 2), according to [8]. Incomplete or inaccessible data was complete from secondary data, extracted from Ecoinvent 3.3.

Life Cycle Impact Assessment

The assessment tool used in order to assist in modeling was SimaPro 9.0. For the impact analysis, the method used was the Recipe Midpoint (V 1.13; Europe

Table 1 Input values considered for the life cycle inventory

Process	S1	S2	Unit
Description	Value	Value	
Input			
Clay[a]	1.35	1.2825	kg
Electricity	3.91E-6	3.91E-6	kWh
Water	7.36E-5	7.36E-5	m^3
Diesel	0.0297	0.0297	MJ
Flat Pallet	1.61E-5	1.61E-5	p
Lubricating oil	1.32E-5	1.32E-5	kg
Tap water	0.027	0.027	kg
Wood Chips	8.9E-3	8.9E-3	kg
Heat—wood chips	0.225	0.225	MJ
OSPW[a]	–	0.064	kg
Output			
Product			
Clay brick	1	1	kg
Emissions to air			
Benzene	2.96E-6	2.81E-6	kg
Carbon dioxide	0.18	0.17	kg
Carbon monoxide	3.9E-4	3.7E-4	kg
Formaldehyde	1.64E-5	1.56E-5	kg
Hydrogen chloride	1.22E-5	1.16E-5	kg
Hydrogen fluoride	1.06E-5	1.007E-5	kg
Nitrogen oxides	2.6E-4	2.5E-4	kg
Phenol	1.3E-7	1.2E-07	kg
Sulfur dioxide	9.98E-5	9.48 E-5	kg
Water	1.51E-5	1.43 E-5	m^3
Particulates, <2.5 um	–	5.1E-7	kg
Particulates, >10 um	–	7.2E-6	kg
Particulates, >2.5 um and <10 um	–	2.6E-6	kg
Emissions to water			
Water	8.57E-5	8.14 E-5	m^3
Waste for treatment			
Wood ash	3.96E-4	3.96E-4	kg

[a]Data from laboratory scale

Table 2 Chemical composition of raw materials [8]

Raw materials (%)	SiO_2	Al_2O_3	FeO_3	K_2O	Na_2O	TiO_2	SO_3	CaO	MnO	LOI[a]
Clay	48.83	35.46	8.87	3.17	–	1.62	0.90	0.89	0.26	14.89
OSPW	55.09	19.86	12.47	3.70	3.05	1.83	–	2.99	1.00	1.86

[a]LOI—Loss on ignition

Recipe H). The midpoint categories analyzed in this study were Global Warming (GW), Stratospheric ozone depletion (OD), Ionizing radiation (IR), Ozone formation, Human health (OFHH), Ozone formation, Terrestrial ecosystems (OFTE), Terrestrial acidification (TA), Freshwater eutrophication (FE), Marine eutrophication (ME), Terrestrial ecotoxicity (TE), Freshwater ecotoxicity (FEC), marine ecotoxicity (MEC), Human carcinogenic toxicity (HCT), Human non-carcinogenic toxicity (HNCT), Land use (LU), Mineral resource scarcity (MRS), Fossil resource scarcity (FRS), and Water Consumption (WC) [15–17].

Results and Discussion

Regarding the comparative system studied and the respective input, Table 3 was obtained from the data characterized and normalized according to SimaPro software. From the values obtained for each impact category evaluated, it was possible to infer that the clay brick incorporated with OSPW (5 W) showed better environmental performance when compared to traditional clay brick (0 W) (Fig. 2). The characterized data represents the impacts recorded in each category according to a specified unit. Normalized data, on the other hand, provide a generalized metric of which categories have the greatest impact on the global analysis.

This analysis did not consider the avoided impact of the landfill for the OSPW. The relative impact refers to the comparative environmental performance, considering the phases of raw material extraction, production, use, and disposal of the products (5 W) and (0 W).

The results, in Fig. 3, show that the FEC, MEC, and HCT categories have a greater participation in the environmental impacts caused for each system analyzed. These categories are related to human exposure to toxic substances, especially through ingestion and inhalation. This is due to the respiratory effects caused by the clay extraction and brick burning process, since this step is largely responsible for CO_2 emissions. These categories are expressed in kg 1.4-dichlorobenzene equivalents (1.4DCB-eq), a unit used as a characterization factor at the midpoint level for human toxicity. In addition, the clay brick (5 W) has positive effects in the categories mentioned, presenting a reduction in impacts to the S2 system, which shows that an incorporation of OSPW in the manufacture of clay bricks is an alternative to reduce the negative effects on human health caused by the ceramics industry (Fig. 3) [18].

Table 3 Impact values—Life Cycle impact assessment

Impact category	Characterized data			Normalized data (%)	
	Unit	Clay brick (0 W)	Clay brick (5 W)	Clay brick (0 W)	Clay brick (5 W)
GW	kg CO_2 eq	0.19	0.18	0.5771	0.5741
OD	kg CFC11 eq	9.36E-09	9.23E-09	0.0036	0.0038
IR	kBq Co-60 eq	5.7E-4	5.4E-4	0.0278	0.0279
OFHH	kg NO_x eq	3.8E-4	3.6E-4	0.4392	0.4335
OFTE	kg NO_x eq	3.9E-4	3.6E-4	0.5150	0.5084
TA	kg SO_2 eq	2.9E-4	2.7E-4	0.1646	0.1638
FE	kg P eq	7.38E-06	7.01E-06	0.2638	0.2639
ME	kg N eq	4.34E-07	4.13E-07	0.0022	0.0022
TE	kg 1.4-DCB	0.17	0.16	3.8495	3.8499
FEC	kg 1.4-DCB	1.1E-3	1.0E-3	20.399	20.403
MEC	kg 1.4-DCB	1.57E-3	1.4E-3	35.456	35.463
HCT	kg 1.4-DCB	3.8E-3	3.6E-3	32.397	32.40
HNCT	kg 1.4-DCB	3.6E-2	3.5E-2	5.7348	5.7353
LU	m^2a crop eq	6.1E-3	5.7E-3	0.0229	0.0227
MRS	kg Cu eq	1.4E-2	1.3E-2	0.0028	0.0028
FRS	kg oil eq	5.5E-3	5.2E-3	0.1302	0.1307
WC	m^3	1.48E-4	1.41E-4	0.0129	0.0129

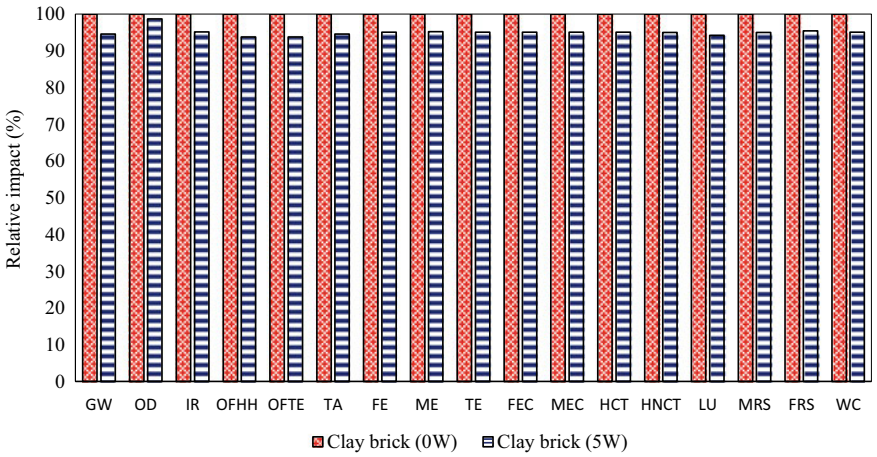

Fig. 2 Characterized data for comparative analyses by relative impact. (Color figure online)

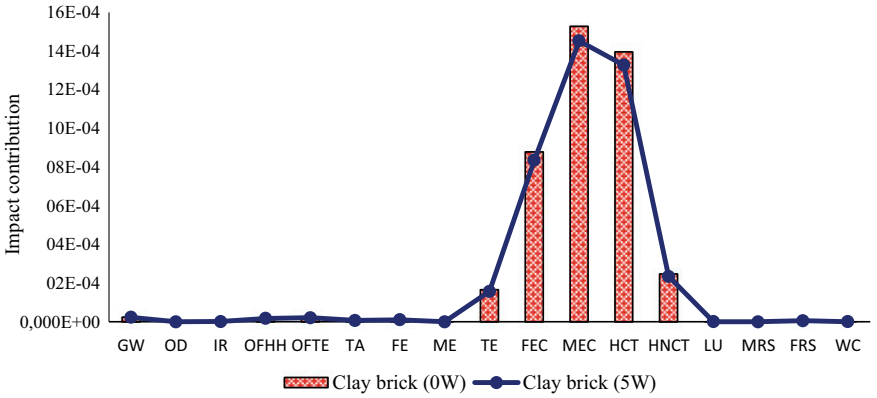

Fig. 3 Normalized data for impact contributions. (Color figure online)

Additionally, the impact assessment of the S2 system was carried out, analyzing the contribution of each input to the categories of impact. According to Fig. 4 it was observed that nine of seventeen evaluated categories contain clay extraction as the main source of impact, registering levels above 70%. Considering the categories FEC, MEC, and HCT, which had a large participation in the global impacts of the evaluated system, it is noted that the impacts caused by the clay extraction activity were around 92%, 91%, and 71%, respectively. This can be attributed mainly to consumption of fossil fuel by equipment used in this stage of the process. Moreover, the addition of OSPW to a ceramic clay (5 W) has a positive effect on WC category by avoiding impact (negative value in the Fig. 4). In that case, the addition of 5% OSPW improved water consumption by 9% compared with conventional bricks [19].

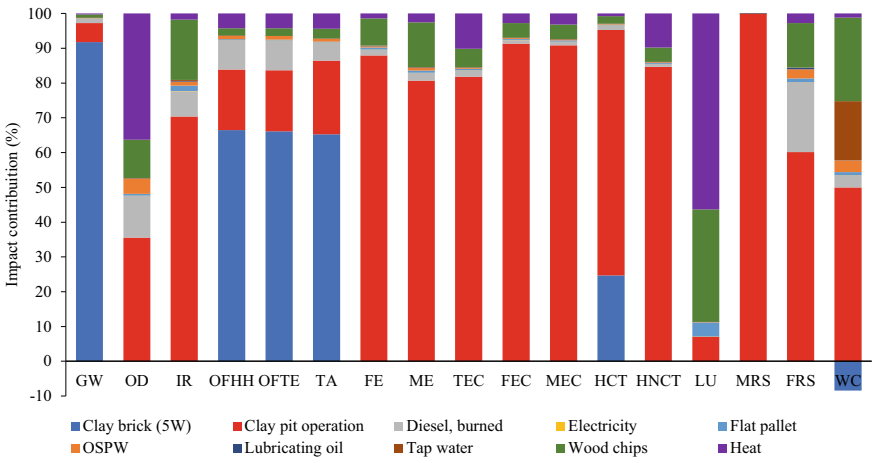

Fig. 4 Impact contribution of each input considered in the S2 system. (Color figure online)

Conclusion

Thus, it is possible to conclude that the main environmental impacts presented by the studied system are associated with the extraction and burning activities of clay production. Due to the use of equipment that requires fossil fuels, the extraction phase of the raw material clay has a considerable contribution to the air emissions. Hence, the mass reduction of the clay raw material in the production of ceramic bricks, when OSPW is incorporated, is a possibility to reduce environmental impacts and improve the sustainability of ceramic bricks. In the clay extraction stage the use of more efficient equipment that uses clean energy sources can contribute to a significant reduction in the global impacts of the evaluated system.

Furthermore, the incorporation with 5% mass of OSPW in the manufacturing of ceramic bricks increased the useful life of red ceramic products. The improvement in the estimated useful life of ceramic bricks can reduce the disposal of these materials in landfills, leading to a reduction in the environmental impacts associated with disposal. Besides that, OSPW is nonhazardous and nontoxic and incorporation into the clay makes the residue inert. Moreover, in situations of disposal due to damage or after the useful life, this material is not considered hazardous.

The main contribution of this work is to subsidize the technological results obtained by [8], evaluating environmentally the process of incorporating residues in ceramic materials and presenting the performance of traditional products and incorporated with OSPW.

References

1. Savadkoohi MS, Reisi M (2020) Environmental protection based sustainable development by utilization of granite waste in Reactive Powder Concrete. J Clean Prod 266:121973
2. Geng Y, Chen W, Liu Z, Chiu ASF, Han W, Liu Z, Zhong S, Qian Y, You W, Cui X (2017) A bibliometric review: energy consumption and greenhouse gas emissions in the residential sector. J Clean Prod 159:301–316. https://doi.org/10.1016/j.jclepro.2017.05.091
3. Campos, Prefeitura Municipal de Campos dos Goytacazes. Planejamento debate a revitalização do setor cerâmico de Campos. https://campos.rj.gov.br/exibirNoticia.php?id_noticia=41258
4. Huedo P, Mulet E, López MB (2016). A model for the sustainable selection of building envelope assemblies. Environ Impact Assess Rev 57:63–77. https://doi.org/10.1016/j.eiar.2015.11.005
5. Sandanayake M, Zhang G, Setunge S (2018) A comparative method of air emission impact assessment for building construction activities. Environ Impact Assess Rev 68:1–9. https://doi.org/10.1016/j.eiar.2017.09.003
6. Mohammadhosseini H, Lim N, Tahir M, Alyousef R, Samadi M (2019) Enhanced performance of green mortar comprising high volume of ceramic waste in aggressive environments. Constr Build Mater 212:607–617
7. Chiu CT, Hsu TH, Yang WF (2008) Life cycle assessment on using recycled materials for rehabilitating asphalt pavements. Resour Conserv Recycl 52(3):545–556. https://doi.org/10.1016/j.resconrec.2007.07.001
8. Xavier G, Azevedo A, Alexandre J, Monteiro S, Pedroti L (2018) Determination of useful life of red ceramic parts incorporated with ornamental stone waste. J Mater Civ Eng. https://doi.org/10.1061/(ASCE)MT.19435533.0002590

9. Azevedo ARGA, Marvila MT, Da Silva LB, Zanelato EB, Alexandre J, Xavier GC, Monteiro SN (2019) Effect of granite residue incorporation on the behavior of mortars. Materials 12:1449
10. Filho RS et al (2013) Atlas de rochas ornamentais do estado do Espírito Santo. Brasília
11. De Paula RR (2016) Avaliação do Ciclo de Vida (ACV) de argamassas e concretos produzidos com Resíduos de Construção e Demolição (RCD). Dissertation, COPPE-UFRJ
12. Ye l, Hong J, Ma x, Qi C, Yang D (2018) Life cycle environmental and economic assessment of ceramic tile production: a case study in China. J Clean Prod. 189:432–441
13. ISO (2006a) ISO 14040 Environmental management—life cycle assessment— principles and framework. Geneve
14. ISO (2006b) ISO 14044 Environmental management—life cycle assessment— requirements and guidelines. Geneve
15. De Azevedo, ARG, Alexandre, J, Marvila, MT, Xavier, GC, Monteiro, SN, Pedroti LG (2020) Technological and environmental comparative of the processing of primary sludge waste from paper industry for mortar. J Clean Prod 32
16. Marvila MT, Azevedo ARG, Cecchin D, Costa J, Xavier GC, Carmo DF, Monteiro SN (2020) Durability of coating mortars containing açaí fibers. Case Studies in Construction Materials 13:10–21
17. De Azevedo ARG, Marvila MT, Rocha HA, Cruz LR, Vieira CM (2020) Use of glass polishing waste in the development of ecological ceramic roof tiles by the geopolymerization process. Int J Appl Ceram Technol
18. Oliveira PS, Antunes MLP, da Cruz NC, Rangel EC, de Azevedo ARG, Durrant SF (2020) Use of waste collected from wind turbine blade production as an eco-friendly ingredient in mortars for civil construction. J Clean Prod 274
19. Amaral LF, Girondi Delaqua GC, Nicolite M, Marvila MT, Azevedo ARG, Alexandre J, Vieira CMF, Monteiro SN (2020) Eco-friendly mortars with addition of ornamental stone waste-a mathematical model approach for granulometric optimization. J Clean Prod 270

Comparison Between Red Ceramic Parts With and Without Ornamental Stone Waste Under Wetting and Drying Cycles

M. S. Moraes, G. C. Xavier, A. R. G. Azevedo, J. Alexandre, M. T. Marvila, S. N. Monteiro, and J. O. Dias

Abstract Various examples of scientific research are promoted in Brazil and in the world to evaluate alternative materials in the industrial process of red ceramics. Thus, the objective is to reduce the amount of clay by incorporating another material in the production line of the red ceramic parts and consequently to prolong the extraction time of the clay reserves. The ornamental stone industries generate a lot of waste when cutting blocks. The research analyzes the behavior of the flexural strength of red ceramic parts with the incorporation of these residues. The percentages of waste addition were 0% (0R) 5% (5R) and 10% (10R) by mass. Three firing temperatures were analyzed: 750, 850, and 950 °C. The main objective is, after 175 cycles of wetting and drying, to compare the flexural strength of ceramic parts with and without the addition of ornamental stone waste. Flexural strength was obtained using the 3-point method. According to the results, samples 0R and 10R at all firing temperatures showed lower flexural strength than samples 5R. The 5R samples sintered at 950 °C were the most resistant with a value of 3.5 MPa after 175 wetting and drying cycles.

Keywords Red ceramic · Ornamental stone waste · Flexural strength

M. S. Moraes · G. C. Xavier · J. Alexandre
LECIV – Civil Engineering Laboratory, UENF - State University of the Northern Rio de Janeiro, Av. Alberto Lamego, 2000, Campos dos Goytacazes, Rio de Janeiro 28013-602, Brazil

A. R. G. Azevedo (✉) · M. T. Marvila · J. O. Dias
LAMAV – Advanced Materials Laboratory, UENF - State University of the Northern Rio de Janeiro, Av. Alberto Lamego, 2000, Campos dos Goytacazes, Rio de Janeiro 28013-602, Brazil
e-mail: afonso.garcez91@gmail.com

A. R. G. Azevedo
TER – Department of Agricultural Engineering and Environment, UFF - Federal Fluminense University, Rua Passo da Pátria, 341, Niterói, Rio de Janeiro 24210-240, Brazil

S. N. Monteiro
Department of Materials Science, IME - Military Institute of Engineering, Square General Tibúrcio, 80, Rio de Janeiro 22290-270, Brazil

J. Li et al., *Characterization of Minerals, Metals, and Materials 2021*,
The Minerals, Metals & Materials Series,
https://doi.org/10.1007/978-3-030-65493-1_28

Introduction

From the dawn of humanity to the present day natural resources are used for survival but in recent years they have been used in an unbridled way, which reflects the consumption behavior of society in this century [1]. The results of these actions to the environment are serious, as they can cause scarcity of resources, in addition to generating large amounts of waste [2]. Civil construction stands out for the expressive volume of raw material consumed which for the most part has a finite origin [2]. The red ceramic industry uses an exhaustible resource, clay. Thus, scientific research is promoted in Brazil and in the world to evaluate alternative materials in the industrial process of red ceramics [3]. So, the objective is to reduce the amount of clay by incorporating another material in the production line of the red ceramic pieces and consequently to prolong the extraction time of the clay reserves. The city of Campos dos Goytacazes, in Brazil, stands out in the production of red ceramic products playing an important role in the economic development of the State of Rio de Janeiro [4].

The ornamental stone sector in addition to being characterized as an extractive activity of exhaustible resources produces a large amount of waste called stone powder. Generally, these materials are not handled properly in their respective deposits and are disposed of inappropriately which causes adverse effects on the environment [2]. Thus, water sources such as rivers and lakes and the soil are polluted with this material which is easily transported by the wind [2]. Ornamental stone residues are identified as possible materials that can participate in the process of making red ceramic arta, including improving certain characteristics such as service life [5]. The residue is generated when cutting the stone blocks, this is due to the abrasion caused by the movement of the diamond saw that cuts the stones. [5]. The municipality of Santo Antônio de Pádua, specifically, stands out as the largest producer of ornamental stones in the state of Rio de Janeiro, in Brazil [6].

In search of sustainable development, companies in the red ceramic sector have played an important role in recycling and using ornamental stone powder residues in their industrial production in recent years [4]. The city of Campos dos Goytacazes and Santo Antônio de Pádua are located in the same state, Rio de Janeiro, this enables the partnership between companies in the field of red ceramics and exploration and production of ornamental stones. The durability of red ceramic parts is affected by wind, air, sun, and water, so those that are exposed to these factors degrade faster [5]. In this research, the wetting and drying cycles performed in the laboratory simulate the cycles of natural degradation of the environment.

Thus, the objective of this research is to compare the red ceramic parts without and with the addition of ornamental stone waste in two situations, intact and after 175 wetting and drying cycles. It is intended to analyze the behavior of the samples submitted to the flexion test which allows to know the time that the parts reach the minimum resistance value after the degradation test. Therefore, the objective is to compare the flexural strength of the different values of percentage of addition of

ornamental stone waste and firing temperature and demonstrate that is possible to produce more resistant and durable red ceramic parts.

Materials and Methods

The main materials used in this research in red ceramic parts with and without the addition of ornamental stone waste are clay and ornamental stone powder. The clay was acquired in a specific red ceramic industry located in the city of Campos dos Goytacazes and the stone waste was supplied by a company in the ornamental stone exploration sector located in the municipality of Santo Antônio de Pádua. The following Figs. 1 and 2 show the images of the clay deposit and the disposal site for the ornamental stone waste.

First, the materials were characterized, in this stage mineralogical analyzes of the clay and ornamental stone waste were carried out. Thus, 200 g of clay and waste were sieved in the 100 mesh (0.074 mm) open mesh and subsequently oven dried at 105 °C. The qualitative mineralogical composition was obtained by X-ray diffraction, using the Shimadzu XRD 7000 equipment. The generator configurations were 30 kV and 30 mA, Cu-Kα1 angular step of 0.02° and time interval 1 s and 2θ with variation between 5° and 60° [5]. The Match3! software was used to quantify the crystalline phases, based on the Rietveld model with the provision of refinement parameters [5].

In the sample preparation process, the clay and the ornamental stone waste were previously oven dried at 105 °C. These materials were then sieved in a 100 mesh (0.149 mm). Three types of samples were prepared for making the ceramic parts, one with only clay and the other two with 5% and 10% mass addition of ornamental

Fig. 1 Clay deposit. (Color figure online)

Fig. 2 Disposal of ornamental stone waste. (Color figure online)

Table 1 Composition of the samples. [5]

Samples	Composition (%)	
	Ornamental stone waste	Clay
0R	0	100
5R	5	95
10R	10	90

stone waste. Materials without addition were classified as 0R, those that received 5 and 10% mass addition of waste, 5R and 10R, respectively (Table 1). Then, the three batches of materials were milled for 30 min for homogenization and moistened with a moisture content of 8%. The following table shows the composition of each of the three sample lots adopted in this research.

To make the ceramic parts in prisms with dimensions of 10 × 2 × 1 cm it was necessary to press the sample with 25 MPa. Thirteen specimens were molded for each percentage of addition and for the three different firing temperatures, 750, 850, and 950 °C. (Figure 3) After modeling the ceramic parts, they were sintered at 750, 850, and 950 °C in an electronic muffle with a heating rate of 2°/min, for 180 min. Cooling took place at room temperature. The image below shows the ceramic parts in the firing phase in an electronic muffle.

After burning, the degradation test was started. The main natural agents of deterioration of ceramic parts are the actions of climatic factors over time, which in tropical climates are more severe [5]. The wetting and drying cycles are considered the most unfavorable condition in the deterioration of red ceramic materials [7]. Thus in this project a laboratory degradation experiment with cycles of temperature and humidity variation was implemented. The wetting and drying cycles simulate the variation of temperature and humidity, called laboratory degradation experiment.

Fig. 3 Ceramic parts in the firing phase in an electronic muffle. (Color figure online)

So, 175 wetting and drying cycles were carried out on 13 ceramic parts from each batch. In each cycle, the samples were immersed in water for 10 h and then placed in an oven at 105°C for 14 h.

After the degradation cycles, all the red ceramic parts were submitted to the flexural strength test, including the intact samples, those that did not participate in the laboratory deterioration process. The samples were tested according to the 3-point method, standardized according to ASTM C-674-77 [8]. The load rate was 0.5 mm/min and the distance between the supports was 9 cm [5].

From the comparison of the flexural strength values of the samples that were degraded ($\boldsymbol{FS}$) in relation to the intact samples ($\boldsymbol{FS}_0$), it is possible to calculate the loss of flexural strength index ($\boldsymbol{I}_{\boldsymbol{LFS}}$) of the red ceramic parts. The formula that allows defining the loss of flexural strength index ($\boldsymbol{I}_{\boldsymbol{LFS}}$) is

$$\boldsymbol{I}_{\boldsymbol{LFS}} = \frac{|\boldsymbol{FS}_0 - \boldsymbol{FS}|}{\boldsymbol{FS}_0} \boldsymbol{X} 100\%$$

The loss of flexural strength index ($\boldsymbol{I}_{\boldsymbol{LFS}}$) value ranges from zero for intact material to a maximum value, always less than 100%, for the most degraded material [5]. Based on the values obtained, the $\boldsymbol{I}_{\boldsymbol{PRF}}$ is calculated for each set of samples after the degradation times. Given the correlation of time in days and the $\boldsymbol{I}_{\boldsymbol{PRF}}$ curves, it is possible to define the time in which the material sample will lose strength, up to the minimum allowed.

Results and Discussion

The following figure shows the X-ray diffractogram of the clay in the Match (3!) program and quantification by Rietveld (Fig. 4).

The diffractogram above shows the presence of kaolinite (55.4%), quartz (23.0%), microcline (17.1%), and gibbsite (4.6%), can be observed in Fig. 5.

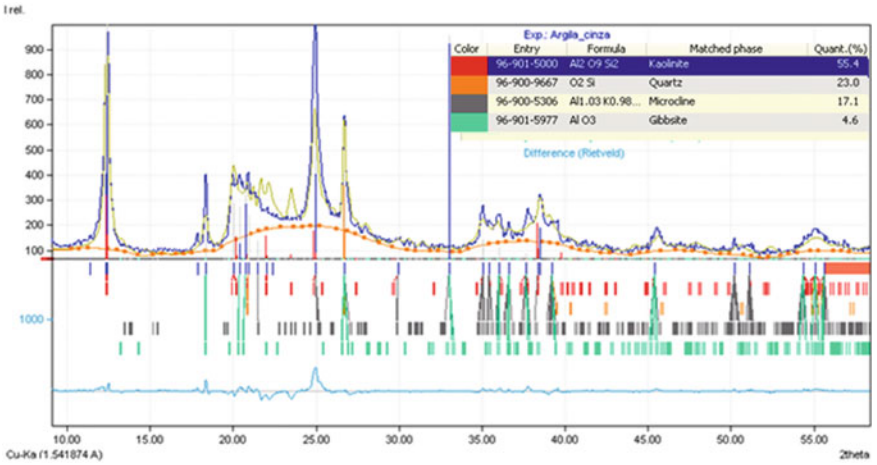

Fig. 4 Clay X-ray diffractogram. (Color figure online)

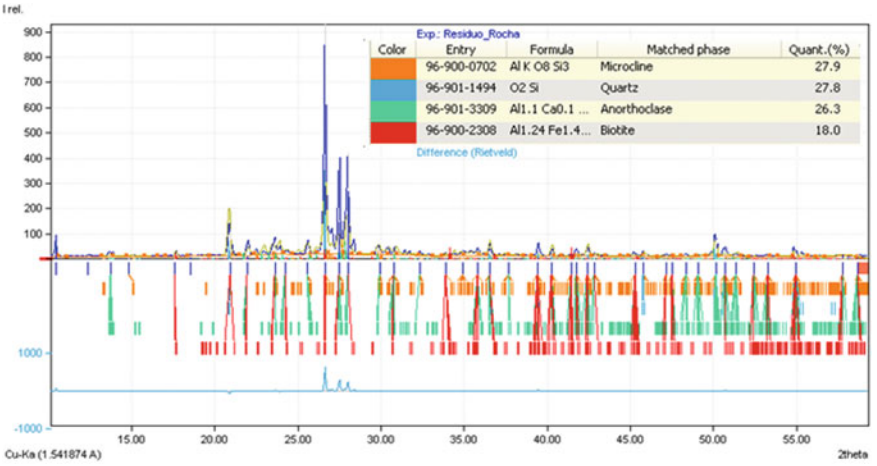

Fig. 5 X-ray diffractogram of the ornamental stone waste. (Color figure online)

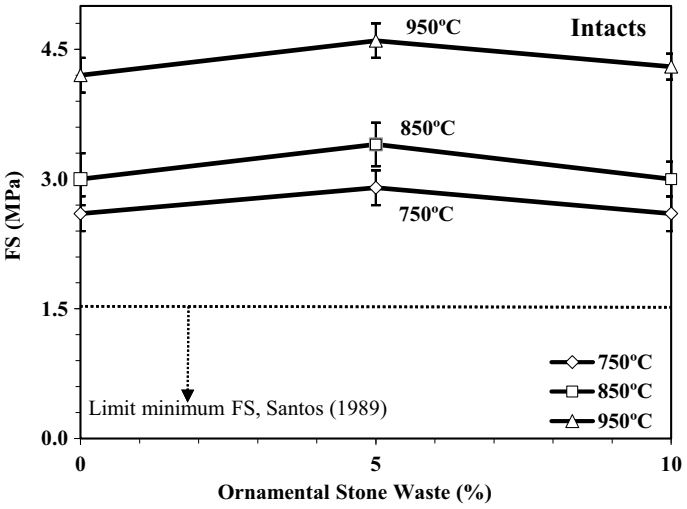

Fig. 6 The flexural strength results of the intact samples [5]

The diffractogram above shows the presence of microcline (27.9%), quartz (27.8%), anorthoclase (26.3%), and biotite (18.0%). The flexural strength results of the intact samples are shown in the following in Fig. 6.

All intact rights have values above the established minimum [8, 9]. As the firing temperature increases, the parts become more resistant to flexural. This occurred in all the percentage of incorporation of ornamental stone waste. The 5R samples sintered at 950 °C reached the highest value of 4.6 MPa [5]. The results of the flexural strength of the samples after 175 wetting and drying cycles are shown in the following in Fig. 7.

There was a loss in flexural strength after 175 cycles of wetting and drying, when compared to the intact samples. All samples sintered at 850 and 950 °C presented values above the established minimum [10–12]. The samples sintered at 750 °C were fragile after 175 cycles, as they reached the established minimum. However, the 5R samples at 750 °C did not reach the minimum, being still in conditions of use. The 5R samples sintered at 950 °C are the most resistant with a value of 3.5 MPa [11].

The following figure shows the flexural strength loss index (I_{LFS}) of samples 5R sintered at 950 °C after 175 cycles of wetting and drying. These samples were chosen because they present greater strength in relation to the others (Fig. 8) [13].

The index of loss of resistance to flexion was higher for samples 0R than for 5R, 59.8% and 39.19%, respectively. This occurs due to the presence of microcline, anorthoclase, and biotite in the ornamental stone waste that forms a liquid phase in the sintering of the samples [14, 15].

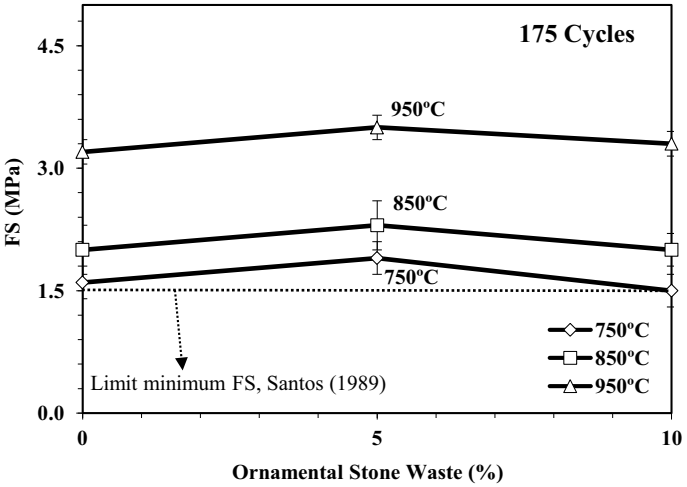

Fig. 7 The flexural strength results of the samples after 175 cycles of wetting and drying

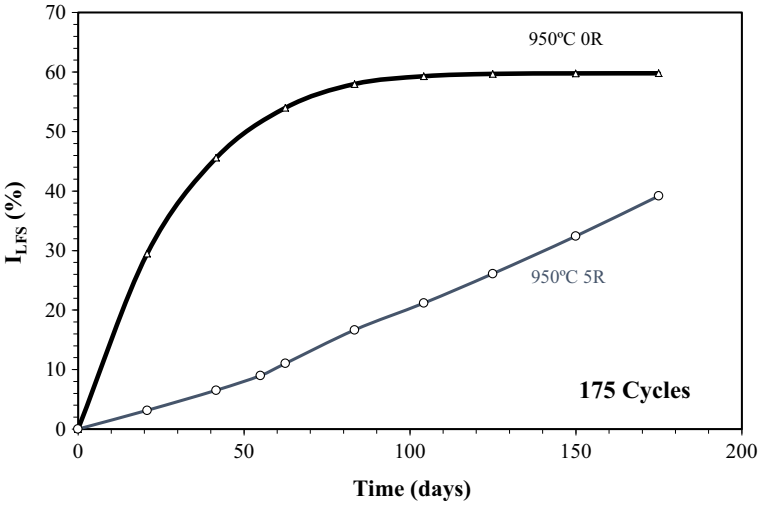

Fig. 8 The results of the flexural strength loss index (I_{LFS}) of samples 0R and 5R sintered at 950 °C after 175 cycles. (Color figure online)

Conclusions

Kaolinite stands out in the mineralogical composition of clay and microcline and quartz in ornamental stone residues. The samples with the addition of 5% by mass, 5R, presented better results. Samples without added ornamental stone residues are less resistant. Analyzing the sintered samples at 950 °C, the 5R are more resistant

than the 0R. The index of loss of resistance to flexion was higher for samples 0R than for 5R. The presence of microcline, anorthoclase, and biotite in the ornamental stone waste improves the performance of the ceramic parts in relation to flexural strength. Therefore, the addition of ornamental stone waste to the ceramic materials improves flexural strength. In addition, there is less clay extraction and an interesting application of the ornamental stone waste. It is suggested for further research that the analyzes be carried out with more wetting and drying cycles.

References

1. Innocent JM, Nandi VS, Rosso F, Oliveira A, Zaccaron A (2018) Vitreous waste recovery study in the formulation of red ceramics [*In Portuguese*]. Ind Ceram 23(3):34–39. https://doi.org/10.4322/cerind.2018.004
2. Moraes JMS et al (2016) Systematization of the characterization of abrasive sludge from ornamental rock cutting to orientate its use as a raw material in the civil construction industry [*In Portuguese*]. Presented at the 18th Brazilian congress of soil mechanics and geotechnical engineering, Belo Horizonte, Minas Gerais, 19–22 Oct 2016
3. Rocha RC (2019) Analysis of the productive agglomeration of red ceramics in Campos dos Goytacazes (2011–2017) [*In Portuguese*]. Braz J Geogr Econ Space Econ 16. https://doi.org/10.4000/spaceeconomy.8930
4. Alexandre J, de Azevedo ARG, de Castro Xavier G, Muylaert Margem F, Monteiro SN, de Oliveira Braga F, de Azeredo NG, Bozzi Piazzarollo C (2016) Influence of weather exposure on dimensional changes in clay ceramics incorporated with granite residue. Mater Sci Forum 869:131–135. https://doi.org/10.4028/www.scientific.net/msf.869.131
5. Xavier GC, Azevedo ARG, Alexandre J, Monteiro SN, Pedroti LG (2019) Determination of useful life of red ceramic parts incorporated with ornamental stone waste. J Mater Civil Eng 31:04018381–04018381-13. https://doi.org/10.1061/(asce)MT.1943-5533.0002590
6. Mineral Resources Department (2012) Mineral Panorama of the state of Rio de Janeiro [*In Portuguese].* State Secretariat for Economic Development, Energy, Industry and Services. http://www.drm.rj.gov.br/index.php/downloads/category/79-panorama-mineral-2014. Accessed 2 July 2020
7. Brooks RM, Cetin M (2013) Water susceptible properties of silt loam soil in sub grades in south west Pennsylvania. Int J Mod Eng Res 3(2):944–948
8. ASTM (1977) Flexural properties of ceramic whiteware materials. ASTM C674. ASTM, West Conshohocken, PA
9. Santos PS (1989) Science and technology of clays [*In Portuguese*]. Edgard Blücher, São Paulo
10. Azevedo ARG, Vieira CMF, Ferreira WM, Faria KCP, Pedroti LG, Mendes BC (2020) Potential use of ceramic waste as precursor in the geopolymerization reaction for the production of ceramic roof tiles. J Build Eng. 29(1):101–156
11. de Azevedo ARG, Alexandre J, Zanelato EB, Marvila MT (2017) Influence of incorporation of glass waste on the rheological properties of adhesive mortar. Constr Build Mater 148:359–368
12. De Azevedo ARG, Alexandre J, Marvila MT, Xavier GC, Monteiro SN, Pedroti LG (2020) Technological and environmental comparative of the processing of primary sludge waste from paper industry for mortar. J Clean Prod 32
13. Marvila MT, Azevedo ARG, Cecchin D, Costa J, Xavier GC, Carmo DF, Monteiro SN (2020) Durability of coating mortars containing açaí fibers. Case Stud Constr Mater 13:10–21

14. De Azevedo ARG, Marvila MT, Rocha, HA, Cruz LR, Vieira CM (2020) Use of glass polishing waste in the development of ecological ceramic roof tiles by the geopolymerization process. Int J Appl Ceram Technol
15. Oliveira PS, Antunes MLP, da Cruz NC, Rangel EC, de Azevedo ARG, Durrant SF (2020) Use of waste collected from wind turbine blade production as an eco-friendly ingredient in mortars for civil construction. J Clean Prod 274

Compressive Properties of Additively Manufactured Titanium-Carbide

Heet Amin, Jianshen Wang, Ali A. H. Ameri, Hongxu Wang, Daniel East, and Juan P. Escobedo-Diaz

Abstract The quasistatic compressive behaviour of additively manufactured titanium-carbide (Ti-6Al4-V-C or Ti-C) was investigated through quasistatic compression and microhardness tests. The carbon content within the titanium-carbide samples was varied in order to identify the influence of graphite on the properties of the material. The information gathered through the mechanical tests and optical microscopy was used in order to identify the effectiveness of titanium-carbide as a functionally graded material applied in ballistic protection. Initial QS compression testing on 5.3 and 6 wt%C content yielded similar results in mechanical properties. This contradicts the hypothesis which predicts an increase in strength with an increase in carbon content. Further details on the results will be presented in this study.

Keywords Additive manufacturing · Titanium-carbide · Microstructure characterisation · Mechanical properties

Introduction

Titanium alone provides desirable mechanical properties such as high strength and corrosion resistance while maintaining a low density as compared to other common metals such as steel, copper, and nickel [1]. Titanium is also abundant in nature in the form of minerals such as rutile, ilmenite, and titanite. Carbon is also abundantly available in the form of diamond, amorphous carbon, and graphite, its most

H. Amin · J. Wang · A. A. H. Ameri · H. Wang · J. P. Escobedo-Diaz (✉)
School of Engineering and Information Technology, University of New South Wales, Canberra, Australia
e-mail: j.escobedo-diaz@unsw.edu.au

D. East
CSIRO Manufacturing, Melbourne, Australia

H. Amin · J. Wang · A. A. H. Ameri · H. Wang · D. East · J. P. Escobedo-Diaz
University of New South Wales at the Australian Defence Force Academy, Canberra, ACT 2600, Australia

J. Li et al., *Characterization of Minerals, Metals, and Materials 2021*,
The Minerals, Metals & Materials Series,
https://doi.org/10.1007/978-3-030-65493-1_29

common form. By alloying titanium and carbon, certain mechanical properties are enhanced. Titanium-carbide (Ti-C) can have various applications where wear resistance, thermal stability, and high strength are necessary such as ballistic armour, aerospace, and turbine parts. Previous studies show increasing carbon content in the Ti-C alloy increases Young's modulus, hardness and yield strength whilst reducing the toughness and ductility of the material [2].

Titanium has shown potential to be formed into a functionally graded material (FGM) where the properties and microstructure of a material changes across a certain distance. With its introduction in 1987 in applications for a high-temperature propulsion system, FGMs have numerous modern-day applications [3]. One such potential application is the use of functionally graded Ti-C for ballistic armour. FGM has shown greater ballistic properties in comparison to homogenous materials [4]. Graded Ti-C with varying ductility, hardness, and strength properties can be arranged so that it can provide desirable protection from high-velocity impacts and compressive forces. There is limited to no relevant research which verifies this theory for Ti-C.

The fabrication method also affects the properties of the material. This study investigates the compressive properties of additively manufactured Ti-C. Ti-C is a relatively modern material, with the introduction of efficient methods to produce Ti-C only beginning in the 1980s (through powder sintering) [5]. A modern Ti-C additive manufacturing process is Laser Engineered Net Shaping (LENS) which was first introduced in 1996 by Sandia National Laboratories and commercialised in 1997 with Optomec. LENS utilises a high-power laser to melt metal powder supplied through a coaxial powder feed system. Depending on the make and model of the LENS machine, the powder feed system can have up to 3–4 nozzles with each nozzle providing different powders allowing the machine to form alloyed products.

Although some research has been conducted into Ti-C. There is minimal research or data which describes the compressive response of additively manufactured Ti-C under quasistatic strain rates. Most of the current research regarding the compressive properties of additively manufactured Ti-C has been conducted by Jianshen Wang in 2019. This study intends on providing more data and information in order to further advance the research into additively manufactured Ti-C and its application as ballistic protection.

Methodology

Fabrication of Samples

An Optomec LENS MR-7 system was used to additively manufacture homogenous Ti-C MMC. This system utilises four nozzles and a 1070 nm wavelength fibre laser to form a melt pool focussed on a targeted area (as illustrated in Fig. 1). The power of the laser ranges from 0.5 to 1 kW. The melt pool then allows the powder fed through the nozzles to be absorbed, forming a composite. Nozzles can feed various

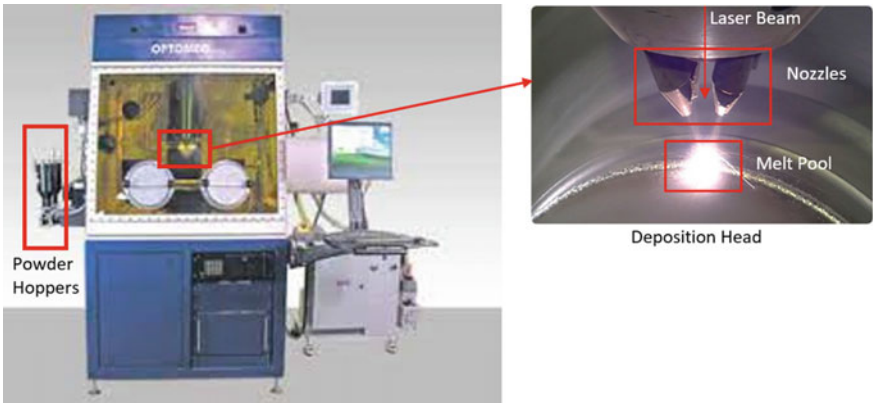

Fig. 1 The image illustrates the key components of the Optomec LENS MR-7 additive manufacturing system (Optomec Inc, 2018). (Color figure online)

powders in order to form numerous composite materials. For the samples used in this study, the nozzles fed Ti-6Al-4 V powder and nickel-coated graphite. Nickel was required whilst feeding through the nozzles, as pure graphite powder was too fine. Fine powder results in blockages in the piping between the powder hopper and the deposition head. In order to prevent this and create more coarse grains in the powder, nickel was added. The carbon (graphite) content was controlled by varying the feed rate of the graphite relative to the deposition rate of the Ti-6Al-4 V powder.

Electric Discharge Wire Cutting

The samples were prepared for testing via EDM wire cutting. EDM cutting processes utilise the electric conductivity of the sample material. An electrically charged wire connected to two spools cuts through a material submerged in dielectric fluid. The dielectric fluid acts as a semi-conductive medium between the electric wires and the workpiece as well as a cooling agent and flushing agent. The most common EDM dielectric fluid is deionised water; however, hydrocarbon oils are also occasionally utilised [6]. The wire cutting process can achieve tolerances up to ± 0.005 mm. The samples used in the study were 6 mm in diameter and length with a design tolerance of ± 0.05 mm for both dimensions. These dimensions will be used for both the quasistatic compression and SHPB testing. Furthermore, the EDM wire cutting generates good, consistent surface finishing, hence further processing is not required for sample preparation.

Sample Preparation and Optical Microscopy

In order to conduct Vickers hardness tests and optical microscopy, the samples were prepared via grinding and polishing in accordance with Titanium preparation methods outlined by Struers (2015). The plane surface of a Ti-C sample was first grinded using an MD-Mezzo 220. The grinding surface was submerged under a thin layer of water which acted as a lubricant. This was followed by a single fine grinding step where an MD-Largo grinding surface was submerged under DiaPro Allegro/Largo 9 μm suspension (lubricant). Finally, the Ti-C surface was polished using a chemical-mechanical technique. A colloidal silica mixture consisting of silica oxide (OP-S) and hydrogen peroxide (H_2O_2) with a volume ratio of 9:1 was used. In an aqueous condition, the Titanium in the Ti-C reacts with the hydrogen peroxide to form titanium dioxide (TiO_2) [7]. The titanium dioxide on the surface of the Ti-C sample is continuously removed by the silica suspension. This leaves the surface free of mechanical deformities that may have occurred due to grinding and prepares the sample for hardness testing (Fig. 2).

After optical microscopy ImageJ software was utilised to calculate the carbon area fractions of the samples. As shown in Table 1, both the 5.3 and 6%wt.C Ti-C samples have similar carbon area fraction with exception of sample 1 of 6%wt.C. This demonstrated how the consistency of the carbon in the samples can vary even when the LENS MR-7 system has been set to generate samples with specific samples. This also highlights the necessity for optical microscopy of the fracture materials after testing.

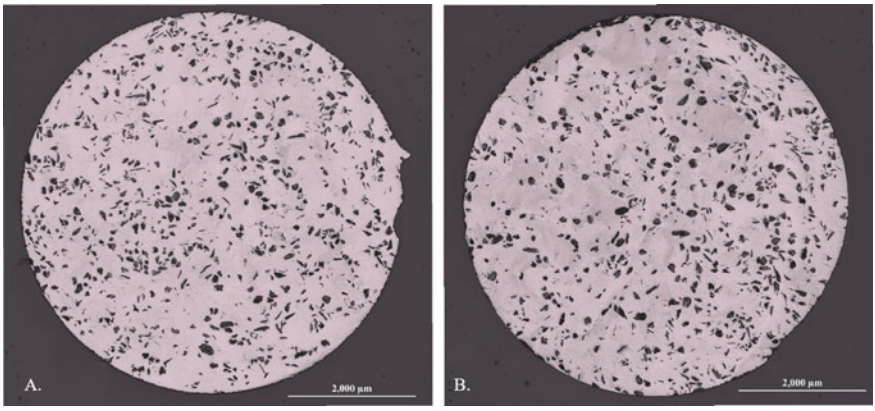

Fig. 2 Image of Ti-6Al-4 V with 5.3 wt%C (**A**) and 6 wt%.C (**B**). (Color figure online)

Table 1 Area fractions of Ti-C samples. Two samples of each carbon percentage were measured to understand the consistency of carbon composition within the samples. Note that these samples are not the same as the samples used for QS compression testing. The analysis was completed using ImageJ

Sample (wt%)	Area (mm^2)	%Area	%Area for Carbon
5.3%C Sample 1	26.78	88.67	11.33
5.3%C Sample 2	27.44	89.59	10.41
6%C Sample 1	27.01	94.20	5.80
6%C Sample 2	27.57	88.10	11.90

Quasistatic (QS) Compression Test Method

QS compression testing describes the behaviour of a material under a load. This testing reveals numerous materials properties such as the yield point, toughness, and elastic modulus. The tests were conducted in accordance with ASTM E9-09 standards. A strain rate of 10^{-3} s^{-1} was used for all tests in order to achieve QS compression. This meant a crosshead velocity of 3.6 mm/min is required for the 6 mm long sample. All samples were compressed until failure.

The uncertainties present in the displacement values measured by the Shimadzu universal testing machine needed to be considered for data analysis. In order to account for this, compliance testing of the machine was conducted prior to all the compression tests in order to ensure accurate readings for measurements.

As illustrated in Fig. 3, the tests were set using inserts which prevent the crosshead from being damaged due to the hard Ti-C specimens. Before each test, the surface of all inserts and samples were lightly lubricated using Molybdenum Disulfide (MoS_2) in order to prevent friction effects on the results. After the completion of each test, the fracture material was collected for further analysis. The inserts and test area were then cleaned using ethanol. The work area was also brushed and cleared using a vacuum in order to remove previous test fragments.

Three tests were conducted at each carbon range. Table 2 shows the parameters the test was conducted within. The dimensions of each sample were measured three times using a digital calliper in order to ensure accurate measurements.

Results and Discussion

Three QS compressions tests were on 5.3 and 6 wt%C Ti-C samples. All tests yielded different stress–strain curves as illustrated in Fig. 4. Only similarity that was noted was the compressions' strengths. Although it was expected that the compressive strengths of the samples would vary with carbon content, the compressive strengths were still similar. With the exception of test 2 for 5.3 wt%C and test 4 for 6 wt%C Ti-C, the compressive strengths of the samples ranged between 1.32 and 1.44 GPa.

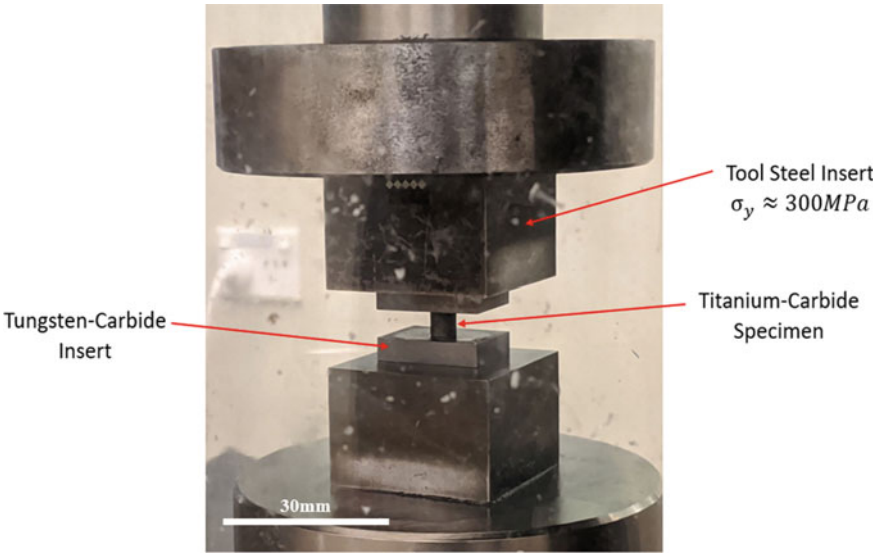

Fig. 3 Image of a QS compression test setup of a titanium-carbide sample being sandwiched between tool steel and tungsten carbide inserts. This setup is on the Shimadzu Autograph AGS-X. (Color figure online)

Table 2 Experiment parameter table showing the dimensions of the samples which were used in QS compression tests

Exp no.	Carbon (wt%)	Average measured dimension ($L_S \times D_S$) (mm)	L_S/D_S Ratios
1.1	5.3	5.993 × 5.980	1.002
1.2	5.3	5.960 × 5.960	1.000
1.3	5.3	5.970 × 5.957	1.002
2.1	6	5.967 × 5.970	0.999
2.2	6	5.963 × 5.983	0.967
2.3	6	5.963 × 5.970	0.999

That is overall quite similar in comparison to additively manufactured pure Ti-6Al-4 V which has a compressive strength ranging between 1.44 and 1.49 GPa [2]. The QS tests alone suggest that carbon significantly affects the material properties at low strain rates, in particularly the compressive strength. As illustrated in Fig. 4, the compressive strength increased with carbon content up until 5.3 wt%C Ti-C. Based on that figure, at some composition between 3.6 and 5.3 wt%C, the carbon begins to act detrimentally towards the compressive strength of the samples. This is shown by the drop in compressive strength for the 5.3 and 6 wt%C Ti-C samples.

Figure 4 also has significant error bars indicating variability in the mechanical properties of the samples. A potential reason behind such varying stress–strain properties (reference error bars in Fig. 4) and presence of anomalies in the compressive

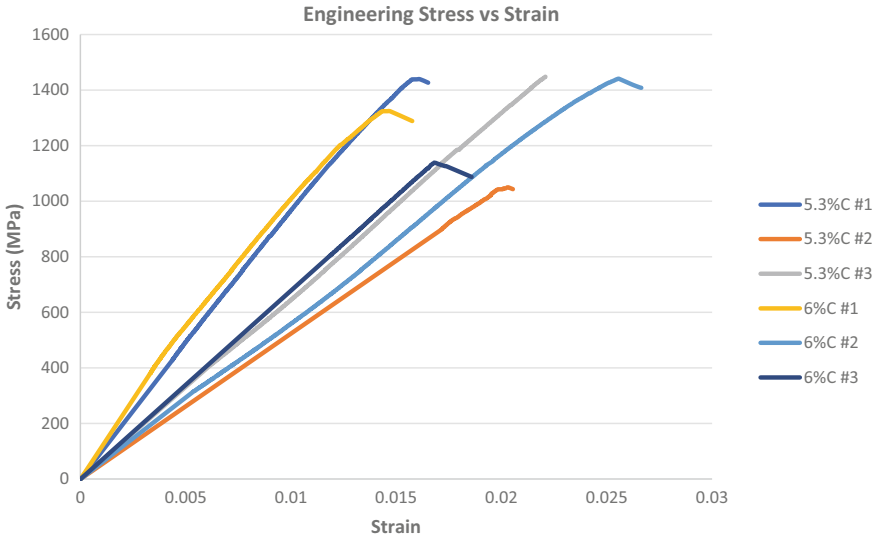

Fig. 4 Stress–strain results from the QS tests on various samples with different carbon contents (wt%). The strain rate of all the tests was 10^{-3} s^{-1}. (Color figure online)

strength could be due to the variability in the carbon composition in the microstructure of the sample. Using the optical microscope, the area fraction of the carbon particles in the alloy was measured. As shown in table, 1, the carbon levels in each sample are slightly different even after the LENS MR-7 system was set to form samples of specified carbon compositions. A major outlier that is noticeable in Table 1 is shown by '6 wt%C Sample 1'. The sample only has 5.8 wt% carbon covering the surface area. This is significantly lower than the other area fractions which range between 10 and 12 wt%.

It is important to note that the percent carbon area of a sample does not indicate the carbon composition with complete accuracy. The distribution of carbon may vary throughout the volume of the sample and the area fraction only represents one cross section. Instead the area fraction provides a sound indication and reasoning as to why some samples may have varying mechanical properties (Fig. 5).

Images were taken using an optical microscope on randomly selected samples. A deeper analysis of the samples showed the presence of dendrites in the grain structure of the material. These dendrites were pure titanium-carbide dendrites. The samples were not etched and hence only the dendrites and graphite particles can be properly visualised under an optical microscope as shown in Fig. 6.

Microhardness tests were conducted on the same samples used for the optical microscopy. Six tests were conducted on each sample to understand the microhardness properties of the samples on different components of the sample surface. It was noticed that dendrites had a hardening effect on samples. Regions with high dendrite concentrations had a significantly greater microhardness value as compared

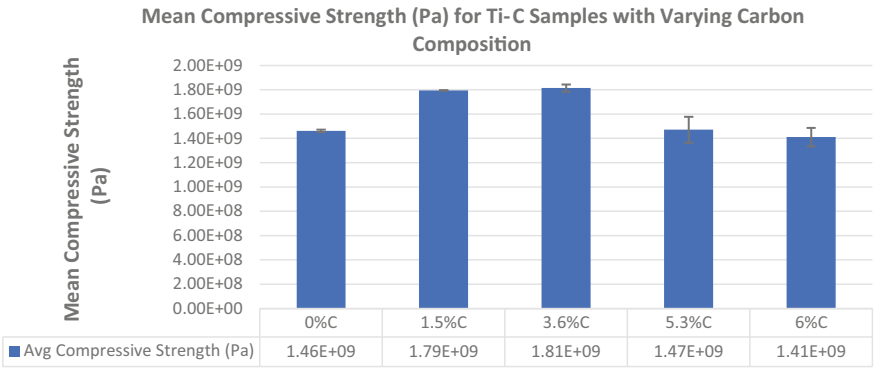

Fig. 5 The figure above shows how the compressive strength of Ti-C varies with carbon composition. Values for 0, 1.5, and 3.6 wt%C were determined by Wang [2]. (Color figure online)

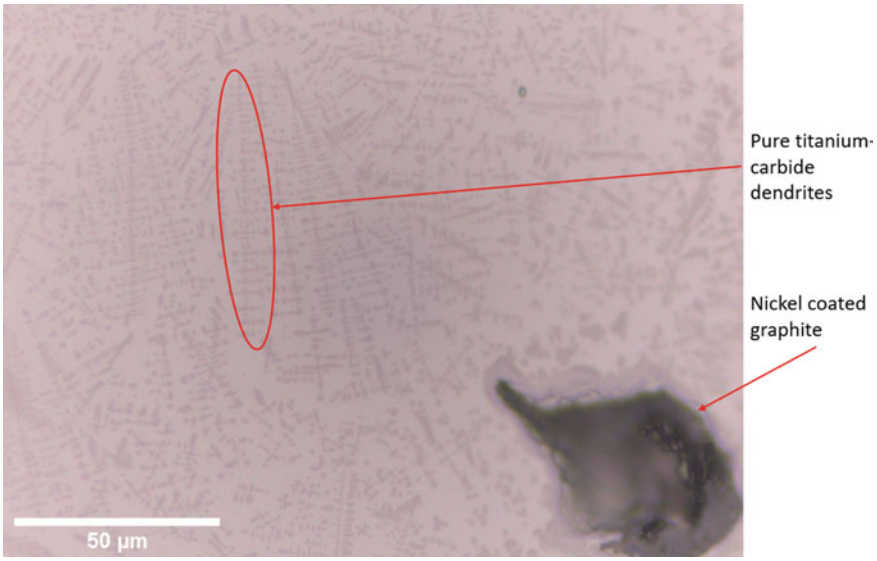

Fig. 6 The image above illustrates the presence pure titanium-carbide dendrites as well as the graphite particles present in the un-etched Ti-C samples. The image above is of '6 wt%C sample #2', captured at a magnification of ×50 by the optical microscope. (Color figure online)

to regions with low dendrite concentrations. Table 3 shows that the pure titanium-carbide dendrites significantly increased the microhardness of the material. Note that the average microhardness values for the low dendrite regions are similar regardless of the sample. However, the microhardness of the high dendrite regions increases at varying rates. Sample 2 with 6 wt%C increased by 115.9% in hardness in comparison to sample 1 with 5.3 wt%C which only increased by 31.3%. The microhardness measurements for sample 1 with 6 wt%C had the lowest microhardness values

Table 3 Table below displays the microhardness values measured for all the samples that were analysed under the optical microscope. Note that sample 2 with 5.3 wt%C did not have a flat surface which resulted in asymmetric indentations and hence did not provide accurate measurements

	Average Microhardness Values (HV)	
Dendrite concentration	5.3 wt%C Sample #1	6 wt%C Sample #2
Low dendrite concentration	611	507
High dendrite concentration	802	1095
Percent increase (%)	31	116

overall; this was expected due to the low carbon area fraction outlined in Table 1 earlier. A low graphite content will result in fewer dendrites being formed hence the lower microhardness measurements.

Figure 7 shows what is meant by 'low' and 'high' dendrite concentrations. Figure 7 further highlights the effects of the dendrites on mechanical properties of the sample. For low dendrite regions, such as 'Ti-C 5.3 wt%C #1', the indentation created slip

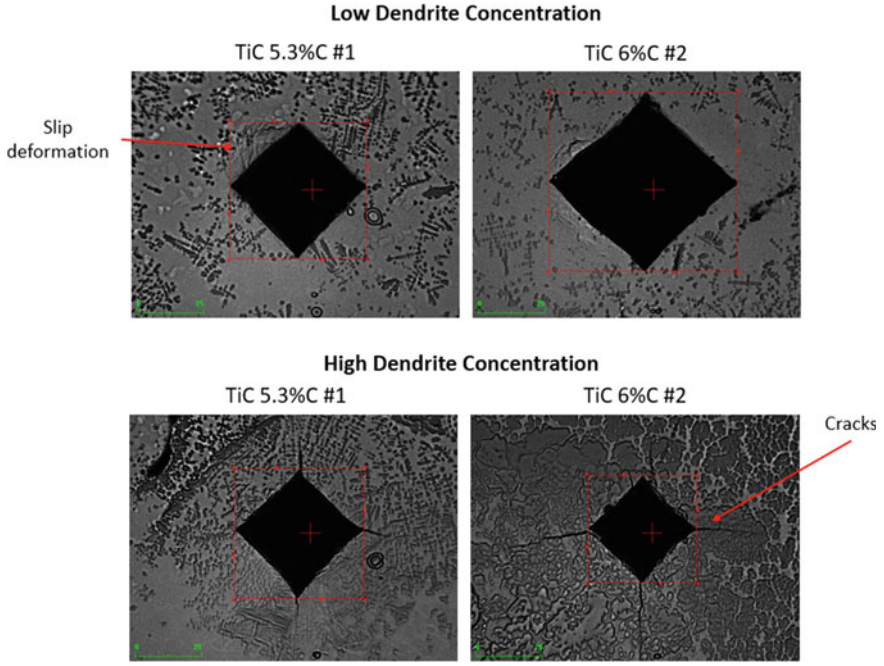

Fig. 7 The figure above displays images of the indentations made on the different samples that were tested. The figure also qualitatively highlights the difference between low and high dendrite regions. (Color figure online)

planes; a property more common in ductile materials. Whereas the high dendrite regions such as 'Ti-C 6 wt%C #2', the indentation created cracks which suggests dendrites also increase the brittleness of the material.

Conclusion

The mechanical response of Ti-C with 5.3 and 6 wt%C were tested. QS compression tests, microhardness tests, and optical microscopy was conducted on samples in order to understand how and why the Ti-C samples reacted to compressive loads. The QS compression tests showed that the compressive strength of the 5.3 and 6 wt%C samples were similar with the exception of certain anomalies. This showed that a difference of 0.7 wt%C does not have a significant effect on the compressive strength of the Ti-C under low strain rates (10^{-3} s^{-1}). However, it also proved that the presence of graphite in the microstructure of the sample has a strengthening effect on the compressive response of the sample as the overall compressive strengths were significantly greater than Ti-6Al-4 V.

Optical microscopy showed that the LENS MR-7 system does not produce samples with complete accuracy in terms of carbon composition. This provides some justification as to why some anomalies were present during the QS compression tests. It also highlights the necessity to analyse the samples after testing in order to correlate the mechanical properties with the microstructure and carbon composition of the sample. A major finding during testing was the effect of carbon on the compressive strength of Ti-C. It was demonstrated that carbon increases the compressive strength of the samples only up to a certain carbon composition. Beyond this point, additional carbon actually reduces the compressive strength of the sample. The exact composition could not be conclusively determined; however, it is likely to range between 3.6 and 5.3 wt%C.

Second, another major finding was the presence of pure titanium-carbide dendrites and its effect on the hardness and brittleness of the Ti-C material. Microhardness testing showed that the dendrites significantly increased the hardness of the samples. Cracks formed by the indentations on regions with high concentrations of dendrites suggests that the brittleness of the samples is also increased by the presence of dendrites. Whereas regions with a low dendrite concentration had lower microhardness values. Slip deformation also occurred as a result of the indentations in these low dendrite regions.

References

1. Densities of Metals and Elements Table (2020) Engineers Edge. https://www.engineersedge.com/materials/densities_of_metals_and_elements_table_13976.htm. Accessed 2 Sept 2020
2. Wang J, Escobedo-Diaz JP, East D, Morozov EV, Yang K (2020) Microstructure evolution of additively manufactured TiC reinforced graded metal matrix composite. In: Characterization of minerals, metals, and materials 2020. Springer
3. Miyamoto WY, Kaysser BA, Rabin AH, Kawasaki A, Reneé GF (1999) Functionally graded material. https://doi.org/10.1007/978-1-4615-5301-4
4. Huang CY, Chen YL (2017) Effect of varied alumina/zirconia content on ballistic performance of a functionally graded material. Int J Refract Metal Hard Mater. https://doi.org/10.4028/www.scientific.net/MSF.928.243
5. Titanium Carbide Nanoparticles: History, Properties, Synthesis, Applications (2019) Nanografi nano technology. Retrieved from https://nanografi.com/blog/titanium-carbide-nanoparticles-history-properties-synthesis-applications/
6. Kibria G, Bhattacharya B (2017) Microelectrical discharge machining of Ti-6Al-4 V: implementation of innovative machining strategies. Microfabr Precis Eng. https://doi.org/10.1016/B978-0-85709-485-8.00004-8
7. Motoshichi M, Muraji S, Eishin K, Syu I (1956) Reaction of hydrogen peroxide with titanium (IV) at different pH values. Bull Chem Soc Jpn. https://doi.org/10.1246/bcsj.29.904

Density Weibull Analysis of Tucum Fiber with Different Diameters

Michelle Souza Oliveira, Fabio da Costa Garcia Filho, Fernanda Santos da Luz, and Sergio Neves Monteiro

Abstract The replacement of synthetic fibers to natural fibers has been the subject of intense research, particularly as applied in composites. *Astrocaryum vulgare* is an important palm tree employed for many people along the Amazonian region in handcrafts and other products, by traditional manipulation techniques. The aim of this work is to perform a density Weibull analysis of *Astrocaryum vulgare* (Tucum) fibers with different diameters. The results obtained may be a database of *Astrocaryum vulgare* fibers, helping future research that will address its application potential as an alternative fiber applied in polymer composites.

Keywords Density analysis · Natural fibers · Tucum fiber · Weibull analysis

Introduction

The technological development and expectations for the use of natural resources have increased [1–10], and this has raised questions related to the availability of materials, such as those derived from sustainable resources, which can be processed with less energy consumption, as well as recyclable materials, including those from which energy can be recovered.

Moreover, the search for new materials, preferably those of natural origin, is constant. Research currently developed needs to consider not only the functionality of the material, but also its production process, products used, as well as the disposal of that material.

Vegetable fibers, such as sisal [11, 12], fique [13], coir [14], and PALF [15] fiber, among others, are sustainable materials, already having current applications (production of yarns, fabrics, nonwovens, composites, etc.) and other applications still being investigated. On the other hand, many other Brazilian plant species and their respective fibers, such as tucum fiber, little or nothing are known about its characteristics and possible applications. The leaves of the *Astocaryum vulgare* palm tree, known

M. S. Oliveira (✉) · F. da Costa Garcia Filho · F. S. da Luz · S. N. Monteiro
Military Institute of Engineering – IME, Rio de Janeiro, Brazil
e-mail: oliveirasmichelle@gmail.com

J. Li et al., *Characterization of Minerals, Metals, and Materials 2021*,
The Minerals, Metals & Materials Series,
https://doi.org/10.1007/978-3-030-65493-1_30

as tucum in the western Brazilian Amazon, are a potential source of vegetable fiber. Such fibers have already been studied by authors, who occasionally related their use to traditional communities [16–18], however, the physical characterization of the fiber was reported only once [18].

Thus, it is necessary to know the physical characteristics of the tucum fiber, which is little investigated in the literature.

Materials and Methods

The basic material investigated in this work was tucum fiber. Here it is worth mentioning that this tucum fiber was obtained from a local market in the state of Amazonas, Brazil.

Determination of Fiber Density: Fiber Geometry

One hundred fibers were randomly separated for a statistical evaluation of their dimension. Based on the diameters obtained in a model Olympus BX53M optical microscope (OM). Five different parts of the same fiber, at 0° and 90°, were analyzed. The rotation ensures the correct values for the average diameter estimate for each fiber.

The histogram in Fig. 1 shows a great dispersion in the values of the diameter of the tucum fiber, considering 6 ranges of diameters, a consequence of the heterogeneity of the physical characteristics of the lignocellulosic fibers.

In this figure it is important to notice that the diameter varies between 0.12 and 0.65 mm with an average diameter of 0.42 mm. The density of each fiber was calculated considering a cylindrical volume of the tucum fibers, using the following mathematical equation.

$$\rho = 4M/(\pi d^2 l) \tag{1}$$

where ρ is the density in g/cm^3, M is the mass in grams, d is the diameter, l is the length of the fiber. From the captured values of mass and volume, a density value was obtained for each tucum fiber. Statistical analyzes were performed using the program Weibull Analysis.

Surface Morphology

The surface morphology and cross section of tucum fiber were analyzed by scanning electron microscopy (SEM) attached by conducting carbon tape to a metallic

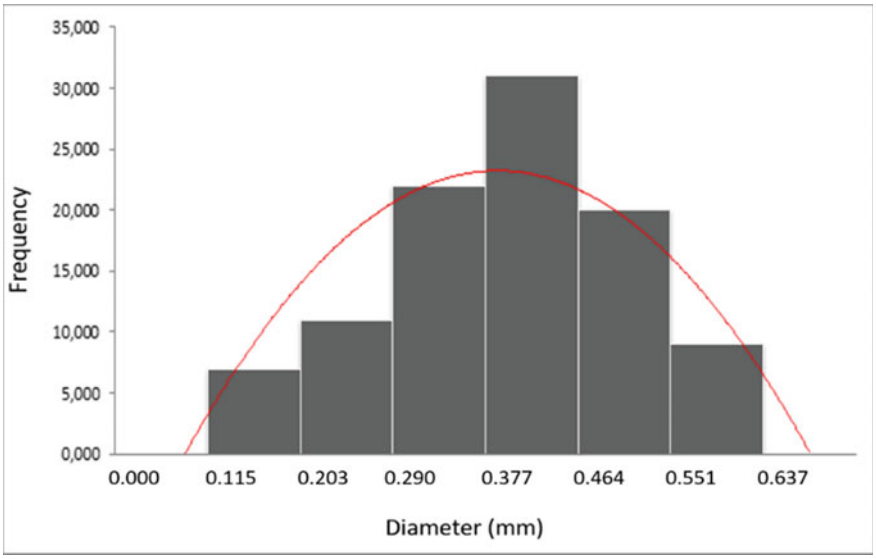

Fig. 1 Histogram of the frequency of the tucum fibers for each diameter range. (Color figure online)

support and then gold sputtered to allow observation in a model SSX-550 Shimadzu microscope operating with secondary electrons accelerated at a maximum voltage of 5 kV.

Results and Discussion

Analysis of the Diameter and Density of the Tucum Fiber

The values of densities were analyzed by the Weibull statistic method for each one of the 6 diameters intervals shown in the histogram of Fig. 1. In addition, the Weibull Analysis computer program provides the following parameters: θ (characteristic density), β (Weibull modulus), R2 (precision adjustment), as well as a mean density based on the Weibull distribution with related deviations. The values of these parameters are listed in Table 1.

Furthermore, the Weibull Analysis program provides the graphs shown in Fig. 2. In this figure it is important to observe that all graphs are unimodal, which indicates that fibers present that same behavior in each diameter interval.

In Fig. 2 there is a clear tendency for the parameter to vary inversely with the average tucum fiber diameter. This indicates that the thinner the fiber the high tends to be the characteristic density. The relationship between diameter and density is inversely proportional.

Table 1 Weibull parameters for the density of tucum fibers associated with the different diameter ranges

Diameter range (mm)	Weibull module (β)	Characteristic density (θ) (g/cm^3)	Precision adjustment (R^2)	Average density (g/cm^3)	Standard deviation (g/cm^3)
$0.12 \leq d < 0.20$	4.202	1.329	0.964	1.532	0.619
$0.20 \leq d < 0.29$	1.892	0.586	0.977	0.543	0.214
$0.29 \leq d < 0.38$	3.076	0.423	0.911	0.404	0.170
$0.38 \leq -d < 0.46$	3.949	0.329	0.975	0.330	0.090
$0.46 \leq d < 0.55$	13.94	0.251	0.983	0.263	0.088
$0.55 \leq d \leq 0.64$	2.522	0.202	0.956	0.178	0.100

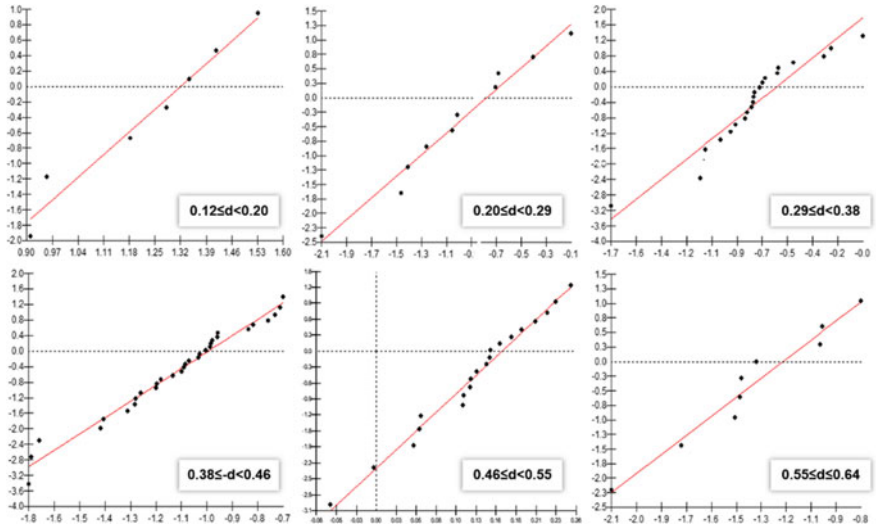

Fig. 2 Graphs of Weibull probability, maximum density, and characteristic density of tucum fibers in different diameter ranges. (Color figure online)

The variation of the characteristic density (θ) with the average fiber diameter for each one of its intervals is presented in Fig. 3. By means of a mathematic correlation, a hyperbolic type of equation was proposed to fit the data. A regular tendency for the θ parameter to vary with the inverse of the tucum fiber diameter.

$$\theta(\mathrm{g/cm^3}) = \mathrm{d}/(3.62\mathrm{d} - 2.87) \tag{2}$$

In order to analyze the physical meaning of Eq. (2), the Weibull average density, ρ¬, evaluated in this work for the tucum fiber was plotted as a function of the equivalent mean diameter in Fig. 4.

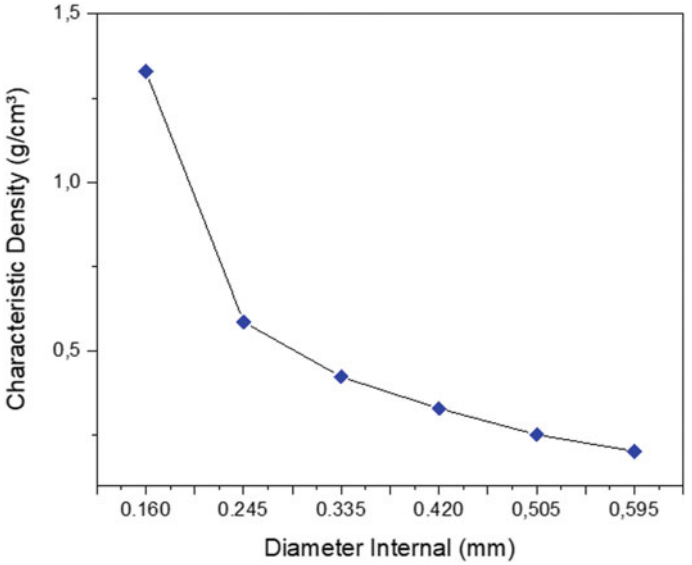

Fig. 3 Variation of the tucum fiber characteristic density, θ, from the Weibull analysis with the corresponding mean equivalent diameter. (Color figure online)

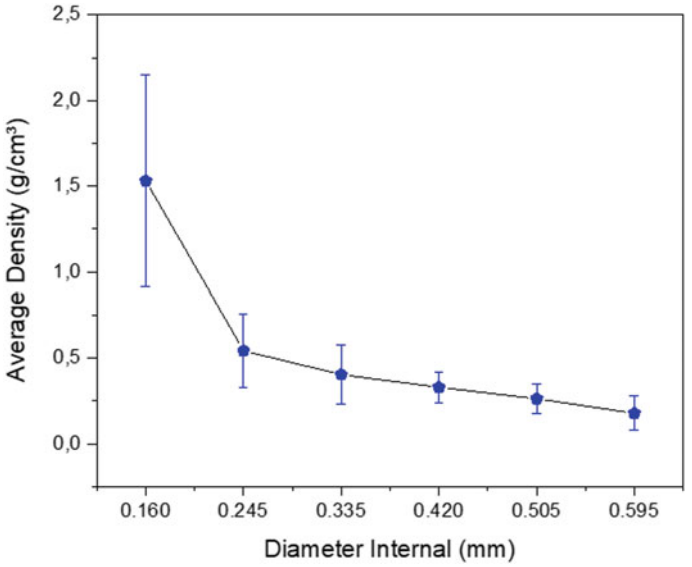

Fig. 4 Variation of the average density with the diameter for each interval in Fig. 1. (Color figure online)

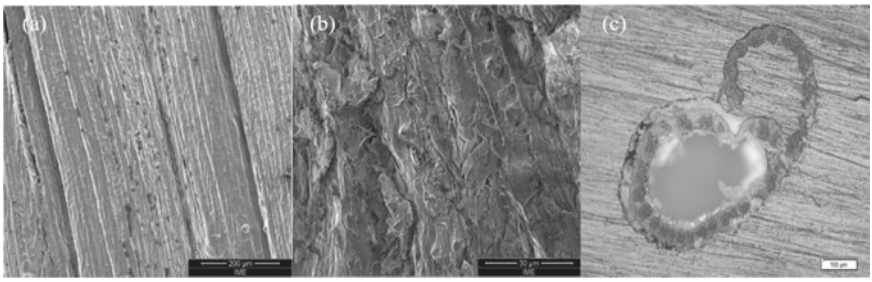

Fig. 5 SEM images longitudinal, (**a**) and (**b**), and OM image (**c**) of tucum fiber

In this figure, an apparent hyperbolic inverse correlation also exists between ρ¬ and d within the error bars (statistical deviations) and investigated limits. Figure 5 reveals by SEM and OM micrographs the aspects of surface morphology, Fig. 5a and b, and cross section, Fig. 5c.

It can be seen in this Fig. 5a displays less a natural flaw and few internal voids, On the other hand, Fig. 5b shows a heterogeneous surface comprising relatively more flaws and voids.

Summary and Conclusions

- The analysis of 100 fibers of tucum fibers showed an inverse dependence between the density and fiber diameter, so that the larger the diameter the lower the density.
- Weibull's statistical method proved to be fundamental for the analysis of density values as a function of the diameter ranges of the tucum fibers.
- A SEM analysis disclosed heterogeneity of tucum fibers.

Acknowledgements The authors thank the Brazilian agencies CAPES and CNPq for the financial support.

References

1. Nayak SY, Sultan MTBH, Shenoy ST, Kini CR, Samant R, Md Shah AU, Amuthakkannan P (2020) Potential of natural fibers in composites for ballistic applications–a review. J Nat Fibers
2. Benzait Z, Trabzon L (2018) A review of recent research on materials used in polymer-matrix composites for body armor application. J Compos Mater 52(23):3241–3263
3. Hassan KMF, Horvath PG, Alpár T (2020) Potential natural fiber polymeric nanobiocomposites: a review. Polymers 12(5):1072
4. Sanjay MR, Madhu P, Jawaid M, Senthamaraikannan P, Senthil S, Pradeep S (2018) Characterization and properties of natural fiber polymer composites: a comprehensive review. J Clean Prod 172:566–581

5. Pickering KL, Efendy MA, Le TM (2016) A review of recent developments in natural fibre composites and their mechanical performance. Compos Part A Appl Sci Manuf 83:98–112
6. Mohammed L, Ansari MNM, Pua G, Jawaid M, Islam MS (2015) A review on natural fiber reinforced polymer composite and its applications. Int J Polym Sci
7. Faruk O, Bledzki AK, Fink HP, Sain M (2014) Progress report on natural fiber reinforced composites. Macromol Mater Eng 299:9–26
8. Shah DU (2013) Developing plant fibre composites for structural applications by optimising composite parameters: a critical review. J Mater Sci 48:6083–6107
9. Shahinur S, Mahbub H (2020) Natural fiber and synthetic fiber composites: comparison of properties, performance, cost and environmental benefits. In: Encyclopedia of renewable and sustainable materials, pp 794–802
10. Monteiro SN, Drelich JW, Lopera HAC, Nascimento LFC, Luz FS, da Silva LC, Pereira AC (2019) Natural fibers reinforced polymer composites applied in ballistic multilayered armor for personal protection—an overview. In: Ikhmayies S, Li J, Vieira C, Margem J, de Oliveira Braga F (eds) Green materials engineering. The minerals, metals and materials series. Springer, Cham, pp 33–47
11. Inacio WP, Lopes FPD, Monteiro SN (2010) Diameter dependence of tensile strength by Weibull analysis: Part III sisal fiber. Matéria (Rio J.), Rio de Janeiro 15(2):124–130
12. Pereira AC, Inácio WP, Margem FM, Monteiro SN (2012) Effect of the fiber equivalent diameter on the elastic modulus and density of sisal fibers. In: Characterization of minerals, metals, and materials 2012, pp 357–364
13. Amoy Netto P, Altoé GR, Muylaert Margem F, de Oliveira Braga F, Monteiro SN, Margem JI (2016) Correlation between the density and the diameter of fique fibers. Mater Sci Forum 869:377–383
14. Monteiro SN, Muylaert Margem F, Guimarães Santafé Júnior HP, de Souza Martins LB, Oliveira MP (2014) Correlation between the diameter and the density of coir fiber using the weibull statistic methodology. Mater Sci Forum 775–776:266–271
15. Oliveira Glória G, Altoé GR, Amoy Netto P, Muylaert Margem F, de Oliveira Braga F, Monteiro SN (2016) Density Weibull Analysis of Pineapple Leaf Fibers (PALF) with different diameters. Mater Sci Forum 869:384–390
16. Bacelar-Lima CG, Mendonça MSD, Barbosa TCT (2006) Floral morphology of one population of Astrocaryum aculeatum Meyer (Arecaceae) in the Central Amazon-Brazil (in Portuguese). Acta Amazonica 36(4):407–412
17. Duarte AYS, Queiroz RS, Sanches RA, Garcia CR, Dedini FG (2012) Ethnobotany of natural fibres-Bactris setosa (tucum) in a traditional rural community. Fibres Text East Eur. 2(91):18–20
18. Pennas LGA, Leonardi B, das Neves P, Coelho LS, Savastano H, Baruque-Ramos J (2020) Amazonian Tucum (Astrocaryum Chambira Burret) Leaf fiber and handcrafted yarn characterization. SN Appl Sci 2(2):1–11

Ecological Mortars with Blast Slag Waste Application

J. A. T. Linhares Jr., M. T. Marvila, A. R. G. Azevedo, L. Reis, A. Azeredo, C. M. Vieira, and S. Monteiro

Abstract The objective of this work is to evaluate the replacement of cement and sand by blast furnace slag waste, in order to produce mortars with better mechanical properties. Mortars were used 1:3:1.5 (cement: sand: water), with substitution of 0, 10, 20, and 30% of cement by slag. A reference mortar was also produced without the application of the waste. Cures were evaluated at normal and thermal temperatures at 60 °C and tests were performed on compressive strength, water absorption, porosity, density, and consistency. The results indicate that the slag is viable in the application of both replacing sand and replacing cement.

Keywords Mortars · Waste · Substitution

Introduction

A variety of studies in the area of ecological mortars have been developed by science, with a tax to reduce the impacts generated by the industry, both the cement industry, and other deliberations that waste in its processes.

J. A. T. Linhares Jr. · M. T. Marvila (✉) · C. M. Vieira
LAMAV–Advanced Materials Laboratory, UENF-State University of the Northern Rio de Janeiro, Av. Alberto Lamego, 2000, Campos dos Goytacazes, Rio de Janeiro 28013-602, Brazil
e-mail: markssuel@hotmail.com

A. R. G. Azevedo (✉)
TER–Department of Agricultural Engineering and Environment, UFF-Federal Fluminense University, Rua Passo Da Pátria, 341, Niterói, Rio de Janeiro 24210-240, Brazil
e-mail: afonso.garcez91@gmail.com

A. R. G. Azevedo · L. Reis · A. Azeredo
LECIV–Civil Engineering Laboratory, UENF-State University of the Northern Rio de Janeiro, Av. Alberto Lamego, 2000, Campos dos Goytacazes, Rio de Janeiro 28013-602, Brazil

S. Monteiro
Department of Materials Science, IME-Military Institute of Engineering, Square General Tibúrcio, 80, Rio de Janeiro 22290-270, Brazil

J. Li et al., *Characterization of Minerals, Metals, and Materials 2021*,
The Minerals, Metals & Materials Series,
https://doi.org/10.1007/978-3-030-65493-1_31

The cement industry has linked to its production processes, stages that generate residues that have a negative impact on human health, such as the emission of pollutants into the air, soil, and water. This industrial branch still has the potential to generate social impacts in communities that occupy the surroundings of production plants [1].

Steel has significant economic importance and many investments are made in its production. It has much required properties such as ductility and mechanical resistance. With the great need for this metal in the world, questions about the wastes and environmental impacts produced in steel mills are beginning to emerge. It becomes necessary to correctly dispose of waste, reduce its impacts and, if possible, generate some economic gain. Legislation further leverages the need to give the most correct destination to waste, seeking greater development, based on sustainability [2].

In an international context, currently the steel industry has made promising advances in reducing the impacts generated by waste, however there is still a good potential for reducing these impacts. In integrated plants, about 80% of the waste generated comes from the steel reduction and refining stages, in semi-integrated plants the refining and raw materials stages generate practically all the waste. Among these steel co-products, blast furnace slag is the one that appears in greater quantity, with a capacity around 210–310 kg of solid waste per ton of pig iron produced. Cement industries already make use of slag generated in blast furnaces, given that, one of the challenges of environmental management in steel mills is better processing of these wastes, to add more quality and value to their specific purposes [3].

In general, there are two ways to produce glassy slag, the same that will be incorporated as a binder in mortar, the first of which is called granulation. In this process, the slag in its liquid state, in free fall, undergoes the action of a jet of water, on average in the proportion of 3 tons of water per 1 of slag, which is placed in a tank with water. Due to the speed of cooling, the slag takes on a glassy granular geometry, as there is not enough time for the crystalline material to form completely. In the second form of processing, pelletizing occurs, where the slag still in a liquid phase falls on a cylinder, which has teeth and rotates in an approximate rotation of 300 RPM, cooled by blasted cold water in a proportion of 1:1 tons of water and slag, the grains are thrown into the air, forming less homogeneous grains. In this second process, grains with a larger diameter are generally used as aggregate and those with a smaller diameter as a binder [4].

The glassy granules formed from blast furnace slag have limited hydraulic properties, however it is necessary to apply activators that speed up the water absorption process. There are generally three types of activators, they are chemical, physical, and thermal activators [5]. The purpose of this work is to use wastes from blast furnaces to incorporate them, in the agglomerating fraction of the mortar, and to observe, from a trace of a parameter, the variation of their mechanical properties. The replacement percentages will be 10, 20, and 30% of agglomerate per slag. The tests used to obtain quantitative data on the mechanical properties are compressive strength, water absorption, porosity, density, and consistency. The cures were carried out at normal and thermal temperatures at 60 °C.

Materials and Methods

The mortars for the tests used in this study were prepared in accordance with NBR 13276 [6], being properly mixed and homogenized. With the mortar still in the fresh state, consistency tests were carried out, to guide the procedures, the guidelines of the NBR 13276 standard were followed [7]. The consistency index recommended by this standard is 260 ± 5 mm.

A tapered trunk of 12.5 cm in diameter at the base, 8 cm in diameter at the top, and with a height of 6 cm. A circular table meeting the minimum diameter of 50 cm, the weight of 12 kg, and the drop height of 14 mm was used in the experiment.

The mortar was introduced into the mold, placed in the center of the table, in three homogeneous layers, and for the first layer 15 strokes were applied with a socket, distributed equally, in the second layer 10 strokes were applied and in the third 5. After the three layers, with the use of a metallic ruler, the mortar was scraped close to the edge of the mold, then it was removed and 30 falls were performed, in an interval of 30 s. Thus, the spreading of the mortar was measured using a ruler in three different directions. The consistency index was then obtained with the average of the three measurements recorded, so the higher this value, the better the workability of the mortar.

For the compressive strength test, three specimens were produced with three layers of the same volume of mortar, and in each layer 15 strokes were applied, evenly distributed, executed with a hammer specific to the procedure, according to specifications of NBR 5739 standard [8]. The dimensions of the specimens were, 50 mm in diameter and 100 mm in height, having reached rupture with the gradual application of 500 ± 10 N/s load, in an EMIC universal testing machine with a capacity of 30 kN as exposed in Fig. 1. The described procedure was performed for

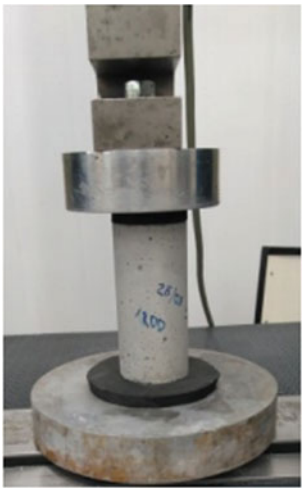

Fig. 1 Compressive strength test, with cylindrical specimen. (Color figure online)

specimens produced with normal curing and with thermal curing at a temperature of 60 °C.

After the rupture, it was possible to calculate the compressive strength using the function below (Eq. 1).

$$R_c = \frac{F_c}{625\pi} \tag{1}$$

where

R_c = compressive strength (MPa);

F_c = maximum applied load (N).

The water absorption and void index test (porosity) were performed in accordance with the NBR 9778 standard [9], three specimens were made to perform the procedures. In the first stage, the specimens were inserted in a greenhouse for 72 h. After time, the masses (M_s) were measured, then immersed in water also for 72 h. With saturation at room temperature, the specimens were brought to a boil, remaining for 5 h, with the volume of water in the container being kept constant. After the time, it was waited until the temperature reached the environment, naturally, then the mass of the immersed specimens (m_i) was recorded, with the use of a hydrostatic scale. In the last stage of the procedure, the specimens were removed from the water and dried with a damp cloth and their saturated masses were measured (m_{sat}).

Using the data recorded during the procedure, it was possible with the use of the equations below, to obtain water absorption (Eq. 2) and voids index (Eq. 3):

$$A = \frac{m_{\text{sat}} - m_s}{m_s} \tag{2}$$

$$I_v = \frac{m_{\text{sat}} - m_s}{m_{\text{sat}} - m_i} \tag{3}$$

$$R_c = \frac{F_c}{625\pi} \tag{4}$$

where

A = water absorption by immersion (%);

I_v = voids index (%);

M_{sat} = sample mass saturated in water after immersion and boiling (g);

M_s = kiln dried sample mass (g);

M_i = mass of the saturated sample immersed in water after boiling (g).

Mass density in the hardened state was measured by tests on submitted specimens, thermal curing, and normal curing, following the procedure described by NBR 13280

[10]. Three cylindrical geometry specimens were made and their measurements were taken using a caliper. Then the masses of the specimens were recorded, with the aid of a laboratory scale. After recording the parameters mentioned above, the volume of the specimens with the expression below was first calculated (Eq. 5).

$$v = \pi * R^2 * h \tag{5}$$

where

V = specimen volume;

R = cylinder base radius;

h = cylinder height.

With the volume of the specimens, mass density was calculated with the following Eq. 6.

$$\rho = \frac{m}{v} * 100 \tag{6}$$

where

ρ = bulk density in the hardened state;

m = mass of the specimen;

V = specimen volume.

Results

With the mortar still in the fresh state, the consistency test was performed, as already described in the methodology, the values obtained were displayed graphically in Fig. 2.

In the mortar without waste, a consistency of 263.33 mm was obtained, with 10% of residue replacing the cement, the value dropped to 259.21 mm, and a slightly sharp fall followed progressively. With 20 and 30% blast furnace waste, the values of 254.23 mm and 252.74 mm were removed in this order [11].

In the compressive strength, there was an increase in the specimens submitted to thermal curing, when incorporated 10 and 20% of the waste, increasing this property from 4.59 MPa to 4.79 and 4.82 MPa, respectively, when added 30% of waste as a binder, there was a drop in resistance, pointing to a possible limit for the improvement of this property, with the use of waste. In normal curing, the compressive strength dropped more linearly, as the percentage of added waste increased. In the parameter mortar, that is, without incorporation, it had a resistance of 4.25 MPa, as the percentage of added waste increased, to 10, 20, and to 30%, the compressive

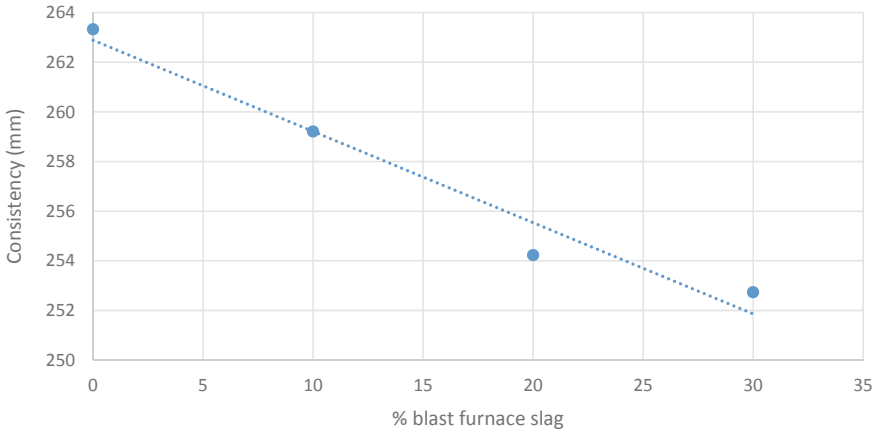

Fig. 2 Behavior of consistency in relation to the substitution of the binder by the waste. (Color figure online)

strength reached the values of 4.08 MPa, 3.88 MPa, and 3.62 MPa, respectively. Figure 3 shows these values [12].

The porosity, or voids index, had a considerable percentage increase in normal cure and a subtle drop, when using thermal cure, this divergence can be better visualized in Fig. 4. In the tests, which used the normal curing process, the mortar without replacing the binder by residue, obtained a porosity of 17.25%, from which an empty index of 18.23% was obtained for 10% and for 20% and 30%, 20.12% and 22.63% were obtained respectively. In the thermal curing process, in the parameter line, the index adopted a value of 16.23%, falling to 16.04% in the mortar with 10% waste, and remaining in decline with 20 and 30% waste, assuming 15.98% and 15.42% in that order [11].

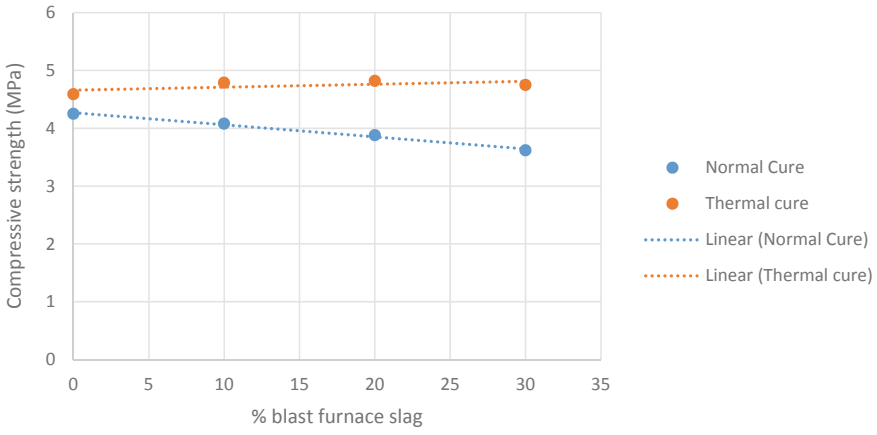

Fig. 3 Behavior of compressive strength, with the incorporation of blast furnace waste. (Color figure online)

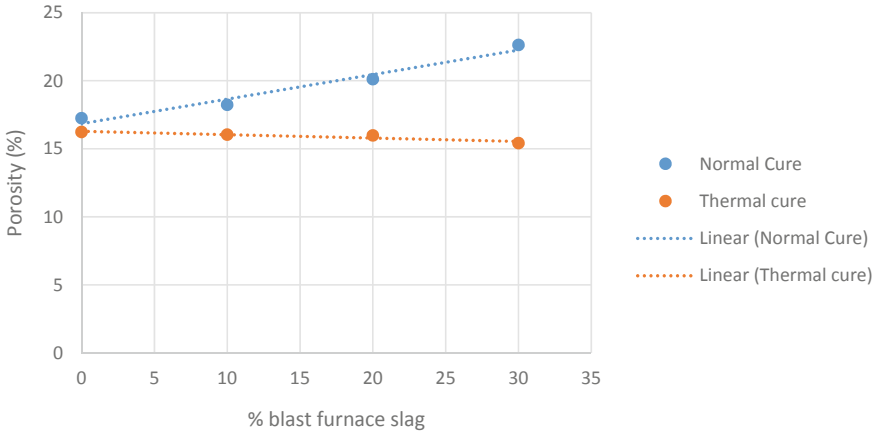

Fig. 4 Normal and thermal curing porosity. (Color figure online)

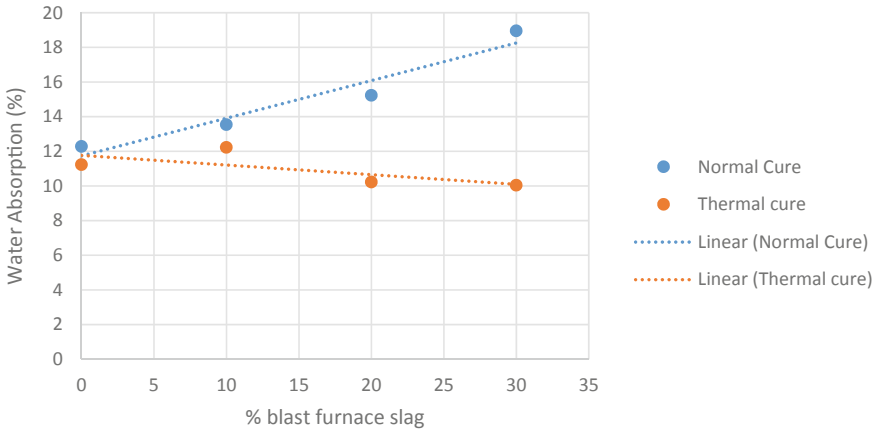

Fig. 5 Behavior of water absorption, in normal and thermal curing. (Color figure online)

In the water absorption tests, a percentage increase occurred, as the percentage of waste was increased, where the specimens were subjected to normal curing. In mortar without replacement of cement by waste, the absorption was 12.28%, with 10 and 20%, the percentages were 13.54 and 15.23%, respectively, where the substitution of the agglomerate portion was 30%, absorption was 18.96% [13].

When thermal curing was used, the highest percentage of absorption was with 10% of the substitution of the agglomerating portion, the value obtained being 12.23%. When 20% of cement was replaced, the absorption percentage was 10.23%, the absorption in the parameter mortar, assumed the value of 11.23%. With 30% replacement, absorption dropped slightly to 10.04% compared to mortar with 20% waste.

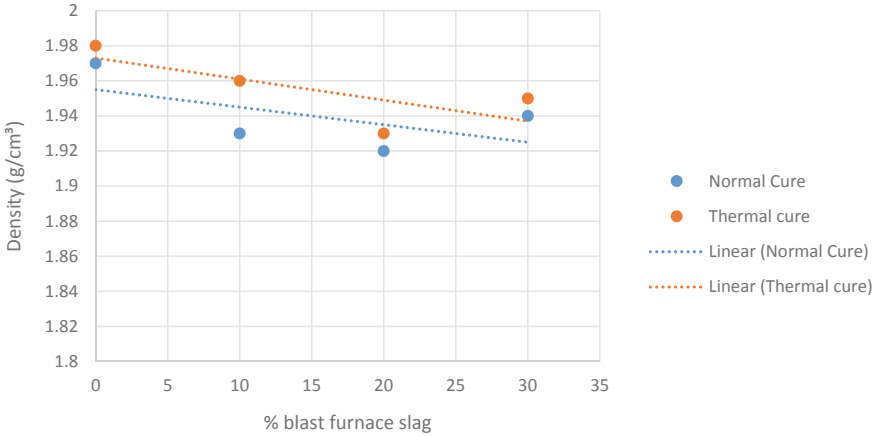

Fig. 6 Density behavior in normal and thermal curing, with the percentage increase of incorporated waste. (Color figure online)

In Fig. 5 below, it is possible to graphically display the difference between the types of curing, in this property as the percentage of waste in the mortar increases [11].

The results obtained in the density tests had a slight drop, when the cement replacement was carried out, both in the specimens where the normal cure was applied, and where the thermal cure was applied, except for the mortars in which 30% were replaced of the agglomerate portion by the waste, reaching a value of 1.94 g/cm^3 for normal curing and 1.95 g/cm^3 for thermal curing. The values obtained from parameter mortars were 1.97 g/cm^3 for normal curing and 1.98 g/cm^3 for thermal. With 10 and 20% waste, the densities obtained were 1.93 g/cm^3 and 1.92 g/cm^3, respectively, when normal curing was used. In thermal curing the values obtained were 1.96 g/cm^3 for 10% and 1.93 g/cm^3 for 20% replacement [13]. The behavior of this property, as the waste content increases, can be described in Fig. 6.

Conclusion

After obtaining the results, it was possible to conclude that

- The use of blast furnace waste, in the agglomerating fraction of the mortar, considerably changes its properties, increasing porosity and consequently water absorption, however this improvement only occurred when the normal curing process was used, in the thermal curing occurred a decline, becoming a healing process not indicated, when necessary the increase of these characteristics.
- When analyzing the behavior of the mortar, in relation to its mechanical properties such as resistance to compression and density of mass, a drop is observed in general. The density decreased in both normal and thermal curing, as expected

due to a considerable increase in porosity and water absorption. The compressive strength was almost linear, as there was only a subtle increase when using the thermal curing process. In normal cure a drop in resistance was observed, as possibly with the increase in porosity and the increase in the formation of potential points of tension accumulation, this property tends to fall.

- Consistency was the property where the greatest drop was observed, as the content of blast slag waste in the mortar increased, this drop showed less workability. Due to this drop, the incorporation of this waste is not indicated, when it is desired to obtain an increase in the workability of the material.
- The incorporation of slag waste, showed a potential for improvement in some properties, giving up the improvement in others. This is something common, when an incorporation is projected. We cannot yet improve so-called antagonistic properties, such as density and porosity. However, the study has a sustainable bias, that is, with the incorporation, there is the potential to reduce major impacts of the steel and cement industry, pointing to healthy economic and social growth.

Acknowledgements The authors thank the Brazilian agencies CNPq, CAPES, and FAPERJ for the support provided to this investigation.

References

1. Maury MB, Blumenschein RN (2012) Cement production: impacts to health and the environment. Debate Sustain 3:75–96 (In Portuguese)
2. Lopes MV, Lima SP (2016). Disposal of steel by-products: steel slag and blast furnace slag. Academic Works Magazine–NO 3. (In Portuguese)
3. Center for Management and Strategic Studies-Technical Documents Series (2010) Steel in Brazil 2010–2025. Brasilia. (In Portuguese)
4. John VM, Agopyan V (2000) Blast furnace slag recycling in Brazil. Industrial waste (In Portuguese)
5. Romério SP (2010) Activation of steel cement. Monograph-Federal University of Minas Gerais. (In Portuguese)
6. Brazilian Association of Technical Standards (2016) NBR13276. Mortar for laying and cladding walls and ceilings-Preparation of mortars. (In Portuguese)
7. Brazilian Association of Technical Standards (2016) NBR13276. Mortar for laying and cladding walls and ceilings-Determination of consistency index. (In Portuguese)
8. Brazilian Association of Technical Standards (2018) NBR5739. Concrete-Cylindrical specimen compression test. (In Portuguese)
9. Brazilian Association of Technical Standards (2005) NBR 9778. Hardened mortar and concrete-Determination of water absorption, voids and specific mass index. (In Portuguese)
10. Brazilian Association of Technical Standards (1995) NBR13280. Mortar for laying and cladding walls and ceilings-Determination of bulk density in the hardened state. (In Portuguese)
11. De Azevedo ARG, Marvila MT, BASSAM TA, Cecchin D, Pereira AC, Monteiro SN (2021) Technological performance of açaí natural fibre reinforced cement-based mortars. J Build Eng 33:101675
12. De Azevedo ARG, Alexandre J, Marvila MT, Xavier GC, Monteiro SN, Pedroti LG (2020) Technological and environmental comparative of the processing of primary sludge waste from paper industry for mortar. J Clean Prod 249:119336

13. Amaral LF, Girondi GC, Nicolite MC, Marvila MT, De Azevedo ARG, Alexandre J, Vieira CM, Monteiro SN (2020) Eco-friendly mortars with addition of ornamental stone waste-a mathematical model approach for granulometric optimization. J Clean Prod 248:119283

Effect of Flying Ash as an Additive or Substitute for Portland Cement on Compression Strength in Concrete Blocks (Vibro-Compacted)

H. G. Ortiz, F. L. García, M. R. Pérez, M. P. Labra, E. C. Legorreta, A. M. T. Ruiz, F. R. B. Hernández, and J. C. J. Tapia

Abstract This study aimed to find the effect of flying ash as an additive or substitute for cement in compression strength of concrete blocks (vibro-compacted). For this purpose, a control specimen was manufactured without Portland cement substitution or addition, denominated as the comparison standard with a strength of 6.99 MPa. With this reference parameter, Portland cement was added with 15% flying ash, reaching a strength of 7.1 MPa and replaced by three different percentages of the mixture, in proportions of 15, 30, and 50%, reaching strengths of 6.92, 6.4, and 5.07 MPa, respectively. The results showed that the compression strength decreases with increasing substitution percentage; however, at low percentages, flying ash can replace Portland cement without compromising compression strength. The physical

H. G. Ortiz · F. L. García · M. R. Pérez · M. P. Labra · E. C. Legorreta · A. M. T. Ruiz · F. R. B. Hernández · J. C. J. Tapia (✉)
Universidad Autónoma del Estado de Hidalgo, Área Académica de Ciencias de la Tierra y Materiales, Cd. Del conocimiento Km 4.5, C.P. 42180 Mineral de la Reforma Hidalgo, Mexico
e-mail: jcjuarez@uaeh.edu.mx

H. G. Ortiz
e-mail: hugo_garcia@uaeh.edu.mx

F. L. García
e-mail: felegorreta@hotmail.com

M. R. Pérez
e-mail: mreyes@uaeh.edu.mx

M. P. Labra
e-mail: miguelabra@hotmail.com

E. C. Legorreta
e-mail: edgarc@uaeh.edu.mx

A. M. T. Ruiz
e-mail: aislinn_teja@uaeh.edu.mx

F. R. B. Hernández
e-mail: frbh68@hotmail.com

J. Li et al., *Characterization of Minerals, Metals, and Materials 2021*,
The Minerals, Metals & Materials Series,
https://doi.org/10.1007/978-3-030-65493-1_32

tests were carried out under the ONNCCE standard. The flying ash was characterized using the techniques of scanning electron microscopy (SEM), X-ray diffraction (XRD), and laser particle size analyzer (LPSA).

Keywords Flying ash · Concrete · Compression strength · Additive · Vibro-compacted

Introduction

The world electrical energy generation in one year is approximately 26,913 Tera watt hours (TWh) [1], and more than 80% are produced with fossil fuels [2]. Owing to that the burning of natural coal is a common practice in countries that have reserves of this mineral. One of the main by-products of this process is flying ash.

The ASTM-C-618-03 [3] standard defines this term as: "The finely divided residue that results from the combustion of mineral or finely ground coal and which is transported in the gaseous flow", and these ashes have been studied already by different researchers as an additive or substitute for Portland cement in concrete high strength to improve compression strength.

For several years, these ashes have covered large areas of land, which is harmful to the waters underground; previous studies have reported that when rainwater comes into contact with these ashes, these are filtered dragging harmful particles, contaminating the earth and the water present in the subsoils [4].

National Geographic conducted a research entitled: "Looking for a safer future for discarded ash from coal-fired power plants", where it has been pointed out that flying ash and other coal residues burned represent one of the most important waste groups for the United States and Europe with figures higher than 136 million and 100 million annually, respectively [5]. Meanwhile, the scientists of the China Academy of Building Materials and Industry Technical Information Institute Construction Materials evaluated that in their country approximately 2,500 million tons of ash come from coal burning [5].

Owing to the alarming figures in tonnage of the ash amounts that are generated and how harmful they are for the environment, it is important to carry out studies focused on applying these residues of carbo-electrics, because it is estimated that its production will hardly stop; on the contrary, it will continue increasing.

Regarding the aforementioned, in 2003 Yasar et al. [6] made a mixture of lightweight concrete, adding 20% flying ash as a replacement for cement based on weight. Tests were performed with cylindrical samples 150 mm in diameter by 300 mm in height. The results obtained from the sample with the addition of ash were favorable and significant, reporting that the resistance compression was 29 MPa and the density of the concrete stepped from 1955 to 1932 kg/m^3, respectively.

Something important to consider when studying compression strength in concrete is the use that will be given to these. So in 2006 Hossain K et al. [7] incorporated different ash percentages, in the range of 5–20%, noting that the addition of flying

ash does not necessarily affects positively the compression strength of the specimens, reporting that by adding 5% of ash, an increase in compression strength is obtained from 79.5–82.4 MPa.

However, in recent years one of the main objectives is to reduce the amount of cement used to make concrete; in this sense, in 2008 Chen et al. [8] performed various tests with flying ash for lightweight, high-strength concrete, replacing Portland cement in the range of 10–40%, and finding the optimization in compression strength between 10 and 20%, with values 2.5 and 6 MPa higher than a control test with a resistance of 50 MPa.

As it could be observed, the central analysis of the investigations carried out by the authors Yasar, Hossain and Chen was the use of different percentages of substitution of Portland cement, using different types of concretes for different objectives, as is the case of the present study, which analyzes the addition and/or substitution of flying ash in the production of vibro-compacted blocks, which have the characteristic of containing low percentages of water, causing the slump in fresh state to be a maximum of two units.

Experimentation

To carry out the elaboration of the vibro-compacted blocks, first, it was necessary to carry out the mineralogical and morphological characterization of the flying ash, using the ray diffraction equipment X (DRX) brand Inel model Equinox 2000, in a range of 5°–100° with cobalt radiation (CoKα1), and a scanning electron microscope (SEM) brand JOEL model JSM-IT300 at different magnifications. For the particle size analysis, the Beckman and Coulter model LS13320 equipment was used.

Subsequently, for manufacture of blocks, the CPO-40R ordinal Portland cement mixture was used: fine stone material (sand), coarse material (gravel), and water. Using a water/cement ratio of 0.48, the dimensions of the block are 20 × 40 × 12 cm with two central holes under the NMX-C-038-2013 [9]. For this study, it was essential to have a comparison sample named “Control”, which is made without additives and is not altered in the water/cement ratio.

For the different mixtures used in the present study, the addition of flying ash was 15%. In addition to the substitution of 15, 30, and 50%, these percentages correspond to the quantity by weight (kg), of the cement used.

The mixing of raw materials for manufacture of vibro-compacted blocks was standardized. The stone materials used, their reduction, and the discrimination of thick and thin materials were governed by the standards NMX-C-030-2004, NMX-C-170-1997, and NMX-C-077-1997 [10–12]. Subsequently, to determine the specific densities of the fine and coarse aggregates, the standards NMX-C-164-2014 and NMX-C-165-2014 [13, 14] were used.

After complying with the parameters established by the standards used, the specimen was elaborated by mixing the stone materials and adding 50% of the total water.

Later the cement was added followed by the flying ash, and finally it was added to the amount of water missing.

The completely homogeneous mixture was poured into the vibro-compacting machine inside the molds, for a time of 7 s to later remove the mold. It should be noted that at the end of this process it is no longer considered a mixture, but a block in state fresh, which only has enough strength to keep its shape; with the passage of time, the compression strength increases, which made it possible to carry out the compression strength tests at 3, 7, 14, and 28 days after its manufacture, under the NMX-C-036-2004 standard [15]. The mechanical tests of the blocks were carried out using an ELVEC equipment model E660. The vibro-compacted blocks were tested in the horizontal direction, previously capped with sulfur mortar. The load was applied with a uniform and continuous speed, without producing impact.

Results

X-Ray Diffraction (XRD)

In the diffractogram of Fig. 1, the results obtained from the mineralogical characterization of flying ash through X-ray diffraction technique are shown, and four mineral phases can be observed to be present in the form of oxides. As expected, the majority

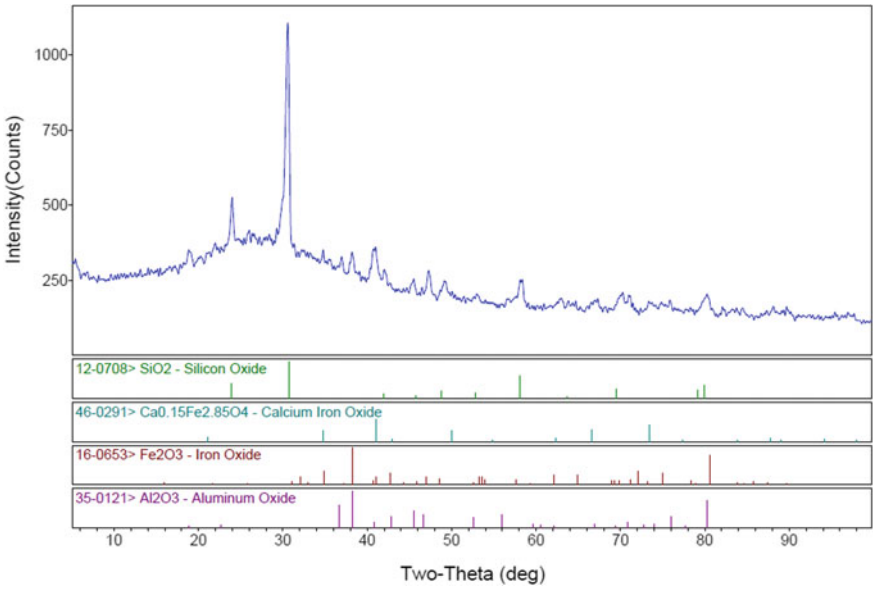

Fig. 1 Mineralogical characterization of flying ash, XRD. (Color figure online)

phase corresponds to quartz [(SiO2) (PDF 12-0708)] with the main peak at 2θ ≈ 30.69°, followed by iron and calcium oxide [(Ca $_{0.15}$ Fe $_{2.85}$ O_4) (PDF 46-0291)] with the main peak at 2θ ≈ 41.03°, hematite [(Fe 2 O 3) (PDF 16-0653)] with the main peak at 2θ ≈ 38.28°, and aluminum oxide Al2O3 (PDF 35-0121) with the main peak at 2θ ≈ 38.25°. It is important to highlight that these results are characteristic of a typical mineralogical composition of flying ash and are consistent with those reported by Gomes and François in 2000 [16].

Scanning Electron Microscopy (SEM)

The morphological study of flying ash was carried out using the scanning electron microscopy (SEM) technique. A micrograph obtained at 500× is showed in Fig. 2, where mainly a solid spherical morphology of the ash with a smooth texture is observed and that the particle size is very heterogeneous. Additionally, the presence of some agglomerations of these particles can be observed to a lesser extent as had already been reported by Kutchko and Kim [17]. It can be noted that the morphology is a function of the carbon particle used, the combustion temperature, and the cooling rate [18]; therefore, from these variables the size and shape of the flying ash can vary.

Laser Particle Analyzer (ATP)

As had already been observed through the scanning electron microscopy technique, there is a wide distribution of particle sizes in the flying ash, which was confirmed by the laser particle analyzer. The results are showed in the graph of Fig. 3. Observe first that the ash sizes are present in the range from 0.868 to 146.8 μm and that the average size is 12.59 μm. In 2006, Kutchko and Kim [17] reported a distribution of particle sizes between 1 and 200 μm and that they were mostly present in sizes of

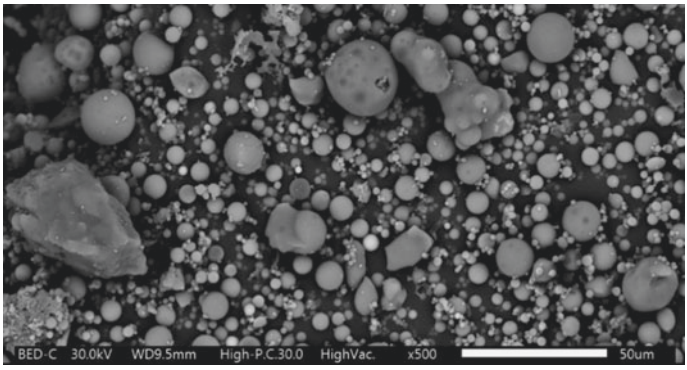

Fig. 2 SEM micrograph, obtained at 500×, revealing the morphology of the fly ash

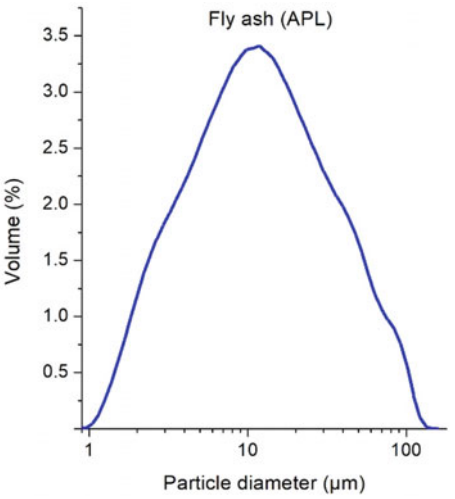

Fig. 3 Volume percentage proportion curve of the diameter of the flying ash. (Color figure online)

1 and 100 μm. These data are of importance because recent research carried out by Yunpeng [19] in 2020 reveals that the distribution and particle size of flying ash can positively affect compression strength.

Compression Strength

Table 1 shows the results obtained from the compression test of the vibro-compacted concrete blocks after 3, 7, 14, and 28 days, as well as the standard deviation of the recorded values of different mixtures, including the standard sample. These values are intended to demonstrate the validation of the reproducibility of the experiments. The data obtained from the compressive strength correspond to the arithmetic mean of five specimens under the NMX-C-036-ONNCCE standard. These results are relevant and are used to determine if the concrete mix meets the specified strength. Mainly

Table 1 Results obtained from the compression resistance tests in MPa of the flying ash and corresponding standard deviation (s)

Mixture	3 Days	7 Days	14 Days	28 Days
15% addition	5.67 *(0.19)*	6.81 *(0.07)*	6.82 *(0.09)*	7.10 *(0.12)*
15% substitution	4.36 *(0.03)*	5.57 *(0.09)*	6.44 *(0.06)*	6.92 *(0.1)*
30% substitution	4.31 *(0.03)*	5.21 *(0.04)*	5.69 *(0.08)*	6.40 *(0.08)*
50% substitution	2.92 *(0.05)*	3.42 *(0.03)*	3.93 *(0.16)*	5.07 *(0.09)*
comparison standard	4.24 *(0.03)*	5.23 *(0.18)*	5.71 *(0.03)*	6.99 *(0.08)*

Average: N = 5/(s is standard deviation)

the compressive strength test at 28 days is essential to evaluate the quality of the concrete [20].

It can be clearly seen that the compression strength is affected in different proportions depending on the amount of addition or substitution of the CPO-40R ordinal Portland cement, by the flying ash, in addition to the setting time of the block. The most significant data can be observed in the sample evaluated at 28 days and with the addition of 15% flying ash, because the resistance is affected positively by increasing 0.11 MPa; however, when evaluating the tests of substitution on the same days of drying, a contrary effect can be seen, mainly with the substitution of 50%. The foregoing suggests that flying ash under these conditions contributes to improving the compression strength only when it is added without replacing the cement for a setting time of 28 days.

In the graphs of Fig. 4, the behavior of the resistance to compression of the standard sample is presented: The mixture with 15% addition and the mixtures with substitutions of 15, 30, and 50% of CPO-40R cement at the different days of setting.

As can be seen, the results of the mixtures with 30% substitution and the reference sample have a comparatively similar compression strength at 28 days. However, the behavior through the setting time is different, observing that at early ages, for example at 3 and 7 days, significant compression strength is obtained only for mixtures with 15% substitution; hence it is not advisable to use in both cases the 50% replacement of flying ash.

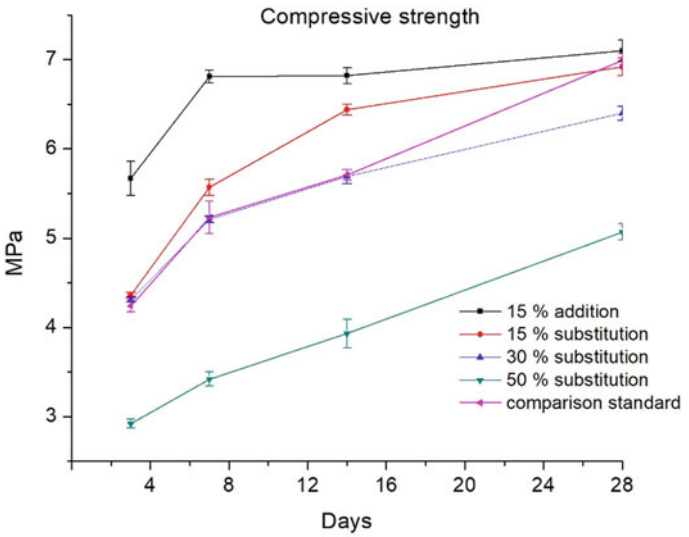

Fig. 4 Graph showing the behavior of compression strength and error bars of different samples at 3, 7, 14, and 28 days of setting. (Color figure online)

Hossain et al. [7] in 2006 reported in concrete set at 28 days that with a 15% substitution, the resistance decreased from 79.5 to 67.4 MPa, being negatively affected due to the fact that these are of high resistance.

Flying ash is not only used as a substitute for cement, but it has also been used by Mien et al. [21]. In 2019, as an additive to improve the workability of concrete mixtures, the substitution or addition of ash does not affect only the resistance to compression but also the behavior of it over time.

Conclusions

The characterization techniques used to reveal the mineralogy, morphology, and particle size distribution of the flying ash confirmed that the results obtained are consistent with those reported in previous research by different authors.

Through the study of compression strength, it is possible to evaluate the effect of flying ash used as an additive or partial substitute for CPO-40R cement in dry concretes, used for the manufacture of vibro-compacted blocks from 0 to 28 days setting.

The results obtained from the mechanical characterization of the vibro-compacted blocks revealed that the resistance to compression has a favorable effect when the flying ash is added without replacing the cement, in the different setting times proposed. However, for early ages, such as at 3 and 7 days of setting, the substitution of 15% ash also favors the resistance to compression, increasing 4.36 and 5.57 MPa with respect to the reference sample. Additionally, it is confirmed that it is not advisable to carry out the replacement of 50% of flying ash in any of the mixtures used.

References

1. Consumo energético mundial|Consumo eléctrico|Enerdata. https://datos.enerdata.net/electricidad/datos-consumo-electricidad-hogar.html. Accessed 04 Sept 2020
2. Consumo de energía procedente de combustibles fósiles (% del total)|Data. https://datos.bancomundial.org/indicator/EG.USE.COMM.FO.ZS?view=map. Accessed 04 Sept 2020
3. ASTM C618-03 (2003) Standard specification for coal fly ash and raw or calcined natural pozzolan for use in concrete
4. Marta J, Sánchez Rojas MI, Frías M (1999) Estudio de las variaciones mineralógicas y morfológicas en cenizas volantes provocadas por fenómenos de lixiviación. Mater Construcc 49(256):43–58. https://doi.org/10.3989/mc.1999.v49.i256.435
5. National Geografic (2011) Buscando un futuro más seguro para la ceniza desechada de las centrales eléctricas de carbón. National Geographic, ago. 15, 2011. https://www.nationalgeographic.es/ciencia/buscando-un-futuro-mas-seguro-para-la-ceniza-desechada-de-las-centrales-electricas-de. Consultado 19 Sept 2019
6. Yasar E, Atis CD, Kilic A, Gulsen H (2003) Strength properties of lightweight concrete made with basaltic pumice and fly ash. Mater Lett 57(15):2267–2270. https://doi.org/10.1016/s0167-577x(03)00146-0

7. Hossain KMA (2006) High strength blended cement concrete incorporating volcanic ash: performance at high temperatures. Cem Concr Compos 28(6):535–545. https://doi.org/10.1016/j.cemconcomp.2006.01.013
8. Chen B, Liu J (2008) Experimental application of mineral admixtures in lightweight concrete with high strength and workability. Constr Build Mater 22(6):08–1113. https://doi.org/10.1016/j.conbuildmat.2007.03.001
9. NMX-C-038-ONNCCE-2013 (2004) Industria de la construcción-mampostería–determinación de las dimensiones de bloques, tabiques o ladrillos y tabicones–método de ensayo
10. NMX-C-030-ONNCCE-2004 (2004) Industria de la Construcción-Agregados-Muestreo
11. NMX-C-170-1997-ONNCCE (1997) Industria de la Construcción–Agregados–Reducción de las Muestras de Agregados Obtenidas en el Campo al Tamaño Requerido para las Pruebas
12. NMX-C-077-1997-ONNCCE (1977) Industria de la Construcción–Agregados para Concreto–Análisis Granulométrico–Método de Prueba
13. NMX-C-164-ONNCCE-2014 (2014) Industria de la construcción-Agregados-Determinación de la densidad relativa y absorción de agua del agregado grueso
14. NMX-C-165-ONNCCE-2014 (2014) Industria de la construcción-Agregados-Determinación de la densidad relativa y absorción de agua del agregado fino-Método de ensayo
15. NMX-C-036-ONNCCE-2013 (2013) Industria de la Construcción–Mampostería–Resistencia a la compresión de bloques, tabiques o ladrillos y tabicones y adoquines–Método de Ensayo
16. Gomes S, François M (2000) Characterization of mullite in silicoaluminous fly ash by XRD, TEM, and 29Si MAS NMR. Cem Concr Res 30(2):175–181. https://doi.org/10.1016/S0008-8846(99)00226-4
17. Kutchko BG, Kim AG (2006) Fly ash characterization by SEM–EDS. Fuel 85(17–18):2537–2544. https://doi.org/10.1016/j.fuel.2006.05.016
18. At H, Vories KC, Throgmorton D, Throgmorton D (2002) Coal combustion by-products and western coal mines: a technical interactive forum. Golden, Colorado
19. Cui Y, Liu J, Wang L, Liu R, Pang B (2020)A model to characterize the effect of particle size of fly ash on the mechanical properties of concrete by the grey multiple linear regression. Comput Concr 26(2):175–183. https://doi.org/10.12989/cac.2020.26.2.175
20. NMX-C-414-ONNCCE-2017 (2017) Industria de la construcción-Cementantes hidráulicos-Especificaciones y métodos de ensayo
21. Van Mien T, Phuc NH, Yen CTH (2019) Effect of fly ash on shrinkage of self-compacting concrete using restrained ring test. J Sci Technol Civil Eng (STCE)-NUCE 13(3):26–33. https://doi.org/10.31814/stce.nuce2019-13(3)-03

Effect of Mg with Different Combination Form of Mg–Ca in MgO-Bearing Fluxes on Fluidity of Liquid Phase in Sintering Process

Shaoguo Chen, Wen Pan, Yapeng Zhang, Huaiying Ma, and Zhixing Zhao

Abstract MgO was considered to be an indispensable mineral composition of the modern sintering process. Fluidity of liquid phase reflecting the scope of effective bonding makes a clear distinction among MgO-bearing fluxes in the sintering process. Mg–Ca combination forms of dolomite, l-dolomite, serpentine and their influence on the fluidity of liquid phase and bonding strength of sinter body were investigated and analyzed. The results showed that there were non-separated, partly-separated, and completely-separated states of Mg–Ca in different MgO-bearing fluxes. Furthermore, development of the separation degree of Mg–Ca combination states led to the decrease of Mg content melt in silico-ferrite of calcium and aluminum (SFCA) and increase of Mg content in magnetite. Consequently, fluidity of liquid phase was improved due to decline of viscosity of liquid phase. Moreover, bonding strength had a good positive correlation with fluidity of liquid phase. Hence, increase of Mg–Ca separation degree was beneficial for improvement of bonding strength.

Keywords Fluidity of liquid phase · Sintering · MgO-bearing fluxes · Mg–Ca combination states

Introduction

Suitable amounts of MgO in sinters can greatly improve the slag properties of blast furnaces. Simultaneously, it plays an important role for alleviating the low temperature reduction degradation phenomenon of sinters in blast furnaces. Hence, MgO was considered to be an indispensable mineral composition of modern sinter [1–4]. In sintering process, MgO is provided by MgO-bearing fluxes. Different types of MgO-bearing fluxes cause significant differences of sintering performance [5–8].

S. Chen (✉) · W. Pan · Y. Zhang · H. Ma · Z. Zhao
Research Institute of Iron & Steel, Shougang Group Co., LTD, Research Institute of Technology, Beijing 100043, China
e-mail: chenshaoguo_0701@163.com

Beijing Key Laboratory of Green Recyclable Process for Iron & Steel Production Technology, Beijing 100043, China

J. Li et al., *Characterization of Minerals, Metals, and Materials 2021*,
The Minerals, Metals & Materials Series,
https://doi.org/10.1007/978-3-030-65493-1_33

Table 1 Chemical composition of fluxes and ores in the study (mass, %)

	TFe	SiO_2	CaO	MgO	Al_2O_3	LOI
Dolomite	0	1.88	31.12	19.64	0.44	45.73
L-Dolomite	0	1.37	49.83	31.69	0	16.85
Serpentine	0	38.19	2.13	38.05	0.93	12.07
Ore-A	65.26	1.92	0.03	0.03	1.27	2.08
Ore-B	60.33	4.30	0.32	0.07	1.50	5.58

Much research on reaction mechanism of MgO and reaction route of MgO-bearing fluxes has been reported in sintering process [9–11]. Influence of Mg–Ca combination states in MgO-bearing fluxes on fluidity and bonding strength of liquid phase in sintering was rarely studied.

In this work, Mg–Ca combination states of different MgO-bearing fluxes were confirmed. Tests of fluidity of liquid phase and bonding strength were carried out with different Mg–Ca combination states. Influence of Mg–Ca combination states on sintering characteristics was discussed.

Experimental Materials

Iron ore fines, dolomite, l-dolomite (light-burned dolomite), serpentine, and pure reagents (including Fe_2O_3, CaO, SiO_2, Al_2O_3) were used, see details in Table 1. All the fluxes were produced in China. Ore-A was hematite from Brazil. Ore-B was blending ore from a large-scale Chinese steel enterprise.

Experimental Methods

Study of Mg–Ca Combination State

Thermogravimetric analysis and differential scanning calorimetry (TG-DSC) method was used to elucidate the differences of Mg–Ca combination states among various MgO-bearing materials.

Fluidity of Liquid Phase

To elucidate the influence of different Mg–Ca combination states of MgO-bearing materials on fluidity of liquid phase during sintering, fluidity tests were carried out

with the method of fluidity of liquid phase test, [12] see details in Figs. 1 and 2. Materials were mixed and compressed as a single cylinder tablet of 0.8 g under a pressure of 15 MPa. Then the tablet of about Φ 8 mm × 5 mm was sent to an infrared heating furnace named Micro-Sinter equipment [13]. The experiment temperature was 1280 °C. After experiments, the fluidity area of liquid phase was obtained. Index of fluidity of liquid phase (*IFL*) was achieved by comparing the area of liquid phase before and after tests. As shown in Eq. (1), IFLs were calculated.

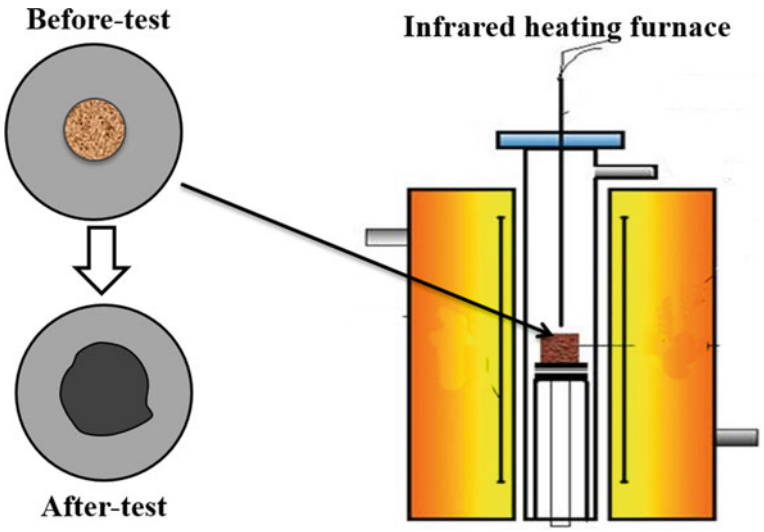

Fig. 1 Schematic diagram of fluidity of liquid phase tests. (Color figure online)

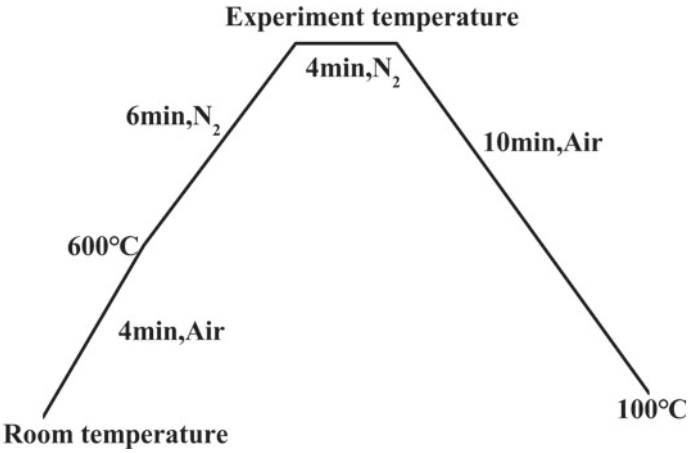

Fig. 2 Temperature system and atmosphere of the liquid phase fluidity tests

Table 2 Mixing conditions of fine materials in fluidity of liquid phase tests (mass, %)

	Case1	Case2	Case3
Dolomite	26.05	0	0
L-Dolomite	0	15.84	0
Serpentine	0	0	15.00
Fe_2O_3	57.38	64.82	63.00
CaO	10.12	11.55	20.00
SiO_2	5.63	6.73	1.10
Al_2O_3	0.82	1.06	0.90
Total	100.00	100.00	100.00

$$IFL = (FA - OA)/OA \tag{1}$$

where *FA* is the flowing area, in mm^2; and *OA* is the original area, in mm^2.

The mixing condition of fine materials used in liquid phase fluidity tests is shown in Table 2. The chemical composition of the fine mixture was maintained constant, that is, $Fe_2O_3 = 45.80$ mass%, $SiO_2 = 6.95$ mass%, CaO = 20.69 mass%, MgO = 5.81 mass%, $Al_2O_3 = 1.06$ mass%, basicity was 3.0, by adjusting the proportion of pure reagent.

Bonding Strength Test

Bonding strength tests were carried out to study the influence of different Mg–Ca combination states on the strength of sinter. Dolomite, l-dolomite, and serpentine below 0.15 mm were used as MgO-bearing materials. Simultaneously, pure reagents were also used, including Fe_2O_3, SiO_2, CaO, MgO, and Al_2O_3. Figure 3 shows the

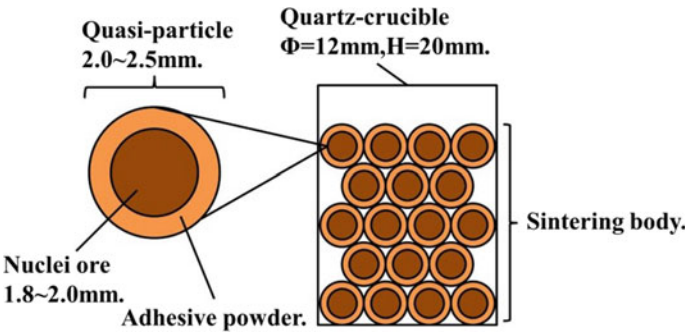

Fig. 3 Schematic diagram of sintering body in bonding strength tests. (Color figure online)

schematic diagram of sintering body in bonding strength tests. About 200 quasi-particles made in disc-pelletizer mixer were put into a quartz crucible. The nuclei ore used in the tests were Ore-A from Brazil, and the adhesive powder consisted of MgO-bearing materials, Ore-B and pure reagents. The chemical composition of quasi-particles was maintained constant, that is, $Fe_2O_3 = 53.30$ mass%, $SiO_2 = 5.93$ mass%, CaO = 11.86 mass%, MgO = 3.70 mass%, $Al_2O_3 = 1.26$ mass%, basicity was 2.0, by adjusting the proportion of pure reagent.

The experiment equipment, temperature system, and atmosphere of bonging strength tests were the same as the fluidity tests. After sintering, the weight (original weight) of sinter body was measured. Then, shatter test was carried out to obtain shatter indexes. The sinter body was freely dropped from a height of 2 m, and screened the pieces with 5 mm perforated screen. The first shatter index was obtained by calculating the pieces weight above 5 mm as a share of the original weight. Sequentially, the above 5 mm pieces were freely dropped from 2 mm height and screened. The second shatter index was obtained by calculating the pieces weight above 5 mm as a share of the original weight. The third to tenth shatter indexes were obtained similarly.

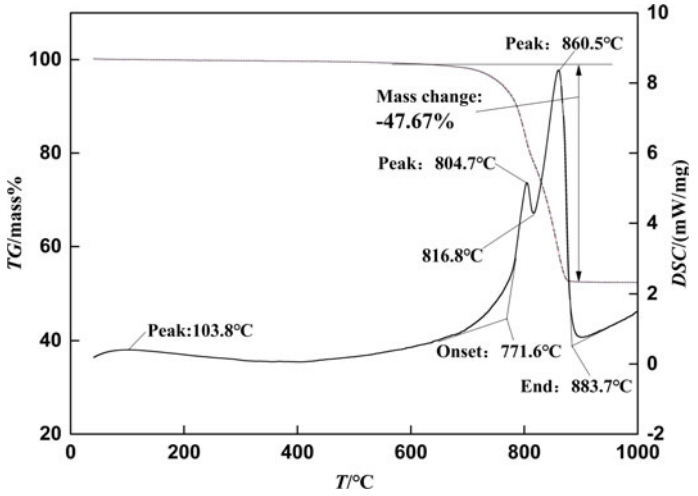

Fig. 4 Thermal decomposition characteristic of dolomite. (Color figure online)

Experimental Results and Analysis

The Mg–Ca Combination State of MgO-Bearing Fluxes

Figure 4 shows the result of thermal decomposition characteristic of dolomite. It can be divided into three stages. But the boundary of second and third stage was not obvious, both of which were continuous endothermic process. The first stage was at about 104 °C where a little weight loss occurred, and it was analyzed to be the removal of physical water. The second stage started at 772 °C and the peak temperature was 816.8 °C. However, when the second did not finish completely, the third stage had already begun, the peak temperature was about 860 °C, and it ended at about 884 °C. Both of the decomposition temperature intervals were relatively narrow, but the weight loss was larger at 48%. It was analyzed that $CaMg(CO_3)_2$ decomposed into MgO, CO_2, and $CaCO_3$ in the second stage, and then $CaCO_3$ decomposed into CaO and CO_2 in the third stage. According to the thermal decomposition process of dolomite, MgO was generated in the second stage and CaO was produced in the third stage, respectively. Therefore, when dolomite is as MgO-bearing material, MgO would be quickly produced accompanying with the generation of CaO during sintering. Mg–Ca state is non-separated state which is defined as Case1.

Figure 5 shows the result of thermal decomposition characteristic of l-dolomite. It consisted of three stages, and the boundaries were relatively obvious. All the stages were endothermic process. Decomposition temperature of the first stage was about 100 °C with a little weight loss, and it was analyzed to be due to removal of physical water. Decomposition temperature of the second stage was between 412 and 495 °C, the weight loss was about 7.6%. It was analyzed to be the decomposition

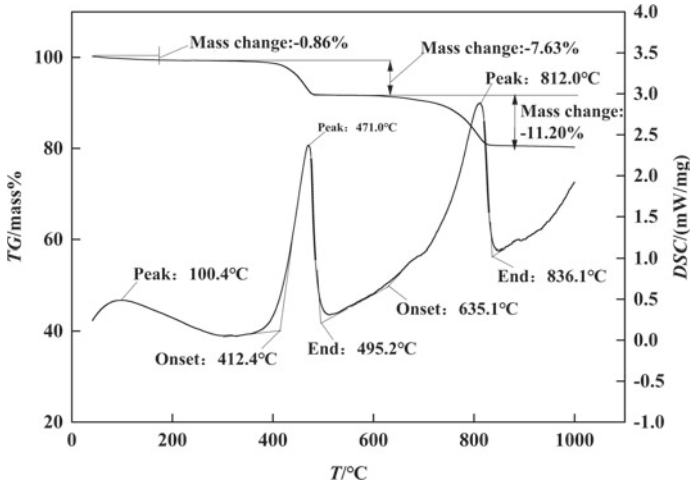

Fig. 5 Thermal decomposition characteristic of l-dolomite

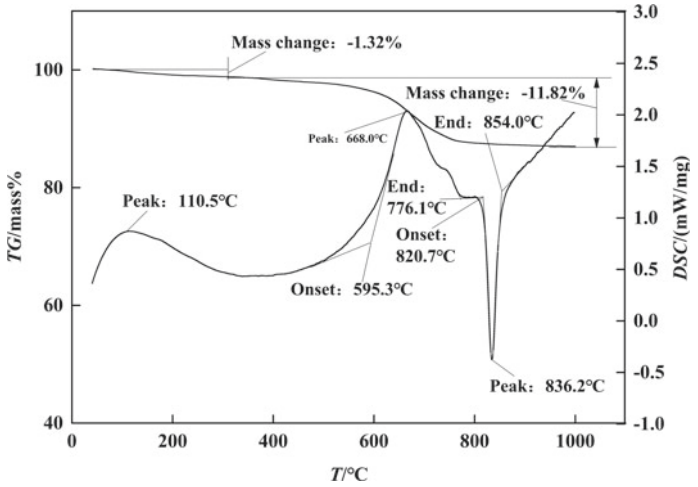

Fig. 6 Thermal decomposition characteristic of serpentine

of modified $Ca(OH)_2$. Thirdly, the temperature range of the third stage was between 635 and 836 °C with weight loss of about 11.2%. It was analyzed that $CaCO_3$ decomposed into CaO and CO_2. According to the thermal decomposition process of l-dolomite, it contained MgO and CaO at room temperature. Additionally, partial CaO was generated in high temperature. Therefore, when l-dolomite is as MgO-bearing material in sintering process, Mg–Ca state is partly-separated state which is defined as Case2.

Figure 6 shows the result of thermal decomposition characteristic of serpentine. It also included three stages. The first stage was at about 110 °C with weight loss of 1.3%. It was analyzed to be the removal of physical water. The second stage was between 600 and 800 °C and had a more powerful endothermic peak. It was analyzed to be the removal of crystal water. The third stage was between 800 and 850 °C. Although it had an obvious exothermic peak, the exothermal interval was narrower. It was analyzed that the enstatites were formed by free silica and partial forsterite. According to the thermal decomposition process of serpentine, when the serpentine is as MgO-bearing material in the sintering process, CaO is completely provided by external CaO-bearing material. Therefore, Mg–Ca state is a completely-separated state which is defined as Case3.

Fluidity of Liquid Phase

Fluidity of liquid phase reflects the flow of generated liquid phase and the ability of bonding material around. Figure 7 shows the pictures of macroscopic feature of liquid phase in the fluidity tests. There were differences in area from Case1 to Case3.

Fig. 7 Macroscopic feature of liquid phase in the fluidity tests. (Color figure online)

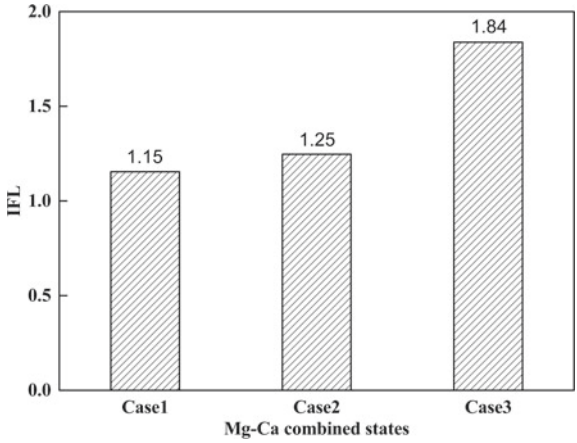

Fig. 8 Fluidity of liquid phase with three kinds of MgO-bearing material

Figure 8 shows the results of fluidity of liquid phase with three kinds of MgO-bearing material which had different Mg–Ca combination states. IFL of Case3 was the highest, then Case2 and Case1. It indicated that separation degree of Mg–Ca could influence the fluidity of liquid phase.

Bonding Strength of Sinter Body

Sinter body was made up of many sinter body sub-units. As shown in Fig. 9, the sub-units of Case1 bonded each other deficiently. However, the sub-units of Case3 bonded each other effectively.

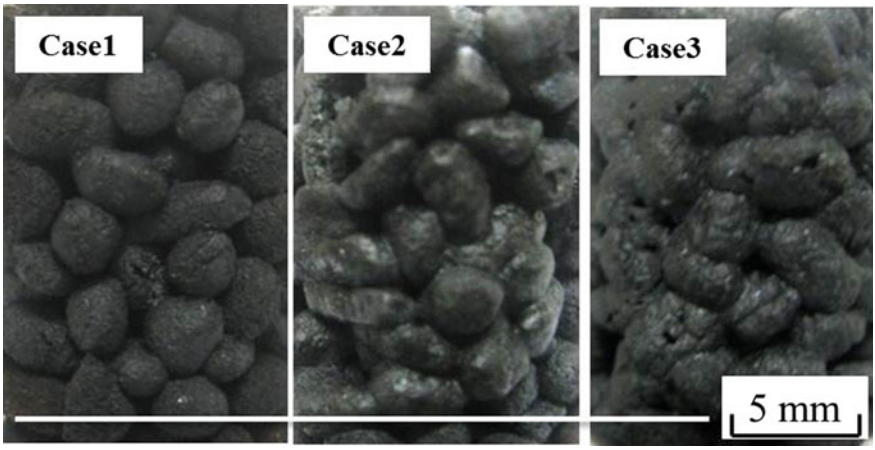

Fig. 9 Macroscopic feature of sinter body in the bonding strength tests. (Color figure online)

Figure 10 shows the results of the eighth shatter index of bonding strength tests. The bonding strength of sinter samples had significant differences based on different Mg–Ca combined state. Similar to the results of fluidity of liquid phase, Case3 which used serpentine had the highest bonding strength, then Case2 (l-dolomite) and Case1 (dolomite). It indicates that increase of Mg–Ca separation degree was conducive to improvement of bonding strength.

Fig. 10 Bonding strength of different Mg–Ca combination states

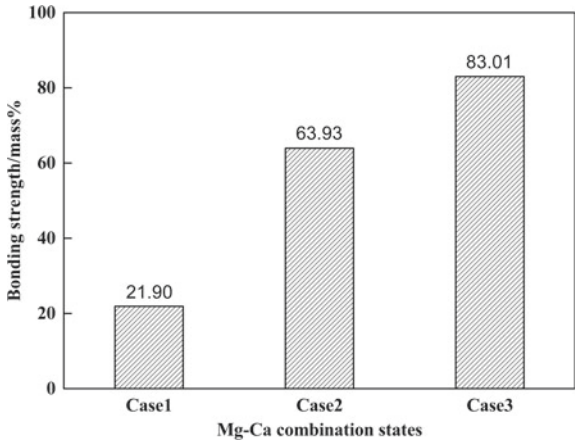

Discussion

Influence of Mg–Ca Combination State on Fluidity of Liquid Phase

In order to clarify the influence of different Mg–Ca separation degree on fluidity of liquid phase, it was analyzed by two aspects of both Mg and Ca.

As for Mg aspect, to further verify the differences of Mg melting in calcium ferrite (CF) based on three kinds of Mg–Ca combination states, microstructure and energy spectrum analysis of liquid phase was performed, as shown in Fig. 11. Magnetite and CF minerals of three kinds Mg–Ca combination states were observed clearly. Table 3 shows the results of energy spectrum analysis of liquid phase. On comparing Mg content in CF, Case3 had the lowest value, then Case2 and Case1. The situation of Mg content in magnetite was the opposite. That means increase of Mg–Ca separation is bad for Mg melting in CF, but good for Mg melting in magnetite.

CF is the main bonding phase of sinter. Viscosity of CF with different MgO contents was calculated with Factsage [14] to clarify the reason of fluidity difference of liquid phase. Table 4 shows the mixing conditions used in viscosity calculation. As shown in Fig. 12, it implied that an increase of MgO content in CF caused an increase of viscosity, which was in accordance with other paper [15]. That is, an increase of MgO melting into CF is bad for fluidity of liquid phase.

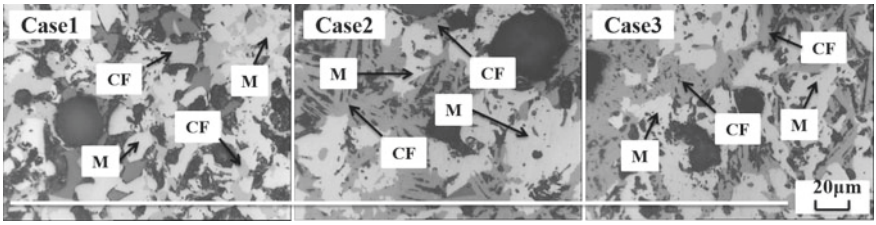

Fig. 11 Microstructure of sintering samples after fluidity of liquid phase tests. M-Magnetite; CF-Calcium ferrite

Table 3 Energy spectrum analysis results of the liquid phase (mass percent, %)

	Liquid phase	O	Si	Mg	Ca	Fe	Total
Case1	CF	28.49	1.53	2.78	7.34	59.86	100.00
	M	31.06	0	3.91	1.54	63.49	100.00
Case2	CF	29.70	4.21	0.78	12.20	53.11	100.00
	M	28.81	0	6.69	2.06	62.44	100.00
Case3	CF	31.69	3.09	0.74	12.37	52.11	100.00
	M	29.41	0	6.71	1.88	62.00	100.00

Table 4 Mixing conditions used in viscosity calculation of liquid phase (mass, %)

	Fe_2O_3	CaO	MgO	Total
Sch1	74.07	25.93	0	100.00
Sch2	73.33	25.67	1.00	100.00
Sch3	72.59	25.41	2.00	100.00
Sch4	71.85	25.15	3.00	100.00
Sch5	71.11	24.89	4.00	100.00
Sch6	70.37	24.63	5.00	100.00

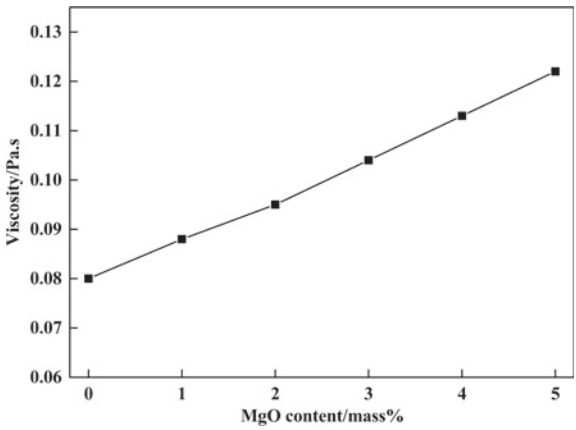

Fig. 12 Relationship between viscosity of calcium ferrite and solubility of MgO

As for Ca aspect, free CaO was introduced to explain the influence of CaO of different Mg–Ca combination states on fluidity of liquid phase. Figure 13 shows the results of correlativity between free CaO content and liquid phase fluidity of

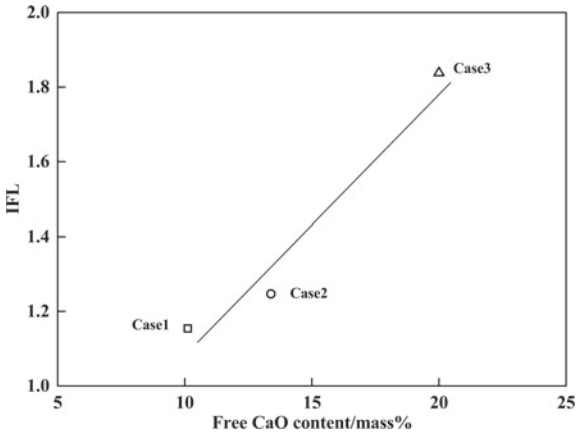

Fig. 13 Relationship between fluidity of liquid phase and free CaO content

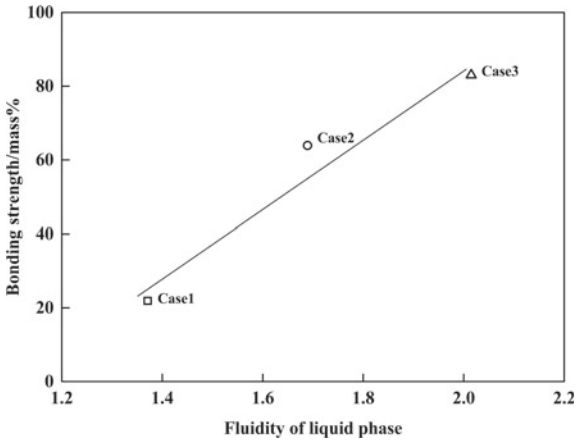

Fig. 14 Correlativity of fluidity of liquid phase with bonding strength

different Mg–Ca combination states of flux materials. Free CaO content was defined as elementary substance content of CaO at room temperature which could be found from Table 2. But one thing to note, free CaO content of Case2 needed to add 11.6% extra CaO content of l-dolomite existing at room temperature. According to Fig. 13, with an increase of Mg–Ca separation degree, free CaO content also increases, which is found as a positive correlation with fluidity of liquid phase. Increase of free CaO would be beneficial to early formation of CF liquid phase, which facilitated improvement of fluidity of liquid phase.

Influence of Mg–Ca Combination States on Bonding Strength

Mg–Ca combination states influenced the fluidity of liquid phase, which could also influence the bonding strength of sinter body further. Figure 14 shows the results analysis of correlativity of fluidity of liquid phase with bonding strength. It means that the bonding strength increased with the increase of fluidity of liquid phase. Bonding phase that had high fluidity of liquid phase could bond the un-melted nuclei ores together better, which led to high bonding strength of sinter body. Therefore, the increase of Mg–Ca separated degree is conducive to the improvement of bonding strength, as a result of an increase of fluidity of liquid phase.

Conclusions

(1) When dolomite, l-dolomite, and serpentine were solely used as MgO-bearing fluxes in the sintering process, Mg–Ca combination state has three kind of states: non-separation, partly-separation, and completely-separation.

(2) Mg–Ca combination state had important effect on fluidity of liquid. An increase of Mg–Ca separated degree was beneficial to improvement of fluidity of liquid phase and further to bonding strength.
(3) The larger the separation degree of Mg–Ca state was, the less Mg content melt in the calcium ferrite and more Mg in magnetite, which cause the increase of fluidity of liquid phase because of decline of liquid phase viscosity.
(4) The bonding strength has a good positive correlation with fluidity of liquid phase, which could explain that increase of separation degree of Mg–Ca was conducive to improvement of bonding strength.

References

1. Wang X (2009) Iron and steel metallurgy: iron part, 2nd edn. Metallurgical Industry Press, Beijing (in Chinese)
2. Fu J, Jiang T, Zhu D (1996) Sintering and pelletizing. Central South University of Technology Press, Changsha (in Chinese)
3. Yadav US, Pandey BD, Das BK et al (2002) Influence of magnesia on sintering characteristics of iron ore. Ironmak Steelmak 29(2):91
4. Matsumura M, Hoshi M, Kawaguchi T (2005) Improvement of sinter softening property and reducibility by controlling chemical compositions. ISIJ Int 45(4):594
5. Kasai E, Sakano Y, Kawaguchi T et al (2000) Influence of properties of fluxing materials on the flow of melt formed in the sintering process. ISIJ Int 40(9):857
6. Umadevi T, Nelson K, Mahapatra PC et al (2009) Influence of magnesia on iron ore sinter properties and productivity. Ironmak Steelmak 36(7):515
7. Feng G, Wu S, Han H, et al (2011) Sintering characteristics of fluxes and their structure optimization. Int J Miner Metall Mater 18(3):270
8. Chen S, Wu S, Zhang G, et al (2014) Blending structure of iron ore for dolomite substitute serpentine in sintering process. Iron and Steel 49(5):24 (in Chinese)
9. Wu S, Han H, Jiang W et al (2009) MgO interaction mechanism in sinter. J Univ Sci Technol Beijing 31(4): 428 (in Chinese)
10. Hsieh L, Whiteman JA (1993) Effect of raw material composition on the mineral phases in lime-fluxed iron ore sinter. ISIJ Int 33(4):462
11. Higuchi K, Tanaka T, Sato T (2007) Reaction behavior of dolomite accompanied with formation of magnetite solid solution in iron ore sintering process. ISIJ Int 47(5):669
12. Wu S, Du J, Ma H, et al (2005) Fluidity of liquid phase in iron ores during sintering. J Univ Sci Technol Beijing 27(3):291 (in Chinese)
13. Duan D, Wang S, Kong L (2000) Analysis on mini-sintering test. J Univ Sci Technol Beijing 22(5):422 (in Chinese)
14. Lv X, Bai C, Deng Q et al (2011) Behavior of liquid phase formation during iron ores sintering. ISIJ Int 51(5):722
15. Machida S, Nushiro K, Ichikawa K et al (2005) Experimental evaluation of chemical composition and viscosity of melts during iron ore sintering. ISIJ Int 45(4):513

Effect of SiO_2 Sources Addition on the Microstructure and Thermal Shock Performance of Alumina–Spinel Castables

Yang Liu, Min Chen, Shan Wang, and Xianglan Yang

Abstract Considering the thermal shock resistance of ladle lining castable, which is strongly dependent on the phase composition and microstructure, the influence of SiO_2 sources on the thermal shock resistance of alumina–spinel castables was studied. The results indicate that trace addition of SiO_2 was detrimental to the mechanical properties of the samples, due to its acceleration on volume expansion of phase formation and the low-melting phase formed at high temperature. However, the formation of low-melting phase has the potential to improve thermal shock resistance attributed to the loose microstructure stacked by equiaxial plate-like calcium hexaluminate owing to its promotion of ion mobility. Meanwhile, it was also confirmed by the samples with the fused silica because of the maximum retained moduli values and relatively slight influence on high temperature mechanical properties in contrast with other SiO_2 sources addition.

Keywords SiO_2 sources · Microstructure · Thermal shock resistance · Alumina–spinel castables

Introduction

Thermal shock is one of the most severe conditions to which a ladle lining can be subjected to during its service. Thus, as a widely used ladle lining material, alumina–spinel castable although known for their outstanding chemical stability and thermomechanical properties, improving their thermal shock performance has always been the focus of research [1–5]. Extensive works related to this subject have been devoted to the study of adjusting the types or grades of corundum and spinel [6–8], the phase composition of matrix [9], or the addition of particle size with specific morphology [10]. Tracing to the fundamental method is to improve the thermal shock resistance of the castable through optimizing the forming material microstructure due to strong correlation between them.

Y. Liu · M. Chen (✉) · S. Wang · X. Yang
School of Metallurgy, Northeastern University, Shenyang 110819, China
e-mail: chenm@smm.neu.neu.cn

J. Li et al., *Characterization of Minerals, Metals, and Materials 2021*,
The Minerals, Metals & Materials Series,
https://doi.org/10.1007/978-3-030-65493-1_34

An important aspect related to microstructure of alumina–spinel castable is the morphology of toughening phase calcium hexaluminate (CA_6), which present with interlaced structures in the refractory. Sako et al. [11] systematically investigated the effect of silica fume on the CA_6 formation in cement-bonded spinel refractory castables, and they found that the morphology of CA_6 crystal was affected by different reaction mechanism, and that the acicular CA_6 is usually generated in the castables matrix when the diffusion mechanism was liquid phase, controlled due to the low-melting point phases formation in Al_2O_3–CaO–SiO_2 system. Braulio et al. [12] pointed out that silica fume addition reduced CA_2 expansion, but led to a greater CA_6 expansion rate while investigating the silica content effects on alumina–magnesia castables. Considering that silica has a great influence of the development of CaO–Al_2O_3 phases, whereas the influence of SiO_2 sources on alumina–spinel castable has not been widely reported in the literature. Hence, alumina–spinel with low silica content—introduced by different SiO_2 sources including silica fume, silica, fused silica, and fused mullite—was developed in this paper. Also, a series of comparison experiments have been carried out among the alumina–spinel castables with different SiO_2 sources, so as to systematically assess their effects on the thermal shock resistance and its associated physical properties of this material.

Experimental

Sample Preparation

In this work, the main starting materials include tabular alumina (T60/T64, Al_2O_3 $\geq$ 99.25wt%, Almatis), pure calcium aluminate cement (Secar 71; Imerys), sintered spinel (AR78, Almatis), and reactive alumina powder (CL370, $Al_2O3 \geq$ 99.56 wt%, Almatis). Four sources of SiO_2 were selected (0.5 wt% in the castable) and their chemical composition is shown in Table 1. Table 2 displays the formulations of the castables with different SiO_2 sources. They were marked as AS0, AS1, AS2, AS3, and AS4, in which sample AS0 has no SiO_2, while the others were respectively added silica fume, silica, fused silica, and fused mullite.

The starting powder mixtures were dry-mixed for 30 s, and then wet-mixed in a compulsory mixer with an appropriate amount of water for 180 s. After mixing, prismatic castables were cast into molds of 40 mm × 40 mm × 160 mm with vibration. Afterwards, the samples were cured at 20 °C and 95% relative humidity for 24 h. In order to remove the free water, binding water, and release water vapor pressure sufficiently, the samples were dried for 24 h at 100 and 400 °C, respectively. Then they were fired in a high temperature electric furnace at a heating rate of 5 °C·min^{-1} up to 1550 °C with a dwell time of 3 h and were furnace cooled.

Table 1 Chemical compositions of different SiO_2 sources

Oxide (wt%)	Silica fume	Silica	Fused silica	Fused mullite
SiO_2	97.03	97.76	99.64	24.16
CaO	0.25	0.05	0.04	0.07
MgO	0.37	0.35	0.02	0.13
Al_2O_3	0.17	0.56	0.03	75.18
Fe_2O_3	0.13	0.97	0.03	0.04
TiO_2	0.07	0.03	0.01	0.07
Na_2O	0.11	0.05	0.06	0.24
K_2O	0.35	0.12	–	0.01
P_2O_5	0.11	–	–	–
Cr_2O_3	0.02	0.08	–	0.01
L.O.I	1.45	0.12	0.17	0.12

Table 2 Composition of alumina–spinel castables containing different SiO_2 sources (wt/%)

Raw materials		AS0	AS1	AS2	AS3	AS4
Tabular alumina	≤6 mm	50	50	50	50	50
	≤0.088 mm	14	14	14	14	14
Sintered spinel(mm)	1–0.2 mm	6	6	6	6	6
	≤0.088 mm	10	10	10	10	10
Calcium aluminate cement	$d_{50} = 3.03$ μm	5	5	5	5	5
Silica fume			0.52			
Silica				0.51		
Fused silica					0.50	
Fused mullite						2.07
Reactive alumina	$d_{50} = 2.00$ μm	5	5	5	5	5
Additives		0.5	0.5	0.5	0.5	0.5

Characterization

It was found that 4.3% water was enough to obtain a well-dispersed castable system. So the flowability of castables with that water addition was evaluated by filling them into an inverted cone placed on a vibration table and then the flow diameter of the castables under vibration (10 s) was measured after removing the cone [13]. The bulk density (B.D.) and the apparent porosity (A.P.) of the material were measured by the Archimedes method with water as medium. The permanent linear change (PLC) of the fired samples was measured by the percentage difference between the final and initial bar length. The linear expansion of samples was tested in a high-temperature thermal dilatometer (model RPZ-04P, Luoyang ATLIRR Instrument for

Testing Refractories Co., Ltd, China). Crystalline phases formed were analyzed by X-ray powder diffraction (XRD, Philips 3020 equipment with Cu-Kα radiation in Ni filter at 40 kV−20 mA) using Cu-Kα1 radiation ($\lambda = 1{\cdot}5406$ Å) at a step of 0.02° (2θ). Field-emission scanning electron microscopy (SEM, SIGMA HD, Zeiss, Germany) was employed to characterize sample's microstructure.

Thermal shock evaluation: The TSR of the fired samples was evaluated using the air quenching method. The heating−cooling group was put into a 1100 °C furnace for 30 min and then were air-cooled with a fan (air speed of 8870 m^3/h) for 20 min. Afterwards, the modulus of rupture (MOR) of the reference group without any thermal shock and the heating−cooling groups after three thermal shock cycles was measured. The retained MOR values, the ratio of the value after three thermal shock to the value without any thermal shock times one hundred to obtain the percentage, were used to verify the TSR of samples.

Results and Discussion

Physical Properties

Figure 1 shows the relationship between SiO_2 sources and the flowability exhibited by the experimental castables. Notice from this figure that the flow diameter of samples varies slightly in the range of 110–130 mm, in which the flow diameter of sample AS1 reaches a maximum and presents well self-flowability. It is attributed to the spherical shape of silica fume which plays an active role in the improvement of flowability. Different from the sample with silica fume, the sample with other silica sources has a slight decrease in flow value due to the relatively increased surface area in contact with water.

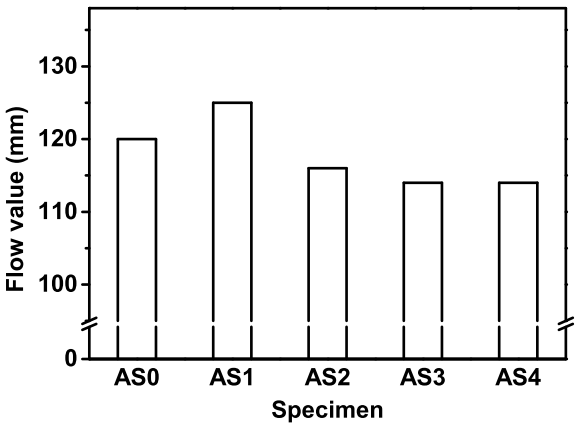

Fig. 1 Effect of SiO_2 sources addition on flowing of alumina–spinel castables

The comparisons of change in MOR and PLC with different SiO_2 sources addition in alumina–spinel castables at different temperatures are given in Figs. 2 and 3, respectively. From Fig. 2, sample AS1 shows relatively mechanical strength after drying at 110 °C for 24 h. This improved castable strength with silica fume can be ascribed to the silanol groups replaced by siloxane groups during the gelling process like the Eq. 1 shows [14]. Siloxane groups and cement hydration products work together to bridge the particles and form close-packed clumps.

$$-\mathrm{SiOH} + \mathrm{HOSi}- \rightarrow -\mathrm{SiOSi}- + \mathrm{H_2O} \quad (1)$$

After treating at 400 °C for 24 h, a lightly loss of strength is found due to reduction of the special surface as well as because of the formation of voids around the C_3AH_6. With the treatment temperature elevating to 1550 °C, an obvious decrease in the MOR

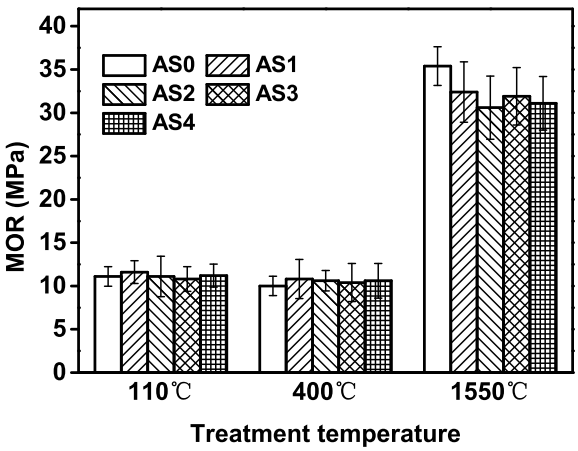

Fig. 2 Modulus of rupture for alumina–spinel castables containing different SiO_2 sources

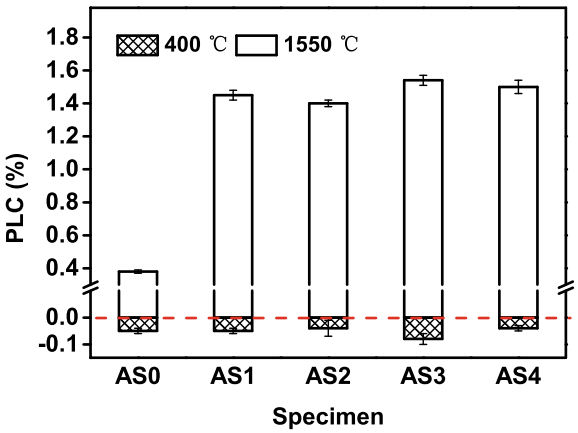

Fig. 3 Permanent linear change for alumina–spinel castables containing different SiO_2 sources. (Color figure online)

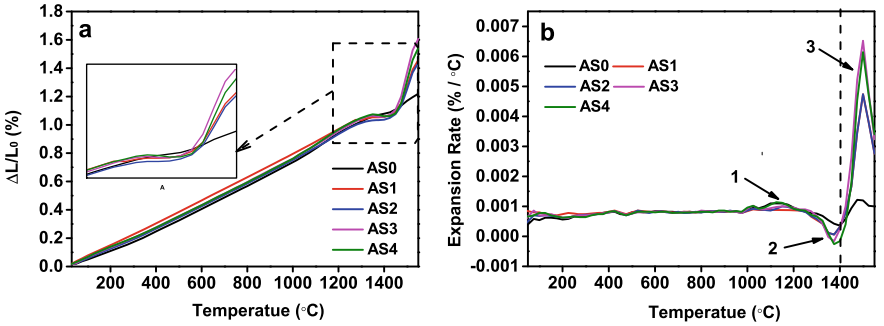

Fig. 4 **a** Linear expansion and **b** expansion rate for alumina–spinel castables containing different SiO_2 sources. (from room temperature to 1550 °C). (Color figure online)

value occurs in the samples containing different SiO_2 sources, and it can be concluded that even trace addition of SiO_2 can reduce MOR at high temperature.

Figure 3 shows the permanent linear change of specimens after drying at 400 °C and firing at 1550 °C for 3 h. It can be seen that all specimens exhibit shrinkage after drying at 400 °C, which is attributed to the dehydration process of a series of hydration products. After firing at 1550 °C for 3 h, specimens present an overall expansion, the introduction of SiO_2 has an obvious effect on the volume expansion, and the PLC of the sample has a step from 0.38% to the maximum value of 1.54%. According to Braulio [15], the excessive expansion due to CA_6 formation could result in cracks and deteriorate the castable's properties, which is confirmed by the decrease of MOR at 1550 °C.

Considering the close correlation between SiO_2 and material expansion, the linear expansion and expansion rate for alumina–spinel castables containing different SiO_2 sources was measured from room temperature to 1550 °C, aiming to understand how various SiO_2 sources affected the overall expansion of the castables. Figure 4a presents the higher expansion behavior of alumina–spinel castables containing different SiO_2 sources. Among them, the sample with silica resulted in the lowest expansion level, pointing out its relatively high lattice defects. The derivative of linear expansion curves results in the castables' expansion rates with the temperature, pointing out the distinct reactions that take place throughout the test. In Fig. 4b, there are three different peaks that can be detected in the expansion rates of each samples containing different SiO_2 sources. As analyzed in previous work of Braulio et al. [12, 15], they are correlated to: (1) the CA_2 formation nearly at 1100 °C; (2) the sintering shrinkage of the samples at the temperature range from 1300 to 1400 °C; and (3) the CA_6 formation at over 1400 °C. Considering the CA_2 formation, the castables with fused silica and fused mullite (AS3 and AS4) showed higher expansion rate due to lack of reactivity to react with CaO at that temperature, which left a free path for the CA_2 formation, and that it also provides a premise for their promotion effect on CA_6 formation than the other sources. In addition, compared with the sample without SiO_2, the peak corresponding to sintering densification of other

samples show a significant deviation toward low temperature, which indicates that the low-melting-point phase, generated by introducing SiO_2, effectively promoted sintering.

Thermal Shock Resistance

The MOR and the residual MOR of fired samples after undergoing three thermal cycles at 1100 °C are depicted in Fig. 5. It can be observed that although a great loss of strength took place after thermal shock for each sample, the residual MOR ratio of the alumina–spinel castables containing different SiO_2 sources is obviously better than the sample AS0 without SiO_2. The maximum residual MOR ratio value is 37.30% from the sample AS3 with fused silica. To further confirm the influence of SiO_2 sources on thermal shock resistance of castable, the microstructure of samples AS1 and AS3 with higher residual MOR rate and blank sample AS0 is compared.

Figure 6 shows the fracture surfaces of a castable after firing at 1550 °C for 3 h and the morphology of CA_6 can be compared with that shown in partial enlarged view. Notice from this figure that although CA_6 crystals develop to an interlocking structure between grain boundaries of corundum and spinel in each sample, the microstructure

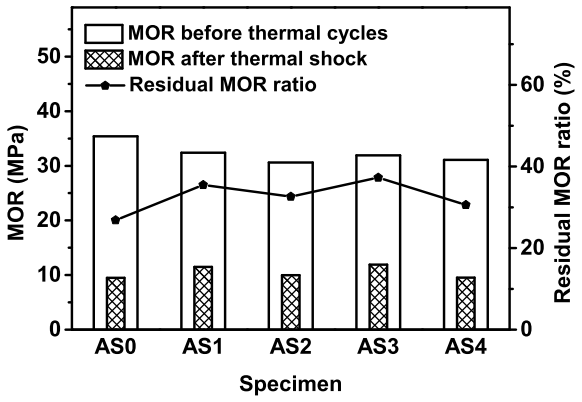

Fig. 5 Effect of SiO_2 sources on thermal shock resistance of specimens

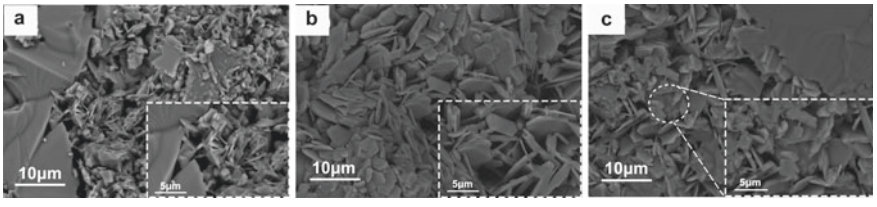

Fig. 6 SEM image of castables fracture with different amount of CAC addition fired at 1550 °C for 3 h: **a** AS0 **b** AS1, **c** AS3

they involved exists obvious differences. The sample AS0 consists of two kinds of CA_6 crystals which are flake and granular crystals (nucleation), respectively. They grow together and adhere to each other, making the structure relatively dense. In comparison, the platelet CA_6 grains gradually increase and grow up for samples of AR1, AR3. According to [16], the mirror layer of CA_6 structure is loose because the large cations stuff; thus, ions are easy to diffuse perpendicularly to the c-axis. The SiO_2 addition just accelerates the ion mobility of Al^{3+} via low-melting-point phase (such as anorthite and gehlenite), and further enhances the formation of hexagonal plate-like microstructure, and that is the reason why CA_6 crystals in the sample with SiO_2 are relatively well developed. The sample AS1 shows obviously thicker CA_6 flake crystals than the one in sample AS3, because the suitable morphology and relatively small particle size of silica fume are conducive to diffusion and mass transfer. Moreover, the glassy phases are detected in the interlocking structure of CA_6 in sample AS3 (Fig. 6c).

Combined with the above analysis, it is not difficult to conclude that the sample with fused silica has favorable thermal shock resistance due to the loose structure and the buffering effect of amorphous relative thermal stress which filled in the reticular structure.

Conclusions

After a series of comparison experiments among the alumina–spinel castables containing different SiO_2 sources, the results show the presence of SiO_2 and its sources significantly influence the CA_6 formation, increasing the expansion rate when compared to the sample without SiO_2. These two factors further affect the microstructure which is strongly related to thermal shock resistance of this material. SiO_2 additions speed up the CA_6 formation via liquid-state reaction, resulting in higher values of expansion due to the abrupt crystal growth. Moreover, although the expansion leads to the strength loss of the sample, it also results in a relatively loose structure of the matrix. The choice of fused silica as silicon source is beneficial to obtain favorable thermal shock resistance of alumina–spinel castables due to the well-developed flake CA_6 crystals interpenetration of the “loose” structure and the buffering effect of glassy phases relative thermal stress which filled in the reticular structure.

Acknowledgements The authors gratefully acknowledge the National Natural Science Foundation of China (No. 51774072,51774073, 51974080), which made this research possible.

References

1. Salvini VR, Pandolfell VC, Bradt RC (2012) Extension of Hasselman's thermal shock theory for crack/microstructure interactions in refractories. Ceram Int 38:5369–5375
2. Moritz K, Aneziris CG (2016) Enhancing the thermal shock resistance of alumina-rich magnesium aluminate spinel refractories by an aluminum titanate phase. Ceram Int 42(12):14155–14160
3. Martinez AGT, Luz AP, Braulio MAL (2012) Creep behavior modeling of silica fume containing Al_2O_3-MgO refractory castables. Ceram Int 38(1):327–332
4. Simonin F, Olagnon C, Maximilien S (2000) Thermomechanical behavior of high-alumina refractory castables with synthetic spinel additions. J Am Ceram Soc 83(10):2481–2490
5. Kubota Y, Matsui T, Kataoka K (2015) The effect of addition of fine powders on generation behavior of hexacalcium aluminate in alumina castable. Taikabutsu 67(6):281–287
6. Schafföner S, Dietze C, Möhmel S, Fruhstorfer J, Aneziris CG (2017) Refractories containing fused and sintered alumina aggregates: Investigations on processing, particle size distribution and particle morphology. Ceram Int 43(5):4252–4262
7. Kakroudia MG, Hugerb M, Gaultb C, Chotard T (2009) Damage evaluation of two alumina refractory castables. J Eur Ceram Soc 29(11):2211–2218
8. Liu J, Gu HZ, Zhang MJ, Huang A, Li HM (2019) Improvement in fatigue resistance performance of corundum castables with addition of different size calcium hexaluminate particles. Ceram Int 45(1):225–232
9. Xu L, Yin XL, Wang N, Chen M (2017) Effect of Y_2O3 addition on the densification, microstructure and mechanical properties of $MgAl_2O_4$-$CaAl_4O_7$-$CaAl_{12}O_{19}$ composites. J Alloy Compd 12:472–478
10. Consonni LB, Luz AP, Pandolfelli VC (2019) Binding additives with sintering action for high-alumina based castables, ceramics international. Ceram Int 45(12):15290–15297
11. Sakoa EY, Braulio MAL, Milaneza DH, Brantb PO, Pandolfelli VC (2009) Microsilica role in the CA_6 formation in cement-bonded spinel refractory castables. J Mater Process Tech 209:5552–5557
12. Braulio MAL, Bittencourt LRM, Poirier J, Pandolfelli VC (2008) Microsilica effects on cement bonded alumina–magnesia refractory castables. J Tech Assn Rec 28(3):180–184
13. Liu Y, Han B, Zhang T, Yu H, Yan W, Wei Y (2016) Effect of zirconia particle size on the properties of alumina-spinel castables. Ceram Int 42:16961–16968
14. Kazemi N (2019) Reasons for crack propagation and strength loss in refractory castables based on changes in their chemical compositions and micromorphologies with heating: special focus on the large blocks. J Asian Ceramic Soc 7(2):109–126
15. Braulio MAL, Milanez DH, Sako EY, Bittencourt LRM, Pandolfelli VC (2007) Expansion behavior of cement bonded alumina–magnesia refractory castables. Am Ceram Soc Bull 86(12):9201–9206
16. Ersson AG, Johansson EM, Jaras SG (1998) Techniques for preparation of manganese-substituted lanthanum hexaaluminates. Stud Surf Sci Catal 98:601–608

Effect of the Incorporation of Bauxite and Iron Ore Tailings on the Properties of Clay Bricks

Beatryz C. Mendes, Leonardo G. Pedroti, Bianca R. Bonomo, Anna Carolina L. Lucas, Lívia S. Silva, Márcia M. S. Lopes, and Gustavo E. S. Lima

Abstract Mining industries generate high amounts of tailings, which are usually allocated in dams. These structures cause severe environmental impacts and serious risks to the safety of the surrounding population. Another way to dispose these wastes is the addition into building materials. This work aimed to study the incorporation of bauxite and iron ore tailings in clay bricks. The raw materials were the tailings and one clay. The mixture design of experiments was applied to obtain the mixtures, and cylinder specimens were produced by pressing. After drying and firing at 950 °C, the specimens were evaluated for mechanical strength, water absorption, linear firing shrinkage, and apparent specific mass. Based on standards criteria, the optimal mixture was determined containing 40% wt. of clay, 45% wt. of bauxite residue, and 15% wt. of iron ore tailings. This study proved the technical feasibility of using high percentages of mining tailings for ceramic production, which is also a sustainable action.

Keywords Red mud · Iron ore tailings · Clay bricks · Sustainability

Introduction

The civil construction sector contributes significantly to the worldwide economy, being responsible for the generation of profits and employment. On the other hand, this sector is also responsible for the exploration and consumption of many natural resources. Some industries still contribute to the emission of pollutant gases and waste generation. One example is the red ceramic industry, which uses clay as raw material. Clays are non-renewable materials and extracted from nature [1, 2].

B. C. Mendes (✉) · L. G. Pedroti · B. R. Bonomo · A. C. L. Lucas · L. S. Silva · M. M. S. Lopes · G. E. S. Lima
UFV - Federal University of Viçosa, DEC – Civil Engineering Department; Av. Peter Rolfs, s/n, Campus Universitário, 36570-000 Viçosa, Brazil
e-mail: beatryz.mendes@ufv.br

J. Li et al., *Characterization of Minerals, Metals, and Materials 2021*,
The Minerals, Metals & Materials Series,
https://doi.org/10.1007/978-3-030-65493-1_35

One way to reduce the impacts caused by red ceramic industries would be the inclusion of guidelines related to sustainable development concept. As clays are naturally heterogeneous materials, the ceramic industry is promising for the absorption of many solid wastes in their productive chain, provided that these wastes ensure or improve the final products quality [3]. Under this point of view, several studies have been carried out in recent years, addressing the incorporation of industrial wastes in the production of red ceramic bricks and tiles: glass waste [4], fly ashes [5], granite and marble wastes [6], grog [7], and so on. The tailings from mining industries should also be mentioned, such as iron ore tailings (IOT), red mud, and copper tailings [8, 9].

Generally, the mining tailings present particle sizes and chemical composition similar to those found in clays. Researches about the partial addition of iron ore tailings showed that the IOT can be included in the ceramic mass as a non-plastic material, which promotes the adjustment of plasticity and improves the control of linear shrinkage in drying and firing stages [10]. Mendes et al. [11] pointed out that approximately 30% of IOT can be added to a mixture with two highly plastic clays, maintaining the quality requirements for construction clay bricks (no structural function). In relation to red mud, some authors have demonstrated that higher contents can be incorporated to ceramic masses. This waste is obtained from bauxite mining, presenting significant amounts of silica, alumina, and iron oxide. Besides, this material can be considered as moderately plastic and shows suitable plasticity behavior for extrusion process. Arhin et al. [12] have evaluated the incorporation of high concentrations of red mud (50, 60, 70, and 80%), mixed with a clay, for the production of prismatic specimens. According to this research, it was possible to add about 50% of red mud to obtain a suitable product.

Although there are several studies, in the technical literature, comprising the application of the two tailings previously mentioned, the addition of both simultaneously is still little explored. Mainly the application of an experimental design allows the optimization of the properties of interest and the definition of an optimal mixture, incorporating the maximum possible levels of the two materials.

The present work aimed to assess the physical and mechanical properties of ceramic mixtures produced from iron ore tailings, red mud, and a highly plastic clayey soil. By means of the mixture design of experiments (simplex network), it was possible to determine the appropriate percentages of incorporation of the wastes, ensuring the required technical performance for construction clay bricks.

Methodology

The raw materials used in this research were iron ore tailings (IOT), red mud (RM), and a clayey soil named as “gray clay” (GC). The materials were previously ground, air-dried, and passed through the ASTM 50 sieve. The characterization of the raw materials consisted of the following determinations: particle size distribution, according to NBR 7181 [13]; specific mass of the grains, following the NBR 6508 [14]; Atterberg limits, according to NBR 7180 [15] and NBR 6459 [16]; and

chemical composition by means of XRF technique, using the spectrometer Philips PANalytical, MagiX - PW2404 model, with automatic sample PW2540 and Rh tube at 2.4 kW.

The mixtures were defined according to the design of experiments (simplex network) with three components, using the special cubic model with the augment of internal points. The intervals of addition were chosen after the performance of preliminary tests, being: 40–70% of gray clay; 20–50% of red mud, and 10–40% of iron ore tailings. Ten mixtures were obtained, following the design and percentages shown in Fig. 1 and Table 1.

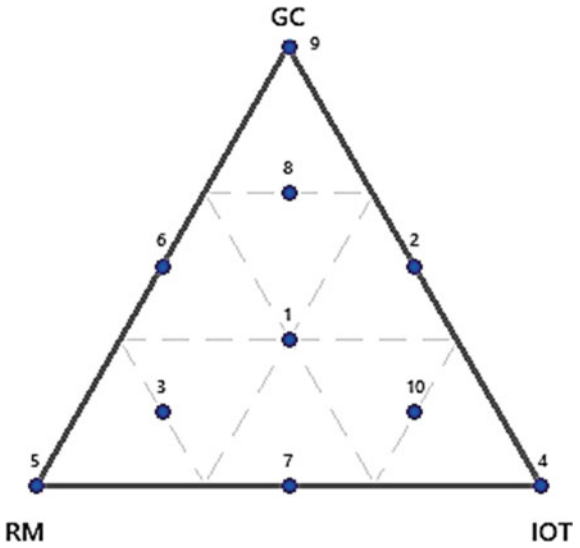

Fig. 1 Pseudo-components triangle with the mixtures defined. (Color figure online)

Table 1 Composition of the mixtures (percentages of incorporation)

Mixtures	Gray clay (GC) (%)	Red mud (RM) (%)	Iron ore tailings (IOT) (%)
1	50	30	20
2	55	20	25
3	45	40	15
4	40	20	40
5	40	50	10
6	55	35	10
7	40	35	25
8	60	25	15
9	70	20	10
10	45	25	30

After the preparation of the mixtures, cylindrical specimens were produced by pressing, with constant moisture of 10%. The pressing load was variable between the mixtures, in order to maintain the green bulk density within the adequate limits (1.8–2.1 g/cm^3). Subsequently, the samples were dried in an oven at 110 °C during 24 h. The firing was applied after the drying, using an electric furnace at 950 °C. The peak temperature was maintained for 3 h. The fired samples were characterized by firing linear shrinkage, apparent specific mass, water absorption, and axial compressive strength. The experimental results were subjected to the Chauvenet test for the elimination of outliers. Using the software Minitab®, the statistical analysis was conducted by ANOVA, with the generation of response surfaces and regression equations. The desirability function was used in order to obtain the optimal composition, according to the national and international standards requirements.

Results and Discussion

Characterization of the Raw Materials

The particle size distributions of gray clay, iron ore tailings, and red mud are shown in Fig. 2. The iron ore tailings are basically composed of sand and silt, with lower content of clay (only 11.9%). The red mud and gray clay presented 48.1 and 62.4% of fine particles (<0.002 mm), respectively. These two materials are mainly constituted by fine particles, unlike the IOT which has the predominance of larger particles. The

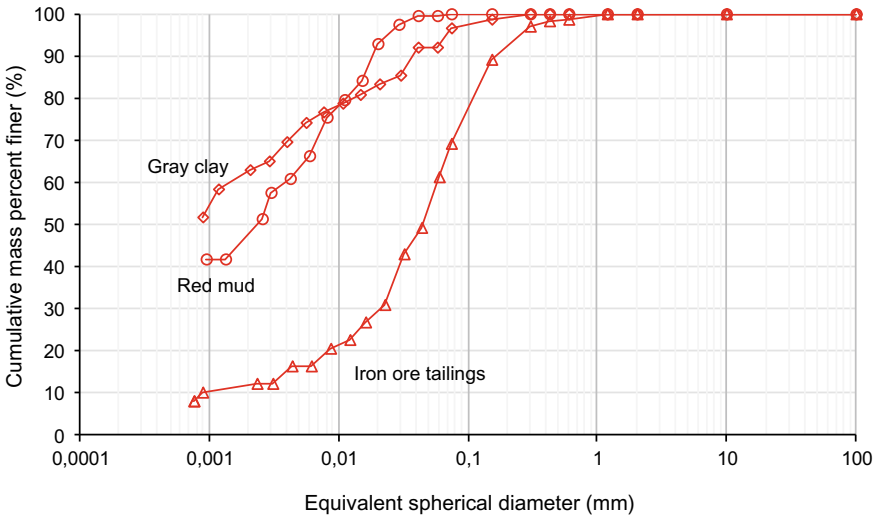

Fig. 2 Particle size distribution of raw materials. (Color figure online)

Table 2 Specific mass and Atterberg limits of raw materials

Raw material	Specific mass (g/cm^3)	Plasticity limit (%)	Liquid limit (%)	Plasticity index (%)
Gray clay	2.609	44	60	16
Iron ore tailings	2.933	0	0	0
Red mud	2.519	24	36	12

significant presence of fine particles is a good characteristic for application in clay bricks. According to Pracidelli and Melchiades [17], the clay fraction is responsible for high plasticity of the soil.

Table 2 shows the specific mass and Atterberg limits of the raw materials. One can notice that the iron ore tailings presented higher specific mass, probably due to the higher amounts of iron and silica in this material. About the Atterberg limits, the gray clay can be classified as very plastic (PI > 15%). The red mud can be defined as medium plastic (7% < PI < 15%), and the iron ore tailings as a non-plastic material. A non-plastic material improves the performance of the ceramic specimens on the drying and firing stages, reducing the shrinkage and any defects. Baccour et al. [18] indicate that values of liquid limit between 30 and 60% are suitable for ceramic production. High plasticity limits, such as the correspondent to gray clay, can lead to problems in the drying and firing stages [19]. As expected by particle distribution, the materials with higher amounts of fine particles (RM and GC) presented higher values of plasticity index.

The extrusion prognostic diagram can be used to classify the materials as suitable or not for extrusion process, according to the results of Atterberg limits [20]. Figure 3 shows that the gray clay is out of the acceptable zone for extrusion, unlike the red mud. Therefore, the mixture of the three materials can form a ceramic mass that falls within the acceptable or even optimal zone.

The chemical characterization of the raw materials is presented in Table 3. The three materials showed great contents of SiO_2, Al_2O_3, and Fe_2O_3. High amounts of

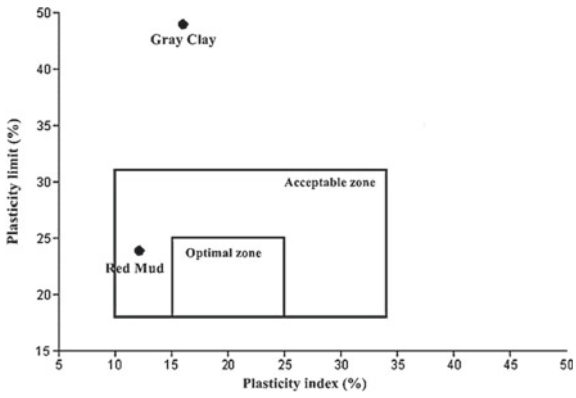

Fig. 3 Extrusion prognostic diagram

Table 3 Chemical composition of raw materials

Chemical composition (%)											
Material	SiO_2	Al_2O_3	Fe_2O_3	TiO_2	CaO	MgO	K_2O	P_2O_5	SO_3	Others	LoI[a]
GC	44.29	32.53	4.62	1.92	0.44	0.09	0.27	0.37	–	0.26	15.21
IOT	63.09	7.17	25.79	0.28	0.20	0.12	0.32	0.39	–	0.26	2.28
RM	30.27	43.14	20.5	1.88	–	–	0.34	–	1.67	0.21	21.3

[a]LOI—Loss on Ignition

SiO_2 and Al_2O_3 can indicate the significant presence of clay minerals, which are responsible for plasticity and formation of important mineral phases (such as mullite and spinel) after firing. Fe_2O_3 is associated with the reddish color of the red ceramic products [21]. Alkaline and earth-alkaline oxides play the role of fluxes, reducing the firing temperature [22].

Characterization of the Ceramic Specimens

All the following response surfaces and equations were obtained from the statistical analysis, performed on the software Minitab®. The signs and values of the coefficients in the equations indicate the influence of each raw material. Figure 4 shows the response surface obtained for firing linear shrinkage, which can be described by Eq. 1. One can notice that the interaction between gray clay and iron ore tailings tends to reduce the shrinkage. Indeed, the iron ore tailings are composed of coarse particles compared to the others materials. These particles can increase the packing of the system and fill the gaps of the matrix. Besides, IOT presented an inert behavior,

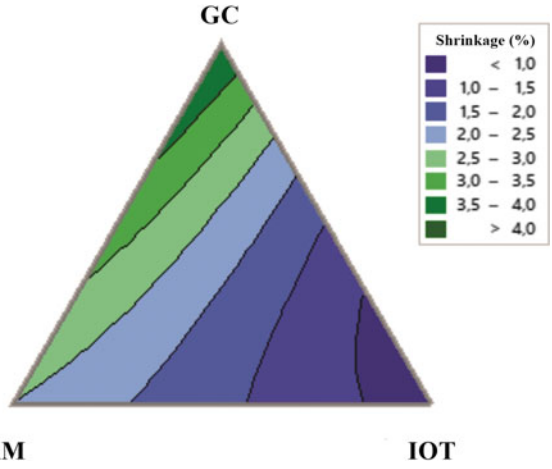

Fig. 4 Surface response of firing linear shrinkage. (Color figure online)

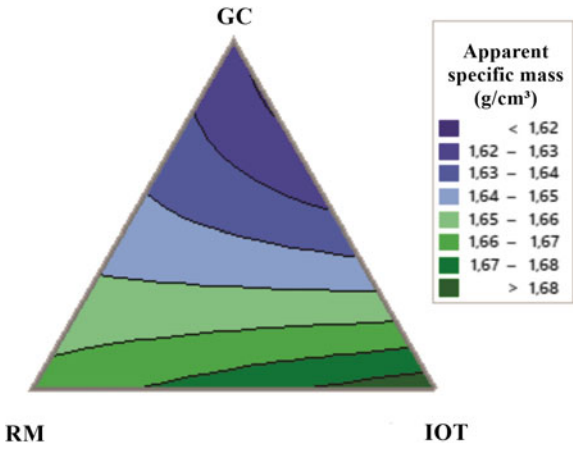

Fig. 5 Surface response of apparent specific mass. (Color figure online)

which is confirmed by the low loss on ignition [11]. The gray clay is the component that more contribute to increase of firing shrinkage. It can be explained by the great amount of mineral clays in this material, which turns it more reactive.

$$\begin{aligned} \text{FLS} &= 8.459 * \text{GC} - 0.511 * \text{RM} + 9.212 * \text{IOT} - 0.391 * \text{GC} * \text{IOT} \\ \text{R}^2 &= 98.25\% \end{aligned} \quad (1)$$

The surface response for apparent specific mass is shown in Fig. 5. Equation 2 indicates that the IOT is mainly responsible for the increase of specific mass (higher coefficient). It can be explained by the higher specific mass of grains correspondent to this component. With the increase of gray clay in the mixture, the values of specific mass are lower.

$$\text{ASM} = 1.554 * \text{GC} + 1.732 * \text{RM} + 1.776 * \text{IOT} \quad \text{R}^2 = 62.64\% \quad (2)$$

The property of water absorption is an important quality indicator for ceramic products. National and international standards specify the range of values suitable for each type of product. In relation to clay bricks, NBR 15270-1 [23] establishes a range of 8–25%. Figure 6 shows the surface response obtained in this experimental program. The incorporation of gray clay tends to reduce the water absorption, unlike the IOT, which promotes the reverse effect. During the firing stage at 950 °C, the beginning of the formation of liquid (or vitreous) phase occurs. This liquid phase fills the porous of ceramic matrix and causes the densification of ceramic bricks. Therefore, the sintering mechanisms lead to reduction of open porosity and absorption. The clay minerals are responsible for vitreous phase formation, and the gray clay is the raw material with greater amount of these compounds.

The higher the IOT and RM contents, the lower the formation of liquid phase, reducing the densification process. The IOT is also an inert material, which increases the concentration of open and interconnect pores [24]. Thus, higher percentages

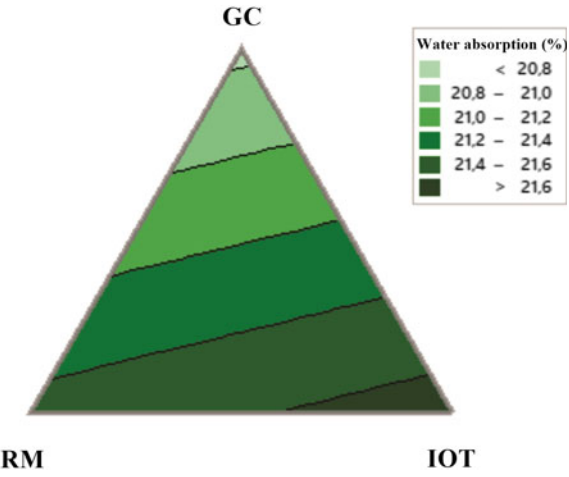

Fig. 6 Surface response of water absorption. (Color figure online)

of IOT and RM promote the increase of water absorption in accordance with the Eq. 3 coefficients. Red mud causes less negative impact compared to IOT, due to its chemical composition—richer in Al_2O_3 and lower content of SiO_2—and particle size distribution.

$$WA = 19.961 * GC + 22.336 * RM + 23.114 * IOT \quad R^2 = 66.14\% \qquad (3)$$

The clay bricks must also meet mechanical strength criteria, even if they are not used as a structural material. The evaluated property was the axial compressive strength, whose response surface is presented in Fig. 7. The ASTM C62 [25] standard

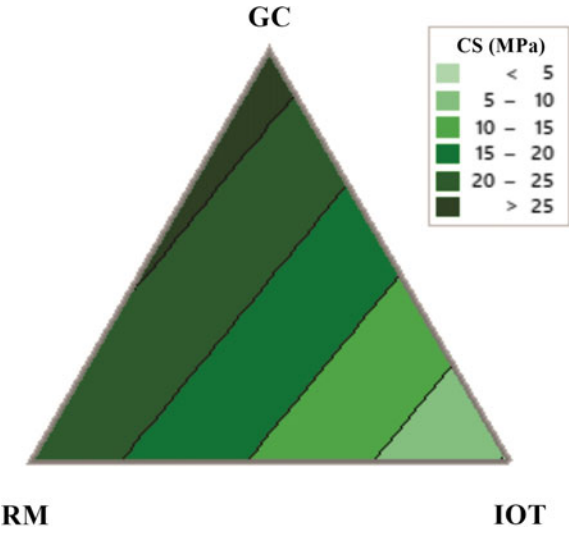

Fig. 7 Surface response of compressive strength. (Color figure online)

specifies a minimum of 17.2 MPa. Both gray clay and red mud contribute to increase of compressive strength, due to the chemical composition of these materials and the presence of clay minerals in GC. The sintering of clay minerals promotes the formation of others mineral phases that are responsible for the gain of strength. The IOT tends to decrease the mechanical strength, which is related to the increase of porosity. Besides, the higher amounts of quartz and hematite particles hinder the sintering process of the clay minerals [10]. Therefore, IOT has a strong negative influence on the compressive strength and Eq. 4 can confirm it.

$$CS = 37.598 * GC + 24.565 * RM - 38.368 * IOT \quad R^2 = 83.75\% \qquad (4)$$

The values of R^2 (determination coefficient) indicate how the fitted equations (or models) can explain the experimental data. This means that high values of R^2 are associated to a better adjustment of the model. For the properties of firing linear shrinkage and compressive strength, the R^2 value was above 80%, indicating a good adjustment of the equations or less variation of the experimental results. On the other hand, the R^2 values of apparent specific mass and water absorption were lower, thus suggesting that the equations fit less well or higher in variation. Considering all the properties, it can be assumed that the equations can describe the experimental data.

In order to prove that the regression analysis performed is valid, the "residuals" versus "predicted values" graphs and the normal probability graphs were analyzed. For all the properties, the errors presented a random distribution around the mean equal to zero, suggesting homogeneity of variances [11]. Besides, the errors are normally distributed in all properties. Thus, one can conclude that the analysis was effective.

Considering the requirements of NBR 15270-1 [23] and ASTM C62 [25] for water absorption and compressive strength, respectively, the optimal zone was determined (Fig. 8). This region includes high percentages of gray clay and red mud. This study aimed to incorporate as much wastes content as possible, meeting the standards

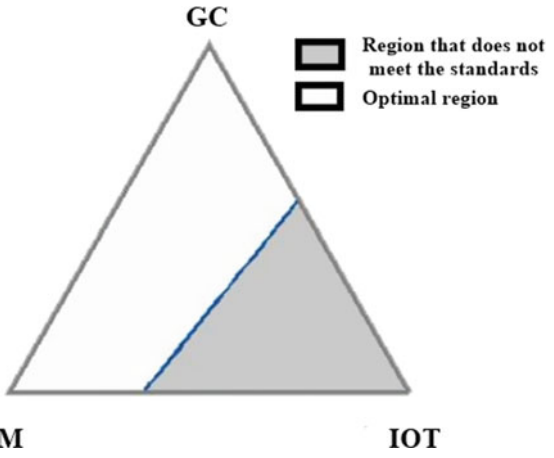

Fig. 8 Optimal region for water absorption and compressive strength properties. (Color figure online)

Table 4 Prediction of behavior of optimal mixture

Properties	Estimated value for optimal mixture
Firing linear shrinkage (%)	2.19
Apparent specific mass (g/cm^3)	1.67
Water absorption (%)	21.51
Axial compressive strength (MPa)	20.34

criterion. Thus, one optimal mixture was defined by means of desirability analysis, composed of 40% GC, 45% RM, and 15% IOT.

It is possible to estimate the values of the analyzed properties, corresponding to optimal mixture, using the regression equations obtained previously. Table 4 shows the results. The optimal composition was also located on Winkler's diagram (Fig. 9). The zones A, B, C, and D correspond to suitable areas for production of high-quality materials, roof tiles, hollow bricks, and solid bricks, respectively. One can notice that the mixture is not situated in the appropriate zone for clay bricks production (C and D zones). However, this diagram is only a referential based on the particle size of the mixture. The quality of ceramic products also depends on the chemical composition and thermal behavior. Even if the composition is out of the suitable area, it can be technically satisfactory. Besides, the optimal composition is closer to B zone, indicating another possible application (roof tiles production).

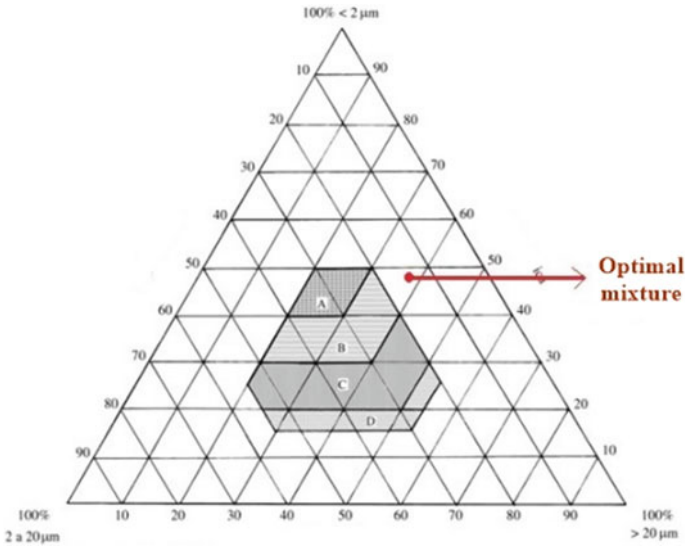

Fig. 9 Location of optimal mixture on Winkler's diagram. (Color figure online)

Conclusions

This study aimed to evaluate the physical and mechanical behavior of clay bricks produced from gray clay, iron ore tailings, and red mud. According to the experimental program and the statistical tools applied (mixture design of experiments), one can conclude the following:

- Both iron ore tailings and red mud presented physical and chemical characteristics that justify their incorporation in fired ceramic products. The IOT can act as a non-plastic material, contributing to better performance on drying and firing stages. RM has great amount of clay and silt fractions, besides high percentages of SiO_2 and Al_2O_3;
- Analyzing the effect of iron ore tailings and red mud, the red mud presented less negative impact on the mechanical strength and water absorption. It can be explained by its chemical composition and particle size distribution (finer material);
- The design of experiments contributed to the optimization of the experimental program, and the regression equations presented significant reliability. It was possible to analyze the effect of each raw material on the final properties of the mixtures;
- The incorporation of red mud and iron ore tailings in the production of clay bricks was proved as technically feasible. Thus, it is an attractive alternative to recycling these wastes, giving them a sustainable destination and preventing the occurrence of security and environmental damages.

Acknowledgements The authors thank the Federal University of Viçosa. This study was financed in part by the Coordenação de Aperfeiçoamento Pessoal de Nível Superior – Brasil (CAPES) – Finance Code 001.

References

1. Monteiro SN, Vieira CMF (2014) On the production of fired clay bricks from waste materials: a critical update. Constr Build Mater 68:599–610
2. Ma B, Cai L, Li X, Jian S (2016) Utilization of iron ore tailings as substitute in autoclaved aerated concrete: physico-mechanical and microstructure of hydration products. J Clean Prod (in press)
3. Silva FL et al (2014) Study of the recovery and recycling of tailings from the concentration of iron ore for the production of ceramic. Ceram Int 40(10):16085–16089
4. Tiffo E et al (2015) Red ceramics produced from mixtures of kaolinite clay and waste glass. Braz J Sci Technol 2:1–13. https://doi.org/10.1186/s40552-015-0009-9
5. Haiying Z, Youcai Z, Jingyu Q (2011) Utilization of municipal solid waste incineration (MSWI) fly ash in ceramic brick: product characterization and environmental toxicity. Waste Manag 31(2):331–341
6. Vieira CMF, Soares TM, Sánchez R, Monteiro SN (2004) Incorporation of granite waste in red ceramics. Mater Sci Eng A 373:115–121

7. Medeiros VSC, Pedroti LG, Mendes BC, Pitanga HN, Silva TOD (2019) Study of mixtures using simplex design for the addition of chamotte in clay bricks. Int J Appl Ceram Technol 16:2349–2361
8. Youngjae K, Youngmin L, Minseuk K, Hyunsik P (2019) Preparation of high porosity bricks by utilizing red mud and mine tailing. J Clean Prod 207:490–497
9. Sglavo VM et al (2000) Bauxite 'red mud' in the ceramic industry. Part 2: production of clay-based ceramics. J Eur Ceram Soc 20(3):245–252
10. Souza CC, Vieira CMF, Monteiro SN (2008) Alterações microestruturais de cerâmica argilosa incorporada com rejeito de minério de ferro. Revista Matéria 13(1):194–202
11. Mendes BC et al (2019) Technical and environmental assessment of the incorporation of iron ore tailings in construction clay bricks. Constr Build Mater 227:116669. https://doi.org/10.1016/j.conbuildmat.2019.08.050
12. Arhin DD et al (2012) Fabrication and characterisation of ghanaian bauxite red mud-clay composite bricks for construction applications. Am J Mater Sci 3(5):110–119
13. ABNT. NBR 7181(1984) Soil - Grain size analysis. ABNT, Rio de Janeiro. (In Portuguese)
14. ABNT (1984) NBR 6508 Soil grains passing through the sieve of 4.8 mm-Determination of specific mass. ABNT, Rio de Janeiro. (In Portuguese)
15. ABNT (2016) NBR 7180 Soil—Plasticity limit determination. ABNT, Rio de Janeiro. (In Portuguese)
16. ABNT (2016) NBR 6459 Soil-Liquid limit determination. ABNT, Rio de Janeiro. (In Portuguese)
17. Pracidelli S, Melchiades F (1997) Importance of granulometric mass composition for red ceramics. Cer Ind 2:31–35 (In Portuguese)
18. Baccour H et al (2008) Mineralogical evaluation and industrial applications of the Triassic clay deposits, Southern Tunisia. Mater Charac 59:1613–1622
19. Celik H (2010) Technological characterization and industrial application of two Turkish clays for the ceramic industry. Appl Clay Sci 50:245–254
20. Marsigli M, Dondi M (1997) Plasticitá delle Argille Italiane per Laterizi e Previsione del Loro Comportamento in Foggiatura. L'Industria dei Laterizi. 46:214–222
21. Mahmoudi S, Srasra E, Zargouni F (2008) The use of Tunisian Barremian clay in the traditional ceramic industry: optimization of ceramic properties. Appl Clay Sci 42:125–129
22. Barba A (1997) Materias Primas para la Fabricación de Soportes de Baldosas Cerámicas. Insituto de Tecnologia Cerámica, Spain
23. ABNT (2017) NBR 15270 Ceramic components. ABNT, Rio de Janeiro. (In Portuguese)
24. Zouaoui H et al (2017) Structure, microstructure and mechanical features of ceramic products of clay and non-plastic clay mixtures from Tunisia. Appl Clay Sci 135:112–118
25. ASTM (2008) ASTM C62 Standard Specification for Building Brick (Solid Masonry Units Made From Clay or Shale). ASTM, West Conshohocken

Effects of K_2O Addition on the Reduction Smelting of Phosphorite for the Yellow Phosphorus Production

Hongquan Jing, Yuan Yao, Cuihong Hou, Haobin Wang, and Shouyu Gu

Abstract Yellow phosphorus produced by electric furnace is an important raw material for the production of high-purity phosphorus fine chemicals. High temperature of the slag system for the smelting of phosphorite resulted in the energy-extensive consumption. Moreover, the low activity of slag led to the low utilization efficiency. In the current study, the effects of K_2O addition on the reduction smelting of phosphorite were investigated via thermodynamic calculations and experiment validation in order to reduce the smelting temperature and increase the activity of the slag. It has been found that K_2O could reduce the melting temperature of SiO_2–CaO–Al_2O_3 ternary system and accelerate the liquid-phase formation. Higher phosphorus volatilization ratio over 97% was obtained when the phosphorite smelted at 1500 °C with binary basicity of 0.8 and 3 wt.% K_2O addition . Moreover, a K-bearing slag with high activity was obtained and it can be used as micronutrient fertilizer.

Keywords SiO_2–CaO–Al_2O_3 · K_2O addition · Yellow phosphorus production · Micronutrient fertilizer

Introduction

Yellow phosphorus is an important raw material used for the preparation of inorganic and organic fine phosphorus chemical products [1, 2]. At present, China is the largest manufacturer of yellow phosphorous, producing about 83% of the world's supply in 2018 [3].

Yellow phosphorus production is the process of carbothermic reduction of phosphorite. Phosphate ore, silica, and coke are evenly mixed with a certain proportion and then are smelted at a phosphorus furnace. When the reaction temperature is heated to

H. Jing · Y. Yao · C. Hou (✉) · H. Wang · S. Gu
Engineering Research Center of Advanced Functional Material Manufacturing of Ministry of Education, Zhengzhou University, Zhengzhou, China
e-mail: hch92@zzu.edu.cn

J. Li et al., *Characterization of Minerals, Metals, and Materials 2021*,
The Minerals, Metals & Materials Series,
https://doi.org/10.1007/978-3-030-65493-1_36

1500 °C by electric energy, the materials generate simple phosphorus gas, and then refined to obtain yellow phosphorus. The general reaction formula of phosphorus production by electric furnace is as follows [1, 3]:

$$4Ca_5(PO_4)_3F + 30C + 21SiO_2 \rightarrow 3P_4 + 20CaSiO_3 + SiF_4 + 30CO \quad (1)$$

Yellow phosphorus production by electric furnace process is characterized as high consumption of energy and material. It consumes 12–14 tonnes of raw materials and about 13,000–15,000 kWh electricity to produce 1 ton yellow phosphorus, accompanied by producing 10 ton slag [4]. Slag is the molten industrial solid waste discharged from the process. However, unlike the regular industrial slag, the slag generated from the phosphate ore covers lots of micronutrients required for the plants, such as CaO, SiO_2, MgO, and Fe_2O_3. The nutrients in the slag are wasted since most of the slag is used to produce cement for the construction industry [5, 6]. The production of yellow phosphorus is a complex process of energy-intensive and environmental pollution, which is facing great challenges of economic and environmental. It is extremely important to study and develop energy-saving, cost-reducing technologies and enhance the utilization efficiency of slag for the sustainable development of furnace-based phosphorous production.

Some attempts were made to reduce the smelting temperature of phosphate ore. It was shown that the melting effect of potash feldspar is better than that of traditional silica flux [7–9]. In our previous work, micronutrients fertilizer rich in various nutrients was prepared in medium- to low-grade phosphate by high temperature melting flowed and quickly quenched by water, which provided an alternative technology for the efficient utilization of yellow phosphorus slag [10].

In order to reduce the energy consumption of yellow phosphorus production and improve the utilization value of water-quenched slag, the carbothermal reduction process of phosphate was conducted using the pure K_2O as the K-bearing addition. Thermodynamic analyses of SiO_2–CaO–Al_2O_3 and SiO_2–CaO–Al_2O_3–K_2O systems were investigated first to determine the melting characteristics of the slag. The activities of the micronutrients and the volatilization of phosphorus and K_2O were also studied.

Experimental

Materials

The phosphate ore, silica, and coke used in the experiments were taken from Yunnan, China. The main compositions of raw phosphate ore and silica samples were listed in Table 1. The coke is with 80.26 wt.% fixed carbon. In order to study the effect of K_2O on slagging and fluxing in yellow phosphorus production process via electric furnace, the chemically pure K_2SO_4 with a purity of 99 wt.% was used as the addition.

Before reduction smelting, all raw materials were dried at 105 °C for 4 h, then were crushed and ground to a particle size less than 180 μm.

Reduction Smelting Procedure

Before reduction smelting, phosphorus, silica, coke, and K_2SO_4 were evenly mixed with a certain proportion of $m(SiO_2)/m(CaO) = 0.8$. Carbothermic reduction of phosphorite process was conducted in the shaft furnace with an inner diameter of 170 mm, which is shown in Fig. 1. Mixture was smelted in a cylindrical graphite crucible (size: 50 mm × 80 mm) under N_2 atmosphere at a given temperature for 1 h, and then the liquid slag was rapidly quenched in cold water. Phosphorus vapor was recycled by a water tank. The slag was dried at 105 °C for the subsequent characterization.

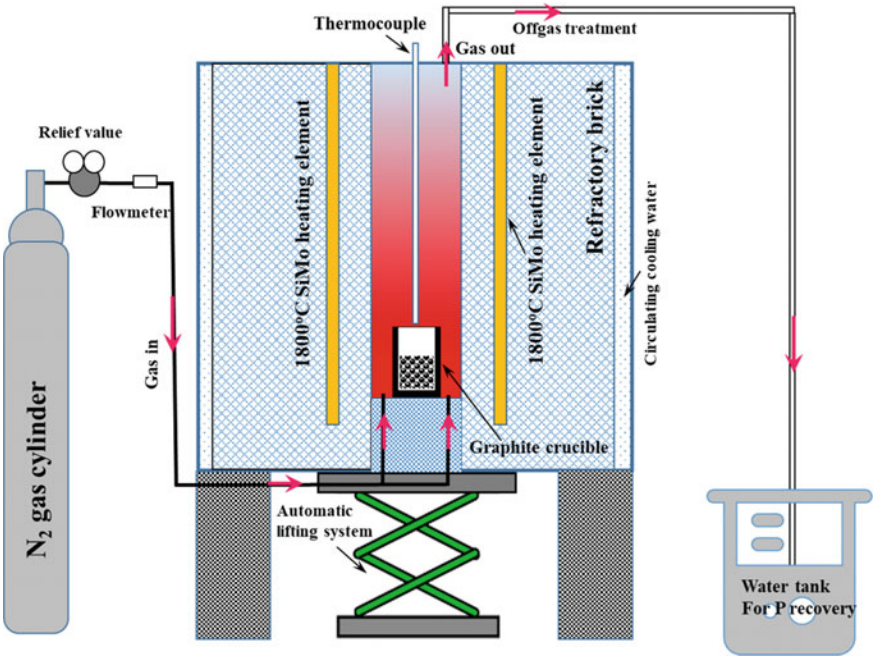

Fig. 1 Schematic diagram of experimental equipment for carbothermal reduction smelting. (Color figure online)

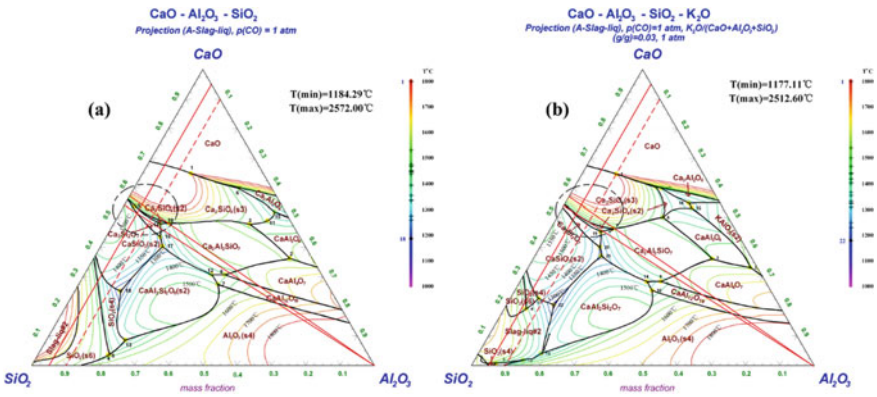

Fig. 2 Ternary phase diagram of SiO_2–CaO–Al_2O_3 (**a**), and quaternary phase diagram of SiO_2–CaO–Al_2O_3 at 3 wt.% K_2O system (**b**). (Color figure online)

Characterization

FactSage 7.3 thermodynamic software was used to analyze the phase diagram. The formation of liquid phase and the volatilization rate of phosphorus about the SiO_2–CaO–Al_2O_3 and SiO_2–CaO–Al_2O_3–K_2O system were analyzed in the module of "Phase Diagram" and "Equilib". The used databases were "FToxid", "FactPS", and "Factsalt".

The mass fraction of phosphorus pentoxide (P_2O_5) and potassium oxide (K_2O) was measured by quinoline phosphomolybdate gravimetric method and sodium tetraphenylborate gravimetric method, respectively. The volatilization ratio of component was calculated as in the following Eq. (2):

$$X = \frac{W_0 - W_1}{W_0} \times 100\% \tag{2}$$

where X is the volatilization ratio of component, wt.%; W_0 is the mass of component in the pre-smelting in the furnace, g; W_1 is the residual mass of component in the slag, g.

For plants, nutrients can be divided into two forms: Absorbable (effective content) and non-absorbable. It is generally difficult for plants to directly absorb the nutrient elements contained in natural ores, so the activation of nutrient elements in minerals is very important. In this experiment, the activation rates of different components were determined. The total mass fraction of SiO_2, CaO, MgO, and K_2O was measured by chemical analyses. In order to simulate the absorption effect of micronutrients by crops, the effective SiO_2 CaO, MgO were determined by 0.5 mol/L HCl solution as the extractant, and the effective contents of K_2O was determined by 2 wt.% citric acid solution [11]. The activation ratios of the micronutrients are according to Eq. (3):

$$\eta = \frac{C_1}{T_0} \times 100\% \tag{3}$$

where η is the activation ratio, wt.%; T_0 is the total mass of component in the slag, g; C_1 is the effective mass of component in the slag, g.

The melting ratio of materials represents the proportion of liquid-phase formation. In this study, the melting ratio of materials was calculated by FactSage 7.3 in the module "Equilib". The melting ratio of materials according to Eq. (4) is

$$C = \frac{Q_1}{Q_0} \times 100\% \tag{4}$$

where C is the melting ratio of materials, wt.%; Q_0 is the total mass of liquid phase and solid phase of SiO_2–CaO–Al_2O_3–K_2O system, g; Q_1 is the mass of liquid phase of SiO_2–CaO–Al_2O_3–K_2O system, g.

Results and Discussion

Phase Diagram of SiO_2–CaO–Al_2O_3–K_2O System

SiO, CaO, and Al_2O_3 are the main components in the slag. In addition, CO and P_4 are the main atmosphere in the furnace, which accounted for 85.93 and 9.97%, respectively [12]. In order to study the influence of K_2O on the melting properties of materials, the phase diagram of SiO_2–CaO–Al_2O_3 and SiO_2–CaO–Al_2O_3–K_2O systems was calculated and analyzed under CO atmosphere.

In the conventional industrial yellow phosphorus production process, the binary basicity of m(SiO_2)/m(CaO) in slag is controlled in the range of 0.75–0.85, and the operation temperature is 1500–1550 °C [1]. As shown in Fig. 2a, when the content of Al_2O_3 is less than 5 wt.%, the formed phases of SiO_2–CaO–Al_2O_3 system lie in the region of alpha-dicalcium silicate (Ca_2SiO_4(s3)), Rankinite ($Ca_3Si_2O_7$), and ps-wollastonite ($CaSiO_3$(s2)), where isotherms distribute closely and the melting temperature increases from 1400 to 1700 °C with increasing basicity. It is also found that Al_2O_3 helps to reduce the melting temperature of slag. Point 9 and point 14 are two special four-phase intersection points in SiO_2–CaO–Al_2O_3 system, which has binary basicity of 0.8, melting temperature decreases from 1437.06 to 1333.15 °C with the Al_2O_3 content increasing from 3.24 to 13.55 wt.%, and with a decreasing extent 103.91 °C.

Compared with SiO_2–CaO–Al_2O_3 system, the lowest fusion point and the highest fusion point of the eutectic mixture are lowered in SiO_2–CaO–Al_2O_3–K_2O system (Fig. 2b), from 1184.29 to 1177.11 °C, and from 2572.00 to 2512.60 °C, separately.

Furthermore, the main phase of SiO_2–CaO–Al_2O_3–K_2O system is Ca_2SiO_4(s3) at the basicity range of 0.75–0.85, where the distribution of isotherms is looser than that of SiO_2–CaO–Al_2O_3 system. As a result, the basicity range is expanded, in which the temperature is controlled lower than 1500 °C.

Liquid-phase and Phosphorus Formation of the SiO_2–CaO–Al_2O_3–K_2O System

The melting rate of materials and the volatilization rate of phosphorus in SiO_2–CaO–Al_2O_3 system are calculated and listed in Fig. 3. As displayed in Fig. 3**a**, it is found that the temperature for 50% melting rate of materials of the SiO_2–CaO–Al_2O_3 system decreases from 1340 to 1190 °C with the K_2O content increase from 0 to 8%. The initial temperatures for the liquid-phase formation from 1225 °C decrease to 1175–1125 °C. It has been demonstrated that the presence of K_2O can accelerate the formation of liquid phase. In special case, when the K_2O content is 0, the temperature for 100% melting rate of materials of the SiO_2–CaO–Al_2O_3 system is over 1400 °C. In other words, the fusion point of the SiO_2–CaO–Al_2O_3 system is 1400 °C. But the temperature of fusion point of the SiO_2–CaO–Al_2O_3 system does not decrease with the increase of K_2O content. The fusion point of the SiO_2–CaO–Al_2O_3 system with 2, 4, 6, and 8 wt.% K_2O is 1375, 1325, 1325, and 1350 °C, separately. Therefore, the addition of K_2O should be less than 6 wt.%.

On the other hand, it is also found that K_2O inhibits the volatilization of phosphorus below 1340 °C, but promotes the volatilization of phosphorus above 1340 °C. As shown in Fig. 3b, below 1340 °C, the volatilization rate of phosphorus is decreased with the increase of K_2O content under the same temperature. When the temperature is increased over 1340 °C, the rate is increased with the increase of

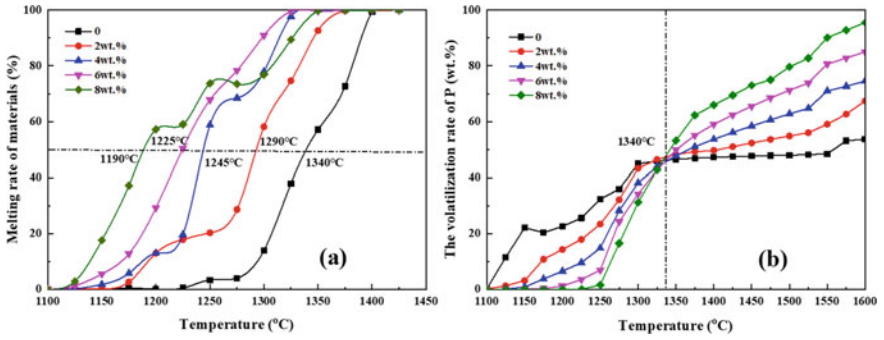

Fig. 3 Effect of K_2O content on the melting rate of materials (**a**) and the volatilization rate of phosphorus (**b**) in SiO_2–CaO–Al_2O_3 system. (Color figure online)

K_2O content. Therefore, considering the fusion point of materials and the yield of yellow phosphorus, when K_2O as an addition is added to the reduction smelting of phosphorite, the reaction temperature should be over 1340 °C.

The Volatilization of Phosphorus and K_2O

As shown in Fig. 4a, the volatilization rate of phosphorus increases with the increase of the temperature and then keep at a steady state when the temperature is further increased to 1500 °C. As consistent with theoretical calculations, the K_2O inhibits volatilization of phosphorus at lower temperature. However, K_2O does not promote the reduction volatilization of phosphate ore after 1340 °C, but this influential of inhibition is reduced or even disappeared with the increase of temperature and the volatilization ratio of phosphorus is over 97 wt.% as the phosphorite is smelted over 1500 °C. In addition, the raw materials of yellow phosphorus production include not only SiO_2, CaO, Al_2O_3, MgO, and Fe_2O_3 but also some other minor elements, such as B, Mn, S, Ni, Zn, and so on [13]. The presence of these substances affects the reduction of phosphate, which makes the experimental results differ from the theoretical calculations. On the whole, K_2O has no unfavorable effect on the reduction volatilization of phosphorite in higher temperature.

Although the overall trend is similar, there are some other differences of the volatilization ratio of phosphorus without K_2O addition between theoretical calculation and experiment. The volatilization ratio of phosphorus experimentally measured is 20–50% higher than that of theoretically calculated at a same temperature. The volatilization rate of phosphorus by theoretically calculated represents the phosphorus yield when the chemical reaction reaches equilibrium. Phosphorus element has a high vapor pressure and is easy to volatilize into the gas phase, so it was directly

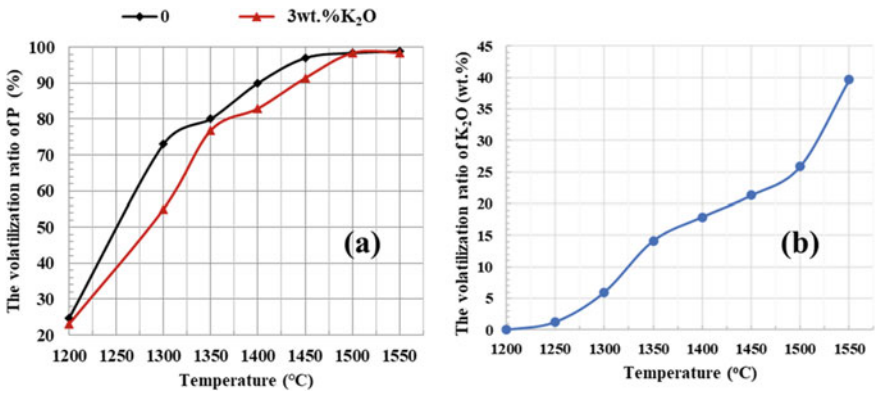

Fig.4 Effect of K_2O addition on the volatilization rate of phosphorus (**a**), and the volatilization rate of K_2O at different temperature (**b**). (Color figure online)

removed from the furnace with N_2 in this experiment, which promoted the movement of reaction (1) to the forward reaction, and increased the reduction rate of phosphate.

Figure 4b presents the temperature dependence of the volatilization ratio of K_2O. The volatilization ratio of K_2O increases with the increase of temperature. And it is less than 26 wt.% below 1500 °C, indicating that more than 2/3 of K_2O remains in the slag. It is inferred that the K-bearing slag is a favorable ingredient for the crop fertilizer.

The Activation Rate of the Slag

The slags with 3 wt.% K_2O addition and without addition obtained at 1500 °C were studied. As shown in Fig. 5, after treatment of high temperature melting and water-quenched, most of the insoluble SiO_2, CaO, MgO, and Fe_2O_3 in the raw materials are transformed into effective status that can be absorbed by plants, and the activation ratio are 74.03, 88.21, 93.12, and 85.30 wt.% in K-bearing slag, respectively. On the other hand, in comparison with the slag without addition, the K_2O has no disappointing effect on the transform of other components. Especially, the total mass of K_2O in K-bearing slag is 3.48 wt.% and the activation ratio of K_2O achieves 90.06 wt.%.

In this case, the value of slag is enhanced with the addition of K_2O and the activation ratio of K_2O was over 90%. No solid waste is generated since the activated slag is used as a favorable ingredient for the crop as fertilizer.

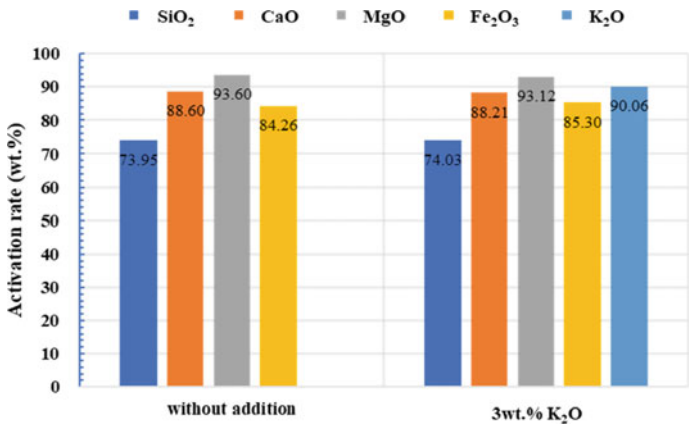

Fig. 5 The activation ratio of the micronutrients in the slag. (Color figure online)

Table 1 Main chemical composition of phosphate ore and silica concentrate (mass fraction, mass%)

Composition	CaO	SiO_2	Al_2O_3	P_2O_5	MgO	Fe_2O_3
Phosphate ore	39.11	21.23	1.88	25.89	1.57	1.32
Silica	0.63	93.2	2.15	0.53	0.76	1.13

Conclusions

(1) Thermodynamic analysis demonstrated that K_2O as an addition can decrease the melting temperature and promote liquid-phase formation of SiO_2–CaO–Al_2O_3 system. The initial temperatures for liquid-phase formation of the SiO_2–CaO–Al_2O_3 system with K_2O addition decrease from 1225 to 1175–1125 °C.

(2) At lower temperatures, the addition of K_2O inhibited the reduction volatilization of phosphorite. With the increase of temperature, the influence of K_2O on the reduction volatilization of phosphorite was reduced or even disappeared. The volatilization rate of phosphorus over 97% as the phosphorite smelted at 1500 °C with 3 wt.% K_2O addition.

(3) The volatilization ratio of K_2O increased with the increase of temperature, and it was less than 26 wt.% at 1500 °C. The activation ratios of SiO_2, CaO, MgO, Fe_2O_3, and K_2O were 74.03, 88.21, 93.12, 85.30, and 90.06 wt.%, separately. It is concluded that no solid waste was generated since the activated slag can be regarded as a favorable ingredient for the crop as fertilizer.

Acknowledgements The authors express their thanks to the National Key Research and Development Program of China (No. 2018YFC1900200, 2016YFD0200401), the Program for Innovative Research Team (in Science and Technology) in University of Henan Province (No. 19IRTSTHN028), and the Special Support Program for High Level Talents in Henan Province (No. ZYQR201912182) for the financial support.

References

1. Du JX, Sun ZL (2010) Furnace-process Yellow Phosphorous. Metallurgical industry press, Beijing China
2. Jiang SX, Fang TH, Dai YF, Lin L (1999) Fertilizer industry series: phoric acid. Chemical Industry Press Beijing China, Phosphorus Fertilizer and Compound Fertilizer
3. Wen LN, Ye LJ (2019) Present situation and development suggestions of phosphorus chemical industry in China. Phosphate Compd Fertil 34(09):1–4
4. Qin YS, Wang CH, Huang XF, Ma LP, Jiang M, Zhou T (2012) Utilization of melting yellow phosphor furnace slag. Chem Ind Eng Prog 31(10): 2319–2323. (Beijing, China)
5. Chen D, Cheng L, Feng H, Hou JJ, Shi K (2010) Study on calcination of quality cement clinker by high addition phosphorous slag. B Chin Ceram Soc 29(3):692–697
6. Sun C, Zheng FW, Ren YY, Li GB, Su Y (2017) Research on utilization of yellow phosphorus slag. Mod Chem Ind 37(8):28–31

7. Geng RX, Xia JP, Chen ZG, Yang J, Zheng S, Liu HL (2017) Effects of potassium feldspar on slagging and fluxing in phosphorus produced via electric furnace.Phosphorus Sulfur Silicon Relat Elem 192(4):475–480
8. Li Y, Xia JP, Liu HL, Cao RF (2017) Mechanism of silica and K-feldspar as flux agents in phosphate ore. J Chem Eng Chin Univ 31(5):1120–1126
9. Zhao Y, Xia JP, Cao RF, Jia Y (2018) Feasibility study on potassium additive promoting carbothermal reduction of phosphate rocks. Bull Chin Silic Soc 37(12):3983–3988
10. Zhang YL, Hou CH, Ji TT, Gu SY, Wang HB, Liu BB (2020) Experimental study on thermal process of preparing phosphorus potassium fertilizers containing medium and trace elements. Multipurp Util Miner Resour
11. Chemical Fertilizer Department of the Ministry of Chemical Industry, China Phosphate Fertilizer Industry Association (1993) Analytical Procedures for the Production of Phosphate Fertilizers and Compound Fertilizers. Chemical industry press Beijing China, Beijing
12. Wang ZH, Jiang M, Ning P, Xie G (2011) Thermodynamic modeling and gaseous pollution prediction of the yellow phosphorus production. I&EC Res 50(21):12194–12202
13. Xu XC, Hou CH, Wang HB, Tang JW (2010) Glass structure of aluminosilicate containing phosphate with low chemical stability and complex component–Development of glass structure model of aluminosilicate containing phosphate and manufacture of glass fertilizer.Sci China Ser B 40 (7):922–926

Evaluation of Different Methods of Surface Treatment of Natural Açai Fiber Added in Cementitious Composites

A. R. G. Azevedo, M. T. Marvila, E. B. Zanelato, T. E. S. Lima, D. Cecchin, J. S. Souza, M. Z. Barbosa, S. N. Monteiro, H. A. Rocha, J. Alexandre, and G. C. Xavier

Abstract Açai fiber has a characteristic that enhances its application as a reinforcement material in mortars. One of the major problems in the use of natural fibers in cementitious composites is the alkalinity of the porous of these materials, which can be solved by applying surface treatment to the fibers. The objective of this work was

A. R. G. Azevedo (✉) · E. B. Zanelato · J. Alexandre · G. C. Xavier
LECIV – Civil Engineering Laboratory, UENF- State University of the Northern Rio de Janeiro, Av. Alberto Lamego, 2000, Campos dos Goytacazes, Rio de Janeiro 28013-602, Brazil
e-mail: afonso.garcez91@gmail.com

E. B. Zanelato
e-mail: ebzanelato@gmail.com

J. Alexandre
e-mail: jonasuenf@gmail.com

G. C. Xavier
e-mail: gxavier@uenf.br

M. T. Marvila · T. E. S. Lima · H. A. Rocha
LAMAV – Advanced Materials Laboratory, UENF - State University of the Northern Rio de Janeiro, Av. Alberto Lamego, 2000, Campos dos Goytacazes, Rio de Janeiro 28013-602, Brazil
e-mail: markssuel@hotmail.com

T. E. S. Lima
e-mail: thuanny@gmail.com

H. A. Rocha
e-mail: higorazevedo@gmail.com

A. R. G. Azevedo · D. Cecchin · M. Z. Barbosa
TER – Department of Agricultural Engineering and Environment, UFF - Federal Fluminense University, 341, Rua Passo Da Pátria, Niterói, Rio de Janeiro 24210240, Brazil
e-mail: daianececchin@yahoo.com.br

M. Z. Barbosa
e-mail: marciozagobarbosa@gmail.com

J. S. Souza
PECC - Civil and Environmental Engineering Department, Campus Darcy Ribeiro, UNB - University of Brasília, Asa Norte, 70910-900 Brasília, Brazil
e-mail: jss.siqueira@gmail.com

J. Li et al., *Characterization of Minerals, Metals, and Materials 2021*,
The Minerals, Metals & Materials Series,
https://doi.org/10.1007/978-3-030-65493-1_37

to evaluate four different forms of surface treatment of natural Açai fibers, washing them with water, with cyclohexane/ethanol, immersing them in a solution of NaOH or alkaline peroxide, adding them in 4% in relation to the mass of cement in mortars of cement, and lime for coating. Properties such as consistency, incorporated air content, linear shrinkage, mechanical resistance, and water absorption were evaluated, according to Brazilian standards. The results showed that the treatment with alkaline NaOH solution is the one that best managed to modify the surface of the fibers, improving the evaluated technological properties.

Keywords Açai fiber · Treatment · Mortar

Introduction

The reduction of resources from non-renewable sources has increased human awareness and induced the use of material from renewable sources [1, 2]. For this reason, several research efforts in the field of sustainability are associated with the use of technology to preserve the environment [3, 4]. Although the series of studies on the behaviour and development of new materials has advanced in recent years, in the reality of Brazilian construction it is still necessary to develop materials that meet the technical and economic needs of sustainable development.

In the context of civil construction, mortars are widely used as a coating material in Brazil. There are several types and compositions of mortars. Since the production of mortar contributes to the scarcity of natural resources, the use of natural fibers has been increasingly frequent. The substitution of some raw materials from non-renewable sources, such as lime and cement, is an ecological practice that reduces the environmental impact [5].

According to Fantilli et al. (2017), more sustainable cement-based composites can be obtained by reinforcing the matrix with short fibers randomly dispersed [6]. In accordance with Pacheco-Torgal and Jalali (2011) [5], the mechanical and chemical performance, the manufacturing technique, the compatibility of the fiber with the cement matrix, the degradation of the fiber, and the appropriate cost to the project must be considered when choosing the fiber. In general, natural fibers have the advantage of increasing the tensile strength and reducing the cost and energy consumption of the cementitious composite. However, it highlights that the use of materials of natural origin can be a complex process and must be carried out consciously in the industry.

Among the various existing reinforce fibers, the Açai fiber is emphasized because in the production of Açai juice the fiber of the seed is not used and becomes an agro-industrial waste. Agro-industrial wastes from the production of Açai juice in northern Brazil are equivalent to more than 93,000 tons per year. In order to take advantage of

S. N. Monteiro
Department of Materials Science, IME - Military Institute of Engineering, Square General Tibúrcio, 80, Rio de Janeiro 22290-270, Brazil
e-mail: snevesmonteiro@gmail.com

this waste, these Açai fibers can be treated and used in cementitious composite [7, 8]. Lima Junior (2007) states that cementitious composites reinforced with Açai fiber do not present significant loss of compressive strength and satisfactorily increase the tensile strength [7].

Açai is a fruit from the Euterpe oleracea palm and is a tropical species, typical of the Amazon rainforest, which grows widely in the northern region of Brazil. Despite the Açai fruit is also found in several Brazilian states, the state of Pará is the largest producer in the country [9]. Generally, the Açai fruit is developed in conditions of warm and humid climate and does not support periods of prolonged drought [10].

In this context of technological application for agro-industrial waste, this research aims to describe a sustainable method for the treatment of Açai fiber and for use in cementitious mortars. For the development of a new technological and sustainable product, the study methodology involves the extraction of fiber from the Açai fruit, the fiber treatment, and application in cement mortars [10]. The efficiency is evaluated by comparing mixtures of different contents of fibers and forms of your superficial treatment. The comparison is made based on the results of the morphological and physical–chemical analysis of the Açai fiber and the results of the rheological and mechanical characteristics of mortars with added fibers. The technical and economic practicality of the methodology for using treatment and the use of Açai fibers in the reinforcement of mortars is revealed in this research.

The objective of this work was to evaluate four different forms of surface treatment of natural Açai fibers, washing them with water, with cyclohexane/ethanol, immersing them in a solution of NaOH or alkaline peroxide, adding them in 4% in relation to the mass of cement in mortars of cement, and lime for coating.

Materials and Methods

For making mortar, ordinary cement Portland (OCP), type III, for Brazilian standards, hydrated lime type III (HL-III), and sand from the Paraíba do Sul river bed are used. The natural fiber used in this research comes from the Açai fruit, which has a hard body, similar to a seed, covered with fibers, which were removed manually [10]. All the Açai used was collected from plantations located in the state of Espirito Santo, Brazil. Upon arriving at the laboratory, the fiber was immediately separated from the core, and subsequently kept in a greenhouse for a period of 24 h, allowing the loss of existing natural moisture and standardization of the fibers for processing [8].

As is known, the use of natural fibers in cementitious matrices, without any type of treatment, causes a series of problems that considerably reduce the useful life and durability of these composites, making their use impossible, requiring the implementation of some treatment technique superficial [11, 12]. For this research, four methodologies for surface treatment of the fibers were defined, before their addition to the mortar mass, which were simple washing with water (treatment A) , washing

with cyclohexane/ethanol (treatment B), immersion in alkaline NaOH solution (treatment C), and the treatment with alkaline peroxide (treatment D), called bleaching [13].

For treatment A, the necessary quantities of fibers were separated for the execution of technological tests, which were soon processed in a microprocessor, grinding the fibers and transforming them into small particles, which were subsequently sieved (16 mesh), reaching fibers with approximately 5 mm long, right after they were submerged in a glass beaker with 200 mL of distilled water, at 80 °C, with magnetic stirring for 1 h. After this process, the fiber was dried in an oven with air circulation at 50 °C until it reached a constant mass, which occurred around 36 h [14].

In treatment B, the same amount of fibers used in treatment A was placed in a container with 200 mL of 1:1 cyclohexane/ethanol solution, for 48 h in a soxhlet and for another 4 h in a row with distilled water. Right after the fiber was dried in an oven with air circulation at 50 °C until they reached constant mass, which occurred after around 24 h [14]. Treatment C occurred in two stages; first, the alkaline treatment with NaOH used approximately 80 g of the ground and sieved fiber (16 mesh) added in a beaker containing 200 mL of sodium hydroxide solution (5% NaOH) at a temperature of 90 °C. The system remained under constant agitation for 60 min, and after cooling to room temperature, vacuum filtration was carried out [14]. The retained solid material was washed with distilled water until it reached neutral pH. The fiber was kiln dried with air circulation at 50 °C until constant mass, which occurred on average within 24 h.

Finally, treatment D used part of the fibers from process C, which were treated with NaOH and subsequently placed in a mixture of hydrogen peroxide (H_2O_2 16%) and sodium hydroxide (NaOH 5%) at a temperature of 55 °C [14]. The system remained under constant agitation for 90 min. After cooling to room temperature, vacuum filtration was performed and the material was washed with distilled water until it reached neutrality [14]. The fiber was kiln dried with air circulation at 50 °C until constant mass, which occurred on average with 27 h.

After all treatments, the fibers could be used in addition to the mortar cement mass. Mortars were made using a 1:1:6 ratio (cement:lime:sand), in relation to the mass of the materials, and the fibers after the four treatments were added in terms of 4% in relation to the cement mass, being added at the time of the mechanical mixing of the mortar, following other works in the literature [8, 10, 15, 16].

The technological properties in the fresh state, such as consistency [17] and incorporated air content [18], were evaluated immediately after being made. In the hardened state, prismatic specimens were molded and submitted to an air cure for a period of 28 days, evaluating immediately after linear retraction, mechanical strength to flexion, and water absorption, always using normative instruments [16].

Results and Discussion

Mortar workability can be measured in relation to the horizontal spreading it has on a slump table. This spreading is measured with a ruler, and its result is shown in Fig. 1.

The fluidity of a mortar must not be too low or too high, as this parameter directly affects the ability to apply this material to structures. The fixed Brazilian standard for coating mortars shows that an acceptable workability range is between 255 and 265 mm; however, in some applications, such as reinforcement and repair of structures, these values are still very high, generating very fluid mortars and are difficult to apply in practice [1].

The addition of natural fibers traditionally reduces fluidity, as the introduction of fibrous elements increases the anchorage area of the cementitious paste [8]. This phenomenon can be seen in Fig. 1, as in all the treatments evaluated, there was a considerable reduction in the standard mean spread [15]. Treatment C, which uses the NaOH solution, was the one that showed values closest to Brazilian standards, in addition to being close to other values found in the literature, for mortars with added fibers [5, 8]. The treatment with only washed water (treatment A) had difficulties in the surface buffering, leaving the surface of the fibers very irregular, similar to the condition without treatment, which significantly reduced their spreading [10]. Figure 2 shows the results of the incorporated air content.

The air incorporated in mortars makes it possible to flow, but in excess it can cause serious problems related to the durability of the composites, mainly linked to the passage of aggressive agents. However, the literature indicates that values between 7 and 17% are those recommended, and that the above values give rise to

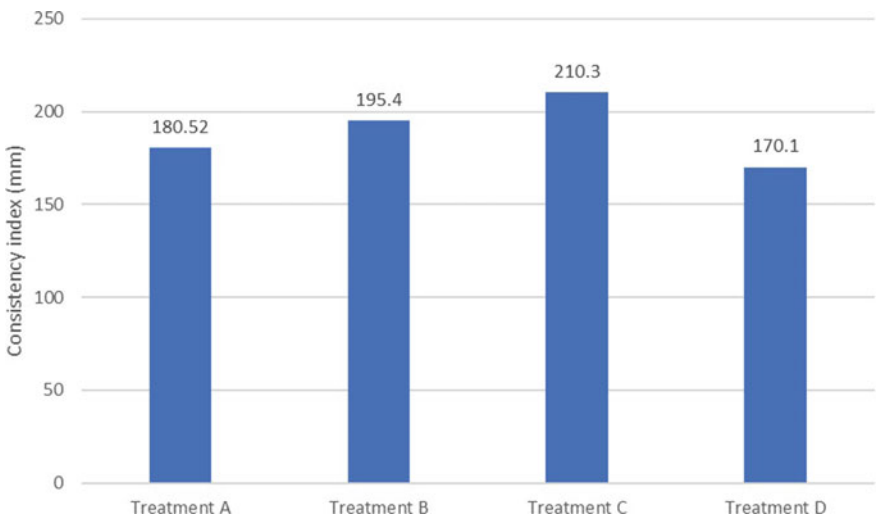

Fig. 1 Result of horizontal spreading, in mm. (Color figure online)

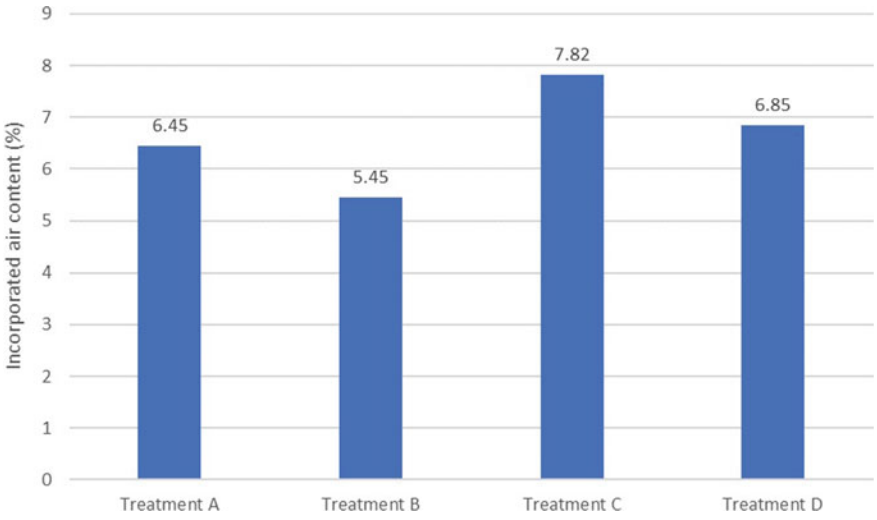

Fig. 2 Result of incorporated air content, in %. (Color figure online)

mortars without application conditions, as other technological properties are directly affected [10].

On the other hand, proportions less than 7% generate mortars without necessary fluids, and for example, in treatment B, the lowest value of incorporated air occurred, since the contact of the fiber with the cyclohexane/ethanol solution caused a reaction with the swelling of the fibers, which generated a significant reduction in the existing pores, and consequently in the air trapped in them, again here, only treatment C obtained values within the specifications of the literature [14, 16]. Figure 3 shows the result of the linear retraction.

Linear shrinkage arises as hydration reactions of cementitious materials occur, changing their dimensions. In the case of applying mortars for coatings and reinforcement of structures, excess shrinkage causes the occurrence of cracks and other openings that can impair the integrity of use [5]. Some studies stipulate that retractions of up to 1% can be allowed for coating mortars [13].

The results shown in Fig. 3 show that all treatments are within the recommended range, in addition it is clear that the insertion of fiber helps in the reduction, when compared to reference mixtures used in other works in the literature [15, 16]. Figure 4 shows the results of the mechanical strength to flexion of the specimens.

Figure 4 indicates that treatment B was the one that resulted in the best resistance results for the specimens, and this is due to the fact that the solution of cyclohexane/ethanol in combination with distilled water has a potential catalyst for the reactions of hydration of the cement paste; however, these values observed in all treatments are still superior to those verified in reference mortars, that is, without the addition of natural fibers [15]. In Fig. 5, the results of water absorption of the specimens can be seen.

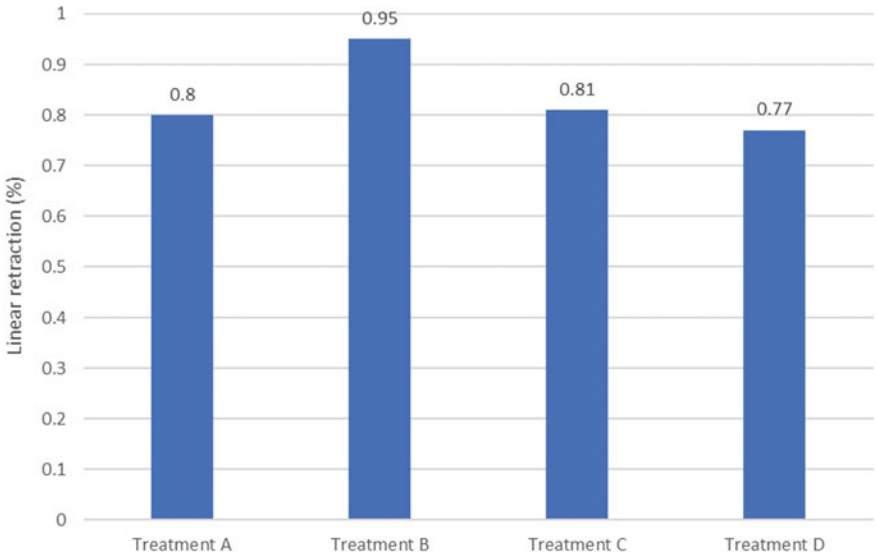

Fig. 3 Result in linear retraction, in %. (Color figure online)

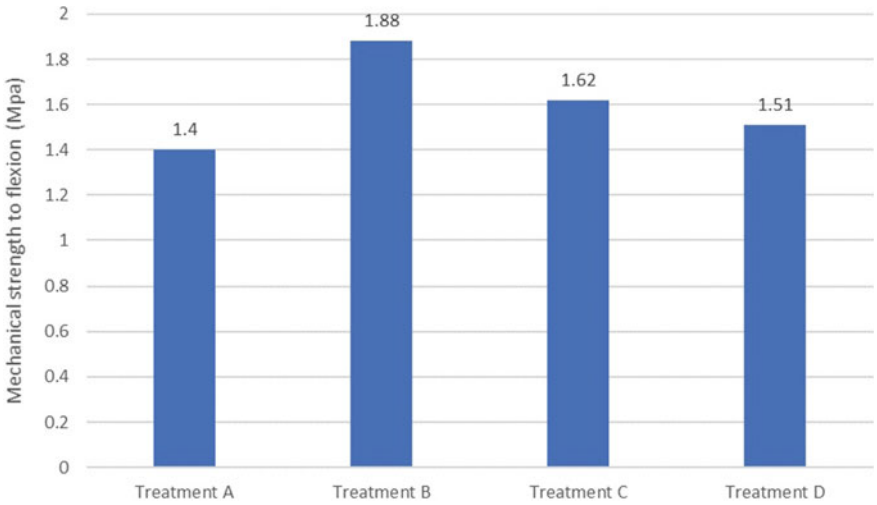

Fig. 4 Result in mechanical strength, in MPa. (Color figure online)

Figure 5 shows the result of water absorption, which corroborates with the result shown in Fig. 4, since in treatments where greater strength is obtained, there is a consequent reduction in water absorption due to greater pore filling [10]. It is desired that water absorption is lower, and in treatments B and C these indicators have been

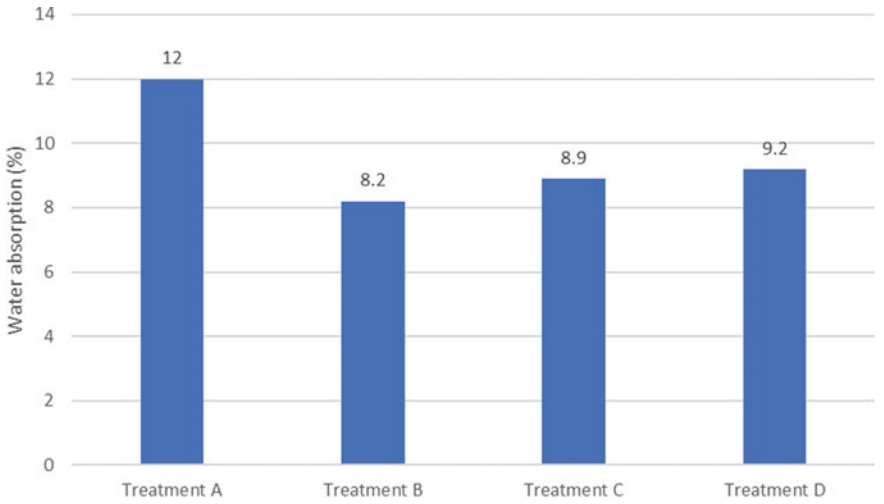

Fig. 5 Result of water absorption, in %. (Color figure online)

validated. For coating mortars, absorptions up to 9% are tolerated, showing that treatments A and D do not meet this parameter [8].

Conclusion

After the results, it can be concluded that:

- The surface treatment of natural fibers for use in cementitious matrices is of fundamental importance, without which this application is not possible from a technological perspective;
- The treatment with alkaline NaOH solution was the one that presented the best results, when considering all the parameters evaluated in this research; in addition, this form of treatment is widely used in the literature and has lower costs and environmental impacts, being the one recommended in this comparative research;
- The use of natural fibers is possible as a reinforcement agent for cement-based matrices, in addition to promoting a potential reuse of agro-industrial waste, contributing to sustainability issues and advancement in the development of new materials.

Acknowledgements The authors thank the Brazilian agencies: CNPq, CAPES and FAPERJ for the support provided to this investigation.

References

1. Joshi SV, Drzal LT, Mohanty AK, Arora S (2004) Are natural fiber composites environmentally superior to glass fiber reinforced composites? Compos A Appl Sci Manuf 35(3):371–376
2. Pereira PHF, Rosa MDF, Cioffi MOH, Benini KCCDC, Milanese AC, Voorwald HJC, Mulinari DR (2015) Vegetal fibers in polymeric composites: a review. Polímeros 25(1):9–22
3. Frollini E, Paiva JMF, Trindade WG, Razera AT, Tita SP (2004) Lignophenolic and phenolic resins as matrix in vegetal fibers reinforced composites. In: Wallenberger FT, Weston N (eds) Natural fibers, plastics and composites. Kluwer Academic Publishers, New York, pp 193–219
4. Hebrisha, SM, Al-Masri AN (2020) Factors affecting the cost of production of electricity and desalination plant for sustainable operation at the libyan iron and steel company. In sustainable development and social responsibility—vol 2, 73–81
5. Pacheco-Torgal F, Jalali S (2011) Cementitious building materials reinforced with vegetable fibers: a review. Constr Build Mater 25(2):575–581
6. Fantilli AP, Sicardi S, Dotti F (2017) The use of wool as fiber-reinforcement in cement-based mortar. Constr Build Mater 139:562–569
7. Lima Júnior UM (2007) Açaizeiro seed fibers (Euterpe oleracea mart.): Evaluation as to the use as reinforcement of fiber cement composites. Master's Dissertation, Faculty of Engineering, Pontifical Catholic University of Rio Grande do Sul, Porto Alegre, Brazil. 145 p (In Portuguese)
8. Marvila MT, Azevedo ARG, Cecchin D, Costa J, Xavier GC, Carmo DF, Monteiro SN (2020) Durability of coating mortars containing Açai fibers. Case Stud Constr Mater 13:10–21
9. Menezes GKA, Couto LL, Flores MDSA (2018) Açai stone waste management as an instrument of local development: The case of the municipality of Ananindeua-PA. Proc Colloq Organ Develop Sustain CODS 9:468–477 (In Portuguese)
10. Azevedo ARG, Marvila MT, Tayeh BA, Cecchin D, Pereira AC, Monteiro SN (2021) Technological performance of Açai natural fiber reinforced cement-based mortars. J Build Eng 33:12–23
11. Azevedo ARG, Marvila MT, Zanelato EB, Alexandre J, Xavier GC, Cecchin D (2020) Development of mortar for laying and coating with pineapple fiber. Rev Bras Eng Agrícola Ambient 21:25–36
12. Kim JT, Netravali AN (2010) Mercerization of sisal fibers: effect of tension on mechanical properties of sisal fiber and fiber-reinforced composites. Compos Part A Appl Sci Manuf 48:125–134
13. Azevedo ARG, Vieira CMF, Ferreira WM, Faria KCP, Pedroti LG, Mendes BC (2020) Potential use of ceramic waste as precursor in the geopolymerization reaction for the production of ceramic roof tiles. J Build Eng 29(1):56–101
14. Campos A, Teodoro KBR, Marconcini JM, Mattoso LHC (2011) Effect of fiber treatments on properties of thermoplastic starch/polycaprolactone/sisal biocomposites. Polimeros 20(10):10–16
15. de Azevedo ARG, Alexandre J, Zanelato EB, Marvila MT (2017) Influence of incorporation of glass waste on the rheological properties of adhesive mortar. Constr Build Mater 148:359–368
16. De Azevedo ARG, Alexandre J, Marvila MT, Xavier GC, Monteiro SN, Pedroti LG (2020) Technological and environmental comparative of the processing of primary sludge waste from paper industry for mortar. J Clean Prod 32:235–249
17. NBR 13276 (2016) Argamassa para assentamento e revestimento de paredes e tetos - Determinação do índice de consistência, Assoc. Bras. Normas Técnicas
18. ABNT (2005) NBR 13278 - Argamassa para assentamento e revestimento de paredes e tetos - Determinação da densidade de massa e do teor de ar incorporado, Assoc. Bras. Normas Técnicas

Evaluation of Full Bedding Concrete Blocks Prisms with Different Laying Mortar Strength

T. E. S. Lima, A. R. G. Azevedo, M. T. Marvila, E. B. Zanelato, J. Alexandre, and S. N. Monteiro

Abstract In the structural masonry system, the wall performs a structural function, absorbing the loads imposed on the system, being formed by blocks joined by seating mortar. In this constructive method, the quality control of the inputs and the correct dimensioning of the components is of paramount importance. In addition to the inputs, other factors can compromise the strength of the wall, for example the mortar bedding types. Two types are recommended, full bedding and face shell bedding. In full bedding, the mortar is disposed in all septum of the block. Therefore, this work has the objective of evaluating concrete blocks prisms with two mixed mortars ratios of different compressive strength. It is concluded that the increase of the compressive strength of the mortar influences the increase in the compressive strength of the prisms with full bedding type.

T. E. S. Lima · A. R. G. Azevedo (✉) · E. B. Zanelato · J. Alexandre
LECIV – Civil Engineering Laboratory, UENF - State University of the Northern Rio de Janeiro, Av. Alberto Lamego, 2000, Campos Dos Goytacazes, Rio de Janeiro 28013-602, Brazil
e-mail: afonso.garcez91@gmail.com

T. E. S. Lima
e-mail: thuanylima.es@gmail.com

E. B. Zanelato
e-mail: ebzanelato@gmail.com

J. Alexandre
e-mail: jonasuenf@gmail.com

A. R. G. Azevedo
TER – Department of Agricultural Engineering and Environment, UFF - Federal Fluminense University, Rua Passo Da Pátria, 341, Niterói, Rio de Janeiro 24210240, Brazil

T. E. S. Lima · M. T. Marvila
LAMAV – Advanced Materials Laboratory, UENF - State University of the Northern Rio de Janeiro, Av. Alberto Lamego, 2000, Campos dos Goytacazes, Rio de Janeiro 28013-602, Brazil
e-mail: markssuel@hotmail.com

S. N. Monteiro
Department of Materials Science, IME - Military Institute of Engineering, Square General Tibúrcio, 80, Rio de Janeiro 22290-270, Brazil
e-mail: snmonteiro@gmail.com

J. Li et al., *Characterization of Minerals, Metals, and Materials 2021*,
The Minerals, Metals & Materials Series,
https://doi.org/10.1007/978-3-030-65493-1_38

Keywords Structural masonry · Prism · Mortar · Strength

Introduction

Structural masonry is a construction system that is on the rise mainly in the construction sector of popular housing, due to the rationality in the consumption of materials and the speed of execution [1]. It is obtained by superimposing structural blocks, tied together, and joined by mortar joint [2].

The importance of the correct dimensioning of the masonry components affects the behavior of the structure [3]. The blocks must have compressive strength compatible with the loads to which they will be subjected, and the laying mortar must develop adequate strength in order not to compromise the structure of which it is part, and should not be more resistant than the block, and still absorb the deformations to which the masonry is submitted [4]. Therefore, [1] limits a maximum value of 70% of the characteristic compressive strength of the block referred to the net area and the compressive strength of the laying mortars for structural masonry [5, 6].

In addition to the characteristics of the materials, several factors interfere in the structural behavior of the masonry, such as the finishing and workmanship qualities, curing conditions, the joint thickness, and the mortar pattern [7, 8].

The most traditional mortar bedding type is the called full bedding, where the mortar is arranged in all the septa of the blocks (Fig. 1).

In this sense, this work aims to evaluate the behavior of full bedding prisms done with concrete block with two mortar ratios of different compressive strengths.

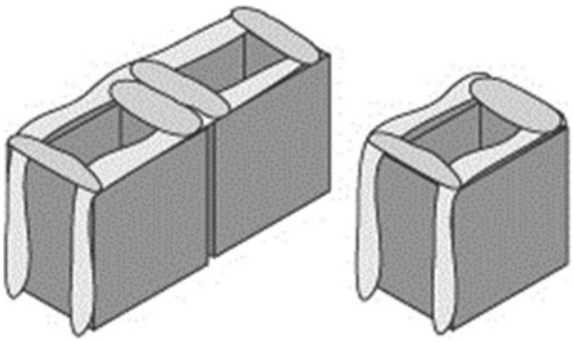

Fig. 1 Full bedding type. *Source* Portella, 2015

Materials and Methods

The hollow concrete blocks used in this work were manufactured in the city of Campos dos Goytacazes/RJ. With dimensions of (14 × 19 × 39) cm (thickness × height × length), water absorption of 6.32%, humidity of 12.34%, and compression strength of 6.01 MPa refer to the gross area and 12.97 MPa refer to the net area [9].

Two mortar ratios were defined for this study, 1:0.5:4.5 and 1:1:6, respectively representing cement:lime:sand. The mortars were produced with Portland cement CPII E-40 with a density of 2.97 g/cm^3, fineness of 4.00%, and a 28th day of compressive strength of 45.3 MPa, hydrated lime CH-III with a density of 2.31 g/cm^3 and washed sand from the Paraíba do Sul River, Campos dos Goytacazes/RJ, with a fineness module of 2.04, maximum size of 2.4 mm, specific weight in bulk of 2.61 g/cm^3 [10]. The water/binder ratio and the compressive strength were 0.9 and 8.93 MPa, respectively, for the mortar 1:0.5:4.5 and 1.26 and 5.72, MPa, respectively, for the mortar 1:1:6 keeping the consistency of the mortar in the range of (260 ± 5) mm. It is noticed that both mortars remained below the limit of 70% of the characteristic compressive strength of the block referring to the net area [11].

To perform the compressive strength test, six prisms were produced for each mortar mix. All prisms had a mortar joint thickness of (10 ± 3) mm and held for 28 days immobile in a weather-free place in the curing process (Fig. 2) [12].

The compression strength test of the prisms followed the procedures of [2] and was performed in the MTS servo-hydraulic system with a capacity of 500 kN, at a rate of 0.05 MPa/s, located in the civil engineering structures laboratory at UENF.

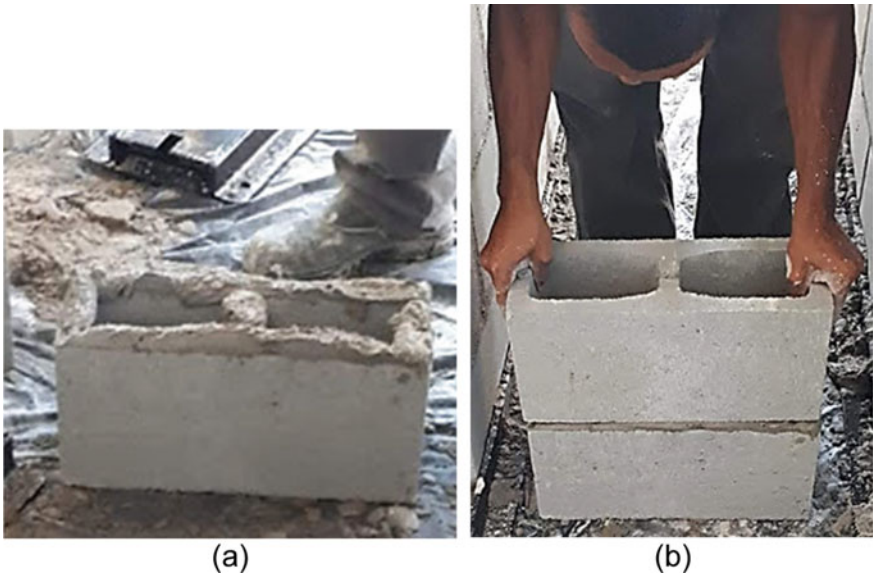

Fig. 2 Construction of the prisms: **a** detail of the full bedding type **b** constructed prism. (Color figure online)

Results and Discussion

The results of the compressive strength tests of the prisms are shown in the Table 1.

Analyzing the results, it can be seen that the 36% increase in compressive strength between the two mortars generated a 28% increase in the compressive strength of the prisms [13].

In addition, the prism/block ratio ranged from 0.5 to 0.8, falling within the allowed range of 0.5–0.9 for concrete blocks in Brazil, according to [3–14].

Regarding the rupture mode, all the prisms ruptured due to the effect of lateral tensile stresses on the block together with the loss of capacity of the mortar, making it possible to visualize the fragmentation of some sections of the block and the presence of vertical cracks parallel to the loading direction, concentrated in the regions of intersection between the longitudinal and transversal septa of the blocks (Fig. 3) [15].

The properties of mortars, together with the masonry blocks used, are responsible for the properties of the walls as a whole, and should always be evaluated [16–19].

Table 1 Results of the compressive strength of the prisms

Mortar ratio	Prisms compressive strength (f_{pm}) (MPa)	Standard deviation (MPa)	Coefficient of variation (%)	Prism/Block ratio (η)	Normalization
1:0.5:4.5	4.64	0.24	5.17	0.77	1
1:1:6	3.36	0.16	4.76	0.56	0.72

Fig. 3 Rupture mode of the prisms with full bedding type. (Color figure online)

Conclusion

As shown by the tests carried out, the compressive strength of the laying mortar influences the compressive strength of structural masonry prisms. Therefore, a 36% increase in the compressive strength of the laying mortars generated a 28% increase in the compressive strength of the prisms.

In the rupture mode of the prisms, there were no notable differences in the cracking and behavior of the specimens, the rupture being presented by all the prisms due to the effect of lateral tensile stresses on the block together with the loss of capacity of the mortar.

Acknowledgements The authors thank the Brazilian agencies: CNPq, CAPES and FAPERJ for the support provided to this investigation.

References

1. Associação Brasileira de Normas Técnicas (2011) Structural masonry–concrete blocks part 1: Design. NBR 15961-1, Rio de Janeiro
2. Associação Brasileira de Normas Técnicas (2016) Masonry of concrete blocks–test methods. NBR 16522, Rio de Janeiro
3. Ramalho MA, Côrrea MRS (2003) Projeto de edifícios de alvenaria estrutural. Pini, São Paulo
4. Nacus CJ (1980) Comparison of fully bedded and face-shell bedded concrete block. Report CE-495, Colorado State University
5. Khalaf FM (1996) Factors influencing compressive strength of concrete masonry prism. Mag Concr Res 48(175):95–101. https://doi.org/10.1680/macr.1996.48.175.95
6. Martins ROG et al (2018) Influence of blocks and grout on compressive strength and stiffness of concrete masonry prisms. Constr Build Mater 182:233–241. https://doi.org/10.1016/j.conbuildmat.2016.12.112
7. Mohamad G, Lourenço PB, Roman HR (2007) Mechanics of hollow concrete block masonry prism under compression: review and prospects. Cement Concr Compos 29(3):181–192. https://doi.org/10.1016/j.cemconcomp.2006.11.003
8. Hilsdorf HK (1969) An investigation into the failure mechanism of brick masonry loaded in axial compression. In: Johnson FB (ed) Designing, engineering and construction with masonry products. Gulf Publishing, Houston, Texas, pp 34–41
9. Santos CFR et al (2017) Numerical and experimental evaluation of masonry prisms by finite element method. IBRACON Struct Mater J 10(2):493–508. https://doi.org/10.1590/s1983-41952017000200010
10. Romagna RH (2000) Resistência à compressão de prismas de blocos de concreto grauteados e não-grauteados. Master's thesis, Universidade Federal de Santa Catarina
11. Mohamad G et al (2017) Strength, behavior, and failure mode of hollow concrete masonry constructed with mortars of different strengths. Constr Build Mater 134:489–496. https://doi.org/10.1016/j.conbuildmat.2016.12.112
12. Camacho JS et al (2015) The influence of grouting and reinforcement ratio in the concrete block masonry compressive behavior. IBRACON Struct Mater J 8(3):353–364. https://doi.org/10.1590/S1983-41952015000300006
13. Portella RP (2015) Fator eficiência da resistência prisma/bloco cerâmico de paredes vazadas. Master's thesis, Universidade Federal de Santa Maria

14. Azevedo ARG et al (2019) Assessing the potential of sludge generated by the pulp and paper industry in assembling locking blocks. J Build Eng 23:334–340. https://doi.org/10.1016/j.jobe.2019.02.012
15. Marvila MT et al (2019) Evaluation of the use of marble waste in hydrated lime cement mortar based. J Mater Cycles Waste Manage 21(5):1250–1261. https://doi.org/10.1007/s10163-019-00878-6
16. França BR et al (2018) Durability of soil-Cement blocks with the incorporation of limestone residues from the processing of marble. Mater Res 21(1). https://doi.org/10.1590/1980-5373-mr-2017-1118
17. Azevedo ARG et al (2020) Potential use of ceramic waste as precursor in the geopolymerization reaction for the production of ceramic roof tiles. J Build Eng 29. https://doi.org/10.1016/j.jobe.2019.101156
18. Marvila MT et al (2019) Correlation between the properties of structural clay blocks obtained by destructive tests and Ultrasonic Pulse Tests. J Build Eng 26. https://doi.org/10.1016/j.jobe.2019.100869
19. Azevedo ARG et al (2015) Addition of paper sludge waste into lime for mortar production. Mater Sci Forum 820:609–614. https://doi.org/10.4028/www.scientific.net/MSF.820.609

Evaluation of Thermal Healing in Pervious Concrete Pavers Produced with Reactive Powders Concrete

Wellington Fernandes, Leonardo Pedroti, Maurício Felisberto, Guilherme Botelho, Gustavo Lima, Beatryz Mendes, Heraldo Pitanga, and André Oliveira

Abstract A solution to mitigate floods in cities is the use of pervious concrete pavements. This is a concrete composed of a structure of interconnected voids allowing the flow of water, reducing the speed of surface runoff. Reactive powders concrete, with the addition of coarse aggregate, propitiates the creation of a pervious material combined with good resistance, hardly found in this type of product. The application of thermal curing allows an acceleration of resistance gain in young ages, making the pieces reach the market in less time. Therefore, we sought to study two traces of pervious concrete with RPC ratios: 1:4.0 and 1:3.5 gravel in mass, evaluating the resistance behavior by means of thermal curing. Significant gain in compressive strength is achieved in the early ages with thermal curing, and the permeability obtained by both lines analyzed was satisfactory.

Keywords Pervious concrete · Thermal cure · RPC

Introduction

The current paving systems in Brazil, asphalt and conventional concrete, generate great waterproofing of the soil on which they are built causing urban problems, such as floods. According to data from the Basic Municipal Information Survey (Munic) 2017, from the Brazilian Institute of Geography and Statistics [1], 1515 municipalities were affected by floods between 2013 and 2017.

These problems tend to worsen due to the growth of the urban population and irregular occupation without planning, with strong disobedience, in many cases, to the guidelines proposed by the Master Plan [2].

Soil waterproofing in urban centers has become directly responsible for the growth of surface runoff in urban basins and for reducing the concentration time, which generates higher and faster flood peaks (Fig. 1) [3].

W. Fernandes (✉) · L. Pedroti · M. Felisberto · G. Botelho · G. Lima · B. Mendes · H. Pitanga · A. Oliveira
Universidade Federal de Viçosa, Departamento de Engenharia Civil, Viçosa, MG, Brazil
e-mail: w.fernandes@ufv.br

J. Li et al., *Characterization of Minerals, Metals, and Materials 2021*,
The Minerals, Metals & Materials Series,
https://doi.org/10.1007/978-3-030-65493-1_39

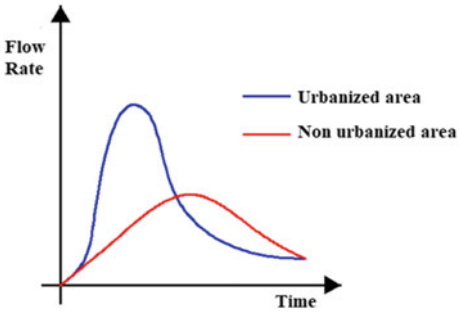

Fig. 1 Urbanized versus non-urbanized area hydrograph. (Adapted from Martins, 2012). (Color figure online)

According to the US Environmental Protection Agency (EPA), pervious concrete is defined as the best management practice for the control of pollution and rainwater, and has been increasingly encouraged by governments due to its environmental aspects, particularly favorable to urban environments. It brings benefits both to the soil, as it provides natural transpiration, to the hydrographic basins, as it allows replenishment, and to vehicle drivers, as drainage prevents the formation of puddles, reducing the effect of glare and aquaplaning in the tracks. However, there is still a great demand for manufacturing and construction standards. Few international studies have been published to evaluate properties on the spot and in the laboratory. The main applications are still limited to areas of little traffic, since this type of concrete still presents problems of durability and resistance [4].

On the other hand, another type of concrete has been studied since the 1990s to meet the needs of prefabricated buildings and constructions that require high performance. It is the concrete of reactive powders (RPC) , which has the capacity to reach between 200 and 800 MPa [5]. Its characteristic is low number of defects and pores, which makes its resistance very high [6]. In the fresh state, it has the characteristic of being self-compacting, managing to completely fill the volumes where it is applied, and which gives good adhesion to other materials [7].

RPC when submitted to thermal curing has its resistance to compression improved, as this treatment accelerates and stimulates new pozzolanic reactions, generating greater resistance at low ages [8]. This characteristic is desired for the production of pervious pavers in large quantities in view of what occurs in the production of precast, where their curing must be accelerated to increase production and turnover of shapes or for concreting in prestressing tracks, already that need a shorter curing time.

Thus, this work had the purpose of manufacturing and evaluating the mechanical resistance, permeability, and porosity of pervious concrete pavers, produced with RPC. The addition of coarse aggregate to the RPC creates a unit of interconnected voids, while its resistance tends to be higher than when produced as a conventional concrete.

Table 1 Cement characteristics

Tests					
		Cement		GBW	Silica
		CP-V	Limits		
			NBR 5733 [9]		
Specific mass (g/cm^3)		3.08	–	2,58	2,2
Fineness (%)		0.06	≤6	–	–
Specific area (m^2/kg)		586	≥300	899	9653
Water for normal consistency paste (%)		29	–	–	–
Setting times (min)	Start	150	–	–	
	End	202	–	–	
Le Chatelier expandability (mm)	Cold	0.1	–	–	
	Hot	0.3	–	–	

Materials and Methods

Materials

The materials used in this work were stored and characterized at the Civil Construction Materials Laboratory of the Federal University of Viçosa, where the entire study was carried out.

Cement, Granite Beneficiation Waste (GBW), and Active Silica

A CP-V cement manufactured by Holcim was used. The granite beneficiation waste is a material resulting from the cutting of ornamental rocks, from the city of Cachoeiro do Itapemirim—ES. The active silica used was produced by Down Corning Brasil in Minas Gerais.

It is presented in Table 1. A description with the characterization tests is presented.

Additive

The superplasticizer additive manufactured by MC-Bauchemie of the SuperFlow 1180 type was used. It is a synthetic additive based on polycarboxylate polymers. It is within the requirements of the Brazilian standard ABNT NBR 11768: 2011 [10] and has a density of 1.09 g/cm^3.

Small and Large Aggregate

The small aggregate comes from Mineração Jundu (Descalvado-SP) SP. The aggregate used was small graded gravel (gravel 0), conventionally crushed and washed, from the Martins Lanna quarry (Belo Horizonte—MG).

A summary of the characteristics of the aggregates is presented in Table 2, while Fig. 2 shows the granulometric curve of the coarse aggregate.

Methodology

The preparation can be divided into two stages. The first stage where the production of RPC (reactive powder concrete, itself) is carried out and the second where the production of pervious concrete takes place (addition of large aggregate to the RPC).

Table 2 Aggregate characteristics

Characteristic	Small aggregate	Large aggregate
Characteristic maximum dimension (mm)		12.5
Fineness module		6.56
Unitary mass dry and loose state (g/cm^3)	1.43	1.38
Unit mass dry and compacted (g/cm^3)		1.49
Specific mass SSS (g/cm^3)	2.65	2.64
Aggregate absorption (%)	0.1	0.47

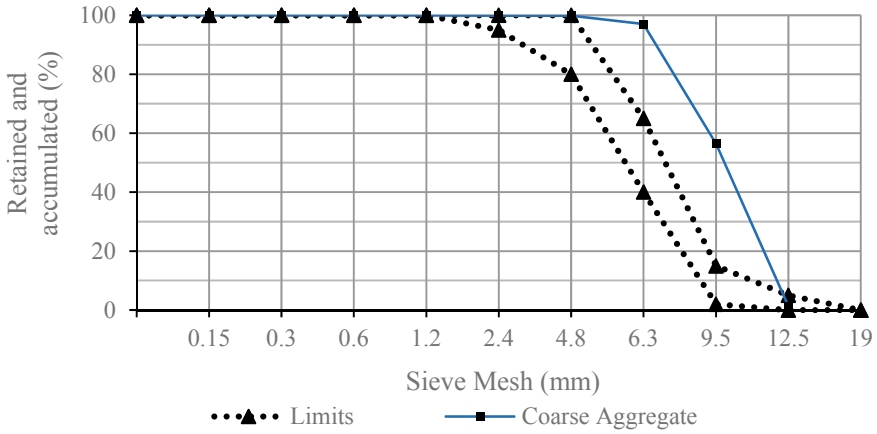

Fig. 2 Granulometric curve of the coarse aggregate. (Color figure online)

RPC Dosage and Production

The RPC dosage was based on the trait proposed by Vanderlei (2004) [5], and adapted by Machado and Lemes (2015) [11], shown in Table 3.

All dry materials (cement, sand, GBW, and silica fume) were previously weighed in and stored in plastic bags. The water used was at 10 °C at the time of its addition, in order to minimize the effects of large amount of heat released during the hydration of the cement in the paste.

The RPC mixing was carried out in a mortar developed in the laboratory. The vat (20 l capacity) was previously moistened, then 80% of the liquid material (water and superplasticizer additive) was added, followed by the dry material, and finally, the rest of the liquid part. A proper rod was used to mix the mortar. The RPC remained in mixture for 4 min at a rotation of 480 rpm.

After mixing, three specimens were molded for each RPC test age (1, 3, 7, and 28 days) and each treatment, that is, 12 for submerged curing at room temperature and 12 for thermal curing, totaling 24 bodies of evidence for determining compressive strength. Only for the age of 1 day, there was no differentiation of type of cure, as they were all in the form and went to rehearsal as soon as they were removed. The cylindrical specimens were molded 50 mm in diameter and 100 mm high, being molded in a single layer and vibrated for 30 s on a vibrating table.

After vibration, the specimens were kept for 24 h inside the humid chamber according to ABNT NBR 5739: 2007 [12]. Subsequently, the specimens were demolded and proceeded to their respective cures: submerged at room temperature and at 90 °C, both in a saturated solution in calcium hydroxide.

In addition to the compressive strength test, the consistency of RPC was evaluated, due to the rapid loss of plasticity that this material presents. The consistency index was obtained according to ABNT NBR 13276: 2005 [13]. The mold is filled in three layers, each of which is dense with 15, 10, and 5 strokes, respectively. After the first densification, the material is again densified through the flow table where it undergoes a process of rising and falling corresponding to 30 revolutions during 30 s. After this process, three mortar diameters were measured on the flow table. The process was repeated every 5 min for an hour to assess the loss of consistency.

Table 3 RPC traits

	Vanderlei (2004)		Machado and Lemes (2015)	
Material	Mass ratio	Consumption (kg/m^3)	Mass ratio	Consumption (kg/m^3)
Cement	1	874	1	853
Sand	1.101	962	1.101	939
GBW	0.235	205	0.235	200
Active silica	0.246	215	0.246	209
Superplasticizer	0.03	26	0.04	34
Water	0.18	157	0.23	197

Pervious Concrete Production

Two strokes were performed with a mass ratio of RPC and coarse aggregate of 1:4.0 and 1:3.5. After the production of the RPC as described in item 2.2.1, a portion was reserved and weighed and an amount of gravel added to it, according to the previously established relationship. The mixture was placed again in the mortar where it remained for 60 s at 480 rpm using a rod suitable for mixing with gravel.

After the addition of the gravel, pavers with dimensions of 100 mm wide, 80 mm high, and 200 mm long were molded for the compression tests, and cubic specimens of 100 mm of edge for the permeability tests.

The RPC: gravel mixture was placed in forms previously greased with mineral oil. The molding took place in two layers and each one was vibrated for 30 s by means of a vibrating table. For each line, 12 pervious concrete pavers were molded in order to determine the compressive strength and three cubic specimens for the extraction of 92 mm diameter cylindrical specimens to determine the permeability.

After molding, the material was taken to a humid chamber, where it remained for 24 h, before being demolded. Upon being unmolded, six pavers went for submerged curing at room temperature and six for curing in a 90 $\pm$ 2 °C thermal bath for 24 h, from where they subsequently went for conventional curing. All curing methods were in saturated calcium hydroxide solution. The cubic specimens were maintained only in conventional curing. Compressive strength was determined at 7 days of age. The permeability test, in turn, was performed at 10 days.

Permeability Test

The permeability test was performed according to the methodology proposed by NEITHALATH (2006) [14]. Therefore, a variable load permeate (Fig. 3) was reproduced in the Building Materials Laboratory (LMC) capable of carrying out this test. It is a nylon mold where a test piece wrapped with a latex membrane is placed so that water does not pass through the side of the test piece, and above it, a PVC tube with piezometric tube is positioned, to determine the water level in the reservoir. At the bottom of the equipment, there is a valve for controlling the water outlet.

The test begins with the placement of the latex band on the specimen, which is subsequently inserted into the nylon mold of the permeameter (Fig. 4). Then the PVC tube with piezometric tube is placed above it. Then water is added until the sample is saturated, and it is observed that the water flow at the drain outlet is not turbulent, so all the air in the set is eliminated. Subsequently, the valve is closed, water is added until the level of the piezometric tube is completed, and the valve is activated so that the water percolates the test piece. During the test, the time (Δt) that the water slide takes to traverse the entire system from point 340 mm (h1) to point 140 mm (h2) of the piezometric tube must be measured.

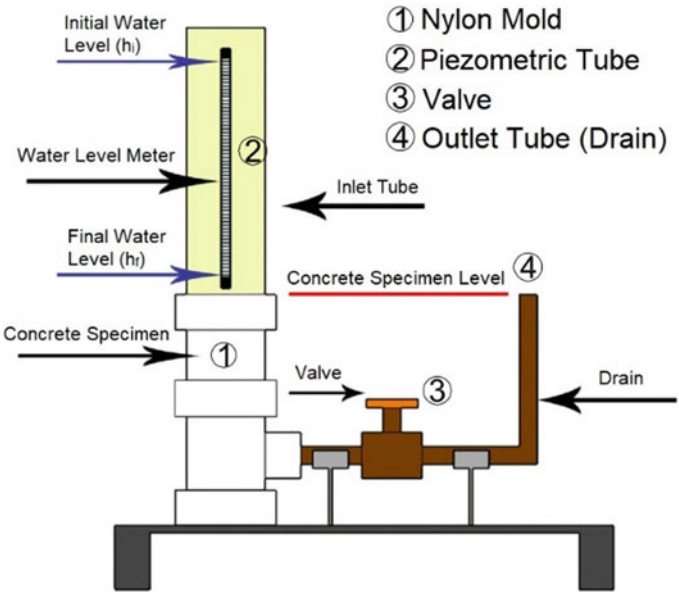

Fig. 3 Scheme of the variable load permeameter used. *Source* Neithalath (2006) (adapted). (Color figure online)

Fig. 4 Variable charge permeameter used. (Color figure online)

The procedure was repeated three times for each specimen, thus obtaining three times (Δt), where for each one the value, the permeability coefficient (k) was determined from Darcy's law (Eq. 1). To determine the permeability of a specimen, the average of the three permeabilities obtained was used.

$$K = \frac{A_1 \times l}{A_2 \times \Delta t} \times log\left(\frac{h_2}{h_1}\right) \quad (1)$$

Being:

- K is the permeability coefficient, expressed in centimeters per second (cm/s);
- A_1 is the cross-sectional area of the sample, expressed in square centimeters (cm^2);
- A_2 is the area of the inlet pipe, expressed in square centimeters (cm^2);
- l is the length of the tube, expressed in centimeters (cm);
- Δt is the duration of the test, expressed in seconds (s);
- h_1 is the initial height of the water column, expressed in centimeters (cm);
- h_2 is the final height of the water column, expressed in centimeters (cm).

Determination of Porosity

The specimens were saturated for 24 h, after which the specimens are weighed and submerged (Mi). Subsequently, the specimens were taken to the greenhouse, where they remain for 24 h and are weighed (Ms) after this process. With the ratio of submerged mass and dry mass, we know the mass of water that penetrates the sample and together with the specific mass of water we have the volume.

Knowing the sample dimensions, we can obtain its volume (V) and thus calculate the porosity P, through the ratio of voids volume and total volume:

$$P(\%) = \left(1 - \frac{M_s - M_i}{V}\right) \times 100 \tag{2}$$

Results

After performing the compression tests on the RPC specimens, strength was found for the ages of 1, 3, 7, and 28 days, as shown in Fig. 5.

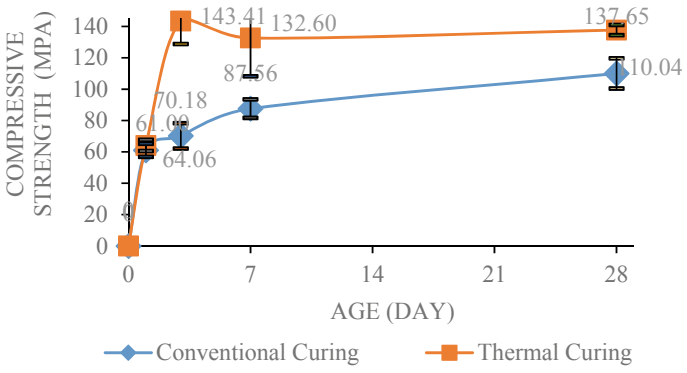

Fig. 5 RPC compressive strength evolution. (Color figure online)

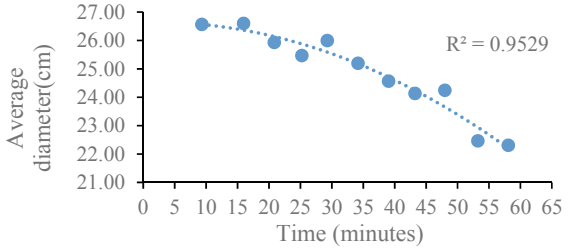

Fig. 6 Evolution of loss of consistency over time. (Color figure online)

It can be seen from Fig. 5 that the resistance in the initial ages was greater in the specimens that had thermal cure and that this difference decreases in the higher ages. Effect caused by thermal curing accelerates resistance gain.

Through the consistency test, as shown in Fig. 6, it can be seen that the RPC loses plasticity very easily, which makes it difficult to work, requiring its use in the best possible time.

Figure 7 shows the resistances, permeability, and pervious concrete.

It is evident how important the thermal cure was in accelerating the resistance gain in both strokes, with gains of around 30%. In relation to the strokes, we noticed that a smaller mass of gravel compared to RPC results in a product with greater resistance. It is an inverse effect for permeability. Higher levels of permeability (136%) were obtained in the mix with greater gravel mass compared to RPC, as well as porosity (18.5%). A porosity of 20.81% was obtained in the mix of 1:3.5 against 24.66% in the 1:4.0 line.

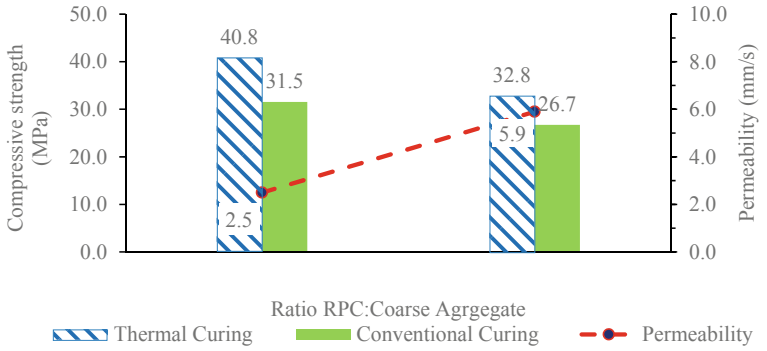

Fig. 7 Resistance and permeability relationship between different paver traits. (Color figure online)

Conclusions

The results allow us to conclude that the two strokes worked reached the requirements of ABNT NBR 16416: 2015, presenting compressive strength above 20 MPa and permeability above 1 mm/s.

The lower the ratio and gravel compared to RPC, the greater the resistance, while the permeability follows the opposite line, but still satisfactory, as well as the porosity. However, care must be taken with this relationship, since the lower the amount of crushed stone, there will be a surplus of RPC which, when vibrated, will be deposited at the bottom of the form, filling the pores and affecting the permeability.

The use of thermal curing is interesting in the acceleration of resistance, allowing in cases of application in industry a greater turnover of forms and shorter curing time.

References

1. IBGE-Brazilian Institute of Geography and Statistics. Basic Municipal Information Survey - MUNIC. https://www.ibge.gov.br/estatisticas-novoportal/sociais/trabalho/10586-pesquisa-de-informacoes-basicas-municipal.html?=&t=downloads. Accessed 22 Nov 2018
2. Tucci CEM (2002) Urban Drainage Management. RBRH Braz J Water Resour 7(1):5–27. Jan/Mar
3. Martins JRS (2012) Urban drainage management: will only technology be enough? Scientific Article, USP, pp 1–11
4. Bonicelli A, Arguellers GM, Pumarejo LGF (2016) Improving pervious concrete pavements for achieving more sustainable Urban roads. Proced Eng 161:1568–1573
5. Vanderlei RD (2004) Experimental analysis of concrete reactive powders: dosage and mechanical properties. 2004. 168 f. Thesis (Doctorate in Civil Engineering) - São Carlos School of Engineering, University of São Paulo, São Carlos
6. Richard P (1996) Reactive powder concrete: A new ultra-high-strength cementitious material. International symposium of high strength/ high performance concrete, 4, 1996. France. Anais… Paris, Paris, pp 1343–1349
7. Moura E (2018) Ultrathin. Téchine Magazine. http://techne.pini.com.br/engenhariacivil/150/artigo285469-1.aspx. Accessed 22 Nov 2018
8. Biz CE (2001) Reactive powder concrete. 112 f. Dissertation (Master in Civil Engineering)-Faculty of Civil Engineering, State University of Campinas, Campinas
9. ABNT-Brazilian Association of Technical Standards (1990) ABNT NBR 5733: Portland cement with high initial resistance-Rio de Janeiro
10. ABNT-Brazilian Association of Technical Standards (2011) ABNT NBR 11768: Chemical additives for Portland cement concretes-Rio de Janeiro, 2011
11. Machado FGD, Lemes JVB (2015) Analysis of the mechanical properties of concrete from reactive powders with the addition of nanofibrilated cellulose. 139f. End of Course Work (Graduation in Civil Engineering)-Federal University of Viçosa, Viçosa, 2015
12. ABNT-Brazilian Association of Technical Standards (2007) ABNT NBR 5739: Concrete-Test of compression of cylindrical specimens-Rio de Janeiro
13. ABNT-Brazilian Association of Technical Standards (2005) ABNT NBR 13276: Mortar for laying and covering walls and ceilings-Preparation of the mixture and determination of the consistency index-Rio de Janeiro
14. Neithalath N, Weiss WJ, Olek J (2006) Characterizing enhanced porosity concrete using electrical impedance to predict acoustic and hydraulic performance. Cem Concr Res 36. September 2006

Evaluation of the Mechanical Behavior of Epoxy Matrix-Hybrid Natural Fabric Composite: Accelerated Aging by UV Radiation

Clara Beatriz Melo Moreira Caminha, Michelle Souza Oliveira, Lucio Fabio Cassiano Nascimento, and Sergio Neves Monteiro

Abstract Thermoset matrix compounds have been used extensively in several industrial sectors. Many of these applications expose the material in environments that compromise its use, inducing, or aging of the material. The process involves several simultaneous and apparently independent mechanisms and, therefore, monitoring the evolution of variables within the specified time is an efficient method used to evaluate the behavior of the natural composites in accelerated conditions. Natural lignocellulosic fibers are important, since their use minimizes environmental pollution and the production costs of composite materials. The aim of this work is to obtain the tensile properties of plain epoxy and epoxy-hybrid natural fabric composite before and after performing aging accelerated by UV radiation. The findings of this work reveal that the epoxy-hybrid composite (50 mallow/50 jute) presents a loss in tensile strength at the first 30 min, and the stiffness decreases from the first exposure. Similar to what happens to living beings, polymers and their composites are also susceptible to the action of ultraviolet radiation.

Keywords Mechanical performance · UV radiation · Aging materials · Tensile test · Natural fabrics · Polymer composites

Introduction

Throughout the twenty-first century, with the evolution of armed conflicts, it became essential to invest in research and technology development in military items, in order to expand the countries' defense capacity and greater security to combat. In this context, although the study of tools for technical improvement and morphological conservation of ballistic protection vests has made it indispensable, cost is a limiting factor in this sector [1, 2].

Currently, ballistic armor has been manufactured primarily based on aramid fibers, polyethylene, and highly resistant polymers, and expensive components susceptible

C. B. M. M. Caminha · M. S. Oliveira (✉) · L. F. C. Nascimento · S. N. Monteiro
Military Institute of Engineering–IME, Rio de Janeiro, Brazil
e-mail: oliveirasmichelle@gmail.com

J. Li et al., *Characterization of Minerals, Metals, and Materials 2021*,
The Minerals, Metals & Materials Series,
https://doi.org/10.1007/978-3-030-65493-1_40

to wear and compromise their performance. The lifespan warranty in Brazil is only 5 years [3]. After this period its incinerated or comminuted and ground up.

Therefore, polymers composites-reinforced with natural fibers [4–10] are taken as potential substitutes for those components, as they are renewable resources and have an excellent cost/benefit ratio [11, 12]. In the current world scenario, it is necessary to search for new technological approaches capable of meeting the growing demand for defense and the operational requirements pre-established by the Brazilian Army, prioritizing the use of national raw material and contributing to the strategic and sustainable development of Brazil [13–18].

The present work investigated the physical properties of the epoxy composites reinforced with 50 mallow/50 jute hybrid fabric, used in the manufacture of rigid ballistic vests, in an environment exposed to ultraviolet radiation (UV). In addition to the aforementioned benefits, the present study aims at enhancing the resources and labor of small rural producers who survive through the extraction of natural fibers, promoting the social and economic development of less favored regions, notably North and Northeast Brazil.

Materials and Methods

The hybrid 50 mallow/50 jute (704 g/m^2) fabric was acquired from Brazilian Companhia Textil Castanhal do Pará, Brazil. The cost was estimated as US$ 5.57/kg [17, 18]. Figure 1 illustrates the hybrid fabric used.

The 120 × 150 mm layers of fabric were dried at 60 °C in an air-oven for 24 h, in order to reduce the inherent moisture. The epoxy resin used was the commercial epoxy type diglycidyl ether of bisphenol A (DGEBA) hardener with triethylenetetramine (TETA), both distributed by Epoxyfiber, Brazil. The DGEBA/TETA epoxy with stoichiometric phr 13 amounts of hardener.

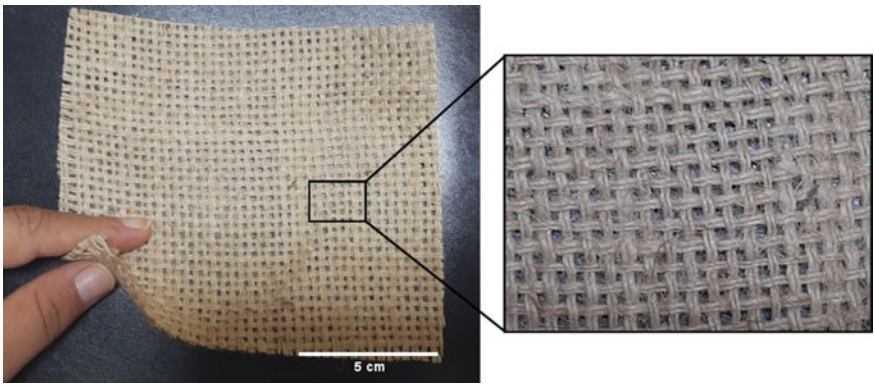

Fig. 1 50 mallow/50 jute hybrid fabric in "*arroyo*" weft configuration. (Color figure online)

Table 1 Evaluation groups and degradation conditions

Specimens group	Conditions
NE	Non-exposed
UV-30 min	Exposed to 30 min of ultraviolet radiation
UV-60 min	Exposed to 60 min of ultraviolet radiation
UV-180 min	Exposed to 180 min of ultraviolet radiation

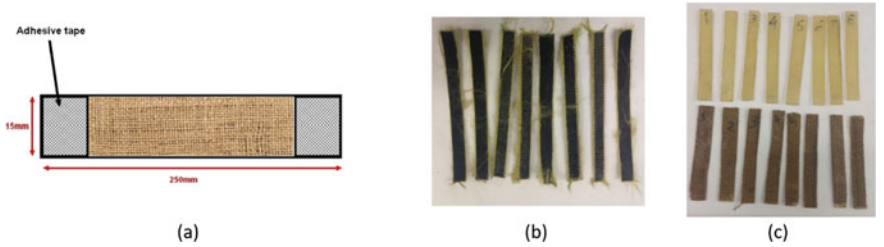

Fig. 2 **a** The scheme of tensile sample, **b** aramid, **c** plain epoxy and composite hybrid after 30 min of UV exposure. (Color figure online)

For the preparation of composites, the proportion used for it was 30 vol.% of hybrid fabric. A pressure of about 3 MPa was applied to the metallic mold. The laminate fabric composite plate, with 3 mm of thickness, was cured at room temperature for 24 h still under pressure. All plates were cut to the dimensions provided by standard [19].

Tensile tests were performed according to the ASTM D3039 standard [19], in an Inston universal equipment, model 3365, with 25 kN load cells. The test speed used in the specimens was 1 mm/min. Eight tensile test samples per group (Table 1) were produced.

The tensile test samples were subjected to an energy sunlight ultraviolet radiation (Fig. 2), on a single face, for 30, 60, and 180 uninterrupted minutes, at 25 °C. An accelerated aging system for non-metallic materials was used with ultraviolet rays A and B in a LABCURA equipment, using a power of 200 W/in. This chamber consists of eight fluorescent lamps (model TKL 40 w/05) that emit ultraviolet radiation in the 200–460 nm region. The samples were placed in the center of the oven, with the face exposed to the UV lamp. UV lamps are used to mimic natural sunlight in accelerated photo-oxidative degradation, and heating at relatively high temperatures in forced air circulation is used to accelerate thermo-oxidative ageing.

Results and Discussion

A possible solution to waste-disposal problems is using biodegradable polymers reinforced by natural fibers instead of traditional petroleum-derived plastics. Direct sunlight can break the covalent bonds in organic polymers. It tends to cause yellowing,

color fading, weight loss, surface roughening, mechanical property deterioration and embrittlement with more reduction in wetter condition. After weathering periods, because of degradation of fibers and matrix, the tensile strength of a composite is decreased. Figure 3 shows the tensile test samples after exposure to UV radiation at different conditions. It is observed that the color of the non-exposed (NE) plain epoxy and epoxy-hybrid fabric composite, Fig. 3a, was slightly modified after UV exposures, suggesting the chemical modification of these materials.

It was hypothesized that polymeric chains and branches would be destroyed by UV radiation, affecting the mechanical performance of the epoxy polymers, but this did not occur in present work. Table 2 shows the results of tensile test for plain epoxy. In this table, it can be verified a slight increase in the modulus of elasticity and the tensile strength of the plain epoxy (PE).

This phenomenon indicates that the free radicals, generated from the exposure of the samples to UV radiation, recombined, making a greater cross-link, which resulted in greater rigidity on the material's surface. Exposure to environmental agents, as UV radiation, produces an increase in the degree of crystallinity. The exposure promotes a reduction in the length of the macromolecular segments that reduce branching and chain entanglement; as a result, the newly formed regions are able to pack together more easily, increasing the crystallinity [20].

Nikafshar et al. [21] reported that increasing UV irradiation time decreased the tensile strength and modulus of epoxy resin and Epikure F204. Nonetheless, it seemed that the tensile modulus was not affected significantly by UV light. After 800 h of UV radiation, tensile strength and elongation at break reduced dramatically to 11.94 and 8.62%, respectively. Table 3 shows the obtained values for epoxy-hybrid fabric composites.

Fig. 3 Tensile test samples, with fragile rupture, under **a** non-exposure, **b** 60 and **c** 180 min of UV radiation exposure. (Color figure online)

Table 2 Plain epoxy at different conditions: NE, UV-30, UV-60 and UV-180 min

Specimens group	Modulus of elasticity (GPa)	Tensile strength (MPa)
NE	13.87 ± 6.88	17,520 ± 9,270
UV-30 min	34.92 ± 7.95	43,619 ± 23,985
UV-60 min	9.87 ± 2.31	77,763 ± 12,324
UV-180 min	5.75 ± 1.81	34,020 ± 9,975

Table 3 Hybrid fabric composite at different conditions: NE, UV-30, UV-60, and UV-180 min

Specimens group	Modulus of elasticity (GPa)	Tensile strength (MPa)
NE	39.62 ± 8.45	66,790 ± 12,585
UV-30 min	32.72 ± 8.27	34,015 ± 11,844
UV-60 min	32.36 ± 6.22	31,109 ± 5,021
UV-180 min	5.68 ± 2.37	34,997 ± 6,616

In particular, the slight increase in strength of epoxy-hybrid fabric composite (HFC) exposed to UV radiation between 60 and 180 min can be attributed to a possible cross-linking of epoxy resin, resulting in greater rigidity of the material. Between 30 and 60 min it could be related to a UV radiation absorbed by lignin in 50 mallow/50 jute hybrid natural fabric. In this case the photodegradation could begin, and the formation of chromophore groups, quinones and hydroperoxyl radicals could happen.

Lignin and extractives (mainly the phenolics) in natural fillers are very sensitive chromophores in the UV region, initiating the degradation processes with formation of new chromophore functional groups such as carboxylic acids, quinones, and hydroepoxy radicals that induce the yellowing aspect of photodegraded wood in wood-based polymer composites [23]. Table 4 presents the values for the aramid laminate in the highest exposure condition.

Alves et al. [20] reported that the mechanical and ballistic characteristics of UHMWPE composite were related to macromolecular modifications induced in the polymer by the environment through physicochemical testing. Exposure to environmental agents induces changes in the UHMWPE macromolecular chains, altering the mechanical properties and the ballistic behavior of the composite. Furthermore, Nascimento et al. [22] reported a decrease in the tensile strength of approximately 20% after UV radiation exposure of 310 h in aramid fabrics. However, no change in total strain was observed. The present work data were plotted to facilitate the comparison among treatments and the type of sample. Figures 4 and 5 summarize the results shown so far.

In general, the tensile strength (Fig. 4) and modulus of elasticity (Fig. 5) epoxy-hybrid fabric composite decreases as the time of exposure to UV radiation increases. One can notice that, similar to what happens to living beings, polymers and their composites are also susceptible to the action of ultraviolet radiation. In particular, the action of UV irradiation on the epoxy-50 mallow/50 jute fabric composites were negative. In the early stages of degradation by UV radiation, epoxy resin plays a fundamental role in stiffening the material.

Table 4 Aramid laminates at UV-180 min exposure

Specimens group	Modulus of elasticity (GPa)	Tensile strength (MPa)
UV-180 min	11.73 ± 2.12	204,409 ± 15,359

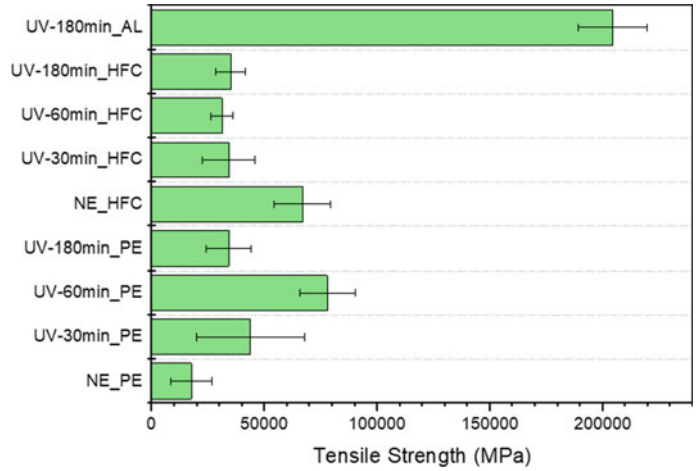

Fig. 4 Comparison of tensile strength among the evaluated groups. (Color figure online)

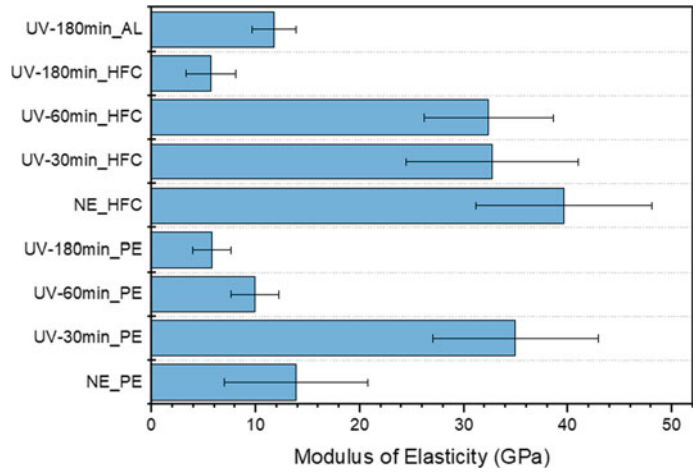

Fig. 5 Comparison of modulus of elasticity among the evaluated groups. (Color figure online)

Therefore, more experiments, like ballistic, UV-Vis, and FTIR, should be done to obtain a better understanding of the relation of UV irradiation in the plain epoxy, epoxy-50 mallow/50 jute fabric composite and aramid, and the time of exposure.

Summary and Conclusions

- Degradation of polymer composites under the action of aggressive environmental factors is a subject of great interest to the scientific community;
- The epoxy-50 mallow/50 jute fabric lose tensile strength at the first 30 min, and the stiffness decreases from the first exposure;
- In particular, the action of UV irradiation on the epoxy-50 mallow/50 jute fabric composites were negative;
- In the early stages of degradation by UV radiation, epoxy resin plays a fundamental role in stiffening the material;
- The use of accelerated tests may be an adequate way to predict the effects of environmental agents on the performance of ballistic armor.

Acknowledgements The authors thank the Brazilian agencies CAPES and CNPq for the financial support; Prof. Renata Antoun Simão, from UFRJ, for providing the UV aging chamber; and LNDC/UFRJ for performing the tensile tests.

References

1. Nayak SY, Sultan MTBH, Shenoy ST, Kini CR, Samant R, Md Shah AU, Amuthakkannan P (2020) Potential of natural fibers in composites for ballistic applications–a review. J Nat Fibers
2. Benzait Z, Trabzon L (2018) A review of recent research on materials used in polymer-matrix composites for body armor application. J Compos Mater 52(23):3241–3263
3. Konarzewski VHC, Spiekemann FL, Santana RMC (2019) Natural ageing of polyaramide fiber from ballistic armor. Polímeros 29(1):e2019002. Epub March 18
4. Hassan KMF, Horvath PG, e Alpár T (2020) Potential natural fiber polymeric nanobiocomposites: a review. Polymers 12(5):1072
5. Sanjay MR, Madhu P, Jawaid M, Senthamaraikannan P, Senthil S, Pradeep S (2018) Characterization and properties of natural fiber polymer composites: a comprehensive review. J Clean Prod 172:566–581
6. Pickering KL, Efendy MA, Le TM (2016) A review of recent developments in natural fibre composites and their mechanical performance. Compos Part A Appl Sci Manuf 83:98–112
7. Mohammed L, Ansari MNM, Pua G, Jawaid M, Islam MS (2015) A review on natural fiber reinforced polymer composite and its applications. Int. J. Polym Sci
8. Faruk O, Bledzki AK, Fink HP, Sain M (2014) Progress report on natural fiber reinforced composites. Macromol Mater Eng 299:9–26
9. Shah DU (2013) Developing plant fibre composites for structural applications by optimising composite parameters: a critical review. J Mater Sci 48:6083–6107
10. Shahinur S, Mahbub H (2020) Natural fiber and synthetic fiber composites: comparison of properties, performance, cost and environmental benefits. Encycl Renew Sustain Mater, 794–802
11. Monteiro SN, Drelich JW, Lopera HA, Nascimento LF, da Luz FS, da Silva LC, dos Santos JL, da Costa Garcia Filho F, de Assis FS, Lima ÉP, Pereira AC (2019) Natural fibers reinforced polymer composites applied in ballistic multilayered armor for personal protection—an overview. In: Ikhmayies S, Li J, Vieira C, Margem J, de Oliveira Braga F (eds) Green materials engineering. The minerals, metals & materials series. Springer, Cham, pp 33–47

12. Rajole S, Ravishankar K, Kulkarni S (2020) Performance study of jute-epoxy composites/sandwiches under normal ballistic impact. Def Technol 16(4):947–955
13. Garcia Filho FC, Oliveira MS, Pereira AC, Nascimento LFC, Matheus JRG (2020) Ballistic behavior of epoxy matrix composites reinforced with piassava fiber against high energy ammunition. J Mater Res Technol 9(2):1734–1741
14. Luz FS, Lima Jr EP, Louro LHL, Monteiro SN (2015) Ballistic test of multilayered armor with intermediate epoxy composite reinforced with jute fabric. Mater Res 18(2):170–177
15. Oliveira MS, da Costa Garcia Filho F, Pereira AC, Nunes LF, da Luz FS, de Braga FO, Monteiro SN (2019) Ballistic performance and statistical evaluation of multilayered armor with epoxy-fique fabric composites using the Weibull analysis. J Mater Res Technol 8(6):5899–5908
16. Moraes YM, Ribeiro CGD, Ferreira CL, Lima ES, Margem JI, Nascimento LFC, Monteiro SN (2018) Mechanical behavior of mallow fabric reinforced polyester matrix composites. J Mater Res Tech 7(4):515–519
17. Nascimento LFC, Louro LHL, Monteiro SN, Lima ÉP, Da Luz FS (2017) Mallow fiber-reinforced epoxy composites in multilayered armor for personal ballistic protection. JOM 69:2052–2056
18. Nascimento LFC, Louro LHL, Monteiro SN, Gomes AV, Marçal RLSB, Lima Júnior ÉP, Margem JI (2017) Ballistic performance of mallow and jute natural fabrics reinforced epoxy composites in multilayered armor. Mater Res 20:399–403. Nascimento RF, da Silva AO, Weber RP, Monteiro SN (2020) Influence of UV radiation and moisten associated with natural weathering on the ballistic performance of aramid fabric armor. J Mater Res Tech 9(5):10334–10345
19. ASTM International. D3039/D3039M-17 (2017) Standard test method for tensile properties of polymer matrix composite materials. ASTM International, West Conshohocken, PA
20. Alves ALS, Nascimento LFC, Suarez JCM (2005) Influence of weathering and gamma irradiation on the mechanical and ballistic behavior of UHMWPE composite armor. Polym Testing 24:104–113
21. Nikafshar S, Zabihi O, Ahmadi M, Mirmohseni A, Taseidifar M, Naebe M (2017) The effects of UV light on the chemical and mechanical properties of a transparent epoxy-diamine system in the presence of an organic UV absorber. Material (Basil.) 10(2):180
22. Nascimento RF, da Silva AO, Weber RP, Monteiro SN (2020) Influence of UV radiation and moisten associated with natural weathering on the ballistic performance of aramid fabric armor. J Mater Res Technol 9(5):10334–10345
23. Brebu M (2020) Environmental degradation of plastic composites with natural fillers–a review. Polymers 12(1):166

Failure Analysis of the Bellows After Service in Hot Blast Stove System by Dissection

Jianlong Wu, Hui Chen, Jian Sun, and Hailong Liang

Abstract High-temperature spot, air leakage, and even burn out accidents occurred frequently in bellows of hot blast systems in the metallurgy industry, which seriously affected the stability of the hot blast system and brought hidden danger to safety production. Although coating, grouting, and other treatment measures had been adopted, the effect was very little. Through dissecting and sampling analysis of the failure bellows, it was concluded that the steel structure of the bellows had cracking hidden danger due to welding quality defects, and other reasons for the failure were high temperature of the bellows steel structure caused by hot air channeling. Therefore, it was proposed that not only the steel structure material and design but also the performance and quality of the internal refractory material of the masonry should be paid attention so as to ensure the air tightness. Only by combining these two aspects can the service life of bellows be effectively improved.

Keywords Hot blast system · Bellows · Lose efficacy · Air tightness

Introduction

Bellows are widely used in pipelines of iron and steel enterprises to compensate for displacement and deformation of pipes [1–4]. In recent years, high-temperature spot, air leakage, and even burn out accidents occurred frequently in bellows in hot blast systems in the metallurgy industry. In addition, the smelting intensity of blast furnace is getting higher and higher, and the requirements for the temperature and stability of air supply are more and more strict, which poses a greater challenge to the stability and safety of hot air pipe system [5, 6]. However, high-temperature spot, air leakage, and even burn out accidents occurred frequently in bellows in hot blast

J. Wu (✉) · H. Chen · J. Sun · H. Liang
Institute of Ironmaking and Steelmaking Technology, Research Institute of Technology, Shougang Group Corporation, Beijing 100043, China
e-mail: jianlong231@163.com

Beijing Key Laboratory of Green Recyclable Process for Iron and Steel Production Technology, Beijing 100043, China

J. Li et al., *Characterization of Minerals, Metals, and Materials 2021*,
The Minerals, Metals & Materials Series,
https://doi.org/10.1007/978-3-030-65493-1_41

system in the metallurgy industry. It has little effect though coating, grouting, and other treatment methods have been adopted, which seriously affected the stability of hot blast system and brought hidden danger to safety production [7–10].

Xue and Cheng [11] analyzed the failure of metal bellows compensator for blast furnace gas pipeline, and pointed out that stress corrosion was the main reason for the failure of bellows compensator. Liang et al. [12] made metallographic analysis on bellows of hot blast stove, and concluded that structural design and welding quality were the main reasons for the failure of bellows steel structure of hot blast stove. In the application of corrugated pipe in iron and steel enterprises, especially in hot air pipe system, the combination of external steel structure and internal refractory was often used. Therefore, when analyzing the failure of bellows, the steel structure and refractory should be considered as a whole structure, which would be more practical. However, the failure analysis of bellows was mainly focused on the metal shell, while the internal refractory was ignored.

Working Condition of Bellows

The bellows studied in this paper had been used in hot air pipe system of an iron and steel enterprise. The main reasons of bellows failure was the loss of compensation function, and there were several high-temperature spots higher than 300 °C on the metal outer surface. Once grouting treatment was adopted in some areas, but the effect was not ideal.

In order to find out the main causes of high-temperature spot and waveform failure of bellows, the metal materials and refractories of the bellows were dissected and analyzed from the surface to the inside. The bellows to be studied was located on the branch pipe connected between the hot blast stove and the hot air main pipe. The gas composition in the pipe was N_2 and O_2, and the content of oxygen was about 25.5%. The gas temperature in the pipeline was about 1300–1400 °C, and the working pressure was 0.55 MPa. The main pipe material was Q_{235} steel, and the bellows was a double-layer structure (the inner layer material was Incoloy825 alloy, and the outer layer material was 316L austenitic stainless steel). The inner wall of the pipe was covered with refractory bricks and from the outside to the inside was clay brick, high alumina brick, and alusite brick in turn.

As shown in Fig. 1, the removed bellows had a complete steel structure and layered refractory. There were small cracks in the carbon steel part connected with the corrugated compensator, and there were obvious grouting repair welding spots on the steel structure near the hot surface (Fig. 1a); there were ring joints and through joints between the three ring refractory bricks built in the corrugated pipe (Fig. 1b); the alusite bricks in the inner ring of the bellows were seriously cracked and holes were formed (Fig. 1c).

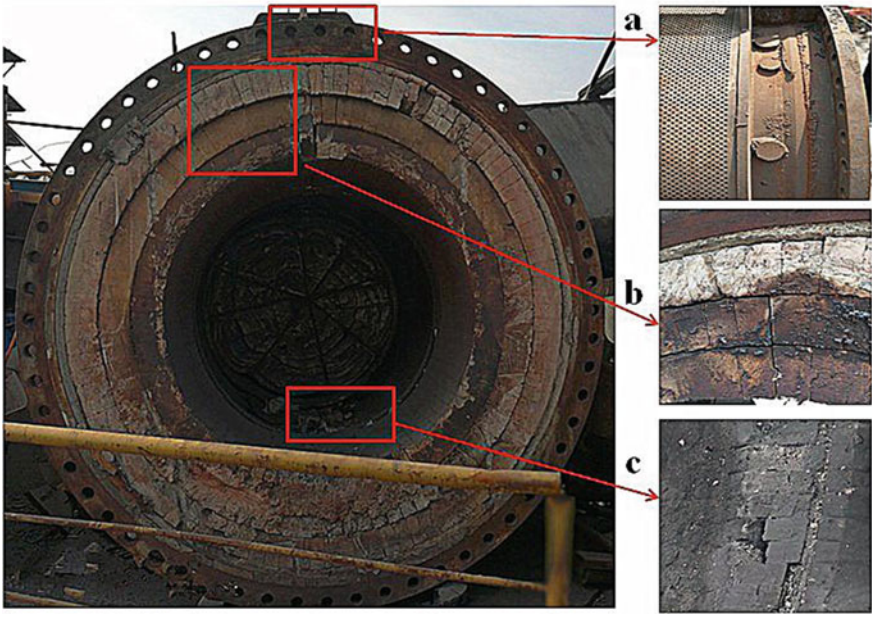

Fig. 1 Bellows and its appearance. (Color figure online)

Dissection and Analysis of Bellows

The upper steel shell was removed first, and then the refractory inside the bellows was removed. Considering that the inner refractory arch structure of bellows had good anti-collapse performance, the corrugated pipe was divided into upper and lower parts according to the horizontal axis.

Dissection Process and Analysis of Bellows

After cutting, the metal shell of the upper half ring of the bellows was lifted out (Fig. 2a). The hoisting process was stable, and the internal masonry refractory had no collapse. The internal spray coating of the upper half of the bellows was relatively complete, and the color of the coating on the hot side was darkened due to over fire, while the coating on the other parts was still the original color (Fig. 2b). When the corrugated pipe waveform was separated from the main steel structure, it could be seen that the internal part of the buffer wave was obviously blackened, which indicated that there was high temperature hot air passing through here, and the overall waveform had no obvious cracking damage phenomenon (Fig. 2c). After the wave shape was removed, the mixture of corrugated fiber felt and mud remains on the main

Fig. 2 Disassembly diagram of the upper steel structure of the bellows. (Color figure online)

steel structure and solidifies into a hard block (Fig. 2d), which was the main reason for the weakening or failure of expansion and contraction of bellows.

As shown in Fig. 3, it was the first light clay brick layer. There were large cracks in the light clay brick layer at the position of the brick retaining ring on the hot surface (the maximum crack size was 110 mm). And there was a certain amount of slurry in the cracks, as shown in Fig. 3a. The brick retaining ring was a steel baffle (as shown in Fig. 2b) protruding inward from the metal main structure of the bellows. The purpose of the installation was to prevent the firebrick from sliding axially in the bellows so that the steel structure of the bellows and the refractory material become an independent whole, which was convenient for disassembly and installation. However, judging from the brick type under the dismantling of the retaining ring (as shown in Fig. 3b), the brick length was 230 mm, while the narrow edge of the groove is only 44 mm, which was less than 20% of the total length of the brick body, and the strength was poor. Therefore, it was considered that the position of the retaining

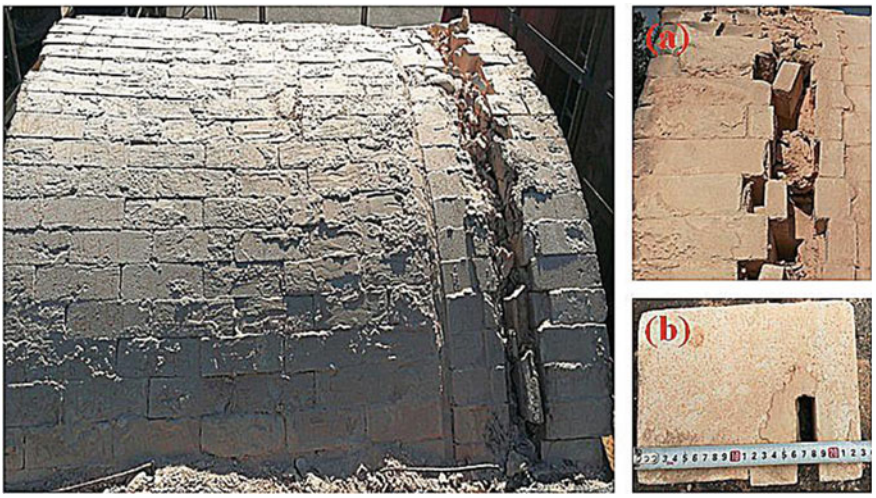

Fig. 3 First ring of clay brick layer. (Color figure online)

ring was easy to fracture due to the unreasonable setting of refractory structure, and the mud entering into the crack was further deteriorated due to the grouting. After the removal of the light clay brick, the second ring of light high alumina brick layer appears ring joint. The maximum gap was 18 mm, which was also located at the retaining ring. There was no obvious crack in the brick layer of the red column of the third ring road.

Through the analysis of the upper part of the bellows, it was found that the inner part of the bellows was filled with hard lumps formed by the solidification of fiber felt and mud, which was the main reason for the weakening or failure of bellows expansion, and these mud were mainly from grouting slurry; on the other hand, the unreasonable structure of refractory brick at the retaining ring was easy to fracture and produce cracks, and the external grouting operation resulted in cracks. The mud entered the fracture and further deteriorated, forming a large fracture with a width of 110 mm.

Through the dissection of the refractory material at the lower part of the bellows, it was found that serious over sintering occurred within the range of 1 m from the lower part of the bellows, forming a smooth ceramic layer with a thickness of about 15 mm (Fig. 4a). It indicated that there was a long period of high temperature wind passing through here. The inner layer of alusite brick was seriously cracked and broken, forming a hole, which was connected with the expansion joint (Fig. 4b), resulting in heat. The wind enters the expansion joint directly through the alusite brick layer.

The internal hot air channeling schematic diagram of the corrugated pipe refractory material (Fig. 5) was sorted out according to the anatomical results of the upper and lower parts of the bellows. Because the alusite brick at the bottom of the bellows was broken and formed a hole connecting with the expansion joint, the high-temperature hot air enters into the expansion joint through the hole, and then it enters the gap between the alumina brick layer and the light high alumina brick

Fig. 4 Refractory material in the lower part of the bellows. (Color figure online)

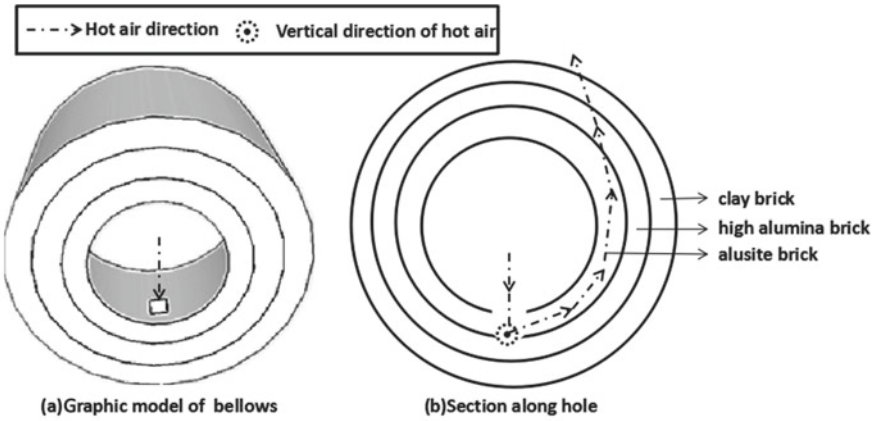

Fig. 5 Schematic diagram of the air leakage channel inside the bellows refractory

layer through the expansion joint. The hot air was divided into two parts: one hot air reached the end face of the corrugated pipe along the gap between the alusite brick layer and the light high aluminum brick layer; whereas another hot air flowed along the alusite brick layer gap between the pillared brick layer and the lightweight high alumina brick layer and reached the upper part of the corrugated pipe, and then passed through the gap between the high alumina brick layer and the clay brick layer to reach the outer steel structure.

Sampling and Analysis of the Bellows

Steel Analysis

After ultrasonic cleaning, microcracks were found in the carbon steel parts connected to the corrugated compensator. Metallographic analysis was carried out for the position containing cracks, and the metallographic photographs were shown in Fig. 6. The black part in the figure was slag inclusion, which was mainly the slag left in the weld during welding, which was one of the causes of crack formation. Although the crack did not penetrate into the inner surface of the steel structure, it was still a big hidden danger, which reflected that the welding quality defect was one of the reasons for the failure of bellows steel structure.

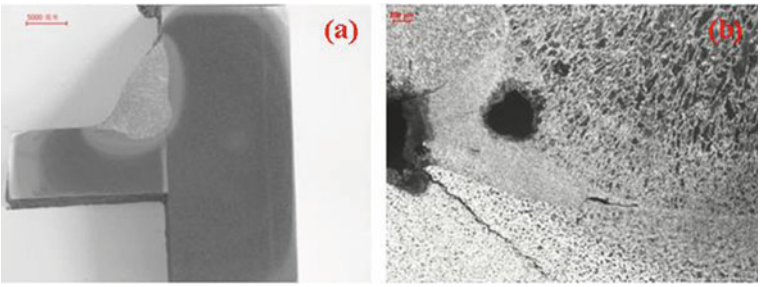

Fig. 6 Metallographic analysis of cracks in the bellows steel. (Color figure online)

Table 1 Component analysis of the bellows refractory bricks (wt.%)

Refractory type	SiO_2	Al_2O_3	Fe_2O_3	CaO	TiO_2	K_2O	Na_2O	S
Clay brick	48.49	44.70	1.49	0.75	1.51	1.57	0.28	0.030
High alumina brick	47.30	46.04	1.48	0.72	1.53	1.66	0.22	0.007
Alusite brick	36.72	60.06	1.14	0.26	0.44	0.26	0.31	0.007

Refractory Analysis

The composition analysis and fire resistance performance test were carried out for the complete refractory brick taken from the disassembly. The composition analysis was shown in Table 1. According to the purchasing standard, the alkali content of light clay brick exceeded the standard (alkali $\leq$ 1.5%), and the other components met the standard; the alumina content of light high alumina brick was lower than the standard ($Al_2O_3 \geq 55\%$), and the contents of Fe_2O_3, TiO_2, and alkali exceeded the standard ($Fe_2O_3TiO_2 \leq 1\%$, alkali $\leq$ 1.5%); the chemical index of andalusite brick met the standard.

According to the physical and chemical standards, the fire resistance of light clay brick, light high alumina brick, and alusite brick were tested. The results were shown in Table 2. The bulk density of the used lightweight clay brick and light high alumina brick was slightly higher, and the compressive strength of the used alusite brick was lower than that of the standard by 26%.

Table 2 Physicochemical indices of refractory bricks

Inspection items	Clay brick	High alumina brick	Alusite brick
Cold crushing strength N/mm^2	1.99 (standard >1)	3.26 (standard >2)	29.6 (standard >40)
Volume density kg/m^3	858 (standard <700)	1015 (standard <975)	2476 (standard >2400)
Apparent porosity (%)	60 (standard)	53.4 (no standard)	14.6 (standard <20)

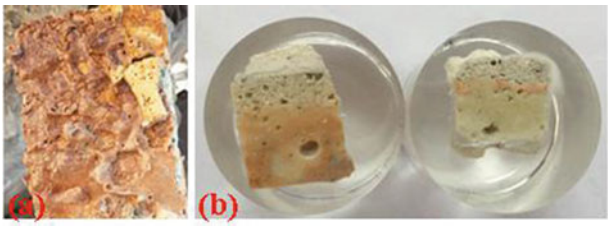

Fig. 7 Sintering between andalusite bricks and high alumina bricks. (Color figure online)

Table 3 Component analysis of sintering between andalusite bricks and high alumina bricks (%)

	SiO_2	Al_2O_3	Fe_2O_3	CaO	MgO	K_2O	Na_2O	S	ZrO_2
Sintering between bricks	53.38	33.70	1.64	0.94	0.48	4.24	3.73	0.042	0.12

It should be noted that the chemical composition of the brick would be changed due to the pollution after use, and the measured results could not be used as the basis for judging whether the brick was qualified or not. However, from the serious cracking situation of the alusite brick, if the nonoriginal alusite brick had a low normal temperature compressive strength, it was necessary to appropriately improve the application standard.

The melting materials between lightweight high alumina brick and andalusite brick were sampled and analyzed, as shown in Fig. 7. The melting temperature was 1371 °C, the softening temperature was 1298 °C, and the flow temperature was 1503 °C. It was estimated from the melting point and softening temperature that the melting temperature was at least 1200 °C.

The chemical composition of sintering between andalusite bricks and high alumina bricks was shown in Table 3. From the view of chemical composition, SiO_2 and Al_2O_3 should come from refractories, but the high contents of Fe_2O_3, K_2O, and Na_2O do not belong to refractories. Therefore, it could be concluded that the molten material was the reaction product of K and Na brought by the hot air of hot blast stove and the fireclay of brick and masonry brick.

On the one hand, the external steel shell of corrugated pipe had cracks due to welding, so the construction quality needed to be strengthened. On the other hand, the normal temperature compressive strength of the alusite brick, one of the refractory materials in the bellows, was lower than 26% of the standard. Hence, it was necessary to increase the compressive strength. According to the composition and characteristics of the melt, it was speculated that there should be a long-term hot wind passing through the area.

Conclusion

(1) Although the welding quality defects of corrugated pipe steel structure had cracking hidden danger, the main reason for the failure of bellows was the poor quality of refractory materials in bellows and the formation of hot air channel. This led to the local high temperature of the corrugated pipe steel structure, and the improper treatment measures led to the formation of a large amount of mud mixture in the corrugated pipe waveform, which made the expansion and contraction function of the bellows invalid.
(2) The structure and performance of refractories needed to be optimized, including that the unreasonable structure of light clay brick at the position of retaining ring, and the normal temperature compressive strength of used andalusite bricks was lower than 26% of the standard.
(3) The bellows of hot air pipe system was the community of steel structure and refractory material. Not only the steel structure material and design should be paid attention to but also the performance and quality of the internal refractory material of the masonry should be paid attention to so as to ensure the air tightness. Only by combining these two aspects could the service life of bellows be effectively improved.

Acknowledgements This study was supported by National Key R&D Program of China (2017YFB0304000).

References

1. Li H-m (1992) Application of corrugated compensator and tie rod in hot air pipeline system. Ironmaking (5):37–40
2. Luo L, Lu J-w, Mi L,Wang W (2014) The application of ripple compensator in angang 3 # blast furnace. Gansu Metall 36(5):105–109
3. Zhang X-p (1992) Application of metal bellows and bellows compensator in thermal pipe system of blast furnace. J KunMing Inst Technol 17(6):92–98
4. Cao W, Chen S-k (2018) Design features and practice operation of hot stove revamping for NO. 1 blast furnace in Ning Steel. China Metall 28(12):45–48
5. Chen G-j, Zhao M-g (2009) Technology progress on high blast temperature of BF stove in Shougang group. China Metall 19(9):18–24
6. Zhang F-m (2013) Developing prospects on high temperature and low fuel ration technologies for blast furnace ironmaking. China Metall 23(2):1–7
7. Qin Z-q, Zhang H-b (2017) Analysis and treatment on the corrosion cracking of bellows compensator in hot blast stove of No. 5 BF. LiuGang Technol 3:27–30
8. Xie D-y, Peng Y-t (2013) Application practice of quick-drying pouring material in integral pouring of hot blast main in large-sized blast furnace. Ind Furn 35(2):52–55
9. Chen H, Ma Z-j, Sun J (2015) Investigation on cracking causes of hot blast pipe system in large blast furnace. In: The 10th China Iron and steel annual meeting. The Chinese Society for Metals, Shanghai, pp 1–6

10. Wan N (2012) Treatment of burning through accident of mixing chamber in hot blast stove of No. 7 BF of Nangang. Ironmaking 31(6):54–59
11. Xue H-b, Cheng S-w (2012) Failure analysis and treatment of metal bellows compensator for blast furnace gas pipeline. J Zhejiang Metall (2):58–63
12. Liang H-l, Ma Z-j, Sun J (2017) Discussion on failure causes of bellows steel structure of hot blast stove. In: 2017 national annual meeting of blast furnace ironmaking. Ironmaking branch of CSM, Kunming, pp 668–671

Flotation Behaviors of Magnesite and Dolomite Using a Mixed Collector

Wencui Chai, Yankun Wu, Huaxia Li, and Yijun Cao

Abstract Magnesite and its main associated mineral dolomite are with a small floatability difference because of similar crystal structure and surface properties, which results in low flotation recovery of magnesite from dolomite. In order to solve the problem, a new mixed collector of sodium oleate (NaOL) for magnesite was proposed in this paper. The effects of flotation behaviors of magnesite and dolomite were investigated by flotation experiments, and the mineral wettability was characterized by contact angle testing. The results show that the mixed collector could greatly reduce the hydrophobicity of dolomite and improve the floatability difference between magnesite and dolomite. The Gaudin's selectivity index of two minerals increased from 1.75 to 3.78.

Keywords Magnesite · Dolomite · Collector · Flotation behaviors

Introduction

Magnesite ($MgCO_3$) is a kind of carbonate mineral and is the main source of magnesium, which has been widely used in metallurgical, chemical, agriculture, construction, and other fields [1]. However, the natural magnesite ore often co-exists with dolomite ($MgCa(CO_3)_2$), another carbonate mineral. Therefore, it is necessary to separate the calcium-containing impurity mineral before the calcination of magnesite to produce qualified magnesium oxide.

Froth flotation is a kind of mineral separation method based on the differences in physicochemical properties, especially wettability between the minerals, and has been proved to be an effective method to separate magnesite and dolomite [2].

W. Chai · Y. Cao (✉)
Henan Province Industrial Technology Research Institute of Resources and Materials, Zhengzhou University, Zhengzhou 450001, Henan, China
e-mail: yijuncao@126.com

Y. Wu · H. Li · Y. Cao
School of Chemical Engineering, Zhengzhou University, Zhengzhou 450001, Henan, China

J. Li et al., *Characterization of Minerals, Metals, and Materials 2021*,
The Minerals, Metals & Materials Series,
https://doi.org/10.1007/978-3-030-65493-1_42

However, the similar crystal structure of magnesite and dolomite increases the difficulty of separation [3, 4]. To achieve more effective separation, several flotation reagents need to be added to the flotation systems to increase the wettability differences between valuable and associated minerals. To separate magnesite and dolomite effectively, a series of novel surfactants have been reportedly used as the collectors, including anion collectors [5–7] (such as sodium oleate (NaOL) and alkane sulfonates) and cation collectors [8, 9] (quaternary ammoniums for example). In addition to the development of new reagents, mixed collectors have been utilized to improve the selectivity and flotation recovery for different kinds of minerals. Most mixed collectors are the combination of traditional collectors and have been proved to be an economical and effective means [10].

In this work, a mixed reagent of NaOL with a kind of amino acid DP was introduced and used as the mixed collector of magnesite. The chemical and mineralogical compositions were analyzed by X-ray fluorescence (XRF) and X-ray diffraction (XRD). The flotation behaviors of magnesite and dolomite with single or mixed collector were investigated through micro-flotation tests. The co-collection mechanisms were simply analyzed by contact angle and zeta potential testing.

Experiments

Materials

Magnesite and Dolomite

Two single minerals, magnesite and dolomite, used in this paper were collected from Liaoning province, China. The typical chemical and mineralogical compositions were determined by EDXRF and XRD technologies, and the results are shown in Table 1 and Fig. 1, respectively.

As can be observed from Table 1, the content of MgO in magnesite is 54.65%, and the contents of MgO and CaO in dolomite are 20.35% and 32.48%, respectively. The chemical analysis results confirm that the purities of the dolomite and magnesite samples are 92.36% and 93.61%, respectively, which meet the desired requirement for single minerals. As shown in Fig. 1, the magnesite sample has little dolomite mineral impurity, and the dolomite sample has almost no impurities.

Table 1 Typical chemical compositions of magnesite and dolomite samples by EDXRF, wt.%

Composition	MgO	CaO	SiO_2	Fe_2O_3
Magnesite	43.98	1.35	1.75	0.25
Dolomite	20.35	32.48	2.08	0.38

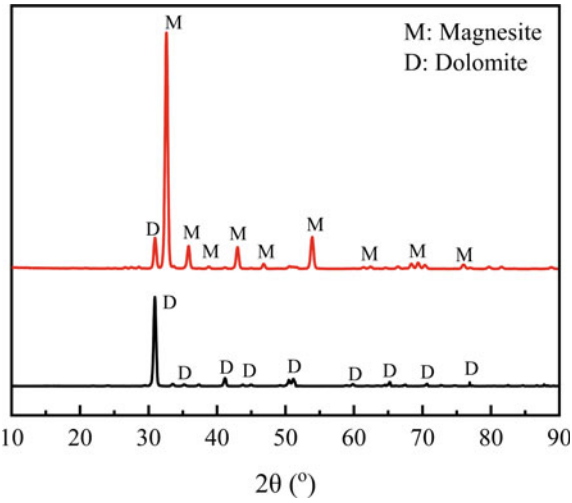

Fig. 1 XRD spectra of magnesite and dolomite samples. (Color figure online)

Chemicals

Unless specifically noted, all chemicals used in the experiments were analytical purity reagents. Sodium oleate (NaOL) and a kind of amino acid (DP) from Aladdin Biochemical Technologies Co., Ltd. (Shanghai, China) were respectively used as the collector and the auxiliary collector. Hydrochloric acid (HCl) and sodium hydroxide (NaOH) were used as pH regulators of the flotation system. Deionized (DI) water with a specific resistance 18.25 MΩ cm was used in all experiments.

Micro-flotation Tests

The micro-flotation tests of magnesite and dolomite were carried out in an XFG II type flotation cell with a 40 mL detachable cell and a stirring speed of 1600 rpm. The flotation slurry was prepared by adding a single mineral (2 g) with a particle size of 37–74 μm into 30 mL DI water in the flotation cell and then stirred for 1 min to achieve an even mix. The different reagents were then sequentially added to the suspension according to the flowsheet in Fig. 2, and the collector dosage was fixed as 60 mg/L. Followed by scraping, filtering, drying, and weighing, concentrate and tailing were collected separately. The typical flowsheet is shown in Fig. 2. The mineral recovery (R) and the selection index (SI) of the two minerals were calculated, respectively, by the Eqs. (1) and (2) as follows.

$$\mathrm{R} = \frac{m_1}{m_1 + m_2} \tag{1}$$

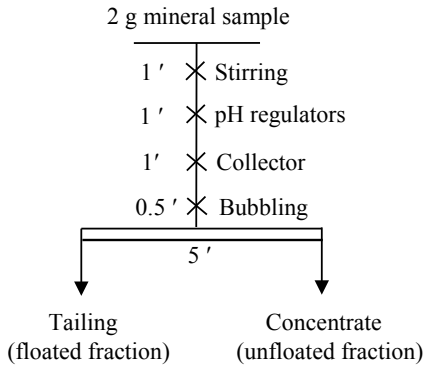

Fig. 2 Flowsheet of single mineral flotation tests

where m_1 and m_2, respectively, represent the mass of the concentrate and the tailing.

$$\mathrm{SI} = \sqrt{\frac{R_1 \times (100 - R_2)}{(100 - R_1) \times R_2}} \tag{2}$$

where R_1 and R_2 represent the flotation recovery of magnesite and dolomite, respectively.

Results and Discussion

Effect of Pulp pH on Flotation Recovery with Single Collector

Pulp pH could have a significant influence on the surface properties and floatability of minerals [11, 12]. Herein, the effect of pulp pH on the flotation recovery of magnesite and dolomite was investigated by using the single collector NaOL. The pH range is alkaline, which is conducive to the flotation of magnesite. The results are shown in Fig. 3.

As observed from Fig. 3, the flotation recovery of magnesite increases first and then decreases with increasing pulp pH from 8 to 12. The flotation recovery reaches maximum at pH 10 as 65% and gets the minimum at pH 12 as 10%. For dolomite, the flotation recovery has a different trend, and reaches the maximum value 75% at pH 12. At this condition, the maximum flotation differences of two minerals were obtained, and the Gaudin's selectivity index (SI) is 0.33, beneficial to reverse flotation. However, the second-best flotation difference was obtained at the condition of pH 10, at which the selectivity index is 1.75, suitable for positive flotation.

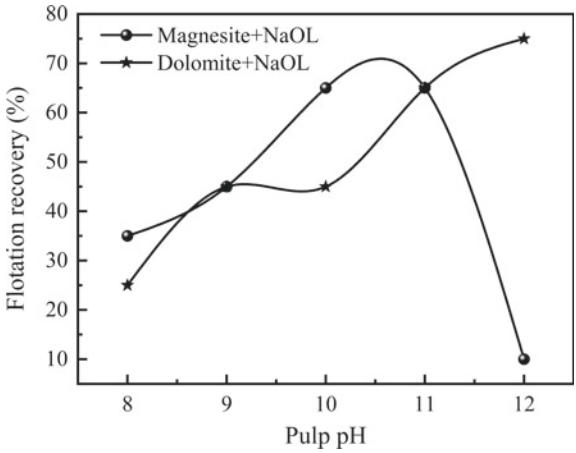

Fig. 3 Effect of pulp pH on flotation recovery with single collector

Effect of Pulp pH on Flotation Recovery with Mixed Collector

In order to explore the strategies improving the flotation differences of magnesite and dolomite at moderately alkaline conditions, a natural amino acid DP was used as the auxiliary collector of NaOL. Also, the effect of pulp pH on the flotation recovery of magnesite and dolomite was investigated using the mixed collector. The dosage ratio of NaOL and DP is 1:1. The results are shown in Fig. 4.

As shown in Fig. 4, compared with the single collector of NaOL, the flotation recovery of magnesite with the mixed collector NaOL-DP improves 10–40% at the specified pH range, except for the condition of pH 11 declining 5%. The maximum recovery of 85% for magnesite was obtained at pH 10, and the selectivity index of two minerals was 3.78. The flotation recovery of dolomite using the mixed collector

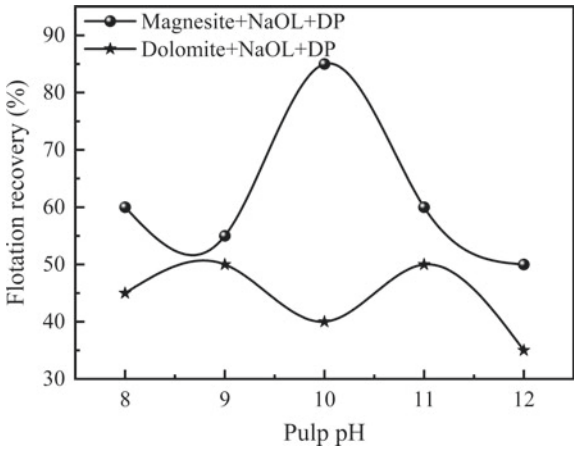

Fig. 4 Effect of pulp pH on flotation recovery with mixed collector

also increased at pH 8–9, but decreased at strong alkali environment. Therefore, the optimal pulp pH of flotation separation of magnesite and dolomite is 10.

Effect of pH on Contact Angle of Two Minerals

To explore the interaction mechanisms of the mixed collector, the contact angle of two single minerals was analyzed before and after treated with NaOL or NaOL-DP, and the results are shown in Fig. 5.

As illustrated in Fig. 5, the contact angles of the raw magnesite and dolomite are similar and is around 20°, which is the main reason for the difficult separation of them. After treated by the collectors, the contact angles of the two minerals increased first and then decreased with the increase of pH solution. The maximum value of magnesite treated with NaOL is about 71° and NaOL+DP 68° at pH 10, and that of dolomite is about 32° and 23° at pH 11, respectively. Whether treated with the single collector NaOL or the mixed collector NaOL+D, the contact angles of both the minerals improved. That is to say, the collectors could increase the hydrophobicity of the two minerals. However, the hydrophobicity of magnesite is higher than that of dolomite, indicating that collector adsorbed more on the magnesite than dolomite. Compared to the single collector NaOL, after treated with the mixed collector NaOL+DP, the contact angles of magnesite slightly decreased while that of dolomite decreased greatly. These results declare that the auxiliary collector DP could largely weaken the hydrophobicity of dolomite treated with NaOL and increase the wettability difference between magnesite and dolomite, which is the benefit to improve the flotation recovery of magnesite against dolomite.

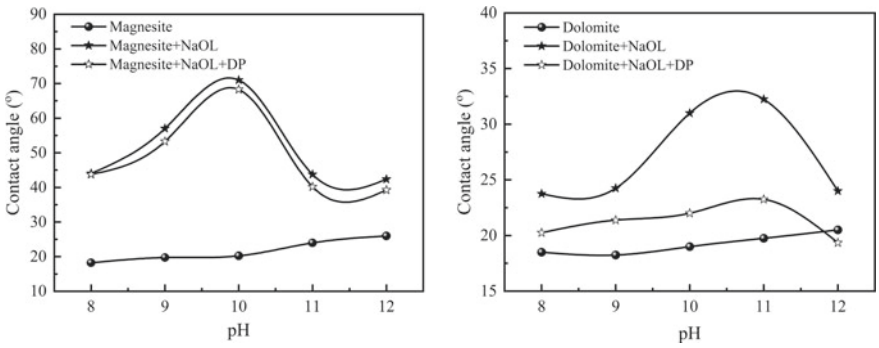

Fig. 5 Effect of pH on contact angle of magnesite (left) and dolomite (right)

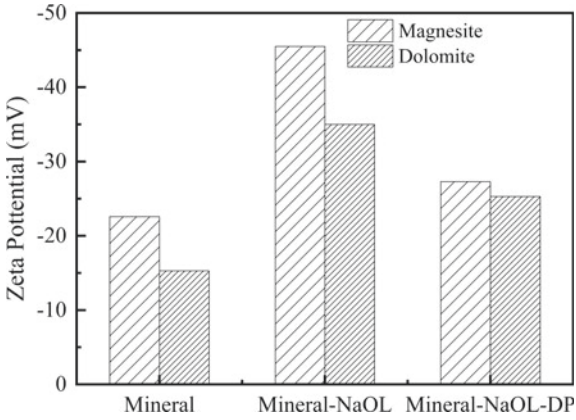

Fig. 6 Effect of pH on zeta potential of two minerals

Effect of pH on Zeta Potential of Two Minerals

Since zeta potential could state the electrical property of the mineral particle surface and its interactions with the surrounding medium, it is significant to study the zeta potential of the two mineral particles before and after treated with the single or mixed collectors. The zeta potential results of the magnesite than dolomite particles at pH 10 are shown in Fig. 6.

Obviously, it can be observed from Fig. 6 that the zeta potential of magnesite and dolomite particles are both negatively charged for the solution with pH 10, and dolomite is with more negative charge than magnesite. After treated with the collectors, the zeta potentials of the two minerals are more negative, indicating that the collectors interacted with the two minerals through chemical adsorption. It is worth noting that the zeta potentials of the two minerals treated with the mixed collector NaOL-DP are less negative than that treated with single collector NaOL. These results declare that another adsorption mechanism of NaOL-DP with the two minerals is electrostatic interaction, since the auxiliary collector DP is an amphoteric reagent.

Conclusions

The flotation behaviors of magnesite and dolomite under different pulp pH using the single collector NaOL and the mixed collector NaOL-DP were investigated through micro-flotation tests. The optimum pulp pH is 10 whether using the single collector or the mixed collector. Under the optimum conditions, the flotation recovery of magnesite and dolomite is 85% and 40%, respectively, and the Gaudin's selectivity index of the two minerals is 3.78, higher than the condition using the single collector. The contact angle analysis results show that the hydrophobicity of dolomite treated with the mixed collector NaOL-DP is greatly lower than that treated with the single

collector NaOL. The mixed collector could improve the hydrophobicity difference and floatability difference of the two minerals, which is beneficial to the flotation separation of magnesite and dolomite. The mixed collector NaOL-DP interacted with the two minerals through chemical and electrostatic adsorptions.

Acknowledgements The authors acknowledge the financial support of the National Natural Science Foundation of China (Nos. 52004249 and U1704252), Open Foundation of Provincial and Ministerial Co-construction of Collaborative Innovation Center for Resource Materials (No. zycl202003), and Program for Innovative Research Team (in Science and Technology) in University of Henan Province (IRTSTHN) (No. 19IRTSTHN028).

References

1. Pagona E, Tzamos E, Grieco G, Zouboulis A, Mitrakas M (2020) Characterization and evaluation of magnesite ore mining by-products of Gerakini mines (Chalkidiki, N. Greece). Sci Total Environ 732:139279
2. Santana AN, Peres AEC (2001) Reverse magnesite flotation. Miner Eng 14:107–111
3. Gence N (2006) Wetting behavior of magnesite and dolomite surfaces. Appl Surf Sci 252:3744–3750
4. Chen G, Tao D (2004) Effect of solution chemistry on flotability of magnesite and dolomite. Int J Miner Process 74:343–357
5. Chen G, Tao D (2005) Reverse flotation of magnesite by dodecyl phosphate from dolomite in the presence of sodium silicate. Sep Sci Technol 39:377–390
6. Tang Y, Yin W, Kelebek S (2020) Magnesite-dolomite separation using potassium cetyl phosphate as a novel flotation collector and related surface chemistry. Appl Surf Sci 508:145191
7. Zhu Z, Wang D, Yang B, Yin W, Ardakani MS, Yao J et al (2020) Effect of nano-sized roughness on the flotation of magnesite particles and particle-bubble interactions. Miner Eng 151:106340
8. Liu W, Liu W, Zhao B, Zhao L, Li D, Fang P et al (2019) Novel insights into the adsorption mechanism of the isopropanol amine collector on magnesite ore: a combined experimental and theoretical computational study. Powder Technol 343:366–374
9. Liu W, Liu W, Wang B, Zhao Q, Duan H, Chen X (2019) Molecular-level insights into the adsorption of a hydroxy-containing tertiary amine collector on the surface of magnesite ore. Powder Technol 355:700–707
10. Jin Y, Haoran S, Bin Y, You Z, Wanzhong Y, Zhanglei Z (2020) Selective co-adsorption of a novel mixed collector onto magnesite surface to improve the flotation separation of magnesite from dolomite. Powder Technol, 371
11. Gence N, Ozbay N (2006) pH dependence of electrokinetic behavior of dolomite and magnesite in aqueous electrolyte solutions. Appl Surf Sci 252:8057–8061
12. Yao J, Sun H, Han F, Yin W, Hong J, Wang Y et al (2020) Enhancing selectivity of modifier on magnesite and dolomite surfaces by pH control. Powder Technol 362:698–706

Incorporation of Porcelain Powder and Mineral Wastes in Epoxy Matrix for Artificial Stone Purchase

Elaine A. S. Carvalho, Vitor da Silva de Souza, Gabriela N. S. Barreto, Sergio N. Monteiro, Rubén J. S. Rodriguez, and Carlos Maurício F. Vieira

Abstract Industrial waste incorporation in artificial stone production has been widely used nowadays, both in search of alternative raw materials as well as for seeking an environmentally correct destination for the waste. During ornamental stones processing, material losses are significant, generating wastes that are often inappropriately disposed of in nature. Quartzite is classified geologically as a metamorphic stone, composed almost entirely of quartz grains and porcelain powder and is characterized by a dense microstructure, consisting of mullite and quartz crystalline phases. The main aim of this work is to characterize and evaluate the effects of incorporating quartzite, quartz, and porcelain powder wastes in an epoxy matrix for artificial stone development. Plates were produced by the vacuum vibrocompression method, already adopted by companies in this field. The highest density mixture was calculated, and the artificial stone developed was characterized to evaluate its physical and mechanical properties. The two most close-packed mixtures were used to produce the plates. The absorption values obtained for the two compositions suggested the artificial stone can be used in external environments, tops, and floating/raised floors, due to the water absorption index $\leq 0.4\%$. The composition in which the porcelain powder was incorporated obtained maximum bending stress of 25 MPa, classifying the artificial stone as high quality to be applied as a coating.

Keywords Artificial stone · Fluorescent lamps · Vacuum · Epoxy resin

E. A. S. Carvalho (✉) · V. da S. de Souza · G. N. S. Barreto · R. J. S. Rodriguez · C. M. F. Vieira
Advanced Materials Laboratory–LAMAV, State University of the Northern Rio de Janeiro-UENF, Av. Alberto Lamego, 2000, Campos dos Goytacazes 28013-602, Brazil

V. da S. de Souza
e-mail: elainesanttos@yahoo.com.br

S. N. Monteiro
Materials Science Department, Military Institute of Engineering-IME, Praça General Tibúrcio, 80, Urca, Rio de Janeiro, RJ 22290-270, Brazil

J. Li et al., *Characterization of Minerals, Metals, and Materials 2021*,
The Minerals, Metals & Materials Series,
https://doi.org/10.1007/978-3-030-65493-1_43

Introduction

Considered as one of the most used products in contemporary architecture, porcelain tile, a type of white ceramic coating, began to gain prominence in Brazil in the early 1990s, influenced by its country of origin, Italy. Its high technical quality enabled a diverse range of applications, although it was initially used for paving. The polishing step of porcelain tiles production aims to remove risks and defects and also to level the surface and shine. Unfortunately, it generates large amounts of waste, and with the recent production increase, the amount of waste is increasing. The need to properly manage and dispose of this waste leads to a new cost to sector producers [1].

All discarded material produced during the manufacturing process is considered waste, which, in most cases, is not reused. Porcelain waste is a material made up of a mixture of abrasive material and porcelain ceramic material, usually made of diamond particles or silicon carbide, agglomerated by cements based on magnesian chlorides [2].

The industrial wastes' inappropriate disposal may cause a lot of environmental problems, such as soil and groundwater contamination and local vegetation damage, in addition to the financial loss caused by fines high costs. To mitigate these impacts, reuse and recycling are the most suitable solutions for the management of the vast majority of industrial wastes, including porcelain polishing waste, enabling cost reduction, preserving non-renewable natural resources, reducing the load of pollutants released into the environment, as well as harmful effects to human health [3–5].

Quartzite contains a high content of quartz (SiO_2) and is considered to be resistant, having properties typical of commercial granites and being classified as metamorphic silicatic ornamental stones. They have a granoblastic texture, are essentially made of quartz, differing due to the degree of recrystallization and granulation [6, 7]. Ornamental quartzite wastes generally come from the diamond blades cutting process, and it is estimated that during the sawing process, 25–30% w of the block becomes waste. Therefore, even though it is an important economic activity, it generates significant amounts of waste that can be harmful to the environment when inappropriately disposed of [8, 9]. It is estimated that more than 5 million tons of coarse wastes and more than 300,000 tons of processing fines wastes are produced per year in quarries in Brazil [9].

An interesting recovering option for this material is adding the wastes in a production cycle, which is interesting in both the environmental and economic aspects. The use of mineral waste for the compacted artificial stone development shows numerous advantages compared to natural stones in technical characteristics, such as reducing the amount of waste to be discarded in nature, adding value to an undesirable waste, and also allowing the generation of a new employability cycle [10].

The possibility of using artificial stone instead of natural stone is based on technical advantages, such as the polymeric matrix lower density (± 1 g/cm^3) that makes it

lighter compared to natural stone (± 2 g/cm^3). The high porosity and the microstructural defects of natural ornamental stones facilitate their contamination by external fluids and the easy propagation of cracks, causing brittle fractures [11–13].

Research on the artificial stone's development has been carried out with various waste types (marble, steel, gravel powder, chamotte) [11, 12, 14] and also research using porcelain powder and quartzite wastes in the incorporation into red ceramics and in the development of silicate glasses [15, 16].

This project's main goal is to produce compacted artificial stones using waste from porcelain tiles cutting as main source, combined with quartz and quartzite in an epoxy matrix through the vacuum, vibration, and compression method that is used by companies for artificial stone's production for commercialization both in Brazil and abroad, by following the protocols and technical standards.

Materials and Methods

The powdered porcelain waste came from the porcelain tiles polishing process, carried out by a ceramic tile industry. The mineral residue (quartz and quartzite) was offered by the company EcologicStone, where this mineral is used for artificial coating manufacture, located in Cachoeiro de Itapemirim, Espírito Santo, Brazil. The waste particles were agglutinated by the epoxy matrix (MC130) of type diglycidyl ether bisphenol A (DGEBA) hardened by FD 139 triethylenetetramine (TETA), both supplied by EPOXYFIBER.

The waste was classified into three granulometric ranges: large (from 2 to 0.42 mm), medium (from 0.42 to 0.075 mm), and fine particles (with grains smaller than 0.075 mm). Large and medium particles were represented by the material provided by EcologicStone, and the porcelain powder was classified in the fine particles range. Based on these three granulometric classifications, ten distinct mixtures were proposed for most close-packed conditions using the simplex-lattice design (SLD) numerical modeling methodology (Fig. 1).

The determination of the most close-packed composition for the waste was associated with the highest dry apparent density. This density was obtained, based on the ABNT/NBR 3388 Brazilian standard [17], for the ten different compositions considered in the simplex method. For each composition, the test was made three times to assure statistical validation. Each sample was placed in a steel vessel and vibrated for 2 min under a 10 kg load. Then, the mixture was weighed, and the apparent density was calculated. The composition with the highest apparent density, associated with the most close-packed particles, was selected for the artificial stone's development.

The minimum amount of resin matrix [18] necessary to thoroughly wet all particles surface and fill in all interstitial voids that the mixture may still contain in a most close-packing aggregation of the filler particles was calculated.

To produce the artificial stone plates, the wastes were placed in an oven at 100 °C for moisture removal. Then, the wastes were weighed and mixed with epoxy resin and the hardener.

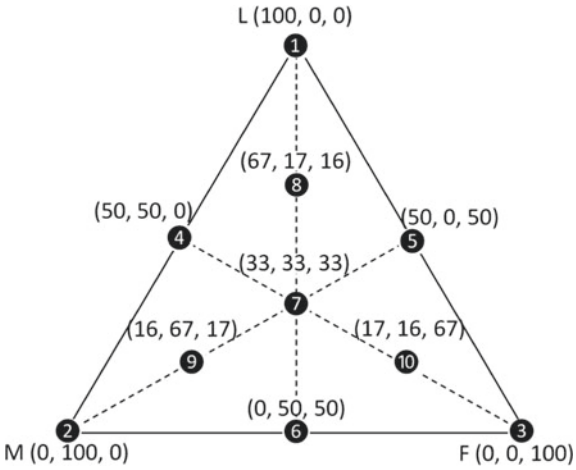

Fig. 1 Ternary diagram with the 10 mixtures based on the complete simplex cubic. Amounts (wt.%) of large (L), medium (M), and fine (F) particles (Carvalho et al. 14)

This mixture was poured into a metallic mold (100 × 100 × 10 mm), and vibrated for 2 min, while simultaneously it was put into a vacuum (600 mmHg); later, it was taken to a hydraulic press under a 10 ton pressure and 90 °C temperature, where it stayed for another 20 min. The plates produced were sanded and then cut to the specific dimensions for the realization of characterization tests.

Density, water absorption, and apparent porosity determination were based in Annex B of ABNT/NBR 15845 Brazilian standard [19], using ten cubic plate samples with 30 × 30 × 30 mm dimensions.

The three-point flexural strength test was performed on the INSTRON universal testing machine, model 5582. For these tests, the recommendations based on Annex F of ABNT/NBR 15845 Brazilian standard [17] and UNE-EN 14617 Spanish standard [18] were followed. Ten prismatic plates with 100 × 25 × 10 mm were used for each flexural test condition, and average stress and corresponding standard deviation were calculated.

Results and Discussion

Table 1 shows the values obtained by the SLD method for the vibrated density of the wastes, according to Fig. 1. The highest density values were obtained for mixtures 5 and 7. Mixture 5, with 50% of large particles (L) and 50% of medium particles (M), has 1.86 g/cm^3 density. The mixture 7 has 1.76 g/cm^3, the second-highest density, with 33.33% of large (L), medium (M), and fine (F) particles.

In Table 1 the mixtures 5 and 7 with the two highest values that were considered the most close-packed mixtures are highlighted. This is due to the fact that mixture 7 is made of two different waste types and may have been influenced by porcelain powder-fine particles. When compared to mixture 5, the lower density maybe, thanks

Table 1 The vibrated density of quartz wastes (coarse granulometry), quartzite (medium granulometry), and porcelain powder (fine granulometry)

Vibrated density (g/cm^3)	
Mixture	Average values
1	0.72 ± 0.03
2	1.75 ± 0.01
3	1.56 ± 0.01
4	1.41 ± 0.04
5	*1.86 ± 0.04*
6	1.43 ± 0.05
7	*1.76 ± 0.01*
8	1.75 ± 0.06
9	1.26 ± 0.01
10	1.74 ± 0.05

to the particle shapes and its infinity of possible combinations, making it difficult to predict the behavior of mixtures involving non-spherical particles. As the particles become non-spherical, there will be a density decrease [11]. In addition, vibration amplitude or frequency, when increased, raise density values and then cause them to decrease [21].

For the artificial stone's development, the combinations were RAQ (quartz and quartzite wastes) and RAP (quartz, quartzite, and porcelain powder wastes), with 18%w epoxy resin as binder, according to the two compositions minimum resin content calculations.

Table 2 presents the apparent density, water absorption, and apparent porosity values obtained in accordance with the Brazilian technical standard. The low density showed by the artificial stones was due to the epoxy matrix with 1.16 g/cm^3. RAQ (quartz and quartzite) density results were lower than RAP and the developed artificial stones (2.10–2.78 g/cm^3) [10, 13, 14, 22]. The RAQ particle adhesion to the epoxy matrix may have been ineffective, and quartz and quartzite particle morphology may have contributed to the decrease in density [22].

Lee et al. observed in their research that a compaction pressure increase, up to 14.7 MPa, was accompanied by increases in density and mechanical properties and a water absorption reduction. On the other hand, when using 19.6 MPa pressure, they observed a decrease in density values as well as in the mechanical properties, with a density variation between 2.03 and 2.45 g/cm^3, which may have happened with the RAQ stone.

Table 2 Physical properties of apparent density, water absorption, and apparent porosity of the RAQ and RAP artificial stones

Physical properties	RAQ	RAP
Density (g/cm^3)	1.84 ± 0.08	2.15 ± 0.03
Warter absorption (%)	0.39 ± 0.08	0.38 ± 0.07
Apparent porosity (%)	0.72 ± 0.12	0.80 ± 0.14

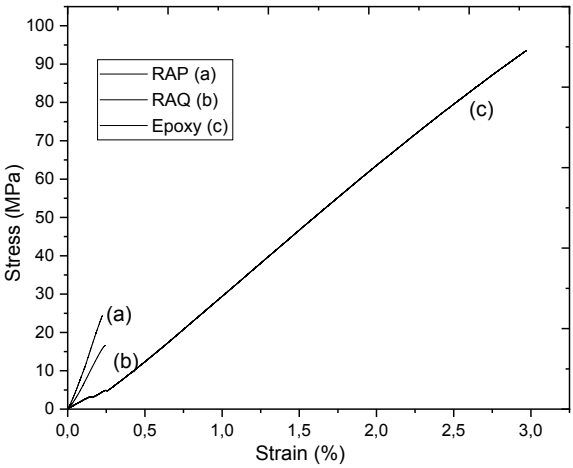

Fig. 2 Flexural rupture stress versus bend strain for artificial stones RAQ, RAP, and epoxy resin

Table 2 shows the water absorption values of 0.39 ± 0.08% (RAQ) and 0.38 ± 0.07% (RAP) that are within the values reported by artificial marble manufacturers in the range of 0.09–0.40% [22] and among those indicated by Chiodi and Rodriguez of 0.1–0.4%, considered a low water absorption material. Quartzite stones should have, preferably, a water absorption index ≤0.4% to be used in homeless outdoor environments, floating / elevated tops, and floors.

For apparent porosity, the values of 0.72 ± 0.12% RAQ and 0.80% RAP were found. Both RAQ and RAP can be, according to Chiodi and Rodriguez, coating materials, classified as low porosity materials, due to apparent porosity, between 0.5 and 1.0%.

Figure 2 shows RAQ 18% epoxy, RAP 18% epoxy, and epoxy resin flexural rupture stress versus bend strain graphs. It presented rupture stress values of 16.98 ± 1.05; 25.13 ± 3.69; and 93.59 ± 4.7 MPa, respectively.

The processed stones showed an elastic deformation, characterizing the material as fragile despite the more resistant structure when compared to the waste incorporation. The difference in the presented value of the developed artificial stones is due to the possible presence of diamond particles, other materials that are used in the lapidating process that improves hardness and resistance [2].

The epoxy resin stress (a) was highest because the chemical bonds of its structures are stronger, and it does not have aggregate grains in its composition, thus being able to equally distribute the forces throughout its body, causing greater deformation.

The decrease in the mechanical properties of RAQ compared to the RAP can also consider that the compaction pressure used was enough to cause a rupture in aggregate particles [18]. RAP, with the addition of porcelain powder, has smaller particle sizes, providing greater mechanical strength since it allows a more efficient interface between the load and the resin. RAQ, for having a coarser granulometry, presents a mechanical strength lower than RAP [22].

It is also important to mention that the ornamental stones used in civil construction are considered to be highly resistant materials when the rupture stress exceeds 20 MPa, which is the case of the porcelain powder waste artificial stone developed (RAP).

Conclusion

This study investigated the artificial stone's development technique as well as its physical and mechanical properties. From the experimental results, the following conclusions can be drawn:

- The incorporation of fine waste from polishing porcelain tiles modified the structure of the stone since the same processing and production steps were followed. These modifications are related to the density of the RAP, since the fine waste was compacted in the middle of the larger grains, making a big difference in the maximum rupture stress, with the possible presence of diamond particles and other resistant materials that could have been added in the porcelain tile polishing process and may have contributed to the increase of this property.
- Both developed artificial stones obtained results that classify them as low water absorption coating materials and can be used in homeless outdoor environments, floating/raised tops, and floors, because of its water absorption index $\leq 0.4\%$.
- RAP's mechanical behavior is considered of high quality to be used in civil construction.

As the developed artificial stones have never been commercialized and there are few theoretical studies in the area, this study is characterized as authentic, unique, and exclusive, being able to supply several segments of architecture and/or civil construction. Once commercialized, the developed artificial stones would generate a new economic cycle that covers from waste collection to cutting, including the final waste use, creating with new stakeholders in addition to adding socioeconomic value to a waste that would be discarded in the environment, generating pollution and soil and groundwater contamination.

Acknowledgements The authors thank the Brazilian agencies CAPES and FAPERJ for financing this research and for providing scholarships. They also thank UENF and coach Renan da Silva Guimarães for their support.

References

1. Breitenbach SB, Santos OC, Andrade CS, Nascimento RM, Martinelli (2017) Addition of porcelain tile polishing residue in lime mortars for restoration. Cerâmica 63:395–401. https://doi.org/10.1590/0366-69132017633672182. (in Portuguese)
2. Bernardin AM, Felisberto DS, Daros MT, Riella HG (2006) Reuse of polishing and enameling residues to obtain cellular ceramics. Cerâm Ind 11:31–34
3. Torres P, Fernandes HR, Aghatopoulos S, Tulyaganov DU, Ferreira JMF (2004) Incorporation of granite cutting sludge in industrial Porcelain tile formulations. J Eur Ceram Soc 24:3177–3181. https://doi.org/10.1016/j.jeurceramsoc.2003.10.039
4. Gomes PC, Alencar TFF, Silva NV, Morais KAM, Angulo SC (2015) Obtaining lightweight concrete using recycled aggregates. AmbienteConstruído 15:31–46. https://doi.org/10.1590/s1678-86212015000300024
5. Andreola F, Barbieri L, Corradi A, Lancellotti I, Manfredini T (2002) Utilisation of municipal incinerator grate slag for manufacturing porcelainized stoneware tiles manufacturing. J Eur Ceram Soc 22:1457–1462. https://doi.org/10.1016/S0955-2219(01)00460-5
6. Peiter CC, Chiodi Filho C (2001) Ornamental stones in the 21st century: bases for a sustainable development policy for Brazilian exports. CETEM/Abirochas, Rio de Janeiro. (in Portuguese)
7. LABTEC Rochas (2012) Ornamental and Coating stones. Definition, classification, applications and the importance of technological characterization. https://www.cpmtc-igc-ufmg.org/labtecrochas/index-51.html. Accessed 6 June 2018. (in Portuguese)
8. Prezotti JCS (2003) Resultados de monitoramentos de estações de tratamento de efluentes líquidos de indústrias de beneficiamento de mármore e granito implantadas no município de Cachoeiro de Itapemirim. In: Sesma–Seminário Estadual sobre Saneamento e Meio Ambiente, FAESA
9. Calmon JL, Silva SAC (2006) Mármore e Granito no Espírito Santo: problemas ambientais e soluções. In: Domingues AF, Boson PHG, Alípaz S (eds) A gestão de recursos hídricos e a mineração. Brasília. Agência Nacional de Águas, Instituto Brasileiro de Mineração, pp 199–231
10. Demartini TJC, Rodriguez RJS, Silva FS (2018) Physical and mechanical evaluation of artificial marble produced with dolomitic marble residue processed by diamond–plated bladed gangsaws. J Mater Res Technol 7:308–313. https://doi.org/10.1016/j.jmrt.2018.02.001
11. Gomes ML, Carvalho EAS, Sobrinho LN, Monteiro SN, Rodriguez RJS, Vieira CMF (2018) Production and characterization of a novel artificial stone using brick residue and quarry dust in epoxy matrix. J Mater Res Technol 7:492–498. https://doi.org/10.1016/j.jmrt.2018.08.012
12. Ribeiro CEG, Rodriguez RJS (2015) Influence of compaction pressure and particle content on thermal and mechanical behavior of artificial marbles with marble waste and unsaturated polyester. Mater Res 18:283–290. https://doi.org/10.1590/1516-1439.372314
13. Ribeiro CEG, Rodriguez RJS, Vieira CMF, Carvalho EA, Candido VS, Monteiro SN (2014) Production of synthetic ornamental marble as a marble waste added polyester composite. Mater Sci Forum 775–776:341–345. https://doi.org/10.4028/www.scientific.net/MSF.775-776.341
14. Carvalho EAS, Vilela NF, Monteiro SN, Vieira CMF, Silva LC (2018) Novel artificial ornamental stone developed with quarry waste in epoxy composite. Mater Res 21:1–6. https://doi.org/10.1590/1980-5373-mr-2017-1104
15. Babisk MP, Vidal FWH, Ribeiro WS, Aguiar MC, Gadioli MCB, Vieira CMF (2012) Incorporation of quartzite waste in red ceramics. Hollos 28(6):169–177
16. Marques LN, Menezes RR, Neves GA, Santana LNL, Lira HI, Ferreira HC (2007) Reuse of polishing residue porcelain tiles for use in ceramic mass. Revista Eletrônica De Materiais E Processos 2(2):34–42
17. Brazilian Association of Technical Norms–ABNT (1991) ABNT NBR 3388: soil: determination of the minimum void index of non-cohesive soils. Rio de Janeiro: ABNT. (in Portuguese)

18. Ribeiro CEG (2015) Development of an alternative artificial marble with residue from the marble and unsaturated unsaturated polyester. Thesis, State University of the Northern Rio de Janeiro. (in Portuguese)
19. Brazilian Association of Technical Norms–ABNT (2010) ABNT NBR 15845-10: stones for linning: test methods. Rio de Janeiro: ABNT (in Portuguese)
20. Spanish Association of Standards and Certification (2008) UNE-EN 14617-2-08: Test methods part 2: determination of the flexural strength. Madrid: UNE-EN (in Spanish)
21. Hettiarachchi HACK, Mampearachchi WK (2018) Effect of vibration frequency, size ratio and large particle volume fraction on packing density of binary spherical mixtures. Powder Technol. https://doi.org/10.1016/j.powtec.2018.05.049
22. Silva FS, Ribeiro CE, Rodriguez RJS (2018) Physical and mechanical characterization of artificial stone with marble calcite waste and epoxy resin. Mater Res 21:1–6. https://doi.org/10.1590/1980-5373-mr-2016-0377

Influence of Modifier Admixture Based on LAS in Cement Pastes

Ana Carolina Pereira Martins, Matheus do Nascimento Duarte, José Maria Franco de Carvalho, André Luís de Oliveira Jr., Gabriel Meireles de Arruda, and Leonardo Gonçalves Pedroti

Abstract The use of modifying admixtures in cement-based composites is mandatory to improve their physical properties with technical and economic advantages. This paper discusses the influences of an alternative admixture based on linear alkyl benzene sodium sulfonate (LAS) in cement pastes. Rheological tests were carried out on a flow table. Setting times and reaction speed were evaluated by ultrasonic pulse velocity (UPV) measurements. Compressive strength tests were performed in mortars. Different LAS contents were evaluated (0, 0.01, 0.1, and 1.0% by cement mass). Contents of up to 0.1% of LAS did not significantly change the rheological behavior in comparison to the reference paste, whereas the content of 1.0% of LAS showed a clear plasticizer effect. The highest levels of LAS resulted in an acceleration in the setting times, which contrasts with the results of UPV. Contents of 0.01 and 0.1% did not impair the strength in the first ages.

Keywords Modifying admixture · LAS · Consistency · Cement pastes · Mechanical strength

A. C. P. Martins (✉) · M. N. Duarte · J. M. F. de Carvalho · A. L. de Oliveira Jr. · G. M. de Arruda · L. G. Pedroti
Department of Civil Engineering, Federal University of Vicosa, Vicosa 36570-900, Brazil
e-mail: ana.martins5@ufv.br

M. N. Duarte
e-mail: duarte.matheus.n@gmail.com

J. M. F. de Carvalho
e-mail: josemaria.carvalho@ufv.br

A. L. de Oliveira Jr.
e-mail: andre.l.junior@ufv.br

G. M. de Arruda
e-mail: gabriel.m.arruda@ufv.br

L. G. Pedroti
e-mail: leonardo.pedroti@ufv.br

J. Li et al., *Characterization of Minerals, Metals, and Materials 2021*,
The Minerals, Metals & Materials Series,
https://doi.org/10.1007/978-3-030-65493-1_44

Introduction

The modern concrete is more than merely a mixture of cement, water, and aggregates; chemical additives and mineral admixtures play an increasingly central role, assigning specific properties to concrete technology [1, 2]. Modifying admixtures are capable of giving considerable physical and economic advantages to cementitious materials, changing the properties of the matrices in the fresh and hardened state [3, 4].

Among the different types of additives available on the market, there are the air-entraining admixtures (AEAs), also known as surfactants, which is an abbreviation of "surface-active admixtures" [3, 5, 6]. The air-entraining agents generally have a molecular structure with a hydrophilic polar group and a non-polar hydrophobic group formed by a long chain of carbon atoms [5, 7]. The volume of entrained air depends on the dosage of admixture: the higher amount of AEAs added, the more air entrained up to a maximum level, beyond which there is no increase in the volume of fair voids in the matrix [4, 8]. The essential requirements of an air-entraining admixture are the rapid production of a stable system of finely divided foam and that the individual bubbles resist coalescence; the foam must not have any chemically harmful effect on the cement [4].

AEAs are substances that introduce a controlled amount of small air bubbles (or voids) during the mixing of the matrix and that remain after it hardens [8–11]. These bubbles are almost spherical and with diameters in the range of 10–100 μm. If homogeneously distributed, they can improve the cohesion and workability of cement-based composites [4, 8, 9]. AEAs can improve some technological advantages to cementitious materials, such as reduce water/cement ratio, reduce cement consumption, increase plasticity and improve consistency, reduce exudation and permeability, refine thermal and acoustic performance, in addition to provide freezing and thawing resistance [3, 4, 6, 8].

Mendes et al. [9] studied a biodegradable surfactant based on linear alkyl benzene sodium sulfonate (LAS) , present in dishwasher detergents, as a sustainable plasticizing and air-entraining agent in mortars. Positive results have been achieved from its application; LAS proved to be more efficient than the commercial AEA, taking into account the volume of fair incorporated and the stability of the pore system formed in the matrix. Also, it achieved an improvement in the workability and cohesion in the fresh state.

In this work, the authors explore the use of a LAS-based admixture in cement-based composites formed by pastes and mortars. The main objective of the research is to investigate and discuss the influence of LAS on workability, hydrated products, setting times, and compressive strength. This study intends to contribute with the knowledge of the effects of this biodegradable and low-cost substance, in the properties of cement-based composites.

Materials and Methods

Materials

A high early strength Portland cement (ASTM Type III equivalent) was used in the production of the pastes and mortars. This Portland cement is specified in Brazil as CPV-ARI type by the standard NBR 16697 [12]. The choice was based on its high fineness and the lack of supplementary cementing materials (95–100% clinker). The data on the physical, chemical, and mechanical characterization of the cement was reported by the producer and are shown in Table 1.

LAS-based additive (linear alkyl benzene sulfonate sodium) was used as an agent to improve plasticity, cohesion, and incorporation of fair microbubbles. It is a biodegradable surfactant present in dishwashing detergents, at a concentration of up to 10% [13], and the proposed AEA consists of homogeneous solutions of detergent and water in different concentrations.

To prepare the mortars, quartz sand extracted in the city of Analândia, state of São Paulo, Brazil, was used. This sand has a maximum diameter of 600 μm, specific gravity of 2.65 g/cm^3, and bulk density of 1.43 g/cm^3.

Evaluation of Rheological Performance in Pastes

Cement pastes with different contents of the LAS-based substance were made to evaluate the effects of this material on the rheological properties and workability. For

Table 1 Chemical, physical, and mechanical properties of Portland cement

Parameter	Value
MgO content, %	0.98
SO_3 content, %	3.43
Na_2O content, %	0.07
K_2O content, %	0.86
Na_2Oeq content, %	0.64
Loss on ignition, %	3.97
Insoluble residue, %	1.48
Density, g/cm^3	3.12
Specific surface area (Blaine), cm^2/g	4372
Hot expandability, mm	0.3
Water for standard cement paste, %	28.8
Initial setting time, min (Initial/Final)	(105/165)
Compressive strength (1/3/7/28 days), MPa	(27.5/37.8/44.3/53.2)

Table 2 Procedure for mixing the pastes

Stage	Speed	Start time (s)	Final time (s)
Mixture of dry materials (100%)	Low	0	60
Addition of water and LAS admixture (100%)	Low	60	90
Mixture	Low	90	150
Scraping of the bowl and paddle	–	150	210
Final mix	High	210	300

Low – 140 ± 5 rpm
High 285 ± 10 rpm

all pastes produced, the water/solids content (ø) was 0.5. The solutions and dosages of the alternative admixture varied from 0.01 to 1.0% by mass of cement named as CP-0.01%LAS, CP-0.1%LAS, and CP-1.0%LAS. A mixture without admixture (0%) was used as a reference (CP-0%LAS) .

The mixtures were performed using a mechanical mixer, and the steps of the mixing procedure are detailed in Table 2. With the prepared pastes, spreading tests were performed using the consistency table, applying 15 strokes in a time interval of 15 s. The measurements were performed at 0, 5, 10, 25, and 50 min. The first spreading test (0 min) started 8 min after the first contact of the cement with water.

Evaluation of the Hydration Kinetics of Pastes

Hydration kinetics evaluations were performed in pastes with four LAS contents (0, 0.01, 0.1, and 1%). To monitor the start and the end of the setting times, tests were performed using the Vicat apparatus and the ultrasonic pulse velocity (UPV), and their results were compared to obtain a relationship between both tests. The setting time test using the Vicat apparatus is prescribed by ABNT NBR 16607 (2018b). The UPV was performed using a Proceq "Pundit Lab" equipment, connected to the computer and operated by the Proceq Punditlink software. The transducer used operates at a frequency of 54 MHz and a pulse width of 9.3 μs. The frequency of measurements was one reading per minute, taken during a 24-h interval.

Evaluation of Mechanical Performance in Mortars

The influence of LAS was also evaluated on the mechanical performance of mortars. For this, mortar specimens with a ratio of 1:3 (cement:sand) were molded in reduced cylindrical molds measuring Ø22 × 22 mm. The compressive strength tests were performed at the ages of 1, 3, 7, and 28 days. The contents of LAS evaluated were

Table 3 Procedure mixture of mortar

Stage	Speed	Start time (s)	Final time (s)
Mixture of water and LAS	Low	0	0
Addition of cement (100%)	Low	0	30
Addition of sand (100%)	Low	30	60
Mixing	High	60	90
Cleaning the container edges	–	90	120
Cover with a damp cloth	–	120	180
Final mix	High	180	240

Low – 140 ± 5 rpm
High 285 ± 10 rpm

the same presented in the study of pastes (0, 0.01, 0.1, and 1%) and the specimens were named as MC-0%LAS, MC-0.01%LAS, MC-0.1%LAS, and MC-1.0%LAS.

The mixing process was carried out with the aid of a mechanical mixer, and the steps of the mixing procedure are detailed in Table 3. For each mixture, 16 specimens were molded and submitted to a process of curing in water. After a period of 24 h, these specimens were demolded and immersed in water saturated with lime, where they remained until the time of the mechanical test.

Results and Discussion

Rheological Performance in Pastes

The results of the rheological tests of the cement pastes containing four percentages of the LAS admixture (0, 0.01, 0.1, and 1.0%) are presented in Fig. 1. A clear tendency of increasing the spread is noticed only in the pastes containing 1.0% of LAS. The contents of 0.01% and 0.1% did not improve the rheological performance. The content of 0.1%LAS produced a paste with behavior very close to the reference paste (0%LAS) , and the content of 0.01% achieved lower spreading values. The surfactant molecules did not provide dispersion of the cement particles, causing retraction in the paste. This indicates that very low concentrations of surfactants did not affect the paste effectively. Similar behavior was identified in the mortars studied by Mendes et al. [9].

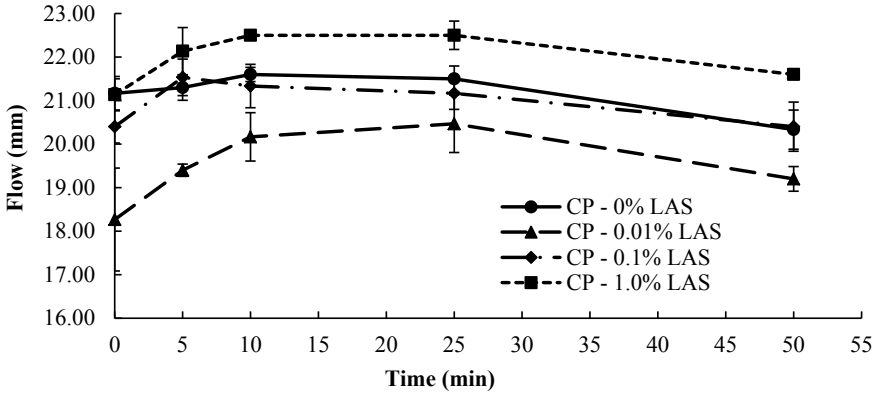

Fig. 1 Results of the flow table for the reference cement pastes (0%) and pastes containing the proposed LAS-based admixture (0.01–1.0%)

Hydration Kinetics of Pastes

The results of the UPV measurements are shown in Fig. 2. The shape of the typical UPV curve for the four proposed mixtures showed three well-defined stages related to the following stages of the hydration kinetics [14]:

I—Dormant: in the first hours, the ultrasonic velocity increases slightly over time, notable for the small slope of the curve. The UPV in this phase does not exceed 1480 m/s, which is the ultrasonic velocity in pure water, due to the existence of voids in the mixture.

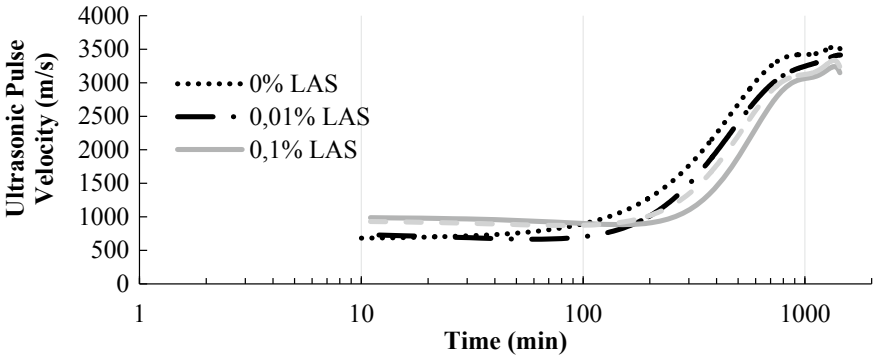

Fig. 2 Ultrasonic pulse velocity of the reference cement pastes (0%) and pastes containing the proposed LAS-based admixture (0.01–1.0%)

II—Acceleration: from a specific moment for each mixture, there is an increase in the UPV rate, indicating a change in the physical structure of the paste. Hydration products are formed more quickly in this phase, which configures the solidification of the material.

III—Deceleration: with the consumption of reagents from cement, the paste hardening phase ends [15]. Thus, the UPV returns to a lower increase over time.

In the first stage, it has been noticed that the UPV of the 0.1% LAS mixture is higher. This can be justified by the increase of ions in the system by the addition of LAS. The dissolution of the ions forms a strong alkaline solution, allowing a greater UPV in the mix [14].

Observing the end of the second stage, the smallest UPV is from the 0.1% LAS mixture. This fact may be linked to the greater incorporation of air in this mixture, which reduces the speed of wave propagation in the material [16].

Therefore, the results point that the mix containing 1% LAS was not the most efficient, because of its dissolution in the first stage, even in the formation of air bubbles in the mixture after his hardening.

Figure 3 shows the results of the setting times using the Vicat apparatus. The mixtures containing 0% LAS and 0.01% LAS showed similar behaviors, both at the beginning and at the end of the setting. This demonstrates that the amount of admixture added is low to affect the setting characteristics of the paste. The mixture with the longest setting time is 0.1% LAS, which indicates that this dosage is the one that most influences the formation of hydration products, as evidenced by the UPV. The initiation of hardening obtained with the Vicat needle test is equivalent to the transition point from stage I to stage II on the UPV curve in mixtures containing 0% LAS and 0.01% LAS. For the mixes containing 0.1% LAS and 1% LAS, there is a lag between the initial setting time and the transition point between stages I and II in the UPV curves, justified by the interval between measurements adopted in the Vicat needle tests.

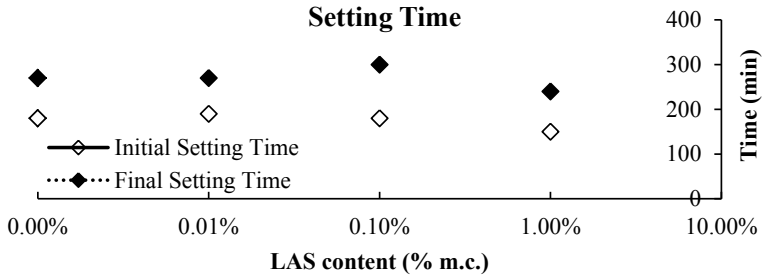

Fig. 3 Setting times of the reference cement paste (0%) and pastes containing the proposed LAS-based admixture (0.01–1.0%)

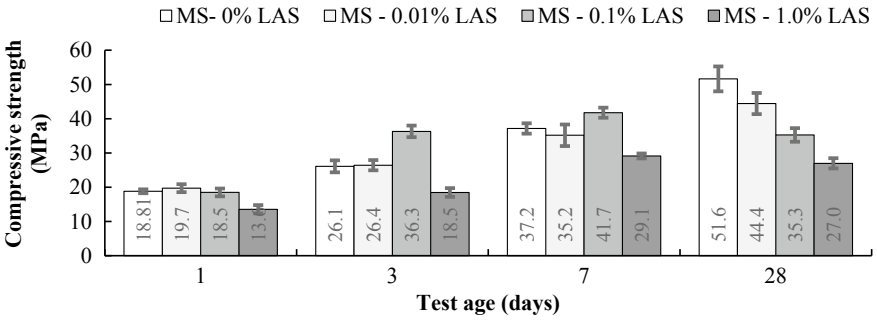

Fig. 4 Compressive strength of the reference cement pastes (0%) and pastes with proposed LAS-based admixture (0.01–1.0%)

Mechanical Performance of Mortars

Figure 4 shows the results of compressive strength for the reference specimens (0%LAS) and the specimens containing the three LAS contents (0.01, 0.1, and 1.0%). It can be observed that LAS in the contents of 0.01% and 0.1% did not decrease the compressive strength in the initial ages compared to the reference mortar, and that the mortar containing 0.1% of LAS presented greater compressive strength in the ages of 3 and 7 days. The mortar containing 1.0% LAS showed a decrease in compressive strength at all test ages. This loss of strength can be related to the increase in the porosity of the matrix as a less integrated and dense matrix has less mechanical strength. Similar results due to the increased concentration of AEAs were obtained in other studies [9, 17].

Conclusions

This research was conducted to explore the potential of using a LAS-based substance as a modifying admixture in cement pastes by evaluating its influence on properties such as workability, setting times, and compressive strength. Based on the results obtained through the proposed methodology, it can be concluded that:

- Lower LAS content (0.01%) practically does not affect the properties analyzed, as observed in the tested pastes and mortars. The spreading was greater in pastes containing 1.0% LAS.
- There was a delay in the initial and final setting times of the mixture containing 0.1% of LAS, which was observed by both Vicat needle test and UPV measurements. Also, the higher dosage of the modifying admixture (1.0%) did not influence the cement setting times.
- The highest LAS content (1.0%) caused a gradual decrease in mechanical strength at all evaluated ages, which is related to the higher air content incorporated into

the matrix. The mortars containing the intermediate LAS content (0.1%) showed the highest compressive strengths at 3 and 7 days, and all the mortars containing LAS showed lower compressive strengths in comparison to the reference mortar at 28 days.

Acknowledgements This study was financed in part by the Coordenação de Aperfeiçoamento de Pessoal de Nível Superior—Brasil (CAPES)—Finance code 001. The authors also acknowledge the support provided by the Fundação de Amparo à Pesquisa do Estado de Minas Gerais (FAPEMIG), Conselho Nacional de Desenvolvimento Científico e Tecnológico (CNPq) and Federal University of Viçosa (UFV). Thanks also due to the Brazilian research groups RECICLOS-CNPq/UFOP and SICon-CNPq/UFV for the infrastructure and collaboration.

References

1. Aïtcin P-C (2000) Cements of yesterday and today Concrete of tomorrow. Cem Concr Res 30:1349–1359. https://doi.org/10.1063/1.1473683
2. Zeng X, Ma C, Long G, Dang H, Xie Y (2019) Hydration kinetics of cement composites with different admixtures at low temperatures. Constr Build Mater 225:223–233. https://doi.org/10.1016/j.conbuildmat.2019.07.153
3. Hartmann C, Jeknavorian A, Silva D, Benini H (2011) Aditivos Químicos para Concretos e Cimentos. In: Isaia GC (ed) Concreto Ciência e Tecnol, 1st ed. IBRACON, São Paulo, pp 347–80
4. Neville AM (2016) Propriedades do Concreto, 5th ed. Bookman, Porto Alegre
5. Atahan HN, Carlos C, Chae S, Monteiro PJM, Bastacky J (2008) The morphology of entrained air voids in hardened cement paste generated with different anionic surfactants. Cem Concr Compos 30:566–575. https://doi.org/10.1016/j.cemconcomp.2008.02.003
6. Mehta PJM, Monteiro PK (2014) Concreto: Microestrutura, Propriedades e Materiais, 2nd ed. IBRACON, São Paulo
7. Seabra MP, Paiva H, Labrincha JA, Ferreira VM (2009) Admixtures effect on fresh state properties of aerial lime based mortars. Constr Build Mater 23:1147–1153. https://doi.org/10.1016/j.conbuildmat.2008.06.008
8. Silva BA, Ferreira Pinto AP, Gomes A, Candeias A (2020) Suitability of different surfactants as air-entraining admixtures for lime mortars. Constr Build Mater 256:118986. https://doi.org/10.1016/j.conbuildmat.2020.118986
9. Mendes JC, Moro TK, Figueiredo AS, do Carmo Silva KD, Silva GC, Silva GJ, Peixoto RA (2017) Mechanical, rheological and morphological analysis of cement-based composites with a new LAS-based air entraining agent. Constr Build Mater 145:648–661. https://doi.org/10.1016/j.conbuildmat.2017.04.024
10. Cultrone G, Sebastián E, Huertas MO (2005) Forced and natural carbonation of lime-based mortars with and without additives: Mineralogical and textural changes. Cem Concr Res 35:2278–2289. https://doi.org/10.1016/j.cemconres.2004.12.012
11. Felice R, Freeman JM, Ley T (2014) Durable concrete with modern air-entraining admixtures. Concr Int, 37–46
12. ABNT, NBR 16697 (2018) Cimento Portland-Requisitos, Associação Brasileira de Normas Técnicas, Rio de Janeiro
13. Bombril SA (2019) Ficha de informações de segurança de produtos químicos-FISPQ-Detergente Limpol
14. Zhang S, Zhang Y, Li Z (2018) Ultrasonic monitoring of setting and hardening of slag blended cement under different curing temperatures by using embedded piezoelectric transducers. Constr Build Mater 159:553–560. https://doi.org/10.1016/j.conbuildmat.2017.10.124

15. Bhalla N, Sharma S, Sharma S, Siddique R (2018) Monitoring early-age setting of silica fume concrete using wave propagation techniques. Constr Build Mater 162:802–815. https://doi.org/10.1016/j.conbuildmat.2017.12.032
16. Lu Y, Ma H, Li Z (2015) Ultrasonic monitoring of the early-age hydration of mineral admixtures incorporated concrete using cement-based piezoelectric composite sensors. J Intell Mater Syst Struct 26:280–291. https://doi.org/10.1177/1045389X14525488
17. Ouyang X, Guo Y, Qiu X (2008) The feasibility of synthetic surfactant as an air entraining agent for the cement matrix. Constr Build Mater 22:1774–1779. https://doi.org/10.1016/j.conbuildmat.2007.05.002

Influence of the Ceramic Block Sorptivity on the Adherence of Rendering Mortars

E. B. Zanelato, A. R. G. Azevedo, M. T. Marvila, T. Lima, J. Alexandre, S. N. Monteiro, G. C. Xavier, and C. M. Vieira

Abstract Adherence is one of the main properties of rendering mortars. Pathologies related to the lack of adherence between the mortar and the ceramic block are frequently seen, especially on facades. A complex system with several variables influences adherence, where the sorptivity of the ceramic block can be highlighted. The objective of this work is to verify the influence that the sorptivity of the ceramic block has on the mortar adhesion in different combinations. Ceramic blocks burned at three temperatures with and without the presence of roughcast were used. The ceramic blocks were evaluated by immersion absorption, mechanical strength, and sorptivity tests. Three traces of mortar were used, characterized by water retention and mechanical resistance tests, in addition to adherence with the ceramic block. The adherence results between the materials indicated that the sorptivity influences the adherence with different behaviors, depending on the mortar used.

Keywords Ceramic · Adherence · Mortar

E. B. Zanelato · A. R. G. Azevedo (✉)
IFF-Federal Institute Fluminese, Rua Cel. Valter Kramer, 357-Parque Vera Cruz, Campos dos Goytacazes, Rio de Janeiro 28080-565, Brazil
e-mail: ebzanelato@gmail.com

E. B. Zanelato · M. T. Marvila · T. Lima · J. Alexandre · G. C. Xavier · C. M. Vieira
LECIV–Civil Engineering Laboratory, UENF-State University of the Northern Rio de Janeiro, Av. Alberto Lamego, 2000, Campos dos Goytacazes, Rio de Janeiro 28013-602, Brazil

A. R. G. Azevedo
TER–Department of Agricultural Engineering and Environment, UFF-Federal Fluminense University, Rua Passo da Pátria, 341, Niterói, Rio de Janeiro 24210240, Brazil

S. N. Monteiro
Department of Materials Science, IME-Military Institute of Engineering, Square General Tibúrcio, 80, Rio de Janeiro 22290-270, Brazil

J. Li et al., *Characterization of Minerals, Metals, and Materials 2021*,
The Minerals, Metals & Materials Series,
https://doi.org/10.1007/978-3-030-65493-1_45

Introduction

Mortar is one of the most versatile materials among construction materials. Its physical and chemical properties combined with its low viscosity allow applications in different stages of a work. Mortars are mainly used as wall coverings, both internal and external [1]. The application of a layer of mortar on the structure, especially concrete, is very common in many countries, especially in large structures. The layer helps to protect both the structure and the masonry [2].

Even with its versatility and extensive use throughout the evolution of construction materials, mortar applications still suffer from several pathological manifestations, where cracking and lack of adhesion with the ceramic block can be highlighted. These phenomena contribute to decrease in the building's useful life [3].

The solution to these problems is not simple, since the adherence is the product of a complex system with several factors that influence it, among which the application technique; the property of the material where the mortar is applied, the curing conditions; the properties of mortar and its constituent materials stand out [4].

Adherence, physically, occurs through micro-anchoring and macro-anchoring. Micro-anchoring occurs by absorbing water with cement particles through the substrate, which when hardened by hydration reactions promotes mechanical anchoring in the pores of the substrate [5]. The micro-anchoring phenomenon is directly affected by the absorptive capacity due to capillarity of the substrate and the water retention capacity of the mortar [6].

Macro-anchoring occurs due to the penetration of the mortar in the irregularities of the substrate. It is directly affected by the topology of the substrate [4] and the rheological capacity of the mortar [7].

To enable a better understanding of this complex system of adherence, several researches are carried out by analyzing individually and globally the variables that affect adherence

The substrate interferes with adhesion mainly due to its ability to absorb water from the mortar. The absorptive capacity of the substrate is given by capillary strength. The suction of the mortar water occurs mainly in the initial moments of contact and decreases exponentially over time [5].

A technique commonly used in buildings is the application of a thin layer of mortar called a roughcast. The roughcast contributes both to the macro-anchoring, since the mortar layer presents high roughness, and to the micro-anchoring, regulating the capillary water absorption of the substrate [8].

Other properties of the substrate also directly affect capillary suction, such as firing temperature, roughness, among others.

The measurement of capillary absorption capacity can be carried out by the absorptivity test, the main test used by authors in the field due to its greater fidelity to what occurs in practice in the interaction of the mortar with the substrate [8].

Regarding the mortar, the properties of the mortar that influence adherence are: water retention, a property responsible for regulating the water transported to the substrate; mechanical resistance, a property that affects adhesion if the mechanical

strength of the mortar is lower than the adhesion between the materials. The mixture of mortars directly affects the properties highlighted above, since the proportion of the different materials used in making the mortar affects the final characteristics of the product.

The objective of this work is to evaluate three firing temperatures of the ceramic and the presence or not of the roughcast in the absorptivity and the adherence of three different mixtures of mortars.

Materials and Methods

Ceramic blocks were collected in the Northern Fluminense region. The blocks were fired at 700, 800, and 900 °C, reference values for ceramics in the region.

CPII-E cement, hydrated lime CHIII, and washed sand taken from the Paraíba do Sul River were used.

The roughcast was made in line 1:3 (cement:sand) in volume.

The mixtures used in the coating mortars are shown in Table 1.

The ceramic blocks were characterized by the initial water absorption test, adapting the test to the American standard ASTM C67 [9]. During the test, the ceramic block comes into contact with water only on a 3 mm high blade. The absorption of the ceramic block depends essentially on the capillary absorption, which is directly related to the adhesion between the mortar and the ceramic block.

During the test, checks are performed at four different times: 5 (W5), 10 (W10), 15 (W15), and 150 (W150) minutes. The absorption test presents a better representation of the duration of the water transport from the mortar to the ceramic block, which is very intense in the first minutes and gradually decreases in the first hours. Absorbency is calculated according to Eq. (1):

$$Sorptivity\left(\text{mm min}^{1/2}\right) = \frac{i}{\sqrt{t}} \tag{1}$$

where i is the accumulated volume of water absorbed per unit area of the absorption surface (mm^3/mm^2); t is the elapsed time (min).

Table 1 Composition of mortar mixtures (in volume)

Mixtures					
Trace	Cement (%)	Hydraulic lime	Sand (%)	Water (%)	w/a
1:3	25	–	75	14.06	0.5624
1:1:6	12.5	12.5	75	14.06	0.5624
1:2:9	8.33	16.67	75	14.06	0.5624

Table 2 Tests carried out on mortar

Tests	Standard
Water retention	NBR 13277 [10]
Compressive strength	NBR 13279 [11]
Flexural tensile strength	NBR 13279 [11]
Tensile adherence strength	NBR 13528 [12]

Absorptivity tests were carried out combining the presence or absence of the roughcast at three different firing temperatures.

In the mortars, the tests indicated in Table 2 were performed.

The retention test was performed by the direct influence on the water transport from the mortar to the substrate.

The mechanical strength must be high enough not to be the place of least resistance during the adhesion test. Compressive strength and flexural tensile strength tests were performed to assess mechanical strength.

The tensile bond strength test was performed to verify the adherence of the three traces of mortar used in the work in each of the substrate combinations.

Results

Figure 1 presents the results obtained in the sorptivity tests.

It can be seen from the results that both the presence of the roughcast and the firing temperature significantly influenced sorptivity.

The increase in temperature, both from 700 to 800 °C and from 800 to 900 °C, promotes an increase in the capillary water absorption capacity. This effect can be justified by the minerals that are formed with the increase in the burning temperature.

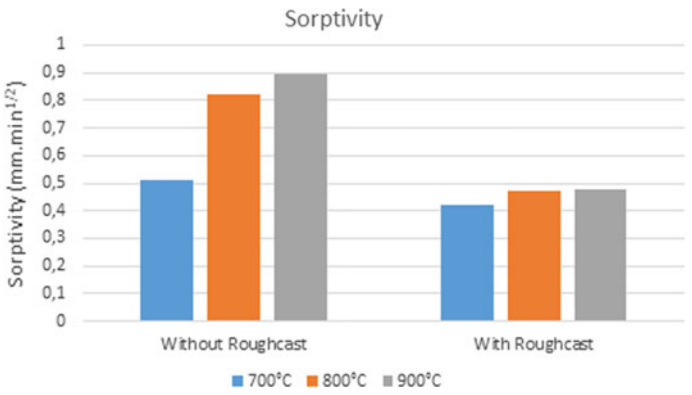

Fig. 1 Sorptivity. (Color figure online)

The increase in the firing temperature promotes greater densification of the ceramic, increases its resistance, and decreases its water absorption by immersion.

The increase in capillary absorption is verified due to the greater presence of small diameter pores, and is more frequent as densification occurs due to the increase in temperature.

The presence of the roughcast promotes the regularization of capillary absorption, presenting similar results for the three temperatures analyzed. Thus, the roughcast had a greater impact, significantly reducing the absorption of ceramic blocks with the lowest firing temperatures.

Figure 2 shows the results obtained in the water retention test.

It can be seen from the results that the water retention of the analyzed lines varies according to the hydrated lime incorporated. Because it is thinner than cement, lime has the capacity to retain a larger volume of the mortar's mixing water, making it difficult to transport it to the substrate.

Figure 3 shows the results of mechanical strength.

It can be seen from the figure that, contrary to what was observed in water retention, the greater the incorporation of hydrated lime, the lower the mechanical resistance. The justification for this result is the lower presence of cement, whose hydration is mainly responsible for the mechanical strength of the mortar.

Figure 4 shows the results of the tensile adhesion test.

It can be seen from the figure that the variables used in the work: firing temperature of the ceramic; presence of roughcast; and trace of the mortar directly influence adherence; however, the analysis is not linear as in previous tests.

The results obtained by the 1:3 mortar indicate that the adhesion decreases as the firing temperature increases. The decrease is justified by the increase in water transport between materials. The 1:3 line showed the lowest water retention capacity, since the increase in temperature increases sorptivity. The increase in water transport benefits micro-anchoring; however, excessive transport hinders the correct hydration of the mortar , with a marked decrease in mechanical strength, becoming the breaking point in the adhesion test.

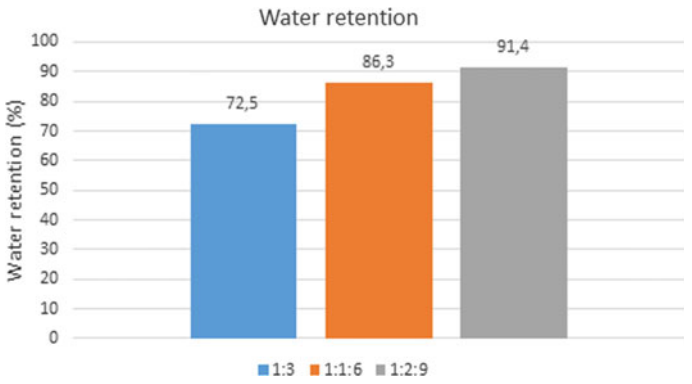

Fig. 2 Water retention. (Color figure online)

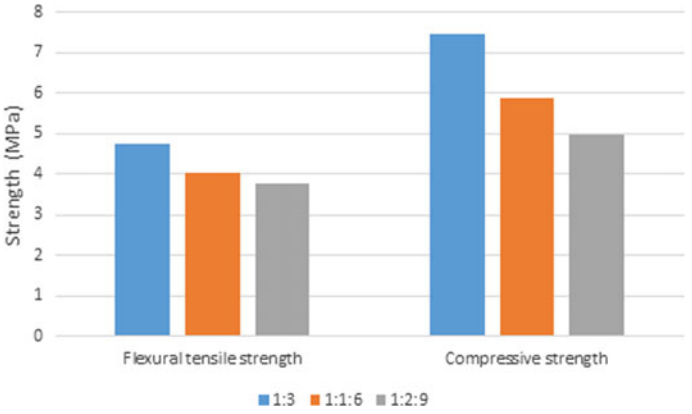

Fig. 3 Mechanical strength. (Color figure online)

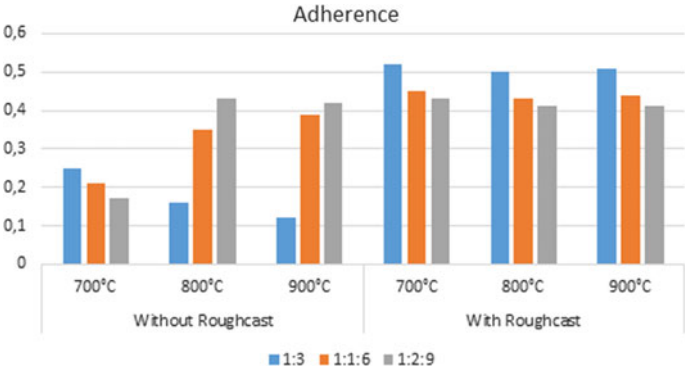

Fig. 4 Tensile adherence strength. (Color figure online)

The 1:1:6 trait, on the other hand, showed an inverse trend to the 1:3 trait, where the increase in the firing temperature increases adherence . This behavior is justified by the high water retention capacity of the 1:1:6 line that when applied on substrates of low sorptivity, there is not enough water transport between the materials, impairing hydration. The increase in the firing temperature increases the water transport gradually and does not significantly affect the hydration of the mortar.

The 1:2:9 line showed a trend similar to the 1:1:6 line. Considering that the line has even greater retention than the line 1:1:6, the adhesion in the ceramic block burned at 700 °C is even lower than the line 1:2:9; however, in the blocks burned at 800 and 900 °C, the adherence was higher.

The use of roughcast changes all the trends mentioned above. With the regularization of the water transport promoted by the application of the roughcast, the adhesion was conditioned to the mechanical resistance of the mortar. Therefore, as

verified in the mechanical strength test, the strokes with a higher proportion of cement have greater mechanical strength and greater adhesion when applied to roughcast substrate.

Conclusion

In this work, it was verified that the firing temperature of the ceramic block, the application of the roughcast, and the trace of the coating mortar influence the resistance. The following points can be highlighted.

- The increase in the firing temperature promotes an increase in the absorptivity of the ceramic.
- The application of the roughcast regularizes the absorptivity of the ceramic.
- Increasing the proportion of hydrated lime promotes increased water retention and decreased mechanical strength.
- The good performance of the adhesion is conditioned to a balanced transport of water from the mortar to ceramic. The balance can be achieved both in the application of a mortar with high retention in a block of high sorptivity, and in the application of a mortar with low water retention in a block of low sorptivity.
- The application of roughcast regularizes and enhances adhesion, being limited by the mechanical strength of the mortar.

Acknowledgements The authors thank the Brazilian agencies IFF, CNPq, CAPES, and FAPERJ for the support provided to this investigation.

References

1. Botas S, Veiga R, Velosa A (2017) Mater Struct 50:211. https://doi.org/10.1617/s11527-017-1086-7
2. Malheiro R, Meira G, Lima M, Perazzo N (2011) Influence of mortar rendering on chloride penetration into concrete structures. Cem Concr Compos 33(2):233–239
3. Nogueira R, Pinto APF, Gomes A (2018) Design and behavior of traditional lime-based plasters and renders. Review and critical appraisal of strengths and weaknesses. Cem Concr Compos 89:192–204
4. Stolz CM, Masuero AB, Pagnussat DT, Kirchhein AP (2016) Influence of substrate texture on the tensile and shear bond strength of rendering mortars. Constr Build Mater 128:298–307
5. Recena FAP (2008) Knowing Mortar, Porto Alegre: EDIPUCRS, 192p. (in Portuguese)
6. Govin MB, Biasotti B, Giudici M, Langella V, Grosseau P (2016) Modification of water retention and rheological properties of fresh cement-based mortars by guar gum derivatives. Constr Build Mater 122:772–780
7. Cardoso FA, John VM, Pileggi RG, Banfill PFG (2014) Characterization of rendering mortars by squeeze-flow and rotational rheometry. Cem Concr Res 57:79–87
8. Zanelato EB, Alexandre J, de Azevedo ARG, Marvila MT (2019) Evaluation of roughcast on the adhesion mechanisms of mortars on ceramic substrates. Mater Struct 52:53

9. ASTM C67 (2018) Standard test methods for sampling and testing brick and structural clay tile.
10. Associação Brasileira De Normas Técnicas. NBR 13277 (2005) Mortars applied on walls and ceilings-determination of the water retentivity. Rio de Janeiro
11. Associação Brasileira De Normas Técnicas. NBR 13279 (2005) Mortars applied on walls and ceilings-determination of the flexural and the compressive strength in the hardened stage. Rio de Janeiro
12. Associação Brasileira De Normas Técnicas. NBR 13528-2 (2005) Render made of inorganic mortars applied on walls-determination of tensile bond strength Part 2: Adherence to the substrate. Rio de Janeiro

Influence of the Granulometry of the Granite Residue on the Sorptivity of Ceramic Blocks

E. B. Zanelato, A. R. G. Azevedo, M. T. Marvila, T. Lima, J. Alexandre, P. Rocha, S. N. Monteiro, and C. M. Vieira

Abstract The ornamental rock industry generates an enormous amount of waste on manufacturing process. Granite is the main rock extracted in Brazil for export blocks, a country that is one of the largest exporters in the world. The expressive volume of powder generated during the manufacturing process can be reused in the manufacture of ceramic pieces. The objective of this work is to evaluate three different particle sizes of the waste and its influence on the ceramic block sorptivity capacity. The clay used in the work and the residue were characterized by chemical analysis test, granulometry, Atterberg limits, and grain density. After the production of ceramic pieces with three levels of incorporation (0, 10, and 20%) of the residue, immersion absorption, sorptivity, mechanical resistance, and adherence tests with mortar were carried out. The results indicate that the granulometry of the residue significantly influences the sorptivity of the ceramic.

Keywords Ceramic · Granite · Sorptivity

E. B. Zanelato (✉) · A. R. G. Azevedo · P. Rocha
IFF-Federal Institute Fluminese, Rua Cel. Valter Kramer, 357-Parque Vera Cruz, Campos dos Goytacazes, Rio de Janeiro 28080-565, Brazil

A. R. G. Azevedo
e-mail: ebzanelato@gmail.com

E. B. Zanelato · M. T. Marvila · T. Lima · J. Alexandre · C. M. Vieira
LECIV–Civil Engineering Laboratory, UENF-State University of the Northern Rio de Janeiro, Av. Alberto Lamego, 2000, Campos dos Goytacazes, Rio de Janeiro 28013-602, Brazil

A. R. G. Azevedo
TER–Department of Agricultural Engineering and Environment, UFF-Federal Fluminense University, Rua Passo da Pátria, 341, Niterói, Rio de Janeiro 24210240, Brazil

S. N. Monteiro
Department of Materials Science, IME-Military Institute of Engineering, Square General Tibúrcio, 80, Rio de Janeiro 22290-270, Brazil

J. Li et al., *Characterization of Minerals, Metals, and Materials 2021*,
The Minerals, Metals & Materials Series,
https://doi.org/10.1007/978-3-030-65493-1_46

Introduction

The ornamental stone industry is an important economic sector for several countries. In Brazil, production and exports increase with each passing year; only in 2017, 2.36 million tons were traded, generating US$ 1,107.1 million in exports. Of the export products, 80% went through processing processes. Among the states mainly responsible for the Brazilian ornamental stone market, the state of Espírito Santo stands out being responsible for 75% of the national physical volume [1].

The processing carried out on the raw rock adds value to the raw material, where cutting and polishing are carried out. Both steps generate huge amounts of dust not used by the industry, causing a great environmental impact on its disposal. The generation of waste is approximately 20% of the weight of the processed raw material. In general, the dust generated in the processing of ornamental rock is dumped into the environment without prior treatment; thus, the industrial sector is penalized by environmentalists for damages caused to the local environment. The destination for landfills has considerably reduced pollution in rivers, a destination that was widely used before environmental standards came into force. However, in places where waste is collected, they have a high maintenance cost and lack of space in landfills, a place where non-recyclable waste is discarded [2].

The reduction of the environmental impact in the disposal of the ornamental rock residue can be obtained by its reuse. The incorporation in different construction materials has been studied, such as the use in concrete [3], mortar [4], ceramic blocks [5], and tiles [6]. The incorporation of the waste not only reduces the environmental impact with its reuse but also improves the performance of the materials.

The incorporation of ornamental rock waste in ceramics directly influences the physical characteristics of the product. The incorporation of the residue tends to increase the packing between the grains, decrease the porosity, and increase the mechanical resistance [7].

The ornamental rock residue, especially granite, can present different granulometries according to the cut made in the industry. Considering that the filling of the voids is directly influenced by the granulometry of the residue, studies that verify how the variation of the proportions of the granulometric fractions influences the properties of the final ceramic piece are necessary [5].

The objective of this work is to evaluate how three different granite residue granulometries influence the sorptivity of the ceramic block. Sorptivity is directly influenced by the porosity of the material and is mainly responsible for the adhesion of mortars of coatings applied on the ceramic block.

Materials and Methods

The clay used in the work was collected directly from the ceramic sector, one being a material used for making ceramic masses in the region.

Table 1 Composition of mixtures (in volume)

Mixtures					
Mixture	Cement (%)	Hydraulic lime (%)	Sand (%)	Water (%)	w/c
1:1:6	12.5	12.5	75	14.06	1.125

The granite residue was collected in waste settling tanks in an ornamental rock industry. The residue was collected in the form of mud and placed to dry in the environment and then in an oven.

The materials used in the mortar were: cement, sand, and water. The cement used was CP-II-E-32. The sand is naturally removed from the river Paraíba do Sul located in Campos dos Goytacazes-RJ. The hydrated lime was CHIII. The mixtures of mortar used are indicated in Table 1. The binder/aggregate ratio was maintained at 1:3 for mixture.

The granulometric analysis was performed following the NBR 7181 standards [8]. The fraction retained the material in the opening sieve 0.074 mm (ABNT # 200), and the samples were classified by sieving. The passing fraction of the material in the same sieve was classified by sedimentation. To perform the sedimentation test, sodium hexametaphosphate, a material with a deflocculating action, was used. The Casagrande standard (1942)-Unified Soil Classification System was used to classify the soil. Classification is also used by the U.S. Army Corps of Engineers (Airports) and U.S. Bureau of Reclamation (Dams).

The material used at the limits of Atterberg was removed and passed through the 0.42 mm sieve (ABNT # 40). The plasticity limit test was carried out in accordance with NBR 7180 [9], while the liquidity limit was carried out in accordance with NBR 6459 [10].

The determination of the real density of the grains was carried out according to NBR 6457 [11] and NBR 6458 [12], using the pycnometer.

The chemical composition was obtained through X-ray dispersive energy spectroscopy (EDX), in the SHIMADZU EDX 700 equipment. With the test it was possible to identify the quantities of each of the chemical elements present in the clay.

Three formulations were made for making ceramics. The reference using only clay, replacement of 10% of the clay mass per residue, and replacement of 20% of the clay mass per residue. For the incorporations of 10 and 20%, each of the three particle sizes of the residue was individually evaluated.

The ceramic formulations were molded by extrusion in the laboratory and burned in an oven at 750 °C.

After firing, immersion absorption, sorptivity, mechanical strength, and mortar adhesion tests were performed.

Results

Table 2 shows the granulometric distribution obtained by the residues and the clay used in the work for making the ceramics.

It can be seen from the figure that the waste used has three different granulometries. Granite 1, the finest among the residues, has a grain distribution similar to that of clay. Granite 2 has intermediate grain distribution, while granite 3 has the largest grain size distribution.

Table 3 shows the results of Atterberg limits and real grain density.

The real density of the grains of the different residue granulometries obtained were close results, and show some similarity with the clay. It was not possible to perform the Atterberg limit test with granite as it does not have sufficient plasticity for the test.

Table 4 presents the results of the chemical analysis of the residue and the clay.

Table 2 Particle size distribution of materials

Sample	Particle size percentages							
	Boulder			Sand			Sílte	Clay
	Gravel	Medium	Fine	Gravel	Medium	Fine		
Clay	–	–	–	0.3	1.2	5.9	31.9	60.7
Granite 1	–	–	0.3	0.6	1.9	5.2	34.1	57.9
Granite 2	–	–	1.1	1.3	1.2	5.6	42.3	48.5
Granite 3	–	1.2	0.9	2.0	2.1	8.1	69.4	16.3

Table 3 Atterberg limits and real grain density

	Clay	Granite 1	Granite 2	Granite 3
LL	47.5	–	–	–
LP	19.5	–	–	–
IP	28.0	–	–	–
Yg	2.82	2.65	2.64	2.65
USCS	CH	SM	CH	CH

Table 4 Chemical analysis

SAMPLE	Elements (%)								
	SiO_2	Al_2O_3	Fe_2O_3	K_2O	TiO_2	SO_3	CaO	BaO	Others
Clay	44.98	40.21	6.79	2.04	1.59	1.49	1.42	–	1.48
Granite 1	60.99	20.31	5.24	6.59	0.58	1.43	3.91	0.64	0.31
Granite 2	61.24	20.01	5.34	6.79	0.76	1.54	3.35	0.56	0.41
Granite 3	60.73	21.03	5.41	6.54	0.64	1.25	3.53	0.62	0.25

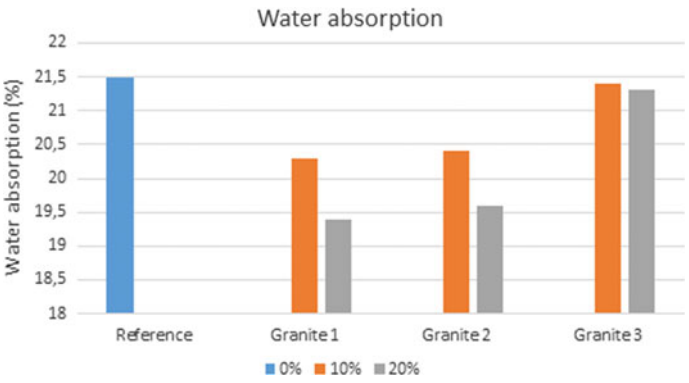

Fig. 1 Water absorption by immersion. (Color figure online)

The clay has an expressive composition of silicon oxide and aluminum, indicating a strong indication of the presence of clay minerals such as kaolinite ($Al_2O_3 \cdot 2SiO_2 \cdot 2H_2O$), which is commonly found in the region where the clay was collected. Granite, on the other hand, has a predominance of silica.

The results obtained by the ceramic in the immersion absorption test are illustrated in Fig. 1.

It can be seen from Fig. 1 results that the water absorption by immersion varies according to the level of incorporation and granulometry of the granite.

Granite 3, which has larger grains, showed greater absorption among the tested granulometries. Granite 1 and 2 showed similar absorption.

The level of incorporation also affected the absorption of water, but with less impact, by slightly increasing the absorption as the incorporation of the residue increases from 10 to 20%. It is noteworthy that both the 10 and 20% incorporations obtained absorption below the reference without residue.

Figure 2 shows the results of mechanical resistance.

Similar to what was verified in the absorption by immersion, the mechanical strength increased in relation to the reference in the same combinations where the absorption by immersion decreased in relation to the reference. This behavior can be justified by the porosity. In general, ceramics with greater porosity have greater absorption by immersion and less mechanical resistance, in the same way that ceramics with less porosity have less absorption by immersion and greater mechanical resistance.

Figure 3 shows the results of the sorptivity test.

It can be seen from the results that the absorptivity is influenced both by the granulometry of the residue and by the level of incorporation of the residue.

Granite 1 stands out with the highest absorptivity values, indicating that the ceramic has a large number of pores of reduced diameter, and therefore, greater capillarity. This effect was already expected by the low immersion absorption obtained by the reduced particle size of the residue.

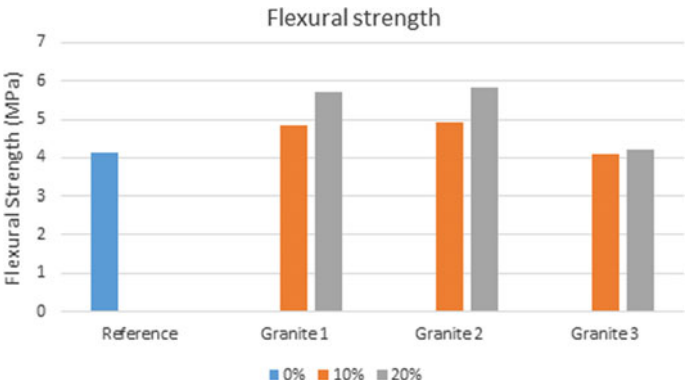

Fig. 2 Flexural strength. (Color figure online)

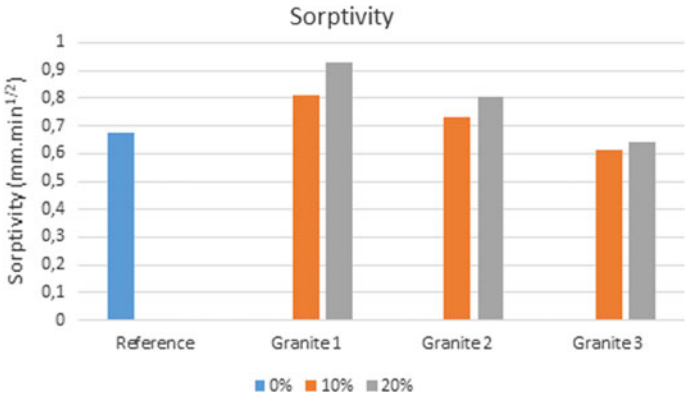

Fig. 3 Sorptivity. (Color figure online)

Granite 2 presents values higher than the reference, but lower than granite 1. In this test there is a differentiation of the results obtained between the granulometry of granite 1 and 2, which until then, obtained similar results.

Granite 3, on the other hand, showed lower values than the reference.

The increase in the level of incorporation from 10 to 20% increased the absorptivity for the three particle sizes of the residue.

Figure 4 shows the results of the adhesion test.

It can be seen from the results obtained, as the absorptivity test had found, that granite 1 significantly increases adherence with mortar. Granite 2 also showed an increase in adhesion in relation to the reference, but slightly lower than granite 1. Granite 3, on the other hand, presented values lower than the reference.

The increase in the level of incorporation of the residue also promoted an increase in adhesion for all granites used.

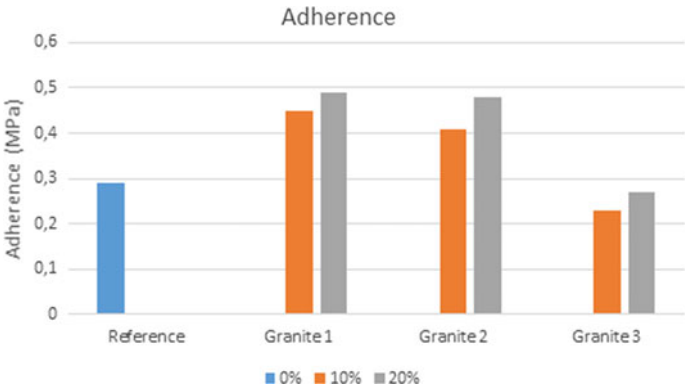

Fig. 4 Adherence. (Color figure online)

Conclusion

In this work, it was found that both the use of the residue significantly influences the physical properties of the ceramic where the following points can be highlighted.

- Granite 1, the finest among those tested, significantly decreases the porosity of the ceramic; consequently, the absorption by immersion is decreased, the mechanical resistance is increased, and both the absorptivity and the adhesion are increased.
- Granite 2, of intermediate granulometry, obtained results similar to granite 1 in absorption by immersion and resistance, but slightly lower in absorptivity and adhesion.
- Granite 3, of greater granulometry, performed less than the reference without residue. Similar immersion absorption and mechanical strength, but lower sorptivity and adhesion.
- The increase in incorporation from 10 to 20% of residue slightly enhances performance for all three granites tested.

Acknowledgements The authors thank the Brazilian agencies IFF, CNPq, CAPES, and FAPERJ for the support provided to this investigation.

References

1. ChiodiFilho C (2017) Balanço das Exportações e ImportaçõesBrasileiras de RochasOrnamentais em 2017. São Paulo: ABIROCHAS, 13p (Informen.01/2017). Brazilian Association of Public Cleaning Companies and Special Waste-ABRELPE 2014. (in Portuguese)
2. Santos PS (1989) Ciência e Tecnologia de Argilas, vol 1, 2ªedição; EditoraEdgardBlücherLTDA
3. Singh M, Choudhary K, Srivastava A, Sangwan KS, Bhunia D (2017) A study on environmental and economic impacts of using waste marble powder in concrete. J Build Eng 13:87–95

4. Singh Y, Vyas AK, Kabeer KISA (2017) Compressive Strength Evaluation of Mortars Containing ISF Slag and Marble Powder. Mater Today Proc 4(9):9635–9639
5. Munir MJ, Kazmi SMS, Wu Y, Hanif A, Khan MUA (2018) Thermally efficient fired clay bricks incorporating waste marble sludge: an industrial-scale study. J Clean Prod 174:1122–1135
6. Moreira JMS, Freire MN, Holanda JNF (2003) Utilização de resíduo de serragem de granito proveniente do estado do Espírito Santo em cerâmica vermelha. Cerâmica 49(312):262–267
7. Souza AJ, Pinheiro BCA, Holanda JNF (2010) Processing of floor tiles bearing ornamental rock-cutting waste. J Mater Process Technol 210(14):1898–1904
8. AssociaçãoBrasileira De NormasTécnicas (2016) ABNTNBR 7181. Soil-Grain size analysis. Rio de Janeiro
9. AssociaçãoBrasileira De NormasTécnicas (2016) ABNTNBR 6459. Soil-Liquid limit determination. Rio de Janeiro
10. AssociaçãoBrasileira De NormasTécnicas (2016) ABNTNBR 7180. Soil-Plasticity limit determination. Rio de Janeiro
11. AssociaçãoBrasileira De NormasTécnicas (2016) ABNTNBR 6458. Gravel grains retained on the 4.8 mm mesh sieve-determination of the bulk specific gravity, of the apparent specific gravity and of water absorption
12. AssociaçãoBrasileira De NormasTécnicas (2016) ABNTNBR 6457. Soil samples-preparation for compactation and characterization tests

Influence of the Incorporation of Granite Waste on the Weathering Resistance of Soil Pigment-Based Paints

Márcia Maria Salgado Lopes, Leonardo Gonçalves Pedroti, Gustavo Emilio Soares de Lima, José Carlos Lopes Ribeiro, Gustavo Henrique Nalon, Beatryz Cardoso Mendes, and André Luís de Oliveira Jr.

Abstract The reuse of granite waste in the manufacture of building paints is an alternative studied to contribute to sustainable development. Therefore, the objective of this study is to evaluate the influence of granite waste, acting as mineral filler, on the weathering resistance of soil pigment-based paints. To manufacture the paint samples, a mixture design of experiments was defined, varying the proportions of soil (pigment), granite waste (mineral filler), and polyvinyl acetate resin (binder). On the other hand, the water (solvent) was varied in each mixture, in order to keep a constant paint viscosity. The weathering resistance test was performed based on the specifications of ASTM G7:2013. A weekly monitoring was carried out to identify the appearance and development of pathological manifestations in the paint films. The color variation was quantified by the delta-E method. The paint film submitted to weathering was compared with the paint film protected from external agents. It was observed that the use of granite waste in soil pigment-based paints delays the appearance of pathological manifestations and reduces the color change of the product. Thus, it is possible to conclude that granite waste has a strong potential to be reused in the production of paints.

Keywords Granite waste · Paint · Soil · Weathering resistance

Introduction

In recent years, Brazil has stood out in the group of major world producers and exporters in the ornamental stone sector. This implies a great concern with the waste generated in this industrial sector, because when these wastes are improperly deposited, they cause damage to the environment and human health [3].

In general, the waste is obtained from several stages of the process of beneficiation of ornamental stones of granitic origin (granites, gabbros, and gneisses), such as the

M. M. S. Lopes (✉) · L. G. Pedroti (✉) · G. E. S. de Lima · J. C. L. Ribeiro · G. H. Nalon · B. C. Mendes · A. L. de Oliveira Jr.
Federal University of Viçosa, Viçosa, Brazil
e-mail: lopes.marcia1993@gmail.com

J. Li et al., *Characterization of Minerals, Metals, and Materials 2021*,
The Minerals, Metals & Materials Series,
https://doi.org/10.1007/978-3-030-65493-1_47

stages of sawing the stone blocks and polishing the plates. During this industrial process, fine particles of granite and water mix and form a mud [4].

Since the civil construction sector consumes a huge volume of natural resources, it is an interesting option for reusing tailings [5]. One of the possibilities for disposal of granite waste is its application in paints as an inert pigment. Inert pigments, mineral fillers, or extenders are chemically stable minerals that can be extracted from deposits or obtained by industrial processes. These minerals must have adequate characteristics of whiteness and granulometry, in addition to low cost. They are incorporated into the paint for technical specifications or just for economic reasons, and can collaborate to improve certain properties of the product, such as the film's mechanical resistance, chemical and weather resistance, porosity, permeability, washability, flexibility, covering power, brightness, uniformity and color development, dispersion, rheology in production, storage, and application [6].

Paints with soil as pigment are often used by the needy people because the soil can be considered a cheap pigment. It is easily accessible and obtainable, which decreases the cost of the paint and contributes to the product sustainability [7].

There are several ways to test the performance and durability of paints. Among them, the natural weathering test is the one that best simulates the real behavior of the paint throughout its useful life. This is because the coating is exposed to all aggressive factors, such as sunlight, rain, humidity, air pollutants, and temperature fluctuations [8, 9]. Therefore, the objective of the present work is to study the influence of granite waste, acting as a mineral filler, in the weathering resistance of building paints with soil pigments.

Materials and Methods

Materials

Two types of soils were collected in the city of Viçosa (Minas Gerais—MG, Brazil): the yellow ocher type and the red ocher type. The granite waste was supplied by the company Decolores Mármores & Granitos, located in the southern region of the state of Espírito Santo, Brazil. It was obtained through the diamond wire cutting process and subjected to the moisture loss treatment in filter press equipment.

The soils and granite waste were subjected to a treatment of de-agglomeration and mechanical dispersion of the particles in an aqueous medium, using the Cowles disk coupled to a mechanical stirrer, at a speed of 1500 rpm. Then, the screening was carried out in a wet environment, using an ASTM 80 mesh (0.177 mm opening), as recommended by Cardoso et al. [7].

The solvent chosen was water and the binder vehicle selected was the polyvinyl acetate resin (PVA) produced by Cascorez (Universal category).

Characterization of Raw Materials

The soils and granite waste were characterized after being subjected to de-agglomeration, dispersion, and sieving processes. For physical characterization, granulometry [10], particle density [11], and specific surface area (through the BET method, using the Quantachrome NOVA equipment and nitrogen adsorption) were determined. For mineralogical characterization, X-ray diffraction (XRD) was performed, using a X'Pert Pro MPD diffractometer (Panalytical) with Co-Kα radiation ($\lambda = 1.789$ Å). Finally, for morphological characterization, scanning electron microscopy (SEM) was performed, using a Leo 1430VP equipment.

Preparation of Paints

To determine the proportions of the materials, a mixture design of experiments was developed. The independent variables of the mix planning were the soil and granite waste pigments, ranging from 0 to 80%, and the resin, ranging from 20 to 40% (considering the total resin, that is, volatile and non-volatile). These ranges of variation were defined according to the study of Silva and Uemoto [12] and according to the values of pigment volume concentration (PVC) expected for economical matte paints, which vary from 55 to 80% [13].

The experimental design was developed in extreme vertices of degree three (complete cubic), with three components and additional central and axial points, using the Minitab® 17 software. The formulations of the paints are presented in Table 1. This design was reproduced twice. In the first one, yellow soil pigments were used, while red soil pigments were used in the second experimental design.

Table 1 Proportions of paints generated by the statistical software Minitab® 17, in mass

Id	Resin	Soil pigment	Granite waste pigment
1	0.200	0.800	0
2	0.300	0.700	0
3	0.400	0.600	0
4	0.250	0.575	0.175
5	0.350	0.475	0.175
6	0.200	0.400	0.400
7	0.300	0.350	0.350
8	0.400	0.300	0.300
9	0.250	0.175	0.575
10	0.350	0.175	0.475
11	0.200	0	0.800
12	0.300	0	0.700
13	0.400	0	0.600

In addition, the water content varied in each mixture, in order to keep the viscosity within a constant range. After a series of preliminary tests, it was defined that the kinematic viscosity considered ideal for the application of the studied paints corresponds to the flow time of 12 ± 1 s, measured by the Ford glass viscometer with hole number 4 [14].

For the production of the paint samples, a certain amount of soil pigments and granite waste was mixed with the water and the PVA resin, according to the proportions defined in Table 1. The Cowles disc coupled to a mechanical stirrer at a speed of 500 rpm was used. Then, the viscosity of the mixture was measured with the Ford glass viscometer, provided with a number 4 hole. When necessary, corrections of paint viscosity were made through the addition of one or more components to the mixture. It should be noted that these corrections have always respected the proportions defined in Table 1.

The Weathering Resistance of Paints

The weathering resistance test was performed based on the specifications of ASTM G7 [15], with appropriate adaptations. Mortar boards, composed of cement, lime, and sand, 1:1:6 (by volume), were used as substrate for the application of paints. Such boards had an area of 20×40 cm^2 and a thickness of 2.5–3.0 cm, representing the external coating used in the constructions. Each of the paint samples was applied on a mortar board, in a total of three coats, according to the specifications of the manufacturers of latex paints of the economic category. These plates were then fixed, randomly, in a wooden structure (Fig. 1a). This structure was oriented to the north with an inclination of 20° in relation to the vertical direction, since the city of Viçosa-MG is at a latitude of 20° 45′ 14″ S. In this way, the paint films were exposed to the maximum incidence of radiation. Finally, the properly painted mortar plates

Fig. 1 Test of paint weathering resistance: **a** before fixing the metal plate; **b** after fixing the metal plate. (Color figure online)

were partially covered with a metal plate (Fig. 1b) so that only half of the dry paint film was exposed to weathering.

The weathering resistance test started on July 10, 2017 and lasted for one year. Monitoring was carried out weekly through visual inspection and image recording, seeking to identify the appearance and development of pathological manifestations in the paint films. The observed changes were linked to temperature and precipitation data obtained from the Main Climatic Station of Viçosa [16, 17]. In addition, at the end of the test, the metal sheets were removed, allowing the comparison between the part subjected to weathering and the part protected by the metal sheets. This comparison was made by determining the color difference, using the delta-E method.

The delta-E method consists of quantitatively obtaining the difference between two colors in the RGB system. The delta-E is a value between 0 and 100, which represents the difference in Euclidean distance between the red, green and blue spectra of an RGB. This is the method adopted by the International Lighting Commission, as it is the one that best represents the perception of color by human beings [1, 19]. The RGB value of the protected paint film and the film exposed to weathering was determined from the average of the RGB values of ten points randomly chosen from each of the studied parts, using the Photoshop® software. Then, the delta-E between the protected and exposed parts of each sample was determined using the Delta-E Calculator software [20].

Results and Discussion

Characterization of Raw Materials

Table 2 shows the results of the physical characterization of the waste and the soils. Regarding the granulometry, it is observed that the red soil is very clayey and the yellow soil is clayey silt. The granite waste has particles predominantly similar in size to the silt fraction. According to the values of average diameter (D50) presented in this table, the granite waste presents particle sizes higher than the particles of the soil. However, the particle diameter of a mineral filler can vary up to 15 μm when it is used in paints [21].

Table 2 Physical characterization of pigments

Pigment	Particle density (g/cm^3)	Specific surface area (m^2/g)	Granulometry (%)			Average diameter (μm)
			Clay	Silt	Thin sand	
Granite waste	2.56	4.42	13.1	73.1	13.8	10
Yellow soil	2.46	34.55	37.5	48.4	14.2	5.5
Red soil	2.65	48.14	63.8	21.9	14.3	<1

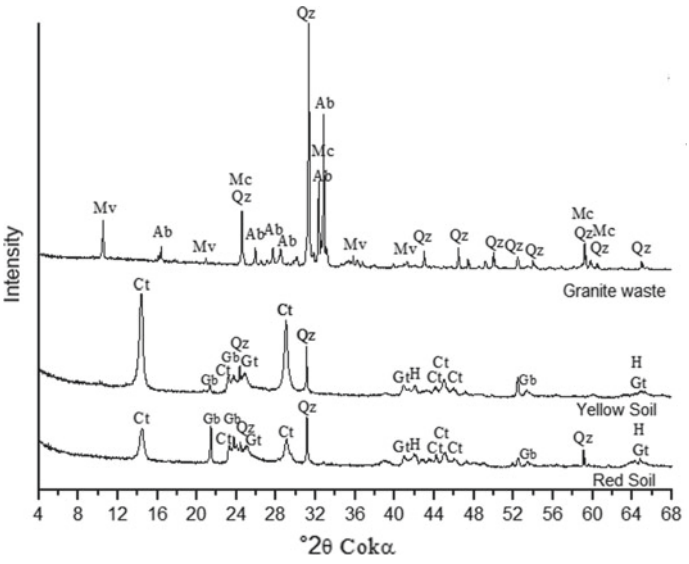

Fig. 2 XRD result of pigments

Regarding the specific surface area, it is observed that the granite waste has a specific surface area much lower than that of the soil. This characteristic provides the manufacture of more economical paints, since the greater the specific surface area of the grains, the greater the amount of resin needed to completely cover the pigment particles in the dry paint film [22].

In addition, the XRD results of those materials are shown in Fig. 2. It seems that the waste has more intense peaks of quartz and albite and less intense peaks of muscovite and microcline. The yellow soil has more intense peaks of kaolinite and quartz, and peaks of low intensity of gibbsite, goethite, and hematite. The red soil has more intense kaolinite, gibbsite, and quartz peaks and some less intense peaks of goethite and hematite.

Subtitle: Ab—Albite ($NaAlSi_3O_8$); Ct—Kaolinite ($Al_2Si_2O_5(OH)_4$); Gb—Gibbsite ($Al(OH)_3$); Gt—Goethite ($FeO(OH)$); H—Hematite (Fe_2O_3); Mc—Microcline ($KAlSi_3O_8$); Mv—Muscovite ($KAl_2Si_3AlO_{10}(OH.F)_2$); Qz—Quartz ($SiO_2$).

Regarding the morphological characterization, the granite waste (Fig. 3a) is a material that has a varied diameter distribution, composed of particles with irregular morphology and angular corners. The yellow soil (Fig. 3b) consists of lamellar and granular particles of different sizes, such as kaolinite and iron oxides, respectively. The red soil (Fig. 3c) is shaped mostly by granular particles of very small dimensions, such as iron oxides, which naturally tend to agglomerate. According to Karakas, Hassas, and Celik [23], the shape and size of the particles interfere in their packaging and, consequently, in the properties of the paint film.

Regarding the weathering resistance test, Fig. 4 shows the images of the mortar boards covered with the paint samples, at the end of one year of exposure. Table 3

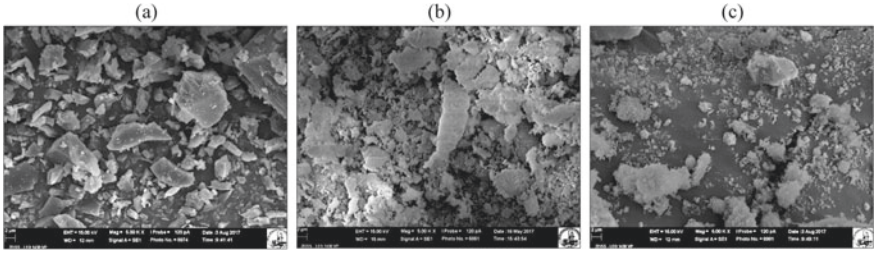

Fig. 3 SEM of pigment particles: **a** granite waste; **b** yellow soil; **c** red soil (Mag. = 5000 X; Scale bar = 2 μm)

Fig. 4 Result of the weathering test of paint samples after one year of exposure. (Color figure online)

shows the color difference results, quantified by the delta-E parameter, between the half of the protected paint film and the half exposed to the weather of all studied samples. This table also presents the pathological manifestations identified in the paint samples, over the year of exposure.

Regarding the meteorological data recorded from July 2017 to July 2018 in Viçosa, there was an average annual temperature of 20 °C, with a minimum value of 5.5 °C (in May 2018) and a maximum value of 34.5 °C (in October 2017). Regarding annual precipitation, an annual average of 1.3 mm and maximum was observed in November (79.4 mm) and December (87.2 mm) of 2017.

Figure 4 and Table 3 show that pathological manifestations were not observed in yellow soil pigment-based paints and most of the red soil pigment-based paints. In red soil-based paints with low contents of granite waste, however, microcracks and peeling were observed. Microcracks appeared during the drying phase and intensified

Table 3 Color difference (delta-E) and pathological manifestations identified in paint samples containing yellow soil and red soil

Id	Yellow soil pigment-based paints			Red soil pigment-based paints		
	Color change (delta-E)	Pathological manifestations		Color change(delta-E)	Pathological manifestations	
		Microcracks	Stripping		Microcracks	Stripping
1	3.30	Absent	Absent	27.07	Present	Present
2	2.95	Absent	Absent	13.36	Present	Present
3	2.44	Absent	Absent	7.21	Present	Present
4	2.36	Absent	Absent	10.87	Present	Present
5	1.51	Absent	Absent	4.51	Present	Present
6	2.23	Absent	Absent	4.89	Absent	Absent
7	1.54	Absent	Absent	4.4	Absent	Absent
8	1.26	Absent	Absent	4.14	Absent	Absent
9	1.92	Absent	Absent	2.04	Absent	Absent
10	1.57	Absent	Absent	1.52	Absent	Absent
11	2.74	Absent	Absent	2.74	Absent	Absent
12	1.42	Absent	Absent	1.42	Absent	Absent
13	1.38	Absent	Absent	1.38	Absent	Absent

with temperature variations. Peeling appeared due to heavy rains. Figure 5 shows images of sample 1 of red soil pigment-based paints with different ages. It exemplifies that the appearance of the microcracks (Fig. 5a) occurred, predominantly, in months when the precipitation was null and the temperature variations were considerable. Peeling (Fig. 5b) was verified when the rainfall was significant. Such pathological manifestation evolved in the following weeks, as shown in Fig. 5c, in accordance with the occurrence of precipitations.

Microcracks generally precede peeling and may be the result, among other factors, of exaggerated dilution of the paint or low levels of resin, which offer little adhesion and flexibility to the film [24, 25]. It can be seen that the red soil has a predominantly

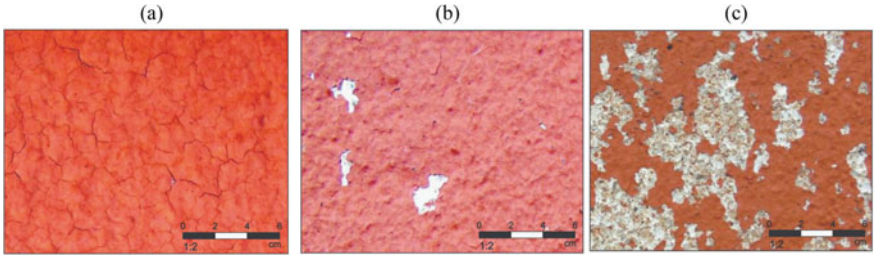

Fig. 5 Red soil pigment-based paint (sample 1): **a** after 5 weeks of exposure; **b** after 20 weeks of exposure; **c** after 23 weeks of exposure. (Color figure online)

clay granulometry and a high specific surface area (Table 2), which shows the need for high levels of resin to involve the pigment particles and high water absorption.

It is also observed that, in addition to the granite waste content, the proportion of resin also influenced the emergence of pathological manifestations, and the greater the amount of resin, the lesser the defects in the paint films. According to Somturk et al. [26], the increase in the volume of binder makes pigments more protected, which results in paints with greater UV resistance and greater weathering resistance. It is exemplified in Fig. 6. Samples 1 (Fig. 6a), 2 (Fig. 6b), and 3 (Fig. 6c) do not have granite waste pigments in their constitutions and have increasing levels of PVA resin. Note that, in sample 1, the paint film is more damaged, followed by sample 2 and, finally, sample 3.

In addition to the microcracks and peeling, the color difference between the half of the protected paint film and the half exposed to weathering was also studied, being quantified by the delta-E method. Table 3 indicates that red soil pigment-based paints showed the greatest color differences. According to Polito [25], fading usually occurs on surfaces constantly exposed to sunlight, with reddish paintings being one of the most affected. Figure 7 exemplifies the color differences when the granite waste was added to the mixture, keeping the resin content constant. Note that the higher the percentage of granite waste present in the mixture, the lower the delta-E values.

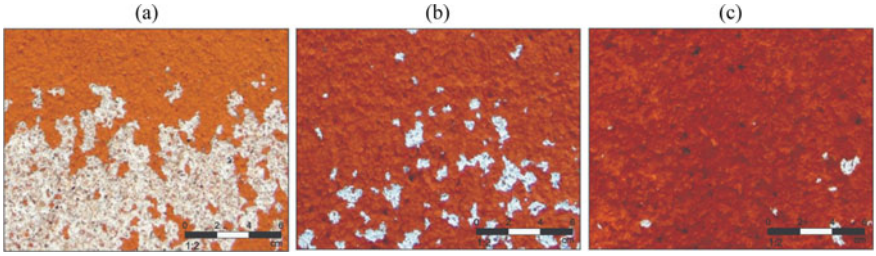

Fig. 6 Red soil pigment-based paints, with variation in the percentage of resin, after one year of exposure: **a** sample 1; **b** sample 2; **c** sample 3. (Color figure online)

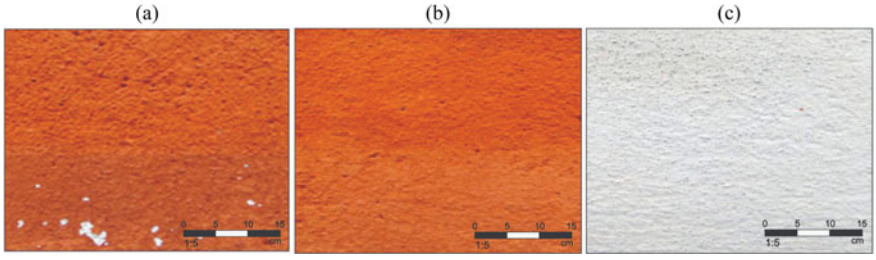

Fig. 7 Red soil pigment-based paints, with variation in the percentage of waste, after one year of exposure: **a** sample 2; **b** sample 7; **c** sample 12. (Color figure online)

Table 3 shows the delta-E results. According to ColorMine [20], delta-E values lower than 2 do not present a noticeable color difference. Table 4 and Fig. 11 show that only formulations with high levels of granite waste satisfy this specification, in the case of yellow and red soil pigment-based paints. It shows that the granite waste slows the appearance of pathological manifestations and reduces the fading of the studied paints. This result is probably due to the high levels of silica in the composition of the granite waste. Silica is highly inert and forms a barrier that prevents the penetration of aggressive agents [27]. However, this result does not mean that soil-based paints with small amounts of granite waste cannot be used. It just means that these paints are recommended for indoor environments, where they will be protected from the agents responsible for weathering.

Conclusions

This research was developed to explore the use of granite waste as mineral filler for soil-based paint production. Based on the results obtained by means of the proposed methodology, it can be concluded that the higher the granite waste content in the soil-based paint composition, the greater the product's weathering resistance. The use of granite waste in soil-based paints delays the appearance of pathological manifestations and reduces the color change of the product.

Acknowledgements The authors thank the CNPq for the support provided to this investigation.

References

1. Sardou Filho R, Matos GMM, Mendes VA, Iza ERHF (2013). Atlas of ornamental rocks of the state of Espírito Santo. Brasília, Brazil. (in Portuguese)
2. Brazilian Association of the Ornamental Stones Industry–Abirochas (2017) Balance of Brazilian Imports and Exports of Ornamental Stones in the 1st Semester of 2017. https://www.abirochas.com.br/noticia.php?eve_id=4195. Accessed 17 Aug 2002. (in Portuguese)
3. Almeida N, Branco F, Santo JR (2007) Recycling of stone slurry in industrial activities: application to concrete mixtures. Build Environ 42:810–819. https://doi.org/10.1016/j.buildenv.2005.09.018
4. Singh S, Nagar R, Agrawal V (2016) A review on properties of sustainable concrete using granite dust as replacement for river sand. J Clean Prod 126:74-87https://doi.org/10.1016/j.jclepro.2016.03.114
5. Blankendaal T, Schuur P, Voordijk H (2014) Reducing the environmental impact of concrete and asphalt: a scenario approach. J Clean Prod 66:27–36. https://doi.org/10.1016/j.jclepro.2013.10.012
6. Fazenda JMR (2009) Paints and varnishes: science and technology, 4th edn. São Paulo, Edgard Blücher. (in Portuguese)

7. Cardoso FP, Alvarenga RCSS, Carvalho AF, Fontes MPF (2016) Production process and evaluation of performance requirements of soil pigments based paint for buildings. Ambiente Construído 16(4):109–125. https://doi.org/10.1590/s1678-86212016000400112. (in Portuguese)
8. Jacques LFE (2000) Accelerated and outdoor/natural exposure testing of coatings. Prog Polym Sci 25:1337–1362. https://doi.org/10.1016/S0079-6700(00)00030-7
9. Fekete E, Lengyel B (2005) Accelerated testing of waterborne coatings. Prog Org Coat 54:211–215. https://doi.org/10.1016/j.porgcoat.2005.06.007
10. Brazilian Association of Technical Norms (2016) NBR 7181–Soil–Grain size analysis. Rio de Janeiro, Brazil. (in Portuguese)
11. EMBRAPA (1997) Guide of soil analysis methods. Rio de Janeiro, Brazil. (in Portuguese)
12. Silva JM, Uemoto KL (2005) Characterization of latex paints for civil construction: diagnosis of the market of the state of São Paulo, Technical Bulletin, Polytechnic Institute of the University of Sao Paulo, Brazil. (in Portuguese)
13. Tiarks F, Frechen T, Kirsch S, Leuninger J, Melan M, Pfau A, Richter F, Schuler B, Zhao CL (2003) Formulation effects on the distribution of pigment particles in paints. Prog Org Coat 48:140–152. https://doi.org/10.1016/S0300-9440(03)00095-X
14. Brazilian Association of Technical Norms (2015) NBR 5849–Paints–Determination of viscosity by Ford glass. Brazil, Rio de Janeiro. (in Portuguese)
15. American Society for Testing Materials (2013) ASTM G7–G7M-13-Standard Practice for Atmospheric Environmental Exposure Testing of Nonmetallic Materials. ASTM International, West Conshohocken, PA
16. Universidade Federal De Viçosa–UFV (2017) Main Climatic Station of Viçosa. Weather report 2017. Viçosa, Brazil. (in Portuguese)
17. Universidade Federal De Viçosa–UFV (2018) Main Climatic Station of Viçosa. Weather report 2018. Viçosa, Brazil. (in Portuguese)
18. Baldevbhai PJ, Anand RS (2012) Color image segmentation for medical images using L*a*b* color space. IOSR J Electron Commun Eng 1(2):24–45
19. Galvão JLB, Matias ACP, Silva KDC, Silva GJB, Peixoto RAF, Mendes JC (2017) Sustainable real estate paints based on iron ore dam tailings. In: Proceedings of the 59th Brazilian Concrete Congress. (in Portuguese)
20. COLORMINE. Delta-E Calculator. ColorMine.org, 2018. https://colormine.org/delta-e-calculator/. Accessed 18 Jan 09. (in Portuguese)
21. Oates JAH (2008) Lime and limestone: chemistry and technology. Production and Uses, Buxton, Wiley-VCH
22. Karakas F, Celik MS (2012) Effect of quantity and size distribution of calcite filler on the quality of water borne paints. Prog Org Coat 74:555–563. https://doi.org/10.1016/j.porgcoat.2012.02.002
23. Karakas F, Hassas BV, Celik MS (2015) Effect of precipitated calcium carbonate additions on waterborne paints at different pigment volume concentrations. Prog Org Coat 83:64–70. https://doi.org/10.1016/j.porgcoat.2015.02.003
24. Paquette E, Poulin P, Drettakis G (2002) The simulation of paint cracking and peeling. In: Proceedings of Graphics Interface 10
25. Polito G (2006) Main painting systems and their pathologies. Federal University of Minas Gerais, Belo Horizonte, Brazil. (in Portuguese)
26. Somturk SM, Emek IY, Senler S, Eren M, Kurt SZ, Orbay M (2016) Effect of wollastonite extender on the properties of exterior acrylic paints. Prog Org Coat 93:34–40. https://doi.org/10.1016/j.porgcoat.2015.12.014
27. Ahmed NM, Abdel-Fatah HTM, Youssef EA (2012) Corrosion studies on tailored Zn·Co aluminate/kaolin core–shell pigments in alkyd based paints. Prog Org Coat 73:76–87. https://doi.org/10.1016/j.porgcoat.2011.09.003

Influence of the Mixing Processes of the Constituents of Incorporated Geopolymer Materials with Glass Waste

L. R. Cruz, A. R. G. Azevedo, M. T. Marvila, A. S. A. Cruz, J. A. T. L. Júnior, N. A. Cerqueira, S. N. Monteiro, and C. M. F. Vieira

Abstract During the production of geopolymeric materials a great challenge exists when it comes to the process of dosing and mixing the constituents, called activators and precursors. In addition, these materials have a great potential for incorporating different solid waste. The objective of this work was to evaluate the different ways of mixing the constituents of the geopolymer materials, evaluating the influence of these variations in the mixing process, molding and curing temperature of the mixtures, and incorporating the glass waste as an activator of the mixture with a molar ratio of 3.5. Prismatic specimens were made and properties such as mechanical resistance

L. R. Cruz · A. R. G. Azevedo (✉) · A. S. A. Cruz
LECIV – Civil Engineering Laboratory, UENF - State University of the Northern Rio de Janeiro, Av. Alberto Lamego, 2000, Campos dos Goytacazes, Rio de Janeiro 28013-602, Brazil
e-mail: afonso.garcez91@gmail.com

L. R. Cruz
e-mail: lucasreis1550@gmail.com

A. S. A. Cruz
e-mail: ariana.sazeredo@gmail.com

M. T. Marvila · J. A. T. L. Júnior · C. M. F. Vieira
LAMAV – Advanced Materials Laboratory, UENF - State University of the Northern Rio de Janeiro, Av. Alberto Lamego, 2000, Campos dos Goytacazes, Rio de Janeiro 28013-602, Brazil
e-mail: markssuel@hotmail.com

J. A. T. L. Júnior
e-mail: tosteslinhares@gmail.com

C. M. F. Vieira
e-mail: vieira@uenf.br

N. A. Cerqueira
UNIREDENTOR - Redentor University Center, BR 356, 25 - Pres. Costa e Silva, Itaperuna, Rio de Janeiro 28300-000, Brazil
e-mail: coord.niander@gmail.com

S. N. Monteiro
Department of Materials Science, IME - Military Institute of Engineering, Square General Tibúrcio, 80, Rio de Janeiro 22290-270, Brazil
e-mail: snmonteiro@gmail.com

J. Li et al., *Characterization of Minerals, Metals, and Materials 2021*,
The Minerals, Metals & Materials Series,
https://doi.org/10.1007/978-3-030-65493-1_48

to flexion, linear shrinkage, and water absorption were evaluated for each condition evaluated. It can be concluded that the order of insertion of the components in the mixture, as well as the molding mode and cure temperature directly influence the technological properties of the specimens.

Keywords Geopolymer · Glass waste · Processes

Introduction

Geopolymeric materials are composed of elements rich in SiO_2 and Al_2O_3 in an amorphous state, called precursors, and of an alkaline activating solution, with different formulations, which in combination encourage the occurrence of reactions called geopolymerization [1]. These materials can be used as a substitute for other construction materials, such as cement-based (mortars and concrete) and ceramics (tiles and blocks). In addition to presenting a series of advantages, such as the high resistance that is obtained in a few curing times, high durability and stability under fire exposure conditions [2–4] are other positive points. In its application to replace traditional ceramic materials, there is no need for the sintering step, that is, there is a great energy saving in the consolidation and hardening process of the ceramic mass [3].

The use of geopolymers has become popular in many countries around the world and its use includes everything from decorative artifacts, thermal insulation to construction materials, such as ceramic tiles, concrete, and mortar [2, 5]. There are also environmental advantages for its use, such as reducing CO_2 emissions and saving natural raw materials [5]. The term "geopolymer" was used in Davidovits patents in 1979 to describe a family of mineral binders similar to artificial zeolites, due to their structure (Si–O-Al) [6].

The various industrial activities generate, every day, greater quantities of solid waste, which are disposed of in industrial sanitary landfills and have their transportation and disposal costs paid by the companies that generate this waste [7]. Environmental legislation for the disposal of solid waste has become more stringent worldwide. On the other hand, the areas available for the construction and expansion of landfills are increasingly scarce, thus encouraging research aimed at the reuse of waste solids [8].

The glass production industry is one that generates large amounts of waste, and only the construction sector consumes a significant amount of flat glass. In its production and polishing process, the glass industry generates waste which is disposed of in landfills after undergoing a process of decanting [8].

The concept of circular economy has been highlighted, as the waste that traditionally err in landfills is reused and is now being integrated into new production chains, such as in the production of civil construction materials [9]. Many researches have already been developed with this theme, showing the great potential that ceramic and cementitious materials have to reinsert solid industrial waste. However, geopolymeric materials also have this advantage, but it is still little explored [3, 5, 8].

A major problem when it comes to geopolymeric materials is due to the difficulty of obtaining a standardized process of mixing, processing, and dosing. This process is not sufficiently described in the literature and hinders its application on a larger scale [5]. Some research gaps arise [3, 5], for example, if the mixing process of the constituent materials (activators and precursors) changes or even influences the properties of the hardened material? Which type of cure and time do you have an impact on? What about the temperature of the molding and curing? These are the questions that are still poorly answered in the literature of these materials, especially those that incorporate industrial solid waste [9].

Therefore, the objective of this work was to evaluate the different forms of mixing of the constituent materials of the geopolymeric artifacts, evaluating the influence of the variations in the mixing process (order of placement of the materials), molding temperature, and curing of the mixtures, incorporating the waste of the mixture, lapidation of flat glass as an activating element of the mixture and metakaolin and sand as precursors, with a molar ratio of 3.5.

Materials and Methods

The materials used in this research were Metacaulim, from the HP ULTRA brand as the precursor to the mixture, and the waste from polishing flat glasses, along with water, as an activating solution. The glass polishing waste was obtained in a materials processing industry located in the municipality of Campos dos Goytacazes, Rio de Janeiro, Brazil. The waste was collected from settling tanks, in the form of a sludge, and went through a drying process, removal and screening in the laboratory, in order to obtain a very fine granulometry (200 mesh sieve) [5]. Another material used was natural sand, collected from the river bed, and sieved, for its use as a correction of the dosage in the precursor materials, forming a granulated mixture.

Traditionally, geopolymeric materials are made using a mixture of granulated part (precursors) with the activating solution, which is made 24 h in advance in a bottle that must be hermetically closed, right after the materials are mixed in a homogenizing equipment for about 20 min, allowing the molding of the specimens. This process was referred to in this work as reference [10].

The proposed alternative process, called model 1, consisted of mixing all materials (activators and precursors) in the form of grains, forming a single granular mixture, which is mixed with water in the appropriate proportion, using the mechanical mixer for about 10 min, to perform the molding of the specimens.

Regarding the temperature and curing time, room temperature (around 23 °C) and thermal curing in an oven (70 °C), with 3 and 7 days of curing, were evaluated for the molding and reference conditions, type 1 [5]. The specimens made were prismatic, measuring 115 × 20 × 3 mm where the prepared mass was poured into the acrylic molds (Fig. 1).

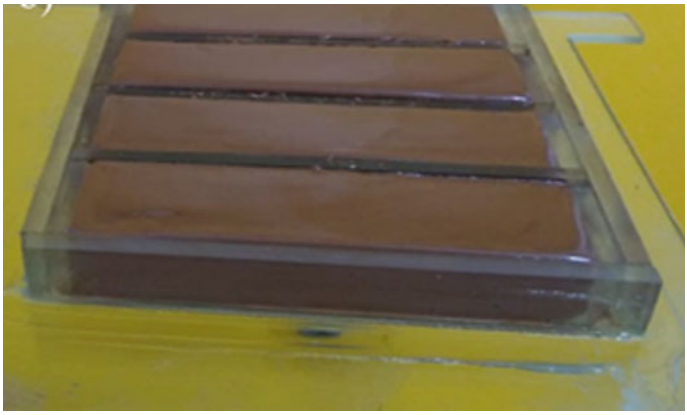

Fig. 1 Specimens molded in an acrylic container. (Color figure online)

All mixtures produced fixed molar ratio of 3.5 and the geopolymeric mass was prepared using materials ratio solution/precursor of 0.26. Table 1 shows the processing information of different mixtures.

After molding and curing the geopolymerized specimens, they were subjected to analysis of mechanical strength to flexion, linear mold retraction, and water absorption. The mechanical strength to flexion was determined using a press of EMIC brand, with a loading rate of 0.5 mm/min. The prismatic specimens were placed on a support to perform a three-point flexion test, according to the technical standard [11]. Linear retraction was measured by comparing the dimension of length, width, and height, before placing the specimens in the curing condition and after the curing time, the result of which was in terms of percentage increase and/or shrinkage of the specimens [5].

Water absorption was performed after the total curing time, immersing the specimens in a water tank at room temperature and buying the mass values obtained before and after submersion in water, in accordance with the technical standard for this test [12].

Table 1 Nomenclature of the mixtures performed

Materials processing	Curing temperature	Curing time	Name
Reference	23 °C	3 days	REF23-3
		7 days	REF23-7
	70 °C	3 days	REF70-3
		7 days	REF70-7
Model 1	23 °C	3 days	MOD23-3
		7 days	MOD23-7
	70 °C	3 days	MOD70-3
		7 days	MOD70-7

Results and Discussion

After the rupture of the prismatic specimens, the values of the mechanical strength to flexion, in MPa, were obtained, as can be seen in Fig. 2.

The results shown in Fig. 2 indicated that the cure thermal, that is, when the specimens were subjected over at a temperature control of 70 °C obtained a greater mechanical strength to flexion, because during that period the reactions geopolymerization have been enhanced. Another point that deserves to be highlighted is that the new model of mixing the materials (model 1) causes a reduction of this property, since the activating solution only begins to rule with longer exposure times, differently from the reference situation, in which the solution is made 24 h in advance, so the kinetics of reactions are favored in this process [13].

Regarding the curing period, as expected and according to other works in the literature, there is an increase in strength with longer curing times. This growth is relatively small, which may suggest that in curing times three-day specimens can be used. This is beneficial in terms of reducing the cost of applying geopolymer materials [3, 5]. In Fig. 3, it is possible to observe the linear retraction during the curing period of the specimens.

In Fig. 3, the results of linear shrinkage were observed. Some studies in the literature have already indicated that a limit of 2% of shrinkage can be tolerated for applications in some construction materials, such as ceramics [13]. Thus, it was observed that in the case of thermal curing there is an increase in retraction, caused by the buffering effect of the geopolymeric matrix, which causes a greater change in the dimensions of the specimens. As in the case of curing at 70 °C for 7 days the

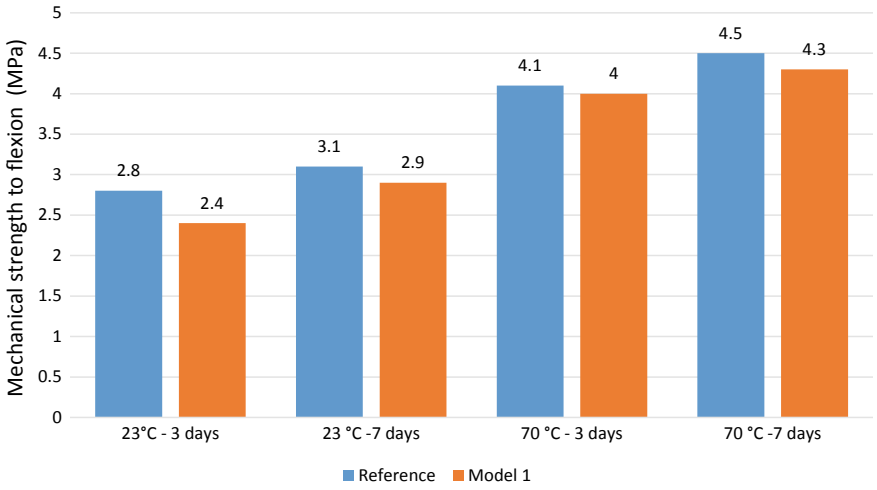

Fig. 2 Result of mechanical strength to flexion, in MPa. (Color figure online)

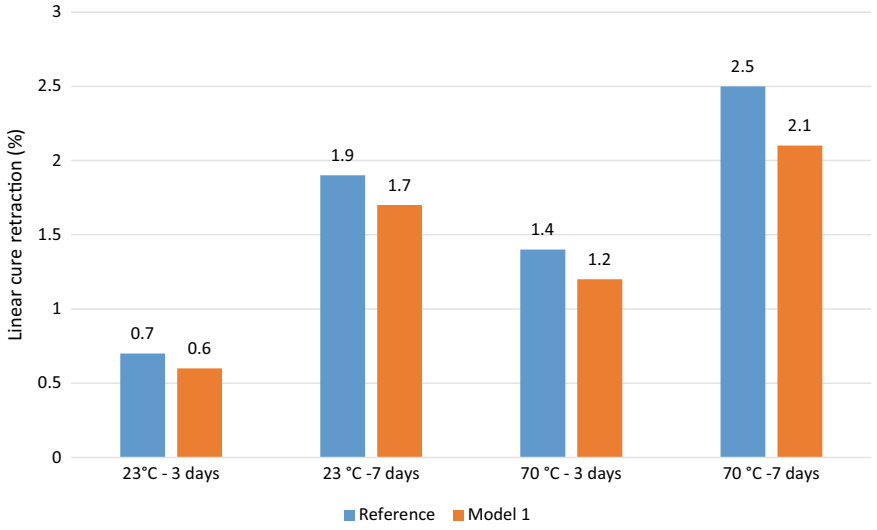

Fig. 3 Linear cure retraction, in %. (Color figure online)

values found are given in Fig. 3. For this property the thermal curing may not be an alternative, which in addition to non-compliance causes an increase in the energy costs of the production process [4, 5].

The temperature of 23 °C with a curing period of 3 days was the one that showed the least retraction, and the comparison between the mixing processes is practically equal, 0.7 and 0.6, respectively for the reference and for the model 1. Figure 4 shows the result of water absorption by simple immersion.

Figure 4 shows the results of water absorption, indicating that processing mode 1 reduces this parameter. This is mainly due to the greater pore filling effect of the geopolymeric matrix, caused by the greater variety of granulometry of the dry mass, before mixing, which contributes to an increase in compactness, further favored after adding the solution. Thermal curing also favors a reduction in these water absorption parameters, due to the higher geopolymeric reaction speed of the matrix [4].

A limit in the literature is that 5% absorption can be applied to some sealing materials in the construction industry, but in other applications, such as tiles, this value can be changed [3]. In general, the values found are within the basic Brazilian normative limits [12].

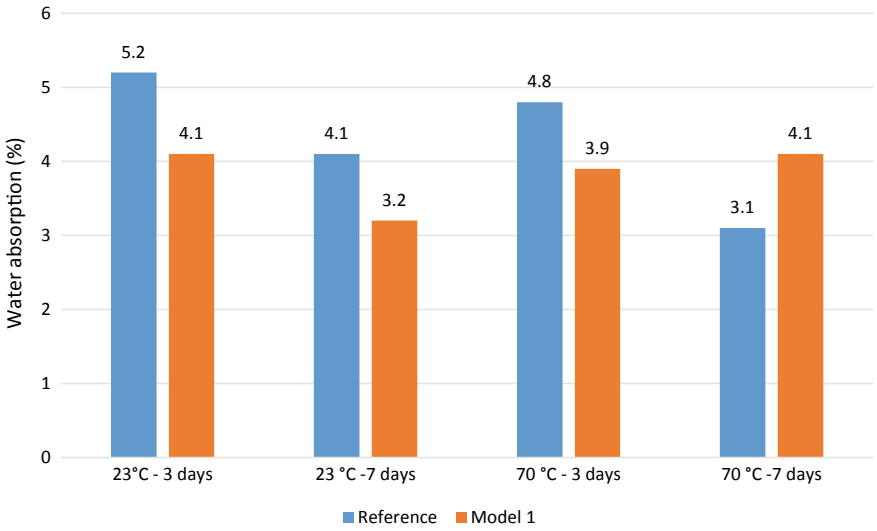

Fig. 4 Water absorption in %. (Color figure online)

Conclusions

After discussing the results, it can be concluded that:

- It is possible to use another methodology, alternative, for mixing and processing the geopolymer materials, allowing a time gain, since the solution does not need to be prepared in advance of 24 h. In addition, the use of geopolymeric materials can be an important tool to gain technological properties and increase the use of these materials;
- Thermal curing, despite guaranteeing greater resistance, does not bring significant advances in the other evaluated practices; therefore, its implementation is not justified from a financial perspective, as it is very expensive, in addition to generating great environmental impacts with energy consumption, for example. Curing in 7 days, despite improving the properties evaluated in relation to 3 days, does not justify its application economically, since within 3 days the materials would have conditions of use for certain applications.
- Thus, mixing at room temperature (23 °C) is the most advisable, in addition to a curing period of just 3 days, which is more economical, and it corroborates other studies in the literature that have already indicated a gain in technological properties with short curing time for geopolymer materials.

Acknowledgements The authors thank the Brazilian agencies CNPq, CAPES, and FAPERJ for the support provided to this investigation.

References

1. Provis JL (2014) Geopolymers and other alkali activated materials: why, how, and what? Mater Struct Constr 47(1–2):11–25
2. Provis JL, Bernal SA (2014) Geopolymers and related alkali-activated materials. Annu Rev Mater Res 44(1):299–327
3. Azevedo ARG et al (2020) Potential use of ceramic waste as precursor in the geopolymerization reaction for the production of ceramic roof tiles. J Build Eng 29(1):101–156
4. Amin SK et al (2017) Fabrication of geopolymer bricks using ceramic dust waste. Constr Build Mater 120:340–356
5. Azevedo ARG et al (2020) Use of glass polishing waste in the development of ecological ceramic roof tiles by the geopolymerization process. Int Appl Ceram Technol 25:1–10
6. Davidovits J (2013) Geopolymer cement a review. Geopolymer Sci Tech 23:45–58
7. Awoyera PO et al (2018) Characterization of ceramic waste aggregate concrete. HBRC J 14:282–287
8. de Azevedo ARG et al (2017) Influence of incorporation of glass waste on the rheological properties of adhesive mortar. Constr Build Mater 148:359–368
9. Azevedo ARG et al (2018) Influence of sintering temperature of a ceramic substrate in mortar adhesion for civil construction. J Build Eng 19:342–348
10. Suweni MM, Ahmadi H (2018) Performance of metakaolin geopolymer ceramic for fiber optic temperature sensor. Mater Today: Proc 5(7):15137–15142
11. ASTM C674–13 (2013) Standard test methods for flexural properties of ceramic whiteware materials. ASTM Int
12. ASTM C373–88 (1999) Standard test method for water absorption, bulk density, apparent porosity, and apparent specific gravity of fired whiteware products. AstmC373–88
13. Duxson P, Provis JL (2008) Designing precursors for geopolymer cements. J Am Ceram Soc 67:78–84
14. Rivera JF et al (2018) Novel use of waste glass powder: production of geopolymeric tiles. Adv Powder Technol 23:67–79

In Situ Investigation of Iron Ore Stock Pile During Its Stacking and Reclaiming Process

Wen Pan, Shaoguo Chen, Yapeng Zhang, Zhipeng Kang, and Dongqing Wang

Abstract The physical properties of a large-scale stock pile of iron ore were in situ investigated during its stacking and reclaiming process. The total weight of the stock pile was around 200,000 tons. The stacking and reclaiming process lasted for 480 h. The tested physical properties included angle of repose, size and shape data, size distribution of the blending ore, and so on. At the initial stage of the stacking process, the angle of repose was 37.1°. A decreasing trend was observed as the stacking process proceeded. In vertical direction, particles at bottom are much coarser than that at upper layer. In longitudinal direction, the head and tail Sect. (5.7 m in length) of the stock pile showed serious particle segregation. According to the testing results during the reclaiming process, the deviation of the particle size at the cross section of the stock pile was above 10%.

Keywords Stock pile · Stacking process · Reclaiming process · Particle size deviation

Introduction

In the process of raw material in a large iron and steel plant, blending stockyard is the core for technical control. The quality of blending ore will directly affect the quality of sinter, and then affect the stability, smooth operation, and high production of blast furnace [1]. The blending process is mainly composed of three steps: blending proportioning, tiling, and cutting. Blending proportioning is used to blend various raw materials according to a certain proportion in the blending batching chamber through the batching tank and the quantitative feeding device. Tiling is used to complete the longitudinal distribution of materials in the blending stockyard by the

W. Pan (✉) · S. Chen · Y. Zhang · D. Wang
Beijing Key Lab of Green Recyclable Process for Iron & Steel Production Technology, Beijing 100043, P. R. China
e-mail: panwen2001@126.com

Z. Kang
Shougang Jingtang United Iron & Steel Co., Ltd, Tangshan 063200, P. R. China

J. Li et al., *Characterization of Minerals, Metals, and Materials 2021*,
The Minerals, Metals & Materials Series,
https://doi.org/10.1007/978-3-030-65493-1_49

input substitution conveyor and the blending stacker. Cutting is used to complete the transverse feeding through the blending reclaimer and the output belt conveyor in the blending stockyard. Among them, the tiling stacking process is the core process which affects the uniformity of the blending stack, and directly affects the particle size distribution, particle size segregation, composition stability, and so on [2–4].

In order to improve the quality of blended ore, many iron and steel enterprises in China have carried out research work on the control of the accumulation process of blended ore [5–7]. In this paper, the online measurement and analysis of the stacking process are carried out. Also, the size distribution of the blend at different locations and the change of the stacking angle are analyzed.

Testing Method

Testing Method of Stacking Process

Iron ore was blended in a large-scale stock pile of 600 m long and 50 m wide, weighing about 200,000 tons after the stacking. During the stacking process, seven sampling points were tracked at the head, 200 m (South 1, North 1), 350 m (South 2, North 2), and 500 m (South 3, North 3), respectively. Each point was divided into two sampling points; the lower sampling point was 0.5 m from the ground and the upper sampling point was 2 m from the ground, as shown in Fig. 1. From the beginning of stacking to 150,000 tons, at every 6,000 tons the angles of repose were measured. After 150,000 tons, at every 8,000 tons the angles of repose were measured. The angle of repose was measured once at the seven points mentioned above, and each point was repeated three times. Around 60 kg of iron ore samples were collected from the 14 measuring points for particle size measurement. Size composition includes > 10, 10–8, 8–5, 5–3, 3–1, and < 1 mm.

Testing Method of Reclaiming Process

When the stock pile was cut vertically after the stacking was completed, the machine stopped at the middle of the stack. The cross-section of the blending stock pile was sampled and the particle size and composition distribution were analyzed. Figure 2 is the partition diagram of the sampling cross-section of large stock pile.

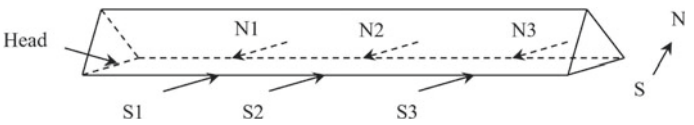

Fig. 1 Measurement schematic diagram

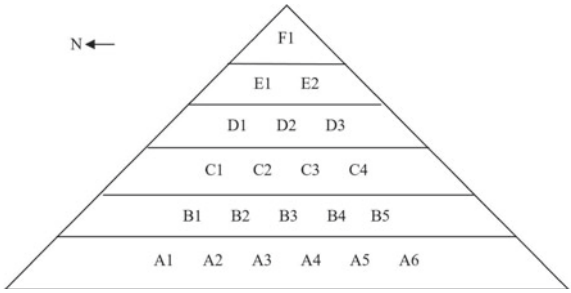

Fig. 2 Partition diagram of cross section of large stock pile

Testing Results

Testing Results of Stacking Process

(1) Repose angle of blended stock pile
Figure 3 shows the change of slope inclination angle (the angle of repose) on the south side and north side during stacking. It can be seen that the angle of repose decreases with the increase of stacking both on the south and north. The angles of repose on the north side are slightly bigger than those on the south side, with an average of 36.2°on the north side and 35.5°on the south side.

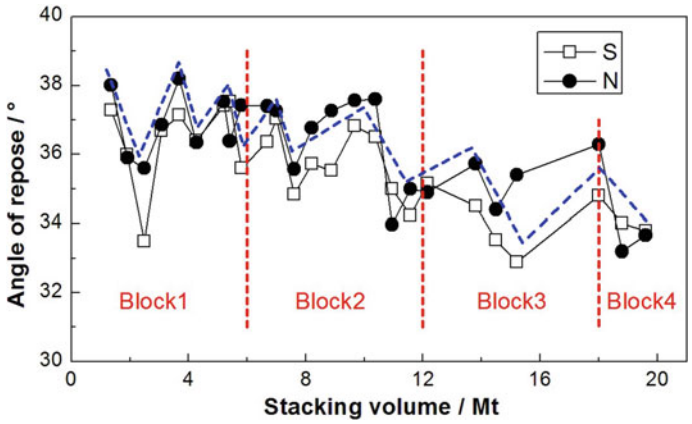

Fig. 3 Change of North–South angle of repose during stacking process. (Color figure online)

(2) Blended stock pile growth

From Fig. 4, the whole process of stacking growth can be observed intuitively. The growth of blended stock pile includes the growth of transverse, longitude, and height dimensions.

The transverse refers to width direction of the north side and south side. Growth in transverse direction can be measured by the distance between the edge of stock pile and stock yard. The measured results are shown in Fig. 5. The ratio of the north and south edge distance to the stacking volume is called the transverse growth speed of the stack, as shown in Fig. 6. From Fig. 5, it can be seen that the southern edge

Fig. 4 Photographs of stacking process. (Color figure online)

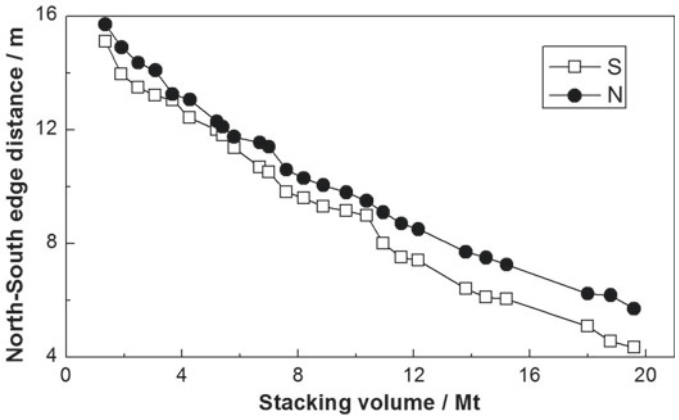

Fig. 5 Dimensional change of North–South edge distance

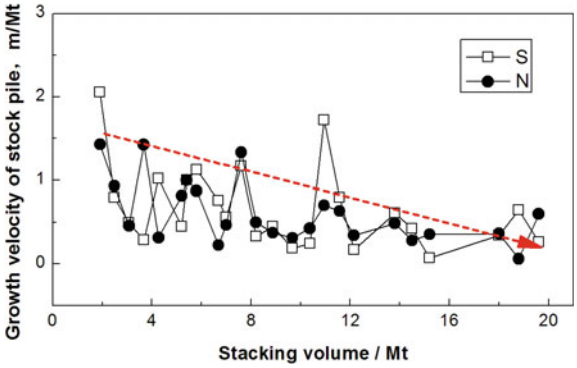

Fig. 6 Transverse growth velocity of stock pile. (Color figure online)

distance of the stock pile is less than 0.7 m on the north, which indicates that the blended stock pile is disposed to the north. The center line of the stock pile is about 0.35 m away from the center line of the stock yard.

According to Fig. 6, the transverse growth speed of the stock pile shows that the growth speed of the southern edge and northern edge is basically the same except for individual measuring points. Figure 7 recorded the change of cantilever pitch angle during the stacking process . The change of cantilever pitch angle is from –15° to + 10°. According to the change of pitch angle and geometric parameters of the stacker, the simulation diagram of the cantilever stacking process is shown in Fig. 8.

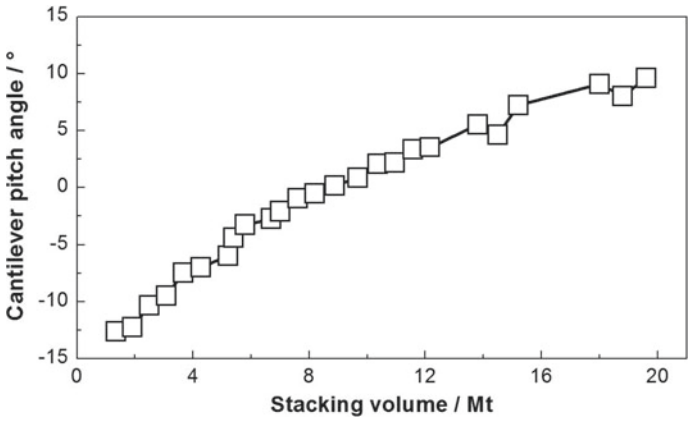

Fig. 7 Change of cantilever pitch angle during stacking

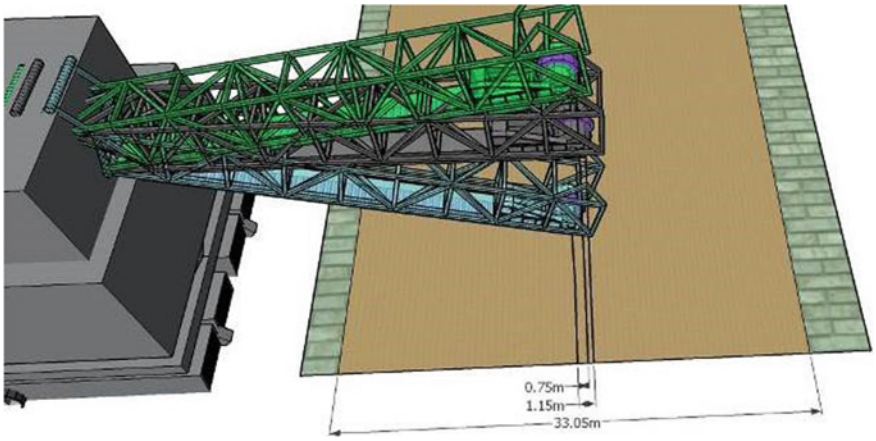

Fig. 8 Simulation diagram of cantilever stacking process. (Color figure online)

Testing Results of Reclaiming Process

(1) Figure 9 shows the particle size composition of blended ores at each point. It can be seen that for the same size of blended ores, the deviation of percentage content in transverse and vertical directions is more than 10%.
(2) Figure 10 shows the statistical result of the average particle size of the cross-sectional blended ore. Particles in the upper layers are bigger on both sides and smaller in the center. In the middle layers, particles on the north side are bigger than that on the south side, while particle size in the lower layers changes in the opposite trend.

Fig. 9 The particle size composition of blended ores

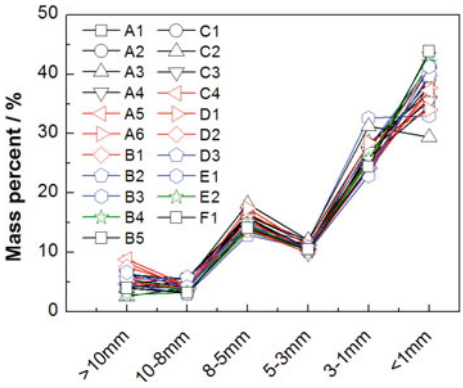

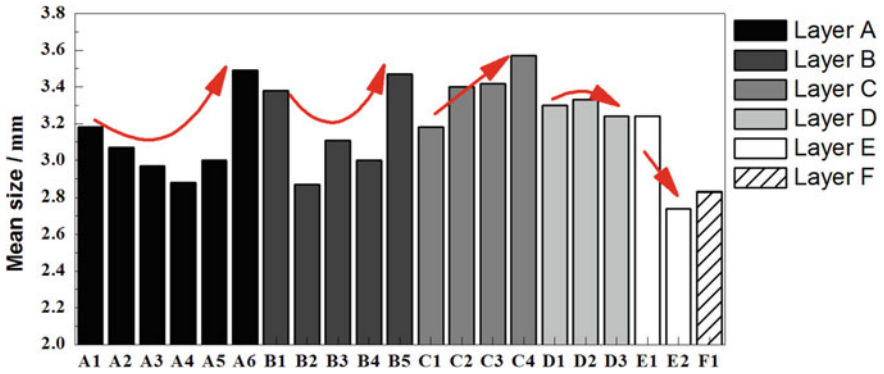

Fig. 10 Statistical result of the average particle size of the cross-sectional blended ore. (Color figure online)

Conclusions

1. With the increase of stacking volume, the angle of repose on both sides shows a downward trend. The angle of repose on both sides shows regular upward and downward fluctuation during the downward process. Comparing the angles of repose on the north side and south side of the stock pile, the angles of repose on the north side are slightly bigger than those on the south side, with an average of 36.2° on the north side and 35.5° on the south side.
2. During the reclaiming process, the deviation of the particle size at the cross-section of the stock pile was above 10%.
3. Particles of iron ore fines in the upper layers are bigger on both sides and smaller in the center. In the middle layers, particles on the south are smaller than that on the north, while it shows an opposite trend in the lower layers.

Acknowledgements Supported by National Key R&D Program of China (2017YFB0304300 & 2017YFB0304302)

References

1. Wenkang L (2013) Technical measures for improving mixing effect of blends. Shanxi Metall 36(02): 42–44+83
2. Haibin L, Tiande X (2011) Reconstruction of blending yard for laisteel 2 × 265 m^2 sintering system. Sinter Pelletizing 36(04): 42–44+52
3. Kang X, Wang D (2017) Application and practice of new technology in modern comprehensive raw material field. Sinter Pelletizing 42(02):57–61
4. Production of Mixing Material Field of Sintering Plant of Shi Steel (2007) Hebei Metall (04):28–30

5. Chang J, Niu Q (2004) Hongli Song. Appl PLC Control Syst Angang Mix Mater Spot 04:45–46
6. Mingyi W, Qinglin N et al. (2004) Control system of mixing yard of Anyang Iron and Steel Company based on PLC. Electr Technol (08): 42–43.
7. Feng L, Sun H, Li B (2000) Revamping of mixing material yard and its production effect in Xinggang. J Hebei Inst Technol S1:81–83

Particle Size Matching Mechanism of Blending Ore and Solid Fuel in Sintering Process

Shaoguo Chen, Yapeng Zhang, Wen Pan, Zhengming Cheng, Zhixing Zhao, Jiangshan Shi, Huaiying Ma, Tongbin Wang, Zhe Wang, and Liping Chen

Abstract The particle size of imported iron ores has gradually become bigger, which is adverse to mineralization and reaction in sintering process. At present, only imported iron ore fines are used in Jingtang sintering plant. And it is hard to control the particle size of imported iron ores. Different iron ore fines are mixed properly before charged to sintering machine. It is an important means to solve this problem to seek the particle size matching between solid fuel and iron ore fines. The suitable matching mode of fuel particle size (d) and blending ore particle size (D) is as follows: d/D = 0.47 ~ 0.54. When the particle size of blending ore changes, the fuel particle size should be controlled according to d/D with fuel crushing process. Since the matching mode was applied, the main quality indexes of sinter improved obviously. The return fine rate of sinter decreased from 25.43 to 24.64%, and the solid fuel consumption decreased from 44.8 to 43.9 kgce/t.

Keywords Particle size matching · Sintering · Solid fuel consumption

Introduction

With the increase of the resource supply of imported iron ore fines and the cost control of mining companies, the imported iron ore resources have gradually deteriorated. Particle size of imported iron ore fines becomes coarser [1–3]. At present, only imported iron ore fines are used in Jingtang sintering plant. And it is hard to control the particle size of imported iron ores. If particle size of iron ore fines was too coarse,

S. Chen (✉) · Y. Zhang · W. Pan · Z. Zhao · H. Ma · L. Chen
Beijing Key Laboratory of Green Recyclable Process for Iron & Steel Production Technology, Beijing 100043, People's Republic of China
e-mail: chenshaoguo_0701@163.com

Shougang Group Co, LTD Research Institute of Technology, Beijing 100043, People's Republic of China

Y. Zhang · Z. Cheng · J. Shi · T. Wang · Z. Wang · L. Chen
Shougang Jingtang United Iron & Steel Co. Ltd, Tangshan 063200, Hebei, People's Republic of China

J. Li et al., *Characterization of Minerals, Metals, and Materials 2021*,
The Minerals, Metals & Materials Series,
https://doi.org/10.1007/978-3-030-65493-1_50

it is adverse to mineralization and reaction in sintering process, especially under the condition of thick layer. Segregation of coarse-grained raw materials to the bottom of the layer will bring obviously negative effect on sinter production [4]. Different iron ore fines are mixed properly before charged to sintering machine. It is an important means to solve this problem to seek the particle size matching between solid fuel and iron ore fines.

Materials and Experiments

Coarsening Condition of Iron Ore Fines

As the main iron ore fines, ore A from Brazil and ore B from Australia were applied in Jingtang sintering process. In 2009, for the measured particle size of ore A, proportion of < 0.15 mm particles was 36%, proportion of > 5 mm particles was 26%, and the average particle size was 3.60 mm. However, they are 15%, 33% and 4.35 mm at present, respectively. The particle size of ore A becomes coarser. Moreover, proportion of < 0.15 mm particles of ore B was about 67% in 2009, and the average particle size was 2.37 mm. At present, they are 57% and 3.12 mm, respectively. As shown in Fig. 1, the average particle size of Jingtang blending ore became larger either.

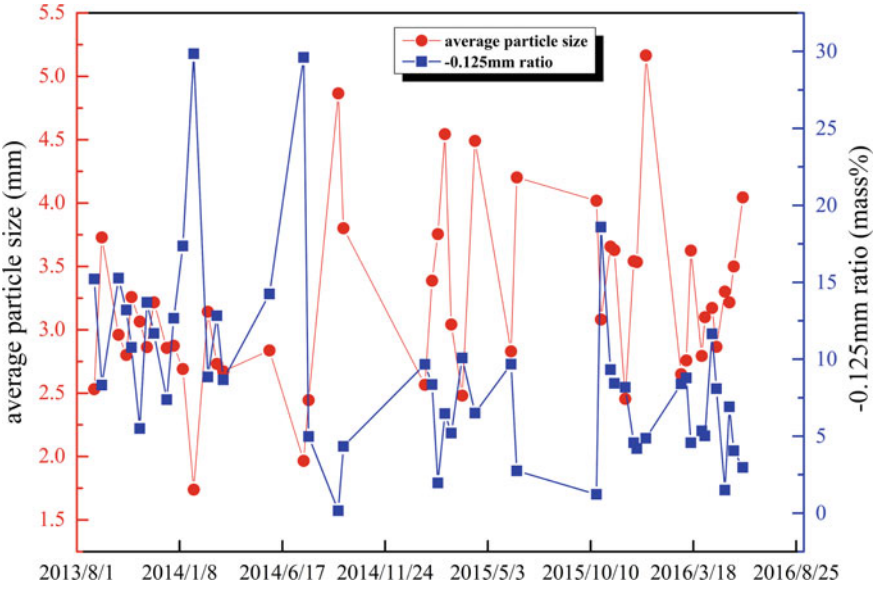

Fig. 1 Variation trend of particle size of Jingtang blending ore. (Color figure online)

Table 1 Blending condition of raw mixtures for sintering pot tests (mass%)

Blending ore	Sinter return	Blast furnace return	Quick lime	Limestone	Coke breeze	Sintering ashes	Blast furnace ashes
70	30	12	3.65	0.5	4.24	1.0	1.0

Thermogravimetric Analysis and Differential Scanning Calorimetry (TG-DSC) Test

TG-DSC test was carried out to study and elucidate the influence of particle size on the thermal decomposition characteristic of coke breeze. Three granulometric classes of coke breeze were tested: < 0.1 mm, 0.1–1 mm, > 1 mm. Each sample of coke breeze with weight of 10 g was introduced into the TG-DSC tester with air atmosphere. The temperature schedule was set to reach 1200 °C at 20 °C/min.

Sinter Pot Test of Particle Size Matching of Coke Breeze and Iron Ore Fines

The sintering test was carried out in the following conditions: sintering pot size, φ300 mm; sintering bed thick, 850 mm; ignition temperature, 1050 °C; ignition time, 3 min; ignition negative pressure, − 12 kPa; and sintering negative pressure, − 16.5 kPa. Table 1 shows the blending condition of raw mixtures.

Results and Discussion

Influence of Particle Size on Combustion Speed of Coke Breeze

As shown in Fig. 2, coke breeze with smaller particle size was faster than that with bigger particle size on combustion speed. It indicates that coke breeze with large particle size can hold high temperature longer in sintering process, which is beneficial to the sintering reaction of coarser iron ore fines.

Influence of Particle Size Matching of Coke Breeze and Iron Ore Fines on Sinter Pot Test Results

As shown in Table 2, when ratio (d/D) of breeze, that is average size coke breeze (d) to average size of blending ore (D), ranged from 0.47 to 0.54, the technical indexes

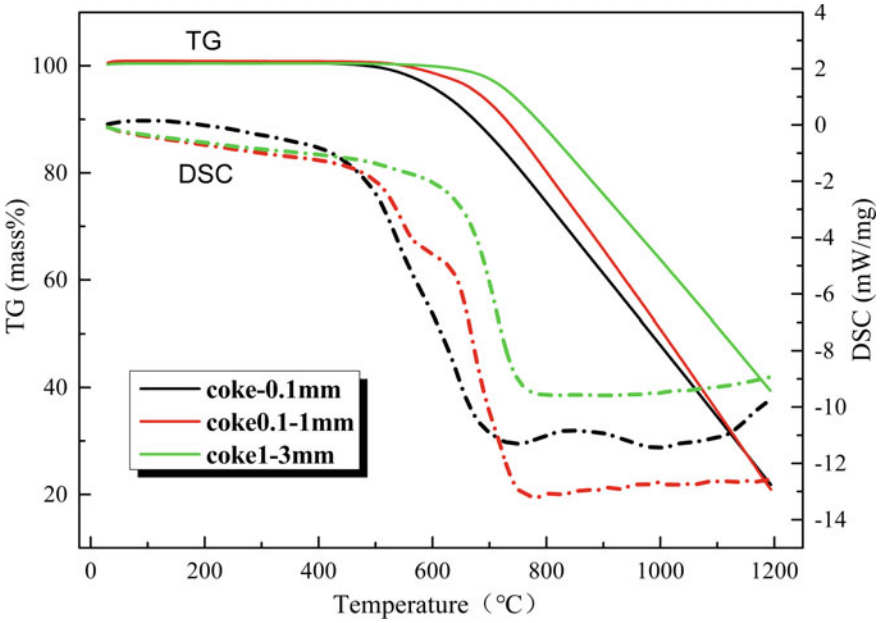

Fig. 2 TG-DSC curve of different particle size of coke powder. (Color figure online)

Table 2 Results of sintering pot tests for matching coke size with blending ore size

No	1	2	3	4	5	6
Average size of coke breeze d/mm	1.95	2.18	2.48	1.65	1.68	1.85
Average size of blending ore D/mm	3.61	3.61	3.61	3.61	3.61	3.61
d/D	0.54	0.6	0.69	0.46	0.47	0.51
Yield/%	83.64	83.62	82.91	84.27	83.65	82.41
Tumbler index/%	66.36	66.87	64.73	67.31	66.2	65.6
Productivity/(t/m^2.h)	1.30	1.15	1.20	1.18	1.35	1.33
Fuel consumption/(kg/t)	45.06	46.28	45.95	45.93	45.13	45.62
Average size of sinter /mm	20.79	23.86	21.35	22.98	21.34	21.06
− 3 mm ratio of coke breeze/%	75.0	75.0	60.0	80.0	85.0	85.0

including productivity and fuel consumption were better than others. So, the suitable matching mode of fuel particle size (d) and blending ore particle size (D) may be as follows: d/D = 0.47 ~ 0.54.

To inspect the quantitative range of matching particle size of coke breeze and particle size of blending ore, the particle size of coke breeze was adjusted and changed according to the particle size of blending ore. Further, sinter pot tests were carried out to verify the matching value. Table 3 shows the verification results of sinter pot

Table 3 Verification results of sintering pot tests for matching coke size with blending ore size

No	7	8	9	10	11	12
Coke breeze average size d/mm	2.33	1.95	2.91	1.63	1.98	2.18
Blending ore average size D/mm	5.01	5.01	5.01	5.01	5.01	5.01
d/D	0.47	0.39	0.58	0.32	0.39	0.44
Yield/%	84.09	81.88	83.22	82.17	82.88	82.64
Tumbler index/%	63.6	63.87	64.27	67.87	67.47	66
Productivity/(t/m^2.h)	1.51	1.49	1.48	1.41	1.38	1.33
Coke consumption/(kg/t)	45.7	47.92	45.14	47.4	46.78	46.78
Sinter average size/mm	22.32	19.36	20.76	20.19	21.47	21.06
Coke − 3 mm ratio/%	70.0	75.0	60.0	85.0	80.0	75.0

tests. In a series of schemes to continuously adjust the ratio of d/D between 0.47and 0.58, the sintering indexes were relatively good.

There was a quantitative matching relationship between fuel particle size and blending ore particle size. The suitable matching mode of fuel particle size (d) and blending ore particle size (D) is as follows: d/D = 0.47 ~ 0.54.

Industrial Application Effects

Based on the matching principle above, industrial test was implemented. Specific changes of sintering indexes before and after the industrial test are shown in Table 4. Compared to base period, the sintering indexes of industrial period improved significantly. Fuel consumption, sinter return ratio, and 0–10 mm sinter ratio decreased by 7.9 kgce/t, 0.47, and 0.74%, respectively. Other indexes are kept stable.

Table 4 Changes of sintering indexes before and after the industrial test

Title	Fuel consumption /(kgce/t)	Tumbler index /%	0–10 mm /%	Average size of sinter /mm	Sinter return ratio /%	d/D
Base period	49.1	82.56	18.11	21.24	25.33	**0.65**
Industrial test period	41.2	82.48	17.37	21.32	24.86	**0.52**
Changes	−7.9	−0.08	−0.74	+0.08	-0.47	–

Conclusions

(1) Particle sizes of iron ore fines used in Jingtang sintering have changed. Due to the increase of particle size of iron ore fines, the coarsening trend of particle size of blending ore occurred.
(2) Coke breeze with larger particle size can make hold of high temperature longer, which is beneficial to the sintering reaction of coarsening iron ore fines.
(3) Under the condition of Jingtang raw materials, the suitable matching mode of particle size of fuel (d) and particle size of blending ore (D) was as follows: d/D = 0.47 ~ 0.54. When the particle size of blending ore changed, the fuel particle size should be controlled according to d/D.
(4) Based on the suitable matching mode, fuel consumption, sinter return ratio, and 0–10 mm sinter ratio in Jingtang sintering process decreased: 0.9kgce/t, 0.79% and 1.05%, respectively.

Acknowledgements Supported by National Key R&D Program of China (2017YFB0304300&2017YFB0304302)

References

1. Gu H-F (2018) The present situation analysis of imported iron ore in China in recent years and the prospect in 2018. Miner Res Res 1:54–56
2. Luo W (2015) Capital expenditure cut by global mining giants to falling mine prices. Shanghai Metals 37(1):57
3. Pei Y-D, An G, Xiong J, Zhao Z-X (2015)Technology progress of Shougang Jingtang sintering in recent years. In: The 10th China steel annual conference and the 6th Baosteel academic annual conference
4. Xu J-L, Dai Y-H, Cheng F-Q (2009) Influence of raw material granularity on sintering, China academic conference on iron raw materials

Research Progress of Aging Effects on Fiber-Reinforced Polymer Composites: A Brief Review

Michelle Souza Oliveira, Fernanda Santos da Luz, and Sergio Neves Monteiro

Abstract Natural fiber-reinforced polymer (NFRP) composites have obtained significance in recent times due to their wide application in different industries, such as automotive, aerospace, construction, home appliances, and ballistic vest because of the high cost of synthetic fibers and environmental issue. These natural fibers are cheaper and lighter but their mechanical properties are lower than the synthetic fibers. In addition, great efforts have been made to understand the phenomenon of weathering of polymeric materials, which ultimately result in the deterioration of the physical and mechanical properties of the polymer. This work aims to present some research in the degradation area of natural fibers and their composites. The components of NFRP and flexural strength and modulus are revealed in the first part. Afterwards, the second part will be devoted to review some methods of aging treatments applied to natural fiber composites. Eventually, a discussion about the optimal approaches for lifetime prediction of NFRPs will be drawn.

Keywords Aging materials · Flexural test · Natural fibers · Polymer composites

Introduction

The reinforcement of the natural fibers into polymer (NFRP) composites has become an attractive research topic over the previous decades [1–10]. NFRP composites, also known as biocomposites, present some advantages compared with composites made of synthetic fibers such as potentially lower material cost, easy access, lower density, good specific strength and stiffness, low manufacturing cost, degradability, promoting human welfare, and ecosystem health. For better understanding, biocomposites can be defined as: (i) biodegradable polymers reinforced with natural fibers; (ii) biodegradable polymers reinforced with man-made fibers; (iii) petroleum based or non-biodegradable polymers reinforced with natural fibers [11]. Thus, no harmful effect on the environment and their specific properties are main causes of

M. S. Oliveira (✉) · F. S. da Luz · S. N. Monteiro
Military Institute of Engineering – IME, Rio de Janeiro, Brazil
e-mail: oliveirasmichelle@gmail.com

J. Li et al., *Characterization of Minerals, Metals, and Materials 2021*,
The Minerals, Metals & Materials Series,
https://doi.org/10.1007/978-3-030-65493-1_51

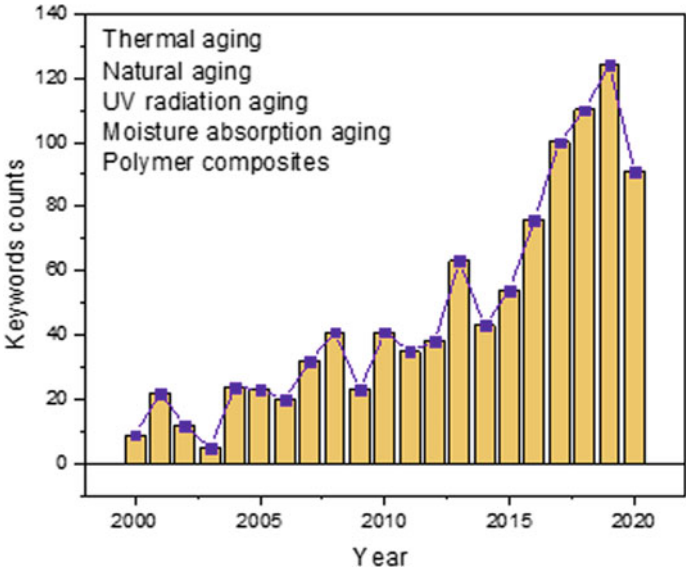

Fig. 1 Number of scientific publications in effects of different types of aging in polymer composites. Data obtained from Science Direct database (accessed on 03.07.20). (Color figure online)

the researcher interest attraction toward natural fiber composites. Figure 1 considers the count of research articles, book chapters, and conference papers for the past 20 years, having as keywords "thermal aging", "natural aging", "UV radiation aging", "moisture absorption aging", and "polymer composites".

Along with number of benefits of NFRP, there are some drawbacks associated with these materials [12]. One of the major drawbacks of biocomposites lies in the fact that both polymers and natural fibers are prone to degradation when exposed to different environmental conditions. After natural weathering periods, biocomposites may suffer from deterioration of several properties, such as discoloration, surface roughness, and loss of mechanical and thermal stability [13]. The mechanical properties of the composites deteriorate due to poor interface bonding between the natural fiber and polymer matrix. It is due to hydrophilic nature of natural fibers and hydrophobic nature of polymer matrix. Several surface treatments of natural fibers were performed to overcome earlier mentioned difficulties during fabrication of the composites to minimize this mechanism [14, 15].

The degradation of physical, thermal, and mechanical properties of NFRP composites owing to long-term exposure to natural weathering, moisture, humidity, and ultraviolet (UV) sunlight was reported in the literature [16]. The major concern regarding outdoor applications of biocomposites consists in its dimensional stability and durability against UV radiation, moisture, and microbial attack, where the degradation comprises the alternations in crystallinity of the matrix phase. In other words, the aging includes mainly chemical changes of the matrix materials, oxidation of composite surfaces, and the interfacial strength degradation.

Composites undergo changes in materials properties under hot–wet conditions also [17]. It is known that composite structures are very sensitive to hydrothermal-elastic stress as composite materials have heterogeneity-related difference in hydrothermal-elastic properties of adjacent entities. The hygrothermal aging at high temperature accelerates the moisture diffusion process. The aging agent can be seawater, distilled water, tap water, demineralized water, or any other application-based chemical [18]. Different aging effects used on synthetic and natural fibers from last decades (2000–2020) and their effect on flexural properties of composites have been reviewed which can edify further possibilities of enhancements of NFRP.

Main Characteristics of Natural Fibers, Epoxy, and Their Individual Behavior Before Aging

Flora-based natural fibers, available in abundance in tropical and subtropical countries, are composed of cellulose, hemicellulose, lignin, pectin, and waxy materials. Cellulose is the major constituent of the natural fiber which provides strength, stability, and stiffness to the fibers. Cellulose's rigid and insoluble micro-fibrils chains enable it to serve as structural content of cellulosic fibers. As a linear polymer made of glucose subunits linked by β-1,4 bonds, cellulose has a basic repeating unit cellobiose. The individual cellulose fiber cells are linked together by means of the middle lamella. Another branched polymer is hemicellulose which is mostly found in the primary wall of the fiber. In contrast to cellulose, hemicellulose represents a type of hetero polysaccharides with complex structures. Its main chain is characterized by a β-1,4-linked-D-xylopyranosyl [18].

As the most abundant natural aromatic polymer, the role of lignin is to bind cellulose microfibrils together in plants and is amorphous in nature. This heteropolymer binding phase has a complex three-dimensional structure with aliphatic and aromatic constituents. The most common linkages formed during lignin biosynthesis are the β-O-4 ether linkages, followed by other types of ether and C–C linkages such as α-O-4, β-β, β-5, and 5–5. The lignin component in natural fibers influences their UV degradation, and water-soluble products, such as carboxylic acids, quinone, and hydroperoxyl radicals, are formed [13]. These three main components assemble together forming a distinct cell wall structure, as shown in Fig. 2, with excellent mechanical properties and ultra-low density. In addition to these, a little amount of organic and inorganic substances—for example, the pectin, mainly constituted with polysaccharides—are also present on the natural fiber which is responsible for color, abrasive nature, odor, and decay resistance of natural fibers. Unfortunately, renewability and durability tend to be mutually exclusive, and the application of natural materials is always a compromise between environmental sustainability and long-term service [18].

Natural fibers are not so much stable at elevated temperature. These have moisture absorption capacity which restricts them for moisture ambient applications. It

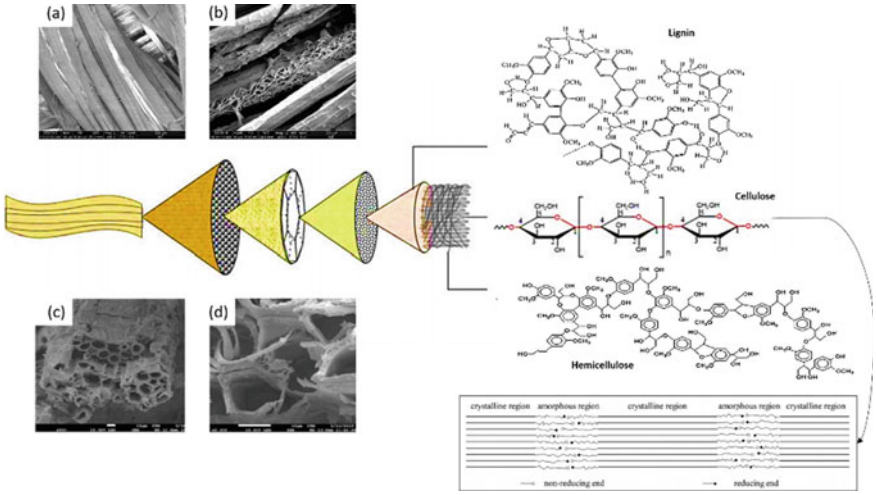

Fig. 2 Schematic diagram and microstructure of fique fiber. Diagrammatic sketch of microstructure of cellulose microfibrils. Adapted from [18–20]. (Color figure online)

also leads to dimension instability problem for fiber composite. The cause for this is hidden in the structure of natural fiber. Furthermore, after a longer period of exposure to humidity, biological activities, such as fungal growth, occur within natural fibers. The hygroscopic behavior of natural fibers influences the biodegradation characteristic of a material. Higher moisture absorption increases the ease of microbial attack. In addition, Sarikaya et al. [21] suggested that used fiber type had great importance on strength characteristics of the composites.

On the other hand, the effects of radiation on polymer structure, and consequently on its physical characteristics, are well known in the plastic industry. Indeed, the mechanisms behind these effects show two opposite trends, depending on irradiation conditions and exposure time: increased cross-linking of the polymer molecules, which increases the mechanical strength, and oxidative degradation, which generally causes material weakening. The last tendency cited will be predominant since it seems to be related to the amount of oxygen available on the material and the capacity to replace the oxygen as it is consumed by chemical reactions with radical produced during irradiation [22]. Currently, considerable efforts have been made to investigate high-performance UV-curable coatings through changing materials or operational parameters. Compared with thermal curing, UV-curing technology is noted as 5E, which stands for efficiency, energy saving, enabling, economical, and environmentally friendly.

Furthermore, epoxy resin (ER) has been widely applied in the field of electronic instruments, construction, machinery, aerospace, coatings, electrical insulation, and advanced composite materials, due to its simple processing, low-cost, and excellent performance with respect to adhesion, wear, electrical insulation, and chemical stability. The properties of ER are affected by light, heat, water, oxygen, and other

atmospheric factors, which degrade its performance and shorten its useful life when used in natural climates. UV irradiation can break some of the chemical bonds of ER, causing aging and degradation of it. Therefore, after long-term UV irradiation, the properties of the ER degrade substantially, and adding a second phase of ER is a common way to improve its anti-UV aging properties [23].

Chen et al. [24] studied the chemical structures, molecular dynamics, and mechanical properties of diglycidyl ether of bisphenol A (DGEBA)/triethylenetetramine (TETA) resins act as a function of the gamma irradiation dose. The authors reported that three distinct relaxations were observed for all polymers. The irradiation process resulted in an increase of local mobility corresponding to β and γ relaxations, and the cooperative mobility associated with α relaxation was also shifted to low temperature with irradiation dose. In this case, it could be attributed to a destruction of cross-linking networks or chain scissions. The flexural and tensile modulus results of ER increased with irradiation dose.

Effects of High Temperature, Moisture Absorption, and UV Radiation on Flexural Properties

Flexural loading of composite components occurs frequently in service, and it is a relatively simple test to carry out and have been widely used to characterize composite structures and materials [25, 26]. For good flexural strength, natural fiber composites should have good interface bonding between fiber/matrix. Mechanical properties such as tensile and compression strength have been reported to decrease at elevated temperature, as well as their viscoelastic properties [25]. The combined effects of water absorption and thermal environment have greater effects on composite materials. As for water absorption, several studies reported that the moisture absorption follows Fickian behavior and depends on both temperature and amount of relative humidity in the environment [17]. In this case, water enters a composite material principally by the mechanism of diffusion. The consequences are mechanical property degradations, thermal degradations mainly with reference to the glass temperature, which in turn affects the composites structural integrity, and a crucial issue related to the composite's applications. Moisture may also accumulate in matrix causing microcrack, pores, cracks, and minor delamination between the layers of the composite laminate. Other possible mechanisms are capillarity along the fiber surface and fiber/matrix interface. Contextualizing, natural fibers swell after moisture absorption and this leads to matrix microcracks around the swollen fibers. In consideration of thermal aging, hot–wet environmental conditions on composite materials play a very important role in performance and durability of composite parts.

The effect of temperature on polymers can be divided into two types, namely short-term and long-term. In general, short-term effects are physical changes reversible when the temperature returns to its original point. Long-term effects are mainly chemical changes which are irreversible. At high temperature ranges (300–500 °C),

polymers decompose and release heat and toxic compounds. When exposed to lower temperatures about 100–200 °C, polymers will soften, creep, distort, and suffer deterioration of mechanical properties [16]. The magnitude of internal stresses, induced from differential thermal coefficients of their components, changes with temperature change. Usually the maximum operating temperature of a polymer is slightly below its T_g, at which the polymer transitions from rigid state to liquid state with significant mechanical property loss happen. This indicates the importance of carrying out studies on moisture absorption at different hot–wet conditions on NFRP composite materials.

Badyankal et al. [15] found that the water absorption test carried out for 15 days shows a minimal absorption of water for NaOH-treated fibers. Chaudhary et al. [27] focused on the effect of water absorption on tensile, flexural, hardness, and impact strength on the jute/flax/epoxy hybrid composite. The authors reported that all mechanical properties were reduced after water absorption, decreased approximately two-thirds of initial tensile and flexural strength of composites before one year of water absorption, followed by a hardness reduction of 2%, and impact strength reduction 4% as compared to dry samples.

Pani et al. [30] observed the water absorption behavior of bamboo/jute/glass (GBJ) fiber-reinforced polymer hybrid composites in seawater aging condition. The GBJ hybrid composite had more seawater absorption tendency, owing the maximum flexural modulus observed. Surprisingly, it also presented the maximum flexural strength among the others two types of hybrid composites in dry conditions.

Lu et al. [31] evaluated the effect of water immersion ageing on flexural and water sorption properties of composites made of non-dry flax fibers and resins which have low sensitivity to water. The authors suggested that composites made of non-dry fiber had considerably lower water absorption and better transverse flexural strength properties than composites made of dried fiber for both polyester/flax and epoxy/flax composites, and could be used for enhancing the water durability of NFRPs.

Moreover, the UV photons absorbed by polymers result in photooxidative reactions which alter the chemical structure, leading to material deterioration. Short-term exposure to UV only causes change in surface morphology, but extended exposure to UV radiation can deteriorate the matrix-dominated properties such as flexural stiffness, interlaminar shear strength, and flexural strength [16].

Photooxidative reactions can also form chromophore chemical species. These chromophores are simple molecules which absorb and transmit light, causing discoloration of the polymer as it absorbs the visible range of light. The NFRP composites have generally poor UV resistance. Chee et al. [11] studied, through accelerated weathering and soil burial, the influence of environmental effects on the color, biodegradability, oxidation stability and complex modulus of bamboo/kenaf fiber reinforced epoxy composites. The authors fixed a loading of 40 wt.% fibers for tree types of hybrid composites: 30/70, 50/50, 70/30, as well as pure epoxy. The kenaf, bamboo, and hybrid composites were exposed to UV radiation at elevated temperature and humidity, for a total exposure period of 156 h. A cycle of UV irradiation of 8 h at 60 °C was followed by 4 h condensation at 50 °C. The investigation of color changes induced after accelerated weathering revealed that higher bamboo fiber,

with the higher lignin content, leads to more pronounced color changes. In terms of thermal stability, the higher bamboo loading demonstrated the most stable hybrid composite, after exposure to accelerated weathering and soil burial. After accelerated weathering, the complex modulus of all the composites shifted to higher values because UV irradiation induced further cross-linking reaction. One can observe that material properties are dependent on temperature and moisture, which are given explicitly in terms of the fiber/matrix properties and fiber volume ratio [28].

Furthermore, direct sunlight exposure will lead to the photodegradation process, which can modify the surface chemistry of the composite. The photodegradation mechanism of the polymer matrix is mainly concentrated on the surface of the composite because the photooxidation is stimulated by UV irradiation and oxygen. Photodegradation can cause changes in the polymer chemical structure, leading to molecular chain scission, reduction in molecular weight, or chain crosslinking due to the presence of catalyst residues, hydroperoxide groups, and carbonyl groups [13].

In the quest for green and energy-efficient product, the requirement of lightweight, low-cost, and high-performance material with exceptional durability was proposed recently [29]. The exposure process to UV radiation and ballistic properties of the epoxy composite with natural fibers were performed by residual velocity with five (5) shoots in each composites plates, as shown in Fig. 3. The epoxy composites reinforced with 30 vol% of 50 jute/50 mallow fabric were prepared in a metallic mold, with dimensions 150 × 120 × 10 mm, exposed to UV radiation and then test by 0.22 ammunition. Characteristic modification of linkages in the polymer main chain were observed after UV exposure.

According to the results in Fig. 3, it is noted that the photodegradation of composites optimized the impact absorption capacity for all conditions. Starting from values of 96.8 J which represents 84.9% of the projectile energy of the control group to

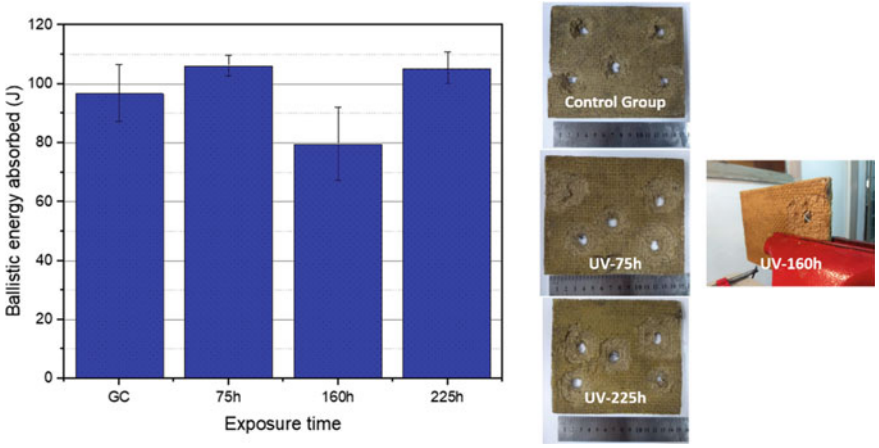

Fig. 3 Graph of the absorbed energy and opposite face of the shots for the Jute/Mallow composites. (Color figure online)

106.3 J which represents 93% of the projectile energy for the group with 75 h of exposure. The integrity of all composite plates after 5 shots remained. Energy dissipation were attributed to the generation of fracture surfaces in composites and are best viewed on the opposite face to the impact of the projectile. Groups that have been exposed to UV radiation presented larger regions of fracture surfaces, which caused a greater absorption of impact energy.

Wang et al. [32] investigated the durability and the effect of natural and accelerated aging on mechanical behavior of flax fiber reinforced composite. The authors found a decrease of 15% on flexural strength and 36% on flexural modulus. The result showed that accelerated and natural aging have different effects on the degradation properties, it could be based on the different mechanism presented by them. The main reason is only limited aging factors are considered in accelerated aging, while natural aging is caused by a combination of various environmental factors.

Natural fiber reinforcement in two directions enhanced mechanical properties significantly compared to unidirectional natural fiber reinforced composite. Bidirectional natural fiber reinforced composites are orthotropic and have nine elastic coefficients. They are very different from the unidirectional fiber reinforced composites which are transversely isotropic. Wang et al. [33] developed the mechanical degradation model for bidirectional NFRP under moisture absorption and hydrothermal loading and used the model to investigate the buckling and vibration behaviors of bidirectional NFRP composites plates. They reported that the elastic module and buckling load decreased monotonously with time and approached to a certain value with time. The degradation of elastic modulus for the composites with high fiber content present larger than with low fiber content. The reason for this phenomenon is the more damaged interfaces are induced by hygrothermal ageing moisture absorption for a composite with higher fiber content.

Most recently, application of graphene in polymer composites has become more common due to the benefits of their two-dimensional atomic carbon sheet structure [34]. This unique material can significantly improve mechanical, electrical, or gas barriers as well as the thermal stability of polymer composites even with a very small filler loading and hence is a promising material for potential diverse applications. With regards to thermal stability, an increase in the onset of non-oxidative degradation temperature by 20–30 °C and even higher has been reported [35]. Moreover, these materials increase the viscosity and hinder the thermal movement of polymer chains. The large specific surface of the graphite may also act as a radical trap for the radicals generated during the combustion and degradation process and further assist in improving the thermal stability.

All these phenomena cited will affect the interfacial adhesion between fiber and matrix, which leads to poor stress transfer and alters the physical, mechanical, and thermal properties of the composites, mainly for ballistic applications. This modality involves an impact mechanism, which is a very complex mechanical/dynamic process. It depends on the thickness, strength, ductility, toughness, and density of the target material and projectile parameters [36]. Therefore, it is necessary to investigate the behavior of NFRPs, applied in ballistic armor, under different types of aging, in order to consolidate these materials as a new technology.

Summary and Conclusions

Day-by-day the NFRPs are increasingly involved in many industrial applications. This review has focused on single-fiber composites, hybrid composites, and their flexural properties. The specific conclusions are:

- The research is still ongoing, and the V50 test can be performed to determine the ballistic limit for the UV exposed composite reinforced with hybrid jute/mallow fabric.
- Based on the residual velocity results obtained, it can be concluded that the photodegradation caused a change in the properties of composites.
- After exposure to UV radiation, epoxy matrix composites reinforced with mallow/jute fabric have optimized their energy absorption capacities impact for 0.22 mm caliber, absorbing 93% of the projectile energy.
- The composites under aging treatments by UV radiation showed a more efficient behavior for impact absorption, generating more surface of fractures which dissipates more energy.
- Thermal degradation of polymer composites is an even more intricate problem, where fillers often seriously affect the stability of polymers.
- Considering the importance of stability, recyclability, and environmental issues, further attention should be paid to this subject.

Acknowledgements The authors thank the Brazilian agencies CAPES and CNPq for their financial support.

References

1. Nayak SY, Sultan MTBH, Shenoy ST, Kini CR, Samant R, Md Shah A.U, Amuthakkannan P (2020) Potential of natural fibers in composites for ballistic applications—a review. J Nat Fibers
2. Benzait Z, Trabzon L (2018) A review of recent research on materials used in polymer-matrix composites for body Armor application. J Compos Mater 52(23):3241–3263
3. Hassan KMF, Horvath PG, e Alpár T (2020) Potential natural fiber polymeric nanobiocomposites: a review. Polymers 12(5): 1072
4. Sanjay MR, Madhu P, Jawaid M, Senthamaraikannan P, Senthil S, Pradeep S (2018) Characterization and properties of natural fiber polymer composites: a comprehensive review. J Clean Prod 172:566–581
5. Pickering KL, Efendy MA, Le TM (2016) A review of recent developments in natural fibre composites and their mechanical performance. Compos Part A Appl Sci Manuf 83:98–112
6. Mohammed L, Ansari MNM, Pua G, Jawaid M, Islam M S (2015) A review on natural fiber reinforced polymer composite and its applications. Int J Polym Sci
7. Faruk O, Bledzki AK, Fink HP, Sain M (2014) Progress report on natural fiber reinforced composites. Macromol Mater Eng 299:9–26
8. Shah DU (2013) Developing plant fibre composites for structural applications by optimising composite parameters: a critical review. J Mater Sci 48:6083–6107

9. Shahinur S, Mahbub H (2020) Natural fiber and synthetic fiber composites: comparison of properties, performance, cost and environmental benefits. Encycl Renew Sustain Mater 794–802
10. Monteiro SN, Drelich JW, Lopera HAC, Nascimento, LFC, Luz FS, da Silva LC, ... Pereira AC (2019) Natural fibers reinforced polymer composites applied in ballistic multilayered Armor for personal protection—an overview. In: Ikhmayies S, Li J, Vieira C, Margem J, de Oliveira Braga F (eds) Green materials engineering. The minerals, metals & materials series. Springer, Cham, pp 33–47
11. Chee SS, Jawaid M, Sultan M, Alothman OY, Abdullah LC (2019) Accelerated weathering and soil burial effects on colour, biodegradability and thermal properties of bamboo/kenaf/epoxy hybrid composites. Polym Test 79:106054
12. Sood M, Dwivedi G (2018) Effect of fiber treatment on flexural properties of natural fiber reinforced composites: a review. Egypt J Pet 27(4):775–783
13. Fei P, Xiong H, Cai J, Liu C, Din Z-u, Yu Y (2016) Enhanced the weatherability of bamboo fiber-based outdoor building decoration materials by rutile nano-TiO2. Constr Build Mater 114:307–316
14. Vedrtnam A, Kumar S, Chaturvedi S (2019) Experimental study on mechanical behavior, biodegradability, and resistance to natural weathering and ultraviolet radiation of wood-plastic composites. Compos B Eng 176:107282
15. Badyankal PV, Manjunatha T, Vaggar GB, Praveen K (2020) Compression and water absorption behaviour of banana and sisal hybrid fiber polymer composites. Mater Today: Proc
16. Ching YC, Gunathilake TU, Ching KY, Chuah CH, Sandu V, Singh R, Liou N-S (2019) Effects of high temperature and ultraviolet radiation on polymer composites. In: Jawaid M, Thariq M, Saba N (eds), Durability and life prediction in biocomposites, fibre-reinforced composites and hybrid composites. Woodhead Publishing, pp 407–426
17. Shetty K et al (2019) Effect of hygrothermal aging on the interlaminar shear strength of a carbon fibre composite. Procedia Struct Integr 14: 849–854
18. Wei J (2018) Degradation behavior and kinetics of sisal fiber in pore solutions of sustainable cementitious composite containing metakaolin. Polym Degrad Stab 150:1–12
19. Rua J, Buchely M, Monteiro S, Colorado H (2019) Structure–property relation of epoxy resin with fique fibers: dynamic behavior using split-hopkinson pressure bar and charpy tests, pp 49–56
20. Oliveira MS, Filho FDCG, Luz FSD, Demosthenes LCDC, Pereira AC, Colorado HA, Nascimento LFC, Monteiro SN (2019) Evaluation of dynamic mechanical properties of fique fabric/epoxy composites. Mater Res 22
21. Sarikaya E et al (2019) Production of epoxy composites reinforced by different natural fibers and their mechanical properties. Compos Part B: Eng 167: 461–466
22. Cota SS et al (2007) Changes in mechanical properties due to gamma irradiation of high-density polyethylene (HDPE). Braz J Chem Eng 24(2):259–265
23. Zhai Z et al (2016) The anti-ultraviolet light (UV) aging property of aluminium particles/epoxy composite. Prog Org Coat 101: 305–308
24. Chen K, Zhao X, Zhang F, Xiaoli Wu, Huang W, Liu W, Wang X (2019) Influence of gamma irradiation on the molecular dynamics and mechanical properties of epoxy resin. Polym Degrad Stab 168:108940
25. Birger S, Moshonov A, Kenig S (1989) The effects of thermal and hygrothermal ageing on the failure mechanisms of graphite-fabric epoxy composites subjected to flexural loading. Composites 20(4):341–348
26. Navaneethakrishnan G et al (2020) Structural analysis of natural fiber reinforced polymer matrix composite. Mater Today: Proc 21:7–9
27. Chaudhary V et al (2020) Comparative study of mechanical properties of dry and water aged jute/flax/epoxy hybrid composite. Mater Today: Proc 25: 857–861
28. Boukhoulda BF, Adda-Bedia E, Madani K (2006) The effect of fiber orientation angle in composite materials on moisture absorption and material degradation after hygrothermal ageing. Compos Struct 74(4):406–418

29. Costa UO, Oliveira MS, Garcia Filho FC, Luz FS, Garcia JM, Silva AO, Figueiredo ABS, Nascimento LFC, Monteiro SN (2019) Influência Da Radiação UV No Comportamento Balístico De Um Compósito De Matriz Epoxídica Reforçada Com Tecido Híbrido De Malva/Juta, 1359–1365. In: 74 Congresso Anual da ABM, São Paulo
30. Pani PR et al (2019) Flexural and specific wear rate of seawater aged bamboo, jute and glass fiber reinforced polymer hybrid composites. Mater Today: Proc 18: 3409–3414
31. Lu, MM, Van Vuure AW (2019) Effects of water immersion ageing on composites made of non-dry flax fibres. Mater Today: Proc
32. Wang X, Petrů M (2020) Degradation of bending properties of flax fiber reinforced polymer after natural aging and accelerated aging. Constr Build Mater 240:117909
33. Wang KF, Wang BL (2018) A mechanical degradation model for bidirectional natural fiber reinforced composites under hydrothermal ageing and applying in buckling and vibration analysis. Compos Struct
34. Ray S, Cooney RP (2018) Thermal degradation of polymer and polymer composites. Handbook of environmental degradation of materials, pp 185–206
35. Potts JR, Dreyer DR, Bielawski CW, Ruoff RS (2011) Graphene-based polymer nanocomposites. Polymer 52(1):5–25
36. Abtew MA, Boussu F, Bruniaux P, Loghin C, Cristian I, Chen Y, Wang L (2019) Ballistic impact performance and surface failure mechanisms of two-dimensional and three-dimensional woven p-aramid multi-layer fabrics for lightweight women ballistic vest applications. J Ind Text

Study of Face Shell Bedding Concrete Blocks Prisms with Different Laying Mortar Strength

T. E. S. Lima, A. R. G. Azevedo, M. T. Marvila, E. B. Zanelato, A. L. C. Paes, J. Alexandre, and S. N. Monteiro

Abstract The structural masonry has as basic characteristic the use of the supporting walls, formed with structural blocks joined by seating mortar. The blocks must have compressive strength compatible with the loads to which they will be subjected to, and the mortar must be adequately resisted in order not to compromise the structure of which it is part of, and absorb the deformations to which the masonry is subjected. Two types of mortar bedding are recommended: full bedding, covering net area for unit, and face shell bedding, where the mortar is placed only in the face shell area of the block. This work aims to test the compression of face shell bedding concrete blocks prisms with two traces of mixed mortar with different compressive

T. E. S. Lima · A. R. G. Azevedo (✉) · E. B. Zanelato · J. Alexandre
LECIV – Civil Engineering Laboratory, UENF - State University of the Northern Rio de Janeiro, Av. Alberto Lamego, 2000, Campos dos Goytacazes, Rio de Janeiro 28013-602, Brazil
e-mail: afonso.garcez91@gmail.com

T. E. S. Lima
e-mail: thuanylima.es@gmail.com

E. B. Zanelato
e-mail: ebzanelato@gmail.com

J. Alexandre
e-mail: jonasuenf@gmail.com

A. R. G. Azevedo
TER – Department of Agricultural Engineering and Environment, UFF - Federal Fluminense University, Rua Passo da Pátria, 341, Niterói, Rio de Janeiro 24210240, Brazil

T. E. S. Lima · M. T. Marvila · A. L. C. Paes
LAMAV – Advanced Materials Laboratory, UENF - State University of the Northern Rio de Janeiro, Av. Alberto Lamego, 2000, Campos dos Goytacazes, Rio de Janeiro 28013-602, Brazil
e-mail: markssuel@hotmail.com

A. L. C. Paes
e-mail: alcpaes@gmail.com

S. N. Monteiro
Department of Materials Science,, IME - Military Institute of Engineering, Square General Tibúrcio, 80, Rio de Janeiro 22290-270, Brazil
e-mail: snmonteiro@gmail.com

J. Li et al., *Characterization of Minerals, Metals, and Materials 2021*,
The Minerals, Metals & Materials Series,
https://doi.org/10.1007/978-3-030-65493-1_52

strength. It has been concluded that the increase of the compressive strength of the mortarinfluences the increase in the compressive strength of the prisms with face shell bedding type.

Keywords Structural masonry · Prism · Mortar · Resistance

Introduction

Structural masonry is a rationalized constructive system, where the elements that perform the structural function are masonry, simultaneously serving the functions of structure and sealing. The main structural concept linked to its use is the transmission of actions through compression stresses. Its main advantages are the rationality in the consumption of materials and the speed of execution. It is obtained by superimposing structural blocks, tied together, and joined by mortar joint.

To estimate the strength of the wall required to support the loads imposed on the structure, the designer needs to know the physical and mechanical characteristics of the component materials. The blocks must have compressive strength compatible with the loads to which they will be subjected to, and the laying mortar must develop adequate strength in order not to compromise the structure of which it is part of, and should not be more resistant than the block, and still absorb the deformations to which the masonry is submitted. Therefore, Brazilian Association of Technical Standards [1] limits a maximum value of 70% of the characteristic compressive strength of the block referred to the liquid area, for the compressive strength of the laying mortars for structural masonry.

However, other factors also interfere with the structural behavior of the masonry; among them are the finishing and workmanship qualities, the curing conditions, and the thickness of the joint and the mortar pattern. The latter can be decisive in the production and performance of the work. Two types of settlement of the units are used, in a relevant and standardized way: face shell bedding and full bedding. The face shell bedding consists of executing the horizontal joint with mortar only in the longitudinal septa of the blocks. On the other hand, in full bedding, the mortar is placed in all the septa of the blocks, including the transversal septa, as seen in Fig. 1. The face shell bedding on horizontal joints has become a widely used option, since it makes execution faster.

In this sense, this work aims to evaluate the behavior of face shell bedding prisms done with concrete blocks with two mortar ratios of different compression strength.

Materials and Methods

The hollow concrete blocks used in this work were manufactured in the city of Campos dos Goytacazes/RJ, with dimensions of (14 × 19 × 39) cm (thickness × height x length), water absorption of 6.32%, humidity of 12.34%, and compression strength of 6.01 MPa referring to the gross area and 12.97 MPa referring to the net area.

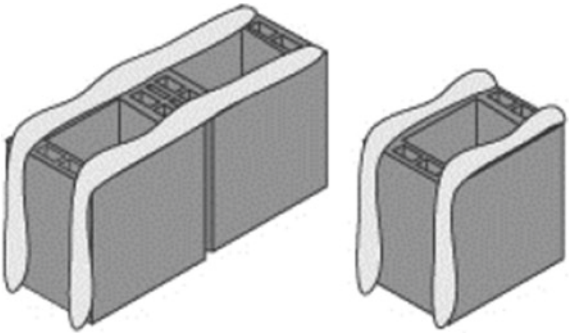

Fig. 1 Face shell bedding type. Source: PORTELLA, 2015

Two mortar ratios were defined for this study, 1:0.5:4.5 and 1:1:6, respectively representing cement:lime:sand. The mortars were produced with Portland cement CPII E-40 with a density of 2.97 g/cm^3, fineness of 4.00%, and a 28th day of compressive strength of 45.3 MPa, hydrated lime CH-III with a density of 2.31 g/cm^3 and washed sand from the Paraíba do Sul River, Campos dos Goytacazes/RJ, with a fineness module of 2.04, maximum size of 2.4 mm, specific weight in bulk of 2.61 g/cm^3. The water/binders ratio and the compressive strength were 0.9 and 8.93 MPa, respectively, for the mortar 1:0.5:4.5 and 1.26 and 5.72 MPa, respectively, for the mortar 1:1:6 keeping the consistency of the mortar in the range of (260 ± 5) mm. It has been noticed that both mortars remained below the limit of 70% of the characteristic compressive strength of the block referring to the net area.

To perform the compressive strength test, six prisms were produced for each mortar mix. All prisms had a mortar joint thickness of (10 ± 3) mm and held for 28 days immobile in a weather-free place in the curing process (Fig. 2).

Fig. 2 Construction of the prisms: **a** detail of the face shell bedding type **b** constructed prism. (Color figure online)

The compression strength test of the prisms followed the procedures of [2] and was performed in the MTS servo-hydraulic system with a capacity of 500 kN, at a rate of 0.05 MPa/s, located in the civil engineering structures laboratory at UENF.

Results and Discussion

The results of the compressive strength tests of the prisms are shown in Table 1.

Analyzing the results, it can be seen that the 36% increase in compressive strength between the two mortars generated a 24% increase in the compressive strength of the prisms.

In addition, the prism/block ratio ranged from 0.5 to 0.7, falling within the allowed range of 0.5–0.9 for concrete blocks in Brazil, according to [3–15].

Regarding the rupture mode, all the prisms ruptured due to the development of tensile stresses on the lateral face of prism, caused by rotation and crushing of the supports (Fig. 3). The crushing of the lateral mortar induces horizontal stresses that cause the material to rupture by flexion, as evidenced by [4–18].

Table 1 Results of the compressive strength of the prisms

Mortar ratio	Prisms compressive strength (f_{pm}) (MPa)	Standard deviation (MPa)	Coefficient of variation (%)	Prism/Block ratio (η)	Normalization
1:0.5:4.5	3.91	0.26	4.32	0.65	1
1:1:6	2.98	0.11	3.69	0.50	0.76

Fig. 3 Rupture mode of the prisms with face shell bedding type. (Color figure online)

Conclusions

As shown by the tests carried out, the compressive strength of the laying mortar influences the compressive strength of structural masonry prisms. Therefore, a 36% increase in the compressive strength of the laying mortars generated a 24% increase in the compressive strength of the prisms.

In the rupture mode of the prisms, there were no notable differences in the cracking and behavior of the specimens, the rupture being presented by all prisms due to the development of tensile stresses on the lateral face, caused by rotation and crushing of the supports, causing crushing of the lateral mortar that induces horizontal stresses that cause failure by flexion.

Acknowledgements The authors thank the Brazilian agencies CNPq, CAPES, and FAPERJ for the support provided to this investigation.

References

1. Brazilian Association of Technical Standards (2011) Structural masonry—concrete blocks part 1: design. NBR 15961–1, Rio de Janeiro
2. Brazilian Association of Technical Standards (2016) Masonry of concrete blocks—test methods. NBR 16522, Rio de Janeiro
3. Ramalho MA, Côrrea MRS (2003) Projeto de edifícios de alvenaria estrutural. Pini, São Paulo
4. Shrive NG (1982) The failure mechanism of face-shell bedded (ungrouted and unreinforced) masonry. University of Calgary, Calgary
5. Khalaf FM (1996) Factors influencing compressive strength of concrete masonry prism. Mag Concr Res 48(175):95–101. https://doi.org/10.1680/macr.1996.48.175.95
6. Martins ROG, Nalon GH, Alvarenga RCSS, Pedroti LG, Ribeiro JCL (2018) Influence of blocks and grout on compressive strength and stiffness of concrete masonry prisms. Constr Build Mater 182:233–241. https://doi.org/10.1016/j.conbuildmat.2016.12.112
7. Mohamad G, Lourenço PB, Roman HR (2007) Mechanics of hollow concrete block masonry prism under compression: review and prospects. Cement Concr Compos 29(3):181–192. https://doi.org/10.1016/j.cemconcomp.2006.11.003
8. Hilsdorf HK (1969) An investigation into the failure mechanism of brick masonry loaded in axial compression. In: Publishing G (ed) Designing, engineering and construction with masonry products, FB Johnson. Houston, Texas, pp 34–41
9. Santos CFR, Alvarenga RCSS, Ribeiro JCL, Castro LO, Silva RM, Santos AAR, Nalon GH (2017) Numerical and experimental evaluation of masonry prisms by finite element method. IBRACON Struct Mater J 10(2):493–508. https://doi.org/10.1590/s1983-41952017000200010
10. Romagna RH (2000) Resistência à compressão de prismas de blocos de concreto grauteados e não-grauteados. Master's thesis, Universidade Federal de Santa Catarina
11. Mohamad G, Fonseca FS, Vermeltfoort T, Martens DRW, Lourenço PB (2017) Strength, behavior, and failure mode of hollow concrete masonry constructed with mortars of different strengths. Constr Build Mater 134:489–496. https://doi.org/10.1016/j.conbuildmat.2016.12.112
12. Camacho JS, Logullo BG, Parsekian GA, Soudais PRN (2015) The influence of grouting and reinforcement ratio in the concrete block masonry compressive behavior. IBRACON Struct Mater J 8(3):353–364. https://doi.org/10.1590/S1983-41952015000300006

13. Portella RP (2015) Fatoreficiência da resistência prisma/blococerâmico de paredesvazadas. Master's thesis, Universidade Federal de Santa Maria
14. Azevedo ARG, Marvila MT, Júnior W, Alexandre J, Xavier GC, Zanelato EB, Cerqueira NA, Pedroti LG, Mendes BC (2019) Assessing the potential of sludge generated by the pulp and paper industry in assembling locking blocks. J Build Eng 23:334–340. https://doi.org/10.1016/j.jobe.2019.02.012
15. Marvila MT, Alexandre J, Azevedo ARG, Zanelato EB (2019) Evaluation of the use of marble waste in hydrated lime cement mortar based. J Mater Cycles Waste Manage 21(5):1250–1261. https://doi.org/10.1007/s10163-019-00878-6
16. França BR, AzevedoARG, Monteiro SN, Filho Garcia FC, Marvila MT, Alexandre J, ZanelatoEB (2018) Durability of soil-cement blocks with the incorporation of limestone residues from the processing of marble. Mater Res 21(1). https://doi.org/10.1590/1980-5373-mr-2017-1118
17. Azevedo ARG, Vieira CMF, Ferreira WM, Faria KCP, Pedroti LG, Mendes BC (2020) Potential use of ceramic waste as precursor in the geopolymerization reaction for the production of ceramic roof tiles. J Buil Eng 29. DOI: https://doi.org/10.1016/j.jobe.2019.101156
18. Marvila MT, Azevedo ARG, Alexandre J, Zanelato EB, Azeredo NG, Simonassi NT, Monteiro SN (2019) Correlation between the properties of structural clay blocks obtained by destructive tests and Ultrasonic Pulse Tests. J Buil Eng 26. https://doi.org/10.1016/j.jobe.2019.100869

Study of Pathologies in Alkali-Activated Materials Based on Slag

M. T. Marvila, A. R. G. Azevedo, E. B. Zanelato, T. E. S. Lima, G. C. G. Delaqua, C. M. F. Vieira, L. G. Pedroti, and S. N. Monteiro

Abstract The main pathogens that occur in alkali-activated materials based on blast furnace slag are efflorescence and the black heart, due to the saturation of very high amounts of sodium. Therefore, the objective of this work was to measure the alkali mortars activated by a solution of 2.5, 5, 7.5, 10, 12.5, and 15M using sodium hydroxide, testing the material under compression and water absorption with 7 days of curing at room temperature, and thermal curing at 60 °C. The results show that the use of 12.5M and 15M causes the appearance of this pathology when curing in a normal environment, while compositions with 10M, 7.5M, and 5M present excellent technological parameters.

Keywords Pathologies · Alkali-activated materials · Slag

M. T. Marvila (✉) · A. R. G. Azevedo · E. B. Zanelato · T. E. S. Lima · G. C. G. Delaqua · C. M. F. Vieira
LECIV – Civil Engineering Laboratory, UENF - State University of the Northern Rio de Janeiro, Av. Alberto Lamego, 2000, Campos dos Goytacazes, Rio de Janeiro 28013-602, Brazil
e-mail: markssuel@hotmail.com

A. R. G. Azevedo
TER – Department of Agricultural Engineering and Environment, UFF - Federal Fluminense University, Rua Passo da Pátria, 341, Niterói, Rio de Janeiro 24210240, Brazil

E. B. Zanelato
DIRINF – Directorate of Infrastructure Rectory, IFF - Federal Institute Fluminese, Rua Cel. Valter Kramer, 357 - Parque Vera Cruz, Campos dos Goytacazes, Rio de Janeiro 28080-565, Brazil

L. G. Pedroti
UFV - Federal University of Viçosa, DEC, Av. Peter Henry Rolfs, s/n - Campus Universty, Viçosa, Minas Gerais 36570-000, Brazil

S. N. Monteiro
Department of Materials Science, IME - Military Institute of Engineering, Square General Tibúrcio, 80, Rio de Janeiro 22290-270, Brazil

J. Li et al., *Characterization of Minerals, Metals, and Materials 2021*,
The Minerals, Metals & Materials Series,
https://doi.org/10.1007/978-3-030-65493-1_53

Introduction

The use of alkali materials activated as building components is increasingly prominent in the civil construction sector [1]. This fact happens due to the great advantages that this type of material has, such as faster gain of resistance than conventional cementitious materials, since the activated alkali materials reach satisfactory resistance values at 3 or 7 days, for example [2].

The other advantages that can be mentioned are: resistance to high temperatures, enabling safety in case of fires [3]; chemical resistance and stability, enabling application in situations of greater aggressiveness; and higher compressive strength values [4]. There is also a benefit related to the possibility of applying waste instead of materials whose production is highly polluting, such as cement [5, 6].

As disadvantages can mention the problems related to the application of alkaline solutions based on NaOH [7], these problems are initially operational, since the material is a very strong base and can cause burns to less careful workers. From the technological point of view, there is also a problem related to the highly exothermic dissolution of NaOH in water, which, if not done in advance, the mixing of the materials that make up the activated alkali compound can cause the occurrence of unwanted cracks and retractions [8, 9].

Other disadvantages are related to the high viscosity of the alkaline solution, which impairs the workability of the activated alkali concretes and mortars, hindering the operations involving the material, and also the occurrence of pathological problems in these materials [8, 9].

Regarding the pathologies that can occur in activated alkali materials, the occurrence of shrinkage and cracks stands out, due to chemical and autogenous principles and the particularities of the reaction itself [10]; and efflorescence, which can be considered the main pathological problem in activated alkali materials. This type of problem occurs when the sodium present in the alkaline solution and necessary to activate the hardening reactions of the slapper reacts with the gases present in the air, such as CO_2, producing a whitish powder that is concentrated on the surface of the material [11, 12]. This powder, in addition to proving the inefficiency of the alkaline activation reaction, is problematic because it causes discomfort to users who have contact with the material, such as skin irritation and minor burns [11, 12].

In the case of calcium-rich strikers, such as blast furnace slag, usually the presence of efflorescence is accompanied by a drop in resistance since the compounds responsible for the resistance formed in the reaction of this material are of the tobermorite type, as shown in Fig. 1 [7, 13]. In Fig. 1 blue triangle represents tetrahedral Si sites; red triangle represents Al substitution into one bridging site; green rectangles denote CaO layers; blue circles denote Al species; yellow circles represent Na+ species; green circles denote Ca^{2+} species.

It is observed that the resistant compounds are C-A-S-H networks [14, 15]. Therefore, if efflorescence is eliminated, two possibilities may occur: excess sodium or deficiency in the alkaline activation reaction due to physical incompatibility, caused

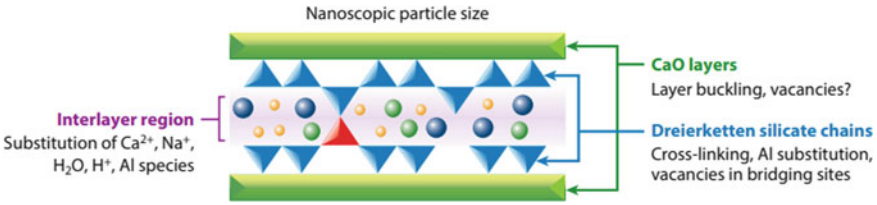

Fig. 1. Tobermorite-like C-A-S-H gel structure from [13]. (Color figure online)

by fineness and granulometry criteria, or chemical, by the absence of calcium or silicates [9, 16].

Another important pathology in activated alkali materials is the black heart, which occurs due to sodium saturation in the central region of the material [17–19]. This defect is more common in burnt ceramic pieces, which due to the heat flow present a concentration of sodium in the central region; however, it can occur in materials formed by alkaline activation [18, 20]. The explanation is the occurrence of a mechanism opposite to that which makes efflorescence possible. That is, while efflorescence occurs due to reaction with ambient air, forming a reaction pile, the black heart occurs when the activated alkali material is confined in an environment with no CO_2, causing the concentration of sodium inside the material [17, 19, 20].

In this context, the objective of this work is to carry out the production of activated alkali materials produced with solutions of different concentrations of sodium and to relate the compounds formed to the pathological problems, also evaluating the influence on the mechanical resistance of the material.

Materials and Methods

The following materials were used to produce the activated alkali materials: granulated blast furnace slag extracted from a Brazilian steel industry located in Vitória-ES, Brazil; river washed sand extracted in Campos dos Goytacazes-RJ, Brazil; and sodium hydroxide micropearls with 99% purity content. The slag is classified as a precursor rich in calcium since the Ca/(Si + Al) ratio was 2.18, greater than 1, necessary to classify the precursor as such [7].

The composition used was 1:2:0.45 (binder:sand:water), with the sum of blast furnace slag and sodium hydroxide present in the activating solution being used as a binder. The solution was produced by dissolving the sodium hydroxide in water through a magnetic mixer, being dosed in different molar ratios, from 2.5 to 15 M. The molarity calculation is performed using equation 1:

$$M = \frac{[NaOH]}{V} \tag{1}$$

where [NaOH] is the number of moles present in the solution, obtained by calculating the sodium mass divided by the molar mass of the compound, which is worth approximately 40 g/mol. V is the volume of the solution.

With this composition of activated alkali material, cylindrical specimens of 50 × 100 mm were produced, using three experimental units per composition, type of cure and per test performed. The specimens were produced through molding, being applied in three different layers, with the application of 25 strokes per layer. Afterwards, they were cured in two different conditions: in normal cure at an ambient temperature of approximately 25 °C and in thermal cure at 60 °C. The cure time was 7 days. The procedure followed the recommendations of the Brazilian standard [21, 22].

Then the specimens were tested through three different tests: resistance to compression, using a hydraulic press brand SOLOTET; water absorption; and mass density in the hardened state. In all tests, the results for activated alkali materials submitted to normal and thermal curing procedures were verified.

Results

Figure 2 shows the results of compressive strength at 7 days for the activated alkali materials studied. It is observed that the best resistance parameters were obtained

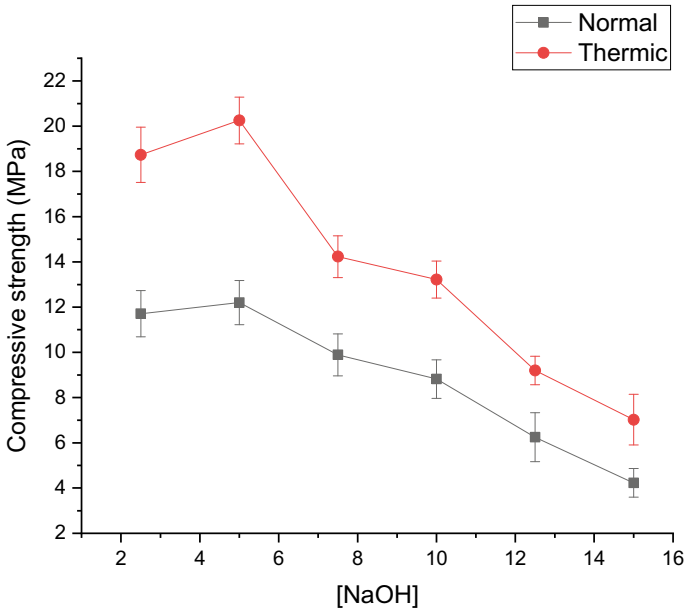

Fig. 2. Compressive strength of activated alkali materials. (Color figure online)

for the solution with molarity 5M performed in thermal curing. The materials cured at normal temperature obtained much lower resistance parameters, which can be attributed to the efflorescence that occurred in the materials, mainly in the compositions with higher sodium content. It is noteworthy that the efflorescence occurred in all the compositions; however, it was more intense in the compositions with higher sodium contents. This indicates that compositions containing lower molar ratios also showed an inefficient reaction, because efflorescence also occurred in these compositions [14, 15].

Figure 3 shows the occurrence of efflorescence in activated alkali materials cured at room temperature. Figure 3a shows the composition with 5M, which showed the best results for compression at normal temperature, while Figure 3b shows the composition 15M, illustrating the excess of sodium and the intensity of efflorescence in the material. Therefore, there is a direct relationship between resistance to this pathology illustrated in the figure.

Regarding the resistance of thermally cured specimens, it is observed that there is no efflorescence in the material, as they were confined in a place without access to CO_2. On the other hand, the excess of sodium accumulated internally, originating with the black heart and forming a critical defect and a point of weakness that was the main responsible for the drop in resistance in the material. This characteristic

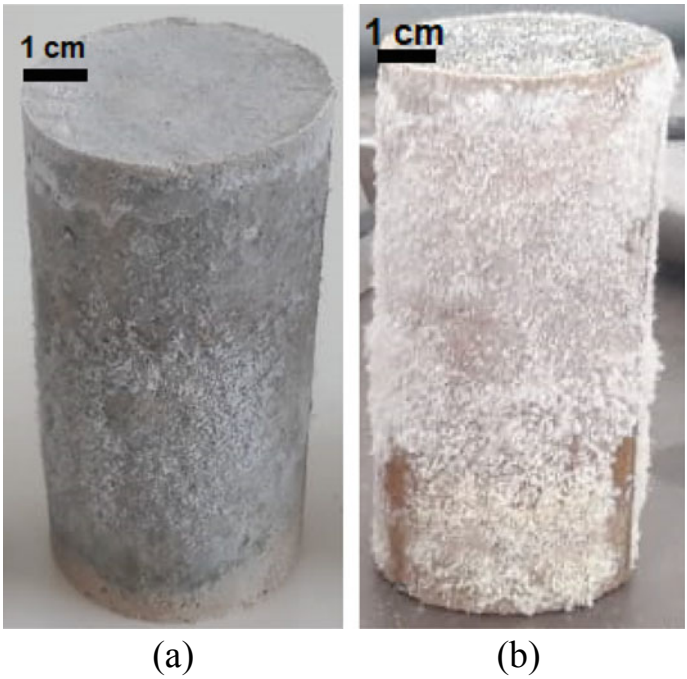

Fig. 3. Efflorescence in activated alkali materials: **a** 5 M; **b** 15 M. (Color figure online)

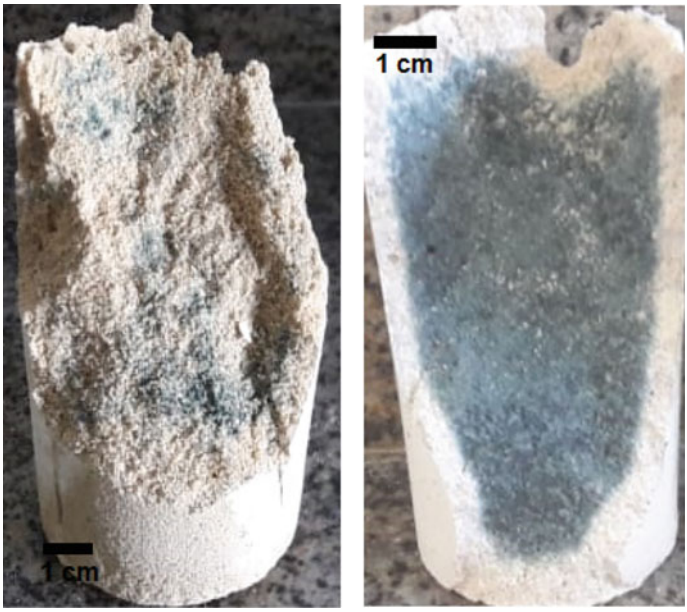

Fig. 4. Black heart in activated alkali materials: **a** 5 M; **b** 15 M. (Color figure online)

even demonstrates that the formation of C-A-S-H networks did not occur sufficiently in compositions with a high sodium content [13].

Fig. 4 shows the rupture surface of the 5M ratio, which presented the main strength values, and of the 15M composition. It is observed that while the 5M composition did not present the black heart defect, the 15M composition was totally blackened. This illustrates the non-formation of the activated and typical alkali networks of this type of material and justifies the low resistance obtained.

Fig. 5 shows the density of the activated alkali materials studied, while Fig. 6 shows the results of water absorption. It is observed that the thermal curing reduces the density of the materials, which is attributed to the elimination of water caused by the heating rates. This affects the porosity and consequently the water absorption of the materials, although the compositions with a lower sodium content do not present statistical difference between the types of cure studied. Given this information, it is possible to attribute the greater water absorption of activated alkali materials produced in thermal cure with higher sodium contents to the black heart defect presented in these compositions. That is, the black heart functions as a region of fragility within the material, being responsible for the increase in water absorption rates.

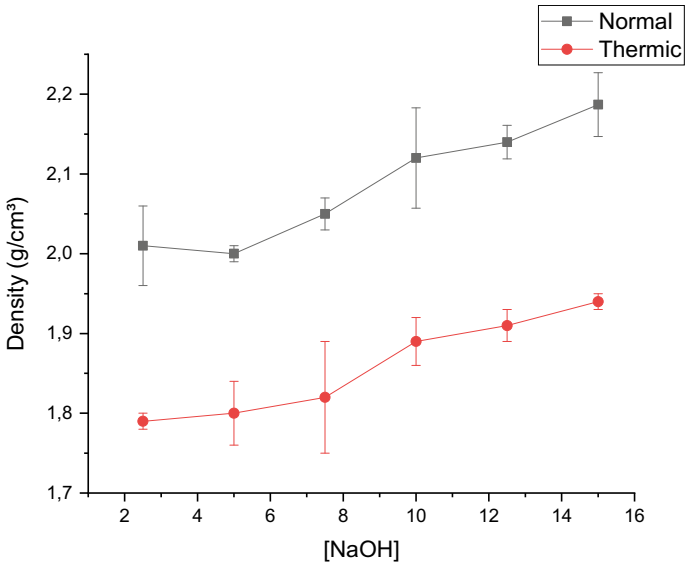

Fig. 5. Density of activated alkali materials. (Color figure online)

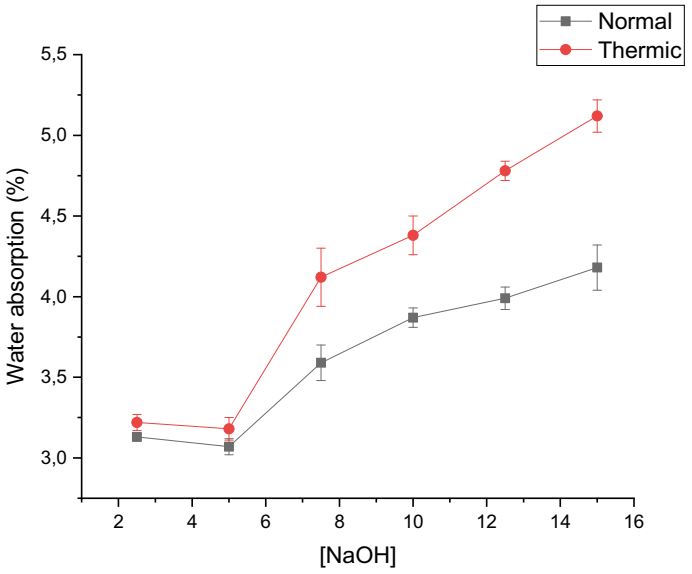

Fig. 6. Water absorption of activated alkali materials. (Color figure online)

Conclusion

After the results, it can be concluded that:

- The use of high levels of sodium in activated alkali materials favors the occurrence of pathologies such as efflorescence and black heart.
- Curing at normal temperature favors the reaction of the sodium present in the composition of the activated alkali materials and the CO_2 present in the atmospheric air, mainly in sodium contents above 7.5M. This considerably reduces the compressive strength of the material.
- Curing at temperatures of 60 °C reduces the occurrence of efflorescence and improves the kinetics of activated alkali reactions, contributing to the increase in resistance to compression. However, if there is excess sodium (above 7.5M in this research), another pathological problem arises due to the concentration of sodium inside the material. It is the black heart, which forms a region of fragility within the material and reduces the resistance to compression.
- Thermal curing reduces the density of activated alkali materials due to the elimination of water by thermal rates and increases the absorption of water in compositions with high levels of sodium due to the occurrence of the black heart defect.

Acknowledgements The authors thank the Brazilian agencies CNPq, CAPES, and FAPERJ for the support provided to this investigation.

References

1. Angulo-Ramírez DE, Mejía de Gutiérrez R, Medeiros M (2018) Alkali-activated Portland blast furnace slag cement mortars: Performance to alkali-aggregate reaction. Constr Build Mater 179:49–56. https://doi.org/10.1016/j.conbuildmat.2018.05.183
2. Ismail I, Bernal SA, Provis JL, San Nicolas R, Hamdan S, van Deventer JSJ (2014) Modification of phase evolution in alkali-activated blast furnace slag by the incorporation of fly ash. CemConcr Compos 45: 125–135. DOI: https://doi.org/10.1016/j.cemconcomp.2013.09.006
3. Lahoti M, Tan KH, Yang EH (2019) A critical review of geopolymer properties for structural fire-resistance applications. Constr Build Mater 221:514–526. https://doi.org/10.1016/j.conbuildmat.2019.06.076
4. Majidi B (2009) Geopolymer technology, from fundamentals to advanced applications: a review. Mater Technol 24:79–87. https://doi.org/10.1179/175355509X449355
5. Marvila MT, Alexandre J, de Azevedo ARG, Zanelato EB (2019) Evaluation of the use of marble waste in hydrated lime cement mortar based. J Mater Cycles Waste Manag 21:1250–1261. https://doi.org/10.1007/s10163-019-00878-6
6. Marvila MT, Azevedo ARG, Barroso LS, Barbosa MZ, de Brito J (2020) Gypsum plaster using rock waste: a proposal to repair the renderings of historical buildings in Brazil. Constr Build Mater 250:118786. https://doi.org/10.1016/j.conbuildmat.2020.118786
7. Provis JL (2014) Geopolymers and other alkali activated materials: why, how, and what? Mater Struct Constr 47:11–25. https://doi.org/10.1617/s11527-013-0211-5

8. Azevedo ARG, Vieira CMF, Ferreira WM, Faria KCP, Pedroti LG, Mendes BC (2020) Potential use of ceramic waste as precursor in the geopolymerization reaction for the production of ceramic roof tiles. J. Build Eng 29:101156. https://doi.org/10.1016/j.jobe.2019.101156
9. de Azevedo ARG, Marvila MT, Tayeh BA, Cecchin D, Pereira AC, Monteiro SN (2021) Technological performance of açaí natural fibre reinforced cement-based mortars. J Build Eng 33:101675. https://doi.org/10.1016/j.jobe.2020.101675
10. Simão L, Hotza D, Ribeiro MJ, Novais RM, Montedo ORK, Raupp-Pereira F (2020) Development of new geopolymers based on stone cutting waste. Constr Build Mater 257:119525. https://doi.org/10.1016/j.conbuildmat.2020.119525
11. Zhang Z, Provis JL, Ma X, Reid A, Wang H (2018) Efflorescence and subflorescence induced microstructural and mechanical evolution in fly ash-based geopolymers. Cem Concr Compos 92:165–177. https://doi.org/10.1016/j.cemconcomp.2018.06.010
12. Longhi MA, Rodríguez ED, Walkley B, Zhang Z, Kirchheim AP (2020) Metakaolin-based geopolymers: Relation between formulation, physicochemical properties and efflorescence formation. Compos Part B Eng 182:107671. https://doi.org/10.1016/j.compositesb.2019.107671
13. Provis JL, Bernal SA (2014) Geopolymers and related Alkali-activated materials. Annu Rev Mater Res 44:299–327. https://doi.org/10.1146/annurev-matsci-070813-113515
14. Provis JL, van Deventer JSJ, kinetics G (2007) 1. In situ energy-dispersive X-ray diffractometry. Chem Eng Sci 62: 2309–2317. DOI: https://doi.org/10.1016/j.ces.2007.01.027
15. Duxson P, Mallicoat SW, Lukey GC, Kriven WM, van Deventer JSJ (2007) The effect of alkali and Si/Al ratio on the development of mechanical properties of metakaolin-based geopolymers. Colloids Surf Physicochem Eng Asp 292:8–20. https://doi.org/10.1016/j.colsurfa.2006.05.044
16. Rivera JF, Cuarán-Cuarán ZI, Vanegas-Bonilla N, Mejía de Gutiérrez R (2018) Novel use of waste glass powder: Production of geopolymeric tiles. Adv Powder Technol. https://doi.org/10.1016/j.apt.2018.09.023
17. Kharol SK, Fioletov V, McLinden CA, Shephard MW, Sioris CE, Li C, Krotkov NA (2020) Ceramic industry at Morbi as a large source of SO_2 emissions in India. Atmos Environ 223:117243. https://doi.org/10.1016/j.atmosenv.2019.117243
18. Cava S, Longo E, Paskocimas CA, Varela JA, Tasca A, Mendonça T, Herter CG, Barbosa JC Jr (2000) Influência da cinética de oxidação no controle da atmosfera de fornos de revestimentos cerâmicos. Cerâmica 46:56–60. https://doi.org/10.1590/S0366-69132000000200002
19. Santos IMG, Silva JM, Trindade MFS, Soledade LEB, Souza AG, Paskocimas CA, Longo E (2005) Efeito da adição de rejeito na redução de coração negro em cerâmicas vermelhas. Cerâmica 51:144–150. https://doi.org/10.1590/S0366-69132005000200012
20. Jin Q, Lu B, Pan Y, Tao X, Himmelhaver C, Shen Y, Gu S, Zeng Y, Li X (2019) Novel porous ceramic sheet supported metal reactors for continuous-flow catalysis. Catal Today. https://doi.org/10.1016/j.cattod.2019.12.006
21. ABNT (2011) NBR 9778—argamassa e concreto endurecidos-Determinação da absorção de água, índice de vazios e massa específica., Assoc Bras Normas Técnicas
22. ABNT (2007) Nbr 5739 :2007 Concreto-Ensaios de compressão de corpos-de-prova cilíndricos, Assoc. Bras. Normas Técnicas

Study of the Feasibility of Incorporation Clay from Campos Dos Goytacazes-RJ, in Mortar Applied on Walls and Ceilings

L. C. G. Botelho, C. G. Xavier, H. A. Colorado, A. R. G. Azevedo, J. Alexandre, C. M. Vieira, and M. T. Marvila

Abstract Civil construction is in constant search for alternatives to reduce the degradation of the environment and, therefore, studies new materials technologies that are sustainable. Mortar is an example whose raw materials involve a high commercial value and highly energetic production processes in relation to CO_2 emissions. This work compares embedded clay mortars for use in wall and ceiling coverings. These are two clays: a clay from Campos dos Goytacazes-RJ and an industrialized clay collected from local businesses. For this purpose, characterization of the aggregates, study of the mortar dosage, consistency indexes, water retention tests, specific gravity, compressive strength, and tensile bond strength were carried out. The results indicated that Campos clay tested as a material for dosing mortar in wall and ceiling was compatible with industrial clay, allowing the commercialization of the studied product.

Keywords Clay · Mortar · Minerals

L. C. G. Botelho · A. R. G. Azevedo (✉) · C. M. Vieira · M. T. Marvila
LAMAV – Advanced Materials Laboratory, UENF - State University of the Northern Rio de Janeiro, Av. Alberto LamegoCampos dos Goytacazes, Rio de Janeiro 200028013-602, Brazil
e-mail: afonso.garcez91@gmail.com

C. G. Xavier · J. Alexandre
LECIV – Civil Engineering Laboratory, UENF - State University of the Northern Rio de Janeiro, Av. Alberto Lamego, 2000, Campos dos Goytacazes, Rio de Janeiro 28013-602, Brazil

H. A. Colorado
CCComposites Laboratory, Universidad de Antioquia UdeA, Medellín, Colombia

A. R. G. Azevedo
TER – Department of Agricultural Engineering and Environment, UFF - Federal Fluminense University, Rua Passo da Pátria, 341, Niterói, Rio de Janeiro 24210240, Brazil

J. Li et al., *Characterization of Minerals, Metals, and Materials 2021*,
The Minerals, Metals & Materials Series,
https://doi.org/10.1007/978-3-030-65493-1_54

Introduction

The major problem presented using Portland cement and lime hydrated in construction materials, with emphasis on the use in mortars, the object of study of this paper, is the great CO_2 emission generated during the manufacture of these two binders [1, 2]. During the last decades there has been an increasing interest in cement industry to incorporate pozzolanic materials to cement and increase the strength and durability of mortars and concretes [3].

The study of new binders to replace the two mentioned above is extremely important and contributes to the sustainable development of the civil construction sector. Besides that, the replacement of these materials by other less reduce the price of the product obtained. One of the materials that can be used in this way and that have been studied for decades is clay.

The use of calcined clays as a pozzolanic material for mortar and concrete has received considerable attention in recent years [3–10]. Another reason, in addition to reducing CO_2 emissions, is that mortar and concrete, which contain pozzolanic materials exhibit considerable enhancement in durability properties [11]. The calcined clays which are rich in kaolinite present the best pozzolanic activity, while the illite and montmorillonite containing a high content of non-clay minerals such as quartz and calcite present a weak pozzolanic activity [4].

However, very few studies have been done on the use of clay as a substitute for lime, which is widely used in an empirical way in civil construction. This material leads to a higher water requirement for a given consistency and then improving the workability of the mixture [12, 13]. The great advantage of this incorporation is that this material does not require any industrial treatment and has low commercial value when compared to lime. The increase of the amount of mixing water does not lead to a decrease of the water retention capacity due to the water retaining properties of the clay minerals. Therefore, the clay fines improve the fresh mortar characteristics. However, the increase in water demand causes a strong decrease in the quality of the mortar concerning mechanical and durability properties [13].

In this context, this paper aims to study the incorporation of two different clays in mortars, one collected in the city of Campos dos Goytacazes-RJ, and the other, industrial, in order to compare them and make their use feasible.

Materials and Methods

The clays used in the mortars of this investigation were one from Campos—RJ and an industrial one. The qualitative mineralogical compositions of the clays, obtained by X-ray diffractometry, in a Shimadzu DXR 7000 equipment, operating with Cu-Kα and 2θ radiation ranging from 5° to 60°, are shown in Figs. 1 and 2. The chemical analysis, obtained by X-ray dispersive energy equipment, model EDX700

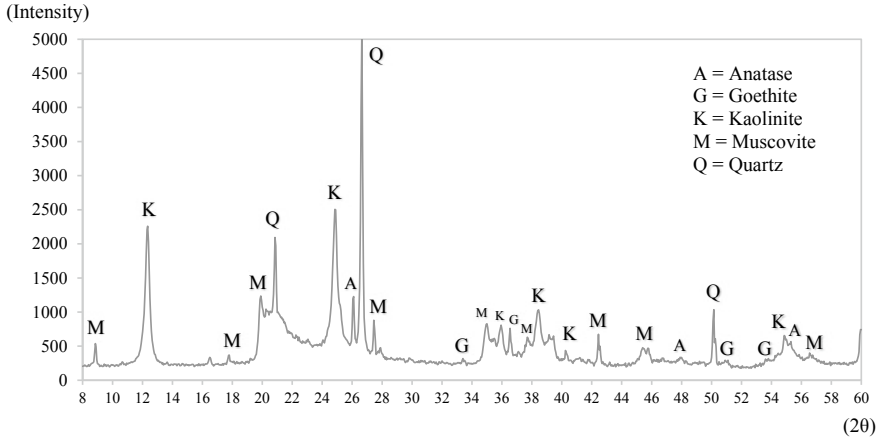

Fig. 1 Crystalline phases identified from the tested clay from Campos—RJ

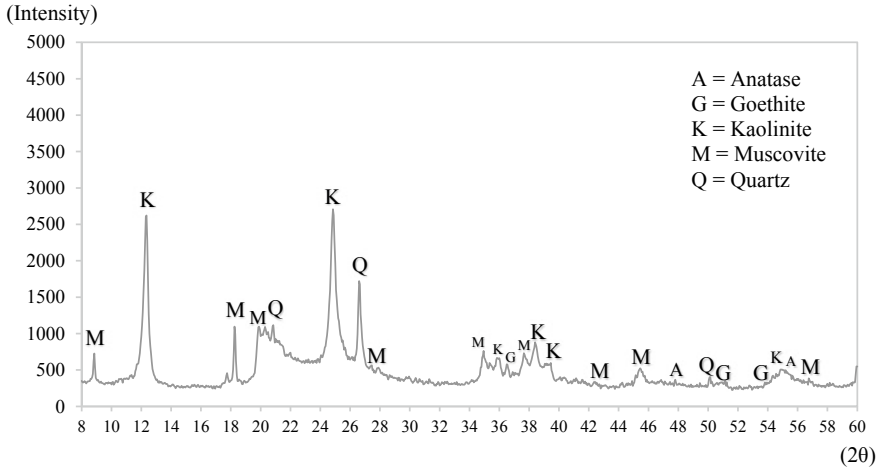

Fig. 2 Crystalline phases identified from an industrialize clay

from Shimadzu, is given in Table 1. With these clays, mortars were produced here denominated as tested clay mortar (TCM) and industrial clay mortar (ICM).

To prepare theses mortars, Brazilian Portland II Cement (2.87 g/cm^3) and Brazilian Portland V Cement (3.02 g/cm^3) were chosen, in order to manufacture the mortar used in this work. These adopted cements are easily found in the civil construction market. The small aggregate selected to produce the mortars was a quartzite sand obtained on the bed of the Paraíba do Sul River and is classified as a natural sand with maximum diameter equal to or lower than 4.8 mm [14] and specific mass 2.73 g/cm^3. The water used was supplied by the concessionaire of Campos dos Goytacazes.

Table 1 Chemical composition of tested clay and industrial clay

	SiO_2 (%)	Al_2O_3 (%)	SO_3 (%)	Fe_2O_3 (%)	TiO_2 (%)	K_2O (%)	CaO (%)	V_2O_5 (%)	ZrO_2 (%)
Tested clay	53.62	39.35	1.92	1.73	1.71	1.29	0.19	0.11	0.08
Industrial clay	51.02	42.2	2.31	1.99	1.79	0.53	-	0.08	0.04

Table 2 Mass values of mortar components

	Cement (g)	Tested clay (g)	Industrial clay (g)	Sand (g)	Water (g)	Total (g)	Maximum aggregate fines content (%)	Proportion of clay minerals (%)
Tested mortar	214.2	304.3	–	1884.3	505.0	2907.8	5.23	2.85
Industrial mortar	214.2	–	319.3	1884.3	570.0	2987.8	5.34	2.87

The granulometric characterization test of the clays studied was carried out according to [15], a Brazilian standard that determines the granulometric analysis of soils. The specific gravity and the Atterberg indices of the tested clay, the industrial clay, and the sand were measured [16, 17].

The mass ratio of 1:1:6 for each mortar with tested clay with CPII and CPV, and with industrial clay with CPII and CPV was corrected to the consistency index of 260 ± 10 mm according to [18]. The mass values of mortar component are given in Table 2. The air entrained content must be between 8.00 and 17.00% according to [19] for the study of dosage and workability. The compressive and the tensile bond strengths tests of mortars containing tested clay and industrial clay at the ages of 7, 14, and 28 days were performed according to [20].

Results and Discussion

The X-ray diffractogram of both the clays shows the presence of the clay mineral kaolinite and the minerals muscovite, quartz, goethite, and anatase, typical of the quaternary region of Campos dos Goytacazes-RJ. The chemical composition (Table 1) shows that the composition of $SiO_2 + Al_2O_3$ above 93.00% characterizes the tested clay as refractory, being able to withstand high temperatures if this material is used in mortar for application in the presence of fire. The amount of aluminum oxide (Al_2O_3: 42.20%) indicates the high presence of kaolinite. Potassium oxide (K_2O: 3.17%) can contribute in the mixture with cement to reduce calcium hydroxide (portlandite), a fragile part of the mortar. The other compounds below 1.00% do not interfere in the final product.

In the granulometric analysis (Fig. 3), the particle size distribution of the tested clay and the industrial clay has significant differences, mainly regarding the clay fraction, 32.00% for the tested clay and 42.00% for industrial clay. This is reflected in the mechanical strength; however, as for the workability measured by the mortar consistency, there was no significant difference. The maximum content of fines for the tested clay is 5.23% and for industrial clay is 5.34%, meeting the criterion < 7.00%.

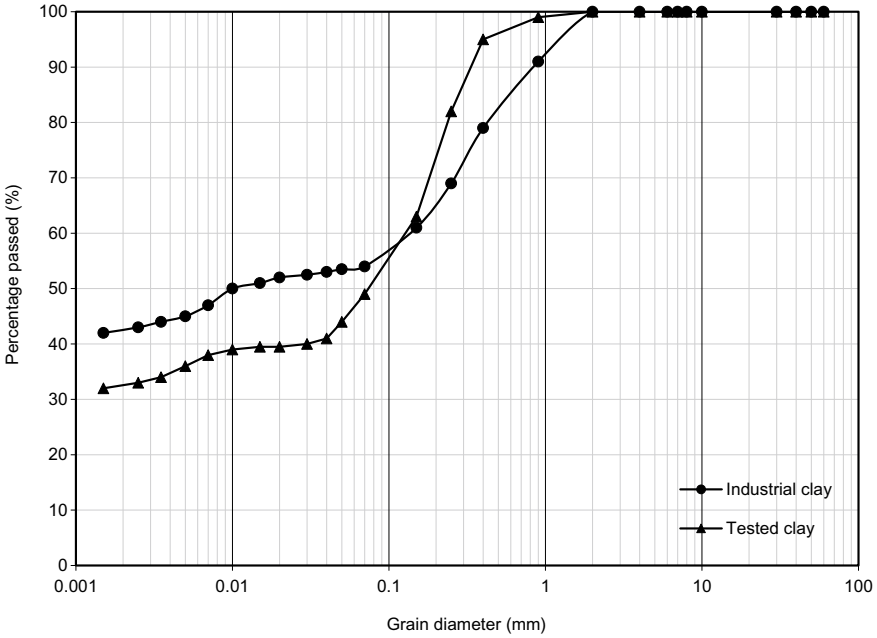

Fig. 3 Granulometric curves of the studied clays

The proportion of mineral clay is 2.85% for tested clay and 2.87% for industrial clay after mixing in the mortar, meeting the < 35.00% criterion.

It can be observed in Table 3 that the tested clay has practically the same specific gravity of the grains (2.60 g/cm^3) in comparison with the industrial clay (2.59 g/cm^3). This means that the mass ratio will be similar. The difference is in the plasticity index, whose lower IP value = 13.00% for the tested clay, presents the possibility of a less fluid mortar compared to the mortar with industrial clay.

Analyzing the test on the flow table, it is observed that to have the desired value of 260 ± 5 mm, it was necessary to add less water (505 g) in the tested clay mortar than the industrial clay mortar (570 g). This means that the workability of the mortar

Table 3 Real specific gravity and Atterberg limits of the clays

	Specific gravity (g/cm^3)	Natural water content (%)	Liquid limit (%)	Plastic limit (%)	Plasticity index (%)	Consistency index (%)	Activity
Tested clay	2.60	1.50	29.00	16.00	13.00	211.54	0.41 (inactive)
Industrial clay	2.59	–	47.40	21.50	25.90	–	0.61 (inactive)

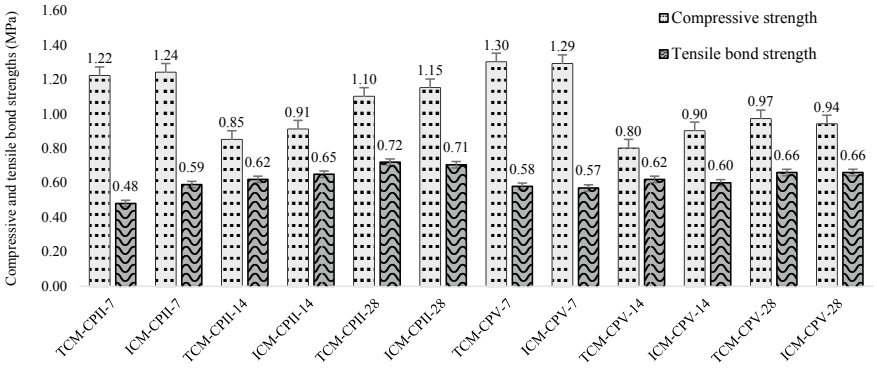

Fig. 4 Compressive and tensile bond strengths of the mortars varying clay, cement, and curing time

with the tested clay uses less water to reach the same consistency, generating less water consumption and less cost in the work.

The tested clay mortar obtained a result in air entrained content of 11.50%, and industrial clay mortar, 10.00%. It is observed that the value practically does not differ and is in accordance with the recommendation of [19]. In this regard, the air entrained content favors the workability of the mortar, that is, making it moldable on walls, ceilings, and brick settlements. This leads to a faster water absorption and a higher total absorption of the material [13].

Figure 4 shows the mechanical strengths of the mortars studied at the ages of 7, 14, and 28 days. The tested clay and industrial clay, at all ages, do not differ, as the deviations are coincident. Only among the cements used, a difference was noticed, that is, at 28 days of age, the tested clay showed higher average resistance with CP II than with CPV. The highest values were reached by the mortars added with tested clay, showing that this clay can be used as an addition to the mortar for laying masonry, wall, and ceiling coverings [21–27].

Conclusions

From the results obtained, it is concluded that:

- The clays have the same mineralogical composition, with the presence of the clay mineral kaolinite and the minerals muscovite, quartz, goethite and anatase. Regarding the chemical composition, they have practically the same components. The clays have $SiO_2 + Al_2O_3$ above 93%, and is characterized as refractory. The amount of aluminum oxide (Al_2O_3) indicates the high presence of kaolinite. Potassium oxide (K_2O) can contribute in the mixture with cement to reduce calcium hydroxide (portlandite), a fragile part of the mortar;

- The particle size distribution of the tested clay and the industrial clay has significant differences, mainly regarding the clay fraction, 32.00% for the tested clay and 42.00% for industrial clay. This reflected in the mechanical strength;
- It is observed that to have the desired value consistency, it was necessary to add less water in the tested clay mortar than the industrial clay mortar, generating less water consumption and less cost in the work;
- In relation to the air entrained content, mortars with the two clays don't differ significantly. The tested clay mortar obtained a result of 11.50%, and industrial clay mortar, 10.00%;
- The tested clay and industrial clay, at all ages, do not differ, as the deviations are coincident, in relation to mechanic strength. Only among the cements used a difference was noticed, that is, at 28 days of age, the tested clay showed higher average resistance with CP II than with CPV. The highest values were reached by the mortars added with tested clay.

The clay tested as a material for dosing mortar in wall and ceiling coverings was compatible with the industrial clay collected in the local trade for use in mortar. This demonstrates the possibility of marketing the product studied. It should be noted that other tests must be carried out to guarantee effective use of the tested clay.

References

1. Arel HS (2016) Recyclability of waste marble in concrete production. J Clean Prod 131:179–188
2. Al-Mulali MZ, Awang H, Abdul Khalil HPS, Aljoumaily ZS (2015) The incorporation of oil palm ash in concrete as a means of recycling: a review. Cem Concr Compos 55:129–138
3. Tironi A, Trezza MA, Scian AN, Irassar EF (2012) Incorporation of calcined clays in mortars: porous structure and compressive strength. Procedia Mater Sci 1:366–373
4. Chakchouk A, Samet B, Mnif T (2006) Study on the potential use of Tunisian clays as pozzolanic material. Appl Clay Sci 33(2):79–88
5. Arce C, Garzón E, Sánchez-Soto PJ (2019) Phyllite clays as raw materials replacing cement in mortars: properties of new impermeabilizing mortars. Constr Build Mater 224:348–358
6. Noor-Ul-Amin (2012) Use of clay as a cement replacement in mortar and its chemical activation to reduce the cost and emission of greenhouse gases. Constr Build Mater 34: 381–4
7. de Oliveira MP, Barbosa NP (2006) Potencialidades de um caulim calcinado como material de substituição parcial do cimento portland em argamassas. Rev Bras Eng Agrícola E Ambient 10(2):490–496
8. Yanguatin H, Tobón J, Ramírez J (2017) Pozzolanic reactivity of kaolin clays, a review | Reactividad puzolánica de arcillas caoliníticas, una revisión. Rev Ing Constr 32(2):13–24
9. Sabir B, Wild S, Bai J (2001) Metakaolin and calcined clays as pozzolans for concrete: a review. Cem Concr Compos 23(6):441–454
10. Shvarzman A, Kovler K, Schamban I, Grader GS, Shter GE (2002) Influence of chemical and phase composition of mineral admixtures on their pozzolanic activity. Adv Cem Res 14(1):35–41
11. Hossain MM, Karim MR, Hasan M, Hossain MK, Zain MFM (2016) Durability of mortar and concrete made up of pozzolans as a partial replacement of cement: a review. Constr Build Mater [Internet] 116: 128–40. DOI: https://dx.doi.org/10.1016/j.conbuildmat.2016.04.147

12. Gomes MI, Diaz Goncalves T, Faria P (2012) Evaluation of effect of water content on workability of earthen mortars. Apunt—J Cult Herit Stud 25(2):258–277
13. Winnefeld F, Böttger KG (2006) How clayey fines in aggregates influence the properties of lime mortars. Mater Struct Constr 39(4):433–443
14. Brazilian Association for Technical Standards (ABNT) (2001) NBR NM 51: small-size coarse aggregate—test method for resistance to degradation by Los Angeles machine
15. Brazilian Association for Technical Standards (ABNT) (2018) NBR 7181: Soil—Grain size analysis, p 12
16. Brazilian Association for Technical Standards (ABNT) (2016) NBR 6457: soil samples—preparation for compactation and characterization tests, p 8
17. National Highway Department (DNER) Soils—determination of specific gravity
18. Brazilian Association for Technical Standards (ABNT) (2016) NBR 13276: mortars applied on walls and ceilings—determination of the consistence index. p 2
19. Brazilian Association for Technical Standards (ABNT) (1995) NBR 13278—mortar—determination of the specific gravity and the air entrained content in the fresh stage—method of test
20. Brazilian Association for Technical Standards (ABNT) (2005) NBR 13279: mortars applied on walls and ceilings—determination of the flexural and the compressive strength in the hardened stage
21. Azevedo ARG, Vieira CMF, Ferreira WM, Faria KCP, Pedroti LG, Mendes BC (2020) Potential use of ceramic waste as precursor in the geopolymerization reaction for the production of ceramic roof tiles. J Build Eng 29(1):101–156
22. de Azevedo ARG, Alexandre J, Zanelato EB, Marvila MT (2017) Influence of incorporation of glass waste on the rheological properties of adhesive mortar. Constr Build Mater 148:359–368
23. De Azevedo ARG, Alexandre J, Marvila MT, Xavier GC, Monteiro SN, Pedroti LG (2020) Technological and environmental comparative of the processing of primary sludge waste from paper industry for mortar. J Clean Prod 32
24. Marvila MT, Azevedo ARG, Cecchin D, Costa J, Xavier GC, Carmo DF, Monteiro SN (2020) Durability of coating mortars containing açaí fibers. Case Stud Constr Mater 13:10–21
25. De Azevedo ARG, Marvila MT, Rocha HA, Cruz LR, Vieira CM (2020) Use of glass polishing waste in the development of ecological ceramic roof tiles by the geopolymerization process. Int J Appl Ceram Technol
26. Oliveira PS, AntunesMLP, da Cruz NC, Rangel EC, de AzevedoARG, Durrant SF (2020) Use of waste collected from wind turbine blade production as an eco-friendly ingredient in mortars for civil construction. J Clean Prod 274
27. Amaral LF, Girondi Delaqua GC, Nicolite M, Marvila MT, Azevedo ARG, Alexandre J, Vieira CMF, Monteiro SN (2020) Eco-friendly mortars with addition of ornamental stone waste—a mathematical model approach for granulometric optimization. J Clean Prod 270

Surface Characterization of Concentrated Jamesonite, in the Collectorless Flotation, in Acid, Neutral, and Alkaline Medium

Jazmín Terrazas Medina, M. Reyes Pérez, Elia Palacios Beas, Iván. A. Domínguez, Mizraim U. Flores Guerrero, Aislinn Michelle Teja Ruiz, Miguel Pérez Labra, Julio Cesar Juárez Tapia, and Francisco Raúl Barrientos Hernández

Abstract The pH is a critical variable and influences the surface state of the float mineral particles and the flotation efficiency. Jamesonite is a sulphosal of lead and antimony with iron content $Pb_4FeSb_6S_{14}$. In this research, the study of the surface state of jamesonite was carried out by means of infrared spectroscopy of particles obtained in flotation without a collector in acid, neutral and alkaline medium. In an alkaline medium, the flotation of the mineral decreases or is depressed, mainly due to the oxidation of the surface iron forming iron oxyhydroxide, α-FeOOH goethite, considered as a hydrophilic species, as well as the division of the main sulfate band indicating the formation of metal sulfates. Meanwhile, when the flotation is carried out without a collector at pH 5.9 and 7.8, a 70% w / w recovery is achieved, and the absorption bands of the covalently bonded species are significantly attenuated.

Keywords Jamesonite · Flotation · Collectorless · Infrared · Oxidation

J. T. Medina · M. R. Pérez (✉) · A. M. T. Ruiz · M. P. Labra · J. C. J. Tapia · F. R. B. Hernández
Academic Area of Earth Sciences and Materials, Autonomous University of the State of Hidalgo, Road Pachuca-Tulancingo Kilometer 4.5, 42180 Mineral de la Reforma, Hidalgo, Mexico
e-mail: mreyes@uaeh.edu.mx

J. T. Medina
e-mail: jazterrazas@gmail.com

E. P. Beas
National Polytechnic Institute unit ESIQUIE, 07738 Mexico City, Mexico

Iván. A. Domínguez
Institute of Metallurgy, Autonomous University of San Luis Potosí, 78210 San Luis Potosí, Mexico

M. U. F. Guerrero
Industrial Electromechanics Area, Technological University of Tulancingo, 43642 Tulancingo, Hidalgo, Mexico

J. Li et al., *Characterization of Minerals, Metals, and Materials 2021*,
The Minerals, Metals & Materials Series,
https://doi.org/10.1007/978-3-030-65493-1_55

Introduction

Jamesonite $Pb_4FeSb_6S_{14}$ is a lead sulfosalt that exists in nature associated with iron sulfide-type minerals such as pyrite and pyrrhotite in hydrothermal deposits [1, 2]. It is also considered a solid solution formed by lead sulfide and antimony sulfide, therefore, the formula can be written as $4PbS{\cdot}FeS{\cdot}3Sb_2S_3$ [3, 4]. Jamesonite presents similar flotation conditions to galena PbS, for this reason, in the mineral processing industry, a lead concentrate composed of both $Pb_4FeSb_6S_{14}$ and PbS species is commonly obtained [4].

The relevance of this mineral, on the one hand, is in lead (Pb), considered an important metal in modern industry. Widely used in chemistry and the military industry, as well as in electronics. The main sources of lead are minerals such as galena, cerussite, and jamesonite [4]. On the other hand, the industrial importance of the jamesonite mineral is in antimony (Sb), this is a strategic metal, used for the production of alloys, chemical products, as well as in the military industry [5].

The fusion of these concentrates leads to excessive production costs due to differences in melting points [6]. For this reason, obtaining individual concentrates of these mineral species is an outstanding issue that is currently being addressed [7]. Jamesonite is a mineral with contents of 40.15% of Pb, 35.39% of Sb, 21.75% of S, and 2.71% of Fe. In the literature, it is established that jamesonite floats without problems at natural pH without the need for activation [8]. In this research work the study of the collectorless flotation of jamesonite will be approached

It has been established that the best flotation conditions for jamesonite are a pH of 8, 20 mg/L of potassium amyl xanthate and 20 mg/L of butyl dithiophosphate. Furthermore, it has been established that activation with metal salts does not improve results. However, at pH 10, the flotation of jamesonite is depressed, similarly $K_2Cr_2O_7$ depresses the flotation, but high dosages are needed, around 2000 g/ton [9]. Therefore, the use of organic and inorganic depressants during the flotation separation of mineral sulfides is constantly the subject of arduous investigation, for example, in the separation of jamesonite from impurities such as marmatite and pyrrhotite mineral in the presence of isobutyl xanthate [10].

In this work, the surface state of the jamesonite obtained in flotation under slightly acidic, neutral, and alkaline pH chemical conditions was studied by Fourier transform infrared spectroscopy, referring the optimal flotation conditions to pulp chemistry and surface state of the jamesonite particles.

Experimental Methodology

The jamesonite used in this experimental work was exhaustively characterized by instrumental techniques of XRD, SEM–EDS and previously reported [11]. The jamesonite flotation tests were carried out in a Denver type flotation cell using for each test 1 L of deionized water and 8 g of mineral particles retained on the 200 mesh

(74 μm). The pH of the flotation pulp was adjusted as appropriate with NaOH and 1 M $H2SO_4$ for alkaline and acid values, respectively.

The conditioning of the flotation pulp was carried out within the same cell, during this stage and at the end of the flotation the potential of hydrogen ions (pH), the oxidation–reduction potential (ORP) referred to as the standard hydrogen electrode (SHE) mV was continuously monitored. As frother agent, methyl iso butyl carbinol MIBC was used in a concentration of 60 mg/L provided by the company Alkemin S.A de S.R.L. In addition, flotation times of; 30 s, 1, 2, 4, 6, 8, and 10 min obtaining the recovery curves versus the flotation time.

The concentrates obtained at different flotation times were characterized by FTIR to determine the surface state of the mineral particles during flotation without a jamesonite collector, under different pH conditions. Therefore, the study of the influence of pH on the flotation without a collector of jamesonite would contribute to provide information on the activation or depression of this mineral species.

Results

Figure 1 shows the results of the evaluation of the effect of activation or depression of the pH in the flotation of jamesonite, it is observed that, when the initial pH of the collectorless flotation is 5.9, natural pH, the cumulative recovery is around the 72% w/w, similar cumulative recoveries are obtained when the pH is 7.8 in a maximum

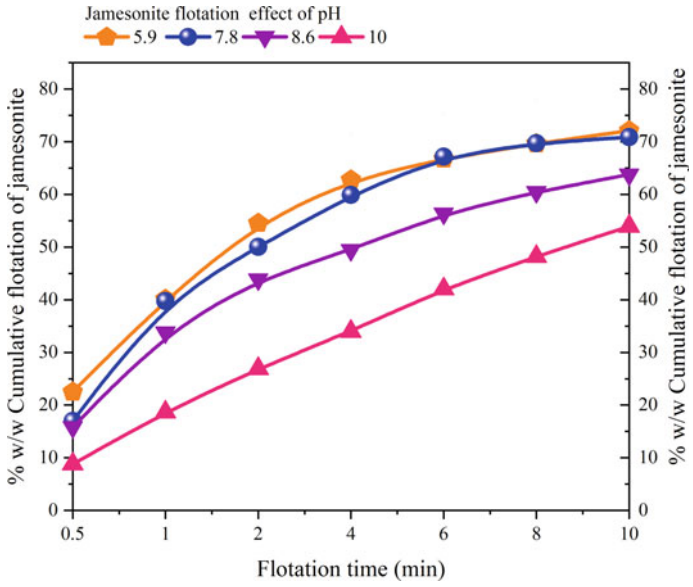

Fig. 1 % of cumulative recovery jamesonite vs. flotation time effect of pH. (Color figure online)

flotation time of 10 min. When the pH is greater than 8 the tendency of the flotation of jamesonite is to decrease.

In this way, when the initial float pH is 8.9 and 10, the maximum cumulative recoveries are 65% w/w and 55% w/w, respectively. Similar results have been found in the literature, but using a diethyl dithiocarbamate collector in concentrations of 1 X 10^{-4} mol/L and terpenic acid as frother agent in concentrations of $6X10^{-5}$ mol/L [12]. From Fig. 1, it can be seen that jamesonite presents excellent flotation at pH between 5.9 and 7.8 without the use of a collector, only using frother agent.

The change in pH, not only alters the concentration of hydrogen ions H^+ and hydroxyl ions OH^- in the flotation pulp, in addition, it decisively influences the success or failure of the flotation of jamesonite, caused by the effect of the variation of chemistry of the pulp specifically by the oxide reduction potential (mV) ORP of the pulp the measured values of the potential are referred to the standard hydrogen electrode (SHE) [13]. This property measures the oxidizing or reducing capacity of a flotation system, in other words, it measures the ability of the pulp to exchange electrons.

With regard to the potential for oxide reduction, previous electrochemical studies of jamesonite show compounds rich in sulfur and deficient in metal, on the surface of the particles, when it has a potential lower than + 80 mV and pH of 6.86. For example, sulfur is passivated at a potential from + 80 mV to + 470 mV, with potentials greater than this last value, $S_2O_3^{-2}$ and SO_4^{-2} are produced. Thus, from these studies, it was found that at pH 9.18 the corrosion of jamesonite is much more intense and the potential of oxidized jamesonite is similar to that of PbS, FeS, and Sb_2S_3 [14].

Figure 2 shows the results obtained in the monitoring of the oxide reduction potential, from this figure it can be seen that the oxidizing character of the solution tends to decrease with the addition of the mineral to the solution, subsequently the pH is adjusted and the potential changes. When this is greater than + 200 mV, good flotation efficiencies are obtained, however, at values lower than this value, the jamesonite is depressed.

The alteration of the jamesonite happens at the surface level in the last atomic layer of the mineral and the activation or depression during the flotation depends on this situation, the phases formed will be determined by the Fourier transform infrared spectroscopy technique FTIR, due to the environment where flotation occurs, mineral particles tend to oxidize forming covalently bonded species such as sulfates, oxides, hydroxides, oxyhydroxides.

To identify the species formed, FTIR spectra were obtained in the spectral region from 400 cm^{-1} to 4000 cm^{-1} in a Perkin Elmer model Spectrum spectrometer, using the potassium bromide pellet preparation method, using 0.01 g of sample and 0.3 g of KBr, which were mixed and compressed in a hydraulic press, the obtained tablets were analyzed by FTIR, obtaining their IR.

The identification of the different bands obtained was supported on the basis of the constitution of an FTIR database of compounds of lead, antimony, and iron oxides. Infrared spectroscopy is a powerful tool for the identification of the surface state of jamesonite particles, the FTIR technique provides information that cannot be obtained in XRD or SEM–EDS.

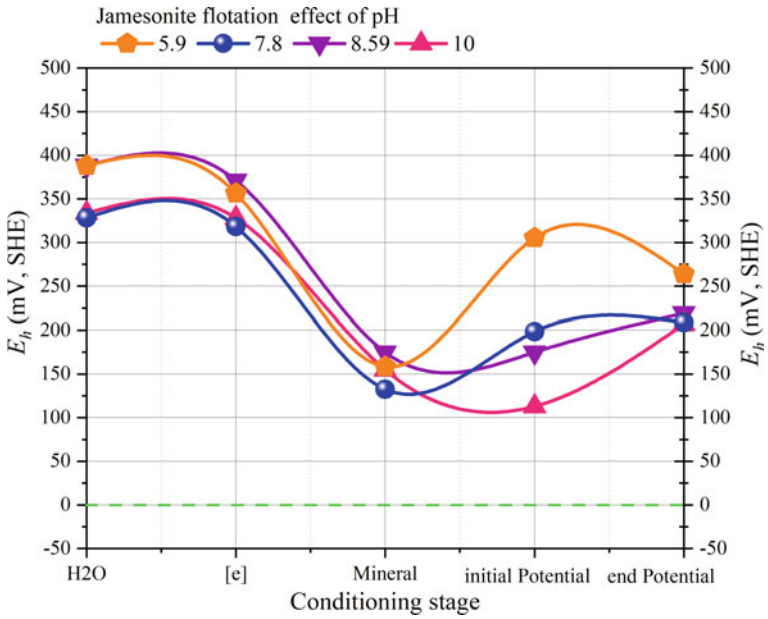

Fig. 2 Oxide reduction potential referred to the Standard Hydrogen Electrode (SHE) mV vs. the conditioning stage. Effect of pH. (Color figure online)

The IR study focused on three spectral domains: the zone corresponding to sulfur species from 1000 cm^{-1} to 1200 cm^{-1}, the zone of metallic oxides, hydroxides, and oxyhydroxides from 400 cm^{-1} to 900 cm^{-1} and the carbonate zone 1300 cm^{-1} to 1400 cm^{-1}. Figure 3 shows the infrared spectra of the jamesonite particles floated at an initial pH of 10, for the first 30 s and 10 min of flotation it is worth mentioning that at this pH the surface is depressed and the maximum cumulative flotation was 55% w/w.

The absorption band at 880 cm^{-1} in the IR spectrum of the floated particles in the first 30 s indicates the presence of the Fe - O vibration bonds of the goethite Fe_2O_3. H_2O, therefore, this phase inhibits flotation of jamesonite from Fig. 1 presented above, it is observed that at this flotation time a flotation of 8% w/w is achieved. The vibration bands at 1049 cm^{-1} and 1088 cm^{-1} are attributed to the vibration of the Sb-O and Pb–O bonds, of the Sb_2O_3 and PbO, respectively.

The weak bands of vibration at 1273 cm^{-1}, 1383 cm^{-1}, and 1641 cm^{-1} correspond to the sulfate ion, the Sb-O bonds of Sb_2O_3 and the bending vibration of the OH^{-1} ion bound at the surface, respectively. Note the presence of a weak signal from the hydroxyl ion. Regarding the IR spectrum of the floating particles at 10 min of flotation, it presents absorption bands at 469 cm^{-1} and 537 cm^{-1} which are assigned to the modes of vibration of the Pb–O bonds of PbO and of Sb-O of Sb_2O_3, respectively, it is worth mentioning that the band of Fe–O bonds is not present in this IR spectrum Fig. 3.

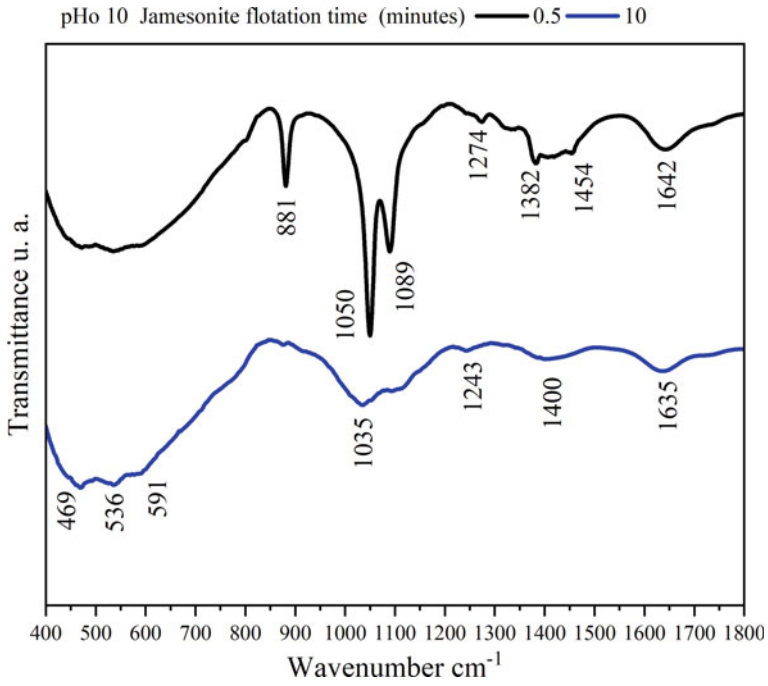

Fig. 3 IR spectra of jamesonite floated at initial pH 10, at 0.5 and 10 min. (Color figure online)

There is also a single absorption band at 1034 cm^{-1} corresponding to the vibration of the free sulfate ion on the surface, weak absorption shoulders are also observed at 1243 cm^{-1}, 1402 cm^{-1}, and 1637 cm^{-1}, it should be noted that the mode of vibration of the hydroxyl bonds increases in this spectrum. On the other hand, Fig. 4 shows the IR spectra of the jamesonite floated at pH 5.9 for the times of 30 s and 10 min of floating, it should be remembered that the maximum recovery achieved in this test was 72% w/w, the spectrum IR of the floating jamesonite in the first 30 s shows weak absorption bands due to the decrease of the covalent binding groups of sulfates, iron hydroxides, lead oxides and antimony, the only absorption band present in a significant way is that corresponding to the hydroxyl ion at 1629 cm^{-1}.

Regarding the IR spectrum of the jamesonite particles obtained at ten minutes of flotation, there are weaker absorption bands, except for the signal at 1113 cm^{-1} and 1618 cm^{-1} that correspond to the sulfate and hydroxyl ion respectively, in previous work has described similar absorption bands [15, 16]. In the field of mineral processing, there is a point of agreement that oxidation of mineral sulfides produces a surface rich in sulfur and deficient in metal [17].

Due to this characteristic, sulfides such as jamesonite experience natural flotation, however, the surface increase of oxide phases such as PbO, PbO_2, Sb_2O_3, significantly decrease the natural flotation of jamesonite, undoubtedly the frother agent favors hydrophobicity—natural flotation of jamesonite, as shown in Fig. 4, the notable

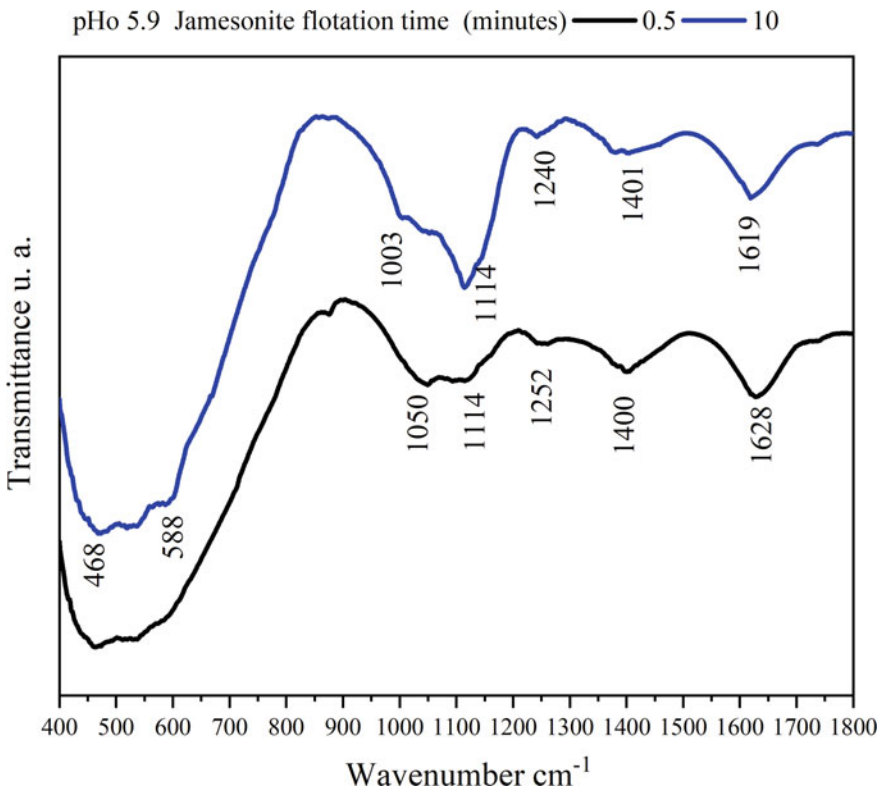

Fig. 4 IR spectra of floating jamesonite at initial pH 5.9, at 0.5 and 10 min. (Color figure online)

decrease in the absorption bands of oxidized species such as lead oxides, antimony, iron hydroxides on the mineral surface substantially improves flotation.

Conclusions

The flotation of jamesonite in alkaline media pH at 8.6 and 10 is significantly depressed, achieving a % w/w of flotation of 65 and 55%, respectively, this is due to the abundant presence of oxidized iron phases such as goethite Fe_2O_3 * H_2O, oxides of lead PbO and antimony oxides Sb_2O_3, while the absence or diminution of the intensity of the absorption bands of the covalent bonds of the oxidized phases on the jamesonite particles lead to an increase in cumulative flotation, achieving a separation efficiency of 70% w/w. Adequate pulp potential to achieve the highest collectorless flotation should be greater than + 200 mV, pulp potentials of + 100 mV lead to jamesonite depression.

Acknowledgements To the Autonomous University of the State of Hidalgo, to the PRODEP Teacher Professional Development Program, and to the National Polytechnic Institute ESIQUIE.

References

1. Luke L, Chang. Xilin Li & Chusheng Zheng. (1987) The jamesonita benavidesite series. Can Mineral 25:667–672
2. Chang LY, Knowles CR (1977) Phase relations in the systems PbS-Fe_{1-x}S-Sb_2S_3 and PbSFe_{1-x}S-Bi_2S_3 Canadian Mineralogist 15:374–379
3. Yang Xu, liang, Hua Yi Xin. (2005) Research on a new process for separating lead and antimony from jamesonite. China's Nonferrous Met Ind 10(5):44–45
4. Chen XF, Peng RM (2008) Effect of calcium hypochlorite on the flotation separation of galena. Nonferr Met 60(3):129–132
5. Chen X, Guohua Gu, Zhu R, Wang C (2019) Selective separation of chalcopyrite from jamesonite with guar gum. Physicochem Probl Miner Process 55(1):237–247
6. Chen JH, Li YQ, Long QR, Wei ZW, Chen Y (2011) Improving the selective flotation of jamesonite using tannin extract. Int J Miner Process 100: 54−56
7. Forssberg LT, K. S. E. (1989) Beneficiation characteristics of antimony minerals a review—part 1. Miner Eng 2(3):321–336
8. Sun W, Sun C, Liu RQ, Cao XF, Tao HB (2016) Electrochemical behavior of galena and jamesonite flotation in high alkaline pulp. Trans Nonferrous Met Soc China 26:551–556
9. Lager T, Forssberg KSE (1989) Beneficiation characteristics of antimony minerals a review—part 1. Miner Eng 2(3):321–336
10. Liu RQ, Sun W, Hu YH, Xiong DL (2006) Depression mechanism of small molecular mercapto organic depressants on flotation behavior of complex sulfide. Chinese J Nonferrous Metals 16(4): 746−751
11. Reyes Pérez M, Palacios Beas EG, Barrientos FR, Pérez Ladra M (2019) The minerals, metals & materials society. In: Li B et al (ed) Characterization of minerals, metals
12. Liu R, Guo Y, Wang Li, Sun W, Tao H, Yuehua Hu (2015) Effect of calcium hypochlorite on the flotation separation of galena and jamesonite in high-alkali systems. Miner Eng 84(2015):8–14
13. Guy PJ, Trahar WJ (1984) the influence of grinding and flotation environments on the laboratory batch flotation of galena. I J Miner Process 12:15–38
14. Yu Rl, Hu YH, Qiu GZ, Qin WQ (2004) Corrosive electrochemistry of jamesonite by cyclic voltammetry. J Cent South Univ Technol 11(3)
15. Nakamoto K (1997) Wiley Interscience, New York
16. M. Reyes P. (2013) Modificación superficial de mineral de pirita y precipitados de Hierro: comportamiento en medios acuosos y de molienda. Tesis Doctoral Morelia, Michoacán, México
17. Zachwieja JB, McCarron JJ, Walker GW, Buckley AN (1989) Correlation between the surface composition and collectorless flotation of chalcopyrite. J Colloid Interface Sci 132:462–468

Superficial Speciation by FTIR Spectroscopy of Floated PbS (Galena) in the Presence of Copper Aqueous (+2)

Jimena Detzamin Ramírez Trejo, M. Reyes Pérez, Elia Palacios Beas, Iván A. Reyes Domínguez, Mizraim U. Flores Guerrero, Aislinn Michelle Teja Ruiz, Miguel Pérez Labra, Julio Cesar Juárez Tapia, and Francisco Raúl Barrientos Hernández

Abstract The presence of copper aqueous (+2) in the pulps that feed the flotation circuits is due to the oxidation of the copper contained in sulfides (chalcopyrite) and in oxides (malachite) as a result of the galvanic reactions that occur during grinding copper aqueous (+2) can have a negative effect during the collectorless flotation of galena. In this investigation, the galena concentrated by collectorless flotation and in the presence of copper aqueous (+2) in alkaline media was superficially characterized by infrared spectroscopy. The results show the depression of galena with the increase of the dosage of copper aqueous (+2) in the pulp at pH 9.6 and Eh of +120 (mV). From the infrared characterization, it was found that the surface state of the galena when it undergoes depression, shows the absence of some of the absorption bands corresponding to the Pb-O and Pb-OH bonds of lead oxide and hydroxide detected when galena flotation reaches maximum recovery.

Keywords Galena · Infrared · Flotation · Collectorless

J. D. R. Trejo · M. R. Pérez (✉) · A. M. T. Ruiz · M. P. Labra · J. C. J. Tapia · F. R. B. Hernández
Autonomous University of the State of Hidalgo, Academic Area of Earth Sciences and Materials, Road Pachuca-Tulancingo Kilometer 4.5 Mineral de La Reforma, 42180 Hidalgo, Mexico
e-mail: mreyes@uaeh.edu.mx

J. D. R. Trejo
e-mail: detzamin.limm@gmail.com

E. P. Beas
National Polytechnic Institute Unit ESIQUIE, C.P. 07738 Ciudad de Mexico, D.F, Mexico

I. A. R. Domínguez
Institute of Metallurgy, Autonomous University of San Luis Potosí, 78210 San Luis Potosí, SLP, Mexico

M. U. F. Guerrero
Industrial Electromechanics Area, Technological University of Tulancingo, 43642 Hidalgo, Mexico

J. Li et al., *Characterization of Minerals, Metals, and Materials 2021*,
The Minerals, Metals & Materials Series,
https://doi.org/10.1007/978-3-030-65493-1_56

Introduction

Galena is a mineral lead sulfide (PbS) very abundant throughout the world and is generally associated with mineral deposits of other base metal sulfides such as sphalerite (ZnS), chalcopyrite (CuFeS2), and bornite (Cu_5FeS_4) among others [1, 2]. Flotation is considered an effective separation process to selectively recover lead sulfide from its accompanying polymetallic sulfides and from mineral gangue. The success of flotation lies in the hydrophobicity which is a superficial property of all sulfides [3, 4].

In the literature, the issue of natural flotation and collectorless flotation of mineral sulphides has been discussed [5]. It has been shown that natural buoyancy is due to the formation of elemental sulfur on the mineral surface (examples of minerals with natural buoyancy are molybdenite, realgar, orpiment) [6], some authors have identified that the hydrophobic species in the collectorless flotation is a surface deficient in metal and rich in poly sulphides [7]. Furthermore, collectorless flotation is also referred to as a foam flotation process because it uses only foaming reagent, the objective of which is to decrease the surface tension of the pulp [2].

The aforementioned surface phenomena substantially improve the hydrophobicity of sulfides and make flotation without a collector possible. This process has advantages such as; the reduction or zero consumption of chemical reagents, the increase in selectivity during flotation, and reduces the number of equipments required to achieve optimal separation. Addition of some metal ions to the flotation system, it can have some negative effects such as the leading to the separation of some undesirable minerals with little flotation capacity [2]. Surface inhibitors or depressants has been reported these can be organic [8] or inorganic such as potassium dichromate, cyanide, sodium sulfite. However, they dangerously damage the environment, they are toxic, poisonous, and their use is increasingly restricted [9–11].

In other works, the use of organic chemical reagents has been reported to depress galena flotation these are carboxymethylcellulose [12], humic acid [13], starch [14], tannin [15] lignin [11], these authors report a selective depressant effect of galena with respect to other sulphides present in the pulp. In the processing of polymetallic mineral sulphides, galena ore is generally floated in a second flotation circuit, for this reason, its surface must initially experience a hydrophilic response [12].

In this research work, the effect of copper aqueous (+2) concentration on galena mineral depression during flotation without a collector is studied evaluating alkaline environment, as well as of pulp potential Eh (mV) and its effect on the success or detriment of galena flotation, the surface speciation of the floated galena particles, was studied by Fourier transform infrared spectroscopy in order to determine the depressive mechanism of galena by effect of copper aqueous (+2) concentration.

Experimental Methodology

To carry out the study of the depressant effect of copper aqueous (+2) in the flotation without a galena collector, a mineral lead sulfide (PbS) was used which was manually sampled and selected from Zimapan, Hidalgo, Mexico. The mineral was fragmented, in a laboratory jaw crusher later it was ground in a mill with steel media for 20 min previously characterized and reported [16].

To perform the flotation tests a 1 L stainless steel laboratory Denver cell was used, the impeller and diffuser made of polypropylene, the impeller stirring speed was 1200 RPM. Deionized water and analytical grade chemical reagents were used in all experiments. During the conditioning of the pulp and at the end of each of the flotation tests both the pH and the oxide reduction potential (ORP) (mV) were monitored these variables were measured with a potentiometer Thermo Scientific Orion 3 Star brand equipped with a pH electrode, Ross ultra triode provided with a temperature sensor.

For each one of the flotation tests, a volume of 1 L of distilled water was used. Pulp conditioning was carried out in the cell. At the beginning, the pH and the potential oxide reduction were measured later the frother agent 60 mgL^{-1} of methyl isobutyl carbinol (MIBC) was added, a dispersion time was given and the mineral lead sulfide galena (PbS) 4 grams was added three minutes later the copper aqueous (+2) was poured as copper sulfate, the concentrations studied were 5, 50, and 75 mgL^{-1} then the pH of the pulp was brought to pH values between 9.5 and 10.5 using NaOH 1 M, this procedure was repeated for each of the flotation tests.

After the conditioning time, the flotation test was started, collecting the concentrate in times of 0.5, 1, 2, 4, 6, 8, and 10 min in previously weighed containers. Once the collection of the foam containing the floated galena particles was concluded, the air valve was closed, this procedure was repeated for each time and the float test was performed. The concentrate obtained in each of the tests were dried, weighed and, by weight difference of the container with and without mineral the floated galena mass was obtained calculating the percentage of flotation obtained in each of the times, analyzed with Eq. 1. Where Wt is the amount of floated mineral at each flotation time and Wo amount of initial mineral.

$$\%Flotation = \frac{W_t}{W_o} * 100 \tag{1}$$

The most significant galena solids were characterized by Fourier transform infrared spectroscopy in order to identify the covalent species present on the surface of the galena mineral, and thus determine the surface speciation and explain the mechanism of depression or activation of the mineral during the float.

Results

Figure 1 shows the results of galena collectorless flotation at pH between 9.5 and 10.5 in the presence of copper aqueous (+2) in concentrations of 5, 50, and 75 mgL^{-1} using a copper sulfate salt, it was decided to evaluate this pH to evaluate the beneficial or harmful effect of the presence of copper aqueous (+2). It is observed that the presence of 5 mgL^{-1} of copper aqueous (+2) improves the flotation efficiency. However, concentrations greater than 50 and 75 mgL^{-1} substantially depress galena flotation having cumulative recoveries of 55% w/w and 45% w/w, respectively.

The origin of copper aqueous (+2), in addition to the copper salt added as a surface activator, comes from the oxidation of copper in minerals such as chalcopyrite, malachite, tenorite, among others, during grinding, as shown in Fig. 1 the increased concentration of copper aqueous (+2) depresses flotation of galena. Copper sulfate is commonly used to activate the mineral surface of sphalerite [10]. It has been identified in the literature that the main species on the surface that influences the flotation of sphalerite are hydrophobic polysulfides [10].

The activation or depression of galena by the action of copper aqueous (+2) of copper sulfate is not described in the literature or is scarcely studied. Some researchers suggest the formation of a hydrophilic surface layer of metallic sulfite, the copper consuming the solution due to the formation of this species and interacting with the surface of the sulfide and reducing its hydrophobic characteristic [2]. The oxide

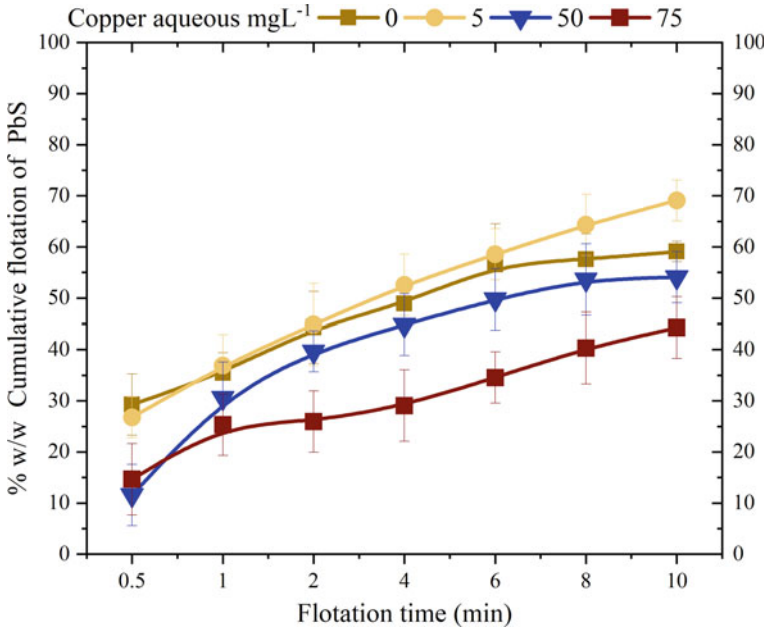

Fig. 1 % of cumulative recovery PbS versus flotation time. Effect of copper concentration. (Color figure online)

reduction potential values, measured in the conditioning stage with a pH of 6.42 and at the beginning of the flotation with a pH of 10.5, containing 1.18 X 10^{-3} M (75 mgL^{-1}) of copper, were expressed in reference to standard hydrogen electrode (SHE) and graphed in the Eh-pH diagrams, Figs. 2 and 3. It is observed that in the conditioning stage when the pH is 6.42, galena interacts with both the aqueous species $Cu_2(OH)_2^{(+2)}$, Cu3 $(OH)_4^{(+2)}$ as with the $Cu(OH)_2$ precipitates. Meanwhile, at the beginning of the flotation test at pH 10.5, the phase in contact with galena is aqueous $CuO_{(a)}$ as seen in Fig. 2 and with precipitates of $Cu(OH)_2$ as seen in Fig. 3.

Figures 2 and 3 show the Eh-pH diagrams of the Cu-H_2O system at 25 °C in a concentration of 1.18 X 10-3 M, Fig. 2 preferentially shows the most thermodynamically stable aqueous copper phases as a function of pH and *Eh,* while Fig. 3 shows the zones of thermodynamic stability of the solid copper phases that eventually precipitate. During the galena pulp conditioning stage, the addition of 1.18 X 10^{-3} M copper aqueous (+2) as copper sulfate gives a pH of 6.24 and an *Eh* of + 0.24 mV under these conditions, copper tends to form $Cu_2(OH)_2^{+2}$ and it is the first aqueous copper species that reacts with the surface of the galena particles, eventually due to the oxide reduction reactions between the species involved, it causes precipitation to CuO.

Cupper aqueous can precipitate and form CuO, the presence of these phases on the surface of the galena will depend on the thermodynamic stability, the interaction

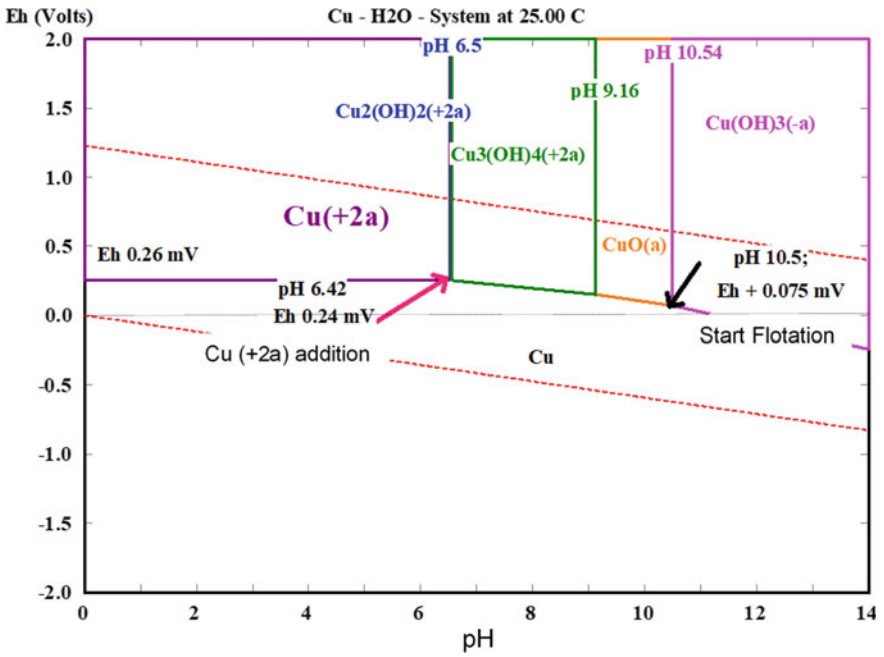

Fig. 2 Pourbaix Eh-pH diagram of the Cu-H_2O system at 25 °C, concentration 1.18 X 10^{-3} M, specifically representing the aqueous copper species. (Color figure online)

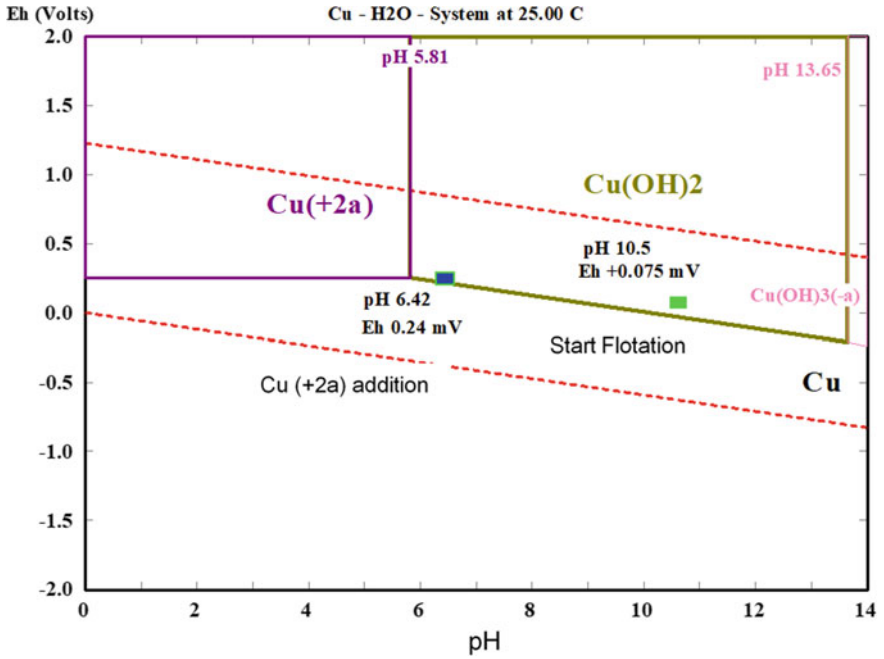

Fig. 3 Diagram of Pourbaix Eh-pH of the Cu-H_2O system at 25 °C, concentration 1.18 X 10^{-3} M. Zone of stability of $Cu(OH)_2$. (Color figure online)

with the mineral surfaces of galena and the chemical conditions of the flotation, dictate their presence on the surface of the particles, the surface speciation of the galena particles obtained during the collectorless flotation in the presence of copper were analyzed by infrared FTIR spectroscopy. This technique is very sensitive to the surface state and can be applied directly for the determination of the surface composition under specific flotation conditions.

Figure 4 shows the infrared spectra of the galena particles floated in the presence of 5 mgL^{-1} of copper aqueous (+2) at pH 10.5 and pulp potential *Eh* of +0.075 mV in times of 0.5 and 10 min. Multiple absorption bands are observed, both spectra show a lot of similarities. During the decrease in size, the atomic bonds are superficially ungrouped, in the case of sulfur in galena, which adsorbs oxygen, forming a double bond S = O between sulfur and oxygen identified with the absorption band at 1385 cm^{-1}.

The signal at 1644 cm^{-1} is assigned to the adsorption of hydroxyl ions OH^- to the surface of the galena mineral. In the zone corresponding to sulfur from 1000 to 1200 cm^{-1}, a single absorption band is observed at 1105 cm^{-1} with very weak absorption shoulders, the main band indicates the presence of the free sulfate ion on the surface of the mineral.

In Fig. 4, multiple absorption bands are observed in the spectral zone from 400 to 900 cm^{-1}, indicating the presence of M-O bonds of both phases formed with lead and

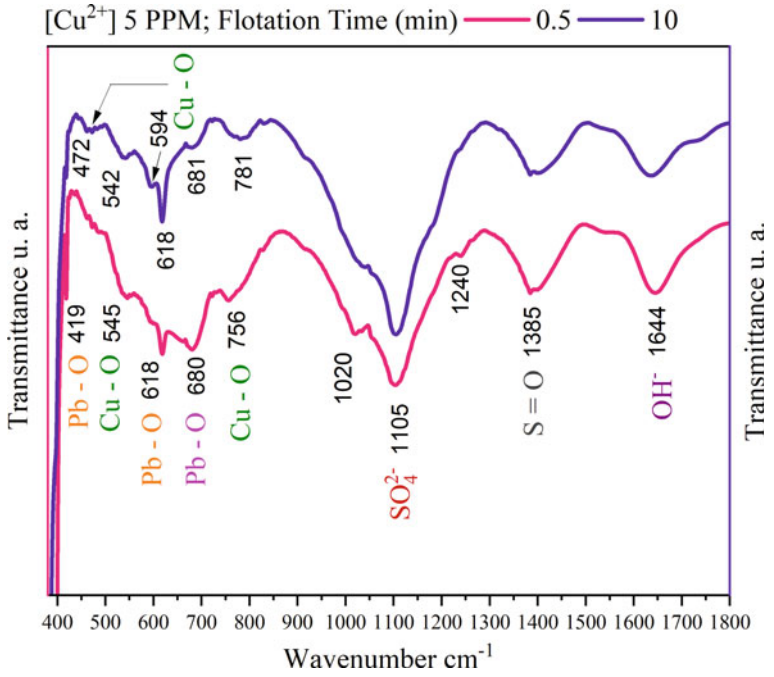

Fig. 4 Infrared spectra of galena floated in the presence of 5 mgL^{-1} copper aqueous (+2). (Color figure online)

copper, the absorption bands in 419 and 618 cm^{-1} show the presence of Pb-O bonds of the PbO_2 species, while the vibration band at around 680 cm^{-1} corresponds to the modes of vibration of the covalent Pb-O bonds of PbO. The spectrum obtained from the galena particles floated in the presence of 5 mgL^{-1} contains multiple absorption bands, the signals detected at 545, 594 and 756 cm^{-1} indicate the surface formation on the surface of galena from Cu-O bonds of CuO, the identification of these species could not be detected by XRD or SEM-EDS.

When galena flotation is carried out in the presence of 50 mgL^{-1} of copper aqueous (+2) as copper sulfate under pH conditions of 9.9 and a pulp potential *Eh* referred to the standard hydrogen electrode of +0.104 mV, Fig. 5 shows the IR spectra of the floated particles in the first 30 s and 10 min of floating. Unlike the spectra shown in Fig. 4, many of the absorption bands found in the galena particles floated in the presence of 5 mgL^{-1} of copper aqueous (+2) are not detected in the IR spectra when you have 50 mgL^{-1} of copper aqueous (+2).

However, the absorption bands at 1101, 1401 and 1633 cm^{-1} increase in intensity, bands corresponding to: the mode of vibration of the tetragonal bonds of the free sulfate ion on the surface of the galena, the presence of S = O type bonds indicating the formation of sulfo oxides and the adsorption of OH^- ions, respectively. Along with these intense bands of vibration, there are lower intensity bands of vibration in 422 and 680 cm^{-1} corresponding to the Pb-O bonds, the absorption band in

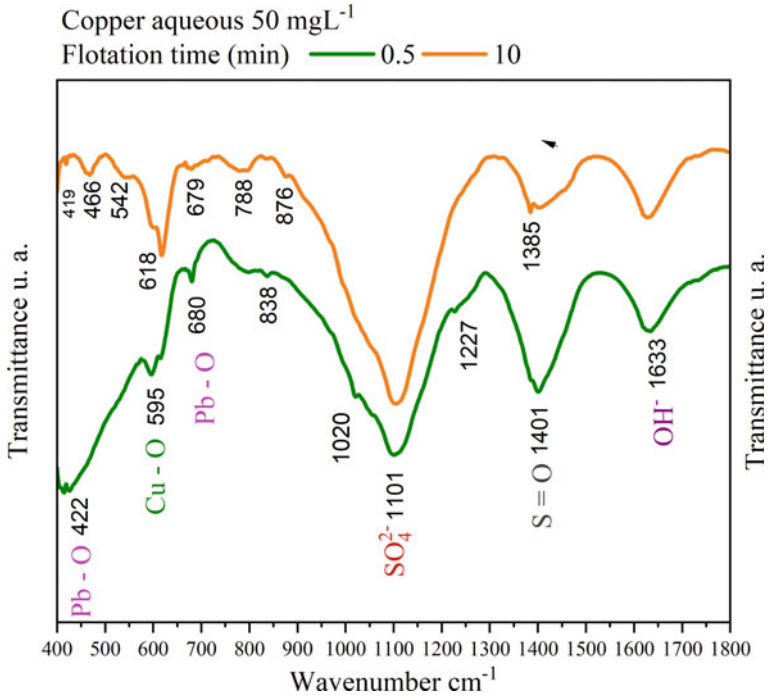

Fig. 5 Infrared spectra of galena floated in the presence of 50 mgL^{-1} of copper aqueous (+2). (Color figure online)

595 cm^{-1} is assigned to the formation of bonds Cu-O. Both IR spectra for galena particles floated in 30 s and the 10 min of float show a lot of similarities.

Therefore, the presence of these absorption bands in these last described spectra is attributed as responsible for the depression of galena in the presence of 50 mgL^{-1} of copper, causing a decrease in the cumulative percentage of galena

Conclusions

The galena collectorless flotation contributes to the industrial process specifically in the decrease in the consumption of collector reagent and increased galena flotation selectivity. The collectorless flotation of galena in the presence of copper aqueous (+2) at pH 9.9 is depressed when the concentration is 50 and 75 mg /L, achieving a % w/w of cumulative flotation of 45% and 55%, respectively, FTIR analysis of floated galena in the presence of these copper concentrations shows intense absorption bands of free sulfate ion, of the S = O double bonds of sulfo oxides and of the hydroxyl ion bound to the surface of galena, while when the galena flotation pulp contains 5 mg /L of copper aqueous (+2) and a pH of 10.5 the collectorless flotation of galena is favorable, achieving a % w/w of cumulative flotation of 70%, the IR spectra of

galena floated under these conditions shows multiple absorption bands of Cu-O and Pb-O bonds.

Acknowledgements To the Autonomous University of the State of Hidalgo, to the PRODEP Teacher Professional Development Program, and to the National Polytechnic Institute ESIQUIE.

References

1. Worner HK, Mitchell RW (eds) Minerals of broken hill, australian mining & smelting limited. Griffin Press: Melbourne, Australia
2. Feng Q, Chen J Electrochemistry of sulfide minerals flotation. Central South University Press
3. Sajjad A, Seyed KM, Mahdi G (2015) Chemical and colloidal aspects of collectorless flotation behavior of sulfide and non-sulfide minerals. Adv Coll Interface Sci 225:203–217
4. Rao SR, Finch JA (2003) Base metal oxide flotation using long chain xanthates. Int J Miner Process 69:251–258
5. Fuerstenau MC, Misra M, Palmer BR (1980) Xanthate adsorption on selected sulphides in the presence of oxygen. Inter J Miner Process 29I(1–2):111–119
6. Finkelstein NP, Allsion SA, Lovell VM, Stewart BV (1975) Advances in Interf Pheno. of Particulate/Solution/Gas Systems (eds. P. Somasundaran and R. B. Grieves). AIChE: New York 71(150):165–175
7. Buckley AN, Hamilton IC, Woods R (1985) Investigation of the surface oxidation of sulphide minerals by linear potential sweep and X-ray photoelectron. In: KSE Forssberg (ed.), Flotation of Sulphide Minerals, Elsevier. Amsterdam 6: 41–60
8. Xingjie W, Wenqing Q, Fen J, Ruizeng L, Daowei W (2019) Inhibition of galena flotation by humic acid: Identification of the adsorption site for humic acid on moderately oxidized galena surface. Miner Eng 137:102–107
9. Bolin N, Laskowski J (1991) Polysaccharides in flotation of sulphides. Part II. Copper/ lead separation with dextrin and sodium hydroxide. Int J Miner Process 33:235–241
10. Bulatovic S, Wyslouzil DM (1995) Selection and evaluation of different depressants systems for flotation of complex sulphide ores. Miner Eng 8(1–2):63–76
11. Sarquís PE, Menéndez Aguado JM, Mahamud MM, Dzioba R (2014) Tannins: the organic depressants alternative in selective flotation of sulfides. J Clean Prod 84(1):723–726
12. Valdivieso A, Ledesma LA, Cabrera A, Navarro OA (2017) Carboxymethylcellulose (CMC) as PbS depressant in the processing of Pb Cu bulk concentrates. Adsor float Stud Miner Eng 112:77–83
13. Wang D, Jiao F, Qin W, Wang X (2017) Effect of surface oxidation on the flotation separation of chalcopyrite and galena using sodium humate as depressant. Sep Sci Technol 53:961–972
14. Kar B, Sahoo H, Rath SS, Das B (2013) Investigations on different starches as depressants for iron ore flotation. Miner Eng 49:1–6
15. Liu R, Sun W, Hu Y (2009) Study on organic depressant FCLS for separation of chalcopyrite and galena. Min Metall Eng 29:29–32
16. Reyes M (2020) El Papel depresor del pH durante la flotación sin colector de mineral de galena conteniendo esfalerita. Tópicos de Investigación en Ciencias de la Tierra y Materiales Publicación anual, vol. 7, no. 7, pp 1–2

Synchronous Extraction of Valuable Metals from Low-Nickel Matte Using Ammonium Sulfate Roasting-Water Leaching Process

Qiangchao Sun, Hongwei Cheng, Qiang Zhang, Guangshi Li, Qian Xu, and Xionggang Lu

Abstract Owing to suffering the poor recovery of valuable metals and the massive loss of Co metal by the traditional pyrometallurgical technology to process the low-nickel matte. Herein, a sulfate roasting followed by a water leaching process was developed as an efficient technology for the simultaneous extraction of Ni, Cu, and Co from low-nickel matte in the presence of $(NH_4)_2SO_4$ additive. The influence of roasting temperature, the dosage of ammonium sulfate, and roasting rules on the leaching efficiency of metals are conducted. Also, the characterizations of phase evolution are complemented with the theoretical analysis of thermodynamic calculation to reveal the mechanism of $(NH_4)_2SO_4$ added sulfate roasting. The results demonstrate that the $(NH_4)_2SO_4$ plays a critical role in reducing the reaction temperature and improving the metal selectivity, achieving higher extraction efficiency of Ni, Cu, and Co (90.12%, 81.82%, and 92.45%, respectively), while Fe is only 10.18% and the high selectivity extraction can be achieved.

Keywords Low-nickel matte · Sulfation roasting · Ammonium sulfate · Water leaching

Introduction

Considering the novel physic-chemical properties of metal nickel, it's widely applied in energy storage devices, catalysts, and mechanical manufacturing [1–4]. The main nickel resources exist in the crust in the form of sulfide ore, the most common phase of Ni is pentlandite ($(Fe, Ni)_9S_8$) in sulfide ore, and copper (Cu), cobalt (Co) are associated metals. For a long time, nickel sulfide ore is the main source of nickel in

Q. Sun · H. Cheng (✉) · Q. Zhang · G. Li · Q. Xu · X. Lu (✉)
Laboratory of Advanced Special Steel & Laboratory of Advanced Ferrometallurgy & School of Materials Science and Engineering, Shanghai University, Shanghai 200444, PR, China
e-mail: hwcheng@shu.edu.cn

X. Lu
e-mail: luxg@shu.edu.cn

J. Li et al., *Characterization of Minerals, Metals, and Materials 2021*,
The Minerals, Metals & Materials Series,
https://doi.org/10.1007/978-3-030-65493-1_57

China, about 70% of nickel is refined from nickel sulfide ore [5–7]. However, continuous overexploitation has led to the impoverishment of nickel ore resources, thus efficient selective extraction in the machining process and comprehensive recovery of valuable metals have promoted a challenge to the extraction of current nickel sulfide ore.

Low-nickel matte is a conventional intermediate product of the nickel sulfide smelting process, which is a complex sulfide co-melt rich in multi-metal elements, like Ni, Cu, Co, and Fe [8]. In the traditional industry, the main processing method for the low-nickel matte is to obtain high-nickel matte through converter blowing, but this production method is inefficient and approximately 70 wt% Co and part of Ni, Cu is transferred to the converter slag, resulting in a large amount of valuable metal loss [9]. Therefore, how to simultaneous and efficient selective extraction of valuable metals from low-nickel matte raw material, and reducing the emissions of harmful gases during the process. That casting an arduous obstacle to facilitate the extraction of the metals from low-grade nickel sulfide.

Currently, with the advantages of low energy consumption and eco-friendly, the hydrometallurgical process has been widely used in recovering metals from low-nickel mattes, such as pressure acid leaching process, oxidation acid leaching process, and oxidation ammonia leaching process [10–12]. However, these extraction strategies usually have poor selectivity in the leaching process (especially for the iron). Hence, an integration method of combination of the pyrometallurgy and the hydrometallurgical process is proposed to meet the aforementioned difficulties. Among them, sulfated roasting couple with water leaching is an effective method to process the low-nickel matte [13]. Although the direct sulfated roasting process has the advantages of easy operation and short process, in general, the metal extraction selectivity of direct sulfated roasting technology needs to further improve. Thus, additive roasting has become a research focus. Roasting low-nickel matte with noncorrosive nature ammonium sulfate ($(NH_4)_2SO_4$) as an effective lixiviant can not only realize the high efficient recovery of valuable metals, but also realize the recycling of additive ammonium sulfate [14–17].

In this study, the sulfated roasting mechanism, the influence of various parameters (roasting temperature, roasting rules, and dosage of additive) on metal's leaching efficiency, and the role of $(NH_4)_2SO_4$ in enhancing metal extraction selectivity is discussed.

Experimental Methods

Raw Materials

The low-nickel matte used in this study was from Jinchuan Group Ltd. (Gansu, China). Table 1 and Fig. 1 shows the X-ray fluorescence spectroscopy (XRF) and the X-Ray diffraction (XRD) pattern of the low-nickel matte, respectively. The main

Table 1 The main chemical composition of low-nickel matte (mass fraction, %)

Fe	Ni	Cu	S	O	Co
26.19	24.69	22.94	21.84	3.69	0.47

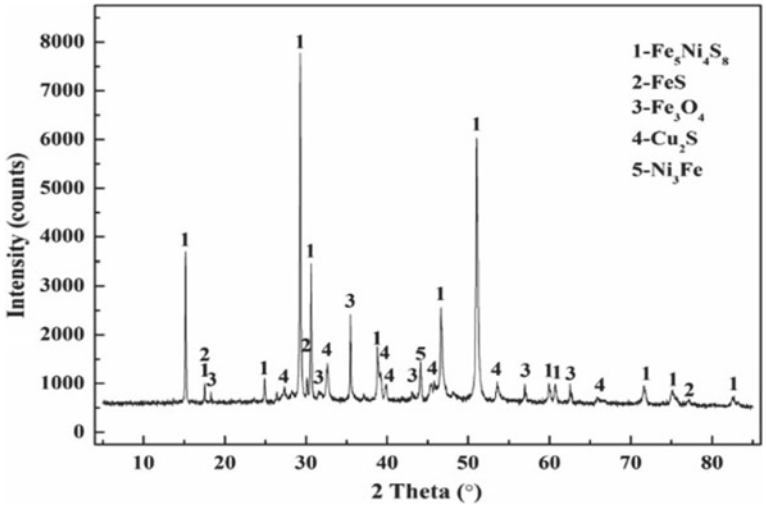

Fig. 1 The XRD pattern of the low-nickel matte sample

phase of the sample are sulfide ($Fe_5Ni_4S_8$), ferrous sulfide (FeS), cuprous sulfide (Cu_2S), magnetite (Fe_3O_4), Fe-Ni alloy (Ni_3Fe), and the Ni and Cu metals are mainly existing in the form of sulfide. The chemical reagent used in the test was commercially pure ammonium sulfate.

Material Characterizations

The composition of the sample was tested by XRF (XRF-1800). The crystalline phase of the low-nickel matte and leaching residue was characterized by XRD (D8 ADVANCE) (from 10 to 90º with a 0.02º/step). The thermomechanical analysis was performed in a thermogravimetric device (TG-DSC, STA 449 F3) under the air atmosphere with a flow rate of 40 mL min^{-1} and heated to 800 °C with a heating rate of 10 °C min^{-1}. The concentration of metal ions in the leachate was analyzed by using an inductively coupled plasma optical emission spectrometer (ICP-OES,). The microstructure of the roasting products was characterized by scanning electron microscope (SEM, SU-1500). The thermodynamic calculation was conducted by HSC 6.1 software system.

Sulfated Roasting and Water Leaching

The minerals are crushed and screened to obtain ~200 mesh powder samples (< 74 μm), then dried at oven 80 ℃ for 24 h. Generally, 1.0 g of low-nickel matte and 0.1 g of ammonium sulfate were mixed in an agate mortar, then transferred to the Al_2O_3 crucible for sulfation roasting in a tube furnace. After roasting, the roasting products were transferred to the 150 mL conical flask, 100 mL of deionized water was added, and the conical flask was placed in a constant temperature (80 °C) water bath for 30 min with strong agitation. After filtering, the filter residue was rinsed with deionized water, placed in a petri dish, and dried in an oven. The filtrate was transferred to the 500 mL volumetric flask. Finally, the leaching efficiency of different metal elements are calculated, respectively, according to the calculation formula as follows:

$$\eta_{\mathrm{X}} = \frac{\mathrm{C}_x \mathrm{V}}{m_0 \omega_{\mathrm{x}}} \times 100\% \tag{1}$$

where C_x is the concentration of metal in the leachate, mg L^{-1}, V is the volume of the volumetric flask, L, m_0 is the total mass of the mineral in the experiment, g, and ω_x is the percentage of the corresponding metal element in the mineral, %.

Results and Discussion

Direct Sulfated Roasting

As illustrated in Fig. 2a, the TG-DSC curves show that low-nickel matte oxidation first under low temperature, then start sulfate reaction with the temperature increased. However, if the temperature is too high, some sulfate began to decompose into metal oxide, even leading to the generation of ferrite species.

The XRD patterns are shown in Fig. 2b, the sulfate and metal oxides phase appear at 450 °C, revealing that the oxidation and sulfate reaction were carried out successively. With the rise of temperature, the intensity of the sulfate phase gradually becomes stronger, but over 500 the peak intensity begins to decline, those results well agree with TG-DSC analysis. Figure 2c shows the leaching rate of metals at different temperatures, with the rise of temperature, the leaching rate of Ni, Cu, and Co increased continuously. However, when the temperature is over 550 °C, the leaching rate of metals began to decline. Based on the XRD results in Fig. 2d, the form of metal oxide and ferrite is the main reason for the low leaching rate under higher temperatures. Besides, according to Figs. 2e and 2f, the optimal roasting time is 2 h. Thus, the direct sulfated roasting process to extract valuable metals from low-nickel matte is inefficient and poor selectively.

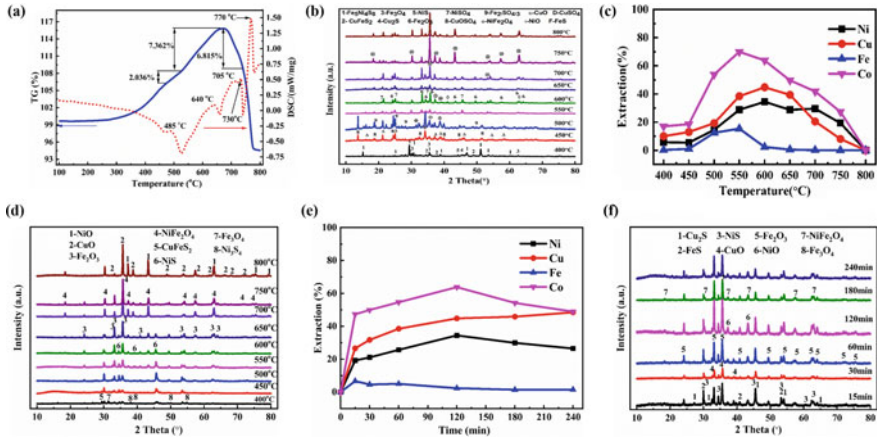

Fig. 2 Direct sulfated roasting of low-nickel matte. **a** TG-DSC analysis, **b** XRD analysis after oxidizing roasting, **c**, **d** Leaching rate, and XRD analysis of leaching residue under different roasting temperatures, **e**, **f** Leaching rate and XRD analysis under different roasting time. (Color figure online)

Sulfated Roasting with $(NH_4)_2SO_4$ Added

As described in Fig. 3a, the TG-DSC curve represents two endothermic peaks at 310 and 405 °C, which was ascribed to the decomposition of $(NH_4)_2SO_4$ additive. The $(NH_4)_2SO_4$ plays a key role in reducing the temperature of sulfation.

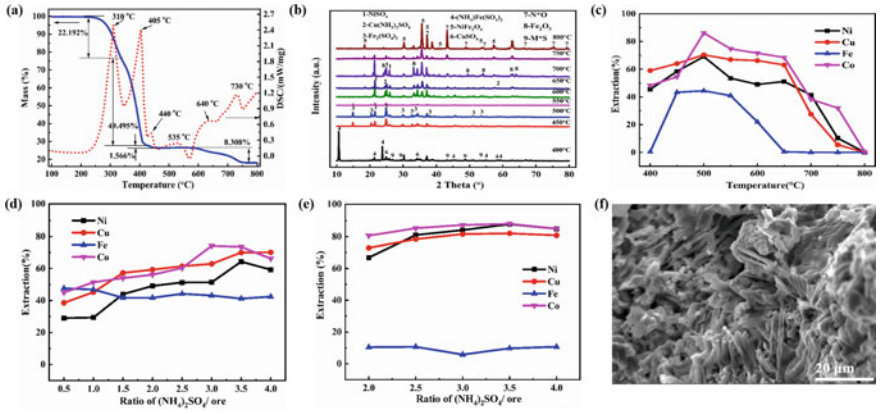

Fig. 3 Sulfated roasting of low-nickel matte with $(NH_4)_2SO_4$ added. **a** TG-DSC analysis, **b** XRD analysis after roasting, **c**, **d** Relationship of leaching rate of metals with temperature and additive ratio, **e** Leaching rate of metals with different ratio of additive under two-step roasting rule (500 °C for 2 h with 5 °C min^{-1} heating rate), **f** SEM image of the roasting product (500 °C for 2 h with 3.5 ratios of $(NH_4)_2SO_4$/material). (Color figure online)

The XRD patterns of roasting products at different temperature are shown in Fig. 3b, in addition to the unreacted metal sulfides, there are $(NH_4)Fe(SO_4)_2$, $NiSO_4$, and traces $Cu(NH_3)_2SO_4$. The formation of compound sulfates well explains that the $(NH_4)_2SO_4$ can reduce the temperature of sulfation, which is agreed with the TG-DSC results. Figure 3c, 3d illustrated the relationship of leaching rate with temperature and ratio, respectively, using the one-step roasting process. Clearly, adding $(NH_4)_2SO_4$ could greatly enhance the leaching rate of Ni, Cu, and Co realized the efficient extraction of valuable metals. To further improve the separation efficiency of different valuable meals in raw materials, the two stages of a roasting rule is adopted to the calcination process. The results represented in Fig. 3e, with 350% $(NH_4)_2SO_4$ added, the corresponding leaching rate of Ni, Cu, and Co are 90.12%, 81.82%, and 92.45%, respectively, whereas the recovery efficiency of Fe is about 10%. The high-efficiency extraction of Ni, Cu, Co, and the removal of Fe are realized. The morphology of calcination product at 500 °C for 2 h with 350% $(NH_4)_2SO_4$ added was analyzed, as shown in Fig. 3f, revealing that the main micro-structure of roasting products is flocculation.

Thermodynamic Calculation and Mechanism Discussion

Based on the calculation results expressed in Fig. 4a, the oxidation order of sulfide in low-nickel matte is $FeS > Ni_3S_2 > Cu_2S$.

Figure 4b depicts the Gibbs free energy of the sulfation process, obviously, the value is negative indicating that the sulfation reaction can happen spontaneously,

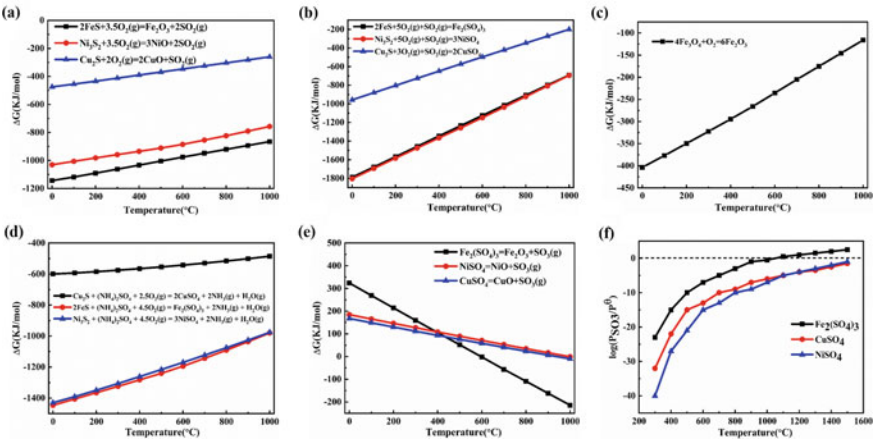

Fig. 4 Thermodynamic calculation of sulfated roasting of low-nickel matte. Gibbs free energy change of, Direct oxidation roasting process **a**, Sulfation process **b**, $(NH_4)_2SO_4$ decomposition **c**, Sulfate roasting with $(NH_4)_2SO_4$ added **d**, MSO_4 (M = Ni, Cu, and Fe) decomposition **e**, **f** Equilibrium partial pressure of SO_3 at different temperatures. (Color figure online)

and the temperature has a crucial influence on sulfation. Thus, in the process of direct roasting, as long as sufficient O_2 and SO_2 are provided, the oxidation reaction and sulfation reaction will continue. The Gibbs free energy change of $(NH_4)_2SO_4$ decomposition is illustrated in Fig. 4c, when the temperature is over 200 °C, the reaction of $(NH_4)_2SO_4$ decomposition is spontaneous, which explains well the two endothermic peak in TG-DSC curves. In the process of roasting of low-nickel matte with $(NH_4)_2SO_4$, the metal sulfides would react with $(NH_4)_2SO_4$ to produce the metal sulfate, the calculation results shown in Fig. 4d demonstrated its spontaneous reaction within the experimental temperature range. According to the results in Fig. 4e, the Fe_2 $(SO_4)_3$ is more prone to decomposition than the $NiSO_4$ and $CuSO_4$, which is consistent with the XRD results. Besides, when the temperature exceeds 700 °C, all the MSO_4 (M = Ni, Cu, and Fe) could decompose spontaneously. As depicted in Fig. 4f, at the same temperature, the equilibrium partial pressure of SO_3 of Fe_2 $(SO_4)_3$ is larger than that of $NiSO_4$ and $CuSO_4$, so that in the presence of Fe_2 $(SO_4)_3$, $NiSO_4$, and $CuSO_4$ are difficult to decompose. Therefore, controlling the roasting temperature that can make Fe_2 $(SO_4)_3$ decompose preferentially, and the NiSO4 and CuSO4 are still exist in the form of sulfate, thus, achieving the selective extraction valuable metals by the subsequent water leaching process. Through thermodynamic calculation and reaction mechanism analysis of this process, it is proved that the $(NH_4)_2SO_4$ additive could lower the roasting temperature and enhance the separation efficiency.

Conclusion

In summary, insufficient degree of sulfation and the formation of $NiFe_2O_4$ are the two main reason for the poor separation efficiency by the direct roasting process to treat the low-nickel matte. The addition of $(NH_4)_2SO_4$ provides sulfur for the roasting reaction, ensuring the sulfation process is fully proceed. Besides, it can reduce the reaction temperature, expanding the stable temperature range of sulfate, therefore, significantly improve the leaching rate of Ni, Cu, and Co. The sulfated roasting with additive added coupling with water-leaching is an efficient strategy to extract valuable metals from low-grade nickel matte.

Acknowledgements This work was supported by the National Natural Science Foundation of China (Nos. 51874196, 51674164), sponsored by Shanghai Pujiang Program (2019PJD015), the Iron and Steel Joint Research Fund of National Natural Science Foundation, and China Baowu Steel Group Corp. Ltd (U1860203), the Science and Technology Commission of Shanghai Municipality (No. 19DZ2270200), and CAS Interdisciplinary Innovation Team.

References

1. Zhang L, Shi D, Liu T, Jaroniec M, Yu J (2019) Nickel-based materials for supercapacitors. Mater. Today 25:35–65
2. Rossin J, Goodlet B, Torbet C, Musinski W, Cox M, Miller J, Groeber M, Mayes A, Biedermann E, Smith S, Dal S, Pollock T (2020) Assessment of grain structure evolution with resonant ultrasound spectroscopy in additively manufactured nickel alloys. Mater Charact 167:110501
3. Ma T, Chen Y, Li Y, Ping Y, Kong W (2019) nickel-catalyzed enantioselective reductive aryl fluoroalkenylation of alkenes. ACS Catal 9(10):9127–9133
4. Li W, Erickson EM, Manthiram A (2020) High-nickel layered oxide cathodes for lithium-based automotive batteries. Nature Energy 5(1):6–34
5. Park K-H, Mohapatra D, Nam C-W, Kim H-I (2007) A comparative study of different leaching processes for the extraction of Cu, Ni and Co from a complex matte. Korean J Chem Eng 24(5):835–842
6. Lu ZY, Jeffrey MI, Zhu Y, Lawson F (2000) Studies of pentlandite leaching in mixed oxygenated acidic chloride-sulfate solutions. Hydrometallurgy 56(1):63–74
7. Zhu D-Q, Cui Y, Hapugoda S, Vining K, Pan J (2012) Mineralogy and crystal chemistry of a low grade nickel laterite ore. Trans Nonferrous Metals Soc China 22(4):907–916
8. Sun Y-J, Diao Y-F, Wang H-G, Chen G, Zhang M, Guo M (2017) Synthesis, structure and magnetic properties of spinel ferrite (Ni, Cu, Co)Fe_2O_4 from low nickel matte. Ceram Int 43(18):16474–16481
9. Chen G-J, Gao J-M, Zhang M, Guo M (2017) Efficient and selective recovery of Ni, Cu, and Co from low-nickel matte via a hydrometallurgical process. Int J Miner Metal Mater 24(3):249–256
10. Muzenda E, Ramatsa IM, Ntuli F, Abdulkareem AS, Afolabi AS (2013) Parametric effects on leaching behavior of nickel-copper matte in ammonia. Particul Sci Technol 31(4):319–325
11. Park KH, Mohapatra D, Reddy BR (2006) A study on the acidified ferric chloride leaching of a complex (Cu–Ni–Co–Fe) matte. Sep Purif Technol 51(3):332–337
12. Yan LIU (2011) Influence of different pretreatment methods on extracting of nickel matte by sulfate roasting [J]. Non Ferrous Mining Metallurgy 27(5):23–25
13. Li J, Chen Z, Shen B, Xu Z, Zhang Y (2017) The extraction of valuable metals and phase transformation and formation mechanism in roasting-water leaching process of laterite with ammonium sulfate. J Clean Prod 140:1148–1155
14. Zhang G, Luo D, Deng C, Lv L, Liang B, Li C (2018) Simultaneous extraction of vanadium and titanium from vanadium slag using ammonium sulfate roasting-leaching process. J Alloys Compd 742:504–511
15. Li Y, Liu H, Peng B, Min X, Hu M, Peng N, Yuang Y, Lei J (2015) Study on separating of zinc and iron from zinc leaching residues by roasting with ammonium sulphate. Hydrometallurgy 158:42–48
16. Liu X-W, Feng Y-L, Li H-R, Yang Z-C, Cai Z-L (2012) Recovery of valuable metals from a low-grade nickel ore using an ammonium sulfate roasting-leaching process. Int J Minerals Metal Mater 19(5):377–383
17. Liu W, Wang X, Lu Z, Yue H, Liang B, Lü L, Li C (2017) Preparation of synthetic rutile via selective sulfation of ilmenite with $(NH_4)_2SO_4$ followed by targeted removal of impurities. Chin J Chem Eng 25(6):821–828

Synthesis and Characterization of ZnO Nanoparticles Obtained from the Extract of *Schinus Molle*

Karime A. Cárdenas, Jenny Domínguez, Estrella Palacios, Laura García, Pedro A. Ramírez, and Mizraim Flores

Abstract Zinc oxide nanoparticles were synthesized using the green chemistry technique, zinc acetate was used as a precursor agent and *Schinus molle* extract as a stabilizer agent the main *Schinus molle* component are carboxylic acids, similarly presents tension bands of the C-H group, the S-O group. A white powder, characteristic of zinc oxide, was obtained. X-ray diffraction was performed on the synthesis product and identified as zincite (ZnO), with a compact hexagonal unit cell, whose network parameters are at a = 3.2490 Å and c = 5.2070 Å, the ICDD-PDF letter is 96-901-1663. Scanning electron microscopy characterization showed that the nanoparticles have a spherical morphology, sizes ranging from 23 to 67.6 nm.

Keywords Synthesis · Characterization · Nanoparticles · Schinus molle

Introduction

The nanoparticle synthesis for a green chemistry approach has had a lot of potential compared with the conventional methods to develop nanostructured materials because it is an economic technique and friendly with the environment that allows to obtain nanoparticulated materials [1, 2]. Researchers have been using green synthesis based on the ecological approach to obtain different metallic nanoparticles for diverse industrial and medical applications, using plants like *Sargassum Algae, Ginko biloba or Panax,* although [1–5], there are many more species to be able to synthesize nanoparticles. Nowadays there is an extensive research known because of the study of the metallic nanoparticles specifically the zinc oxide due to its low cost thanks to the easy technic to be obtained.

Zinc oxide (ZnO) is a broadband (3.37 eV) piezoelectric and semiconductor material with a high exciton binding energy (60 meV) at room temperature [6–8], it is a white powder that is insoluble in water but soluble in weak and strong mineral acids,

K. A. Cárdenas · J. Domínguez · E. Palacios (✉) · L. García · P. A. Ramírez · M. Flores
Área Electromecánica Industrial, Universidad Tecnológica de Tulancingo, Camino a Ahuehuetitla #301 Col. Las Presas, 43642 Tulancingo, Hidalgo, Mexico
e-mail: palaciosestrella07239@gmail.com

J. Li et al., *Characterization of Minerals, Metals, and Materials 2021*,
The Minerals, Metals & Materials Series,
https://doi.org/10.1007/978-3-030-65493-1_58

ammonia, acetic acid or formic acid [9, 10], its structure is relatively open with a very compact hexagonal network where zinc atoms occupy half of the tetrahedral sites, while all the octahedral sites are empty. The open structure also influences the nature of the diffusion mechanism defects. The identity, quantity, and stability of these vacancies or radicals are characteristics to consider when this material is required in an application [11]. Based on its properties such as high chemical stability, wide radiation absorption range, biocompatibility, biodegradability, etc., it becomes a good material for technological applications [8]. Applications for this type of material depend due to its electrical and magnetic properties and the method by which they were prepared [10], nanometric ZnO has important properties that contribute to the production of thin films which are used in steels to avoid corrosion processes.

Corrosion is the process of deterioration of metal materials (including pure metals and such as alloys) through chemical and electrochemical reactions. Under certain conditions, such as high salt concentrations, variations between dry and humid climate, high temperatures and radiation rates, chemical, and electrochemical reactions occur that cause loss of material properties or accelerated damage. Corrosion is the physical-chemical interaction between a metal and its environment. It is a spontaneous phenomenon, as all metals used tend to lose electrons (oxidize) and return to their natural state by forming oxides, salts, hydroxides, etc. Oxidation is the chemical reaction from which an atom, ion or molecule gives up electrons [12, 13]. Currently, there are several methods to control, reduce, and prevent metallic corrosion. However, these attempts to interfere with the corrosion process cannot completely prevent it. One of the traditional methods is the use of inhibitors that are incorporated into coatings or paints.

The present work focuses on the biosynthesis of zinc oxide nanoparticles through green chemistry, using the *Schinus molle* plant, which is a family of the Cassia alata plant, being the phytochemicals that serve as reducing agents and stabilizing agents through reduction and oxidation reaction [14].

Methods and Materials

For the synthesis of zinc oxide nanoparticles, the green chemistry technique was used, where the *Schinus molle* tree leaves were used. The leaves that were used were healthy, fresh, free of pests, and green in color, thus preventing the synthesis from becoming contaminated. Twenty grams of *Schinus molle* leaves were weighed, then washed with tap water, and rinsed with ultra-pure water, then dried at room temperature. 500 mL of ultra-pure water was measured and placed in a Pyrex reaction jar with a hermetically sealed four-necked lid, the reaction jar was placed on a heating plate with magnetic stirring (Thermo, Supernuova model RS-232), and maintained at a speed of 400 rpm. When the solution reached 75 °C the *Schinus molle* leaves were deposited, after 10 min the zinc acetate solution (0.4 mol L^{-1}) began to be deposited, 10 mL every after 10 min (Scheme 1), the solution changed color when making the first deposit of the zinc acetate solution, and turned green, the temperature of the

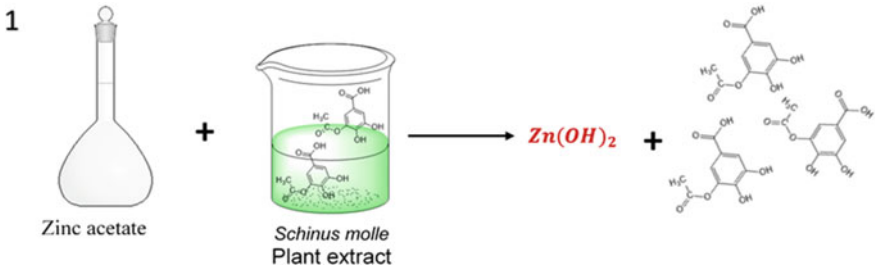

Scheme 1 Representation of the zinc acetate reduction process. (Color figure online)

solution rose to 92 °C. After having made the nine zinc acetate deposits, the solution was cooled and filtered, using Whatman filter paper, No. 4, the filtration process was maintained for 150 min. The filtered solution was brought to refrigeration and the powder that remained on the filter paper was used for characterization by different techniques. *Schinus molle* leaves were characterized by Fourier Transform Infrared (FTIR) to determine the organic groups present in the plant. Powders obtained after synthesis were analyzed by X-ray diffraction (XRD). For the characterization by scanning electron microscopy (SEM), two drops of the filtered solution were taken, which were deposited on the surface of a Cu sample holder. When the drops dried, the nanoparticles that were intended to be in the solution were impregnated in the said sample holder.

Results and Discussion

Schematic representation for the first equation of the ZnO nanoparticle synthesis mechanism, in which the zinc acetate and the active compounds (Tannin) of the leaves of the tree (*Shinus molle*) react leading to the formation of zinc hydroxide and carboxylic acid. Scheme 2 shows the second equation where zinc hydroxide reacts with the amines, leading to the formation of nanoparticulate zinc oxide.

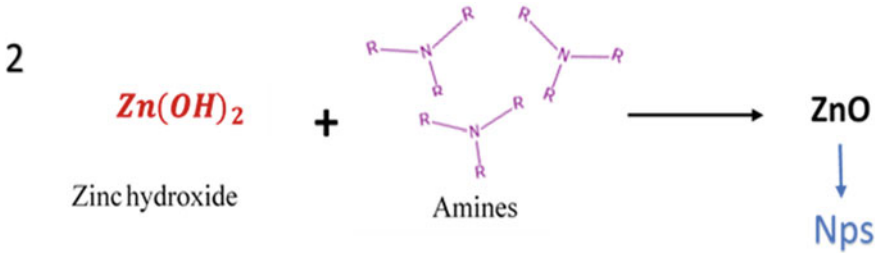

Scheme 2 Representation of the zinc hydroxide reduction process. (Color figure online)

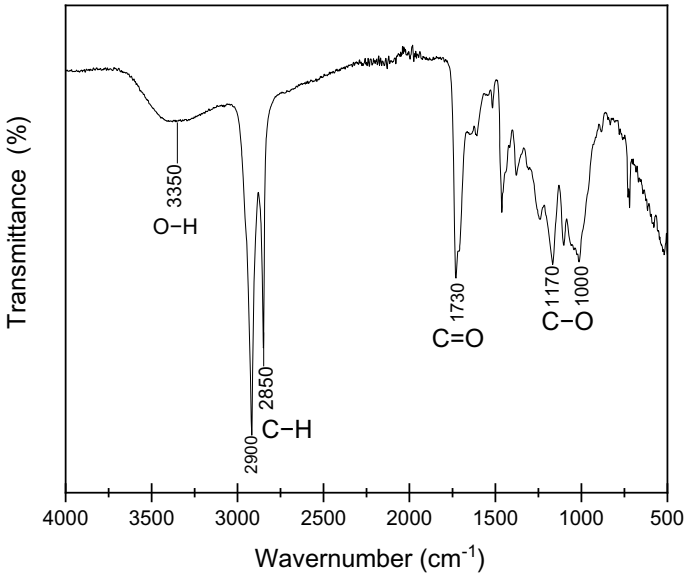

Fig. 1 FTIR spectrum of *Schinus molle* leaves

A spectrum of FTIR was made to the leaves of *Schinus molle*, which were washed with ultra-pure water, then dried and crushed. Figure 1 shows the FTIR spectrum where a stretch broadband is present, characteristic of the O−H link, which represents the phenolic groups in the region of 3200 to 3400 cm^{-1}. Two intensity stretches bands belonging to the C−H link are shown; one in the region 2900 cm^{-1} and one 2850 cm^{-1}. A characteristic stretch band of carboxylic acids (C = O) is observed in the region 1730 cm^{-1}, which shows a high stretch band. In the region of 1000 to 1170 $cm^{-1,}$ there are a series of bands belonging to the C−O link.

To confirm the presence of ZnO in the synthesis, it was characterized by X-Ray Diffraction. The results are displayed on a spectrum presented in Fig. 2, which was indexed with ICDD-PDF 96-901-1663, where it is confirmed the presence of zinc oxide in zincite shape (mineral of zinc oxide) the same which crystalline hexagonal compact structure with a red parameter of a = 3.2490 Å and c = 5.2070 Å.

Figure 2 shows a diffractogram sampling thirteen crystallographic planes from where only three peaks show the highest intensity, there the highest one is placed 36.31° with the crystallographic plane 101 has a interplanal distance 2.4754 Å, the second one has medium intensity in reference with the last one and it´s located 31.76° with the crystallographic plane 100 which interplanal distance 2.8137 Å and the last peak presents a lower intensity found in 34.43° with the crystallographic plane 002 with an interplanal distance 2.6035 Å. The remaining peak show medium or lower intensity as shown in Fig. 2, it is worth to emphasize that being an indexed graphic with the chard previously mentioned, all of the peaks concur at 100%.

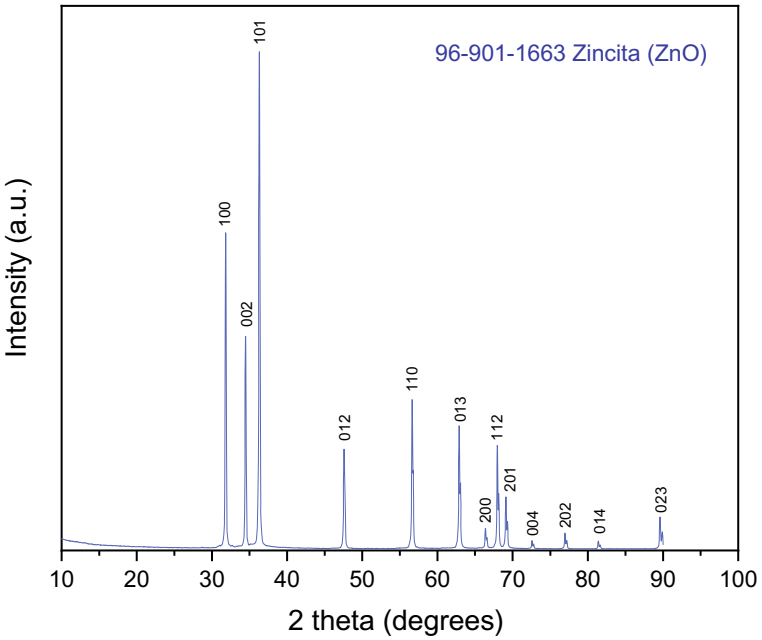

Fig. 2 XRD spectrum of the ZnO powder. (Color figure online)

A sample was taken which was characterized by SEM at 200,000X magnifications in the first micrograph present in Fig. 3, while in Fig. 4 it is at 100,000X magnifications and both at an acceleration of 5.0 kV. The results that were obtained were favorable, showing that nanoparticles with a spherical morphology and sizes ranging from approximately 23 to 67 nm were obtained.

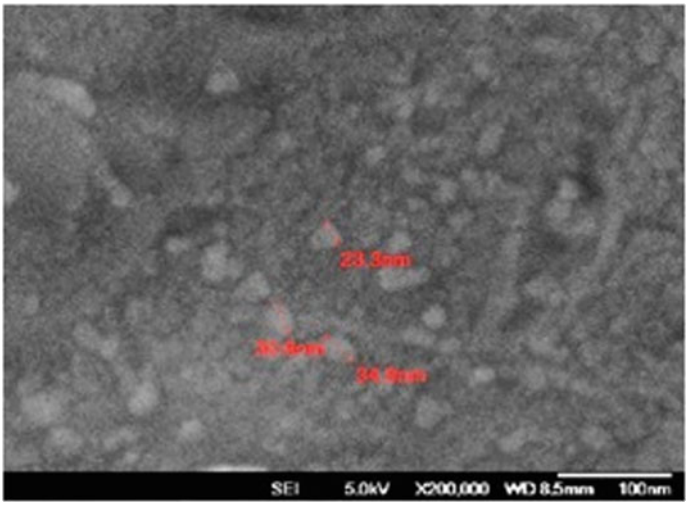

Fig. 3 Micrograph of ZnO nanoparticles ranging from 23.3 nm to 34.8 nm. (Color figure online)

Fig. 4 Micrograph of ZnO nanoparticles ranging from 25.5 nm to 67.6 nm. (Color figure online)

Conclusions

It was possible to synthesize zinc oxide nanoparticles (ZnO) by the green chemistry method using the leaves of *Schinus molle*. The samples were characterized by X-ray Diffraction showing that zinc oxide (ZnO) was obtained in the form of zincite whose crystalline structure is compact hexagonal with a parameter of a network of a =

3.2490 and c = 5.207. The samples were characterized by SEM, showing that the morphology of the nanoparticles is spherical, ranging from 23.3 nm to 67.6 nm, with good dispersion of the nanoparticles.

Schinus molle leaves were characterized by FTIR and the presence of phenolic groups and carboxylic acids was confirmed.

References

1. Rajit R, Bhabhin NM, Dharsan MV, Nivedit CV, Sindhu S (2015) Green synthesis of copper nanoparticles using Ginkgo biloba L. leaf extract and their catalytic activity for the Huisgen [3 + 2] cycloaddition of azides and alkynes at room temperature. J Colloid Inter Sci 6
2. Mirza AU, Kareem A, Nami SAA, Bhat SA, Mohammad A, Nahi N (2016) Biological Synthesis of nanoparticles from plants and microorganisms. Cellpress 596
3. Islan GA, Durán M, Cacicedo ML, Nakazat G, Kobayash RKT, Martinez D, Castro GR, Durán N (2013) Potential therapeutic and diagnostic applications of one-step in situ biosynthesized gold nanoconjugates (2-in-1 system) in cancer treatment. RSC Advances 10
4. Javadi E, Ghaffari M, Bahlakeh G, Taher P (2019) Photocatalytic, corrosion protection and adhesion properties of acrylic nanocomposite coating containing silane treated nano zinc oxide: a combined experimental and simulation study. Progr Org Coatings 14
5. Sing M, Wang Q, Xia X (2015) A strategic approach for rapid synthesis of gold and silver nanoparticles by Panax ginseng leaves. Cells Nanomed Biotechnol 14
6. Al-Asedy HJ, Bidin N, Abbas KN, Al-Azaw MA (2018) Structure, morphology and photoluminescence attributes of Al/Ga co-doped ZnO nanofilms: Role of annealing time. Mater Res Bull 10
7. Hamzaou N, Boukhache A, Ghamni M, Fauque C (2005) A comprehensive review of ZnO materials and devices. J Appl Phys 8
8. Chen L, Batjikh I, Hurh J, Han Y, Huo Y, Alia H, Lib JF, Rupa EJ, Ahna J, Mathiyalagan R, Yang DC (2019) Green synthesis of zinc oxide nanoparticles from root extract of Scutellaria baicalensisandits photocatalyticde gradation activity using methylene blue. Optik 8
9. Jaramillo AF, Montoya LF, Prabhakar JM, Sanhueza JP, Fernández K, Rohwerder M, Rojas D, Montalba C, Melendrez MF (2019) Formulation of a multifunctional coating based on polyphenols extracted from the Pine radiata bark and functionalized zinc oxide nanoparticles: Evaluation of hydrophobic and anticorrosive properties. Progr Org Coatings 14
10. Pouy Marzbani YM (2015) The effect of nano-zinc oxide on particleboard. Maderas. Ciencia y tecnología 14
11. Acosta-Humánez M, Agarwal H (2015) Sol-gel synthesis of zinc oxide nanoparticle at three different. DYNA 10
12. Jayabala J, Mani G, Krishna N, Pernaba J, Devados JM, Jang HT (2015) Green Synthesis of palladium nanoparticles with sargassum alga and their electrocatalytic activities towards hydrogen peroxide. Biochem Biotechnol 9
13. Pourhashem S, Machado CD, Raman V, Rehman JU, Maia BH, Meneghett EK, Almeida VP, Silv RZ, Farago PV, Khan IK, Bude JM (2018) Schinus molle: anatomy of leaves and stems, chemical composition and insecticidal activities of volatile oil against bed bug (Cimex lectularius). J Alloys Compounds 11
14. Happy A, Soumya M, Kumar SV, Rajeshkumar S, Sheb RD, Lakshmi T, Nallaswam VD (2019) Phyto-assisted synthesis of zinc oxide nanoparticles using Cassia alata and its antibacterial activity against Escherichia coli. Biochem Biophys Reports 4

Technical, Environmental, and Economic Advantages in the Use of Asphalt Rubber

Mariáh P. S. P. Soares, Niander A. Cerqueira, Felipe Fraga de Almeida, Afonso R. G. Azevedo, and Markssuel Teixeira Marvila

Abstract The correct disposal of tires is a major concern for the environment. A part of the waste is used to manufacture rubber asphalt, providing environmental, technical, and economic advantages. In the present work, it was identified that the permanent deformation at 60 °C in 10,000 cycles for CAP 50/70 (traditional asphalt) is 4.7%, while rubber asphalt is 2.5%. In addition, the permanent deformation at 60 °C in 30,000 cycles for CAP 50/70 is 6.2%, and for rubber asphalt, it is 3.2%. Thus, the pavement with rubber asphalt is more durable compared to the pavement with CAP 50/70. So, even though rubber asphalt is a little more expensive, in the end, it becomes more economical because it has greater durability. Moreover, over the years the CAP 50/70 will need more maintenance, while rubber asphalt promises a much lower amount of maintenance.

Keywords Asphalt rubber · Composites · Environmental effects · Sutainability

Introduction

The increase in population, the advancement of new technologies, and the growth of the economy have resulted in an increase in the disposal of solid waste in nature. In 1999, with the approval of CONAMA Resolution 258/99 [1], there was a significant growth in the recycling of waste tires in Brazil.

The CNT (National Confederation of Transport) Survey of Highways 2019, states that the road modal is the main one for the movement of cargo and people, but it does not receive significant investments for the growth of highways to accompany

M. P. S. P. Soares · N. A. Cerqueira (✉) · F. F. de Almeida · A. R. G. Azevedo · M. T. Marvila
Sociedade Universitária Redentor, Redentor, BR 356 Km 25, Itaperuna, Rio de Janeiro, Brazil
e-mail: prniander@gmail.com

A. R. G. Azevedo
Universidade Federal Fluminense—UFF, Rio de Janeiro, Brazil

M. T. Marvila
Universidade Estadual Do Norte Fluminense Darcy Ribeiro—UENF, Rio de Janeiro, Brazil

J. Li et al., *Characterization of Minerals, Metals, and Materials 2021*,
The Minerals, Metals & Materials Series,
https://doi.org/10.1007/978-3-030-65493-1_59

the economic growth of the country. The quality and maintenance of most roads are not satisfactory.

Combining economic development and environmental issues, rubber asphalt brings simple and effective perspectives in the short, medium, and long term related to the durability and quality of the pavement, automobiles, the environment, and even the health of citizens. This technology occurs through the range of useless tires with no destination, with promising innovation for the paving part.

Tire Collection and Recycling in Brazil

Although the tire has been very useful since it was created, it is also a big problem when it comes to the environment, because when the tire wears out completely it becomes unusable. According to Reciclanip in 1999, to meet CONAMA resolution 258/99 [1], the National Waste Collection and Disposal Program began, which was created by ANIP (National Association of the Pneumatic Industry), over time the program was expanded and they decided to create Reciclanip, in 2007, which is an institution focused on correctly collecting and disposing of waste tires in the country. It was founded by the new tire manufacturers Bridgestone, Goodyear, Michelin, and Pirelli. Subsequently, Continental and Dunlop joined the group.

Reciclanip has been working on reverse logistics, giving waste tires a correct destination. In 2019, they had more than 1026 collection points and correctly disposed of 471 tonnes of waste tires. Between 1999 and 2019, correctly collected and disposed of more than 5.23 million tons of waste tires, which corresponds to 1.04 billion passenger tires [2].

Lagarinhos [3] says that before the CONAMA Resolution, the country only recycled 10% of tires. Soon after the legislation was passed, companies registered to collect waste tires grew considerably. In Brazil, there is no government incentive in favor of tire recycling. Reverse logistics is paid for by new tire manufacturers and importers.

The Road Modal in Brazil

In Brazil, the main mode of transportation of people and cargo is the road, data from the CNT Highway Survey 2019, show that only 12.4% of the highways are paved. Despite being a very important modal, there are still few paved stretches [4]. And road conditions are not satisfactory.

The search [4] shows that the growth of the vehicle fleet is greater than the growth of the road network, the road mode is the most appropriate for short and medium distance journeys and there is an overload of vehicles circulating on the highways, with these aspects, combined, make it necessary for investment levels to expand and maintain roads to be significant.

The non-compliance with technical requirements related to the structure of the flexible pavements, which was also observed in the CNT Roads Survey 2019, points out that, both in the support capacity of the layers, as well as in the quality of the materials used in the coating, it results in a more accelerated deformation [4].

Transport in Brazil is an activity that is part of the base of the economy in the country, allowing functionality in several sectors, and should go hand in hand with environmental issues. The quality of the road network, its state of conservation, and its proper maintenance interferes mainly in safety, but also in costs and energy efficiency of transport, influencing the environment. When vehicles travel on roads in inadequate conditions, they generate some damage, such as accidents, higher fuel consumption, wear and tear on vehicle parts, among other factors [4].

In view of the current situation of the road network in the country, it is necessary to invest more in road infrastructure, both for paving new roads and for maintaining existing roads; so that economic growth goes hand in hand with environmental issues.

Rubber Asphalt

Rubber asphalt is the integration of rubber in the asphalt mixture, which in addition to offering desirable properties to the pavement, also presents a significant environmental perspective, since it enables a more sustainable destination for millions of scrap tires discarded every year [4].

Similarly, it is also defined as an asphalt binder that brings innovation, economy, and sustainability to the pavement generated through investments in research for a product of high durability and safety, which presents an attention to the reduction of environmental problems [5].

Brief History of Asphalt Rubber

According to Di Giulio [6], the first studies on the use of rubber tires on asphalt were around the 1950 s. However, it was only in the following decade that the technological development of the material was verified, when the engineer Charles Mc Donald traveled United States highways in a trailer, applied a mixture of rubber tire powder with asphalt to seal the cracks in the roof of his vehicle. Over time, he observed that the mixture did not oxidize, in the opposite way of those with conventional asphalt. From there, engineers began to experiment with the mix for plug-in services. In the United States, there is a law that requires the application of a minimum percentage of recycled rubber in asphalt mixtures.

Since the 1960s, countries such as the United States, South Africa, Portugal, China, and Australia have performed services with rubber asphalt. The first studies on rubber asphalt in Brazil took place in 1999 [5]. In the same year, article No. 2 of CONAMA resolution 258/99 [1], the article prohibits the disposal of waste tires in

the environment, arising the need to give these tires a sustainable destination. The first test application of rubber asphalt in the country was in 2001, at kilometer 319 of BR116 in Rio Grande do Sul [7]. From then on, several other stretches were submitted to rubber asphalt, with positive results in the applications. In September 2009, DNIT publishes material and service specifications for rubber-modified asphalt with its wet use [8, 9].

Today rubber asphalt is a reality in several countries, in Brazil, several stretches were built, recovered or restored. More than 10 million scrap tires have been used in the production of rubber asphalt [5].

Getting the Rubber Powder

The rubber powder, used in rubber asphalt, is obtained by grinding the tire at recycling plants or companies specializing in tire retreading. There are three types of methods for obtaining this rubber powder [10]:

- Cryogenics: Addition of liquid nitrogen to ground rubber. The rubber is frozen and, after freezing, it is crushed until the desired granulometry is acquired.
- Regeneration: Extraction by means of solvent that separates the rubber from the other components, such as metals, fabrics, and others. The ground chips of the tire are subjected to water vapors together with chemicals, such as alkalis and mineral oils, until the desired product is acquired.
- Cold grinding: Most common and cheap, a process in which the tire is ground and sieved, then passed through magnets that remove the remaining metal parts.

The most used method of the three is cold grinding, as the other two methods have a higher cost.

Methods for Obtaining Asphalt Rubber

There are two methods of incorporating tire rubber powder into asphalt mixtures [11, 12]:

- Dry route: consists of the mixture of crushed rubber particles as an aggregate of the mixture, producing the so-called aggregate-rubber. In this method, rubber is added to the mixture as part of the stone aggregate and not as part of the asphalt binder;
- Wet way: represents the mixture of small fine particles of rubber with asphalt, giving rise to the so-called asphalt-rubber. The small rubber particles act as a modifying agent and are added directly to the heated CAP (Asphalt Petroleum).
- This method has two types of manufacturing process; it can be stock or non-stock.

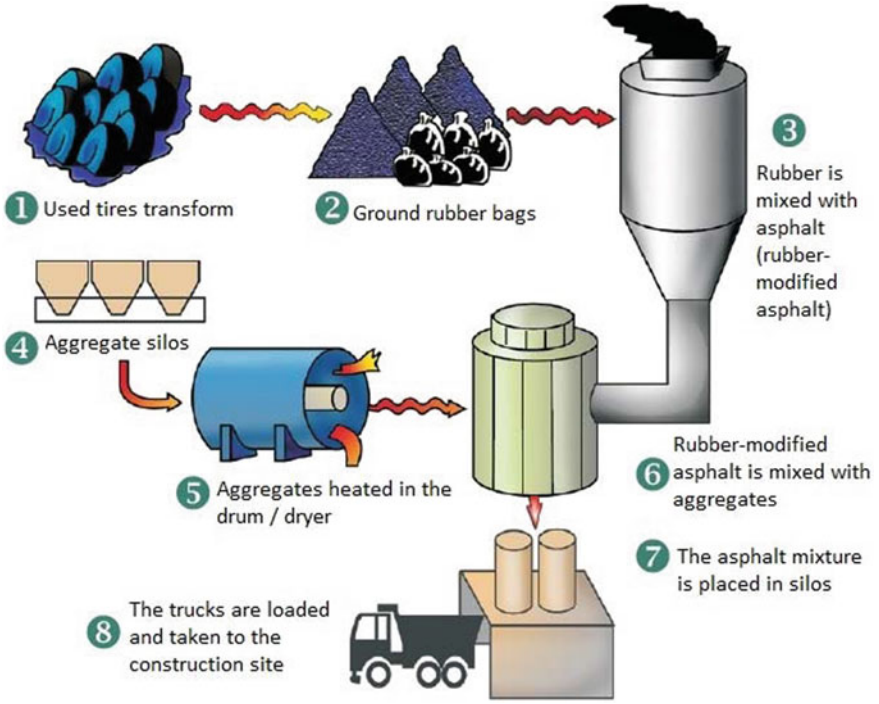

Fig. 1 Scheme of manufacture of rubber asphalt by the wet process by the stocking mixing process (blending terminal) *Source* Bernucci et al. [11]. (Color figure online)

- The non-stocking process, also known as continuous blending, is produced on site with a mixing equipment and needs to be applied at the same time, due to its instability. The stocking process, which is known as the blending terminal, is appropriately mixed in a special terminal, resulting in a stable and relatively homogeneous binder. Then having a more reliable quality control. Subsequently, the asphalt binder is transported to each site.

Figure 1 shows a scheme for manufacturing rubber asphalt using the stockpile manufacturing process, which is the process standardized by DNIT 112/2009−ES [9].

Standards and Technical Characteristics of Rubber Asphalt

In 2009, developed the first Brazilian standards for rubber asphalt were by DNIT. The DNIT Standard 111/2009-EM [8] has the purpose of specifying the material used for paving with asphalt cement modified by rubber from unserviceable tires by the wet process of the terminal blending type. The standard defines wet asphalt

rubber as "Petroleum asphalt cement modified by the wet process addition of ground rubber from unserviceable tires (particles passing through sieve No. 40), resulting in a mixture in which ground rubber generally represents 15 to 20% of the binder mass."

This regulation presents some specific conditions that the asphalt rubber must have, such as: the ground rubber must represent a minimum rubber content of 15% by weight, incorporated into the asphalt binder by the wet method and it is also necessary to check in advance if the results of the tests match the characteristics of the two rubber asphalts, AB-8 and AB-22, as shown in Table 1.

In addition, the DNIT 111/2009-EM [8] standard indicates that the wet-blending process of the terminal blending type is that which obtains the stockpile rubber asphalt, where the elements are mixed in a special terminal by agitation with high shear and subjected to high temperatures, originating in a stable and homogeneous ligand. However, the standard in question does not indicate the maximum time between the production of rubber asphalt and its use in the field and leaves the manufacturer to define the conditions for storage and storage of rubber asphalt.

The DNIT 112/2009-ES [9] standard regulates the specification of the service and quality control of asphalt concrete with rubber asphalt, which must be manufactured in an appropriate plant, obtained through the wet process of the terminal blending type. The standard also recommends the use of two types of rubber asphalt for specific granulometric bands:

Table 1 Result of characteristic tests of rubber asphalt

Technical Characteristics	Unity	Asfalto Borracha		Test methods
		Type AB 8	Type AB 22	
Penetration,100 g, 5 s, 25 °C	0,1 mm	30–70	30–70	DNER ME 003/99
Softening point, min, °C	°C	55	57	DNER ME- 247/94
Brookfield Viscosity, 175 °C, 20 rpm, Spindle 3	cP	800–2000	2200–4000	NBR 15529
Flash Point, min	°C	235	235	DNER ME 148/94
Elastic Recovery Ductilometer, 25 °C, 10 cm, min	%	50	55	NBR 15086:2006
Storage stability, max	°C	9	9	DNER ME-384/99
Effect of heat and air (RTFOT), 163 °C:				
Mass variation, max	%	1	1	NBR 15235:2006
Softening Point Variation, max	°C	10	10	DNER ME-247/94
Percentage of Original Penetration, min	%	55	55	DNER ME 003/99
Percentage of Original Elastic Recovery, 25 °C 10 cm, min	%	100	100	NBR 15086:2006

Source DNIT 111/2009-EM [8]

- AB-8: for bands A, B, and C of DNIT and for discontinuous band type Gap Graded;
- AB-22: for Gap Graded discontinuous band.

Technical Advantages in the Use of Asphalt Rubber

The use of rubber asphalt results in a pavement with greater resistance to cracks and permanent deformations (wheel tracks), this is because the asphalt mixture gains part of the rubber's elastic capacity, consequently, the pavement reduces undesirable deformations, since modified asphalt has the ability to deform when vehicles pass and return to their initial position. Furthermore, rubber asphalt also shows late aging and oxidation, due to certain elements present in rubber, such as carbon black, which preserve the asphalt by combating the chemical wear caused by the exposure of the floor to ultraviolet and infrared rays [10].

A study carried out at USP (University of São Paulo) analyzed the behavior, in relation to permanent deformation, of conventional asphalt mixtures and asphalt mixtures modified by rubber asphalt. Those modified by rubber asphalt show values of deformation in the simulator much lower than mixtures with conventional binders. Coming to the conclusion that the modified mixture with rubber asphalt proved to be less vulnerable to the formation of wheel tracks. Figure 2 shows the two plates subjected to the test, the direct one is with rubber asphalt and only 5% was deformed after 30,000 simulation cycles and the left plate with conventional ligand was deformed 13% after 10,000 cycles [7].

CNT 2019 [4] also points out other benefits such as less thermal vulnerability; the reduction of noise when passing vehicles, improving the well-being of passengers and inhabitants of the areas adjacent to the highways; and the best grip between the tire and the pavement, making passengers safer.

Fig. 2 Two plates after being submitted to the traffic simulator *Source* Greca Asfaltos [7]

Environmental Advantages in the Use of Asphalt Rubber

With the approval of CONAMA Resolution 258/99 [1], there was a significant advance in the recycling of waste tires in Brazil. In 2009, CONAMA Resolution No. 416/09 [12] was approved, changing the formula for calculating production for the aftermarket. The new resolution obliges manufacturers and importers to allocate 100% of the tires that enter the aftermarket. That is, for each new tire sold in the aftermarket, importers, and manufacturers must give a correct destination for a waste tire [5].

The CNT [4] shows that between 2009 and 2019, there was an increase of 80.8% in the vehicle fleet in Brazil, generating more and more waste tires annually. The use of rubber from these tires on paving reduces the deposit of this material in landfills or other inappropriate places, and up to a thousand tires per kilometer can be used [6].

The incorrect destination of the tires endangers the health of the population, as it is a place for the development of parasites and insects that transmit diseases. In addition, if they are burned, they generate toxic smoke, also attacking the environment. Thus, a great alternative for the correct destination of these tires is to use rubber on pavements, where a large amount of waste tires will be destined [10]

Economic Advantages in the Use of Asphalt Rubber

In 2009, Greca asfaltos made a comparative study between a 30 km pavement restoration work, comparing the use of conventional asphalt with CAP-50/70 asphalt binder and rubber asphalt. The purpose was to show the use of the technical characteristics of rubber asphalt [7].

The section was reversed with a 5 cm thick conventional asphalt layer and 3.5 cm thick asphalt rubber layer, having the same strength and stability as the conventional asphalt section.

The execution price of rubber asphalt costs approximately 15% more expensive than conventional asphalt. This is due to the fact that its manufacture requires high machining temperatures to increase the efficiency of compacting the coating.

Table 2 shows that considering only the execution of machining and application of CBUQ (Hot Machined Bituminous Cement) and the cost of the ton of conventional asphalt and rubber asphalt, it is concluded that in these two points the rubber asphalt has a higher value. However, when checking the work as a whole, taking into account the quantity of CBUQ applied, which is lower in the case of rubber asphalt and also its durability, the final cost of the work is less and the savings are in the long run.

Table 2 Comparison of cost between rubber asphalt and conventional asphalt

Quantities	Calculation	Unity	Asphalt Type	
			CAP 50/70	Rubber Asphalt (Ecoflex)
Mass quantity asphalt from CBUQ produced	–	ton	26,25	18,375
Machining Cost/ Application per ton of CBUQ applied	–	R$/ton	200	230
Mass quantity x Machining Cost/ Application	A X B	R$	5.250.000,00	4.226.250,00
Asphalt Content	–	% em peso	5	5,5
Asphalt Cost Per Ton	–	R$/Ton	1.150,00	1.550,00
Asphalt Cost at CBUQ	A x D x E	R$	1.509.375,00	1.566.468,75
Total Cost of Work	C + F	RS	6.759.375,00	5.792.718,75

Source Greca [7]

Conclusion

Due to the aforementioned facts, it can be realized that the use of rubber asphalt is considerably higher than that of conventional asphalt, since with the superior quality, costs are reduced because rework and intermittent repairs are not necessary. Runner asphalt decreases the amount of car maintenance related to defects or irregularities in the pavements. It guarantees the preservation of the environment and positively influences the health of citizens, due to the fact that it can have an adequate destination for waste tires, incorrect disposal is reduced, avoiding the proliferation of vectors in accumulated, burnt water, among others.

References

1. National Environment Council (Conama) (1999) Resolution nº 258, of August 26 (In Portuguese)
2. Reciclanip (2020) Volume of intended tires (In Portuguese). http://www.reciclanip.org.br/destinados/. Accessed 22 May 2020
3. Lagarinhos L, Tenório CAF, Jorge AS (2013) Reverse logistics for post-consumer tires in Brazil (In Portuguese). Polímeros 23(1), 49–58. Epub October 11, 2012. https://dx.doi.org/10.1590/S0104-14282012005000059
4. National Transport Confederation Cnt Highway Survey (2019) Management Report (In Portuguese). https://pesquisarodovias.cnt.org.br/relatorio-gerencial. Accessed 31 October 2019
5. Zatarin, APM, da Silva ALF, dos Anemam LS, de Barros MR, Chrisostomo W (2017) Viability of asphalt-rubber paving (In Portuguese). R. gest. sust. ambient Florianópolis 5(2):649–674, out.2016/mar

6. Digiulio G (2007) Environmental and economic advantages in using rubber on asphalt (In Portuguese). Inovação Uniemp, vol.3, pp. 12–15
7. Greca Asfaltos. ECOFLEX–Rubber Asphalt (In Portugues). http://grecaasfaltos.com.br/asfalto-borracha-ecoflex-asfalto-ecologico/. Accessed 22 May 2020
8. DNIT 111/2009–EM: Flexible paving–Asphalt cement modified by rubber from waste tires by the wet process, of the type "Terminal Blending"–Material Specification (In Portugues)
9. DNIT 112/2009–ES: Flexible floors–Asphalt concrete with rubber asphalt, wet, "Terminal Blending" type–Service Specification (In Portugues)
10. de Almeida, VS, GOMES ACC (2018) Conventional asphalt and rubber asphalt: a comparative study (In Portugues). Episteme Transversalis [S.l.], v. 9, n. 1, maio. ISSN 2236-2649
11. Bernucci, LB, da Motta, LMG, Ceratti, JAP, Soares JB (2008) Asphalt paving: basic training for engineers (In Portugues). (1ed.) Programa Asfalto nas Universidades, Petrobrás Distribuidora S.A., 2008
12. Camargo, Felipe Filizzola. Field and Laboratory Performance Evaluation of a Field-blended Rubber Asphalt (In Portugues) (2016) Thesis (Doctorate in Transport Engineering)- Polytechnic School, University of São Paulo, São Paulo. https://doi.org/10.11606/t.3.2016.tde-01072016-111905

The Incorporation of the Light Green Clay in the Textile Polyamide Residues

M. N. Sartori, D. P. Castro, F. R. Valenzuela-Diaz, and L. G. A. Silva

Abstract The aim of this work is to evaluate the possibility to use textile residues of polyamide with elastane that are discarded by the industry as a matrix of a new polymer-clay composite material, evaluated on a manometric scale, and to propose a way of recycling for these materials. At the same time, with nanocomposite technology, value is added to this material. In this work, polyamide of textile residues from industry was used. These materials were first processed in a compacter machine. Composites at 1, 2, and 3% by weight of Light Green clay/polyamide were prepared by double screw extrusion. The properties of the composite were characterized by X-ray diffraction (XRD), tensile, flexural, impact tests, and thermogravimetric analysis (TGA). Results obtained were compared with the neat textile polyamide properties. It was concluded that it is feasible to recycle the textile residues of polyamide, and that the addition of clay, at the doses studied in this work, could lead to the obtaining of composite materials with better mechanical than untreated ones.

Keywords Recycling · Textile residues · Polyamide · Clay

Introduction

In Brazil, the textile, industry is relevant to the generation of wealth and jobs. This manufacturing activity consolidated strongly, making the country a major world producer of textile, the 5th largest producer in the world, with an approximate production of 1.8 million tons of made-up articles [1, 2].

M. N. Sartori (✉) · D. P. Castro · L. G. A. Silva
Nuclear and Energy Research Institute, IPEN, CNEN/SP, Av. Prof. Lineu Prestes, 2242, São Paulo, SP 05508-000, Brazil
e-mail: marianasartori@usp.br

F. R. Valenzuela-Diaz
Dep. de Eng. Metalúrgica E de Materiais, Universidade de São Paulo, Escola Politécnica, Av. Prof. Mello de Moraes, 2463, São Paulo, SP 05508-030, Brazil

J. Li et al., *Characterization of Minerals, Metals, and Materials 2021*,
The Minerals, Metals & Materials Series,
https://doi.org/10.1007/978-3-030-65493-1_60

With such a large manufacturing activity, the generation of waste is unavoidable, around 175 thousand tons of textile shavings per year coming only from cuts in the mold of clothing in Brazil [3].

The study of polymer waste is a current and important theme, considering its increasing presence in solid urban waste and being recyclable materials with high potential for reuse.

Polyamides have been on the market for nearly 80 years. Fibers made of PA6 and PA 6.6 were the first commercialized polyamide products. Until to-day, these two polyamides have played a dominant role in the production and on the Market [4, 5].

These two types of polyamides belonging to the group of polymer thermoplastic fibers have a very wide spectrum of applications, especially in the field of thermal underwear and hosiery products, in which, plain stitch knitwear plays a predominant role and are produced in the form of filaments and staple fibers. Polyamide fibers show very good mechanical properties, and the high abrasion resistance is the most valuable feature of these fibers [6, 7].

Polymer–clay nanocomposites, have attracted much attention from both industry and academia over the past decade because they frequently exhibit unexpected properties. In contrast to the traditional fillers, nanofillers, in particular, nanoclay is found to be effective. The addition of a small amount (< 5 wt%) can show significant improvement in mechanical, thermal and barrier properties, flammability resistance, and electrical/electronic properties of the final polymer nanocomposite without requiring special processing techniques [8, 9].

Experimental

Materials

The materials used in this work were the polyamide textile residues from postindustrial supplied by NZ Cooperpolymer Thermoplastic Engineering and Brazilian bentonite Light Green clay from Boa Vista−PB. This clay did not undergo any purification process and was only strained (D = 0.074 mm) to exclude larger particles.

Methodology

Firstly, the polyamide textile residues were processed in a compacting machine for volume reduction. Before the extrusion process, the polyamide compacts and Light Green clay were kept in an oven for 4 h at 100 °C to remove moisture. The clay was mixed with the polymer matrix manually.

The incorporation of Light Green clay into the polyamide was carried out in a twin screw extruder using temperatures from 200 to 250 °C and thread rotation speed

Table 1 Formulations of textile polyamide with Light Green clay (%, by weight)

Samples	Textile polyamide	% clay
PA 0	100	0
PA1	99	1
PA2	98	2
PA3	97	3

of 60 rpm. The extruded material was dried, pelletized by a pelletizer, fed into an injection molding machine and specimen test samples were obtained. The mergers were made according to Table 1.

The aim of this work is to develop a method for recycling the polyamide textile residues and analyses the mechanical properties. As an important part of the paper, the experimental parts are shown in steps in Fig. 1 below, to demonstrate how the samples were obtained. The step (1) shows the polyamide textile residues from postindustrial that were used in this work. Step (2) present the material after the compaction process. Is it possible to notice reductions in the total volume of the material, small particles were obtained in this process. The granules obtained in the extrusion process are shown in step (3). Step (4) is the final of the experimental part, the samples of the materials.

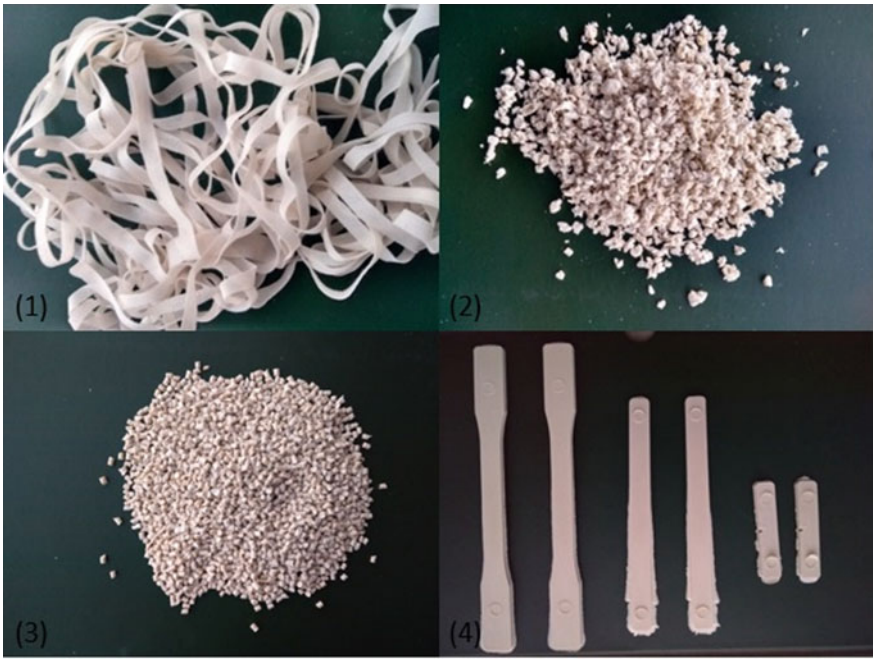

Fig. 1 Steps of the experimental part. **1** polyamide textile residues; **2** compacted polyamide textile residues; **3** polyamide extruded; **4** samples of polyamide textile residues. (Color figure online)

The formulations were evaluated by tensile strength at rupture (ASTM D 638) and flexural resistance (ASTM D 790) for both tests were used ten specimens for each formulation. The Izod impact resistance (ASTM D 256) was also examined and seven specimens were used for each composition.

The X-ray diffraction study was performed using the Rigaku DMAX 2100 equipment with CuKα ($\lambda = 1.54$ nm) operated at 40 kV and 40 mA, with 2θ varying between 2nd and 50th. This technique was performed to evaluate the formation of nanocomposites.

To perform the thermogravimetric analysis (TGA) in an inert nitrogen atmosphere using a heating rate of 20 °C/min, the samples were warmed from room temperature to 800 °C.

Results and Discussion

X-Ray Diffraction (XRD)

Figure 2 show the results of diffraction of samples of pure polyamide and systems with the addition of 1%, 2%, and 3%.

The results showed a change in the intensity and inclination of the peaks, which indicates that the clay was interspersed with the polyamide matrix. No completely exfoliated structures were obtained, as the appearance of the d_{001} peaks indicates at least a certain degree of intercalation.

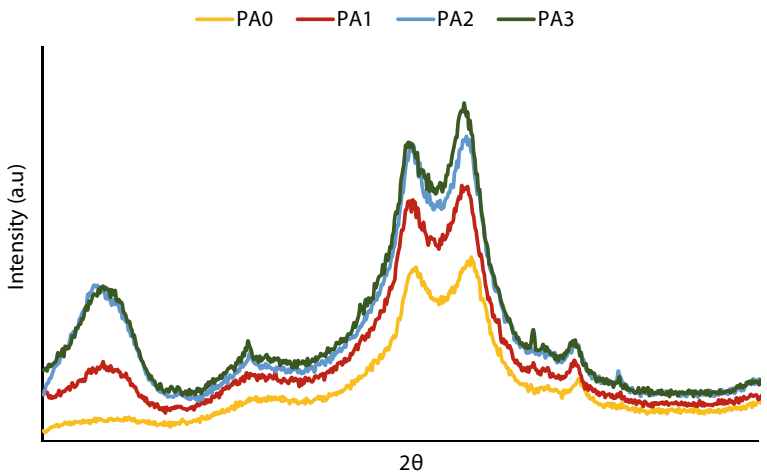

Fig. 2 X-ray diffraction patterns of PA0, PA1, PA2, and PA3 samples. (Color figure online)

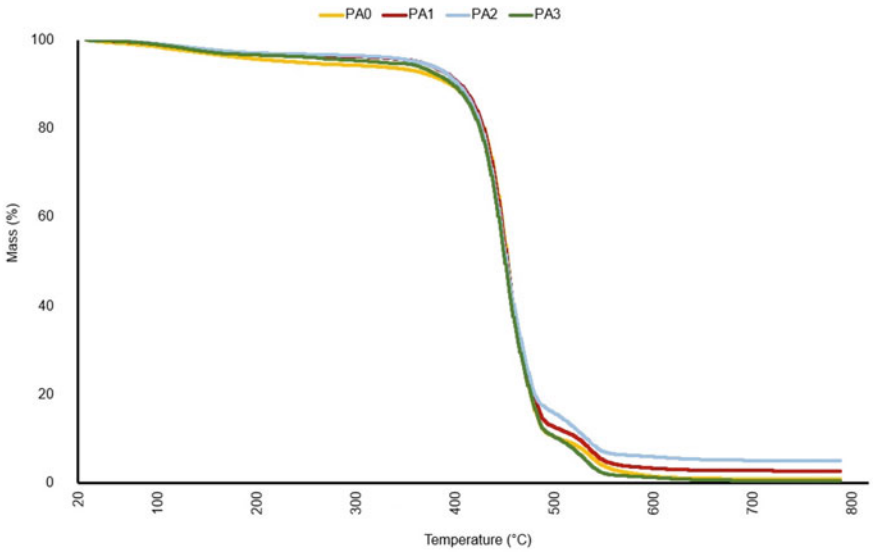

Fig. 3 Thermogravimetric curves of the PA0, PA1, PA2, and PA3 samples. (Color figure online)

Thermogravimetric Analysis (TGA)

Some works [10, 11] in the literature have found no difference in the thermal stability of polyamide/clay nanocomposites. In this work, the same behavior was observed (Fig. 3). No system obtained with clay showed thermal stability superior to that of pure polymer, regardless of the clay content used. The analysis showed that the thermal stability was the same both for the pure polymer and for the nanocomposites produced with the unmodified clays.

Mechanical Tests Results

Mechanical test results are shown in Table 2.

Table 2 Mechanical test results for PA0, PA1, PA2, and PA3

	Tensile strength at break (MPa)	Elongation (%)	Izod impact (J/m)	Flexural strength (MPa)
PA 0	29.31 ± 1.64	4.17 ± 1.21	109.38 ± 9.81	283.90 ± 24.16
PA 1	48.86 ± 3.65	5.96 ± 1.65	124.40 ± 2.87	278.03 ± 11.38
PA 2	65.58 ± 4.88	9.04 ± 0.52	120.92 ± 2.52	284.57 ± 16.75
PA 3	31.95 ± 4.81	5.39 ± 0.34	119.80 ± 2.18	283.66 ± 13.91

The addition of 1% of clay promoted an increase in tensile strength at break of 67% when compared to neat polymer. In the formulation with 3%, this increase was about 120% (Table 2). This improvement in the mechanical property of tensile, when compared to the properties of polyamide without the addition of clay, indicates that the clay acted as a reinforcing load increasing the sample stiffness.

The addition of clay, in all formulations, promoted an increase bigger than 10% in the impact resistance of the material (Table 2). This improvement can be attributed to the absorption of impact energy by the clay with the consequent reduction in the propagation of micro-cracks.

The flexural strength values found for PA0, PA1, PA2, and PA3 were the same, considering the measurement error, which indicates that the clay, in the percentages added does not interfere with the flexural strength of the recycled textile polyamide. In addition, some nanocomposites dissipated small deviations, being smaller than pure material, which gives greater reliability to the results (Table 2).

For a recycled material reinforced with clay without modification, the result is considered significant, showing it a real possibility of use.

Conclusions

The objective of the present study was to develop a method for recycling the polyamide textile residues and to evaluate the contribution of the natural Brazilian bentonite Light Green clay on the properties of the polyamide textile residues. As for processing, the materials formulated with clay showed a behavior according to that used by the recycled polymer industry. This particularity observed in the process was a positive point for the material formed, suggesting that the method used can be repeated by the industry on a regular basis. The results showed that the incorporation of nanoclay represented a significant gain in tensile strength at break and also an improvement in impact resistance. The superior mechanical properties of nanocomposite observed in this study can be attributed to the stiffness of Light Green clay, to the degree of the intercalation, and good dispersion of the clay layers in the polyamide residues.

Acknowledgements The authors acknowledge CAPES and CNPq for financial support.

References

1. Iemi (2014) Relatório Setorial da Indústria Têxtil Brasileira, Brasil Têxtil. São Paulo
2. Loga (2014) Coleta domicilar
3. Sinditêxtil–SP (2012) Retalho Fashion, Projeto de reciclagem une meio ambiente e inclusão social. Ano VII, n 25
4. Wiebeck H, Harada J (2005) Plásticos de Engenharia: Tecnologia e Aplicações Artliber, São Paulo

5. Deopura BL et al. (2008) Polyesters and polyamides. Woodhead Publishing
6. Lewandowski GS, Perzyna EB, (2005) Structure and mechanical properties of polyamid fibres. Fibres & Textile in Eastern Europe
7. Vananthan N (2009) Polyamide fiber formation: structure properties and characterization. Fundamentals and Manufactures Polymer Fibres, Handbook of Textile Fibre Structure
8. Ray SS, Okamoto M (2003) Polymer/layered silicate nanocomposites: a review from preparation to processing. Progr Poly Sci 28(2003):1539–1641
9. Alexandre M, Dubois P (2000) Polymer-layered silicate nanocomposites: preparation, properties and uses of a new class of materials. Mater Sci Eng Rep 28:1–63
10. Jang BN, Wilke CA (2005) The effect of clay on the thermal degradation of polyamde 6 and polyamide 6/clay nanocomposites. Polymer 46:264–3274
11. Pramoda KP, Liu Z, He C, Sue HJ (2003) Thermal degradation behavior of poliamide 6/clay nanocomposites. Poly Degr Stab 81 47–56

The Simpex-Lattice Method Application to Optimize the Design of Soil-Slag-Fly Ash Mixtures

Mateus Henrique R. Rodrigues, Leonardo G. Pedroti, Taciano O. da Silva, Heraldo N. Pitanga, Klaus Henrique de P. Rodrigues, and Emerson C. Lopes

Abstract Ladle furnace slags and fly ashes may be utilized as soil stabilizers in road construction as an option to reuse these by-products. However, there is no method grounded on experimental design to optimize the dosage of those by-products in mixtures with soil. This study applied the Simplex-Lattice method to perform the experimental design to optimize the design of soil-slag-fly ash mixtures. The soil was geomechanically characterized and the by-products were subjected to scanning electronic microscopy (SEM), X-ray diffraction (XRD), pozzolanic activity, and specific surface area analysis. The experimental mixtures were submitted to an unconfined compressive strength test and the results led to a response surface and a mathematical model that described the interaction between the components and allowed the mixture design optimization. This study highlights the potential of the Simplex-Lattice method to optimize soil-slag-fly ash mixtures and the technical suitability of utilizing those by-products as soil stabilizers.

Keywords Steel slag · Fly ash · Simplex-Lattice · Soil stabilization

M. H. R. Rodrigues (✉) · L. G. Pedroti · T. O. da Silva · H. N. Pitanga · K. H. de P. Rodrigues · E. C. Lopes
DEC–Civil Engineering Department, Federal University of Viçosa–UFV, Av. Peter Rolfs, S/N, Campus Universitário, Viçosa 36570-000, Brazil
e-mail: mateus.ribeiro@ufv.br

L. G. Pedroti
e-mail: leonardo.pedroti@ufv.br

T. O. da Silva
e-mail: taciano.silva@ufv.br

H. N. Pitanga
e-mail: heraldo.pitanga@ufv.br

K. H. de P. Rodrigues
e-mail: klaus@ufv.br

E. C. Lopes
e-mail: emerson.lopes@ufv.br

J. Li et al., *Characterization of Minerals, Metals, and Materials 2021*,
The Minerals, Metals & Materials Series,
https://doi.org/10.1007/978-3-030-65493-1_61

Introduction

The steelmaking industry in Brazil is responsible for producing around 35.4 million tons of steel annually; therefore, it is responsible for generating approximately 20 million tons of waste per year. From this total, 27% are classified as steel slag and 6% as fines (including fly ashes) [1]. This considerable volume of waste makes the by-products an undesirable, but inevitable, environmental liability, emphasizing the necessity to find alternatives for their utilization rather than just disposal in nature [2].

These by-products have been successfully applied on the mortars [3], cement [4], and asphalt concrete production [5]. In highway engineering, these materials have shown promising results when used as chemical soil stabilizer agents [6, 7]. The stabilizing potential of those by-products can be optimized when combined with other steelmaking by-products, which is the case of the combined application of ladle furnace slag (LFS) and fly ashes (FA) [8] .

Fly ashes are defined as an artificial pozzolan that, by itself, has few or no agglomeration properties, but when in contact with water, can react with calcium hydroxides creating binding compounds [9]. LFS is a material resulting from secondary steel refining, presenting low hydraulic reactivity, but shows great potential as a chemical agent in soil stabilization applications [6]. Research involving LFS, FA, and other by-products in soil stabilization applications have been carried out using empirical methods based on professional experience to design the mixtures with soil [10]. However, the lack of a consolidated methodology that allows an optimized design of mixtures composed of these by-products and soil, makes it difficult to apply these materials for large-scale production. In order to suppress this difficulty, some statistical design methods have been studied for this purpose, such as the Simplex-Lattice method, which is a promising method that has been successfully used in the optimized design of ceramic compounds [11], mortars [12], and other product varieties.

The Simplex-Lattice method can be described as an ordered system consisting of a uniformly spaced points arrangement, that must be tested, and which results are used to fit a regression model. An advantage of applying this method while designing mixtures is to reduce the number of trials required to get a regression model to predict the mixtures response in function of mix ratio components [13].

The present paper evaluates the Simplex-Lattice method technical applicability on the optimized design of Soil-Ladle Furnace Slag-Fly Ash (SLF) mixtures, aiming to maximize the unconfined compressive strength of these mixtures. To study the mixtures responses and to evaluate the potential of the application of these by-products as a chemical stabilizer in soil stabilization applications, it was also proposed performing the physical, mineralogical, and chemical characterization of the raw materials.

Materials and Methods

Materials

The soil sample used in this study was collected in Viçosa, Minas Gerais State, Brazil, submitted to air-drying, and prepared to perform the laboratory tests in accordance with NBR 6457 [14].

The LFS sample was obtained from a steelmaking company located in Jeceaba, Minas Gerais State, Brazil. The material sampling was carried out in accordance with NBR 10007 [15]. After transporting the material to the Civil Engineering Laboratory at the Federal University of Viçosa, the material was air-dried, milled, and submitted to a sieving process to retain the particles larger than 0.6 mm (sieve nº 30).

The FA used in this study was obtained from a company responsible for processing and commercialize pozzolanic fly ash from coal burning, located in Capivari de Baixo, Santa Catarina State, Brazil. The material is classified as class-C fly ash and meets the pozzolanic requirements prescribed in technical standard NBR 12653 [16].

Characterization of Raw Materials

Soil sample was submitted to characterization laboratory tests to determine: (i) the particle size distribution [17]; (ii) specific gravity [18]; and (iii) Atterberg Limits and Plasticity Index [19, 20]. Samples of LFS and FA were submitted to laboratory tests to determine the specific gravity [21], the finesses by sieving [22], and the specific surface area by Brunauer, Emmett, Teller (BET) method. The pozzolanic activity test performed on steel slag and fly ash samples were carried out following the procedures proposed by Lúxan et al. [23].

The mineralogical characterization of soil, ladle furnace steel slag and fly ash, were carried out by means of XRD diffraction test, utilizing Brunker D-8 Discover diffractometer (CuKα radiation, 40 kV, 30 mA, $\lambda = 1.5418$ Å, θ–2θ angles, 5º a 80º range, 0.02°/step, 1 s/step). Scanning electron microscopy (SEM) analysis was also performed on LFS and FA samples, utilizing JOEL JSM-6010LA equipment, utilizing sputter coated specimens to prevent charging in the SEM.

Experimental Design of Mixtures

The method chosen to design the experimental mixtures was the Simplex-Centroid method. The experimental mixtures were composed of three components (soil, LFS, and FA), therefore, the total experimental mixtures to be tested in this experimental program is given by $(2^q–1)$, where "q" corresponds to the number of components on the mixture [24], totalizing 7 mixtures. Additionally, it was proposed that the

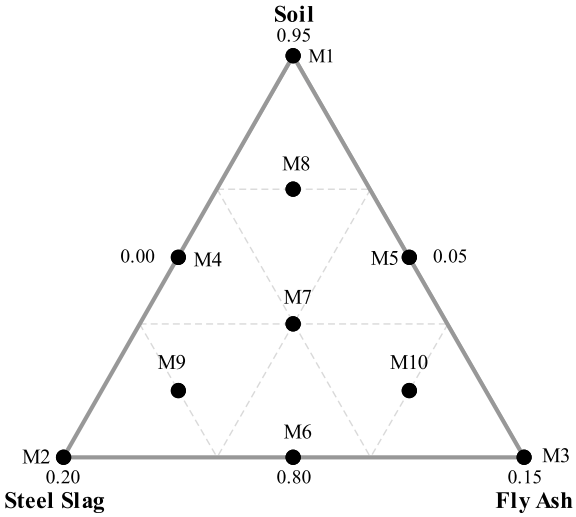

Fig. 1 Simplex-Centroid triangular diagram and testing mixtures identification

Table 1 Component contents of the experimental mixtures (dry mass composition)

Material	M1	M2	M3	M4	M5	M6	M7	M8	M9	M10
Soil (%)	95.0	87.5	80.0	80.0	80.0	87.5	85.0	82.5	82.5	90.0
LFS (%)	5.0	12.5	20.0	12.5	5.0	5.0	10.0	7.5	15.0	7.5
Fly Ash (%)	0.0	0.0	0.0	7.5	15.0	7.5	5.0	10.0	2.5	2.5

3 intermediate mixtures were to be tested, as shown in Fig. 1. The maximum and minimum limits that all components can assume in the mix proportion were defined based on values verified in the technical literature [25], being defined that the mixtures would be composed by 5–20% of LFS and 0–15% of FA. The composition of each experimental mixture is presented on Table 1.

Testing Methods

The natural soil and all the experimental mixtures were submitted to a compaction test, in accordance with NBR 7182 [26], to define the maximum dry unit weight and the optimum moisture content. Three specimens of each experimental mixture and three specimens of natural soil were submitted to unconfined compressive strength (UCS) test in accordance with NBR 12770 [27], considering the Standard Proctor compaction energy and 7 days curing period. The UCS of each mixture was determined from the mean value obtained from the three tested specimens. The UCS of the natural soil was determined following the same procedure adopted for the experimental mixtures.

Table 2 Geotechnical characterization of soil

Geotechnical parameter	Result	Geotechnical parameter	Result
Clay (%) ($\Phi \leq 0.002$ mm)	5	Bulk Specific Gravity (g/cm^3)	2.657
Silt (%) (0.002 mm < $\Phi \leq$ 0.06 mm)	24	Liquidity Limity (LL) (%)	36
Fine sand (%) (0.06 mm < $\Phi \leq$ 0.2 mm)	13	Plasticity Limit (PL) (%)	18
Medium Sand (%) (0.2 mm < $\Phi \leq$ 0.6 mm)	40	Plasticity Index (PI) (%)	18
Gravel Sand (%) (0.6 mm < $\Phi \leq$ 2 mm)	15	USCS Classification	SC
Gravel (%) ($\Phi >$ 2.0 mm)	3	TRB Classification	A-2-6

The UCS result for each mixture was uploaded in Minitab® software to generate the mathematical model that describes the interaction between components and their impact on the product mechanical behavior. To the statistical analysis it was setup a confidence level of 95%.

Results and Discussion

Geotechnical Characterization of Soil

Table 2 presents the results from the geotechnical characterization of soil and the soil classification according to the Unified System of Classification of soils (USCS) and Transportation Research Board (TRB). The soil can be classified as a clayed sand soil according to USCS and as A-2-6 soil according to (TRB). The soil particle size distribution is shown in Fig. 2.

Mineralogical Characterization

Figure 3a and b show, respectively, the ladle furnace steel slag and the fly ash SEM images. From the SEM images, it is noted that LFS has very irregular shaped particles, while the fly ash is composed of particles fine-grained and spherical in shape. Irregularly shaped particles have a lower specific surface area compared to spherical particles. For materials that present cementitious properties, it is desirable that these materials show high specific surface area since the amount of chemical reactions tends to be proportional to this factor.

Figures 4 and 5 presents the major mineralogic phases identified in the ladle furnace slag and in the fly ash samples, respectively. The major phases identified in the ladle steel slag were the portlandite, olivine, calcite, dolomite, brucite, artinite,

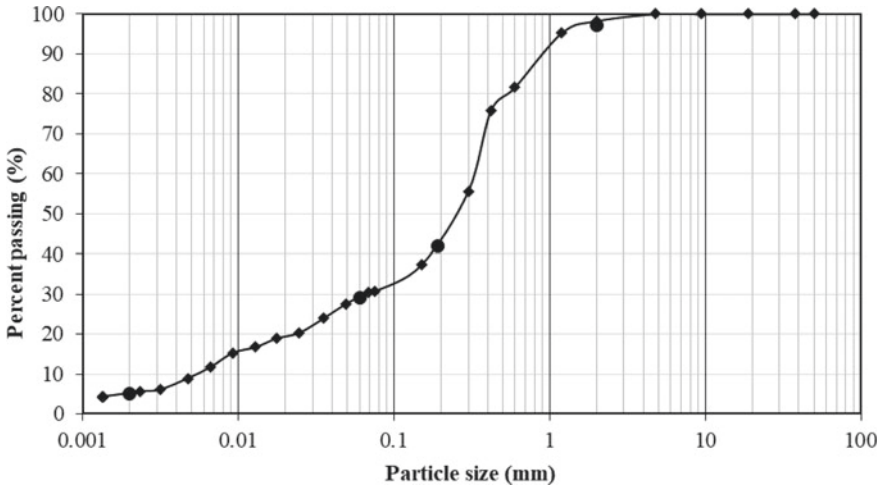

Fig. 2 Soil grain size distribution

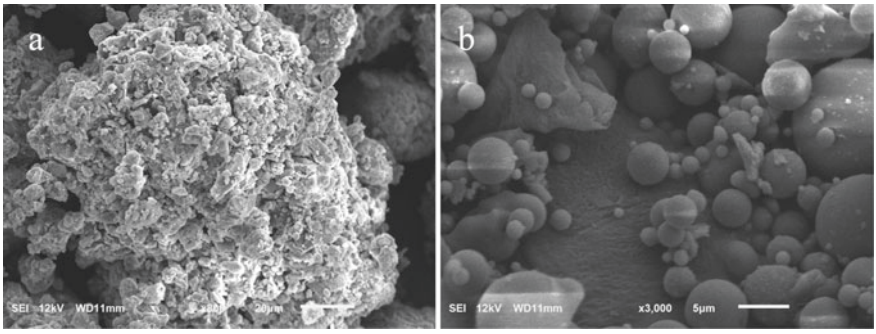

Fig. 3 Ladle furnace steel slag **a** SEM image and fly ash **b** SEM image

and larnite, while in the fly ash sample were identified the mullite, wollastonite, quartz, lime, calcite, albite, anhydrite. The peaks on the XRD patterns indicate the amount of the mineralogic phases in the materials composition. Both the mineralogic phases and the amount of these phases in the materials compositions were the same verified in some studies approaching the same type of materials, except for the olivine in the LFS, and for the mullite in the FA, which has shown a larger amount than what is observed in the technical literature consulted [6–8, 28].

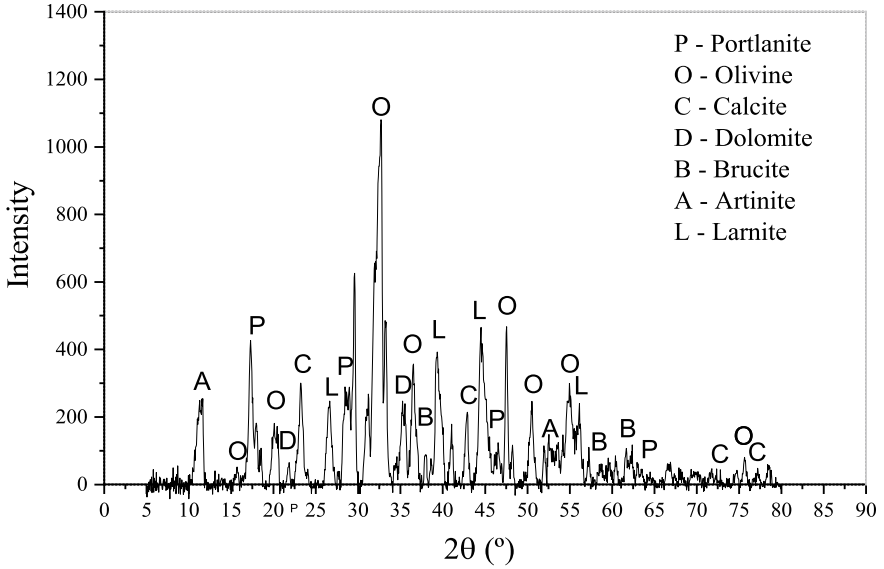

Fig. 4 Results of the XRD analysis of the ladle furnace steel slag sample

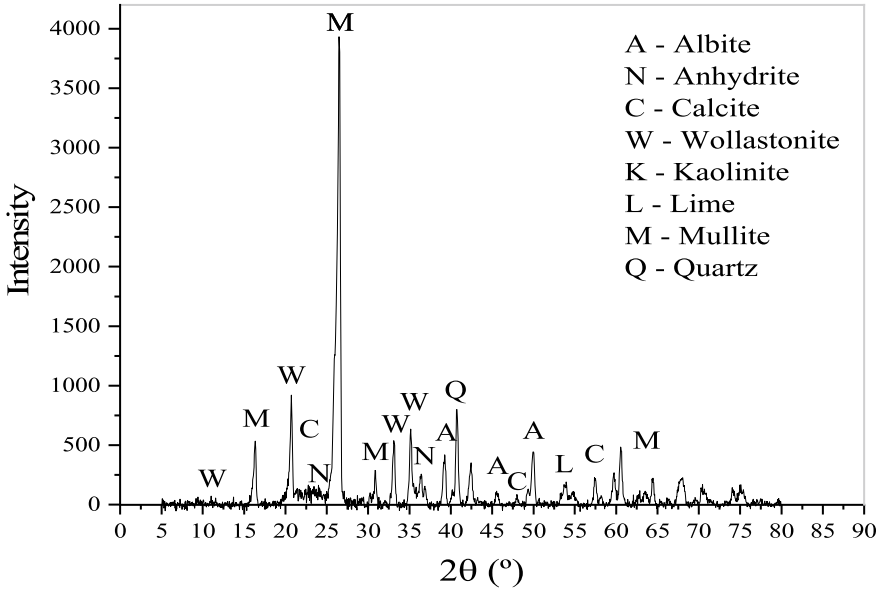

Fig. 5 Results of the XRD analysis of the fly ash sample

Table 3 Physical and chemical characterization of ladle furnace steel slag and fly ash samples

Properties	LFS	Fly Ash
Finesses index (%)	55.8	23.71
Blaine Specific Surface Area (cm^2/g)	1906.4	1788.24
Specific Gravity (g/cm^3) -	2.91	2.08
Pozzolanic Activity (Lúxan et al. 1989)	Low	Medium

Chemical and Physical Characterization of Raw Materials

The results from the characterization tests performed on the by-products are shown in Table 3. The LFS has larger specific gravity compared to fly ash, which is in accordance with usual values for the specific gravity of these materials [29]. Both materials have shown a high specific surface area, indicating a favorable condition to occur hydration reactions. The finesses index for both materials indicates that the fly ash has a larger amount of fines compared to the ladle furnace slag. The fly ash response to the pozzolanic activity test performed indicates that this material has medium pozzolanic activity, while the ladle furnace slag sample presented low pozzolanic activity. Even though those materials have not shown good pozzolanic activity, the combined application of those materials may be interesting; the fly ash has a higher amount of artificial pozzolanic components and the steel slag has higher contents of cementitious compounds, which when combined, favors hydration reactions [25].

Geotechnical Characterization of Experimental Mixtures and Natural Soil

Figure 6 shows the maximum dry unit weight and the optimum moisture content for each experimental mixture and for the natural soil submitted to the compaction test. From Fig. 6, the variation in the maximum dry unit weight and moisture content between the mixtures can be observed, showing that the by-products addition has increased the maximum dry unit weight and the optimum moisture content of the mixtures when compared to the natural soil. The soil maximum dry unit weight was 1.717 g/cm^3 at 15.1% of water content. The higher maximum dry unit weight was observed for the mixture containing 20% of ladle steel slag on its composition. Also, an increase in the optimum moisture content proportional to the amount of by-product in the mixture was observed. This behavior is assigned due to the amount of fines in the mixture increase, which increases the mixture specific surface area and requires higher amount of water to hydrate the cementitious compounds added to the mixtures [16].

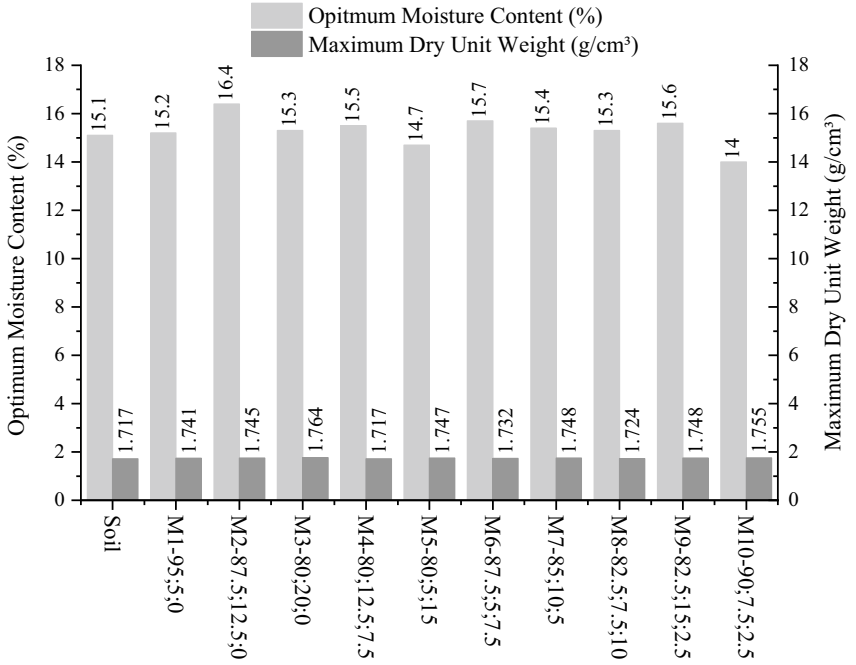

Fig. 6 Experimental mixtures optimum water content and maximum dry unit weight

Unconfined Compressive Strength Tests

The results from the UCS tests performed are shown in Fig. 7. The addition of steelmaking by-products in the mixtures has improved the compressive strength of the natural soil, by 14 to 62%. The experimental mixtures that shown the highest UCSs were mixtures M3, M4, M5, and M7, with a maximum UCS of 166 kPa corresponding to the M5 mixture. This value represents a significant increase of 62% in the unconfined compressive strength of natural soil, suggesting a baseline for optimization of materials combinations.

The verified gain in soils compressive strength can be assumed as a consequence of cementitious and hydration reactions that originate cemented components along the curing time considered. This hypothesis is taken as an explanation when considering the XRD analyses indicating the presence of minerals such as larnite, mayenite, and wollastonite in the materials structure desirable hydraulic properties [6, 10].

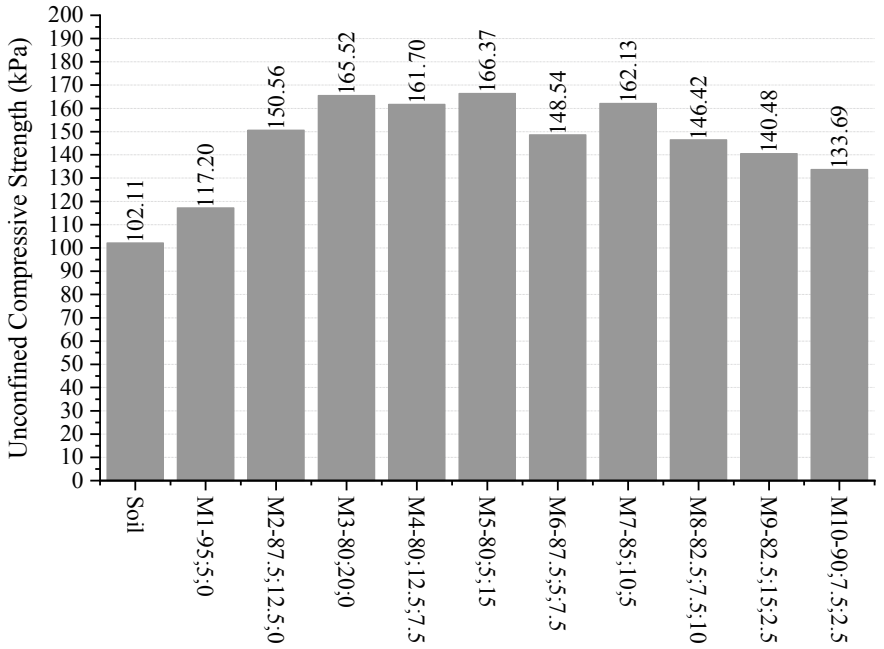

Fig. 7 Unconfined Compressive Strength tests results

Simplex-Lattice Method Analysis

The UCS results from each experimental mixture were assessed in Matlab 2018® software to obtain the triangular response surface shown in Fig. 8, from which can be observed the resistance intervals as a function of the proportion of each component in the mixture.

As the mixtures were composed of three materials, the mathematical model proposed to describe the UCS behavior of the mixtures has the structure presented in Eq. 1 [25], where "Y" represents the unconfined compressive strength, *"β_x"* the regression coefficients, and *"x_i"* the amount of each component in the mixture.

$$Y(x_1x_2x_3) = \beta_1x_1 + \beta_2x_2 + \beta_3x_3 + \beta_{12}x_1x_2 + \beta_{13}x_1x_3 + \beta_{23}x_2x_3 + \beta_{123}x_1x_2x_3 \quad (1)$$

The most statistically fitted regression model calculated, considering 95% of confidence level, is shown in Eq. 2. In this equation, the UCS is expressed as a function of the proportion of soil (S), ladle furnace slag (L), and Fly ash (F) in the mixture composition.

$$UCS(kPa) = 109.6\,S + 369.6\,L + 382.1F \quad (2)$$

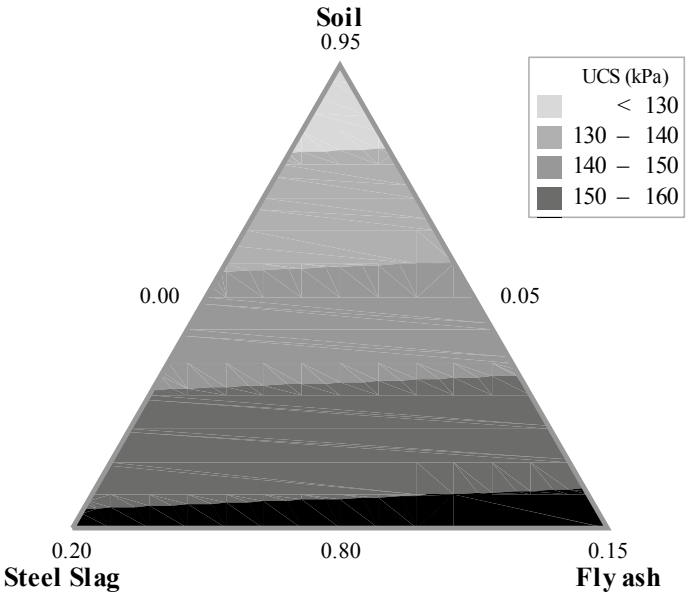

Fig. 8 Response surface for UCS as a function of material content

From the regression model coefficients presented in Eq. 2, can be inferred that the LFS and the FA addition in the mixture composition has a positive influence on the mixture's unconfined compressive strength. The coefficients that represent the interaction between the components as shown in Eq. 1 (β_{12}, β_{13}, β_{23}, β_{123}) did not present statistical relevance and have been removed from the regression model. The regression model presented in Eq. 2 resulted in R^2 equals to 71.72%.

From the mathematical model presented in Eq. 2, it was possible to optimize the mix design through the statistical tool "desirability" available from the Minitab® software to maximize the UCS. This approach was carried out with a set UCS target value of 170 kPa. As a result of this optimizing procedure, the Minitab ® software returned the mixture composed of 80% of soil, 5% of LFS, and 15% of FA as the optimal mixture with a desirability value equal to 0.962, and a maximum UCS of 166.4 kPa.

Conclusion

The Simplex-Lattice method is a powerful tool to perform the experimental design of mixtures aiming to evaluate the product's responses as a function of the mixture components contents. This method significantly reduces the number of trials required to achieve the balance between the materials ratio in the mixture and their mechanical response. In addition, the Simplex-Lattice method can establish a response surface

consistent with the testing results, allowing the possibility to define different proportions that are able to reach the same range of UCS, and making suitable the optimized design of mixtures.

The unconfined compressive strength of the natural soil has increased up to 62% by applying different materials proportions in the mixtures. The observed behavior is attributed to pozzolanic and cementitious reactions between the steelmaking by-products and the soil, since the mineralogical characterization of those materials verified the presence of mineralogic phases that indicates high cementitious potential, such as larnite, mayenite and wollastonite, and belite.

From the significant improvement on soil performance under this loading condition, it is verified the technical suitability of the application of ladle furnace slag and fly ash as soil stabilizer agents, consolidating an interesting alternative to reuse a large amount of those by-products.

Acknowledgements The authors thank Federal University of Viçosa, Brazil and Coordenação de Aperfeiçoamento Pessoal de Nível Superior–Brasil (CAPES) for supporting this study.

References

1. Instituto aço brasil (IAB) (2018) Relatório de Sustentabilidade. Rio de Janeiro–RJ: Instituto Aço Brasil. http://www.acobrasil.org.br/sustentabilidade/. Accessed 3th Aug 2019
2. Palod R, Deo S, Ramtekkar G (2017) Review and Suggestions on use of steel slag in concrete and its potential use as cementitious component combined with GGBS. Int J Civil Eng Technol 8:1026–1035
3. Santamaría A, González JJ, Losáñez MM, Skaf M, Ortega-Lopez V (2020) The design of self-compacting structural mortar containing steelmaking slags as aggregate. Cement Concr Compos 111 (103627). https://doi.org/10.1016/j.cemconcomp.2020.103627
4. Shi Z, Shi C, Zhao R, Wang D, He F (2016) Factorial design method for designing ternary composite cements to mitigate ASR expansion. J Mater Civil Eng 28(9). https://doi.org/10.1061/(asce)mt.1943-5533.0001568
5. Oluwasola EA, Hainin MR, Aziz MMA (2015) Comparative evaluation of dense-graded and gap-graded asphalt mix incorporating electric arc furnace steel slag and copper mine tailings. J Cleaner Product 122:315–325. https://doi.org/10.1016/j.jclepro.2016.02.051
6. Aldeeky H, Al Hattamleh O (2017) Experimental study on the utilization of fine steel slag on stabilizing high plastic subgrade soil. Advan Civil Eng (9230279)
7. Zumrawi MM, Babikir AAA (2016) Laboratory study of steel slag used for stabilizing expansive soil. Univer Khartoum Eng J 6(2):30–35
8. Yildirim IZ, Prezzi M (2017) Experimental evaluation of EAF ladle steel slag as a geo-fill material: Mineralogical, physical & mechanical properties. Constr Buil Mater 154:23–33
9. ABNT NBR 12653 (2014) Materiais pozolânicos. Rio de Janeiro: ABNT. (Portuguese version)
10. Diniz DH, Carvalho JMFD, Mendes JC, Peixoto RAF (2017) Blast oxygen furnace slag as chemical soil stabilizer for use in roads. J Mater Civil Eng 29:04017118
11. Medeiros VSC, Pedroti LG, Mendes BCM, Pitanga HN, Silva TO (2019) Study of mixtures using simplex design for the addition of chamotte in clay bricks. Int J Appl Ceram Technol 16:2349–2361. https://doi.org/10.1111/ijac.13346
12. He P, Zhang B, Lu J, Poon CS (2020) A ternary optimization of alkali-activated cement mortars incorporating glass powder, slag and calcium aluminate cement. Constr Buil Mater 240:117983. https://doi.org/10.1016/j.conbuildmat.2019.117983

13. Abbas YM (2018) Simplex-lattice strength and permeability optimization of concrete incorporating silica fume and natural pozzolan. Constr Buil Mater 168:199–208
14. ABNT NBR 6457 (2016) Soil samples – Preparation for compaction and characterization tests. Rio de Janeiro: ABNT (Portuguese version)
15. ABNT NBR 10007 (2004) Sampling of solid waste. Rio de Janeiro: ABNT. (Portuguese version)
16. ABNT NBR 12653 (2014) Pozzolanic materials–Requirements. Rio de Janeiro: ABNT. (Portuguese version)
17. ABNT NBR 7181 (2016) Soil–Grain size analysis. Rio de Janeiro: ABNT. (Portuguese version)
18. ABNT NBR 6458 (2016) Gravel grains retained on the 4,8 mm mesh sieve–Determination of the bulk specific gravity, of the apparent specific gravity and of water absorption. Rio de Janeiro: ABNT. (Portuguese version)
19. ABNT NBR 6459 (2016) Soil–Liquid limit determination. Rio de Janeiro: ABNT. (Portuguese version)
20. ABNT NBR 7180 (2016) Soil–Plasticity limit determination. Rion de Janeiro: ABNT. (Portuguese version)
21. ABNT NBR 16605 (2017) Portland cement and other powdered material–Determination of the specific gravity. Rio de Janeiro: ABNT. (Portuguese version)
22. ABNT NBR 11579 (2012). Portland cement–Determination of fineness index by means of the 75 μm sieve (nº 200). Rio de Janeiro: ABNT. (Portuguese version)
23. Luxán MP, Madruga F, Saavedra J (1989) Rapid evaluation of pozzolanic activity of natural products by conductivity measurement. Cement Concr Res 19(1):63–68
24. Jiao D, Shi C, Yuan Q, An X, Liu Y (2018) Mixture design of concrete using simplex centroid design method. Cement Concr Compos 89:76–88. https://doi.org/10.1016/j.cemconcomp.2018.03.001
25. Santos AL, Pitanga HN, Silva ACB, Silva TO (2018) Caracterização do comportamento mecânico de misturas de solo-escória de aciaria-cinza volante visando a aplicação em obras de pavimentação. Revista Brasileira de Energias Renováveis 7(1):16–29. https://doi.org/10.5380/rber.v7i1.57963
26. ABNT NBR 7182 (2016) Soil–Compaction test. Rio de Janeiro: ABNT. (Portuguese version)
27. ABNT NBR 12025 (2012) Soilcement–Simple compression test of cylindrical specimens–Method of test. Rio de Janeiro: ABNT. (Portuguese version)
28. Vassileva SV, Menendez R, Alvarez D, Diaz-Somoanob M (2003) Phase-mineral and chemical composition of coal fly ashes as a basis for their multicomponent utilization. 1. Characterization of feed coals and fly ashes. Fuel 82:1793–1811
29. Grubeša IN, Barišić I, Fučić A, Bansode SS (2016) Characteristics and uses of steel slag in building construction. Chennai, India: Elsevier, Woodhead Publishing. ISBN 978-0-08100976-5

Variation of the Silica Module for Dosing Activated Alkali Mortars

M. T. Marvila, A. R. G. Azevedo, E. B. Zanelato, T. E. S. Lima, S. N. Monteiro, C. M. F. Vieira, J. Alexandre, and G. C. Xavier

Abstract The dosage of activated alkali materials, as is the case with blast furnace slag mortars, is one of the great complexities of materials science. In this context, the objective of this work is to propose the mortar dosage 1: 1: 0.5 (precursor: aggregate:

M. T. Marvila (✉) · A. R. G. Azevedo · E. B. Zanelato · T. E. S. Lima · C. M. F. Vieira · J. Alexandre · G. C. Xavier
UENF–State University of the Northern Rio de Janeiro, LAMAV–Advanced Material Engineering Laboratory, Av. Alberto Lamego, 2000, Campos Dos Goytacazes, Rio de Janeiro 28013-602, Brazil
e-mail: markssuel@hotmail.com

A. R. G. Azevedo
e-mail: Afonso.garcez91@gmail.com

E. B. Zanelato
e-mail: ebzanelato@gmail.com

T. E. S. Lima
e-mail: thuanylima.es@gmail.com

C. M. F. Vieira
e-mail: vieira@uenf.br

J. Alexandre
e-mail: jonas.uenf@gmail.com

G. C. Xavier
e-mail: gxavier@uenf.br

A. R. G. Azevedo
TER–Department of Agricultural Engineering and Environment, UFF– Federal Fluminense University, Rua Passo Da Pátria, 341, Niterói, Rio de Janeiro 24210240, Brazil

E. B. Zanelato
DIRINF –Directorate of Infrastructure Rectory, IFF–Federal Institute Fluminese, Rua Cel. Valter Kramer, 357 –Parque Vera Cruz, Campos Dos Goytacazes, Rio de Janeiro 28080-565, Brazil

S. N. Monteiro
Department of Materials Science, IME –Military Institute of Engineering, Square General Tibúrcio, 80, Rio de Janeiro 22290-270, Brazil
e-mail: snevesmonteiro@gmail.com

J. Li et al., *Characterization of Minerals, Metals, and Materials 2021*,
The Minerals, Metals & Materials Series,
https://doi.org/10.1007/978-3-030-65493-1_62

activator), varying the silica module of the solution by 0.3, 0.6, 0.9, 1.2, and 1.5, and performing compression, density, water absorption, and porosity tests, performing thermal curing at 60 °C and normal curing, with curing of 7 days. The results showed that the variation of the silica module significantly changes the results of the evaluated properties, with the best parameters obtained for a 1.2 module of silica.

Keywords Silica module · Alkali activated materials · Slag

Introduction

One of the most important factors in the dosage of activated alkali materials is the definition of the materials present in the activating solution [1]. Usually, sodium and potassium hydroxides and silicates are used, due to their availability and high alkalinity. In case of materials produced with calcium-rich strikers, as is the case with blast furnace slag, the application of the alkaline solution is responsible for accelerating the hydration reaction of the slag, since the alkaline materials induce a greater break in the bonds present in the slag, producing resistant components in the material [2, 3].

It is known that the structure of the blast furnace slag hardened and produced through alkaline activation is the basis of C-A-S-H crystals, named as tobermorite [4]. The sodium or potassium, present in the activators, are necessary to occupy the interstices and balance the electrical charges of C-A-S-H, making the material stable and resistant. It is clear to observe, however, the presence of silicate in the structure of tobermorite. However, blast furnace slag has a predominantly very large amount of calcium oxide in its structure [5, 6]. This indicates a need for silicates in the alkaline activation reaction.

Therefore, it is essential to apply silicates in the alkaline solution, to complete the formation of the structure of tobermorite [7]. However, the use of silicates in activated alkali materials can impair other properties, such as the viscosity of the formed material. The application of silicates, therefore, can impair workability parameters and consequently reduce the compaction and densification of the material.

Another important fact is the pH of the alkaline solution. The application of silicates reduces the pH of the solution, and may indirectly reduce the efficiency of the activated alkali reaction that occurs in high pH media [8, 9]. In addition, it is known that there is a maximum amount of silicates that can be absorbed by the structure of tobermorite without the fragility of the formed network occurring. Figure 1, for example, illustrates the microscopy of an activated alkali material formed with excess silicate [10], which induces the formation of less resistant secondary phases than the classic tobermorite (C-A-S-H) [11, 12].

All of these factors lead to the conclusion that there is an optimum amount of silicates that should be used in the alkaline activation process. The use of silicates at levels less than optimal does not form the tobermorite network in a complete way, however, the use of silicates at levels above optimum may affect the alkaline

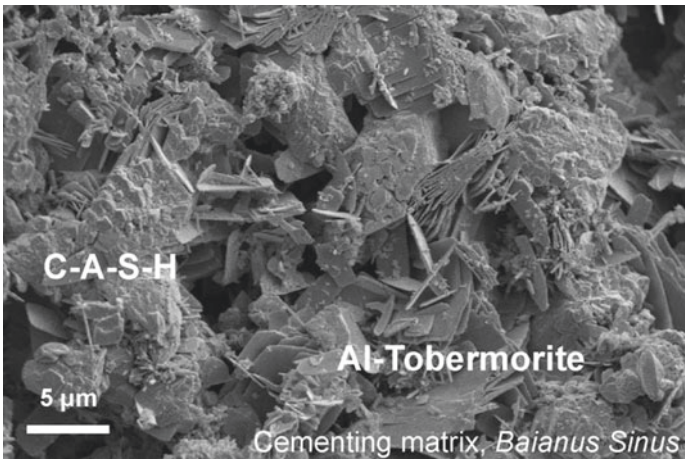

Fig. 1 Microscopy of tobermorite and secondary phases [10]

activation reaction due to the drop in pH, due to the lack of densification of the materials produced. and due to the saturation of silicate phases within the tobermorite network.

In this context, the objective of this work is to evaluate the influence of the silica module, which is the relationship between silicon oxide and sodium oxide used for alkaline activation, through the analysis of the compressive strength obtained by the materials.

Materials and Methods

The materials used to produce the activated alkali materials were blast furnace slag extracted from a Brazilian steel industry and river sand extracted in Brazil. For the production of the alkaline solution, two components were used, the first being sodium silicate with 63% SiO_2, 18% Na_2O, and 19% H_2O, leading to a 3.5 silica module. The second component is sodium hydroxide micropearls with a purity of 99%, necessary to enable variation in the silica module. This module, presented by Eq. (1), was varied from 0.3 to 1.5, according to data consulted by the bibliography for similar precursors [13].

$$M_s = \frac{[Si\,O_2]}{[Na_2\,O]} \tag{1}$$

where:

Ms is the silica module.

Table 1 Chemical composition of blast furnace slag

Ca	Si	Al	Mg	S	Ti	Fe	K	Others
62.49	22.00	6.69	3.96	1.95	0.86	0.58	0.45	1.02

[SiO_2] is the number of moles of SiO_2 present in the solution, obtained by calculating the mass divided by the molar mass of the compound.

[Na_2O] is the number of moles of Na_2O present in the solution, obtained by calculating the mass divided by the molar mass of the compound.

The slag used presents the chemical composition shown in Table 1, where it is possible to perceive the high amount of Ca and low Si content, leading to a Ca / Si ratio of 2.84, illustrating the need for the application of silicates in the activator solution to correct the absent contents.

For this reason, alkali mortars activated in the proportion 1: 1: 0.5 (binder: sand: water) were produced, varying the silica module from 0.3 to 1.5. For each studied composition, cylindrical specimens of 50 × 100 mm were produced, using 3 experimental units for each test, as showed in Fig. 2. Two curing procedures were used, at room temperature and at a temperature of 60 °C, and the tests were carried out after 7 days of molding. Then the specimens were tested through three different tests: resistance to compression, using a hydraulic press brand SOLOTET; water absorption; porosity; and mass density in the hardened state.

Fig. 2 Samples produced. (Color figure online)

Results and Discussion

Figure 3 shows the results of compressive strength. It is observed that the strength of the material is increased as the silica module of the solution is increased. The optimum silica modulus occurs with the amount of 1.2, justified by the formation of tobermorite gels in the material, composed of C-A-S-H [10]. Table 1 shows that blast furnace slag contains 22% SiO_2, with the complementary material obtained by sodium silicate present in the activating solution. However, the use of 1.5 in the silica module is excessive, forming additional, less resistant phases, reducing the strength of the material.

Figure 4 shows the density of the activated alkali materials studied as a function of the silica module and the type of cure performed. It is observed that there is no statistical difference in density between the applied silica modules, however, the thermal curing causes a reduction in the density of the material, due to the elimination of water during the curing procedure of the material.

Figures 5 and 6 show the results of porosity and water absorption, respectively, for the studied materials. It is observed that there was an increase in porosity, and consequently in water absorption, as there was an increase in the silica module up to 1.5. It is also possible to identify a direct relationship between porosity and mechanical strength for activated alkali materials, differently from what occurs with most cementitious materials. This is because the mechanism of reaction and formation of gels in this class of materials is not just a physical characteristic, being mainly related to mineralogical and chemical issues [12, 13].

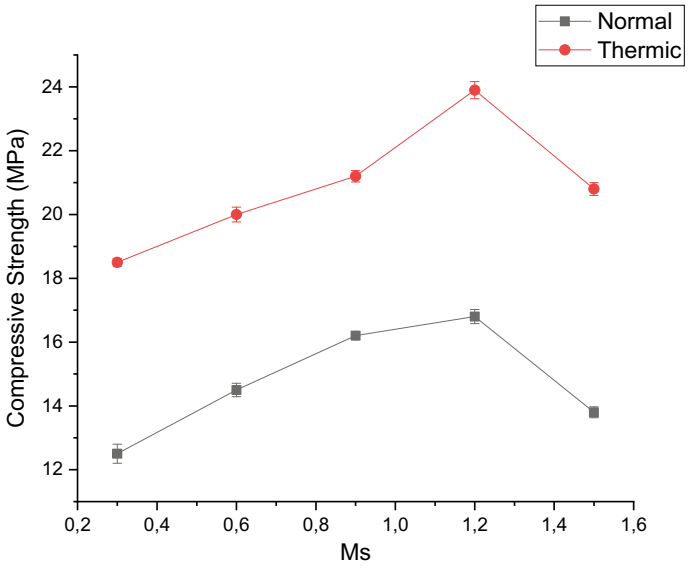

Fig. 3 Compressive strength of materials studied. (Color figure online)

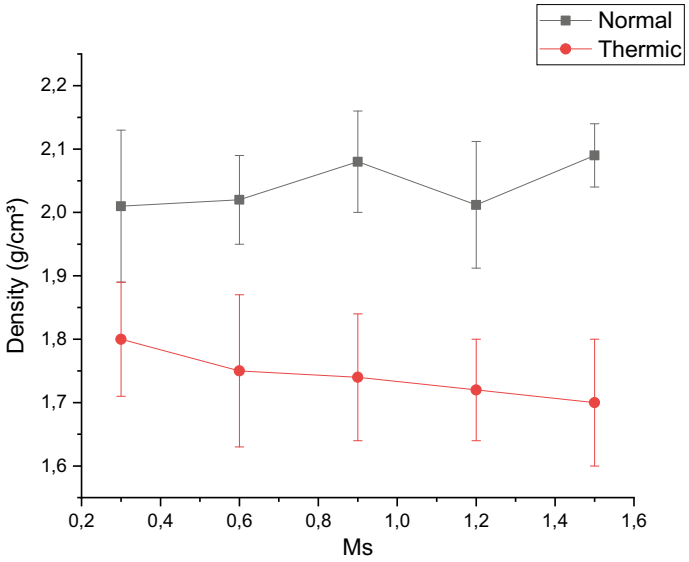

Fig. 4 Density of materials studied. (Color figure online)

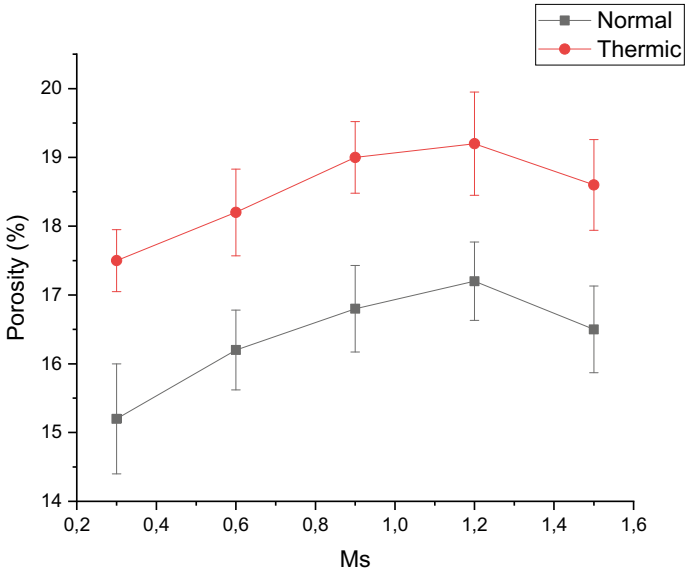

Fig. 5 Porosity of materials studied. (Color figure online)

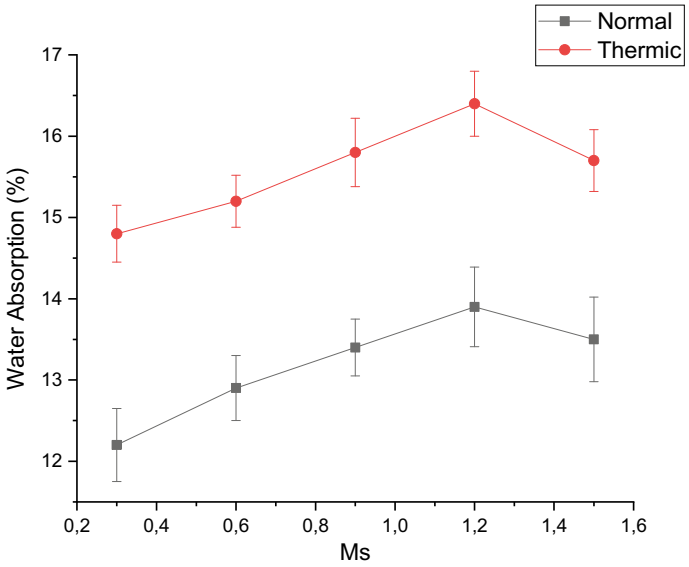

Fig. 6 Water absorption of materials studied. (Color figure online)

Conclusions

After discussing the results, it can be concluded that:

- The blast furnace slag studied has a low amount of SiO_2, requiring the application of silicate in the solution to correct the levels and greater efficiency in alkaline activation.
- The dosage of the materials through the silica module showed that the optimum content is obtained with a ratio of 1.5, as observed by the resistance values. This is attributed to the formation of tobermorite gels, responsible for the mechanical behavior of the material. Above this content, less resistant secondary phases are formed.
- There is no statistical difference in the density of the materials due to the silica modulus factor.
- Alkali activated materials do not obey the indirect relationship between resistance to compression and porosity and water absorption, in the same way as cementitious materials. This is because the principles of resistance are not only physical, but mainly chemical.

Acknowledgements The authors thank the Brazilian agencies CNPq, CAPES, and FAPERJ for the support provided to this investigation.

References

1. Palomo A, Krivenko P, Garcia-Lodeiro I, Kavalerova E, Maltseva O, Fernández-Jiménez A (2014) A review on alkaline activation: new analytical perspectives; Activación alcalina: Revisión y nuevas perspectivas de análisis. Mater Construcción 64:22. https://doi.org/10.3989/mc.2014.00314
2. Lahoti M, Tan KH, Yang EH (2019) A critical review of geopolymer properties for structural fire-resistance applications. Constr Build Mater 221:514–526. https://doi.org/10.1016/j.conbuildmat.2019.06.076
3. Phoo-ngernkham T, Hanjitsuwan S, Damrongwiriyanupap N, Chindaprasirt P (2017) Effect of sodium hydroxide and sodium silicate solutions on strengths of alkali activated high calcium fly ash containing Portland cement, KSCE. J Civ Eng 21:2202–2210. https://doi.org/10.1007/s12205-016-0327-6
4. Duxson P, Provis JL (2008) Designing precursors for geopolymer cements. J Am Ceram Soc. https://doi.org/10.1111/j.1551-2916.2008.02787.x
5. Provis JL, van Deventer JSJ (2007) Geopolymerisation kinetics. 1. In situ energy-dispersive X-ray diffractometry. Chem Eng Sci 62:2309–2317. https://doi.org/10.1016/j.ces.2007.01.027
6. Provis JL, Bernal SA (2014) Geopolymers and related alkali-activated materials. Annu Rev Mater Res 44:299–327. https://doi.org/10.1146/annurev-matsci-070813-113515
7. Provis JL (2014) Geopolymers and other alkali activated materials: Why, how, and what? Mater Struct Constr 47:11–25. https://doi.org/10.1617/s11527-013-0211-5
8. Rożek P, Król M, Mozgawa W (2019) Geopolymer-zeolite composites: a review. J Clean Prod 230:557–579. https://doi.org/10.1016/j.jclepro.2019.05.152
9. Pérez-Villarejo L, Bonet-Martínez E, Eliche-Quesada D, Sánchez-Soto PJ, Rincón-López JM, Castro-Galiano E (2018) Biomass fly ash and aluminium industry slags-based geopolymers. Mater Lett 229:6–12. https://doi.org/10.1016/j.matlet.2018.06.100
10. Jackson MD, Mulcahy SR, Chen H, Li Y, Li Q, Cappelletti P, Wenk HR (2017) Phillipsite and Al-tobermorite mineral cements produced through low-temperature water-rock reactions in Roman marine concrete. Am Miner 102:1435–1450. https://doi.org/10.2138/am-2017-5993CCBY
11. Kani EN, Allahverdi A, Provis JL (2017) Calorimetric study of geopolymer binders based on natural pozzolan. J Therm Anal Calorim 127:2181–2190. https://doi.org/10.1007/s10973-016-5850-7
12. Azevedo ARG, Vieira CMF, Ferreira WM, Faria KCP, Pedroti LG, Mendes BC (2020) Potential use of ceramic waste as precursor in the geopolymerization reaction for the production of ceramic roof tiles. J Build Eng 29:101156. https://doi.org/10.1016/j.jobe.2019.101156
13. Azevedo ARG, Marvila MT, Rocha HA, Cruz LR, Vieira CMF (2020) Use of glass polishing waste in the development of ecological ceramic roof tiles by the geopolymerization process. Int J Appl Ceram Technol.13585. https://doi.org/10.1111/ijac.13585

Author Index

J. Li et al., *Characterization of Minerals, Metals, and Materials 2021*,
The Minerals, Metals & Materials Series,
https://doi.org/10.1007/978-3-030-65493-1

Subject Index

J. Li et al., *Characterization of Minerals, Metals, and Materials 2021*,
The Minerals, Metals & Materials Series,
https://doi.org/10.1007/978-3-030-65493-1

N

O

P

Q

R

S